Real-frequency dynamics of quantum impurity models studied with fRG, NRG, CFT

Elias Walter

SIGIL·UNIVERSI·TAT·LUDOVIC·MAXIM·

Munich 2021

© 2021 Elias Walter

Real-frequency dynamics of quantum impurity models studied with fRG, NRG, CFT

Elias Walter

A dissertation submitted
to the Faculty of Physics at the
Ludwig–Maximilians–Universität München
for the degree of
Doctor rerum naturalium

Munich, December 17, 2021

First referee: Prof. Dr. Jan von Delft
Second referee: Prof. Dr. Michael Knap
Day of submission: December 17, 2021
Day of the oral examination: February 17, 2022

Zusammenfassung (Summary in German)

Quantenstörstellenmodelle stellen eine einfache, aber mächtige Plattform für die Untersuchung von elektronischen Korrelationen in der Festkörperphysik dar. Hierbei wird der exponentiell große Hilbertraum eines wechselwirkenden Quantenvielteilchenproblems auf eine einzelne Störstelle reduziert, welche alle relevanten Freiheitsgrade enthält, während die Umgebung durch ein nichtwechselwirkendes Bad approximiert wird. Dies erlaubt eine detaillierte Untersuchung physikalischer Eigenschaften, die aus lokalen Korrelationen resultieren. Gleichzeitig können Störstellenmodelle als Ausgangspunkt für eine systematische Integration von lokalen und nichtlokalen Korrelationen über die Störstelle hinaus dienen. Interessante Observable für Quantenstörstellenmodelle sind dynamische Korrelationsfunktionen wie beispielsweise Spin- und orbitale Suszeptibilitäten, welche Informationen zu Quantenfluktuationen enthalten. Viele theoretische Zugänge zu solchen Korrelationsfunktionen werden im sogenannten Imaginärzeit-Matsubara-Formalismus konstruiert. Das erschwert den Vergleich mit experimentellen Daten, die natürlich in reeller Zeit gemessen werden. Daher ist es wünschenswert, mit Methoden zu arbeiten, die direkt auf der reellen Zeit- oder Frequenz-Achse konstruiert werden.

In dieser Dissertation werden zwei Projekte vorgestellt, in denen zwei verschiedene Quantenstörstellenmodelle mit unterschiedlichen Realfrequenzmethoden studiert werden. Der erste Teil konzentriert sich auf eine methodische Weiterentwicklung der Funktionalen Renormierungsgruppe (fRG), ein vielseitiges Tool für die Berechnung von Ein- und Zweiteilchen-Korrelationsfunktionen. Einige Probleme der konventionellen sogenannten Ein-Loop-Trunkierung wurden durch die kürzlich vorgestellte Multiloop-fRG (mfRG) behoben. Dieser Ansatz wurde aber bislang nur im Matsubara-Formalismus angewandt. Andererseits wurde fRG bereits im sogenannten Keldysh-Formalismus implementiert, welcher Realfrequenz-Rechnungen ermöglicht. Aufgrund der größeren numerischen Komplexität des Keldysh-Formalismus wurden dabei aber stets Näherungen bemüht, die noch stärkere Einschränkungen als die Ein-Loop-Trunkierung darstellen. Wir verbinden nun die Möglichkeiten des Keldysh-Formalismus mit den Vorteilen von Multiloop-fRG und implementieren zum ersten Mal einen Keldysh-mfRG-Code, der fRG zu einer quantitativen Realfrequenz-Methode weiterentwickelt. Wir testen diese Methode für das Single-Impurity-Anderson-Modell, das bereits gut verstanden ist und leicht zu komplexeren Modellen verallgemeinert werden kann. Dies erlaubt uns, Keldysh-mfRG als quantitative Methode systematisch zu testen, und eröffnet die Möglichkeit verschiedenster zukünftiger Erweiterungen der Methodik.

Im zweiten Teil beantworten wir eine viel direktere physikalische Fragestellung, nämlich die nach dem Ursprung und den Eigenschaften von Nicht-Fermi-Flüssigkeitsverhalten (NFL) in Hund-Metallen. Diese Materialien zeichnen sich durch elektronische Korrelationen aus, die von der ersten Hund'schen Regel verursacht werden, welche besagt, dass der gesamte Elektronenspin eines multiorbitalen Atoms im Grundzustand maximal ist. Charakteristische Eigenschaften einer Nicht-Fermi-Flüssigkeit wurden in solchen Systemen bereits vorhergesagt, speziell fraktionales Potenzverhalten der dynamischen Spin- und orbitalen Suszeptibilitäten, wobei der Ursprung dieses Verhaltens jedoch bislang unklar blieb. Hund-Metalle werden gut durch ein Kondo-Störstellenmodell mit drei Orbitalen beschrieben. Wir untersuchen dieses Modell mit einem kombinierten numerischen und analytischen Ansatz. Dabei verbinden wir eine numerisch exakte Lösung des Modells mittels der Numerischen Renormierungsgruppe (NRG) mit einem analytischen Ansatz ausgehend von einer konformen Feldtheorie (CFT).

Dies erlaubt uns, das NFL-Regime ausführlich zu charakterisieren. Wir können insbesondere das charakteristische Potenzverhalten, welches vermutlich für die supraleitende Phase in Hund-Metallen verantwortlich ist, analytisch erklären. Außerdem liefern wir eine Erklärung für die außergewöhnlich niedrige Kohärenzskala vom Nicht-Fermi-Flüssigkeits- zum Fermi-Flüssigkeitsverhalten in Hund-Metallen.

Summary

(Summary in English)

Quantum impurity models provide a simple but powerful framework for studying electronic correlations in solid-state physics. Reducing an exponentially large interacting quantum many-body problem to a single impurity containing all relevant degrees of freedom—immersed in a noninteracting bath that approximately describes its environment—allows for a detailed study of physical properties originating from local correlations. At the same time, impurity models provide a starting point for systematically incorporating local and nonlocal correlations beyond the impurity level. Useful observables for quantum impurity models are dynamical correlation functions such as spin or orbital susceptibilities, since they allow for important insights on quantum fluctuations in the system of interest. Many theoretical approaches for computing correlation functions are formulated in the imaginary-time Matsubara formalism, which complicates the comparison to experimental data measured (obviously) in real time. Therefore, methods working directly on the real-time or real-frequency axis are highly desirable.

In this thesis, we present two projects studying two different quantum impurity models with different real-frequency methods. In the first part, we focus on methodological advancement in the context of the functional renormalization group (fRG), a versatile tool for computing dynamical one- and two-particle correlation functions. Many caveats of the conventional so-called one-loop approximation in fRG have recently been overcome through the development of multiloop fRG (mfRG). The mfRG approach has however only been implemented in the Matsubara formalism yet, bringing along the issues mentioned above. On the other hand, fRG has been implemented in the Keldysh formalism before, which allows for direct real-frequency calculations. However, due to the increased numerical complexity of the Keldysh framework, approximations even stronger than the one-loop truncation were made. Here, we combine the power of the Keldysh formalism with the benefits of the multiloop extension and implement for the first time a full Keldysh mfRG code, which elevates fRG to a quantitative real-frequency method. We test this method for the single-impurity Anderson model, which is well understood and straightforwardly generalizable to more complex models. This allows for a systematic evaluation of the capabilities of Keldysh mfRG and opens up the route to various nontrivial extensions of the method in the near future.

In a second part, we aim to answer a much more direct physical question, namely, on the origin and nature of non-Fermi-liquid (NFL) behavior in so-called Hund metals. These materials are characterized by electronic correlations that originate from Hund's first rule, stating that the total electronic spin of a multiorbital atom should be maximized. Properties characteristic of a non-Fermi liquid have been observed in such systems before, in particular through fractional power laws in dynamical spin and orbital susceptibilities, but a detailed understanding was lacking thus far. The physics of Hund metals is well captured by a three-orbital Kondo impurity model. To study this model, we combine a numerically exact solution by means of the numerical renormalization group (NRG) and an analytical treatment within a conformal field theory (CFT). This hybrid numerical and analytical approach allows us to fully characterize the NFL regime in this model for Hund metals. We provide analytical explanations for the characteristic power laws in the susceptibilities, which have been conjectured to be relevant for superconductivity in Hund metals, and explain the origin of the unusual suppression of the Fermi-liquid coherence scale.

Publications

This dissertation contains the following journal articles, listed in order of appearance:

P1 *Uncovering Non-Fermi-Liquid Behavior in Hund Metals: Conformal Field Theory Analysis of an* $SU(2) \times SU(3)$ *Spin-Orbital Kondo Model*
E. Walter, K. M. Stadler, S.-S. B. Lee, Y. Wang, G. Kotliar, A. Weichselbaum, and J. von Delft
Sec. 10.2 / arXiv:1908.04362 Phys. Rev. X **10**, 031052 (2020)

P2 *Global Phase Diagram of a Spin-Orbital Kondo Impurity Model and the Suppression of Fermi-Liquid Scale*
Y. Wang, **E. Walter**, S.-S. B. Lee, K. M. Stadler, J. von Delft, A. Weichselbaum, and G. Kotliar
Sec. 10.3 / arXiv:1910.13643 Phys. Rev. Lett. **124**, 136406 (2020)

Acknowledgments

Everything presented in this thesis was only possible due to the direct and indirect support and assistance of many people, to whom I would like to express my deepest gratitude.

First and foremost, I would like to thank Jan von Delft for four fantastic years as a PhD student in his group. He has been a perfect supervisor by keeping the balance between giving the academic freedom to develop own ideas, and always having an open door (or an open Zoom room) for discussions and for sharing his enthusiasm to understand every detail about a scientific problem. Even more, I am grateful for his understanding and support in personal matters beyond science. I really appreciated his commitment to always rank his students' needs highest, in particular during the last year working remotely and with a fixed deadline in mind. Furthermore, Jan's dedication for teaching, working on excellent lectures and exercises with the same passion as for his research, left a lasting impression on me. Overall, I have really learned a lot during the last years, and I am very thankful for that.

I would further like to thank my collaborators on the (chronologically) first project pursued during my PhD (Part II of this thesis): Kathi Stadler, whose excellent work initiated this project, Gabi Kotliar, for numerous discussions in which he shared his deep understanding of condensed matter physics and always provided new ideas, Yilin Wang, who did most of the hard work for the second paper that evolved from this project. Many thanks to Andreas Weichselbaum, who developed the `QSpace` tensor network library, and Seung-Sup Lee, who wrote the NRG routines that were used for all numerical calculations, and was always a great help with NRG numerics.

For the (chronologically) second project (Part I of this thesis), I would like to express my gratitude to Santiago Aguirre, with whom I have jointly worked on the Keldysh mfRG implementation for one and a half years. Without his passion and commitment, contributing thousands of lines of code and numerous creative ideas, this project would by far not have reached the point where it is now. I would like to thank Fabian Kugler, who has the most profound knowledge about diagrammatic field theory of everybody I know. His deep understanding of the matter and his tireless striving for fully grasping every detail significantly helped to lead the project into the right direction. I would further like to thank Julian Thönniß, who helped a lot with technical issues at the beginning of the project and even implemented some functionality from his code to ours, and Marc Ritter, whose expert knowledge about C++ programming solved various implementation problems. Many thanks go to Anxiang Ge, Nepomuk Ritz and Marcel Gievers, who joined our efforts about a year ago and since then extensively improved, restructured and extended the code. I am extremely glad that they are continuing this project into various new directions. Thanks also to Seung-Sup for providing NRG data of the four-point vertex shown in Fig. 9.3, and to Fabian for computing the NRG benchmark data used in Chapters 7 and 8.

I would further like to thank Michael Knap for corefereeing this thesis.

Beyond the scientific work, my PhD would not have been half the fun without the great people and enjoyable working atmosphere at the chair for Theoretical Solid State Physics. I particularly thank my office mates Frauke Schwarz, Kathi Stadler, Bin-Bin Chen, Florian Stäbler, Nick Zhou, Jheng-Wei Li, and Marc Ritter. Furthermore, I have enjoyed very much numerous discussions and a lot of good mood on the way to the Mensa, in cake breaks, on group hikes and conferences, with the current and former group members Santiago

Aguirre, Bin-Bin Chen, Gianni Del Bimbo, Maximilian Dorfner, Johannes Feldmeier, Anxiang Ge, Marcel Gievers, Andreas Gleis, Johannes Halbinger, Sebastian Huber, Fabian Kugler, Seung-Sup Lee, Jheng-Wei Li, Wei Li, Michael Lichtenegger, David Moser, Felix Palm, Dima Pimenov, Matthias Punk, Marc Ritter, Nepomuk Ritz, Dimitris Saraidaris, Björn Sbierski, Benedikt Schneider, Dennis Schimmel, Frauke Schwarz, Florian Stäbler, Kathi Stadler, Koushik Swaminathan, Julian Thönniß, Andreas Weichselbaum, Lukas Weidinger, and Oleg Yevtushenko. I have particularly good memories of the 2018 CECAM conference in Vienna with Andreas Gleis, Fabian and Seung-Sup, and the shared flat with Fabian, Sebastian and Dima in Boston during the 2019 APS March Meeting. Our Mensa group would not be complete without many (former and current) members of the Schollwöck chair, including Maximilian Buser, Jonas Greitemann, Ke Liu, Rajah Nutakki, Lode Pollet, Nihal Rao, Andreas Swoboda, Tuomas Vanhala, and Stefan Wittlinger.

I am very grateful for being part of the research school IMPRS-QST. Several summer schools (both in person and online), workshops, and lab tours allowed to broaden the scientific horizon beyond my own research projects, and also to meet many great people, including students from ICFO in Barcelona, from Harvard, Innsbruck, and Vienna, during our joint summer schools and workshops. In particular, I would like to thank the IMPRS coordinator Sonya Gzyl, who significantly contributed to the success of these great events.

Special thanks go to Andreas Gleis for accommodation during occasional trips to Munich in the last year. Furthermore, I would like to thank Marcel, Anxiang and in particular Nepomuk for the very careful proofreading of this thesis.

I wish to thank our secretaries Stéphane Schoonover and Kathrin Higgen for help with administrative issues, and for always promoting the nice atmosphere in the group.

IT support by the Rechnerbetriebsgruppe of the Arnold Sommerfeld Center is acknowledged. Thanks to Kalle Bamberg for support on the KCS cluster. The Gauss Centre for Supercomputing is acknowledged for providing computing time on the GCS Supercomputer SuperMUC-NG at Leibniz Supercomputing Centre.

Eventually, I would like to thank my family for constant support throughout the last decades, and my wife Lisa, whose unconditional love and support have helped me in a way that cannot be overestimated.

Contents

Zusammenfassung (Summary in German) **i**

Summary (Summary in English) **iii**

Publications **v**

Acknowledgments **vii**

1 Introduction **1**
- 1.1 Motivation 1
  - 1.1.1 Keldysh mfRG for the single-impurity Anderson model 2
  - 1.1.2 NRG+CFT for a three-channel spin-orbital Kondo model 4
- 1.2 Outline 6

I Keldysh multiloop fRG study of the single-impurity Anderson model **7**

2 Quantum field theory in the Keldysh formalism **9**
- 2.1 Keldysh time contour 9
- 2.2 Quantum field theory in the Keldysh formalism 11
  - 2.2.1 Building blocks of diagrammatic quantum field theory 11
  - 2.2.2 Single-particle correlation functions 14
  - 2.2.3 Two-particle correlation functions 17
    - 2.2.3.1 Symmetries 17

3 Multiloop functional renormalization group **21**
- 3.1 Functional renormalization group 21
- 3.2 Multiloop fRG 23
  - 3.2.1 Parquet formalism 23
  - 3.2.2 mfRG flow equations 25

4 Keldysh vertex parametrization **27**
- 4.1 Frequency structure 28
  - 4.1.1 Channel decomposition 28
  - 4.1.2 Asymptotic classes 31
  - 4.1.3 Susceptibilities 33
  - 4.1.4 Flow equations for the asymptotic classes 34
- 4.2 Spin structure 38
- 4.3 Keldysh structure 39
  - 4.3.1 Parity symmetries 41
  - 4.3.2 Crossing symmetries and complex conjugation 42
    - 4.3.2.1 Symmetry transformations 42
    - 4.3.2.2 Mixing of channels, asymptotic classes and spin components 43
    - 4.3.2.3 Treatment of nonsymmetric vertices 44
    - 4.3.2.4 Simplification of the Keldysh structure 45

4.3.3 Keldysh components of n-point functions 49

5 Single-impurity Anderson model 53
5.1 Definition of the model 53
5.2 SIAM within fRG 55
5.3 Physics of the SIAM 57

6 Implementation details 61
6.1 General structure 61
6.2 Frequency grid 63
6.3 Frequency integration 65
6.3.1 Numerical integration 66
6.3.1.1 Adaptive integrator 66
6.3.1.2 Guiding the integrator 68
6.3.2 Analytic integration of asymptotic tails 69
6.3.2.1 Bubble integrals 70
6.3.2.2 Loop integrals 72
6.4 Numerical parameters and validity of the numerics 73

7 Perturbation theory and consistency checks 77
7.1 4$^{\text{th}}$-order perturbation theory 77
7.1.1 Zero-temperature perturbation theory 77
7.1.2 Zero-frequency perturbation theory 79
7.2 Generic properties of correlation functions 84
7.2.1 Causality 84
7.2.2 Kramers-Kronig relation 84
7.2.3 Fluctuation-dissipation theorems 85
7.3 Specific properties of the SIAM 87

8 Dynamical and static properties 91
8.1 Dynamical correlation functions 92
8.2 Static properties 94
8.2.1 One-particle Ward identity 96
8.2.2 Korringa-Shiba relation 97
8.3 Sum rule for susceptibility 98
8.4 Two-particle Ward identity 99

9 Frequency-dependent two-particle vertex 103

II NRG+CFT analysis of a three-channel spin-orbital Kondo model 109

10 Non-Fermi-liquid behavior in a three-channel spin-orbital Kondo model 111
10.1 Overview 111
10.2 Publication: *Uncovering Non-Fermi-Liquid Behavior in Hund Metals: Conformal Field Theory Analysis of an* $SU(2) \times SU(3)$ *Spin-Orbital Kondo Model* 113
10.3 Publication: *Global Phase Diagram of a Spin-Orbital Kondo Impurity Model and the Suppression of Fermi-Liquid Scale* 141

11 Conclusion and outlook 167

A Vertex frequency parametrizations 171

B Multiloop flow equations in the single-boson exchange parametrization 175
B.1 SBE decomposition in the diagrammatic channels 175
B.2 Relation between SBE and asymptotic decomposition 178
B.3 Multiloop flow equations in the SBE decomposition 179

Bibliography 189

1 Introduction

1.1 Motivation

Interacting quantum many-body systems are among the most fascinating and intriguing problems theoretical condensed matter physics is faced with. On the one hand, a naive treatment of a full many-body system is immediately deemed to fail due to the macroscopically large number of coupled degrees of freedom. On the other hand, a purely reductionist approach that treats the individual constituents independently can never account for the extremely rich variety of emergent phenomena that have been observed in such systems [And72]. Examples include high-temperature superconductivity, novel non-Fermi-liquid phases, or magnetic phases with fractional excitations such as spin liquids. Many of those phenomena have been lacking theoretical understanding for decades, and the reason is that they cannot be explained from a single-particle picture, while a full many-body description is notoriously hard. Therefore, the challenge is to neglect enough details to allow for predictions with a limited amount of computational resources, while concurrently keeping all necessary ingredients responsible for the fascinating phenomena to be described in the system of interest.

A prototypical attempt to bridge this gap between simplification and completeness of the description of the relevant physics are quantum impurity models. This class of models focuses on a single impurity, representing e.g. a single atom, on which interactions between constituents are incorporated to a maximal degree. In contrast, the environment of the impurity, e.g. the surrounding atoms in a solid, is treated as a noninteracting "bath", such that its influence on the impurity is only captured approximately. Impurity models have proven to be a very useful framework for the description of phenomena that are caused by the interplay and correlations of local degrees of freedom. A prime example is the Kondo effect [Kon64], i.e., the screening of a magnetic impurity in a solid by the surrounding conduction electrons. Despite their apparent simplicity, impurity models often host emergent energy scales (such as the Kondo temperature) that cannot be explained from the single-particle properties of the model, but instead require a genuine many-body treatment. On the other hand, impurity models serve as an excellent starting point for a systematic inclusion of correlations beyond the bare impurity level, e.g. within the dynamical mean field theory (DMFT) [MV89, GKKR96] and diagrammatic extensions thereof [RHT+18], which can account for nonlocal correlations to some degree.

While a lot of the complication is reduced by treating the surroundings of the impurity as a noninteracting bath, solving impurity models often still remains a very nontrivial task on its own, which requires sophisticated many-body techniques. Many available methods for this purpose originate from the ideas of quantum field theory and are often formulated in the imaginary-time Matsubara formalism. A prime example is the widely-used continuous-time quantum Monte Carlo (CTQMC) method [GML+11], but also the functional renormalization group (fRG) [KBS10, MSH+12] is usually implemented on the imaginary-time axis. The Matsubara formalism is a very convenient framework for computing dynamical correlation functions. However, in experiment, dynamical properties are of course measured as a function of real frequencies, and the analytic continuation of numerical data from the imaginary- to the real-frequency axis is numerically ill-conditioned [SS86, GJSS91], which poses a major obstacle for comparing Matsubara results to experiments. It is therefore desirable to work with methods that provide numerical data for dynamical correlation functions directly on the real-frequency axis, without the need for analytic continuation.

In this thesis, we present the results of two independent projects, studying two different quantum impurity models with different methodological approaches, which both accomplish this task. Conceptually, they are in a sense complementary: The (multiloop) functional renormalization group (mfRG) [KvD18b, KvD18c, KvD18a] studied in Part I is very flexible and not even restricted to impurity models. However, for practical purposes, certain truncations are necessary, and as a result the method only works reliably for weak to intermediate interaction strength and cannot fully capture the strongly correlated regime. By contrast, the numerical renormalization group (NRG) [Wil75, BCP08] and the conformal field theory (CFT) analysis of fixed points [Aff90, AL91b, AL91a, AL93, LA94] used in Part II are both fully nonperturbative and thus allow for full control of the physical behavior at arbitrarily large interaction strength. However, they are limited to the impurity picture, and cannot simply be extended from local to nonlocal correlations on a lattice. Nevertheless, the impurity picture is still understood to be a valid approximation if the physics in the system of interest is dominated by the interplay of local degrees of freedom.

Despite being conceptually quite different, all methods used in this thesis share the ability to compute real-frequency dynamical quantities: The mfRG will be formulated in the Keldysh formalism, which alleviates the constraints of Matsubara formalism at the expense of increased numerical costs. NRG is not formulated in quantum field theoretical language, but instead works with quantum states and thus is constructed directly on the real-frequency axis. The CFT description of fixed points is also based on a Hamiltonian picture and does not require artificial imaginary times. In the following, we introduce the models and methods studied in these two projects in more detail.

1.1.1 Keldysh mfRG for the single-impurity Anderson model

The functional renormalization group (fRG) [KBS10, MSH$^+$12] is a conceptually extremely versatile tool for studying interacting quantum many-body systems: It is *a priori* exact, can treat both local and nonlocal correlations, and if formulated in the Keldysh formalism, it allows to treat systems in and out of thermal equilibrium. However, for actual calculations approximations need to be made, and thereby the method loses its initially nonperturbative character. As a consequence, reliable predictions can only be made at not too large interaction strength, beyond which fRG loses its validity.

The standard so-called one-loop truncation introduces a variety of problems, which are partially cured in multiloop fRG (mfRG) [KvD18b, KvD18c, KvD18a]. In particular, multiloop fRG restores the independence of physical results on the so-called regulator, a technical ingredient of fRG that can be chosen arbitrarily and thus should not affect physical results. Thereby, the multiloop extension turns fRG into a quantitatively reliable method [Kug19]. mfRG has so far only been implemented in the imaginary-frequency Matsubara formalism (e.g. [KvD18c, THK$^+$19]). Here, we extend it to the Keldysh formalism, within which correlation functions are computed directly on the real-frequency axis, thereby avoiding the need for performing analytic continuation numerically. Even further, the Keldysh formalism is not restricted to thermodynamic equilibrium, but allows for nonequilibrium studies without further complication. However, this power comes at the price of strongly increased numerical complexity.

Keldysh fRG has been frequently used before (e.g. [JMS07, JPS10a, SBvD17, WvD19]). However, due to the large numerical costs, it has not been extended beyond the one-loop truncation so far, and even further, a strong simplification of the frequency dependence of the four-point vertex has routinely been applied. However, the four-point vertex is known to be important for accurately capturing two-particle properties [RHT+18], hence a parametrization of the Keldysh vertex including its full frequency dependence is highly desirable. To achieve this, and thereby to allow to elevate Keldysh fRG to the (quantitative) multiloop level, has been the main goal of this project.

We study the single-impurity Anderson model (SIAM) [And61] as a testbed for method development. The SIAM is one of the most iconic models in condensed-matter physics [Hew93]. It involves a single energy level that can be occupied by up to two electrons and is immersed in a noninteracting bath to which it hybridizes. On the impurity level, electrons experience a Coulomb repulsion. Originally introduced to study the behavior of magnetic impurities in metals [And61], it has much wider implications: Physically, it also serves as a simple model for a single-electron quantum dot [GGSM+98, GGGK+98]. More generally, it can be understood as a minimal model for studying electron-electron interactions in solids: It allows for interactions at one single "impurity" site, and treats the surrounding electrons as a noninteracting bath that couples to the impurity. This concept is the starting point for a zoo of models: It can be extended from a single impurity orbital to multiorbital impurities, a Schrieffer-Wolff transformation at low energies leads to the Kondo model that describes the formation of a Kondo singlet between the localized impurity and the bath [SW66], and an extension of the Anderson model to a lattice of impurities is called periodic Anderson model, which is the prototypical model for heavy-fermion systems [Hew93]. Furthermore, a lattice of Anderson-like impurities with hopping between neighboring sites and interaction on every site leads to Hubbard-like models that are believed to be a useful starting point for studying the cuprate high-T_c superconductors [ZR88, Dag94]. The Anderson model is also of central importance in the study of lattice models: In the context of DMFT [MV89, GKKR96], the lattice is mapped to an effective Anderson-type impurity again, but the coupling to the bath now has to be determined self-consistently.

Due to its long history, there are many previous works on the SIAM: Exact perturbation theory results [YY70, Yam75a, YY75, Yam75b], analytic solutions via the Bethe ansatz [TW83, ZH83], fRG studies, e.g. [HMPS04, GPM07, KHP+08, JPS10a, RMJ16, CGKH+21], and NRG calculations, e.g. [KmWW80a, KmWW80b, BPH97, BHP98].

Our goal here is to reproduce known results with Keldysh mfRG, and answer the following questions: How well does the method perform on a *quantitative* level? Which parameter regimes can we reach, and where does also multiloop fRG fail due to inevitable truncations? Can we improve (compared to the standard one-loop truncation) on the fulfillment of Ward identities, which are important in particular for computing transport properties [WvD19]? Answering these questions for the SIAM in equilibrium, where numerically exact benchmark results from NRG are available, allows us to characterize the capabilities of Keldysh mfRG as a quantitative method. This is essential if one wants to study the SIAM in nonequilibrium, which is not accessible by NRG.

Furthermore, applications of Keldysh mfRG beyond the SIAM, which can build on the developments presented in this thesis, are manifold:

- Introducing an orbital degree of freedom to the impurity allows to study multiorbital quantum dots. Here, one would focus on nonequilibrium transport properties, which are directly accessible in the Keldysh formalism.
- As a further generalization, one can add one spatial dimension to the zero-dimensional SIAM and continue on previous work on transport through a 1-dimensional nanoconstriction (or quantum point contact) [BHS+13, SBvD17, WSSvD18], where one-loop fRG has been shown to be insufficient due to the violation of Ward identities [WvD19].

- One can include a rotationally-invariant momentum dependence to the bath and the impurity in order to study the so-called Fermi-polaron problem [SEPD12, Gie21].
- By adding a lattice-momentum dependence to the impurity, one can extend the SIAM to the (2-dimensional) Hubbard model [Hub63, Rit21b], which is believed to be relevant for the physics of the cuprate high-temperature superconductors [ZR88, Dag94].
- One could overcome some limitations of fRG by starting an mfRG flow not from a trivial initial condition, but from a DMFT vertex and self-energy. In this way, one would use mfRG to include nonlocal correlations in addition to the local ones captured in DMFT, thereby curing issues induced by conventional approximations. This method, combining the power of DMFT to study strongly correlated systems nonperturbatively and of fRG to compute nonlocal correlations, has been coined DMF^{2}RG [TAB$^+$14, VTM19]. It has only been implemented in the Matsubara formalism so far, but it would be very interesting to elevate it to the Keldysh framework as well, in order to obtain real-frequency spectral information for the 2d Hubbard model. A method to compute the DMFT vertex in the Keldysh formalism has been introduced very recently by an extension of NRG from two-point to multipoint correlation functions [KLvD21, LKvD21].

For the last three projects, first steps have already been taken by Marcel Gievers and Nepomuk Ritz in the group of Jan von Delft, alongside further methodological advances pursued by Anxiang Ge.

1.1.2 NRG+CFT for a three-channel spin-orbital Kondo model

While the first project presented in this thesis pursued methodological advances, the second one was guided by a very direct physical question: Can the incoherent low-temperature regime in Hund metals be attributed to a non-Fermi-liquid (NFL) fixed point, and what is the origin and the nature of this non-Fermi liquid?

Hund metals [GdMM13] are multiorbital materials in which electronic correlations originate not primarily from the Coulomb repulsion, but from Hund's first rule [dMMG11, SKWvD19, DSH$^+$19]: This phenomenological rule states that for a multiorbital atom with a given number of electrons in some shell, the ground state is the one where the total spin is maximal. Since a maximized spin corresponds to a symmetric representation of the SU(2) spin symmetry group, due to the fermionic statistics of electrons it is accompanied by an antisymmetric orbital configuration, which lowers the potential energy [GdMM13]. Typical Hund metals are transition metal oxides with partially filled d shells, such as the ruthenates [WGTM08, MAM$^+$11, TZR$^+$19], iron pnictides and chalcogenides [YHK11b, YHK11a, YHK12, YLY$^+$13, HBA$^+$13], and also nickelates [WH20]. Hund metals have raised a lot of interest in recent years. Originally, this was mainly triggered by the discovery of unconventional superconductivity in the iron pnictides [KWHH08, Ste11]. However, also the normal state of Hund metals is of great interest, since it shows bad-metal behavior in a large incoherent regime and a very low Fermi liquid coherence scale, related to a large effective mass of quasiparticles [dMMG11, YLY$^+$13, HBA$^+$13]. The superconductivity is believed to originate from strong spin fluctuations in the incoherent regime [LCMK18], which enhances the need for thoroughly understanding the normal state of Hund metals.

In typical Hund metals, the five $3d$ orbitals are split into three so-called t_{2g} and two e_g orbitals through the presence of oxygen ligands, with the t_{2g} orbitals being most relevant for electronic properties [YHK12]. Therefore, the natural minimal model for describing Hund physics is a three-band Hubbard model with an onsite Hund coupling that enforces Hund's rule by favoring maximal spin [GdMM13]. In the context of DMFT [MV89, GKKR96], this model is mapped onto a three-orbital Anderson model [GdMM13, SYvD$^+$15], which is a multiorbital generalization of the aforementioned SIAM, but in addition also includes a Hund coupling J, making it a "Hund impurity model". This model shows a remarkable behavior, coined spin-orbital separation (SOS) [SYvD$^+$15, SKWvD19, DSH$^+$19]: A Kondo-like screening of the impurity happens both in the spin and orbital sector, but spin and orbital degrees of freedom are screened on different energy scales, $T_{\mathrm{sp}} < T_{\mathrm{orb}}$. Below the spin Kondo temperature T_{sp}, coherent Fermi-liquid behavior is observed. However, in the intermediate SOS energy window $[T_{\mathrm{sp}}, T_{\mathrm{orb}}]$, incoherent behavior is visible, characterized by screened orbital degrees of freedom but an unscreened spin [YHK12, SYvD$^+$15]. This behavior was conjectured to be a non-Fermi liquid [AT13], but the nature of this NFL state remained unclear, in particular since the SOS regime is rather small, preventing a more detailed analysis.

Here, we go one step further: Just as the Kondo model emerges from the SIAM [SW66], one can do a Schrieffer-Wolff transformation on the three-orbital Anderson model, projecting out charge fluctuations, to arrive at a three-orbital Kondo-type model [AK15]. This Kondo model has not only a spin-spin Kondo coupling, but also an orbital-orbital one (and even one that mixes the spin and orbital degrees of freedom). By (artificially) tuning those couplings, one can open up the SOS regime and study its nature in detail. In particular, we identify a fixed point in the renormalization group (RG) flow of the model that is responsible for the NFL, and study it in detail.

Methodologically, we use a combined numerical and analytical approach: On the one hand, we solve the model numerically using NRG [Wil75, BCP08]. Its implementation within the `QSpace` library [Wei12a, Wei12b] enables us to exploit Abelian and non-Abelian symmetries, which makes a numerically exact treatment of three-orbital models possible. On the other hand, fixed points in the RG flow identified by NRG can be expected to be scale-invariant, which allows a description in terms of a conformal field theory (CFT). We generalize the CFT approach to fixed points of multichannel Kondo models devised by Affleck and Ludwig [Aff90, AL91b, AL91a, AL93, LA94] from multichannel spin to multiorbital impurities, which allows us to study the fixed points of our multiorbital Kondo model analytically. The numerical and the analytical approach work hand in hand very fruitfully: NRG can provide numerically exact results for spectra and dynamical correlation functions; but of course it cannot deliver explanations for the observed behavior, which we do get from analytical understanding, thereby enhancing the abilities of numerics by helping to interpret numerical results. On the other hand, our extension of the CFT methodology was guided by the numerical results, which provided insights about the fixed points that the model hosts and their qualitative (and quantitative) behavior. As a result, we get a very detailed understanding of the NFL fixed point and regimes influenced by it: One can compute the exact fixed point spectrum (both numerically and analytically) and derive power laws of dynamical spin and orbital susceptibilities with fractional exponents. These directly relate to previous observations in the incoherent regime of Hund metals, e.g. in [SYvD$^+$15]. Note that a real-frequency treatment (built in to our approach) is indispensable for the description of dynamical spin fluctuations, which are believed to be responsible for the pairing in the iron-pnictide superconductors.

In a further step, we freely tune the couplings of the model to compute its full phase diagram. One can identify three different phases, a Fermi liquid (FL), an NFL, and a so-called singular Fermi liquid (SFL) obtained by incomplete spin screening, featuring a fluctuating (residual) spin with a marginal coupling to the bath. These phases are connected by quantum phase transitions at zero temperature, i.e., quantum critical points (QCP) (or lines in the phase diagram). The proximity to such a QCP leads to the suppression of the Fermi liquid scale in the FL phase, which explains the unusually small coherence scale of Hund metals.

1.2 Outline

As introduced above, this thesis is divided into two parts, discussing two separate projects.

Part I (comprising Chapters 2 – 9) presents the background, methodological advances and results of the first project. In Chapter 2, we introduce the basic building blocks of quantum field theory in the Keldysh formalism: The Keldysh time contour that is crucial for finite-temperature real-frequency calculations, and definitions of the fundamental elements of diagrammatic field theory in this framework, namely, one- and two-particle correlation functions, or propagators and interaction vertices. Chapter 3 provides a brief introduction to fRG, the method we use to explicitly compute such correlation functions. We explain the basic idea and the conventional one-loop truncation, and then focus on the multiloop extension which overcomes limitations thereof. mfRG is most elegantly defined in the framework of parquet theory, which provides relations that connect different classes of diagrams in a self-consistent manner.

To implement mfRG in the Keldysh formalism, we need to treat the Keldysh four-point vertex in its full glory, which is a very complicated object. In Chapter 4, we illustrate how to efficiently parametrize it. Here we employ simplifications that go beyond the state of the art (as opposed to previous chapters). The main achievement of this chapter is the parametrization of the combined frequency and Keldysh structure of the four-point vertex, making use of various symmetries. While in Chapters 2 and 3 we try to keep the discussion almost entirely on a diagrammatic level (allowing for a particularly concise and illustrative notation of all important equations), in Chapter 4 we will provide more explicit expressions in terms of useful parametrizations.

After this methodological part (Chapters 2 – 4), which aims to be as generic (i.e., model-independent) as possible, we focus on a specific model as a proof of principle. Chapter 5 introduces the model of interest—the single-impurity Anderson model—and model-specific simplifications. In Chapter 6, we discuss specific issues that arise in the numerical treatment of real frequencies, and how to solve them. While the problems discussed in this section are generic for a real-frequency implementation, some details of the solutions are specific for the SIAM.

Chapters 7 – 9 present results for the SIAM within our implementation of Keldysh mfRG. In Chapter 7, we first study the SIAM in perturbation theory, where analytical benchmark results are available. We then perform various other consistency checks that allow for a systematic evaluation of the validity of the code. In Chapters 8 and 9 we continue with presenting mfRG results for one- and two-particle correlation functions.

In Part II (Chapter 10) we present the results of the second project. These are summarized in two journal publications that are reprinted in this chapter.

Finally, we conclude the thesis in Chapter 11.

Appendix A provides details on the Keldysh vertex frequency parametrization that are omitted in Chapter 4 for clarity. In Appendix B we briefly outline a different frequency parametrization as the one used in Chapter 4 which was recently introduced [KVC19], the so-called single-boson exchange decomposition, and we derive mfRG flow equations within this parametrization. We also illustrate how the two parametrizations are related.

Part I

Keldysh multiloop fRG study of the single-impurity Anderson model

2 Quantum field theory in the Keldysh formalism

The Keldysh formalism is a very powerful framework extending quantum field theory to nonequilibrium systems. The basic idea was introduced by Keldysh in 1964 [Kel64], following work by Schwinger [Sch61] and Kadanoff and Baym [KB62], thus sometimes also called Schwinger-Keldysh formalism. An extensive pedagogical discussion of the topic can be found in [Kam11], more compact introductions in the context of fRG are also given in related PhD theses [Jak09, Sch17, Klö19].

Here, we only give a very brief summary of the key ideas that allow to do nonequilibrium quantum field theory on the real-frequency axis, and present the most important formulas necessary for the rest of the thesis. We start by introducing the notion of a Keldysh contour for computing the time evolution of expectation values (roughly following [Kam11]). Without going into details, we will sketch the main idea and in particular point out the conceptual difference to the widely-used equilibrium imaginary-time Matsubara formalism. Then we define the basic building blocks of quantum field theory in the Keldysh formalism. Here we adopt a diagrammatic language from the very beginning, since it proves very useful in particular in the context of the functional renormalization group and the parquet formalism.

2.1 Keldysh time contour

Consider some physical system described by a (potentially time-dependent) model Hamiltonian $H(t)$. The goal is to compute correlation functions (i.e., expectation values of some linear operators) for this model, since they correspond to experimentally measurable quantities. A general thermal (finite-temperature) expectation value of an operator $\hat{O}$ in a quantum state at time t described by a density matrix $\rho(t)$ is

$$\langle \hat{O} \rangle(t) = \frac{\mathrm{Tr}\, \hat{O}\rho(t)}{\mathrm{Tr}\, \rho(t)} = \frac{1}{\mathcal{Z}} \mathrm{Tr}\, \hat{O}\rho(t) \,, \quad \text{with the partition function} \quad \mathcal{Z} = \mathrm{Tr}\, \rho(t) \,. \tag{2.1}$$

The time evolution of $\rho(t)$ from a given initial state $\rho_0 = \rho(t_0)$ can be obtained from an equation of motion (von Neumann equation), which is formally solved by the time-evolution operator,

$$\rho(t) = U(t, t_0)\, \rho_0\, U(t_0, t) \,, \tag{2.2}$$

with (in units where $\hbar = 1$)

$$U(t, t_0) = \mathcal{T} \exp \left(-i \int_{t_0}^{t} \mathrm{d}t' H(t') \right) \,, \tag{2.3}$$

and $U(t_0, t) = (U(t, t_0))^\dagger$. Here $\mathcal{T}$ denotes time ordering of the operators in the exponential. Using the cyclicity of the trace, we obtain

$$\langle \hat{O} \rangle(t) = \frac{1}{\mathcal{Z}} \mathrm{Tr} \left[U(t_0, t)\, \hat{O}\, U(t, t_0)\, \rho_0 \right] = \langle \hat{O}(t) \rangle \,, \tag{2.4}$$

which we can also interpret as the operator being time-evolved from time t_0 to t and back, and evaluated in the initial state ρ_0. The time evolution thus goes in two different directions, which seems cumbersome at first view. With the Matsubara and the Keldysh formalism, two different strategies of handling this complication have been established.

(A) Matsubara formalism: In equilibrium, we have no explicit time-dependence of the Hamiltonian, $H(t) = H$, therefore the time-evolution operator simplifies to

$$U(t, t_0) = e^{-iH(t-t_0)} \,. \tag{2.5}$$

On the other hand, the equilibrium density matrix is just a thermal state and can thus be expressed through U,

$$\rho_0 = e^{-\beta H} = U(-i\beta, 0) \,, \tag{2.6}$$

with the inverse temperature $\beta = 1/k_B T$. Due to time-translational invariance in equilibrium, we can define $t_0 = 0$. We then have (using cyclicity of the trace again)

$$\langle \hat{O}(t) \rangle = \frac{1}{\mathcal{Z}} \operatorname{Tr} \left[U(-i\beta, 0) U(0, t) \, \hat{O} \, U(t, 0) \right] \,. \tag{2.7}$$

Defining an imaginary time $\tau = it$ and $\tilde{U}(\tau, \tau_0) = e^{-(\tau-\tau_0)H} (= U(t, t_0))$, we can substitute

$$\langle \hat{O}(\tau) \rangle = \frac{1}{\mathcal{Z}} \operatorname{Tr} \left[\tilde{U}(\beta, 0) \tilde{U}(0, \tau) \, \hat{O} \, \tilde{U}(\tau, 0) \right] = \frac{1}{\mathcal{Z}} \operatorname{Tr} \left[\tilde{U}(\beta, \tau) \, \hat{O} \, \tilde{U}(\tau, 0) \right] \,. \tag{2.8}$$

This can be interpreted as an evolution along the compact imaginary time interval $(0, \beta)$ according to the imaginary time evolution operator $\tilde{U}$. While this trick of rotating the time onto the imaginary axis strongly simplifies the expression Eq. (2.4), it strictly relies on the assumption of the system being in equilibrium. Furthermore, correlation functions that are computed on the imaginary time or frequency axis have to be analytically continued to real frequencies. For discrete numerical data, this is an ill-defined problem [SS86, GJSS91]. Thus, a different approach to this problem is desirable.

(B) Keldysh formalism: Here we simply accept the fact that we have to do forward and backward time evolution. Taking Eq. (2.4) at face value, we have

$$\langle \hat{O}(t) \rangle = \frac{1}{\mathcal{Z}} \operatorname{Tr} \left[U(t_0, t) \, \hat{O} \, U(t, t_0) \, \rho_0 \right] = \frac{1}{\mathcal{Z}} \operatorname{Tr} \left[\tilde{\mathcal{T}} e^{-i \int_t^{t_0} \mathrm{d}t' H(t')} \, \hat{O} \, \mathcal{T} e^{-i \int_{t_0}^{t} \mathrm{d}t' H(t')} \, \rho_0 \right] \,, \tag{2.9}$$

where $\tilde{\mathcal{T}}$ indicates anti-time ordering, i.e., the operators in the expansion of the exponential are placed from right to left with decreasing times. We can interpret the forward and backward time evolution as a closed time contour $\mathcal{C}$,

$$\langle \hat{O}(t) \rangle = \frac{1}{\mathcal{Z}} \operatorname{Tr} \left[\mathcal{T}_{\mathcal{C}} \left\{ e^{-i \int_t^{t_0} \mathrm{d}t' H^+(t')} \, \hat{O} \, e^{-i \int_{t_0}^{t} \mathrm{d}t' H^-(t')} \, \rho_0 \right\} \right] =$$

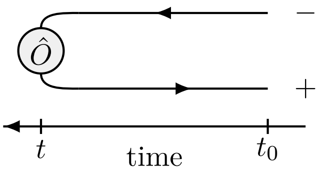

, (2.10)

where now each operator has an additional contour index $j = \mp$, indicating whether it has to be put on the forward $(-)$ or backward $(+)$ branch of this “Keldysh” contour.[1] The contour time ordering $\mathcal{T}_{\mathcal{C}}$ puts all operators on the backward branch left of those on the forward branch, and anti-time-orders (time-orders) them on the backward (forward) branch. The operator $\hat{O}$ is inserted at time t.

This structure implies that if $\hat{O}$ consists of several operators, they also need to be equipped with contour indices to ensure correct ordering. Consider e.g. the correlation function of two operators $\hat{O}_1, \hat{O}_2$ inserted at times $t_1 > t_2$:

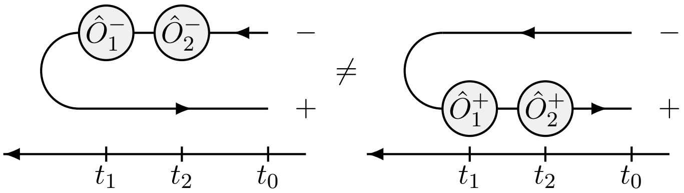

$$\langle \mathcal{T}_{\mathcal{C}}\, \hat{O}_1^-(t_1)\hat{O}_2^-(t_2)\rangle = \langle \hat{O}_1^-(t_1)\hat{O}_2^-(t_2)\rangle \neq \langle \hat{O}_2^+(t_2)\hat{O}_1^+(t_1)\rangle = \langle \mathcal{T}_{\mathcal{C}}\, \hat{O}_1^+(t_1)\hat{O}_2^+(t_2)\rangle\,, \tag{2.11}$$

where clearly the order of the two operators along the contour is exchanged between the left and the right expression, since time-ordering exchanges the operators on the backward branch. This implication in particular holds for field operators appearing in one- and two-particle correlation functions, which we are usually interested in. As a conclusion, all fields have to bear a contour index, thus n-point correlation functions will generically have 2^n Keldysh components. This makes it very challenging to compute such functions numerically. We will see later how to simplify the Keldysh structure of the four-point function to deal with this problem at least to some degree.

2.2 Quantum field theory in the Keldysh formalism

2.2.1 Building blocks of diagrammatic quantum field theory

Let us now move to the convenient path integral formalism. We will be interested in fermionic theories henceforth, thus we replace the trace over states by a functional integral over fermionic Grassmann fields $\psi, \bar{\psi}$. We again leave out the details and refer the reader to the standard literature (e.g. [NO88], or [Kam11] in the Keldysh context).

To be specific, we will assume that the Hamiltonian of the system of interest consists of two terms, $H = H_0 + H_I$: a noninteracting (quadratic) part H_0 that describes free dynamics in some potential, and a two-particle interaction H_I. The partition function $\mathcal{Z}$ then becomes a path integral over the action S[2]:

$$\mathcal{Z} = \int \mathcal{D}\bar{\psi}\,\mathcal{D}\psi\, e^{iS[\bar{\psi},\psi]}\,, \quad S[\bar{\psi},\psi] = \underbrace{\bar{\psi}_{1'}(G_0^{-1})_{1'|1}\psi_1}_{S_0} + \underbrace{\tfrac{1}{4}(\Gamma_0)_{1'2'|12}\,\bar{\psi}_{1'}\bar{\psi}_{2'}\psi_2\psi_1}_{S_I}\,. \tag{2.12}$$

For notational brevity, we use a multi-index $1 \mathrel{\hat{=}} (j_1, \sigma_1, \nu_1, k_1, m_1, \dots)$, combining the Keldysh contour index $j_1 = \mp$, spin $\sigma_1 = \uparrow, \downarrow$, time t_1 (or frequency ν_1 in the Fourier domain), position

---

[1] This convention is used in [Jak09, Sch17, HBSvD17], while in [Kam11] the contour labels $-$ and $+$ are exchanged.

[2] Note that this definition of S_I includes a relative minus sign compared to the usual convention in the Keldysh context, e.g. [Kam11] or [Jak09]. This is motivated by the fact that in this way, the bare vertex Γ_0, which absorbs this relative minus sign, has the same sign as the one typically used in the Matsubara context (compare Eq. (2.13) to Fig. 2(a) of [Kug18]).

x_1 (or momentum k_1), orbital m_1 etc. Repeated indices are always understood to be summed or integrated over, respectively.

The action again consists of a noninteracting part S_0 and a two-particle interaction S_I, specified by G_0 and Γ_0, respectively. These are derived from their Hamiltonian counterparts and are thus the basic constituents of the theory. It is very useful to introduce diagrammatic representations for them: If one expands the exponential e^{iS_I} in Eq. (2.12) (and similarly in general correlation functions introduced below in Eq. (2.16)) in powers of the bare interaction Γ_0 and decomposes the resulting noninteracting correlation functions using Wick's theorem [NO88, Wic50], one obtains products of bare propagators and bare vertices, connected in all possible different ways. This is most conveniently noted in a diagrammatic language.[3] Its building blocks are[4]

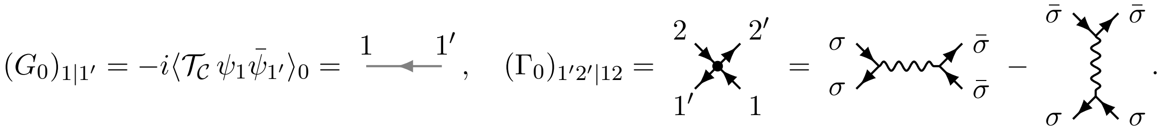

$$(G_0)_{1|1'} = -i\langle \mathcal{T}_\mathcal{C}\, \psi_1 \bar{\psi}_{1'} \rangle_0 = \qquad , \qquad (\Gamma_0)_{1'2'|12} = \qquad = \qquad - \qquad . \tag{2.13}$$

Here we have identified G_0 with the noninteracting one-particle correlation function, or bare propagator, with

$$\langle \cdots \rangle_0 = \frac{1}{\mathcal{Z}_0} \int \mathcal{D}\bar{\psi}\, \mathcal{D}\psi\, e^{iS_0[\bar{\psi},\psi]} (\cdots) \,, \quad \text{with} \quad \mathcal{Z}_0 = \int \mathcal{D}\bar{\psi}\, \mathcal{D}\psi\, e^{iS_0[\bar{\psi},\psi]} \,. \tag{2.14}$$

For the bare vertex, we use the compact Hugenholtz notation (single dot) [NO88], which is an antisymmetric combination of the direct and exchange Feynman vertices (boson line). In Eq. (2.13) we have also indicated that for local vertices, Pauli's principle ensures that only opposite spins can interact, i.e., the bare vertex has only two possible spin components. Furthermore, for all models where the bare interaction is local (instantaneous) in time (i.e., frequency-independent), all four legs of the bare vertex have the same Keldysh contour index [Jak09]. This property turns out to be very useful in a numerical treatment, and it is quite generic, since it holds in particular for all impurity as well as lattice models with a Hubbard-like interaction (including the single-impurity Anderson model studied in this thesis). In summary, we have explicitly [Jak09]

$$\begin{aligned}&(\Gamma_0)^{j_1'j_2'|j_1j_2}_{\sigma_1'\sigma_2'|\sigma_1\sigma_2}(t_1',t_2'|t_1,t_2;q_1',q_2'|q_1,q_2)\\ &\quad = -j_1\,\delta(t_1'\!=\!t_2'\!=\!t_1\!=\!t_2)\,\delta_{j_1'=j_2'=j_1=j_2}\,\delta_{\sigma_1,\bar{\sigma}_2'}(\delta_{\sigma_1',\sigma_2}\delta_{\sigma_2',\sigma_1} - \delta_{\sigma_1',\sigma_1}\delta_{\sigma_2',\sigma_2})\,(\Gamma_0)_{q_1',q_2'|q_1,q_2}\,,\end{aligned} \tag{2.15}$$

where the q's encode momentum or position dependence of the bare interaction. (For the SIAM, $(\Gamma_0)_{q_1',q_2'|q_1,q_2} \mapsto U$, the bare interaction strength.) The bare interaction acquires a minus sign $-j_1$ when moved from the forward ($j_1 = -$) to the backward ($j_1 = +$) branch of the Keldysh contour.

---

[3] Technical remark: As a result of the factors of i appearing in the expansion of e^{iS_I} (along with a minus sign coming from the definition of the bare vertex, see Footnote 2 above), each sum over independent internal arguments (only implicit in the diagrammatic language) comes with a prefactor $(-i)$. Working in the frequency domain, we will absorb this into the integrals over internal frequencies ν_j, which we define as $\int \frac{\mathrm{d}\nu_j}{2\pi i}$, the factor 2π coming from the definition of the Fourier transform Eq. (2.27). Note that here we have again a relative minus sign compared to the convention of [Jak09], where frequency integrals are defined as $\frac{i}{2\pi}\int \mathrm{d}\nu_j$. This exactly cancels the relative sign of the bare vertex (cf. previous footnote), such that the values of all diagrams are equivalent.

[4] Notational remark: We will use the convention that barred fields have indices with a prime, while unbarred fields have unprimed indices. As a result, for vertices, arguments at outgoing legs have a prime, while those at incoming legs do not, and for propagators vice versa.

Experimental observables can be expressed through n-point correlation functions of the interacting theory, defined as

$$\langle \psi_1 \cdots \bar{\psi}_n \rangle = \frac{1}{\mathcal{Z}} \int \mathcal{D}\psi\, \mathcal{D}\bar{\psi}\, e^{iS[\psi,\bar{\psi}]}\, \psi_1 \cdots \bar{\psi}_n \,. \tag{2.16}$$

Of particular interest are one- and two-particle correlation functions, which describe dynamics of particles in their interacting environment as well as their effective (dressed) interactions.

The one-particle propagator G can be expressed through the bare propagator G_0 and the self-energy Σ via the Dyson equation

$$G_{1|1'} = -i\langle \mathcal{T}_\mathcal{C}\, \psi_1 \bar{\psi}_{1'} \rangle =$$

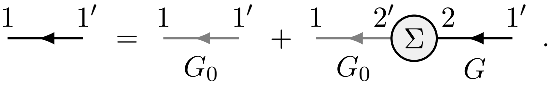

(2.17)

This self-consistent equation can be solved, $G = (G_0^{-1} - \Sigma)^{-1}$. The two-particle correlation function $G^{(4)}$ can be expressed through the 4-point vertex Γ,

$$G^{(4)}_{12|1'2'} = i\langle \mathcal{T}_\mathcal{C}\, \psi_1 \psi_2 \bar{\psi}_{2'} \bar{\psi}_{1'} \rangle =$$

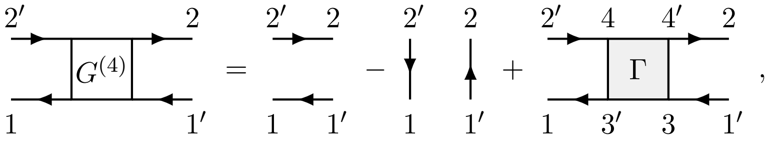

(2.18)

i.e., the 4-point vertex is the connected amputated part of the 4-point function. Internal arguments $(3, 3', 4, 4')$ are again summed over. One- and two-particle properties are thus fully captured by the self-energy and the 4-point vertex,

$$\Sigma_{1'|1} =$$

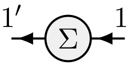

$$, \quad \Gamma_{1'2'|12} =$$

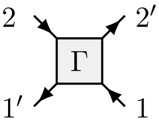

, (2.19)

which contain all amputated connected one-particle-irreducible one- and two-particle vertex diagrams, i.e., diagrams that cannot be split into two pieces by cutting a single bare propagator line [NO88].

The structure of Σ and Γ becomes most transparent by studying their leading contributions in perturbation theory (PT). Up to 2nd order (PT2) we obtain[5]

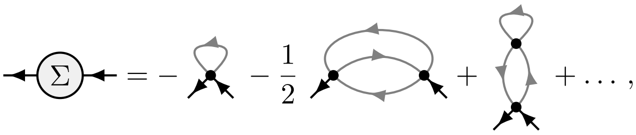

(2.20a)

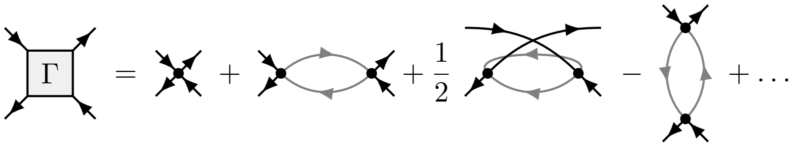

(2.20b)

---

[5] A complete list of all vertex diagrams for the spin component $\Gamma_{\uparrow\downarrow|\uparrow\downarrow}$ up to 4th order (PT4) is presented in Sec. 7.1.2 below.

Here gray lines are again identified with the bare propagator G_0, while external lines are amputated. The sign prefactors come from the fermionic anticommutation relations, and the prefactors 1/2 are introduced to avoid overcounting diagrams with two indistinguishable parallel lines.

Having defined the central objects of interest, Σ and Γ, let us now investigate their structure in the Keldysh formalism. For the rest of this chapter, we follow the notational conventions of [Jak09], and we recommend the corresponding chapters there for more details on the Keldysh structure of correlation functions.

2.2.2 Single-particle correlation functions

Recall that all fields carry a contour index, specifying the branch of the Keldysh contour on which they are to be placed. G thus has a matrix structure,

$$G^{-|+}(t_1,t_2) = -i\langle \mathcal{T}_\mathcal{C}\, \psi^-(t_1)\bar{\psi}^+(t_2)\rangle \equiv +i\langle \bar{\psi}(t_2)\psi(t_1)\rangle = G^<(t_1,t_2)\,, \tag{2.21a}$$

$$G^{+|-}(t_1,t_2) = -i\langle \mathcal{T}_\mathcal{C}\, \psi^+(t_1)\bar{\psi}^-(t_2)\rangle \equiv -i\langle \psi(t_1)\bar{\psi}(t_2)\rangle = G^>(t_1,t_2)\,, \tag{2.21b}$$

$$G^{-|-}(t_1,t_2) = -i\langle \mathcal{T}_\mathcal{C}\, \psi^-(t_1)\bar{\psi}^-(t_2)\rangle \equiv \Theta(t_1-t_2)\, G^>(t_1,t_2) + \Theta(t_2-t_1)\, G^<(t_1,t_2)\,, \tag{2.21c}$$

$$G^{+|+}(t_1,t_2) = -i\langle \mathcal{T}_\mathcal{C}\, \psi^+(t_1)\bar{\psi}^+(t_2)\rangle \equiv \Theta(t_1-t_2)\, G^<(t_1,t_2) + \Theta(t_2-t_1)\, G^>(t_1,t_2)\,. \tag{2.21d}$$

In the expressions on the right-hand side, fields are brought into the correct order along the Keldysh contour $\mathcal{C}$, therefore the contour index is dropped. For $G^{-|+}$ and $G^{+|-}$, the order is fixed independent of the order of t_1 and t_2, and for $G^{-|-}$ and $G^{+|+}$, Θ functions ensure correct contour ordering.

For $t_1 > t_2$, we immediately see that $G^{-|+} = G^{+|+}$ and $G^{+|-} = G^{-|-}$. Analogously, for $t_1 < t_2$ we have $G^{-|+} = G^{-|-}$ and $G^{+|-} = G^{-|-}$. We can combine these causal relations to obtain

$$G^{-|+} + G^{+|-} - G^{-|-} - G^{+|+} = 0\,. \tag{2.22}$$

The Keldysh structure of G can thus be simplified by the so-called Keldysh rotation,

$$\psi^1 = \tfrac{1}{\sqrt{2}}(\psi^- - \psi^+)\,, \quad \psi^2 = \tfrac{1}{\sqrt{2}}(\psi^- + \psi^+)\,, \tag{2.23}$$

and equivalently for bar fields.[6] We can define a basis transformation matrix D via $\psi^\alpha = D^{\alpha|j}\psi^j$[7]:

$$D = \tfrac{1}{\sqrt{2}}\begin{pmatrix} 1 & -1 \\ 1 & 1 \end{pmatrix}\,, \quad D^{-1} = \tfrac{1}{\sqrt{2}}\begin{pmatrix} 1 & 1 \\ -1 & 1 \end{pmatrix}\,. \tag{2.24}$$

If we rotate G to this new basis, $G^{\alpha|\alpha'} = D^{\alpha|j}G^{j|j'}(D^{-1})^{j'|\alpha'}$, we have

$$G^{\alpha|\alpha'} = \begin{pmatrix} G^{1|1} & G^{1|2} \\ G^{2|1} & G^{2|2} \end{pmatrix} = \begin{pmatrix} 0 & G^A \\ G^R & G^K \end{pmatrix}\,, \tag{2.25}$$

---

[6] Note that this convention is different from [Kam11], but follows the convention of [Jak09] and [HBSvD17] (and [Sch17] with the Keldysh indices $(1,2)$ identified with (q,c)).

[7] In [Jak09], D and D^{-1} are exchanged.

where $G^{1|1} = 0$ follows from the causality argument mentioned above. The remaining nonzero components in Eq. (2.25) are

$$G^R(t_1, t_2) = -i\Theta(t_1 - t_2)\langle\{\psi(t_1), \bar{\psi}(t_2)\}\rangle \,, \tag{2.26}$$

the retarded propagator, $G^A(t_1, t_2) = (G^R(t_2, t_1))^*$ the advanced one, and $G^K(t_1, t_2) = G^> + G^< = -(G^K(t_2, t_1))^*$ the Keldysh propagator [Jak09]. $\{\bullet, \bullet\}$ denotes the anticommutator.

In equilibrium as well as in a nonequilibrium steady state, we have time-translational invariance, $G(t_1, t_2) = G(t_1 - t_2)$, and therefore energy conservation. Going to Fourier space,

$$G(\nu) = \int \mathrm{d}t \, e^{i\nu t} \, G(t) \,, \quad G(t) = \int \frac{\mathrm{d}\nu}{2\pi} \, e^{-i\nu t} \, G(\nu) \,, \tag{2.27}$$

the propagator is thus diagonal in the frequency arguments.[8] In equilibrium, the Keldysh components of the propagator fulfill the fluctuation-dissipation theorem (FDT) [Kam11, Jak09]

$$G^K(\nu) = (1 - 2n_F(\nu))(G^R(\nu) - G^A(\nu)) = 2i \tanh\left(\frac{\nu - \mu}{2T}\right) \mathrm{Im}\, G^R(\nu) \,, \tag{2.28}$$

where $n_F(\nu) = 1/(\exp(\frac{\nu - \mu}{T}) + 1)$ is the Fermi-Dirac distribution function (in natural units where $k_B = 1$), μ is the chemical potential, and T the temperature. This result is a special case of the more general FDTs for n-point functions mentioned below.

The bare propagator G_0 is related to the noninteracting Hamiltonian $H_0 = c^\dagger_1 \epsilon_{1|1'} c_{1'}$, with fermionic creation (annihilation) operators $c^\dagger$ (c). In the eigenbasis of H_0 where $\epsilon_{1|1'} = \epsilon_1 \delta_{1|1'}$, it has the well-known form

$$(G_0^{R/A})_{1|1'}(\nu) = \frac{\delta_{1|1'}}{\nu - \epsilon_1 \pm i0^+} \,. \tag{2.29}$$

With Eq. (2.28), its Keldysh component reads

$$(G_0^K)_{1|1'}(\nu) = -2i(1 - 2n_F(\nu)) \lim_{\eta \to 0^+} \frac{\eta}{(\nu - \epsilon_1)^2 + \eta^2} = -2i(1 - 2n_F(\nu))\delta(\nu - \epsilon_1) \,. \tag{2.30}$$

The self-energy has a similar structure as the propagator after Keldysh rotation, inferred from the defining Dyson equation $G = G_0 + G_0 \, \Sigma \, G$:

$$\Sigma^{\alpha_1'|\alpha_1} = \begin{pmatrix} \Sigma^{1|1} & \Sigma^{1|2} \\ \Sigma^{2|1} & \Sigma^{2|2} \end{pmatrix} = \begin{pmatrix} \Sigma^K & \Sigma^R \\ \Sigma^A & 0 \end{pmatrix} \,. \tag{2.31}$$

Here causality implies $\Sigma^{2|2} = 0$ [Jak09], and we have $\Sigma^A = (\Sigma^R)^*$. In complete analogy to Eq. (2.28) we have the FDT

$$\Sigma^K(\nu) = 2i \tanh\left(\frac{\nu - \mu}{2T}\right) \mathrm{Im}\, \Sigma^R(\nu) \,. \tag{2.32}$$

---

[8] Notational remark: We will use ν for fermionic frequencies and ω for bosonic ones. (In the Keldysh formalism, there is no conceptual difference between bosonic and fermionic frequencies, but it still is useful to make this notational distinction when comparing to the Matsubara formalism, where bosonic and fermionic (imaginary) frequencies are inherently different.)

The Dyson equation reads component-wise[9]

$$G^R = G_0^R + G_0^R\,\Sigma^R\,G^R\,, \tag{2.33a}$$
$$G^A = G_0^A + G_0^A\,\Sigma^A\,G^A\,, \tag{2.33b}$$
$$G^K = G^R\,\Sigma^K\,G^A\,. \tag{2.33c}$$

Note that Eqs. (2.21) are ambiguous at $t_1 = t_2$, since the step functions $\Theta(t_1 - t_2)$ are not uniquely defined at this point. This is related to the fact that if the two fields $\psi, \bar{\psi}$ are at the very same point on the Keldysh contour, it is not *a priori* clear how to order them. The ambiguity is resolved by demanding that in this case barred fields should be ordered to the left of unbarred ones. This implies that $G^{-|-}(t,t) = G^{<}(t,t) = G^{+|+}(t,t)$, so that Eq. (2.22) does not hold at $t_1 = t_2 = t$. Therefore, one also has to be careful with Keldysh-rotated quantities in this case. Since the point $t_1 = t_2$ is of zero measure in integrals over time arguments, which we have to perform when computing diagrams, this subtlety is irrelevant for almost all practical purposes, at least in our context. However, there is indeed one exception that explicitly has an equal-time nature: The first-order PT (or Hartree) contribution to the self-energy,

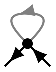

$$\Sigma_H = - \qquad . \tag{2.34}$$

Due to the instantaneous nature of the bare interaction, both incoming and outgoing legs have the same time argument. A naive computation of the retarded component of this diagram after the Keldysh rotation (and in the frequency domain) would yield

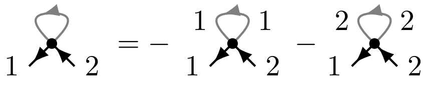

$$\Sigma_H^R = \Sigma_H^{1|2} = - \qquad = - \underbrace{\qquad}_{G_0^{1|1} \overset{?}{=} 0} - \qquad \overset{?}{=} -\Gamma_0 \int \frac{\mathrm{d}\nu'}{2\pi i}\, G_0^K(\nu')\,. \tag{2.35}$$

(Other terms in the internal Keldysh sum are zero due to the Keldysh structure of the bare vertex mentioned below in Eq. (2.39), and other quantum numbers are dropped for simplicity.) This result is however *not* correct: Since Eq. (2.22) does not hold at equal times, we have $G_0^{1|1}(t|t) \neq 0$ after Keldysh rotation.

We get the correct result by staying in the contour basis: At equal times, retarded and advanced components do not differ, and indeed, since only $\Sigma_H^{-|-}(t,t) = -\Sigma_H^{+|+}(t,t)$ are nonzero at equal time arguments, after Keldysh rotation one finds that $\Sigma_H^R(t,t) = \Sigma_H^{-|-}(t,t)$. For this component, however, we obtain in the frequency domain

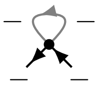

$$\Sigma_H^R = \Sigma_H^{-|-} = - \qquad = -\Gamma_0 \int \frac{\mathrm{d}\nu'}{2\pi i}\, G_0^{<}(\nu') = \Gamma_0\,\langle n \rangle\,, \tag{2.36}$$

which is the known result for the Hartree term, relating it to the particle density $\langle n \rangle$.[10]

---

[9] Writing out the Dyson equation (2.17) explicitly in the Keldysh basis, one obtains for the Keldysh component $G^K = G^R\left[(G_0^R)^{-1} G_0^K (G_0^A)^{-1} + \Sigma^K\right] G^A$. Since $(G_0^{R/A})^{-1}_{1|1'} = (\nu - \epsilon_1)\,\delta_{1|1'}$ and $(G_0^K)_{1|1'} \sim \delta(\nu - \epsilon_1)\,\delta_{1|1'}$, the first term in the square brackets vanishes.

[10] Explicitly including spin indices, we have $\Sigma^R_{H,\sigma} = -(\Gamma_0/2\pi i)\int \mathrm{d}\nu'\, G^{<}_{0,\bar{\sigma}}(\nu') = \Gamma_0\langle n_{\bar{\sigma}}\rangle$ due to the structure of the bare vertex (Eq. (2.15)), connecting opposite spins σ and $\bar{\sigma}$.

If one needs to compute this expression explicitly, one can relate $G^<$ to G^R by use of an FDT [Jak09] (see also section on FDTs below)

$$G^<(\nu) = -n_F(\nu)(G^R(\nu) - G^A(\nu))\,. \tag{2.37}$$

This issue is also discussed in more detail in Section 2.1.13 of [Wei20]. An introduction to the Keldysh formalism with a careful distinction between equal and different time arguments is given in [Klö19] (followed by a detailed analysis of Keldysh perturbation theory, including the Hartree diagram mentioned here).

2.2.3 Two-particle correlation functions

General n-point functions have 2^n Keldysh indices, thus the 4-point vertex is a 4×4 matrix in Keldysh space. After the Keldysh rotation, similar to the self-energy (2-point vertex), causality implies that the Keldysh component with only indices 2 is zero,

$$\Gamma^{22|22} = 0\,, \tag{2.38}$$

which generalizes to all n-point vertices. A special candidate is the bare vertex: Since all its contour indices are equal (see Eq. (2.15)), after Keldysh rotation it strongly simplifies to

$$(\Gamma_0)^{\alpha_1'\alpha_2'|\alpha_1\alpha_2}_{q_1'q_2'|q_1q_2} = \begin{cases} \frac{1}{2}(\Gamma_0)_{q_1'q_2'|q_1q_2}\,, & P_\alpha \text{ odd}\,, \\ 0\,, & \text{else}\,, \end{cases} \tag{2.39}$$

where

$$P_\alpha = \alpha_1' + \alpha_2' + \alpha_1 + \alpha_2 \tag{2.40}$$

is the sum of all four Keldysh indices.

2.2.3.1 Symmetries

The vertex has a number of generic symmetries that are crucial in particular for a numerical calculation, since they allow us to simplify the structure of the vertex, which strongly reduces the numerical cost. These symmetries are discussed in great detail in [Jak09, JPS10b]. Here we only briefly summarize the main results.

Crossing symmetries: Since the fields in S_I anticommute, exchanging any pair of incoming or outgoing legs of the bare vertex just gives a minus sign. This property translates to the full vertex also:

$\Gamma_{1'2'|12} =$

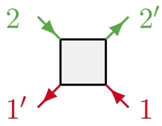

$= -$

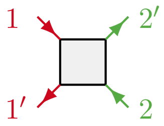

$= -\Gamma_{1'2'|21}\,,$ $\quad\mathcal{S}_1$ (exchange incoming legs), (2.41a)

$= -$

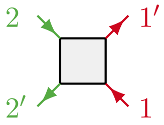

$= -\Gamma_{2'1'|12}\,,$ $\quad\mathcal{S}_2$ (exchange outgoing legs), (2.41b)

$= +$

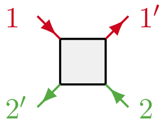

$= +\Gamma_{2'1'|21}\,,$ $\quad\mathcal{S}_3$ (exchange incoming and outgoing legs). (2.41c)

Here the subscript indices are again composite indices, i.e., all external arguments attached to a pair of legs have to be exchanged. Graphically, these symmetries $\mathcal{S}_i$ correspond to mirroring the diagrams along one of the diagonals (or both for $\mathcal{S}_3$). Obviously, $\mathcal{S}_3 = \mathcal{S}_1\mathcal{S}_2 = \mathcal{S}_2\mathcal{S}_1$.

From this the prefactors in the perturbation expansion Eq. (2.20) become directly apparent:

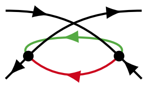

$= +$

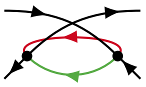

$,$

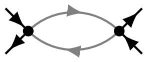

$= -$

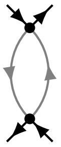

$.$ (2.42)

Complex conjugation: Exchanging incoming with outgoing fields is essentially equivalent to complex conjugation of the corresponding correlation function. The acquired sign is less trivial to see than for the crossing symmetries; we again refer to [Jak09, JPS10b] for a detailed derivation. The vertex transforms under complex conjugation as

$$\Gamma_{1'2'|12} = (-1)^{1+P_\alpha}\left(\Gamma_{12|1'2'}\right)^*\,, \qquad \mathcal{S}_\mathcal{C}\text{ (complex conjugation).} \tag{2.43}$$

Fluctuation-dissipation theorems (FDT): In equilibrium, the cyclicity of correlation functions on the imaginary time axis can be expressed via the so-called Kubo-Martin-Schwinger (KMS) conditions [Kub57, MS59, Kub66]. Together with time-reversal symmetry, the KMS conditions lead to so-called fluctuation-dissipation theorems, which are linear relations between different Keldysh components. While the FDT one the one-particle level (Eq. (2.28)) has been well-known for a long time, the generalization to n-point functions is due to [WH02] (also see [Ge20]). A detailed summary is again given in [Jak09, JPS10b].

In the contour basis, the FDTs for n-point vertices $\Gamma^{(n)}$ read [Jak09]

$$e^{\Delta^{\boldsymbol{j}'|\boldsymbol{j}}(\boldsymbol{\nu}'|\boldsymbol{\nu})/T}\,(\Gamma^{(n)})^{\boldsymbol{j}'|\boldsymbol{j}}_{J'|J} = -(-1)^{m^{\boldsymbol{j}'|\boldsymbol{j}}}\left[(\Gamma^{(n)})^{\bar{\boldsymbol{j}}'|\bar{\boldsymbol{j}}}_{J'|J}\right]^*\,, \tag{2.44}$$

and similarly for correlation functions, where $\boldsymbol{j}'|\boldsymbol{j} = (j_1', \ldots|\ldots, j_n)$, $\bar{j} = \mp$ for $j = \pm$, $\boldsymbol{\nu}'|\boldsymbol{\nu} = (\nu_1', \ldots|\ldots, \nu_n)$, and $J'|J = (1', \ldots|\ldots, n)$, with $1'$ etc. again being composite indices collecting all other quantum numbers. Furthermore,

$$\Delta^{\boldsymbol{j}'|\boldsymbol{j}}(\boldsymbol{\nu}'|\boldsymbol{\nu}) = \sum_{\substack{j_i \in \boldsymbol{j} \\ j_i = +}} (\nu_i - \mu) - \sum_{\substack{j'_i \in \boldsymbol{j}' \\ j'_i = +}} (\nu'_i - \mu) \,, \quad m^{\boldsymbol{j}'|\boldsymbol{j}} = \sum_{\substack{j_i \in \boldsymbol{j} \\ j_i = +}} 1 - \sum_{\substack{j'_i \in \boldsymbol{j}' \\ j'_i = +}} 1 \,. \tag{2.45}$$

On the two-point level, this simplifies to Eq. (2.37). The rotation of Eq. (2.44) into the Keldysh basis is quite tedious. It is done in detail in [WH02], including explicit expressions for two-, three-, and four-point functions. On the two-point level, the Keldysh-rotated FDT gives the well-known Eq. (2.28).

3 Multiloop functional renormalization group

In the last chapter, we have defined the basic objects we are interested in, namely, one- and two-particle correlation functions in the Keldysh formalism, or more precisely, the self-energy Σ and the 4-point vertex Γ. We have seen that we can easily write down a diagrammatic perturbation series for them, but ultimately we are interested in resumming infinitely many diagrams in order to go beyond the perturbative regime. The functional renormalization group is a powerful method that can achieve this; *a priori* it allows us to compute Σ and Γ exactly. The goal of this chapter is to introduce the general framework and provide the flow equations that will be used in later chapters. Naturally, this introduction is by no means meant to be complete. For a more in-depth discussion, we refer the reader to the pertinent literature. Compact introductions to fRG with different perspectives are given in several PhD theses [Jak09, Sch17, Kug19]; the more extensive standard literature in the context of condensed matter physics contains [MSH$^+$12, KBS10]. For multiloop fRG, we strongly recommend reading the original papers [KvD18c, KvD18b, KvD18a], summarized in [Kug19].

3.1 Functional renormalization group

The name “functional” RG indicates that this method originated in the context of quantum field theory in the path integral formulation, where one can derive a flow equation for the generating functional of one-particle-irreducible vertices, called Wetterich equation [Wet93]. An expansion of this functional equation in terms of n-point correlation functions leads to an infinite hierarchy of flow equations for n-point vertices [MSH$^+$12].

Here, we take a slightly different, very pragmatic point of view: We are interested in finding the solution of an interacting theory, which is inaccessible from a perturbative point of view, since it requires a resummation of infinitely many diagrams. The fRG provides a “trick” that allows to compute such an infinite sum of diagrams directly without the necessity of actually computing diagrams perturbatively. The general strategy can be summarized in four steps (we restrict ourselves to fermionic fRG):

- The starting point is a (fermionic) theory, as introduced Section 2.2. It is governed by a self-energy Σ and a two-particle vertex Γ. These objects can be derived from a generating functional, but one can also view self-energy and vertex as the collection of all one-particle-irreducible one- or two-particle diagrams, respectively, as already argued in Chapter 2. The goal is to compute Σ and Γ explicitly.

- We introduce a parameter Λ into the bare propagator G_0 such that G_0^Λ vanishes for an initial value $\Lambda = \Lambda_i$, while the full theory is recovered at a final value $\Lambda = \Lambda_f$. From the perturbation expansion Eq. (2.20) we see that Σ and Γ inherit a Λ dependence from G_0. In this way, we smoothly connect the theory to a very simple solvable one: At $\Lambda = \Lambda_i$, we see from Eq. (2.20) that if all bare propagator lines G_0 vanish, the self-energy vanishes as well, $\Sigma^{\Lambda_i} = 0$, and the vertex is just the bare interaction, $\Gamma^{\Lambda_i} = \Gamma_0$ ($\Rightarrow$ the problem is solved at Λ_i!). The dependence on the parameter Λ, called regulator, can in principle be arbitrary. Usually, one might choose a Λ dependence that resembles an infrared cutoff (connecting to the original physical picture of RG, where high-energy degrees of freedom are successively integrated out) or another way of systematically suppressing "complicated" behavior. For the SIAM (introduced in Chapter 5), we will use the hybridization Δ as a flow parameter: At $\Delta_i \to \infty$, the impurity is strongly hybridized to the bath and interactions become negligible, such that the model is solvable. At Δ_f, the interacting model is recovered.

- Now we take the derivative of Σ and Γ w.r.t Λ. This is in general a nontrivial step, since one would need an explicit form of Σ and Γ in terms of G_0 and Γ_0 in order to obtain closed expressions. Usually, this is circumvented by deriving a flow equation for the generating functional of n-point vertices [Wet93], which can be expanded in the fields in order to obtain $\dot{\Sigma} = \partial_\Lambda \Sigma$ and $\dot{\Gamma} = \partial_\Lambda \Gamma$. In this way, one obtains flow equations

$\dot{\Sigma} \;=\; -$ 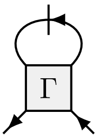

, (3.1a)

$\dot{\Gamma} \;=$ 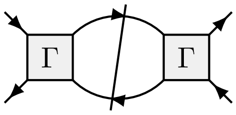

$+\ \frac{1}{2}$ 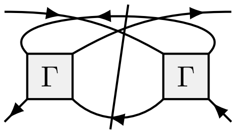

$-$ 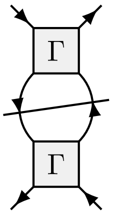

$+$ 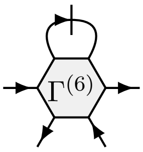

, (3.1b)

$$\dot{\Gamma}^{(6)} \;=\; \ldots\,, \tag{3.1c}$$

$$\vdots$$

Here propagator lines with a dash correspond to the so-called single-scale propagator

$$S = \partial_\Lambda G|_{\Sigma=\text{const.}}\,, \tag{3.2}$$

and bubbles with a dash are understood as a sum of two terms,

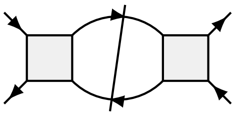
$=$ 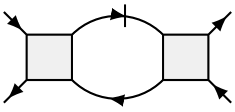
$+$ 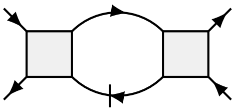
. (3.3)

- The flow equations are ordinary differential equations for self-energy and vertex, with the known initial condition $\Sigma^{\Lambda_i} = 0$, $\Gamma^{\Lambda_i} = \Gamma_0$. Hence, they can be integrated,

$$\Sigma^{\Lambda_f} = \int_{\Lambda_i}^{\Lambda_f} \mathrm{d}\Lambda\, \dot{\Sigma}^{\Lambda}\,, \quad \Gamma^{\Lambda_f} = \int_{\Lambda_i}^{\Lambda_f} \mathrm{d}\Lambda\, \dot{\Gamma}^{\Lambda}\,, \tag{3.4}$$

yielding the solution of the interacting problem.

This elegant strategy *a priori* allows one to obtain the exact solution of the interacting theory. However, looking at Eq. (3.1), a problem becomes immediately clear: The flow equation for Γ includes a contribution from the 6-point vertex $\Gamma^{(6)}$, the flow equation for $\Gamma^{(6)}$ depends on $\Gamma^{(8)}$ etc. One obtains an infinite hierarchy of equations that cannot be solved exactly and thus needs to be truncated. The standard one-loop truncation simply sets $\Gamma^{(6)} = 0$. Since $\Gamma^{(6)}$ depends on six external arguments, it would be far too complicated for a realistic numerical treatment. In this way, one obtains a closed set of relations for Σ and Γ that can be solved numerically. Note that even without the input of the 6-point vertex Eq. (3.1b) contains all three diagrammatic channels (formally introduced below) and thus provides a channel-unbiased approach, in contrast to a mere resummation of ladder diagrams in one particular channel.

However, the approximation $\Gamma^{(6)} = 0$ still comes at a price. Since the right-hand side of the flow equation for Γ is truncated, it does not form a total derivative w.r.t Λ any more. Therefore, the result of the flow will acquire an unphysical dependence on the choice of regulator, which was *a priori* completely arbitrary. This strongly limits the quantitative predictive power of the approach. Furthermore, ladder-type diagrams are fully captured even in this truncation, while other classes of diagrams are not. This leads to a bias toward ladder diagrams, which are particularly prone to divergences [KvD18b]. In the following section, we discuss a way to cure these issues without strongly increasing the numerical complexity, introduced in [KvD18c, KvD18b, KvD18a].

3.2 Multiloop fRG

For any realistic numerical calculation, approximations of the exact flow equations are unavoidable. However, they can be done more systematically than a crude one-loop truncation. In particular, it is possible to capture parts of the 6-point vertex while staying on the two-particle (4-point) level, and thereby restore the total derivative structure of the flow equations, such that the flow stays independent of the choice of regulator. This is achieved in the multiloop flow equations, which are most conveniently derived from the parquet formalism.

3.2.1 Parquet formalism

The parquet formalism (for a review see [Bic04]) provides a systematic classification of vertex diagrams on the two-particle level, by distinguishing diagrams w.r.t their two-particle reducibility. It constitutes a set of equations that can again be deduced from generating functionals of correlation functions (a concise overview is given in [Kug19]). From a diagrammatic perspective, the parquet equations self-consistently relate different classes of diagrams to each other.

The parquet formalism is defined through the following set of equations:

- Firstly, the one-particle self-energy is related to the two-particle vertex via the **Schwinger-Dyson equation (SDE)**:

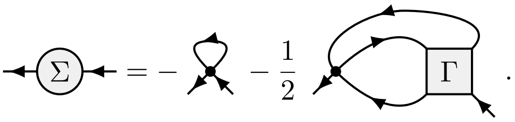

(3.5)

- On the two-particle level, the starting point of the parquet classification is the so-called **parquet equation**,

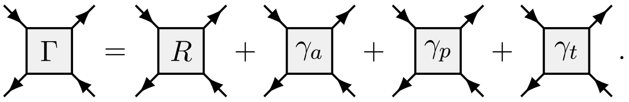

(3.6)

It states that all vertex diagrams can be assigned to one of the following four classes: those diagrams γ_r, $r = a, p, t$, which are reducible in either the antiparallel (a), parallel

(p), or transverse antiparallel (t) channel,[1] and the fully two-particle-irreducible vertex R. Importantly, these four classes are exclusive. To illustrate the notion of two-particle reducibility, we show the lowest-order contributions in perturbation theory for each of these classes:

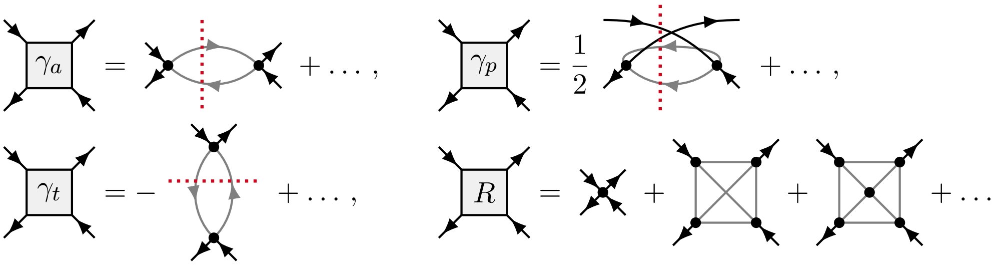

(3.7)

Diagrams reducible in the a, p, or t channel can be split into two parts by cutting two antiparallel, parallel, or transverse antiparallel propagator lines, respectively. The diagrams in R cannot be cut into two parts by cutting two propagator lines.

- Since the four classes in the parquet equation are exclusive, one can decompose Γ w.r.t its reducibility in one of the channels r: $\Gamma = I_r + \gamma_r$, where $I_r = R + \gamma_{\bar{r}}$, with $\gamma_{\bar{r}} = \sum_{r' \neq r} \gamma_{r'}$, the sum of all diagrams irreducible in channel r. The **Bethe-Salpeter equations (BSE)** relate the irreducible diagrams to the reducible ones:

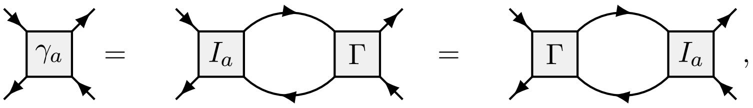

(3.8a)

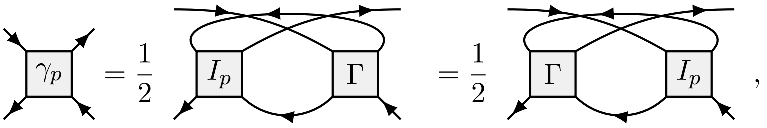

(3.8b)

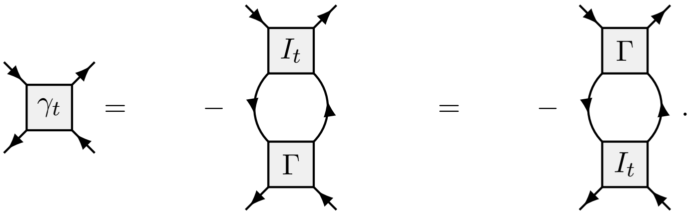

(3.8c)

  This closes the set of self-consistent relations, with R remaining as an input. Note that all propagator lines in these equations are full propagators, which leads to feedback of the self-energy into the vertex.

The only class of diagrams that is not related to other classes is the fully irreducible vertex R. If R is known, everything else can be computed self-consistently via the parquet equations. But R itself is the most complicated object: R diagrams contain several nested integrals/sums over internal arguments, while the integrals in reducible diagrams partially factorize. This makes R diagrams beyond the bare vertex hardly tractable numerically. Therefore, one usually approximates $R \approx \Gamma_0$, which is known as the parquet approximation (PA). The PA results in an error in 4th order in the bare interaction (cf. Eq. (3.7)), but otherwise provides a solvable set of equations that give an infinite set of diagrams, the so-called parquet diagrams.

---

[1] In the literature, there are various different names for these channels: In [RVT12, Roh13] and related works, $a \mathrel{\widehat{=}} \overline{\mathrm{ph}}$ (particle-hole crossed), $p \mathrel{\widehat{=}} \mathrm{pp}$ (particle-particle), $t \mathrel{\widehat{=}} \mathrm{ph}$ (particle-hole). In [Jak09, Sch17] and related works, $a \mathrel{\widehat{=}} x$ (exchange particle-hole), $p \mathrel{\widehat{=}} p$ (particle-particle), $t \mathrel{\widehat{=}} d$ (direct particle-hole), sometimes also capitalized (X, P, D). In [HS09], $a \mathrel{\widehat{=}} \mathrm{ph,cr}$ (crossed particle-hole), $p \mathrel{\widehat{=}} \mathrm{pp}$ (particle-particle), $t \mathrel{\widehat{=}} \mathrm{ph,d}$ (direct particle-hole). In [Reu11] and related works, $(a, p, t) \mathrel{\widehat{=}} (u, s, t)$.

The PA is a useful approximation for various reasons, which are nicely summarized in Section 2.3.1.7 of [Kug19]: Besides including all diagrams that are still numerically tractable with available resources, the parquet diagrams are a fully self-consistent set of diagrams which is therefore channel-unbiased, and they fulfill various diagrammatic identities, and in particular also fulfill the Mermin-Wagner theorem. In Chapter 4, we will keep all relations general, allowing for a future extension beyond the PA in the context of DMF^{2}RG. From Chapter 5 on, we will explicitly work in the parquet approximation.

3.2.2 mfRG flow equations

The mfRG flow equations [KvD18b] are derived by again introducing a regulator Λ into the bare propagator G_0, which makes all objects in the parquet equations Λ-dependent [KvD18a]. Here, the fully irreducible vertex R is treated as an input to the theory and is thus assumed to be Λ-independent, $R^\Lambda \approx R$. (This is trivially fulfilled in the PA.) Taking the derivative of the SDE and the BSE w.r.t Λ gives flow equations for Σ and Γ.

When computing $\dot{\gamma}_r$ via the BSE, one obtains terms including $\dot{I}_r = \sum_{r' \neq r} \dot{\gamma}_{r'}$. Thus, one has to iteratively insert the flow equation for γ_r into the equations of the other channels $r' \neq r$, yielding an infinite set of contributions of increasing “loop order”:

$$\dot{\Gamma} = \dot{\gamma}_a + \dot{\gamma}_p + \dot{\gamma}_t \,, \quad \dot{\gamma}_r = \sum_{\ell=1}^{\infty} \dot{\gamma}_r^{(\ell)} \,. \tag{3.9}$$

The individual ℓ-loop contributions in the a channel are

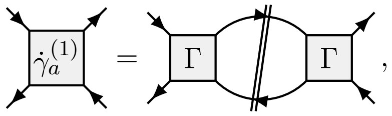

(3.10a)

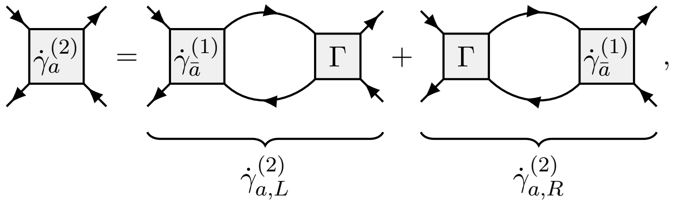
$\dot{\gamma}_a^{(2)}$
=
$\dot{\gamma}_{\bar{a}}^{(1)}$
Γ
+
Γ
$\dot{\gamma}_{\bar{a}}^{(1)}$
,
$\dot{\gamma}_{a,L}^{(2)}$
$\dot{\gamma}_{a,R}^{(2)}$

(3.10b)

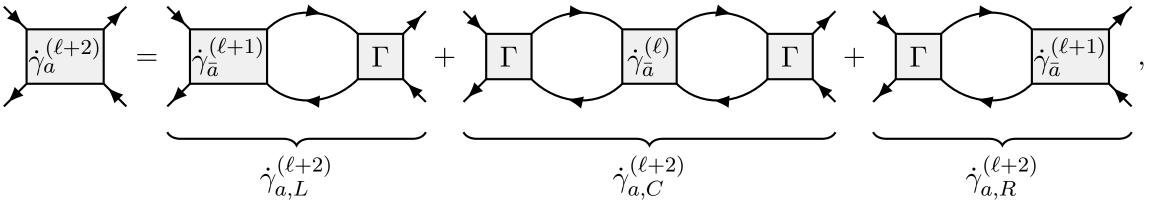
$\dot{\gamma}_a^{(\ell+2)}$
=
$\dot{\gamma}_{\bar{a}}^{(\ell+1)}$
Γ
+
Γ
$\dot{\gamma}_{\bar{a}}^{(\ell)}$
Γ
+
Γ
$\dot{\gamma}_{\bar{a}}^{(\ell+1)}$
,
$\dot{\gamma}_{a,L}^{(\ell+2)}$
$\dot{\gamma}_{a,C}^{(\ell+2)}$
$\dot{\gamma}_{a,R}^{(\ell+2)}$

(3.10c)

where Eq. (3.10c) applies for $\ell + 2 \geq 3$. Here $\gamma_{\bar{r}}^{(\ell)} = \sum_{r' \neq r} \gamma_r^{(\ell)}$. The double-dashed bubble corresponds again to a sum of two terms (cf. Eq. (3.3)), where double-dashed propagators are fully differentiated ones,

$$\partial_\Lambda G = S + G \dot{\Sigma} G \,, \tag{3.11}$$

with the single-scale propagator S from Eq. (3.2).

The flow equations for $\gamma_p^{(\ell)}$ and $\gamma_t^{(\ell)}$ follow completely analogously: All subscripts a simply have to be replaced by p or t, and the (regular and differentiated) a bubbles (i.e., pairs of propagators reducible in the a channel) are replaced by p or t bubbles.

The self-energy flow equation reads

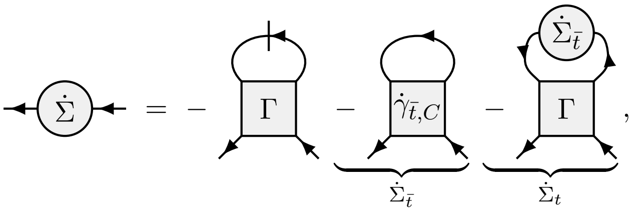

(3.12)

with $\dot\gamma_{\bar t,C} = \sum_\ell \dot\gamma^{(\ell)}_{\bar t,C} = \sum_\ell(\dot\gamma^{(\ell)}_{a,C} + \dot\gamma^{(\ell)}_{p,C})$. Note that there are two more terms in addition to Eq. (3.1a), even though the latter is in principle exact and is not truncated even in the one-loop approximation. However, if the vertex Γ has been truncated, the first term alone would not yield a total derivative any more. The multiloop corrections to the self-energy flow restore this total derivative structure. These terms naturally arise in the Λ derivative of the SDE within the PA [KvD18a]. One should also mention that the differentiated propagators (Eq. (3.11)) appearing in the flow equation (3.10a) of the vertex include the differentiated self-energy, while the flow equation for the self-energy includes parts of the differentiated vertex. Therefore, the flow equations for vertex and self-energy are coupled and should in principle be iterated in order to get the correct derivative of Γ and Σ.

Note that the one-loop contribution Eq. (3.10a) of the vertex flow with a single-dashed bubble (i.e., with the single-scale propagator) would be equivalent to the usual one-loop flow equation Eq. (3.1b), neglecting the contribution of the 6-point vertex. Replacing the single-scale propagator by the fully differentiated one, $S \mapsto \partial_\Lambda G$, as done in Eq. (3.10a), corresponds to the so-called Katanin substitution [Kat04] that contains the feedback of the differentiated self-energy into the vertex flow, and already goes beyond the standard one-loop approximation. By adding higher-loop contributions until convergence is reached, one effectively solves the self-consistent parquet equations through an fRG flow. On the one hand, this strongly improves upon the standard one-loop approximation; in particular, regulator independence is restored, curing issues mentioned above [KvD18c, THK+19]. On the other hand, it also provides a more stable way of reaching a solution of the parquet equations by simply integrating ordinary differential equations. This is numerically favorable compared to an iteration of the self-consistent equations, which is generically much harder to get converged.

It is also worth mentioning that while the mfRG equations are derived from the parquet equations, no assumption is made on the fully irreducible vertex R, except for the fact that its Λ dependence is ignored. And indeed, the resulting equations only need the full Γ (and Σ) at $\Lambda = \Lambda_i$ as an input. Therefore, the limitations of the parquet approximation can be overcome by starting the mfRG flow from an initial Γ^{Λ_i} that is not just the bare vertex Γ_0, but a correlated one, e.g. obtained from DMFT, which implicitly contains nontrivial information from R as well [TAB+14, VTM19]. Furthermore, sometimes vertex divergences of the building blocks I_r and γ_r of the parquet formalism appear, while the full vertex stays finite [SRG+13, SCW+16, GRS+17, CGS+18, TGCR18]. Such unphysical divergences, which are a huge problem for numerics, do not show up in mfRG, since only the full vertex enters the right-hand side of the flow equations.

4 Keldysh vertex parametrization

In the previous two chapters, we have introduced all ingredients in terms of diagrammatic equations that are necessary to perform Keldysh mfRG computations. However, when it comes to an actual calculation, we need to think carefully about how to handle the building blocks of these equations numerically.

The Keldysh vertex is a huge and complicated object: it depends on four Keldysh indices α_i, spin indices σ_i, frequencies ν_i, and potentially other quantum numbers q_i that can include momentum, position, orbital, etc.:

$$\Gamma = \Gamma_{1'2'|12} = \Gamma^{\alpha'_1\alpha'_2|\alpha_1\alpha_2}_{\sigma'_1\sigma'_2|\sigma_1\sigma_2}(\nu'_1\nu'_2|\nu_1\nu_2\,;q'_1q'_2|q_1q_2)\,. \tag{4.1}$$

When evaluating the right-hand sides of the flow equations introduced in the previous chapter, we need to perform sums and integrals over internal arguments. For bubbles $B_r(\Gamma^L,\Gamma^R)$ in the $r = a, p, t$ channel, connecting a left and right vertex Γ^L and Γ^R, we have explicitly

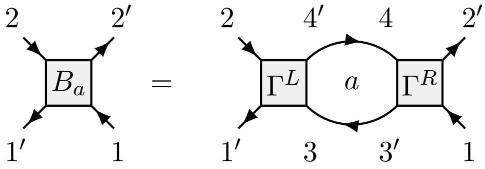

$$(B_a)_{1'2'|12} = \cdots = \cdots = \sum_{3,3',4,4'} \Gamma^L_{1'4'|32}\, G_{3|3'}\, G_{4|4'}\, \Gamma^R_{3'2'|14}\,, \tag{4.2a}$$

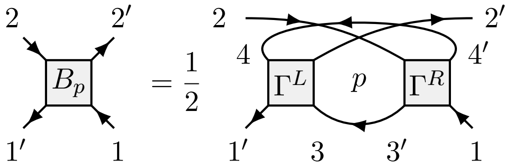

$$(B_p)_{1'2'|12} = \cdots = \frac{1}{2}\cdots = \frac{1}{2}\sum_{3,3',4,4'} \Gamma^L_{1'2'|34}\, G_{3|3'}\, G_{4|4'}\, \Gamma^R_{3'4'|12}\,, \tag{4.2b}$$

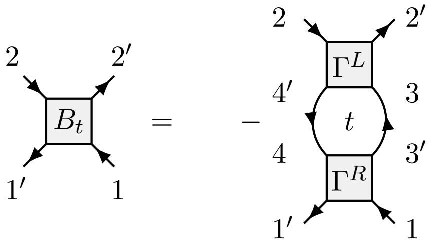

$$(B_t)_{1'2'|12} = \cdots = -\cdots = -\sum_{3,3',4,4'} \Gamma^L_{4'2'|32}\, G_{3|3'}\, G_{4|4'}\, \Gamma^R_{1'3'|14}\,, \tag{4.2c}$$

and for a self-energy loop $L(\Gamma, G)$

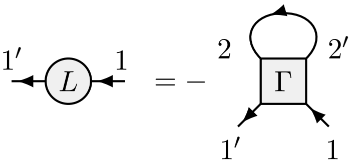

$$L_{1'|1} = \cdots = -\cdots = -\sum_{2,2'} \Gamma_{1'2'|12}\, G_{2|2'}\,, \tag{4.3}$$

where we have included a minus sign into the definition of L, since such loops always come with a minus sign in the self-energy flow equations (3.1a) or (3.12), the SDE (3.5), or in perturbation theory (cf. Eq. (2.20a)). Each sum includes a sum over Keldysh indices and spins (and potentially lattice sites, orbitals etc.) and integration over frequencies (and potentially momenta).

For completeness, we also introduce differentiated bubbles and loops,

$$\dot{B}(\Gamma^L, \Gamma^R) \sim \Gamma^L \circ [\partial_\Lambda (G \circ G)] \circ \Gamma^R , \quad \dot{L}(\Gamma, G) = L(\Gamma, S) , \tag{4.4}$$

which appear in the flow equations (3.10a) and (3.12), respectively. Here the $\circ$ operation is defined in complete analogy to Eq. (4.2), and the product rule has to be applied as indicated in Eq. (3.3).

By doing a rough estimate, it quickly becomes clear that even for quite simple models such as a single-band Hubbard model in a naive treatment the required numerical resources easily surpass the limits even of the largest supercomputers. Therefore, it is vital to efficiently store the vertices and efficiently compute bubbles and loops by finding a suitable parametrization and employ all available symmetries, and thereby reduce the numerical cost as much as possible. In the following sections, we will analyze the three generic dependencies that have to be dealt with always, independent of the specific model: The frequency structure, spin structure, and Keldysh index structure. We employ symmetries to simplify the structure in each of these sectors, and find ways to compactly represent the vertex, bubbles, and loops.

Remark: While the decomposition into diagrammatic classes according to their high-frequency asymptotic behavior was introduced in [WLT+20] and the spin structure is also well-known (see e.g. [RVT12]), the simplification of the Keldysh structure of those asymptotic classes using parity and crossing symmetries is new. The latter work was done in close collaboration with Santiago Aguirre. Many of the following relations are therefore already presented in his master's thesis [Agu20]. We still give a summary here including all essential ideas and relations, for completeness of this thesis, and to give somewhat more details on the symmetry reduction of the vertex. We refer the interested reader to [Agu20] for additional details that are only briefly mentioned here.

4.1 Frequency structure

4.1.1 Channel decomposition

To simplify the frequency structure, we first recall the parquet decomposition of the vertex into different diagrammatic channels (Eq. (3.6)), $\Gamma = R + \sum_{r=a,p,t} \gamma_r$. While this decomposition relies purely on diagrammatic properties, it has direct consequences for the frequency (and momentum) structure, since one can choose different natural parametrizations for each channel.[1] Energy conservation implies $\nu'_1 + \nu'_2 = \nu_1 + \nu_2$, hence three frequencies are sufficient to parametrize the vertex. In each channel, we express the four fermionic frequencies $\nu'_1, \nu'_2, \nu_1, \nu_2$ at the vertex legs through one bosonic transfer frequency ω_r and two fermionic frequencies ν_r, ν'_r:

---

[1] For DMF^{2}RG [TAB+14, VTM19] (cf. Sec. 1.1.1), the input of the fRG flow is the full DMFT vertex that is only known numerically. In this case, a channel decomposition is *a priori* not possible. However, by taking appropriate limits of combinations of frequencies, one can in fact deduce the asymptotic classes $\mathcal{K}_1^r$ and $\mathcal{K}_{2^{(\prime)}}^r$ (introduced in the next subsection) in each channel $r = a, p, t$, such that the channel-dependent frequency parametrization is indeed useful also in this context. Only $\mathcal{K}_3 + R$ has to be treated on general grounds (also discussed in [Kug19], Fig. 2.15). This is in fact ongoing work in the group of Jan von Delft, pursued by Johannes Halbinger [Hal21].

$\Gamma(\nu'_1\nu'_2|\nu_1\nu_2)$

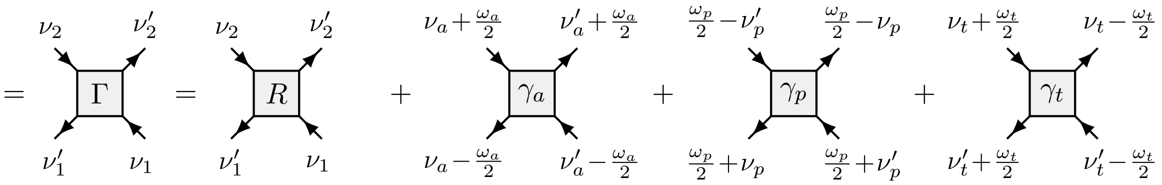
=
ν_2
ν'_2
Γ
ν'_1
ν_1
=
ν_2
ν'_2
R
ν'_1
ν_1
+
$\nu_a + \frac{\omega_a}{2}$
$\nu'_a + \frac{\omega_a}{2}$
γ_a
$\nu_a - \frac{\omega_a}{2}$
$\nu'_a - \frac{\omega_a}{2}$
+
$\frac{\omega_p}{2} - \nu'_p$
$\frac{\omega_p}{2} - \nu_p$
γ_p
$\frac{\omega_p}{2} + \nu_p$
$\frac{\omega_p}{2} + \nu'_p$
+
$\nu_t + \frac{\omega_t}{2}$
$\nu_t - \frac{\omega_t}{2}$
γ_t
$\nu'_t + \frac{\omega_t}{2}$
$\nu'_t - \frac{\omega_t}{2}$

$$= \Big[R(\nu'_1\nu'_2|\nu_1\nu_2) + \gamma_a(\omega_a,\nu_a,\nu'_a) + \gamma_p(\omega_p,\nu_p,\nu'_p) + \gamma_t(\omega_t,\nu_t,\nu'_t)\Big] \times \delta(\nu'_1+\nu'_2-\nu_1-\nu_2)\,. \tag{4.5}$$

Note that we choose symmetric parametrizations with $\pm\frac{\omega_r}{2}$ on all vertex legs. This ensures that the peaks of the vertices are centered around $\omega_r = 0$,[2] which is numerically preferable. However, other conventions are of course possible, e.g. the parametrization obtained by adding $\frac{\omega_a}{2}$ on all legs in the a channel (and similar replacements in the p and t channel).[3]

When inserting γ_r into the flow equation of a different channel r', one needs to express ω_r, ν_r, ν'_r in the parametrization of channel r'. The corresponding transformations are simple linear combinations which are given explicitly in Appendix A (cf. [Agu20], Sec. 3.1).

The bubbles can be written as follows in these natural parametrizations of the channels (for clarity ignoring the dependence on all other arguments):

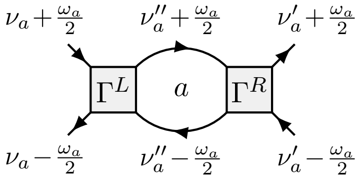
$\nu_a + \frac{\omega_a}{2}$
$\nu''_a + \frac{\omega_a}{2}$
$\nu'_a + \frac{\omega_a}{2}$
Γ^L
a
Γ^R
$\nu_a - \frac{\omega_a}{2}$
$\nu''_a - \frac{\omega_a}{2}$
$\nu'_a - \frac{\omega_a}{2}$

$$= \int \frac{d\nu''_a}{2\pi i}\, \Gamma^L(\omega_a,\nu_a,\nu''_a)\, G(\nu''_a - \tfrac{\omega_a}{2})\, G(\nu''_a + \tfrac{\omega_a}{2})\, \Gamma^R(\omega_a,\nu''_a,\nu'_a)\,, \tag{4.6a}$$

$$\frac{1}{2}$$

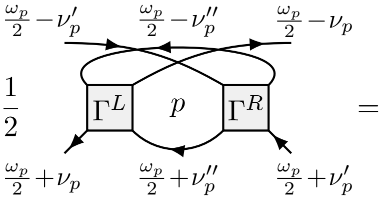
$\frac{\omega_p}{2} - \nu'_p$
$\frac{\omega_p}{2} - \nu''_p$
$\frac{\omega_p}{2} - \nu_p$
Γ^L
p
Γ^R
$\frac{\omega_p}{2} + \nu_p$
$\frac{\omega_p}{2} + \nu''_p$
$\frac{\omega_p}{2} + \nu'_p$

$$= \frac{1}{2}\int \frac{d\nu''_p}{2\pi i}\, \Gamma^L(\omega_p,\nu_p,\nu''_p)\, G(\tfrac{\omega_p}{2} + \nu''_p)\, G(\tfrac{\omega_p}{2} - \nu''_p)\, \Gamma^R(\omega_p,\nu''_p,\nu'_p)\,, \tag{4.6b}$$

$$-$$

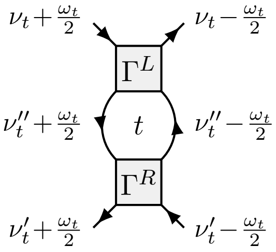
$\nu_t + \frac{\omega_t}{2}$
$\nu_t - \frac{\omega_t}{2}$
Γ^L
$\nu''_t + \frac{\omega_t}{2}$
t
$\nu''_t - \frac{\omega_t}{2}$
Γ^R
$\nu'_t + \frac{\omega_t}{2}$
$\nu'_t - \frac{\omega_t}{2}$

$$= -\int \frac{d\nu''_t}{2\pi i}\, \Gamma^L(\omega_t,\nu_t,\nu''_t)\, G(\nu''_t - \tfrac{\omega_t}{2})\, G(\nu''_t + \tfrac{\omega_t}{2})\, \Gamma^R(\omega_t,\nu''_t,\nu'_t)\,. \tag{4.6c}$$

---

[2] To see this, consider Eq. (4.6): The frequency arguments of the two internal bubble lines are shifted by $\pm\frac{\omega_r}{2}$, i.e., the combination of the two propagators is symmetric or antisymmetric around $\omega_r = 0$. This of course has to hold as well for the result of the diagram after integration over ν''_r.

[3] Such a parametrization can be useful in particular in the Matsubara formalism. There, ω_r is of bosonic nature, while ν_r, ν'_r are fermionic frequencies. Importantly, the external frequencies $\nu_i^{(\prime)}$ at all legs have to be fermionic as well. While e.g. $\nu_a + \frac{\omega_a}{2}$ is either bosonic or fermionic (since $\frac{\omega_a}{2}$ is alternatingly bosonic or fermionic) and thus requires cumbersome rounding procedures, $\nu_a + \omega_a$ would always be fermionic (since it is a sum of a bosonic and a fermionic Matsubara frequency).

Each bubble thus involves an integral over one single internal (fermionic) frequency. We can write the corresponding expressions more compactly by defining the product of two propagators,

$$\Pi(\nu_1,\nu_2) = G(\nu_1)\,G(\nu_2)\,. \tag{4.7}$$

Encoding the channel-specific frequency dependence as

$$\Pi_a(\omega_a,\nu''_a) = \Pi\left(\nu''_a - \tfrac{\omega_a}{2}, \nu''_a + \tfrac{\omega_a}{2}\right)\,, \tag{4.8a}$$

$$\Pi_p(\omega_p,\nu''_p) = \Pi\left(\tfrac{\omega_p}{2} + \nu''_p, \tfrac{\omega_p}{2} - \nu''_p\right)\,, \tag{4.8b}$$

$$\Pi_t(\omega_t,\nu''_t) = \Pi\left(\nu''_t - \tfrac{\omega_t}{2}, \nu''_t + \tfrac{\omega_t}{2}\right)\,, \tag{4.8c}$$

the frequency-dependence of the bubbles simplifies to

$$B_r(\omega_r,\nu_r,\nu'_r) = \frac{\alpha_r}{2\pi i}\int \mathrm{d}\nu''_r\,\Gamma_L(\omega_r,\nu_r,\nu''_r)\,\Pi_r(\omega_r,\nu''_r)\,\Gamma_R(\omega_r,\nu''_r,\nu'_r)\,, \tag{4.9}$$

with the channel-specific prefactors

$$\alpha_a = 1\,, \quad \alpha_p = \tfrac{1}{2}\,, \quad \alpha_t = 1\,. \tag{4.10}$$

For the loop, it is most convenient to stay in the natural fermionic frequency parametrization,

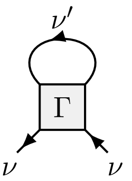

$$- \qquad = -\int \frac{\mathrm{d}\nu'}{2\pi i}\,\Gamma(\nu\nu'|\nu\nu')\,G(\nu') \tag{4.11}$$

To illustrate the usefulness of these channel-dependent frequency parametrizations, we consider the vertex in 2nd order perturbation theory (Eq. (2.20b)):

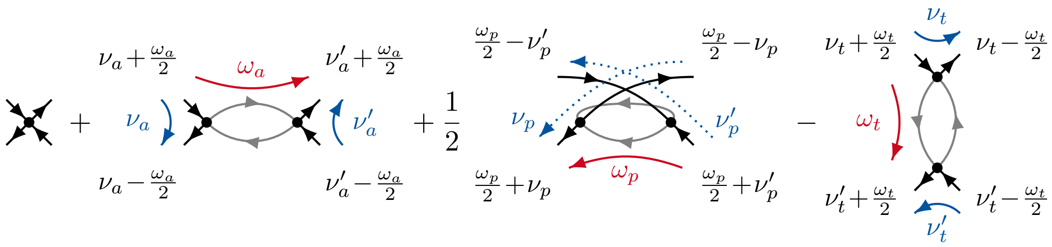
+
$\nu_a+\frac{\omega_a}{2}$
ω_a
$\nu'_a+\frac{\omega_a}{2}$
ν_a
ν'_a
$\nu_a-\frac{\omega_a}{2}$
$\nu'_a-\frac{\omega_a}{2}$
$+\frac{1}{2}$
$\frac{\omega_p}{2}-\nu'_p$
$\frac{\omega_p}{2}-\nu_p$
ν_p
ν'_p
ω_p
$\frac{\omega_p}{2}+\nu_p$
$\frac{\omega_p}{2}+\nu'_p$
−
ν_t
$\nu_t+\frac{\omega_t}{2}$
$\nu_t-\frac{\omega_t}{2}$
ω_t
$\nu'_t+\frac{\omega_t}{2}$
$\nu'_t-\frac{\omega_t}{2}$
ν'_t

. (4.12)

The bosonic frequency ω_r is “transferred” through the bubble in which each diagram is reducible, while the fermionic frequencies ν_r, ν'_r parametrize the frequency dependence on each side of the bubble.

Another important implication becomes very clear in PT2: Obviously, the internal propagator lines only depend on the bosonic transfer frequency of the corresponding channel (and the internal integration frequency), while the external fermionic frequencies directly flow in and out of the diagram at the same bare vertex, such that the value of each diagram is independent of ν_r, ν'_r. This notion can be generalized, leading to the decomposition of each reducible vertex γ_r into four different asymptotic classes.

4.1.2 Asymptotic classes

This decomposition was introduced in [WLT+20] to correctly capture the high-frequency asymptotic behavior of the vertices. The authors realized the following: Since the frequency dependence enters the denominator of the propagators, diagrams decay as a function of all frequencies which appear in internal propagator lines. However, diagrams that do not depend on some external frequency ν, as illustrated for PT2 above, will stay finite in the limit $\nu \to \infty$. Therefore, sampling the vertices γ_r in a finite three-dimensional frequency box will not properly capture the high-frequency asymptotic behavior. Instead, one should treat classes of diagrams with nontrivial asymptotics separately.

Schematically, we define these classes as follows:

$$\gamma_a(\omega_a, \nu_a, \nu'_a) \; =$$

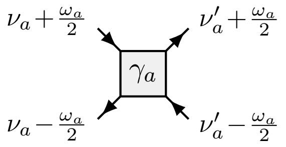
$\nu_a + \frac{\omega_a}{2}$
$\nu'_a + \frac{\omega_a}{2}$
γ_a
$\nu_a - \frac{\omega_a}{2}$
$\nu'_a - \frac{\omega_a}{2}$

$$=$$

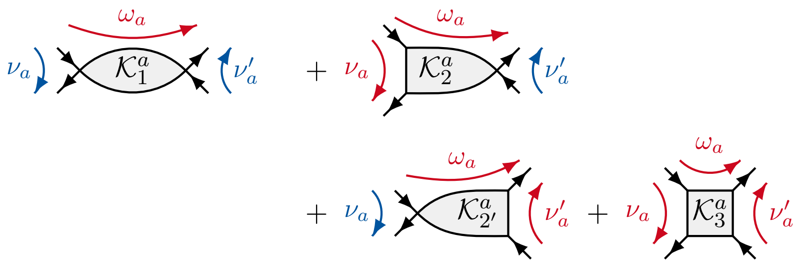
ω_a
ν_a
$\mathcal{K}_1^a$
ν'_a
$+$
ω_a
ν_a
$\mathcal{K}_2^a$
ν'_a
$+$
ω_a
ν_a
$\mathcal{K}_{2'}^a$
ν'_a
$+$
ω_a
ν_a
$\mathcal{K}_3^a$
ν'_a

$$= \; \mathcal{K}_1^a(\omega_a) \; + \; \mathcal{K}_2^a(\omega_a, \nu_a) \; + \; \mathcal{K}_{2'}^a(\omega_a, \nu'_a) \; + \; \mathcal{K}_3^a(\omega_a, \nu_a, \nu'_a)\,, \tag{4.13a}$$

$$\gamma_p(\omega_p, \nu_p, \nu'_p) \; =$$

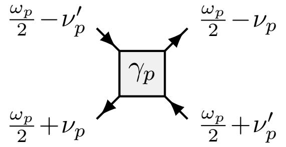
$\frac{\omega_p}{2} - \nu'_p$
$\frac{\omega_p}{2} - \nu_p$
γ_p
$\frac{\omega_p}{2} + \nu_p$
$\frac{\omega_p}{2} + \nu'_p$

$$=$$

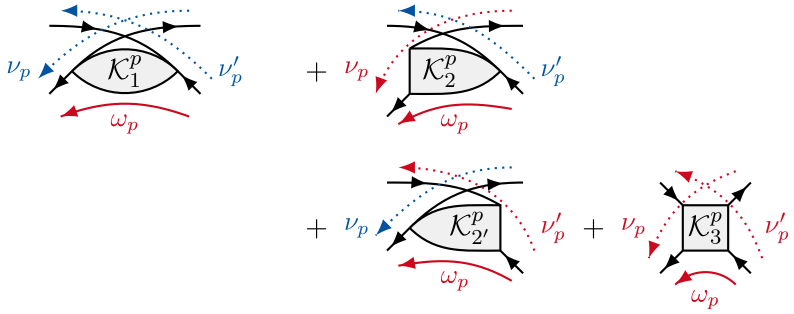
ν_p
$\mathcal{K}_1^p$
ν'_p
ω_p
$+$
ν_p
$\mathcal{K}_2^p$
ν'_p
ω_p
$+$
ν_p
$\mathcal{K}_{2'}^p$
ν'_p
ω_p
$+$
ν_p
$\mathcal{K}_3^p$
ν'_p
ω_p

$$= \; \mathcal{K}_1^p(\omega_p) \; + \; \mathcal{K}_2^p(\omega_p, \nu_p) \; + \; \mathcal{K}_{2'}^p(\omega_p, \nu'_p) \; + \; \mathcal{K}_3^p(\omega_p, \nu_p, \nu'_p)\,, \tag{4.13b}$$

$$\gamma_t(\omega_t, \nu_t, \nu'_t) \; =$$

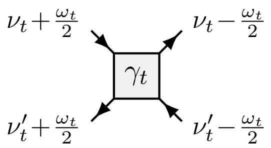
$\nu_t + \frac{\omega_t}{2}$
$\nu_t - \frac{\omega_t}{2}$
γ_t
$\nu'_t + \frac{\omega_t}{2}$
$\nu'_t - \frac{\omega_t}{2}$

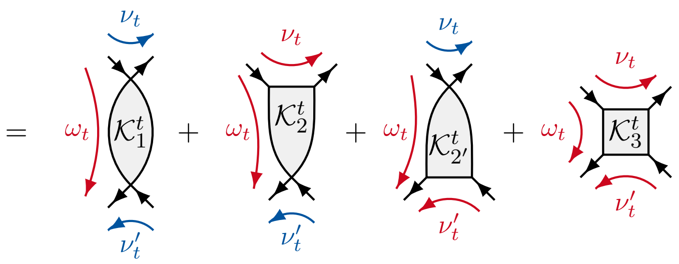

$$= \mathcal{K}_1^t(\omega_t) + \mathcal{K}_2^t(\omega_t,\nu_t) + \mathcal{K}_{2'}^t(\omega_t,\nu_t') + \mathcal{K}_3^t(\omega_t,\nu_t,\nu_t')\,. \tag{4.13c}$$

Formally, $\mathcal{K}_1^r$ contains those diagrams where (in r parametrization) the left two legs connect to the same bare vertex, and the right two legs also connect to the same bare vertex. Those diagrams are thus independent of ν_r, ν_r' and stay finite in the limit $\nu_r \to \infty$, $\nu_r' \to \infty$,

$$\lim_{\nu_r\to\infty} \lim_{\nu_r'\to\infty} \gamma_r(\omega_r,\nu_r,\nu_r') = \mathcal{K}_1^r(\omega_r)\,. \tag{4.14}$$

$\mathcal{K}_2^r$ ($\mathcal{K}_{2'}^r$) analogously contains the part of the vertex that is finite for $\nu_r' \to \infty$ ($\nu_r \to \infty$), while decaying in the limit $\nu_r \to \infty$ ($\nu_r' \to \infty$),

$$\lim_{\nu_r'\to\infty} \gamma_r(\omega_r,\nu_r,\nu_r') = \mathcal{K}_1^r(\omega_r) + \mathcal{K}_2^r(\omega_r,\nu_r)\,, \tag{4.15a}$$

$$\lim_{\nu_r\to\infty} \gamma_r(\omega_r,\nu_r,\nu_r') = \mathcal{K}_1^r(\omega_r) + \mathcal{K}_{2'}^r(\omega_r,\nu_r')\,. \tag{4.15b}$$

$\mathcal{K}_3^r$ contains all diagrams that depend on all three frequencies and thus decay if any of them is sent to infinity. It is also worth mentioning that the reducible vertex in a channel r' decays as a function of both fermionic frequencies of the other channels $r \neq r'$,

$$\lim_{\nu_r\to\infty} \gamma_{r'\neq r} = \lim_{\nu_r'\to\infty} \gamma_{r'\neq r} = 0\,. \tag{4.16}$$

Since the fully two-particle-irreducible vertex R decays to the bare vertex for any frequency going to infinity (see the structure of its perturbation expansion in Eq. (3.7)), similar equations to Eqs. (4.14) and (4.15) consequently also hold for the full vertex Γ, the only exception being that the (frequency-independent) bare vertex Γ_0 appears on the right-hand side as well.

The asymptotic decomposition is also useful since for not too strong interaction (i.e., in the perturbative regime), the diagrams in $\mathcal{K}_3$ that do depend on all three frequencies are observed to be smaller than those in $\mathcal{K}_1, \mathcal{K}_{2^{(\prime)}}$, which might justify resolving them more coarsely in a numerical implementation. This is very helpful since $\mathcal{K}_3$ is most expensive numerically, due to the three-dimensional frequency dependence, while $\mathcal{K}_{2^{(\prime)}}$ only needs to be sampled on a two-dimensional frequency grid (and $\mathcal{K}_1$ on a one-dimensional one).[4]

It is important to mention that in previous works on Keldysh fRG (e.g. [JMS07, JPS10a, SBvD17, WvD19]), the vertices γ_r have always been approximated to depend on the bosonic transfer frequency ω_r only. This is equivalent to neglecting all diagrams in $\mathcal{K}_{2^{(\prime)}}$ and $\mathcal{K}_3$ altogether. While this approach drastically reduces the numerical complexity by going from a three-dimensional to a one-dimensional frequency dependence, it is clear that neglecting a huge part of the vertex will certainly have implications on the results of a calculation. Here, we incorporate the dependence on the fermionic frequencies also, by including all asymptotic classes, and we will show later that this indeed strongly improves the results for physical observables.

---

[4] One might also be tempted to assume that $\mathcal{K}_3$ should be more localized in frequency space than $\mathcal{K}_1$ and $\mathcal{K}_{2^{(\prime)}}$, such that a smaller frequency box would be sufficient to properly sample it numerically. However, in our calculations we have not been able to confirm this; $\mathcal{K}_{2^{(\prime)}}$ and $\mathcal{K}_3$ usually have similar extent and decay even less quickly than $\mathcal{K}_1$. This tendency can be seen in Fig. 9.1 below. A more localized behavior of diagrams with a 3-dimensional frequency dependence has however been observed for φ^{irr} in the so-called SBE (single-boson exchange) decomposition [BTH+21], which is discussed in Appendix B.

4.1.3 Susceptibilities

The asymptotic classes also have a physical interpretation: $\mathcal{K}_1^r$ is related to a susceptibility in channel r, $\mathcal{K}_2^r$ has properties of a 3-point (fermion-boson) vertex, while $\mathcal{K}_3^r$ contains genuine 4-point diagrams.[5] The susceptibilities in channel r are obtained from the 4-point correlation function $G^{(4)}$ (Eq. (2.18)) by closing two pairs of legs in the corresponding channel and subtracting the disconnected parts afterwards [Roh13],

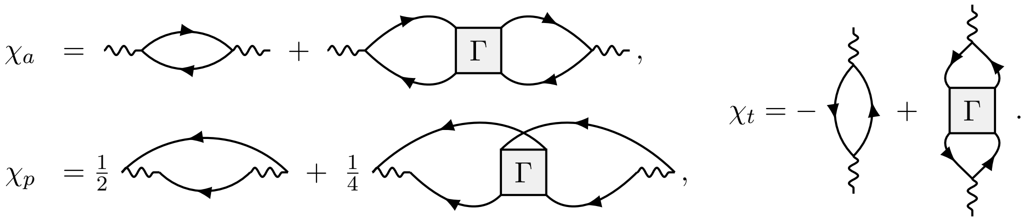

(4.17)

The wiggly lines are amputated bare vertices Γ_0. The generalized particle-hole susceptibility is usually defined as (cf. [RVT12], Fig. 3, or [VT97])

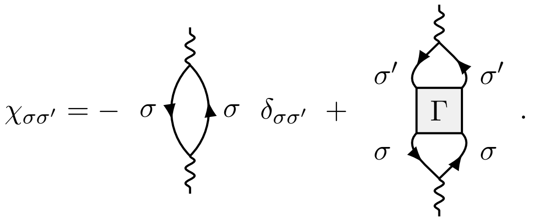

(4.18)

The classes $\mathcal{K}_1^r$ can be shown to be directly related to these susceptibilities,[6]

$$\mathcal{K}_1^r = \Gamma_0\, \chi_r\, \Gamma_0\,. \tag{4.19}$$

It is easily seen that $\chi_{\sigma\sigma'} = (\chi_t)_{\sigma\sigma'} = \Gamma_0^{-1} (\mathcal{K}_1^t)_{\sigma\sigma'|\sigma\sigma'}\, \Gamma_0^{-1}$. The physical spin and charge susceptibilities are then given by [VT97]

$$\chi_{\mathrm{sp/ch}} = \chi_{\uparrow\uparrow} \mp \chi_{\uparrow\downarrow}\,. \tag{4.20}$$

We thus have $\Gamma_0\, \chi_{\mathrm{sp/ch}}\, \Gamma_0 = (\mathcal{K}_1^t)_{\uparrow\uparrow|\uparrow\uparrow} \mp (\mathcal{K}_1^t)_{\uparrow\downarrow|\uparrow\downarrow}$. Making use of SU(2) symmetry $(\mathcal{K}_1^t)_{\uparrow\uparrow|\uparrow\uparrow} = (\mathcal{K}_1^t)_{\uparrow\downarrow|\uparrow\downarrow} + (\mathcal{K}_1^t)_{\uparrow\downarrow|\downarrow\uparrow}$ ([Roh13], see Eq. (4.34) below) and crossing symmetry $(\mathcal{K}_1^t)_{\uparrow\downarrow|\downarrow\uparrow} = -(\mathcal{K}_1^a)_{\uparrow\downarrow|\uparrow\downarrow}$ (see Sec. 4.3.2 below), we eventually obtain

$$\Gamma_0\, \chi_{\mathrm{sp}}\, \Gamma_0 = -(\mathcal{K}_1^a)_{\uparrow\downarrow|\uparrow\downarrow}\,, \quad \Gamma_0\, \chi_{\mathrm{ch}}\, \Gamma_0 = 2(\mathcal{K}_1^t)_{\uparrow\downarrow|\uparrow\downarrow} - (\mathcal{K}_1^a)_{\uparrow\downarrow|\uparrow\downarrow}\,. \tag{4.21}$$

---

[5] This becomes particularly apparent in the SBE decomposition (Appendix B).

[6] This can be derived from the BSE (3.8): In symbolic notation (summation over internal indices is understood), we have $\gamma_r = \alpha_r\, I_r\, \Pi_r\, \Gamma = \alpha_r\, I_r\, \Pi_r\, (I_r + \gamma_r) = \alpha_r\, I_r\, \Pi_r\, (I_r + \alpha_r\, \Gamma\, \Pi_r\, I_r)$. In the limit $\nu_r, \nu_r' \to \infty$, we have $I_r \to \Gamma_0$, $\gamma_r \to \mathcal{K}_1^r$, and thus $\mathcal{K}_1^r = \alpha_r\, \Gamma_0\, \Pi_r (\Gamma_0 + \alpha_r\, \Gamma\, \Pi_r\, \Gamma_0) = \alpha_r\, \Gamma_0\, \Pi_r\, \Gamma_0 + \alpha_r^2\, \Gamma_0\, \Pi_r\, \Gamma\, \Pi_r\, \Gamma_0$, reproducing the diagrams shown in Eq. (4.17).

4.1.4 Flow equations for the asymptotic classes

As we represent the vertex through its asymptotic classes, we would like to compute them directly during the flow, without the need of numerically taking the limits of certain frequencies to infinity. In this way we can also systematically add or neglect higher asymptotic classes. Therefore, we now derive flow equations for them explicitly, starting from the general multiloop flow equations (3.10). We will restrict the explicit derivation to the a channel. The equations for the p and t channels follow directly by replacing all sub-/superscripts a by p or t and the a bubbles by p or t bubbles.

Recall the one-loop flow equation in the a channel (3.10a),

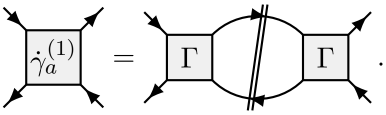

(4.22)

We can decompose $\dot{\gamma}_a^{(1)}$ on the left-hand side into its asymptotic classes,

$$\dot{\gamma}_a^{(1)} = \dot{\mathcal{K}}_1^{a\,(1)} + \dot{\mathcal{K}}_2^{a\,(1)} + \dot{\mathcal{K}}_{2'}^{a\,(1)} + \dot{\mathcal{K}}_3^{a\,(1)} \,. \tag{4.23}$$

On the right-hand side of the flow equation (4.22), we insert the diagrammatic decomposition of Γ w.r.t the a channel,

$$\Gamma = \Gamma_0 + \mathcal{K}_1^a + \mathcal{K}_2^a + \mathcal{K}_{2'}^a + \mathcal{K}_3^a + \gamma_{\bar{a}} + R - \Gamma_0 \,. \tag{4.24}$$

We have already written the fully irreducible vertex R as the sum of the (frequency-independent) bare vertex Γ_0 and other diagrams $R - \Gamma_0$, which depend on all frequencies and thus decay to zero in the limits $\nu_r \to \infty$ and $\nu_r' \to \infty$ in all channels r. (Of course in the PA we have $R - \Gamma_0 = 0$.) In order to see which parts contribute to the flow of which asymptotic class, we formally take the limits of frequencies $\nu_a \to \infty$, $\nu_a' \to \infty$ on both sides of the flow equation. We define the parts of Γ that do not decay for $\nu_r' \to \infty$, $\nu_r \to \infty$ as

$$\Gamma_2^r(\omega_r, \nu_r) = \lim_{\nu_r' \to \infty} \Gamma(\omega_r, \nu_r, \nu_r') = \Gamma_0 + \mathcal{K}_1^r + \mathcal{K}_2^r \,, \tag{4.25a}$$

$$\Gamma_{2'}^r(\omega_r, \nu_r') = \lim_{\nu_r \to \infty} \Gamma(\omega_r, \nu_r, \nu_r') = \Gamma_0 + \mathcal{K}_1^r + \mathcal{K}_{2'}^r \,. \tag{4.25b}$$

Correspondingly, we define

$$\bar{\Gamma}_2^r(\omega_r, \nu_r, \nu_r') = \Gamma - \Gamma_2^r = \mathcal{K}_{2'}^r + \mathcal{K}_3^r + \gamma_{\bar{r}} + R - \Gamma_0 \,, \tag{4.26a}$$

$$\bar{\Gamma}_{2'}^r(\omega_r, \nu_r, \nu_r') = \Gamma - \Gamma_{2'}^r = \mathcal{K}_2^r + \mathcal{K}_3^r + \gamma_{\bar{r}} + R - \Gamma_0 \,, \tag{4.26b}$$

which contain all diagrams that *do* decay for $\nu_r' \to \infty$, $\nu_r \to \infty$, respectively. Diagrammatically, the left (right) pair of legs (in the r parametrization) of $\Gamma_{2'}^r$ (Γ_2^r) connect to the same bare vertex, while the left (right) pair of legs of $\bar{\Gamma}_{2'}^r$ ($\bar{\Gamma}_2^r$) connect to different bare vertices.

The resulting flow equations can also be clearly seen from the diagrams directly: In the a channel, all diagrams where the left and the right pairs of legs connect to the same bare vertex, respectively, contribute to the flow of $\mathcal{K}_1^a$, while diagrams, where only the right pair of legs connect to the same bare vertex but the left one does not, contribute to $\dot{\mathcal{K}}_2^{a,(1)}$ etc. We show all contributions for $\dot{\mathcal{K}}_1^{a,(1)}$ explicitly; for the other classes they can be written down analogously:

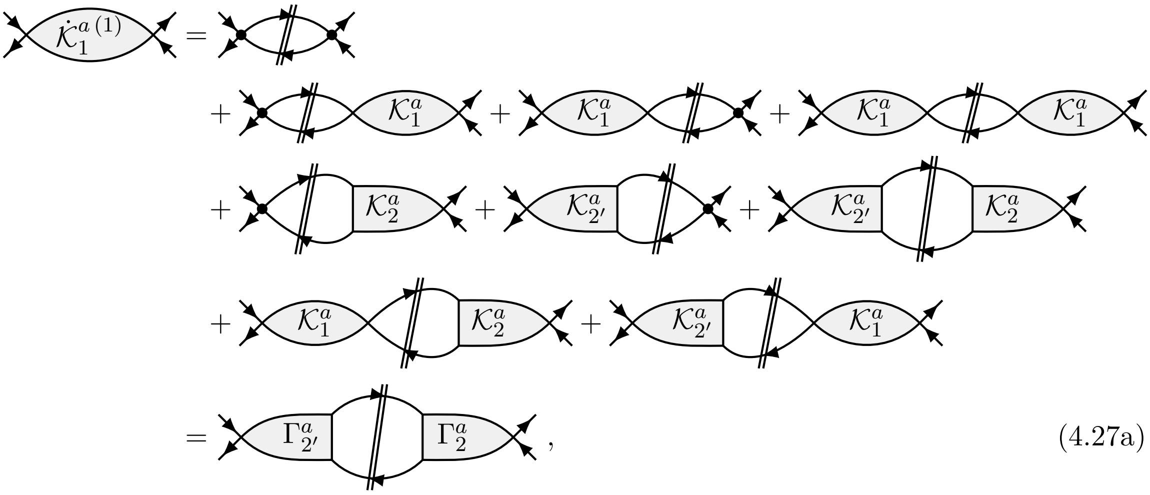
$\dot{\mathcal{K}}_1^{a\,(1)}$
=
+
$\mathcal{K}_1^a$
+
$\mathcal{K}_1^a$
+
$\mathcal{K}_1^a$
$\mathcal{K}_1^a$
+
$\mathcal{K}_2^a$
+
$\mathcal{K}_{2'}^a$
+
$\mathcal{K}_{2'}^a$
$\mathcal{K}_2^a$
+
$\mathcal{K}_1^a$
$\mathcal{K}_2^a$
+
$\mathcal{K}_{2'}^a$
$\mathcal{K}_1^a$
=
$\Gamma_{2'}^a$
Γ_2^a
,

(4.27a)

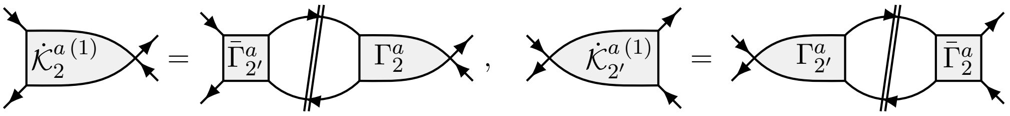
$\dot{\mathcal{K}}_2^{a\,(1)}$
=
$\bar{\Gamma}_{2'}^a$
Γ_2^a
,
$\dot{\mathcal{K}}_{2'}^{a\,(1)}$
=
$\Gamma_{2'}^a$
$\bar{\Gamma}_2^a$
,

(4.27b)

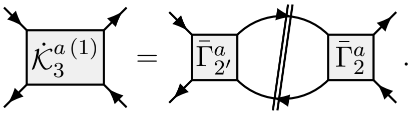
$\dot{\mathcal{K}}_3^{a\,(1)}$
=
$\bar{\Gamma}_{2'}^a$
$\bar{\Gamma}_2^a$
.

(4.27c)

We continue with the two-loop contribution (3.10b)

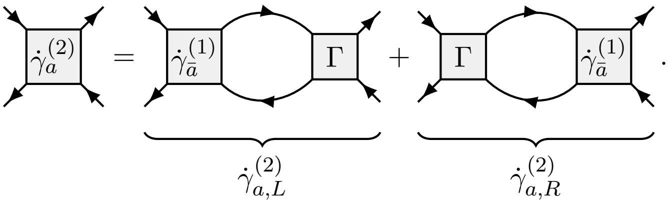
$\dot{\gamma}_a^{(2)}$
=
$\dot{\gamma}_{\bar{a}}^{(1)}$
Γ
+
Γ
$\dot{\gamma}_{\bar{a}}^{(1)}$
.
$\dot{\gamma}_{a,L}^{(2)}$
$\dot{\gamma}_{a,R}^{(2)}$

(4.28)

Since $\dot{\gamma}_{\bar{a}}^{(1)}$ has no contribution where the left two or the right two legs connect to the same vertex, as it only contains contributions from the p and t channel, there is no 2-loop contribution to $\dot{\mathcal{K}}_1^a$. In a similar fashion as before, we obtain

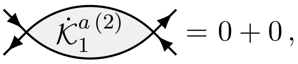
$\dot{\mathcal{K}}_1^{a\,(2)}$
$= 0 + 0\,,$

(4.29a)

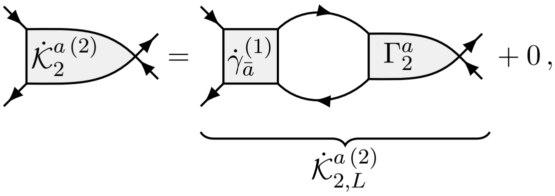
$\dot{\mathcal{K}}_2^{a\,(2)}$
=
$\dot{\gamma}_{\bar{a}}^{(1)}$
Γ_2^a
$+\,0\,,$
$\dot{\mathcal{K}}_{2,L}^{a\,(2)}$

(4.29b)

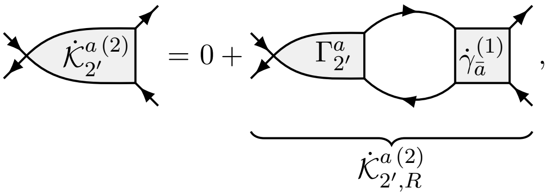
$\dot{\mathcal{K}}_{2'}^{a\,(2)}$
$= 0 +$
$\Gamma_{2'}^a$
$\dot{\gamma}_{\bar{a}}^{(1)}$
,
$\dot{\mathcal{K}}_{2',R}^{a\,(2)}$

(4.29c)

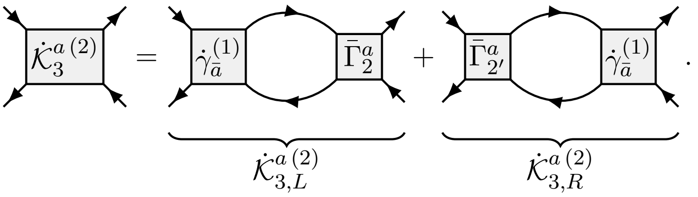
$\dot{\mathcal{K}}_3^{a\,(2)}$
=
$\dot{\gamma}_{\bar{a}}^{(1)}$
$\bar{\Gamma}_2^a$
+
$\bar{\Gamma}_{2'}^a$
$\dot{\gamma}_{\bar{a}}^{(1)}$
.
$\dot{\mathcal{K}}_{3,L}^{a\,(2)}$
$\dot{\mathcal{K}}_{3,R}^{a\,(2)}$

(4.29d)

For the $\ell + 2$-loop contribution (3.10c), with $\ell \geq 1$,

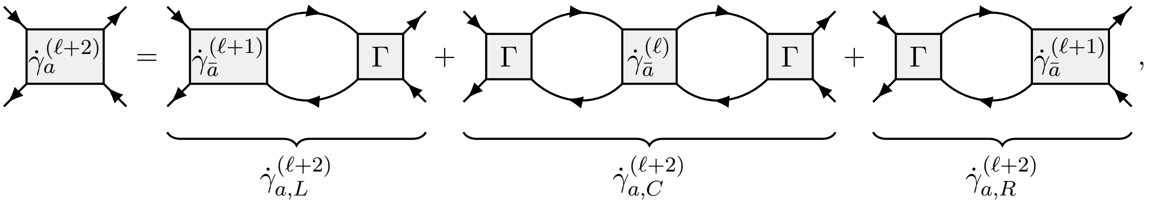
$\dot{\gamma}_a^{(\ell+2)}$
=
$\dot{\gamma}_{\bar{a}}^{(\ell+1)}$
Γ
+
Γ
$\dot{\gamma}_{\bar{a}}^{(\ell)}$
Γ
+
Γ
$\dot{\gamma}_{\bar{a}}^{(\ell+1)}$
,
$\dot{\gamma}_{a,L}^{(\ell+2)}$
$\dot{\gamma}_{a,C}^{(\ell+2)}$
$\dot{\gamma}_{a,R}^{(\ell+2)}$

(4.30)

the procedure is just the same. Here, $\dot{\mathcal{K}}_1^a$ *does* have contributions again, namely from the central term $\dot{\mathcal{K}}_{1,C}^{a\,(\ell+2)}$:

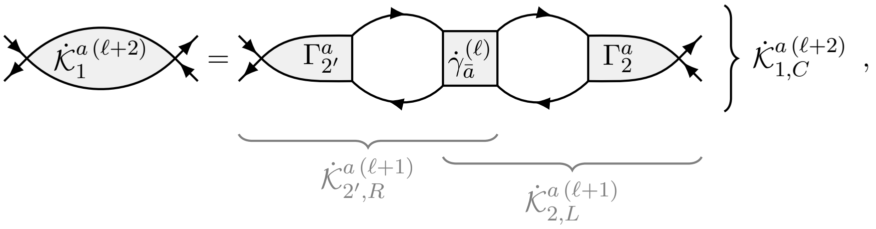
$\dot{\mathcal{K}}_1^{a\,(\ell+2)}$
=
$\Gamma_{2'}^a$
$\dot{\gamma}_{\bar{a}}^{(\ell)}$
Γ_2^a
$\dot{\mathcal{K}}_{1,C}^{a\,(\ell+2)}$
,
$\dot{\mathcal{K}}_{2',R}^{a\,(\ell+1)}$
$\dot{\mathcal{K}}_{2,L}^{a\,(\ell+1)}$

(4.31a)

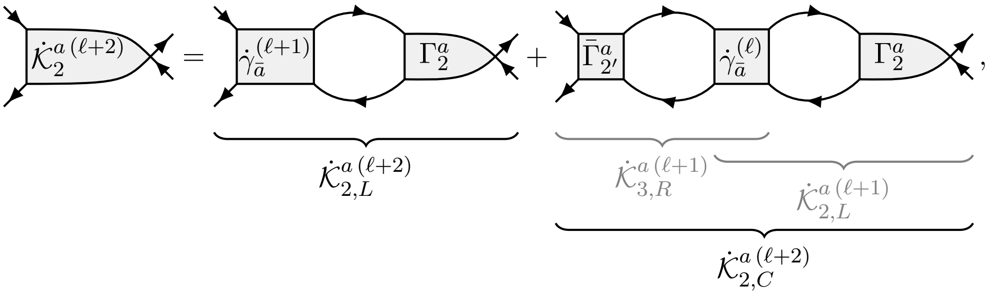
$\dot{\mathcal{K}}_2^{a\,(\ell+2)}$
=
$\dot{\gamma}_{\bar{a}}^{(\ell+1)}$
Γ_2^a
+
$\bar{\Gamma}_{2'}^a$
$\dot{\gamma}_{\bar{a}}^{(\ell)}$
Γ_2^a
,
$\dot{\mathcal{K}}_{2,L}^{a\,(\ell+2)}$
$\dot{\mathcal{K}}_{3,R}^{a\,(\ell+1)}$
$\dot{\mathcal{K}}_{2,L}^{a\,(\ell+1)}$
$\dot{\mathcal{K}}_{2,C}^{a\,(\ell+2)}$

(4.31b)

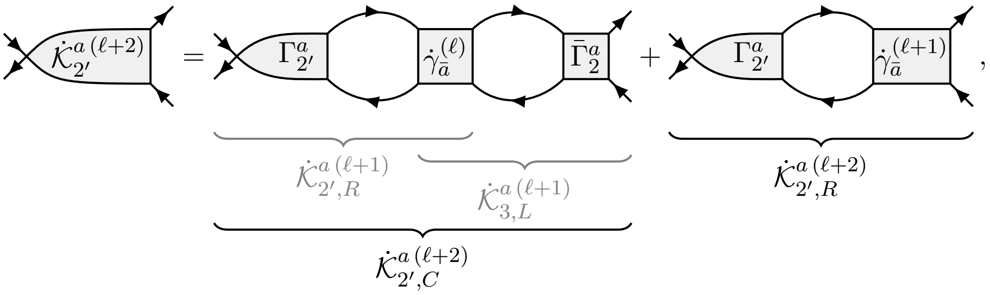
$\dot{\mathcal{K}}_{2'}^{a\,(\ell+2)}$
=
$\Gamma_{2'}^a$
$\dot{\gamma}_{\bar{a}}^{(\ell)}$
$\bar{\Gamma}_2^a$
+
$\Gamma_{2'}^a$
$\dot{\gamma}_{\bar{a}}^{(\ell+1)}$
,
$\dot{\mathcal{K}}_{2',R}^{a\,(\ell+1)}$
$\dot{\mathcal{K}}_{3,L}^{a\,(\ell+1)}$
$\dot{\mathcal{K}}_{2',R}^{a\,(\ell+2)}$
$\dot{\mathcal{K}}_{2',C}^{a\,(\ell+2)}$

(4.31c)

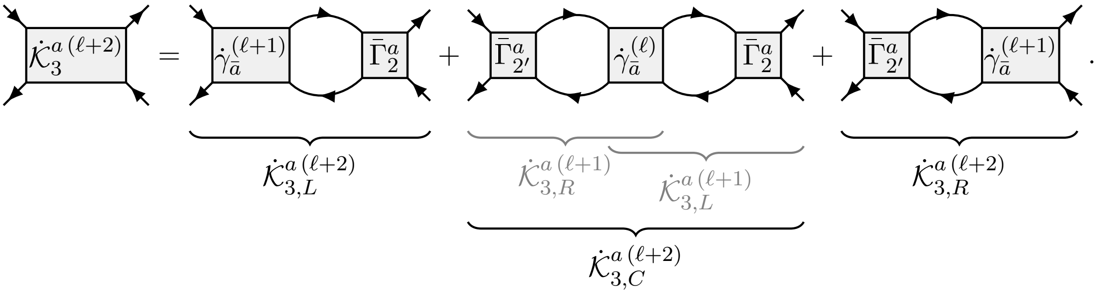
$\dot{\mathcal{K}}_3^{a\,(\ell+2)}$
=
$\dot{\gamma}_{\bar{a}}^{(\ell+1)}$
$\bar{\Gamma}_2^a$
+
$\bar{\Gamma}_{2'}^a$
$\dot{\gamma}_{\bar{a}}^{(\ell)}$
$\bar{\Gamma}_2^a$
+
$\bar{\Gamma}_{2'}^a$
$\dot{\gamma}_{\bar{a}}^{(\ell+1)}$
.
$\dot{\mathcal{K}}_{3,L}^{a\,(\ell+2)}$
$\dot{\mathcal{K}}_{3,R}^{a\,(\ell+1)}$
$\dot{\mathcal{K}}_{3,L}^{a\,(\ell+1)}$
$\dot{\mathcal{K}}_{3,R}^{a\,(\ell+2)}$
$\dot{\mathcal{K}}_{3,C}^{a\,(\ell+2)}$

(4.31d)

Note that these equations can also be used in the context of DMF^{2}RG [TAB$^+$14, VTM19]. As already mentioned in Footnote 1 in Sec. 4.1.1, in DMF^{2}RG only the full vertex Γ is given as an input. While $\mathcal{K}_1^r$, $\mathcal{K}_2^r$ and $\mathcal{K}_{2'}^r$ can be derived from Γ by considering limits of certain frequencies to infinity [Hal21], a channel decomposition is not possible on the level of $\mathcal{K}_3 (= \mathcal{K}_3^a + \mathcal{K}_3^p + \mathcal{K}_3^t)$. However, the classes $\mathcal{K}_3^r$ also do not enter the right-hand sides of Eqs. (4.27), (4.29), (4.31) individually (which is already clear from the general formulation of the mfRG flow equations (3.10)). Consider e.g. the one-loop contribution to the flow of $\mathcal{K}_2^a$, Eq. (4.27b). If we define $\gamma_{\bar{r}}^{1,2} = \sum_{r' \neq r} (\mathcal{K}_1^{r'} + \mathcal{K}_2^{r'} + \mathcal{K}_{2'}^{r'}) = \gamma_{\bar{r}} - \sum_{r' \neq r} \mathcal{K}_3^{r'}$, we can write

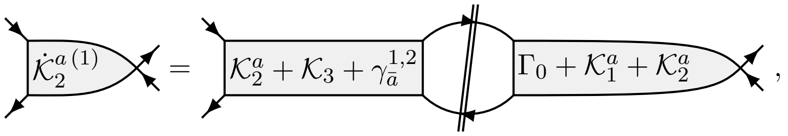
$\dot{\mathcal{K}}_2^{a\,(1)}$
=
$\mathcal{K}_2^a + \mathcal{K}_3 + \gamma_{\bar{a}}^{1,2}$
$\Gamma_0 + \mathcal{K}_1^a + \mathcal{K}_2^a$
,

(4.32)

which only requires knowledge about the full $\mathcal{K}_3$. This holds equivalently for all insertions of the full vertex into flow equations at any loop order. Note that insertions of the *differentiated* vertex in loop order ℓ into the flow equations of order $\ell + 1$ and $\ell + 2$ *do* require a channel decomposition on the level of $\mathcal{K}_3$, e.g. the two-loop contribution to the flow of $\mathcal{K}_2^a$, Eq. (4.29b), contains $\dot{\gamma}_{\bar{a}}^{(1)} = \dot{\gamma}_{\bar{r}}^{1,2\,(1)} + \dot{\mathcal{K}}_3^{p\,(1)} + \dot{\mathcal{K}}_3^{t\,(1)}$. However, this is not an issue since the *differentiated* vertices $\dot{\mathcal{K}}_3^{p\,(1)}$ and $\dot{\mathcal{K}}_3^{t\,(1)}$ are indeed computed independently via equations analogous to Eq. (4.27c). Therefore, in the DMF^{2}RG context, one would start with $\mathcal{K}_1^r$, $\mathcal{K}_2^r$, $\mathcal{K}_{2'}^r$ and the full $\mathcal{K}_3$ from DMFT, compute the differentiated vertices $\dot{\mathcal{K}}_i^r$ independently (including $\dot{\mathcal{K}}_3^r$), and successively insert them in higher loop-orders, and eventually update $\mathcal{K}_3$ using $\dot{\mathcal{K}}_3 = \sum_{\ell,r} \dot{\mathcal{K}}_3^{r\,(\ell)}$ in each step of the flow.

At this point, it is also worth mentioning that quite recently a new parametrization of the vertex has been developed, namely, the single-boson exchange (SBE) decomposition [KVC19, KV19]. This parametrization is based on reducibility in bosonic lines instead of pairs of fermionic ones, motivated by the physical interpretation of boson exchange processes. It is related to the asymptotic decomposition into $\mathcal{K}_i^r$ used here, in that its constituents can be expressed through the asymptotic classes $\mathcal{K}_i^r$. We briefly introduce the SBE parametrization in Appendix B and also derive multiloop flow equations for its constituents, which can be done in the same spirit as the derivation of the flow equations for $\mathcal{K}_i^r$ above.

4.2 Spin structure

As mentioned in Sec. 2.2.1, due to Pauli's principle, a local bare vertex can only involve interactions between particles with different spins, i.e., it connects one incoming and outgoing spin ↑ to one incoming and outgoing spin ↓. The full (screened) interaction vertex can also mediate interactions between equal spins, but it still needs to fulfill spin conservation, $\sigma'_1 + \sigma'_2 = \sigma_1 + \sigma_2$, since all propagator lines and bare vertices in each diagram conserve spin. Generically, we thus have 6 spin components,

$$\Gamma_{\sigma\bar{\sigma}|\sigma\bar{\sigma}} =: \Gamma_{\sigma\bar{\sigma}} =: V\,, \tag{4.33a}$$

$$\Gamma_{\sigma\bar{\sigma}|\bar{\sigma}\sigma} =: \Gamma_{\overline{\sigma\bar{\sigma}}} =: \hat{V}\,, \tag{4.33b}$$

$$\Gamma_{\sigma\sigma|\sigma\sigma} =: \Gamma_{\sigma\sigma} \overset{SU(2)\text{ symmetry}}{=} V + \hat{V}\,, \tag{4.33c}$$

with $\sigma = \uparrow, \downarrow$, and $\bar{\sigma}$ means spin inversion. Here we have already indicated that for SU(2) symmetry, one can deduce that [Roh13]

$$\Gamma_{\sigma\sigma|\sigma\sigma} = \Gamma_{\sigma\bar{\sigma}|\sigma\bar{\sigma}} + \Gamma_{\sigma\bar{\sigma}|\bar{\sigma}\sigma}\,. \tag{4.34}$$

Of course with SU(2) symmetry we also have $\Gamma_{\sigma_1\sigma_2} = \Gamma_{\bar{\sigma}_1\bar{\sigma}_2}$, such that the components $V = \Gamma_{\uparrow\downarrow}$ and $\hat{V} = \Gamma_{\overline{\uparrow\downarrow}}$ are sufficient. We will see later that these are in fact related by crossing symmetry, such that we only need to compute the V component explicitly. We treat the relation between V and $\hat{V}$ in conjunction with the Keldysh structure in the next section to reduce the number of independent components as much as possible.

For systems with SU(2) symmetry, bubbles contributing to the V component have the following structure (again ignoring other dependencies for clarity):

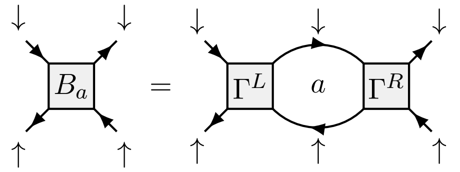

$$= V^L G_\uparrow G_\downarrow V^R\,, \tag{4.35a}$$

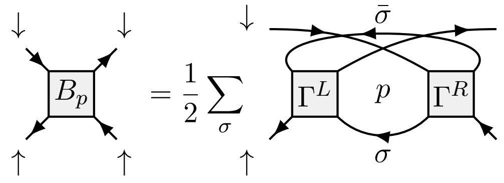

$$= \frac{1}{2}\left(V^L G_\uparrow G_\downarrow V^R + \hat{V}^L G_\downarrow G_\uparrow \hat{V}^R\right) \overset{(*)}{=} V^L G_\uparrow G_\downarrow V^R\,, \tag{4.35b}$$

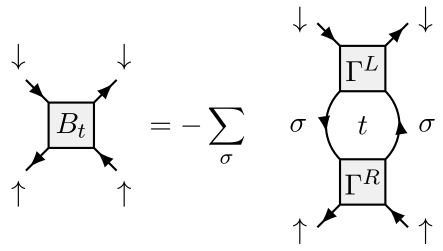

$$= -\left[(V^L + \hat{V}^L) G_\downarrow G_\downarrow V^R + V^L G_\uparrow G_\uparrow (V^R + \hat{V}^R)\right]. \tag{4.35c}$$

Of course with SU(2) symmetry, $G_\uparrow = G_\downarrow$. We see that due to the spin structure of the vertices, an explicit spin sum is necessary in the t, but not in the a and p channel. Note that in the p channel, the last equality $(*)$ holds if the left and right vertex are crossing symmetric[7] (cf. Eq. (2.41)). We then only need to compute the first term, and the sum simply cancels the prefactor $1/2$. This is the case for full vertices $\Gamma^{L/R} = \Gamma$ as well as for $I_p = R + \gamma_a + \gamma_t$ appearing in the BSE (3.8), and also for $\dot\gamma_{\bar p}^{(\ell)} = \dot\gamma_a^{(\ell)} + \dot\gamma_t^{(\ell)}$ in the mfRG flow equations (3.10). Note that even the not fully symmetric vertices $\dot\gamma_{p,L}^{(\ell)}$ and $\dot\gamma_{p,R}^{(\ell)}$, which have to be inserted into the $(\ell+1)$-loop equation (3.10c) for computing $\dot\gamma_{p,C}^{(\ell+1)}$, are crossing-symmetric w.r.t $\mathcal{S}_1$ and $\mathcal{S}_2$ (cf. Eq. (4.55) below), since both incoming and both outgoing legs are attached to a fully crossing-symmetric vertex ($\dot\gamma_{\bar p}^{(\ell)}$ or Γ, respectively). Therefore, the last equality $(*)$ in Eq. (4.35b) holds generically for all p bubbles.

In loops, even with SU(2) symmetry a spin sum is in general necessary:

$$-\sum_\sigma$$

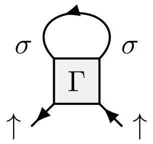

$$= -\Big[(V+\hat V)\,G_\uparrow + V G_\downarrow\Big] \overset{G_\uparrow = G_\downarrow}{=} -(2V+\hat V)G\,. \qquad (4.36)$$

An exception are diagrams where at least one of the external legs connects to a bare vertex, e.g. in 2nd order PT:

$$-\frac{1}{2}\sum_\sigma$$

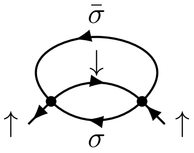

$$\overset{\text{two identical terms}}{=} \;-$$

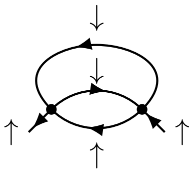

$$= -V_a^{\mathrm{PT2}} G_\downarrow\,. \qquad (4.37)$$

Here, the structure of the bare vertex (allowing only different spins to scatter) fixes the spin of the middle propagator line. Thus, in conjunction with crossing symmetry of the left and right bare vertex, it removes the spin sum (canceling the prefactor $1/2$, similar to the p bubble). The same holds accordingly for the second diagram in the SDE (3.5).

For systems without SU(2) symmetry, one needs to replace $V + \hat V$ in the t bubble and in the loop by the equal-spin components $\Gamma_{\sigma\sigma}$. Since the two components $\Gamma_{\sigma\sigma}$ are independent in this case, one additionally needs to compute them separately. The structure of the corresponding bubbles is similar, but involves a spin sum in the a channel as well.

4.3 Keldysh structure

Here we first briefly investigate the structure of bubbles and loops, before turning to the vertex Keldysh structure which requires more careful treatment.

For the bubbles, we define the Keldysh structure of the product of two propagators Π (Eq. (4.7)) as

$$\Pi^{\alpha_3\alpha_4|\alpha_3'\alpha_4'}(\nu_1,\nu_2) = G^{\alpha_3|\alpha_3'}(\nu_1)\, G^{\alpha_4|\alpha_4'}(\nu_2)\,. \qquad (4.38)$$

---

[7] Applying $\mathcal{S}_1$ on the left and $\mathcal{S}_2$ on the right only gives minus signs on both sides (which cancel) and exchanges the arguments of the propagator lines. With $G_\uparrow = G_\downarrow$, they are however indistinguishable.

With this definition we obtain from Eq. (4.2) (again dropping other quantum numbers)

$$B_a^{\alpha_1'\alpha_2'|\alpha_1\alpha_2} = \sum_{\alpha_3,\alpha_3',\alpha_4,\alpha_4'} \Gamma_L^{\alpha_1'\alpha_4'|\alpha_3\alpha_2}\, \Pi_a^{\alpha_3\alpha_4|\alpha_3'\alpha_4'}\, \Gamma_R^{\alpha_3'\alpha_2'|\alpha_1\alpha_4}\,, \tag{4.39a}$$

$$B_p^{\alpha_1'\alpha_2'|\alpha_1\alpha_2} = \frac{1}{2} \sum_{\alpha_3,\alpha_3',\alpha_4,\alpha_4'} \Gamma_L^{\alpha_1'\alpha_2'|\alpha_3\alpha_4}\, \Pi_p^{\alpha_3\alpha_4|\alpha_3'\alpha_4'}\, \Gamma_R^{\alpha_3'\alpha_4'|\alpha_1\alpha_2}\,, \tag{4.39b}$$

$$B_t^{\alpha_1'\alpha_2'|\alpha_1\alpha_2} = - \sum_{\alpha_3,\alpha_3',\alpha_4,\alpha_4'} \Gamma_L^{\alpha_4'\alpha_2'|\alpha_3\alpha_2}\, \Pi_t^{\alpha_3\alpha_4|\alpha_3'\alpha_4'}\, \Gamma_R^{\alpha_1'\alpha_3'|\alpha_1\alpha_4}\,. \tag{4.39c}$$

The sums over internal Keldysh indices can be further simplified, since each propagator has only three nonzero Keldysh components, $G^{2|1} = G^R, G^{1|2} = G^A, G^{2|2} = G^K$ (cf. Eq. (2.25)). The auxiliary object Π thus has 9 nonvanishing Keldysh components,

$$\Pi(\nu_1,\nu_2) = \begin{pmatrix} 0 & 0 & 0 & G^A(\nu_1)\,G^A(\nu_2) \\ 0 & 0 & G^A(\nu_1)\,G^R(\nu_2) & G^A(\nu_1)\,G^K(\nu_2) \\ 0 & G^R(\nu_1)\,G^A(\nu_2) & 0 & G^K(\nu_1)\,G^A(\nu_2) \\ G^R(\nu_1)\,G^R(\nu_2) & G^R(\nu_1)\,G^K(\nu_2) & G^K(\nu_1)\,G^R(\nu_2) & G^K(\nu_1)\,G^K(\nu_2) \end{pmatrix}. \tag{4.40}$$

Denoting a collection of four Keldysh indices as $i_j = (\alpha_{j_1}, \alpha_{j_2}|\alpha_{j_3}, \alpha_{j_4})$, we can write

$$B_r^{i_0} = \alpha_r \sum_{i_2 \in \mathcal{I}_\Pi} \Gamma_L^{i_1^r(i_0,i_2)}\, \Pi_r^{i_2}\, \Gamma_R^{i_3^r(i_0,i_2)}\,, \tag{4.41}$$

where the sum over i_2 only includes the nonzero components of Π,[8]

$$\mathcal{I}_\Pi = \{(11|22), (12|21), (12|22), (21|12), (21|22), (22|11), (22|12), (22|21), (22|22)\}\,. \tag{4.42}$$

For a given set of external Keldysh indices i_0, the Keldysh indices of the left and right vertex, i_1 and i_3, need to be determined for each $i_2 \in \mathcal{I}_\Pi$, and they differ between the three channels a, p, t. The corresponding combinations of indices can be read off from Eq. (4.39). With $i_0 = (\alpha_1'\alpha_2'|\alpha_1\alpha_2)$ and $i_2 = (\alpha_3\alpha_4|\alpha_3'\alpha_4')$, they read

$$i_1^a(i_0,i_2) = (\alpha_1'\alpha_4'|\alpha_3\alpha_2)\,, \quad i_3^a(i_0,i_2) = (\alpha_3'\alpha_2'|\alpha_1\alpha_4)\,, \tag{4.43a}$$

$$i_1^p(i_0,i_2) = (\alpha_1'\alpha_2'|\alpha_3\alpha_4)\,, \quad i_3^p(i_0,i_2) = (\alpha_3'\alpha_4'|\alpha_1\alpha_2)\,, \tag{4.43b}$$

$$i_1^t(i_0,i_2) = (\alpha_4'\alpha_2'|\alpha_3\alpha_2)\,, \quad i_3^t(i_0,i_2) = (\alpha_1'\alpha_3'|\alpha_1\alpha_4)\,, \tag{4.43c}$$

also described in [Agu20] (Sec. 2.4.1).

The Keldysh sum of the self-energy loop Eq. (4.3) only involves three terms, since it only contains a single propagator to be integrated over. Due to the Keldysh structure of the self-energy (Eq. (2.31)), we usually only need to compute loops for two combinations of external Keldysh indices (namely for $\Sigma^{1|2} = \Sigma^R$ and $\Sigma^{1|1} = \Sigma^K$). For these components, we have explicitly

$$L^{1|2} = -\left(\Gamma^{11|22}\, G^R + \Gamma^{12|21}\, G^A + \Gamma^{12|22}\, G^K\right)\,, \tag{4.44a}$$

$$L^{1|1} = -\left(\Gamma^{11|12}\, G^R + \Gamma^{12|11}\, G^A + \Gamma^{12|12}\, G^K\right)\,. \tag{4.44b}$$

---

[8] In the numerical implementation, we use a flattened version of the indices i_j, counting the components in Eq. (4.40) or Eq. (4.45) from left to right and top to bottom from 0 to 15. This is discussed in detail in [Agu20], Sec. 2.3.1; the flattened Keldysh indices are also denoted explicitly in Table 4.2. In this notation, we have $\mathcal{I}_\Pi \mathrel{\widehat{=}} \{3, 6, 7, 9, 11, 12, 13, 14, 15\}$.

Now let us investigate the Keldysh structure of the 4-point vertex. Generically, the vertex is a 4×4 matrix in Keldysh space,

$$\Gamma = \begin{pmatrix} 11|11 & 11|12 & 11|21 & 11|22 \\ 12|11 & 12|12 & 12|21 & 12|22 \\ 21|11 & 21|12 & 21|21 & 21|22 \\ 22|11 & 22|12 & 22|21 & 22|22 \end{pmatrix} . \tag{4.45}$$

Causality requires $\Gamma^{22|22} = 0$ (cf. Eq. (2.38) and the discussion there). We can further reduce the number of independent Keldysh components by considering parity symmetries (originating from the Keldysh structure of the bare vertex) and crossing symmetries and complex conjugation (generic properties of the 4-point vertex introduced in Chapter 2, Eqs. (2.41)). This will be discussed in the following two subsections.

4.3.1 Parity symmetries

The bare vertex only depends on the parity of the sum of the Keldysh indices, see Eq. (2.39). Therefore, all transformations that conjugate any pair of Keldysh indices simultaneously (see [Agu20], Sec. 3.3.3),

$\mathcal{P}^a_L(\alpha'_1\alpha'_2|\alpha_1\alpha_2) = (\bar{\alpha}'_1\alpha'_2|\alpha_1\bar{\alpha}_2)$: 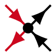 , $\mathcal{P}^a_R(\alpha'_1\alpha'_2|\alpha_1\alpha_2) = (\alpha'_1\bar{\alpha}'_2|\bar{\alpha}_1\alpha_2)$: 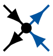 , (4.46a)

$\mathcal{P}^p_L(\alpha'_1\alpha'_2|\alpha_1\alpha_2) = (\bar{\alpha}'_1\bar{\alpha}'_2|\alpha_1\alpha_2)$: 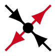 , $\mathcal{P}^p_R(\alpha'_1\alpha'_2|\alpha_1\alpha_2) = (\alpha'_1\alpha'_2|\bar{\alpha}_1\bar{\alpha}_2)$: 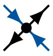 , (4.46b)

$\mathcal{P}^t_L(\alpha'_1\alpha'_2|\alpha_1\alpha_2) = (\alpha'_1\bar{\alpha}'_2|\alpha_1\bar{\alpha}_2)$: 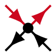 , $\mathcal{P}^t_R(\alpha'_1\alpha'_2|\alpha_1\alpha_2) = (\bar{\alpha}'_1\alpha'_2|\bar{\alpha}_1\alpha_2)$: 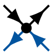 , (4.46c)

are symmetries of the bare vertex, $\Gamma_0 = \mathcal{P}^r_{L/R}\Gamma_0$, for all channels r. Here "conjugation" of Keldysh indices means $\bar{\alpha} = \{ {2 \atop 1}$ for $\alpha = \{ {1 \atop 2}$, and the red/blue arrows indicate graphically the positions of the indices that are affected by the corresponding transformation.

This has direct implications on the Keldysh structure of the asymptotic classes. As can directly be seen from the definition of the asymptotic classes, $\mathcal{P}^r_{L/R}$ are both symmetries of $\mathcal{K}^r_1$, and $\mathcal{P}^r_L$ ($\mathcal{P}^r_R$) is a symmetry of $\mathcal{K}^r_{2'}$ ($\mathcal{K}^r_2$):

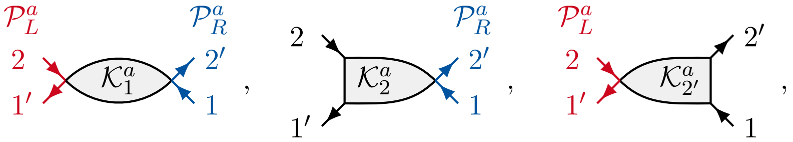
$\mathcal{P}^a_L$
2
1′
$\mathcal{K}^a_1$
$\mathcal{P}^a_R$
2′
1
,
2
$\mathcal{K}^a_2$
1′
$\mathcal{P}^a_R$
2′
1
,
$\mathcal{P}^a_L$
2
1′
$\mathcal{K}^a_{2'}$
2′
1
,
(4.47a)

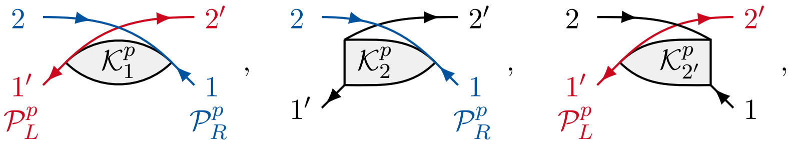
2
1′
$\mathcal{P}^p_L$
$\mathcal{K}^p_1$
2′
1
$\mathcal{P}^p_R$
,
2
1′
$\mathcal{K}^p_2$
2′
1
$\mathcal{P}^p_R$
,
2
1′
$\mathcal{P}^p_L$
$\mathcal{K}^p_{2'}$
2′
1
,
(4.47b)

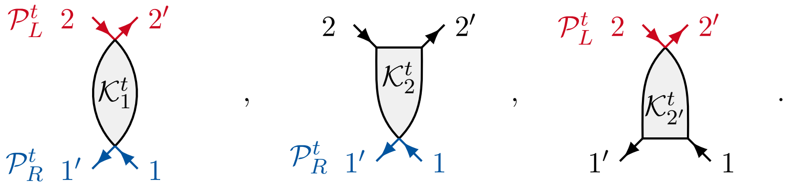
$\mathcal{P}^t_L$
2
2′
$\mathcal{K}^t_1$
$\mathcal{P}^t_R$
1′
1
,
2
2′
$\mathcal{K}^t_2$
$\mathcal{P}^t_R$
1′
1
,
$\mathcal{P}^t_L$
2
2′
$\mathcal{K}^t_{2'}$
1′
1
.
(4.47c)

Here applying the transformations $\mathcal{P}^r_{L/R}$ at the indicated positions does not change the value of the corresponding asymptotic class. The Keldysh structure of $\mathcal{K}^r_1$ and $\mathcal{K}^r_{2(')}$ thus simplifies as follows,

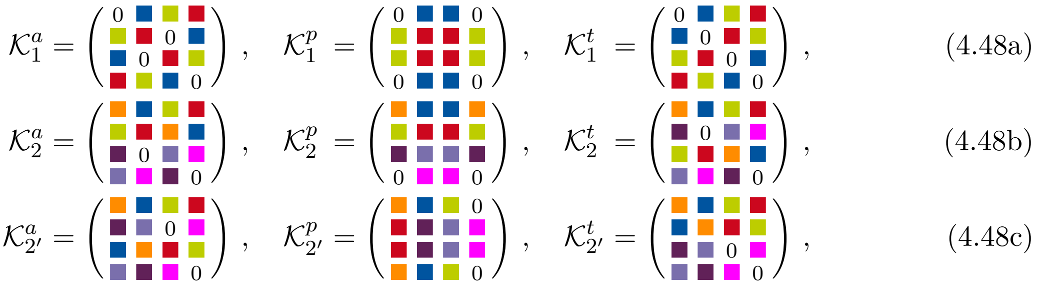

where boxes with the same color indicate Keldysh components that are equal, as they are connected by parity transformations. All zero components are symmetry-related to the (22|22) component, which is zero by causality. The number of independent Keldysh components thereby already reduces from 15 to 7 for $\mathcal{K}_{2^{(\prime)}}$, and to 3 for $\mathcal{K}_1$. Further simplifications are obtained by the application of crossing symmetries.

4.3.2 Crossing symmetries and complex conjugation

4.3.2.1 Symmetry transformations

The general symmetries $\mathcal{S}_1, \mathcal{S}_2, \mathcal{S}_3, \mathcal{S}_\mathcal{C}$ have already been introduced in Chapter 2, Eqs. (2.41) and (2.43). We can use them to additionally simplify the vertex: We can relate two Keldysh and spin components, if we simultaneously transform the frequencies (and other quantum numbers) accordingly. For this purpose, we define further transformations[9]:

$$\begin{aligned}
\text{incoming legs } (\mathcal{S}_1): &\quad \mathcal{T}_1\,\Gamma(\nu_1'\nu_2'|\nu_1\nu_2;q_1'q_2'|q_1q_2) = -\Gamma(\nu_1'\nu_2'|\nu_2\nu_1;q_1'q_2'|q_2q_1)\,, &(4.49\text{a})\\
\text{outgoing legs } (\mathcal{S}_2): &\quad \mathcal{T}_2\,\Gamma(\nu_1'\nu_2'|\nu_1\nu_2;q_1'q_2'|q_1q_2) = -\Gamma(\nu_2'\nu_1'|\nu_1\nu_2;q_2'q_1'|q_1q_2)\,, &(4.49\text{b})\\
\text{inc.} + \text{outg. legs } (\mathcal{S}_3): &\quad \mathcal{T}_3\,\Gamma(\nu_1'\nu_2'|\nu_1\nu_2;q_1'q_2'|q_1q_2) = +\Gamma(\nu_2'\nu_1'|\nu_2\nu_1;q_2'q_1'|q_2q_1)\,, &(4.49\text{c})\\
\text{comp. conj. } (\mathcal{S}_\mathcal{C}): &\quad \mathcal{T}_\mathcal{C}\,\Gamma(\nu_1'\nu_2'|\nu_1\nu_2;q_1'q_2'|q_1q_2) = (-1)^{1+P_\alpha}\Big[\Gamma(\nu_1\nu_2|\nu_1'\nu_2';q_1q_2|q_1'q_2')\Big]^*\,. &(4.49\text{d})
\end{aligned}$$

Note that these transformations only manipulate frequencies (and other quantum numbers such as momenta, orbitals, etc.), while Keldysh and spin indices are not affected and thus dropped in Eq. (4.49) for clarity. The translation of Eq. (4.49) into the natural parametrizations of the channels is straightforward and given in Appendix A, Eq. (A.3).

Since we want to keep the following discussion general, without the assumption of SU(2) symmetry, we additionally need an auxiliary transformation that flips all spins,

$$\mathcal{T}_\mathcal{S}\,\Gamma_{\sigma_1'\sigma_2'|\sigma_1\sigma_2} = \Gamma_{\bar\sigma_1'\bar\sigma_2'|\bar\sigma_1\bar\sigma_2} \tag{4.50}$$

(trivial in the SU(2) symmetric case), while leaving all other quantum numbers (including Keldysh indices) unchanged.

---

[9] Note that this definition formally differs from the one given in [Agu20]: There, the transformations T_i are applied to the Keldysh and spin indices, while here they transform all other quantum numbers, including a sign prefactor. These two definitions are closely related and just different interpretations of the same symmetry relations: The lower equality signs instead of the upper ones in Eqs. (3.28)–(3.32) of [Agu20] would give the exact same definition as presented here. We use Eq. (4.49) here since it defines what has to be done in an actual calculation: transformations need to be applied to frequencies and other quantum numbers of some Keldysh component in order to get a symmetry-related one.

Using these transformations, we can relate different Keldysh/spin components to each other, e.g. (skip q's for simplicity)

$$\Gamma^{\alpha_1'\alpha_2'|\alpha_1\alpha_2}_{\sigma_1'\sigma_2'|\sigma_1\sigma_2}(\nu_1'\nu_2'|\nu_1\nu_2) \overset{\text{symmetry } \mathcal{S}_1}{=} -\Gamma^{\alpha_1'\alpha_2'|\alpha_2\alpha_1}_{\sigma_1'\sigma_2'|\sigma_2\sigma_1}(\nu_1'\nu_2'|\nu_2\nu_1) \overset{\text{def.}}{=} \mathcal{T}_1\Gamma^{\alpha_1'\alpha_2'|\alpha_2\alpha_1}_{\sigma_1'\sigma_2'|\sigma_2\sigma_1}(\nu_1'\nu_2'|\nu_1\nu_2)\,. \tag{4.51}$$

Equating the leftmost and rightmost side of this equation, we obtain a recipe for computing a Keldysh+spin component $\Gamma^{\alpha_1'\alpha_2'|\alpha_1\alpha_2}_{\sigma_1'\sigma_2'|\sigma_1\sigma_2}$ that we did not store in memory: Take the symmetry-related component $\Gamma^{\alpha_1'\alpha_2'|\alpha_2\alpha_1}_{\sigma_1'\sigma_2'|\sigma_2\sigma_1}$ and apply the corresponding symmetry transformation to its frequency arguments (and other quantum numbers).[10]

4.3.2.2 Mixing of channels, asymptotic classes and spin components

A further complication comes from the fact that some of the symmetries relate different diagrammatic channels, different asymptotic classes $\mathcal{K}_i$ and different spin components. This can all be understood on purely diagrammatic grounds, viewing these symmetries as mirror symmetries of the diagrams along their diagonals, as already mentioned in Chapter 2 (also explained in detail in [Agu20], Sec. 3.3). The crossing symmetries relate the a and t channel and their asymptotic classes $\mathcal{K}_2^{a,t}$, $\mathcal{K}_{2'}^{a,t}$ as follows:

exchange incoming legs ($\mathcal{S}_1$) :

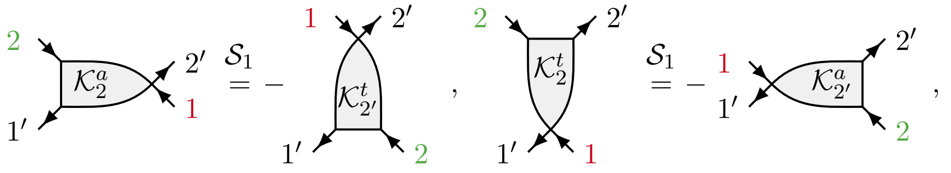

(4.52a)

exchange outgoing legs ($\mathcal{S}_2$) :

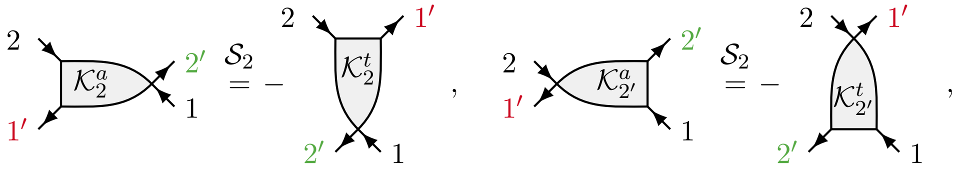

(4.52b)

---

[10] There is an important subtlety involving the order in which several (noncommuting) transformations have to be applied: Assume we have obtained the relation $B(\omega_r,\nu_r,\nu_r') = \mathcal{T}_i\mathcal{T}_j A(\omega_r,\nu_r,\nu_r')$ between two Keldysh components A and B (noted in this order in Table 4.2). We use this to only compute and store A in a numerical calculation, and if we need B, we will employ this relation to obtain it from A. However, since we want to evaluate B at some given frequency arguments (ω_r,ν_r,ν_r'), we need to apply the *inverse* transformation on those frequency arguments in order to obtain the correct arguments at which to evaluate A. Inverting the transformation amounts to an exchange of the order of the two transformations, since all transformations are self-inverse, $(\mathcal{T}_i\mathcal{T}_j)^{-1} = \mathcal{T}_j^{-1}\mathcal{T}_i^{-1} = \mathcal{T}_j\mathcal{T}_i$.
Example: We see from Table 4.2 that $(\mathcal{K}_3^a)^{21|11}_{\sigma\bar{\sigma}|\bar{\sigma}\sigma} = \mathcal{T}_S\mathcal{T}_C\mathcal{T}_1(\mathcal{K}_3^t)^{11|12}_{\sigma\bar{\sigma}|\sigma\bar{\sigma}}$. We want to compute $(\mathcal{K}_3^a)^{21|11}_{\sigma\bar{\sigma}|\bar{\sigma}\sigma}$ at frequencies (ω_a,ν_a,ν_a'), therefore, we need to apply the inverse transformation, $\mathcal{T}_1\mathcal{T}_C$ ($\mathcal{T}_S$ has no effect on frequencies), in order to obtain the frequencies at which we have to evaluate $(\mathcal{K}_3^t)^{11|12}_{\sigma\bar{\sigma}|\sigma\bar{\sigma}}$ instead. This is important since $\mathcal{T}_1\mathcal{T}_C(\omega_a,\nu_a,\nu_a') = \mathcal{T}_1(\omega_a,\nu_a',\nu_a) = (-\omega_t,\nu_t,\nu_t') \neq \mathcal{T}_C\mathcal{T}_1(\omega_a,\nu_a,\nu_a') = \mathcal{T}_C(-\omega_t,\nu_t',\nu_t) = (\omega_t,\nu_t',\nu_t)$.

exchange incoming and outgoing legs ($\mathcal{S}_3$) :

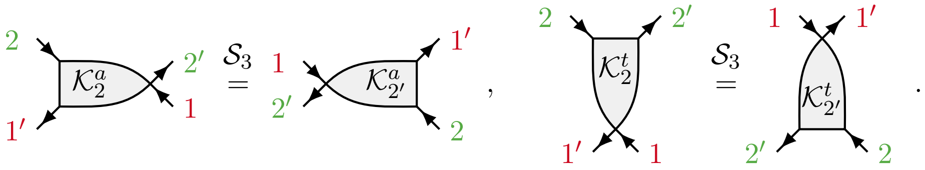

(4.52c)

Similarly, $\mathcal{S}_1$ and $\mathcal{S}_2$ transform between $\mathcal{K}_1^a \longleftrightarrow \mathcal{K}_1^t$ and $\mathcal{K}_3^a \longleftrightarrow \mathcal{K}_3^t$. In the p channel, the asymptotic classes are not mixed by these symmetries.

Complex conjugation ($\mathcal{S}_\mathcal{C}$) can be understood as reversing the direction of the arrows of the legs, since it transforms unbarred fields into barred ones, corresponding to mirroring diagrams at the vertical axis. It thus relates the following asymptotic classes:

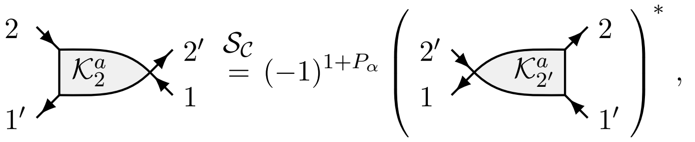

(4.53a)

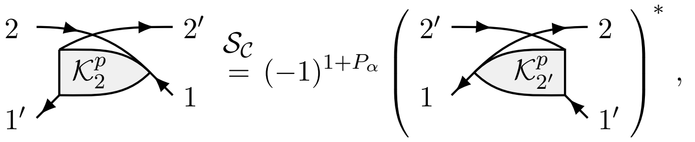

(4.53b)

while $\mathcal{K}_{2^{(\prime)}}^t$ and $\mathcal{K}_1^r$ and $\mathcal{K}_3^r$ are not mixed.

The spin components transform as follows:

$$V = \Gamma_{\sigma\bar{\sigma}|\sigma\bar{\sigma}} \xleftrightarrow{\mathcal{S}_1} \Gamma_{\sigma\bar{\sigma}|\bar{\sigma}\sigma} = \hat{V}\,, \qquad V = \Gamma_{\sigma\bar{\sigma}|\sigma\bar{\sigma}} \xleftrightarrow{\mathcal{S}_2} \Gamma_{\bar{\sigma}\sigma|\sigma\bar{\sigma}} = \mathcal{T}_\mathcal{S}\hat{V}\,, \tag{4.54a}$$

$$V = \Gamma_{\sigma\bar{\sigma}|\sigma\bar{\sigma}} \xleftrightarrow{\mathcal{S}_3} \Gamma_{\bar{\sigma}\sigma|\bar{\sigma}\sigma} = \mathcal{T}_\mathcal{S}V\,, \quad \hat{V} = \Gamma_{\sigma\bar{\sigma}|\bar{\sigma}\sigma} \xleftrightarrow{\mathcal{S}_3} \Gamma_{\bar{\sigma}\sigma|\sigma\bar{\sigma}} = \mathcal{T}_\mathcal{S}\hat{V}\,, \tag{4.54b}$$

$$V = \Gamma_{\sigma\bar{\sigma}|\sigma\bar{\sigma}} \xleftrightarrow{\mathcal{S}_\mathcal{C}} \Gamma_{\sigma\bar{\sigma}|\sigma\bar{\sigma}} = V\,, \qquad \hat{V} = \Gamma_{\sigma\bar{\sigma}|\bar{\sigma}\sigma} \xleftrightarrow{\mathcal{S}_\mathcal{C}} \Gamma_{\bar{\sigma}\sigma|\sigma\bar{\sigma}} = \mathcal{T}_\mathcal{S}\hat{V}\,. \tag{4.54c}$$

4.3.2.3 Treatment of nonsymmetric vertices

The full vertex as well as the reducible vertices γ_p and $\gamma_a + \gamma_t$ always fulfill all of the above symmetries (where γ_a and γ_t are related by $\mathcal{S}_1, \mathcal{S}_2$). However, one can construct diagrams that do not fulfill crossing symmetries on their own, and such contributions do occur in the multiloop flow equations. More precisely, the contributions $\dot{\gamma}_{r,L/R}^{(\ell)}$ in Eq. (3.10) consist of a differentiated vertex on the left/right and a full vertex on the other side and thus are clearly not left-right symmetric. This is in principle not an issue since the left and right part always appear together in the flow equations, and the sum is symmetric again. However, when computing the central part $\dot{\gamma}_{r,C}^{(\ell)}$, we need to insert either $\dot{\gamma}_{\bar{r},L}^{(\ell-1)}$ or $\dot{\gamma}_{\bar{r},R}^{(\ell-1)}$ on the right/left side of an r bubble, and for this, in numerics we temporarily need to store such a nonsymmetric vertex. Fortunately, it is still possible to only compute part of e.g. $\dot{\gamma}_{r,L}^{(\ell)}$ by reconstructing the rest from $\dot{\gamma}_{r,R}^{(\ell)}$. If for a certain Keldysh/spin component of $\dot{\gamma}_{r,L}^{(\ell)}$ a symmetry transformation is used that relates these two parts, the corresponding values are read from $\dot{\gamma}_{r,R}^{(\ell)}$ instead.

Generally, the crossing symmetries and complex conjugation relate such nonsymmetric vertices as follows[11]:

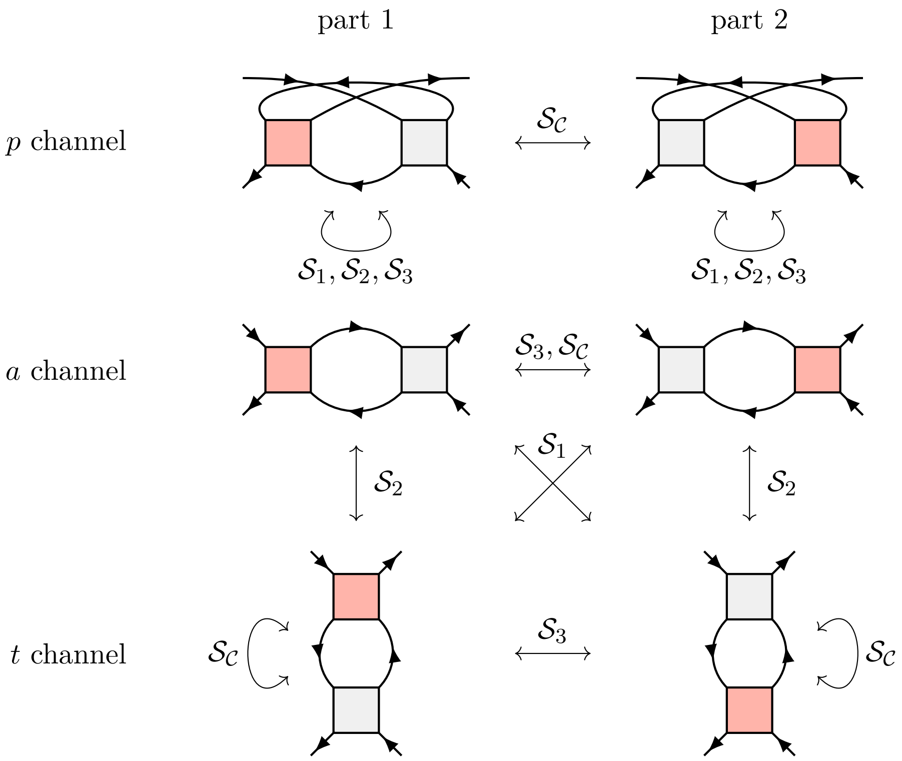

(4.55)

Whenever we would like to make use of the symmetry $\mathcal{S}_C$ for a component of a nonsymmetric vertex in the a or p channel, or of the symmetry $\mathcal{S}_1$ or $\mathcal{S}_3$ in the a or t channel, we need to access the symmetry-related part. This procedure requires that we always compute both types of nonsymmetric vertices in order to have full access to either of them. Again, this is no actual constraint for a multiloop flow, since both parts appear in the flow equations (3.10). Note that a similar asymmetry seems to appear in the Bethe-Salpeter equations (3.8), where an r-irreducible vertex and a full vertex are connected by an r bubble. However, since the result is the reducible vertex γ_r, it *does* in fact fulfill the crossing symmetries. A potential numerical asymmetry can be cured by computing both equivalent forms of the BSE (irreducible vertex inserted on the left or right side of the bubble) and symmetrizing the result.

Nonsymmetric vertices also arise in the multiloop corrections to the self-energy flow (cf. Eq. (3.12)): The vertex $\dot{\gamma}_{\bar{t},C}$ contains only diagrams reducible in the a and p channel, but no t-reducible diagrams, and is thus not crossing-symmetric. As a consequence, the numerical implementation of $\dot{\gamma}_{\bar{t},C} = \dot{\gamma}_{a,C} + \dot{\gamma}_{p,C}$ needs to have access to $\dot{\gamma}_{t,C}$ as well in order to make use of symmetry relations involving $\dot{\gamma}_{a,C}$.

A summary of all considerations of the last three subsections is given in Table 4.1.

4.3.2.4 Simplification of the Keldysh structure

By repeatedly applying these symmetry transformations, one can find symmetry-related Keldysh/spin components and thereby reduce the number of independent components that

---

[11] Note that in the p channel, $\mathcal{S}_1$, $\mathcal{S}_2$ and $\mathcal{S}_3$ do not mix nonsymmetric vertices. Instead, $\mathcal{S}_1$ only acts on the vertex on the right of the p bubble, and $\mathcal{S}_2$ only acts on the vertex on the left. $\mathcal{S}_3$ thus acts on both vertices *independently*. Similarly, nonsymmetric diagrams in the t channel are not mixed by $\mathcal{S}_C$.

Table 4.1 Crossing symmetries $\mathcal{S}_1, \mathcal{S}_2, \mathcal{S}_3$ and complex conjugation symmetry $\mathcal{S}_\mathcal{C}$, and their effect of mixing channels, asymptotic classes ($\mathcal{K}_2^r$, $\mathcal{K}_{2'}^r$) and spin components, and the corresponding symmetry transformations that need to be applied when using the symmetries to simplify the Keldysh structure. The column "asym." denotes in which channels each symmetry relates two nonsymmetric vertices (cf. Eq. (4.55)).

symmetry	channel	diag. class	spin	asym.	transf.	sign	frequencies
$\mathcal{S}_1 \circlearrowleft {}^{1'2'\vert 12}_{1'2'\vert 21}$	$a \leftrightarrow t$	$\mathcal{K}_2^{a,t} \leftrightarrow \mathcal{K}_{2'}^{t,a}$	$V \leftrightarrow \hat{V}$	a, t	$\mathcal{T}_1$	$-$	$(\omega_a, \nu_a, \nu'_a) \leftrightarrow (-\omega_t, \nu'_t, \nu_t)$ $(\omega_p, \nu_p, \nu'_p) \leftrightarrow (\omega_p, \nu_p, -\nu'_p)$
$\mathcal{S}_2 \circlearrowleft {}^{1'2'\vert 12}_{2'1'\vert 12}$	$a \leftrightarrow t$		$V \leftrightarrow \mathcal{T}_\mathcal{S}\hat{V}$		$\mathcal{T}_2$	$-$	$(\omega_a, \nu_a, \nu'_a) \leftrightarrow (\omega_t, \nu_t, \nu'_t)$ $(\omega_p, \nu_p, \nu'_p) \leftrightarrow (\omega_p, -\nu_p, \nu'_p)$
$\mathcal{S}_3 \circlearrowleft {}^{1'2'\vert 12}_{2'1'\vert 21}$		$\mathcal{K}_2^{a,t} \leftrightarrow \mathcal{K}_{2'}^{a,t}$	$V \leftrightarrow \mathcal{T}_\mathcal{S} V$ $\hat{V} \leftrightarrow \mathcal{T}_\mathcal{S}\hat{V}$	a, t	$\mathcal{T}_3$	$+$	$(\omega_a, \nu_a, \nu'_a) \leftrightarrow (-\omega_a, \nu'_a, \nu_a)$ $(\omega_p, \nu_p, \nu'_p) \leftrightarrow (\omega_p, -\nu_p, -\nu'_p)$ $(\omega_t, \nu_t, \nu'_t) \leftrightarrow (-\omega_t, \nu'_t, \nu_t)$
$\mathcal{S}_\mathcal{C} \circlearrowleft {}^{1'2'\vert 12}_{12\vert 1'2'}$		$\mathcal{K}_2^{a,p} \leftrightarrow \mathcal{K}_{2'}^{a,p}$	$V \leftrightarrow V$ $\hat{V} \leftrightarrow \mathcal{T}_\mathcal{S}\hat{V}$	a, p	$\mathcal{T}_\mathcal{C}$	$(-)^{1+P_\alpha}$	$(\omega_a, \nu_a, \nu'_a) \leftrightarrow (\omega_a, \nu'_a, \nu_a)$ $(\omega_p, \nu_p, \nu'_p) \leftrightarrow (\omega_p, \nu'_p, \nu_p)$ $(\omega_t, \nu_t, \nu'_t) \leftrightarrow (-\omega_t, \nu_t, \nu'_t)$

have to be computed numerically. This is particularly efficient for the asymptotic classes $\mathcal{K}_1$, $\mathcal{K}_{2^{(\prime)}}$, where the Keldysh structure is already simpler due to the parity symmetries discussed above.

We exemplify this derivation by investigating the Keldysh structure of the V ($\hat{V}$) component of $\mathcal{K}_1^a$ ($\mathcal{K}_1^t$):

$$\mathcal{K}^a_{1,\sigma\bar{\sigma}|\sigma\bar{\sigma}} = \begin{pmatrix} 0 & \bar{B}_1^a & \mathcal{T}_3\bar{B}_1^a & \bar{C}_1^a \\ \mathcal{T}_3\bar{B}_1^a & \bar{C}_1^a & 0 & \bar{B}_1^a \\ \bar{B}_1^a & 0 & \bar{C}_1^a & \mathcal{T}_3\bar{B}_1^a \\ \bar{C}_1^a & \mathcal{T}_3\bar{B}_1^a & \bar{B}_1^a & 0 \end{pmatrix} \underset{\mathcal{S}_1}{\overset{\mathcal{S}_2}{\begin{matrix} \longleftrightarrow \\ \times \\ \longleftrightarrow \end{matrix}}} \begin{pmatrix} 0 & \mathcal{T}_2\bar{B}_1^a & \mathcal{T}_1\bar{B}_1^a & \mathcal{T}_1\bar{C}_1^a \\ \mathcal{T}_2\bar{B}_1^a & 0 & \mathcal{T}_1\bar{C}_1^a & \mathcal{T}_1\bar{B}_1^a \\ \mathcal{T}_1\bar{B}_1^a & \mathcal{T}_1\bar{C}_1^a & 0 & \mathcal{T}_2\bar{B}_1^a \\ \mathcal{T}_1\bar{C}_1^a & \mathcal{T}_1\bar{B}_1^a & \mathcal{T}_2\bar{B}_1^a & 0 \end{pmatrix} = \mathcal{K}^t_{1,\sigma\bar{\sigma}|\bar{\sigma}\sigma} \, . \tag{4.56}$$

$\mathcal{S}_1$ relates columns of $\mathcal{K}^a_{1,\sigma\bar{\sigma}|\sigma\bar{\sigma}}$ to columns of $\mathcal{K}^t_{1,\sigma\bar{\sigma}|\bar{\sigma}\sigma}$, $\mathcal{S}_2$ relates rows. $\mathcal{S}_3 = \mathcal{S}_1\mathcal{S}_2$ does not switch between channels, but relates components within the same channel. Combining the parity symmetries Eq. (4.48) and the crossing symmetries, one can reduce the naively 30 components of $\mathcal{K}^a_{1,\sigma\bar{\sigma}|\sigma\bar{\sigma}}$ and $\mathcal{K}^t_{1,\sigma\bar{\sigma}|\bar{\sigma}\sigma}$ to 2, which we call $\bar{B}_1^a$ and $\bar{C}_1^a$.

The result of this analysis in all channels and asymptotic classes is presented in Table 4.2. Effectively, the number of independent Keldysh components is reduced to 2 for $\mathcal{K}_1^r$ in each channel r, to 5 per channel for $\mathcal{K}_2^r$ and $\mathcal{K}_{2'}^r$ together, and to 6 per channel for $\mathcal{K}_3^r$. In the SU(2)-symmetric case, only a single spin component $V = \Gamma_{\sigma\bar{\sigma}|\sigma\bar{\sigma}}$ needs to be computed explicitly.

Table 4.2 Independent Keldysh components and transformations between symmetry-related components for all asymptotic classes $\mathcal{K}_1^r$, $\mathcal{K}_2^r$, $\mathcal{K}_{2'}^r$, $\mathcal{K}_3^r$ in all channels $r = a, p, t$ and both equal-spin and different-spin sectors. Components in the different-spin sector are denoted with a bar. This table was derived in collaboration with Santiago Aguirre and thus is presented in similar form in [Agu20] (Tables 3.1–3.5).

		$\sigma\sigma\|\sigma\sigma$			$\sigma\bar{\sigma}\|\sigma\bar{\sigma}$			$\sigma\bar{\sigma}\|\bar{\sigma}\sigma$		
		$\mathcal{K}_1^a$	$\mathcal{K}_1^p$	$\mathcal{K}_1^t$	$\mathcal{K}_1^a$	$\mathcal{K}_1^p$	$\mathcal{K}_1^t$	$\mathcal{K}_1^a$	$\mathcal{K}_1^p$	$\mathcal{K}_1^t$
11|11	0	0	0	0	0	0	0	0	0	0
11|12	1	B_1^a	B_1^p	B_1^t	$\bar{B}_1^a$	$\bar{B}_1^p$	$\bar{B}_1^t$	$\mathcal{T}_S\mathcal{T}_2\bar{B}_1^t$	$\mathcal{T}_1\bar{B}_1^p$	$\mathcal{T}_S\mathcal{T}_2\bar{B}_1^a$
11|21	2	$\mathcal{T}_3B_1^a$	B_1^p	$\mathcal{T}_3B_1^t$	$\mathcal{T}_S\mathcal{T}_3\bar{B}_1^a$	$\bar{B}_1^p$	$\mathcal{T}_S\mathcal{T}_3\bar{B}_1^t$	$\mathcal{T}_1\bar{B}_1^t$	$\mathcal{T}_1\bar{B}_1^p$	$\mathcal{T}_1\bar{B}_1^a$
11|22	3	C_1^a	0	C_1^t	$\bar{C}_1^a$	0	$\bar{C}_1^t$	$\mathcal{T}_1\bar{C}_1^t$	0	$\mathcal{T}_1\bar{C}_1^a$
12|11	4	$\mathcal{T}_3B_1^a$	$\mathcal{T}_CB_1^p$	B_1^t	$\mathcal{T}_S\mathcal{T}_3\bar{B}_1^a$	$\mathcal{T}_C\bar{B}_1^p$	$\bar{B}_1^t$	$\mathcal{T}_1\bar{B}_1^t$	$\mathcal{T}_1\mathcal{T}_C\bar{B}_1^p$	$\mathcal{T}_S\mathcal{T}_2\bar{B}_1^a$
12|12	5	C_1^a	D_1^p	0	$\bar{C}_1^a$	$\bar{D}_1^p$	0	$\mathcal{T}_1\bar{C}_1^t$	$\mathcal{T}_1\bar{D}_1^p$	0
12|21	6	0	D_1^p	C_1^t	0	$\bar{D}_1^p$	$\bar{C}_1^t$	0	$\mathcal{T}_1\bar{D}_1^p$	$\mathcal{T}_1\bar{C}_1^a$
12|22	7	B_1^a	$\mathcal{T}_CB_1^p$	$\mathcal{T}_3B_1^t$	$\bar{B}_1^a$	$\mathcal{T}_C\bar{B}_1^p$	$\mathcal{T}_S\mathcal{T}_3\bar{B}_1^t$	$\mathcal{T}_S\mathcal{T}_2\bar{B}_1^t$	$\mathcal{T}_1\mathcal{T}_C\bar{B}_1^p$	$\mathcal{T}_1\bar{B}_1^a$
21|11	8	B_1^a	$\mathcal{T}_CB_1^p$	$\mathcal{T}_3B_1^t$	$\bar{B}_1^a$	$\mathcal{T}_C\bar{B}_1^p$	$\mathcal{T}_S\mathcal{T}_3\bar{B}_1^t$	$\mathcal{T}_S\mathcal{T}_2\bar{B}_1^t$	$\mathcal{T}_1\mathcal{T}_C\bar{B}_1^p$	$\mathcal{T}_1\bar{B}_1^a$
21|12	9	0	D_1^p	C_1^t	0	$\bar{D}_1^p$	$\bar{C}_1^t$	0	$\mathcal{T}_1\bar{D}_1^p$	$\mathcal{T}_1\bar{C}_1^a$
21|21	10	C_1^a	D_1^p	0	$\bar{C}_1^a$	$\bar{D}_1^p$	0	$\mathcal{T}_1\bar{C}_1^t$	$\mathcal{T}_1\bar{D}_1^p$	0
21|22	11	$\mathcal{T}_3B_1^a$	$\mathcal{T}_CB_1^p$	B_1^t	$\mathcal{T}_S\mathcal{T}_3\bar{B}_1^a$	$\mathcal{T}_C\bar{B}_1^p$	$\bar{B}_1^t$	$\mathcal{T}_1\bar{B}_1^t$	$\mathcal{T}_1\mathcal{T}_C\bar{B}_1^p$	$\mathcal{T}_S\mathcal{T}_2\bar{B}_1^a$
22|11	12	C_1^a	0	C_1^t	$\bar{C}_1^a$	0	$\bar{C}_1^t$	$\mathcal{T}_1\bar{C}_1^t$	0	$\mathcal{T}_1\bar{C}_1^a$
22|12	13	$\mathcal{T}_3B_1^a$	B_1^p	$\mathcal{T}_3B_1^t$	$\mathcal{T}_S\mathcal{T}_3\bar{B}_1^a$	$\bar{B}_1^p$	$\mathcal{T}_S\mathcal{T}_3\bar{B}_1^t$	$\mathcal{T}_1\bar{B}_1^t$	$\mathcal{T}_1\bar{B}_1^p$	$\mathcal{T}_1\bar{B}_1^a$
22|21	14	B_1^a	B_1^p	B_1^t	$\bar{B}_1^a$	$\bar{B}_1^p$	$\bar{B}_1^t$	$\mathcal{T}_S\mathcal{T}_2\bar{B}_1^t$	$\mathcal{T}_1\bar{B}_1^p$	$\mathcal{T}_S\mathcal{T}_2\bar{B}_1^a$
22|22	15	0	0	0	0	0	0	0	0	0
		$\mathcal{K}_2^a$	$\mathcal{K}_2^p$	$\mathcal{K}_2^t$	$\mathcal{K}_2^a$	$\mathcal{K}_2^p$	$\mathcal{K}_2^t$	$\mathcal{K}_2^a$	$\mathcal{K}_2^p$	$\mathcal{K}_2^t$
11|11	0	A_2^a	A_2^p	$\mathcal{T}_2A_2^a$	$\bar{A}_2^a$	$\bar{A}_2^p$	$\bar{A}_2^t$	$\mathcal{T}_S\mathcal{T}_2\bar{A}_2^t$	$\mathcal{T}_1\bar{A}_2^p$	$\mathcal{T}_S\mathcal{T}_2\bar{A}_2^a$
11|12	1	B_2^a	B_2^p	$\mathcal{T}_2B_2^a$	$\bar{B}_2^a$	$\bar{B}_2^p$	$\bar{B}_2^t$	$\mathcal{T}_S\mathcal{T}_2\bar{B}_2^t$	$\mathcal{T}_1\bar{B}_2^p$	$\mathcal{T}_S\mathcal{T}_2\bar{B}_2^a$
11|21	2	C_2^a	B_2^p	$\mathcal{T}_2C_2^a$	$\bar{C}_2^a$	$\bar{B}_2^p$	$\bar{C}_2^t$	$\mathcal{T}_S\mathcal{T}_2\bar{C}_2^t$	$\mathcal{T}_1\bar{B}_2^p$	$\mathcal{T}_S\mathcal{T}_2\bar{C}_2^a$
11|22	3	D_2^a	A_2^p	$\mathcal{T}_2D_2^a$	$\bar{D}_2^a$	$\bar{A}_2^p$	$\bar{D}_2^t$	$\mathcal{T}_S\mathcal{T}_2\bar{D}_2^t$	$\mathcal{T}_1\bar{A}_2^p$	$\mathcal{T}_S\mathcal{T}_2\bar{D}_2^a$
12|11	4	C_2^a	C_2^p	$\mathcal{T}_C\mathcal{T}_2B_2^a$	$\bar{C}_2^a$	$\bar{C}_2^p$	$\mathcal{T}_C\bar{B}_2^t$	$\mathcal{T}_S\mathcal{T}_2\bar{C}_2^t$	$\mathcal{T}_1\bar{C}_2^p$	$\mathcal{T}_1\mathcal{T}_C\bar{B}_2^a$
12|12	5	D_2^a	D_2^p	0	$\bar{D}_2^a$	$\bar{D}_2^p$	0	$\mathcal{T}_S\mathcal{T}_2\bar{D}_2^t$	$\mathcal{T}_1\bar{D}_2^p$	0
12|21	6	A_2^a	D_2^p	$\mathcal{T}_C\mathcal{T}_2D_2^a$	$\bar{A}_2^a$	$\bar{D}_2^p$	$\mathcal{T}_C\bar{D}_2^t$	$\mathcal{T}_S\mathcal{T}_2\bar{A}_2^t$	$\mathcal{T}_1\bar{D}_2^p$	$\mathcal{T}_1\mathcal{T}_C\bar{D}_2^a$
12|22	7	B_2^a	C_2^p	$\mathcal{T}_2F_2^a$	$\bar{B}_2^a$	$\bar{C}_2^p$	$\bar{F}_2^t$	$\mathcal{T}_S\mathcal{T}_2\bar{B}_2^t$	$\mathcal{T}_1\bar{C}_2^p$	$\mathcal{T}_S\mathcal{T}_2\bar{F}_2^a$
21|11	8	$\mathcal{T}_C\mathcal{T}_3B_2^a$	$\mathcal{T}_3C_2^p$	$\mathcal{T}_2C_2^a$	$\mathcal{T}_S\mathcal{T}_C\mathcal{T}_3\bar{B}_2^a$	$\mathcal{T}_S\mathcal{T}_3\bar{C}_2^p$	$\bar{C}_2^t$	$\mathcal{T}_S\mathcal{T}_C\mathcal{T}_1\bar{B}_2^t$	$\mathcal{T}_S\mathcal{T}_2\bar{C}_2^p$	$\mathcal{T}_S\mathcal{T}_2\bar{C}_2^a$
21|12	9	0	$\mathcal{T}_3D_2^p$	$\mathcal{T}_2D_2^a$	0	$\mathcal{T}_S\mathcal{T}_3\bar{D}_2^p$	$\bar{D}_2^t$	0	$\mathcal{T}_S\mathcal{T}_2\bar{D}_2^p$	$\mathcal{T}_S\mathcal{T}_2\bar{D}_2^a$
21|21	10	$\mathcal{T}_C\mathcal{T}_3D_2^a$	$\mathcal{T}_3D_2^p$	$\mathcal{T}_2A_2^a$	$\mathcal{T}_S\mathcal{T}_C\mathcal{T}_3\bar{D}_2^a$	$\mathcal{T}_S\mathcal{T}_3\bar{D}_2^p$	$\bar{A}_2^t$	$\mathcal{T}_S\mathcal{T}_C\mathcal{T}_1\bar{D}_2^t$	$\mathcal{T}_S\mathcal{T}_2\bar{D}_2^p$	$\mathcal{T}_S\mathcal{T}_2\bar{A}_2^a$
21|22	11	F_2^a	$\mathcal{T}_3C_2^p$	$\mathcal{T}_2B_2^a$	$\bar{F}_2^a$	$\mathcal{T}_S\mathcal{T}_3\bar{C}_2^p$	$\bar{B}_2^t$	$\mathcal{T}_S\mathcal{T}_2\bar{F}_2^t$	$\mathcal{T}_S\mathcal{T}_2\bar{C}_2^p$	$\mathcal{T}_S\mathcal{T}_2\bar{B}_2^a$
22|11	12	$\mathcal{T}_C\mathcal{T}_3D_2^a$	0	$\mathcal{T}_C\mathcal{T}_2D_2^a$	$\mathcal{T}_S\mathcal{T}_C\mathcal{T}_3\bar{D}_2^a$	0	$\mathcal{T}_C\bar{D}_2^t$	$\mathcal{T}_S\mathcal{T}_C\mathcal{T}_1\bar{D}_2^t$	0	$\mathcal{T}_1\mathcal{T}_C\bar{D}_2^a$
22|12	13	F_2^a	F_2^p	$\mathcal{T}_2F_2^a$	$\bar{F}_2^a$	$\bar{F}_2^p$	$\bar{F}_2^t$	$\mathcal{T}_S\mathcal{T}_2\bar{F}_2^t$	$\mathcal{T}_1\bar{F}_2^p$	$\mathcal{T}_S\mathcal{T}_2\bar{F}_2^a$
22|21	14	$\mathcal{T}_C\mathcal{T}_3B_2^a$	F_2^p	$\mathcal{T}_C\mathcal{T}_2B_2^a$	$\mathcal{T}_S\mathcal{T}_C\mathcal{T}_3\bar{B}_2^a$	$\bar{F}_2^p$	$\mathcal{T}_C\bar{B}_2^t$	$\mathcal{T}_S\mathcal{T}_C\mathcal{T}_1\bar{B}_2^t$	$\mathcal{T}_1\bar{F}_2^p$	$\mathcal{T}_1\mathcal{T}_C\bar{B}_2^a$
22|22	15	0	0	0	0	0	0	0	0	0

Table 4.2 (continued)

		$\sigma\sigma\vert\sigma\sigma$			$\sigma\bar{\sigma}\vert\sigma\bar{\sigma}$			$\sigma\bar{\sigma}\vert\bar{\sigma}\sigma$		
		$\mathcal{K}_{2'}^a$	$\mathcal{K}_{2'}^p$	$\mathcal{K}_{2'}^t$	$\mathcal{K}_{2'}^a$	$\mathcal{K}_{2'}^p$	$\mathcal{K}_{2'}^t$	$\mathcal{K}_{2'}^a$	$\mathcal{K}_{2'}^p$	$\mathcal{K}_{2'}^t$
1111	0	$\mathcal{T}_3 A_2^a$	$\mathcal{T}_\mathcal{C} A_2^p$	$\mathcal{T}_1 A_2^a$	$\mathcal{T}_\mathcal{S}\mathcal{T}_3 \bar{A}_2^a$	$\mathcal{T}_\mathcal{C} \bar{A}_2^p$	$\mathcal{T}_\mathcal{S}\mathcal{T}_3 \bar{A}_2^t$	$\mathcal{T}_1 \bar{A}_2^t$	$\mathcal{T}_\mathcal{S}\mathcal{T}_\mathcal{C}\mathcal{T}_1 \bar{A}_2^p$	$\mathcal{T}_1 \bar{A}_2^a$
1112	1	$\mathcal{T}_3 C_2^a$	$\mathcal{T}_\mathcal{C} C_2^p$	$\mathcal{T}_1 C_2^a$	$\mathcal{T}_\mathcal{S}\mathcal{T}_3 \bar{C}_2^a$	$\mathcal{T}_\mathcal{C} \bar{C}_2^p$	$\mathcal{T}_\mathcal{S}\mathcal{T}_3 \bar{C}_2^t$	$\mathcal{T}_1 \bar{C}_2^t$	$\mathcal{T}_\mathcal{S}\mathcal{T}_\mathcal{C}\mathcal{T}_1 \bar{C}_2^p$	$\mathcal{T}_1 \bar{C}_2^a$
1121	2	$\mathcal{T}_3 B_2^a$	$\mathcal{T}_\mathcal{C}\mathcal{T}_3 C_2^p$	$\mathcal{T}_1 B_2^a$	$\mathcal{T}_\mathcal{S}\mathcal{T}_3 \bar{B}_2^a$	$\mathcal{T}_\mathcal{S}\mathcal{T}_\mathcal{C}\mathcal{T}_3 \bar{C}_2^p$	$\mathcal{T}_\mathcal{S}\mathcal{T}_3 \bar{B}_2^t$	$\mathcal{T}_1 \bar{B}_2^t$	$\mathcal{T}_1\mathcal{T}_\mathcal{C} \bar{C}_2^p$	$\mathcal{T}_1 \bar{B}_2^a$
1122	3	$\mathcal{T}_3 D_2^a$	0	$\mathcal{T}_1 D_2^a$	$\mathcal{T}_\mathcal{S}\mathcal{T}_3 \bar{D}_2^a$	0	$\mathcal{T}_\mathcal{S}\mathcal{T}_3 \bar{D}_2^t$	$\mathcal{T}_1 \bar{D}_2^t$	0	$\mathcal{T}_1 \bar{D}_2^a$
1211	4	$\mathcal{T}_\mathcal{C} B_2^a$	$\mathcal{T}_\mathcal{C} B_2^p$	$\mathcal{T}_1 C_2^a$	$\mathcal{T}_\mathcal{C} \bar{B}_2^a$	$\mathcal{T}_\mathcal{C} \bar{B}_2^p$	$\mathcal{T}_\mathcal{S}\mathcal{T}_3 \bar{C}_2^t$	$\mathcal{T}_1\mathcal{T}_\mathcal{C} \bar{B}_2^t$	$\mathcal{T}_1\mathcal{T}_\mathcal{C} \bar{B}_2^p$	$\mathcal{T}_1 \bar{C}_2^a$
1212	5	$\mathcal{T}_\mathcal{C} D_2^a$	$\mathcal{T}_\mathcal{C} D_2^p$	$\mathcal{T}_1 A_2^a$	$\mathcal{T}_\mathcal{C} \bar{D}_2^a$	$\mathcal{T}_\mathcal{C} \bar{D}_2^p$	$\mathcal{T}_\mathcal{S}\mathcal{T}_3 \bar{A}_2^t$	$\mathcal{T}_1\mathcal{T}_\mathcal{C} \bar{D}_2^t$	$\mathcal{T}_\mathcal{S}\mathcal{T}_\mathcal{C}\mathcal{T}_1 \bar{D}_2^p$	$\mathcal{T}_1 \bar{A}_2^a$
1221	6	0	$\mathcal{T}_\mathcal{C}\mathcal{T}_3 D_2^p$	$\mathcal{T}_1 D_2^a$	0	$\mathcal{T}_\mathcal{S}\mathcal{T}_\mathcal{C}\mathcal{T}_3 \bar{D}_2^p$	$\mathcal{T}_\mathcal{S}\mathcal{T}_3 \bar{D}_2^t$	0	$\mathcal{T}_1\mathcal{T}_\mathcal{C} \bar{D}_2^p$	$\mathcal{T}_1 \bar{D}_2^a$
1222	7	$\mathcal{T}_3 F_2^a$	$\mathcal{T}_\mathcal{C} F_2^p$	$\mathcal{T}_1 B_2^a$	$\mathcal{T}_\mathcal{S}\mathcal{T}_3 \bar{F}_2^a$	$\mathcal{T}_\mathcal{C} \bar{F}_2^p$	$\mathcal{T}_\mathcal{S}\mathcal{T}_3 \bar{B}_2^t$	$\mathcal{T}_1 \bar{F}_2^t$	$\mathcal{T}_\mathcal{S}\mathcal{T}_\mathcal{C}\mathcal{T}_1 \bar{F}_2^p$	$\mathcal{T}_1 \bar{B}_2^a$
2111	8	$\mathcal{T}_3 C_2^a$	$\mathcal{T}_\mathcal{C} B_2^p$	$\mathcal{T}_\mathcal{C}\mathcal{T}_1 B_2^a$	$\mathcal{T}_\mathcal{S}\mathcal{T}_3 \bar{C}_2^a$	$\mathcal{T}_\mathcal{C} \bar{B}_2^p$	$\mathcal{T}_\mathcal{S}\mathcal{T}_\mathcal{C}\mathcal{T}_3 \bar{B}_2^t$	$\mathcal{T}_1 \bar{C}_2^t$	$\mathcal{T}_1\mathcal{T}_\mathcal{C} \bar{B}_2^p$	$\mathcal{T}_\mathcal{S}\mathcal{T}_\mathcal{C}\mathcal{T}_1 \bar{B}_2^a$
2112	9	$\mathcal{T}_3 A_2^a$	$\mathcal{T}_\mathcal{C} D_2^p$	$\mathcal{T}_\mathcal{C}\mathcal{T}_1 D_2^a$	$\mathcal{T}_\mathcal{S}\mathcal{T}_3 \bar{A}_2^a$	$\mathcal{T}_\mathcal{C} \bar{D}_2^p$	$\mathcal{T}_\mathcal{S}\mathcal{T}_\mathcal{C}\mathcal{T}_3 \bar{D}_2^t$	$\mathcal{T}_1 \bar{A}_2^t$	$\mathcal{T}_\mathcal{S}\mathcal{T}_\mathcal{C}\mathcal{T}_1 \bar{D}_2^p$	$\mathcal{T}_\mathcal{S}\mathcal{T}_\mathcal{C}\mathcal{T}_1 \bar{D}_2^a$
2121	10	$\mathcal{T}_3 D_2^a$	$\mathcal{T}_\mathcal{C}\mathcal{T}_3 D_2^p$	0	$\mathcal{T}_\mathcal{S}\mathcal{T}_3 \bar{D}_2^a$	$\mathcal{T}_\mathcal{S}\mathcal{T}_\mathcal{C}\mathcal{T}_3 \bar{D}_2^p$	0	$\mathcal{T}_1 \bar{D}_2^t$	$\mathcal{T}_1\mathcal{T}_\mathcal{C} \bar{D}_2^p$	0
2122	11	$\mathcal{T}_3 B_2^a$	$\mathcal{T}_\mathcal{C} F_2^p$	$\mathcal{T}_1 F_2^a$	$\mathcal{T}_\mathcal{S}\mathcal{T}_3 \bar{B}_2^a$	$\mathcal{T}_\mathcal{C} \bar{F}_2^p$	$\mathcal{T}_\mathcal{S}\mathcal{T}_3 \bar{F}_2^t$	$\mathcal{T}_1 \bar{B}_2^t$	$\mathcal{T}_\mathcal{S}\mathcal{T}_\mathcal{C}\mathcal{T}_1 \bar{F}_2^p$	$\mathcal{T}_1 \bar{F}_2^a$
2211	12	$\mathcal{T}_\mathcal{C} D_2^a$	$\mathcal{T}_\mathcal{C} A_2^p$	$\mathcal{T}_\mathcal{C}\mathcal{T}_1 D_2^a$	$\mathcal{T}_\mathcal{C} \bar{D}_2^a$	$\mathcal{T}_\mathcal{C} \bar{A}_2^p$	$\mathcal{T}_\mathcal{S}\mathcal{T}_\mathcal{C}\mathcal{T}_3 \bar{D}_2^t$	$\mathcal{T}_1\mathcal{T}_\mathcal{C} \bar{D}_2^t$	$\mathcal{T}_\mathcal{S}\mathcal{T}_\mathcal{C}\mathcal{T}_1 \bar{A}_2^p$	$\mathcal{T}_\mathcal{S}\mathcal{T}_\mathcal{C}\mathcal{T}_1 \bar{D}_2^a$
2212	13	$\mathcal{T}_\mathcal{C} B_2^a$	$\mathcal{T}_\mathcal{C} C_2^p$	$\mathcal{T}_\mathcal{C}\mathcal{T}_1 B_2^a$	$\mathcal{T}_\mathcal{C} \bar{B}_2^a$	$\mathcal{T}_\mathcal{C} \bar{C}_2^p$	$\mathcal{T}_\mathcal{S}\mathcal{T}_\mathcal{C}\mathcal{T}_3 \bar{B}_2^t$	$\mathcal{T}_1\mathcal{T}_\mathcal{C} \bar{B}_2^t$	$\mathcal{T}_\mathcal{S}\mathcal{T}_\mathcal{C}\mathcal{T}_1 \bar{C}_2^p$	$\mathcal{T}_\mathcal{S}\mathcal{T}_\mathcal{C}\mathcal{T}_1 \bar{B}_2^a$
2221	14	$\mathcal{T}_3 F_2^a$	$\mathcal{T}_\mathcal{C}\mathcal{T}_3 C_2^p$	$\mathcal{T}_1 F_2^a$	$\mathcal{T}_\mathcal{S}\mathcal{T}_3 \bar{F}_2^a$	$\mathcal{T}_\mathcal{S}\mathcal{T}_\mathcal{C}\mathcal{T}_3 \bar{C}_2^p$	$\mathcal{T}_\mathcal{S}\mathcal{T}_3 \bar{F}_2^t$	$\mathcal{T}_1 \bar{F}_2^t$	$\mathcal{T}_1\mathcal{T}_\mathcal{C} \bar{C}_2^p$	$\mathcal{T}_1 \bar{F}_2^a$
2222	15	0	0	0	0	0	0	0	0	0
		$\mathcal{K}_3^a$	$\mathcal{K}_3^p$	$\mathcal{K}_3^t$	$\mathcal{K}_3^a$	$\mathcal{K}_3^p$	$\mathcal{K}_3^t$	$\mathcal{K}_3^a$	$\mathcal{K}_3^p$	$\mathcal{K}_3^t$
1111	0	A_3^a	A_3^p	$\mathcal{T}_2 A_3^a$	$\bar{A}_3^a$	$\bar{A}_3^p$	$\bar{A}_3^t$	$\mathcal{T}_1 \bar{A}_3^t$	$\mathcal{T}_1 \bar{A}_3^p$	$\mathcal{T}_1 \bar{A}_3^a$
1112	1	B_3^a	B_3^p	$\mathcal{T}_2 B_3^a$	$\bar{B}_3^a$	$\bar{B}_3^p$	$\bar{B}_3^t$	$\mathcal{T}_\mathcal{S}\mathcal{T}_2 \bar{B}_3^t$	$\mathcal{T}_\mathcal{S}\mathcal{T}_2 \bar{B}_3^p$	$\mathcal{T}_\mathcal{S}\mathcal{T}_2 \bar{B}_3^a$
1121	2	$\mathcal{T}_3 B_3^a$	$\mathcal{T}_3 B_3^p$	$\mathcal{T}_1 B_3^a$	$\mathcal{T}_\mathcal{S}\mathcal{T}_3 \bar{B}_3^a$	$\mathcal{T}_\mathcal{S}\mathcal{T}_3 \bar{B}_3^p$	$\mathcal{T}_\mathcal{S}\mathcal{T}_3 \bar{B}_3^t$	$\mathcal{T}_1 \bar{B}_3^t$	$\mathcal{T}_1 \bar{B}_3^p$	$\mathcal{T}_1 \bar{B}_3^a$
1122	3	C_3^a	C_3^p	$\mathcal{T}_2 C_3^a$	$\bar{C}_3^a$	$\bar{C}_3^p$	$\bar{C}_3^t$	$\mathcal{T}_1 \bar{C}_3^t$	$\mathcal{T}_1 \bar{C}_3^p$	$\mathcal{T}_1 \bar{C}_3^a$
1211	4	$\mathcal{T}_\mathcal{C} B_3^a$	$\mathcal{T}_\mathcal{C} B_3^p$	$\mathcal{T}_1\mathcal{T}_\mathcal{C} B_3^a$	$\mathcal{T}_\mathcal{C} \bar{B}_3^a$	$\mathcal{T}_\mathcal{C} \bar{B}_3^p$	$\mathcal{T}_\mathcal{C} \bar{B}_3^t$	$\mathcal{T}_1\mathcal{T}_\mathcal{C} \bar{B}_3^t$	$\mathcal{T}_1\mathcal{T}_\mathcal{C} \bar{B}_3^p$	$\mathcal{T}_1\mathcal{T}_\mathcal{C} \bar{B}_3^a$
1212	5	D_3^a	D_3^p	D_3^t	$\bar{D}_3^a$	$\bar{D}_3^p$	$\bar{D}_3^t$	$\mathcal{T}_1 \bar{E}_3^t$	$\mathcal{T}_1 \bar{E}_3^p$	$\mathcal{T}_1 \bar{E}_3^a$
1221	6	$\mathcal{T}_1 D_3^t$	$\mathcal{T}_1 D_3^p$	$\mathcal{T}_1 D_3^a$	$\bar{E}_3^a$	$\bar{E}_3^p$	$\bar{E}_3^t$	$\mathcal{T}_1 \bar{D}_3^t$	$\mathcal{T}_1 \bar{D}_3^p$	$\mathcal{T}_1 \bar{D}_3^a$
1222	7	F_3^a	F_3^p	$\mathcal{T}_1 F_3^a$	$\bar{F}_3^a$	$\bar{F}_3^p$	$\bar{F}_3^t$	$\mathcal{T}_1 \bar{F}_3^t$	$\mathcal{T}_1 \bar{F}_3^p$	$\mathcal{T}_1 \bar{F}_3^a$
2111	8	$\mathcal{T}_\mathcal{C}\mathcal{T}_3 B_3^a$	$\mathcal{T}_\mathcal{C}\mathcal{T}_3 B_3^p$	$\mathcal{T}_\mathcal{C}\mathcal{T}_1 B_3^a$	$\mathcal{T}_\mathcal{S}\mathcal{T}_\mathcal{C}\mathcal{T}_3 \bar{B}_3^a$	$\mathcal{T}_\mathcal{S}\mathcal{T}_\mathcal{C}\mathcal{T}_3 \bar{B}_3^p$	$\mathcal{T}_\mathcal{S}\mathcal{T}_\mathcal{C}\mathcal{T}_3 \bar{B}_3^t$	$\mathcal{T}_\mathcal{S}\mathcal{T}_\mathcal{C}\mathcal{T}_1 \bar{B}_3^t$	$\mathcal{T}_\mathcal{S}\mathcal{T}_\mathcal{C}\mathcal{T}_1 \bar{B}_3^p$	$\mathcal{T}_\mathcal{S}\mathcal{T}_\mathcal{C}\mathcal{T}_1 \bar{B}_3^a$
2112	9	$\mathcal{T}_2 D_3^t$	$\mathcal{T}_2 D_3^p$	$\mathcal{T}_2 D_3^a$	$\mathcal{T}_\mathcal{S}\mathcal{T}_3 \bar{E}_3^a$	$\mathcal{T}_\mathcal{S}\mathcal{T}_3 \bar{E}_3^p$	$\mathcal{T}_\mathcal{S}\mathcal{T}_3 \bar{E}_3^t$	$\mathcal{T}_\mathcal{S}\mathcal{T}_2 \bar{D}_3^t$	$\mathcal{T}_\mathcal{S}\mathcal{T}_2 \bar{D}_3^p$	$\mathcal{T}_\mathcal{S}\mathcal{T}_2 \bar{D}_3^a$
2121	10	$\mathcal{T}_3 D_3^a$	$\mathcal{T}_3 D_3^p$	$\mathcal{T}_3 D_3^t$	$\mathcal{T}_\mathcal{S}\mathcal{T}_3 \bar{D}_3^a$	$\mathcal{T}_\mathcal{S}\mathcal{T}_3 \bar{D}_3^p$	$\mathcal{T}_\mathcal{S}\mathcal{T}_3 \bar{D}_3^t$	$\mathcal{T}_\mathcal{S}\mathcal{T}_2 \bar{E}_3^t$	$\mathcal{T}_\mathcal{S}\mathcal{T}_2 \bar{E}_3^p$	$\mathcal{T}_\mathcal{S}\mathcal{T}_2 \bar{E}_3^a$
2122	11	$\mathcal{T}_3 F_3^a$	$\mathcal{T}_3 F_3^p$	$\mathcal{T}_2 F_3^a$	$\mathcal{T}_\mathcal{S}\mathcal{T}_3 \bar{F}_3^a$	$\mathcal{T}_\mathcal{S}\mathcal{T}_3 \bar{F}_3^p$	$\mathcal{T}_\mathcal{S}\mathcal{T}_3 \bar{F}_3^t$	$\mathcal{T}_\mathcal{S}\mathcal{T}_2 \bar{F}_3^t$	$\mathcal{T}_\mathcal{S}\mathcal{T}_2 \bar{F}_3^p$	$\mathcal{T}_\mathcal{S}\mathcal{T}_2 \bar{F}_3^a$
2211	12	$\mathcal{T}_\mathcal{C} C_3^a$	$\mathcal{T}_\mathcal{C} C_3^p$	$\mathcal{T}_1\mathcal{T}_\mathcal{C} C_3^a$	$\mathcal{T}_\mathcal{C} \bar{C}_3^a$	$\mathcal{T}_\mathcal{C} \bar{C}_3^p$	$\mathcal{T}_\mathcal{C} \bar{C}_3^t$	$\mathcal{T}_1\mathcal{T}_\mathcal{C} \bar{C}_3^t$	$\mathcal{T}_1\mathcal{T}_\mathcal{C} \bar{C}_3^p$	$\mathcal{T}_1\mathcal{T}_\mathcal{C} \bar{C}_3^a$
2212	13	$\mathcal{T}_\mathcal{C} F_3^a$	$\mathcal{T}_\mathcal{C} F_3^p$	$\mathcal{T}_2\mathcal{T}_\mathcal{C} F_3^a$	$\mathcal{T}_\mathcal{C} \bar{F}_3^a$	$\mathcal{T}_\mathcal{C} \bar{F}_3^p$	$\mathcal{T}_\mathcal{C} \bar{F}_3^t$	$\mathcal{T}_\mathcal{S}\mathcal{T}_\mathcal{C}\mathcal{T}_1 \bar{F}_3^t$	$\mathcal{T}_\mathcal{S}\mathcal{T}_\mathcal{C}\mathcal{T}_1 \bar{F}_3^p$	$\mathcal{T}_\mathcal{S}\mathcal{T}_\mathcal{C}\mathcal{T}_1 \bar{F}_3^a$
2221	14	$\mathcal{T}_\mathcal{C}\mathcal{T}_3 F_3^a$	$\mathcal{T}_\mathcal{C}\mathcal{T}_3 F_3^p$	$\mathcal{T}_\mathcal{C}\mathcal{T}_2 F_3^a$	$\mathcal{T}_\mathcal{S}\mathcal{T}_\mathcal{C}\mathcal{T}_3 \bar{F}_3^a$	$\mathcal{T}_\mathcal{S}\mathcal{T}_\mathcal{C}\mathcal{T}_3 \bar{F}_3^p$	$\mathcal{T}_\mathcal{S}\mathcal{T}_\mathcal{C}\mathcal{T}_3 \bar{F}_3^t$	$\mathcal{T}_1\mathcal{T}_\mathcal{C} \bar{F}_3^t$	$\mathcal{T}_1\mathcal{T}_\mathcal{C} \bar{F}_3^p$	$\mathcal{T}_1\mathcal{T}_\mathcal{C} \bar{F}_3^a$
2222	15	0	0	0	0	0	0	0	0	0

As seen from Eq. (A.3), the crossing transformations act on the natural channel-dependent frequencies ω_r, ν_r, ν'_r by flipping the sign or exchanging ν_r and ν'_r. If one has redundant symmetries (e.g. $\mathcal{T}_\mathcal{C}$ has not been used in the example Eq. (4.56)), one can use them to e.g. only compute some Keldysh component for negative frequencies and obtain the values for positive frequencies afterwards by applying the corresponding transformation $\mathcal{T}_i$. This has been worked out and implemented into our code by Anxiang Ge [Ge21].

4.3.3 Keldysh components of n-point functions

As discussed in Sec. 4.1.3, the asymptotic classes $\mathcal{K}_1^r$ are related to susceptibilities, which have the nature of a bosonic self-energy, and $\mathcal{K}_{2^{(\prime)}}^r$ have the nature of three-point functions. In principle, n-point functions only have n Keldysh indices, therefore one can express $\mathcal{K}_1^r$ and $\mathcal{K}_{2^{(\prime)}}^r$ in terms of 2 and 3 Keldysh indices, respectively. To achieve this, the parity of Keldysh indices (even e or odd o) of the two legs connecting to one bare vertex can be considered as one effective Keldysh index: As can be seen from Eq. (4.47), each pair of legs with a parity symmetry only depends on the parity of Keldysh indices. We identify $o \,\widehat{=}\, 1$, $e \,\widehat{=}\, 2$.[12] In analogy to Eq. (2.31) we thus have

$$(\mathcal{K}_1^r)^R = (\mathcal{K}_1^r)^{1|2} = (\mathcal{K}_1^r)^{o|e}\,, \quad (\mathcal{K}_1^r)^A = (\mathcal{K}_1^r)^{2|1} = (\mathcal{K}_1^r)^{e|o}\,, \quad (\mathcal{K}_1^r)^K = (\mathcal{K}_1^r)^{1|1} = (\mathcal{K}_1^r)^{o|o}\,. \tag{4.57}$$

The order of the Keldysh indices (incoming and outgoing) is determined by the flow direction of the bosonic frequency ω_r,

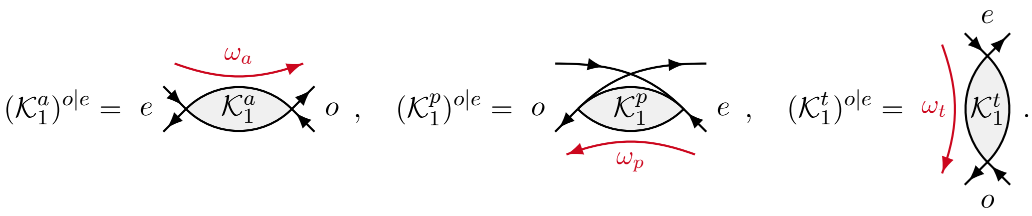

(4.58)

In the a channel, we have explicitly

$$(\mathcal{K}_1^a)^R = (\mathcal{K}_1^a)^{11|21} = (\mathcal{K}_1^a)^{12|11} = (\mathcal{K}_1^a)^{21|22} = (\mathcal{K}_1^a)^{22|12} = \mathcal{T}_3 \bar{B}_1^a\,, \tag{4.59a}$$
$$(\mathcal{K}_1^a)^A = (\mathcal{K}_1^a)^{11|12} = (\mathcal{K}_1^a)^{12|22} = (\mathcal{K}_1^a)^{21|11} = (\mathcal{K}_1^a)^{22|21} = \bar{B}_1^a\,, \tag{4.59b}$$
$$(\mathcal{K}_1^a)^K = (\mathcal{K}_1^a)^{11|22} = (\mathcal{K}_1^a)^{12|12} = (\mathcal{K}_1^a)^{21|21} = (\mathcal{K}_1^a)^{22|11} = \bar{C}_1^a\,. \tag{4.59c}$$

Similarly, in the p and t channel we have

$$(\mathcal{K}_1^p)^R = \mathcal{T}_\mathcal{C} \bar{B}_1^p\,, \quad (\mathcal{K}_1^p)^A = \bar{B}_1^p\,, \quad (\mathcal{K}_1^p)^K = \bar{D}_1^p\,, \tag{4.60a}$$
$$(\mathcal{K}_1^t)^R = \mathcal{T}_3 \bar{B}_1^t\,, \quad (\mathcal{K}_1^t)^A = \bar{B}_1^t\,, \quad (\mathcal{K}_1^t)^K = \bar{C}_1^t\,. \tag{4.60b}$$

We can also express the physical components of the physical susceptibilities (Eq. (4.21)) in terms of $\mathcal{K}_1^{a,t}$:

$$\Gamma_0\, \chi_{\mathrm{sp}}^R\, \Gamma_0 = -(\mathcal{K}_1^a)_{\uparrow\downarrow}^R\,, \quad \Gamma_0\, \chi_{\mathrm{ch}}^R\, \Gamma_0 = 2(\mathcal{K}_1^t)_{\uparrow\downarrow}^R - (\mathcal{K}_1^a)_{\uparrow\downarrow}^R\,. \tag{4.61}$$

---

[12] This can be seen very easily: $(\mathcal{K}_1^r)^{22|22} = 0$ by causality (cf. Eq. (2.38)), i.e., $(\mathcal{K}_1^r)^{e|e} = 0$, but interpreting χ_r as a bosonic self-energy, we have $(\mathcal{K}_1^r)^{2|2} = 0$ (cf. Eq. (2.31)). This allows us to identify $e \,\widehat{=}\, 2$, and correspondingly $o \,\widehat{=}\, 1$.

Since the susceptibilities have the nature of (bosonic) self-energies, in equilibrium their Keldysh components are connected to the retarded ones by FDTs (cf. Eq. (2.32)),

$$(\mathcal{K}_1^r)^K(\omega) = 2i \coth\left(\frac{\omega-\mu}{2T}\right) \operatorname{Im}(\mathcal{K}_1^r)^R(\omega)\,, \tag{4.62a}$$

$$\chi_r^K(\omega) = 2i \coth\left(\frac{\omega-\mu}{2T}\right) \operatorname{Im}\chi_r^R(\omega)\,, \tag{4.62b}$$

and equivalently for the physical susceptibilities $\chi_{\mathrm{sp/ch}}$. Note that due to their bosonic nature, $(1-2n_F(\nu)) = \tanh((\nu-\mu)/2T) \to (1-2n_B(\omega)) = \coth((\omega-\mu)/2T)$ compared to Eq. (2.32), with the Bose-Einstein distribution function $n_B(\omega) = 1/(\exp(\frac{\omega-\mu}{T})-1)$.

For $\mathcal{K}_2$, we define

$$(\mathcal{K}_2^a)^{\alpha_1\alpha_2\alpha_3} =$$

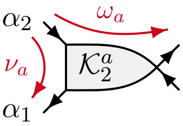

,

$$(\mathcal{K}_2^p)^{\alpha_1\alpha_2\alpha_3} =$$

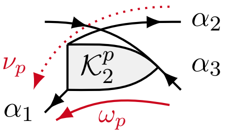

,

$$(\mathcal{K}_2^t)^{\alpha_1\alpha_2\alpha_3} = \tag{4.63}$$

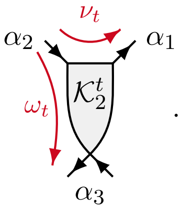

.

With this definition, the order of Keldysh indices is equivalent to that in [WH02]. Therefore, in equilibrium a set of 3-point FDTs (cf. last paragraph of Sec. 2.2.3.1) directly follows from Eq. (64) of [WH02],[13]

$$\begin{aligned}
\operatorname{Im}\left\{(\mathcal{K}_2^r)^{22o} + (\mathcal{K}_2^r)^{21e} + (\mathcal{K}_2^r)^{12e} + (\mathcal{K}_2^r)^{11o}\right\} &= 0\,,\\
\operatorname{Re}\left\{(\mathcal{K}_2^r)^{21o} + (\mathcal{K}_2^r)^{12o} + (\mathcal{K}_2^r)^{11e}\right\} &= 0\,,\\
\operatorname{Im}\left\{(\mathcal{K}_2^r)^{21o} - (\mathcal{K}_2^r)^{12o} - (\mathcal{K}_2^r)^{11e}\right\} &= \tanh\left(\frac{\nu_1'}{2T}\right) \operatorname{Im}\left\{(\mathcal{K}_2^r)^{22o} + (\mathcal{K}_2^r)^{21e}\right.\\
&\qquad \left. -(\mathcal{K}_2^r)^{12e} - (\mathcal{K}_2^r)^{11o}\right\}\,,\\
&\vdots
\end{aligned} \tag{4.64}$$

As an example, in the a channel one obtains

$$\begin{aligned}
\operatorname{Im}\left\{\bar{F}_2^a + \mathcal{T}_\mathcal{S}\mathcal{T}_\mathcal{C}\mathcal{T}_3\bar{B}_2^a + \bar{B}_2^a + \bar{C}_2^a\right\} &= 0\,,\\
\operatorname{Re}\left\{\mathcal{T}_\mathcal{S}\mathcal{T}_\mathcal{C}\mathcal{T}_3\bar{D}_2^a + \bar{D}_2^a + \bar{A}_2^a\right\} &= 0\,,\\
\operatorname{Im}\left\{\mathcal{T}_\mathcal{S}\mathcal{T}_\mathcal{C}\mathcal{T}_3\bar{D}_2^a - \bar{D}_2^a - \bar{A}_2^a\right\} &= \tanh\left(\frac{\nu_a - \frac{\omega_a}{2}}{2T}\right) \operatorname{Im}\left\{\bar{F}_2^a + \mathcal{T}_\mathcal{S}\mathcal{T}_\mathcal{C}\mathcal{T}_3\bar{B}_2^a - \bar{B}_2^a - \bar{C}_2^a\right\}\,,\\
&\vdots
\end{aligned} \tag{4.65}$$

---

[13] In [WH02], labels a, r correspond to our Keldysh indices $1, 2$. Furthermore, one has to exchange the functions coth ↔ tanh appearing there, since [WH02] treats real bosonic fields, while we are dealing with fermionic ones.

These equations can be solved for individual Keldysh components (cf. Eq. (65) of [WH02]). To use them explicitly to further reduce the number of independent Keldysh components in equilibrium, along with the analogous equations for $\mathcal{K}_3$ depending on four Keldysh indices (cf. Eq. (67) of [WH02]), is ongoing work pursued by Anxiang Ge [Ge21].

5 Single-impurity Anderson model

In the last chapters, we have described the methodology of Keldysh mfRG. We now introduce the single-impurity Anderson model [And61] that we will be studying in the rest of Part I of this thesis as a proof of principle for this method. Many of the definitions and notational conventions are again following [Jak09]. After defining the model Hamiltonian and the bare propagator G_0 and bare vertex Γ_0 derived from it as the building blocks of our field theoretical approach in Section 5.1, in Section 5.2 we define the regulator we use in order to implement fRG. Section 5.3 gives a very brief recap of the physics of the SIAM.

5.1 Definition of the model

In order to be able to also study nonequilibrium transport through the impurity in the future, we generalize the original Anderson model [And61] to one with two different baths (or reservoirs),[1] which can be interpreted as the left and right lead of a quantum dot represented by the impurity [Jak09]. We consider bath electrons with momentum k and spin σ in reservoir $m = L, R$, created by $c^\dagger_{mk\sigma}$, and impurity electrons with spin σ created by $d^\dagger_\sigma$. The bath electrons are noninteracting and moving freely with only a kinetic term that is diagonal in momentum space, while the impurity electrons are localized but interacting. In addition, electrons can hop between the baths and the impurity site. The Hamiltonian thus consists of three terms,

$$H = \underbrace{\sum_{mk\sigma} \epsilon_m(k) c^\dagger_{mk\sigma} c_{mk\sigma}}_{H_{\text{bath}}} + \underbrace{\sum_{\sigma} \epsilon_\sigma d^\dagger_\sigma d_\sigma + U d^\dagger_\uparrow d_\uparrow d^\dagger_\downarrow d_\downarrow}_{H_{\text{imp}}} + \underbrace{\sum_{mk\sigma} (t_m d^\dagger_\sigma c_{mk\sigma} + \text{h.c.})}_{H_{\text{hyb}}} . \tag{5.1}$$

H_{bath} describes the kinetic energy of the noninteracting bath electrons with dispersion relations $\epsilon_m(k)$, and H_{hyb} describes the hybridization via hopping of electrons between the baths and the impurity site, with (momentum-independent) hopping amplitudes t_m. H_{imp} describes the impurity energy levels

$$\epsilon_\sigma = eV_g - \sigma B - \frac{U}{2} \tag{5.2}$$

and the onsite interaction U on the impurity. Here V_g is a gate voltage that allows to shift the impurity energy levels, with the elementary charge e, and B is a Zeeman splitting of the two spin directions $\sigma = \uparrow, \downarrow \mathrel{\widehat{=}} \pm$ induced by a magnetic field. Note that a finite magnetic field of course breaks SU(2) symmetry, which increases the number of independent vertex spin components, as argued in Sec. 4.2. In the following chapters, we will always consider the SU(2)-symmetric case $B = 0$, such that we can drop the spin index, $\epsilon_\sigma = \epsilon$. By including the term $-U/2$ in the definition of ϵ_σ, V_g is defined relative to the particle-hole-symmetric point at half-filling [Jak09]: For $V_g = 0$ (and $B = 0$), the single-particle levels lie at $\epsilon = -U/2$ and $\epsilon + U = U/2$ (cf. Fig. 5.1).

---

[1] One can straightforwardly generalize this to any number of reservoirs N, by considering $m = 1, \dots, N$ everywhere in the following.

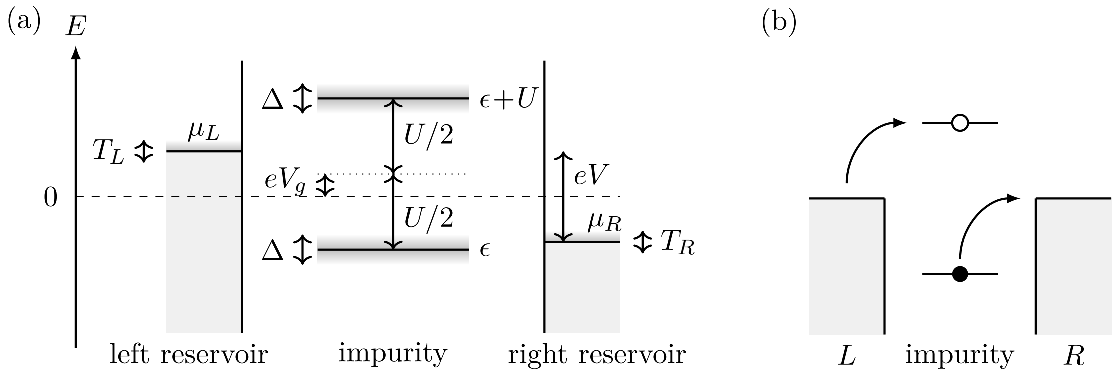

Figure 5.1 (a) Sketch of the SIAM with two reservoirs, showing all relevant energy scales (for $B = 0$): Each reservoir $m = L, R$ is in thermal equilibrium at the temperature T_m and is filled up to its chemical potential μ_m. A difference in the chemical potentials leads to a voltage drop eV across the impurity. The single-particle energy levels ϵ and $\epsilon + U$ for the first and second electron on the impurity are broadened by the hybridization Δ (Eq. (5.5)) and can be shifted by the gate voltage eV_g. (b) For $V_g = 0$ and $\mu_L = -\mu_R$ (=0 in equilibrium), the impurity is singly occupied (i.e., half-filled), and fulfills particle-hole symmetry: Adding a second electron or removing the first electron from the impurity both costs an energy penalty $U/2$.

The bare vertex Γ_0 of the SIAM is governed by the onsite interaction term $Ud^\dagger_\uparrow d_\uparrow d^\dagger_\downarrow d_\downarrow$ in the Hamiltonian. In Keldysh formalism, according to Eqs. (2.15) and (2.39) it is given by

$$(\Gamma_0)^{\alpha_1'\alpha_2'|\alpha_1\alpha_2}_{\sigma_1'\sigma_2'|\sigma_1\sigma_2} = \left(\delta_{\sigma_1',\sigma_2}\delta_{\sigma_2',\sigma_1} - \delta_{\sigma_1',\sigma_1}\delta_{\sigma_2',\sigma_2}\right) \begin{cases} \frac{U}{2}\,, & P_\alpha \text{ odd,} \\ 0\,, & \text{else.} \end{cases} \tag{5.3}$$

The bare impurity propagator reads (cf. Eqs. (2.29) and (2.30), [Jak09])

$$G^{R/A}_{0,\sigma}(\nu) = \frac{1}{\nu - \epsilon_\sigma \pm i0^+}\,, \quad G^K_{0,\sigma}(\nu) = -2i(1 - 2\langle n_\sigma\rangle)\delta(\nu - \epsilon_\sigma)\,, \tag{5.4}$$

with the (spin-dependent) impurity occupation $n_\sigma = d^\dagger_\sigma d_\sigma$. At $B = 0$ and half filling, $\langle n_\uparrow\rangle = \langle n_\downarrow\rangle = 1/2$ (i.e., single occupation of the impurity $\langle(n_\uparrow + n_\downarrow)\rangle = 1$), we thus have $G^K_0 = 0$.

The Hamiltonian is quadratic in the bath c electrons. Therefore, when going to the functional integral, they can be integrated out. Due to the coupling H_{hyb} to the impurity site, this leads to an additional quadratic term for the impurity d electrons, which can be interpreted as a reservoir-induced self-energy Σ_{res} for the impurity electrons. Assuming flat bands $\epsilon_m(k) = v_m k$ of the baths with bandwidths D_m, in the wide-band limit $D_m \to \infty$ the influence of the bath simply takes the form of a constant hybridization $\Delta = \Delta_L + \Delta_R$, with $\Delta_m = \pi|t_m|^2/v_m$ [Jak09],

$$\Sigma^{R/A}_{\text{res}} = \mp i\Delta = \sum_m \Sigma^{R/A}_{\text{res,m}}\,, \quad \Sigma^{R/A}_{\text{res,m}} = \mp i\Delta_m\,. \tag{5.5}$$

We can assume each reservoir m to be in thermal equilibrium by itself, with chemical potential μ_m and temperature T_m (cf. Fig. 5.1). Thus, for the Keldysh component we have

$$\Sigma^K_{\text{res}}(\nu) = \sum_m \Sigma^K_{\text{res,m}}(\nu) \overset{(2.32)}{=} -2i\sum_m \Delta_m \tanh\left(\frac{\nu - \mu_m}{2T_m}\right) = -2i\Delta N_{\text{eff}}(\nu)\,, \tag{5.6}$$

with the effective distribution factor[2]

$$N_{\text{eff}}(\nu) = \frac{1}{\Delta}\sum_m \Delta_m \tanh\left(\frac{\nu-\mu_m}{2T_m}\right) = \frac{1}{\Delta}\sum_m \Delta_m(1-2n_{F,m}(\nu))\,, \tag{5.7}$$

where $n_{F,m}$ is the Fermi distribution function of reservoir m.

Including Σ_{res}, we define the reservoir-dressed bare impurity propagator, for which we will reuse the symbol G_0, since it effectively takes over the role of the bare impurity propagator further on. It is obtained from Eq. (5.4) via the Dyson equation (2.33) and reads

$$G^{R/A}_{0,\sigma}(\nu) = \frac{1}{\nu-\epsilon_\sigma \pm i\Delta}\,, \quad G^K_{0,\sigma}(\nu) = G^R_{0,\sigma}(\nu)\,\Sigma^K_{\text{res}}(\nu)\,G^A_{0,\sigma}(\nu) = -2iN_{\text{eff}}(\nu)\frac{\Delta}{(\nu-\epsilon_\sigma)^2+\Delta^2}\,. \tag{5.8}$$

In equilibrium, we can simplify all expressions by removing one reservoir, $\Delta_R = 0$, such that $\Delta = \Delta_L$, $\mu = \mu_L$, $T = T_L$, and $N_{\text{eff}}(\nu) = \tanh((\nu-\mu)/2T)$.

Physically, Δ corresponds to a broadening of the impurity levels due to the presence of the bath (cf. Fig. 5.1), or in turn, the impurity d electrons acquire a finite lifetime. In the following chapters, we will use Δ as energy unit, and the dimensionless quantity U/Δ determines the effective interaction strength.

After having integrated out the bath electrons, we remain with the problem of computing the full dynamics of the interacting impurity electrons, governed by the full propagator G. It includes correlation effects via the self-energy Σ,

$$G^{R/A}_\sigma(\nu) = \frac{1}{\nu-\epsilon_\sigma \pm i\Delta - \Sigma^{R/A}_\sigma(\nu)}\,, \tag{5.9a}$$

$$G^K_\sigma(\nu) = G^R_\sigma(\nu)\left(\Sigma^K_\sigma(\nu)+\Sigma^K_{\text{res}}(\nu)\right)G^A_\sigma(\nu) \tag{5.9b}$$

$$\overset{\text{equilibrium}}{=} -2i\tanh\left(\frac{\nu-\mu}{2T}\right)\frac{\Delta - \operatorname{Im}\Sigma^R_\sigma(\nu)}{(\nu-\epsilon_\sigma-\operatorname{Re}\Sigma^R_\sigma(\nu))^2+(\Delta-\operatorname{Im}\Sigma^R_\sigma(\nu))^2}\,. \tag{5.9c}$$

5.2 SIAM within fRG

In order to compute Σ with fRG, we have to introduce a flow parameter into G_0, as explained in Chapter 3. We will use Δ as flow parameter (the so-called hybridization flow [Jak09])[3,4]: For $\Delta \to \infty$, we have $G^R_0 \to 0$, such that the theory becomes trivial. Physically, an infinitely strong hybridization essentially corresponds to an absorption of the impurity into the bath, and the interaction U/Δ becomes negligible. When flowing toward small Δ, we recover the interacting theory, as U/Δ becomes large. By keeping the numerical value of U fixed

---

[2] In [Jak09], the effective distribution function is defined as $N_{\text{res}}(\nu) = \sum_m(\Delta_m/\Delta)n_{F,m}(\nu)$ (Eq. (6.7) there), such that $N_{\text{eff}}(\nu) = 1-2N_{\text{res}}(\nu)$.

[3] A detailed discussion of various possible regulators for the Keldysh propagator is given in [Jak09]. An important realization made there is that sharp frequency cutoffs lead to various issues, including violations of causality. [Jak09] therefore concludes that the hybridization flow is beneficial for finite systems such as impurity models. An alternative for lattice systems is a momentum cutoff.

[4] In some works, including [Jak09, JPS10a] to which we frequently refer, the bare propagator Eq. (5.8) is defined with $\Delta \mapsto \Gamma/2$. (Here Γ should not be confused with the full vertex.) In our numerical implementation (and also in [Agu20]), we thus use the substitution $\Delta = (\Gamma+\Lambda)/2$ for historical reasons (equivalently used in [Jak09]), where Λ flows from a large value to zero, such that $\Delta_i = (\Gamma+\Lambda_i)/2$ and $\Delta_f = \Gamma/2$. For the single-scale propagator, this leads to a prefactor of 1/2 compared to Eq. (5.10):

$$S^\Lambda = \partial_\Lambda G|_{\Sigma=\text{const.}} = \partial_\Delta G|_{\Sigma=\text{const.}}\cdot\frac{\partial\Delta}{\partial\Lambda} = \frac{1}{2}S^\Delta\,.$$

and flowing in Δ from large to small values, we can thus sweep from the noninteracting to the strongly interacting limit of the model, where every step of the flow corresponds to the solution of the model at a different interaction strength U/Δ, which is thereby turned on during the flow.

For the hybridization flow, the single-scale propagator (Eq. (3.2)) reads [Jak09]

$$S^{R/A}(\nu) = \partial_\Delta G^{R/A}(\nu)\Big|_{\Sigma=\text{const.}} = \mp i(G^{R/A}(\nu))^2\,, \tag{5.10a}$$

$$S^K(\nu) = \partial_\Delta G^K(\nu)\Big|_{\Sigma=\text{const.}} = -iG^R(\nu)G^K(\nu) - 2iN_{\text{eff}}(\nu)G^R(\nu)G^A(\nu) + iG^K(\nu)G^A(\nu) \tag{5.10b}$$

$$\overset{\text{equilibrium}}{=} 2i\tanh\left(\frac{\nu-\mu}{2T}\right)\operatorname{Im} S^K(\nu)\,. \tag{5.10c}$$

The initial values of Γ and Σ at $\Delta_i = \infty$ are [Jak09]

$$\Gamma^{\Delta_i=\infty} = \Gamma_0\,, \quad (\Sigma_\sigma^{R/A})^{\Delta_i=\infty} = U\langle n_{\bar\sigma}\rangle\,, \quad (\Sigma^K)^{\Delta_i=\infty} = 0\,. \tag{5.11}$$

Note that while all vertex diagrams of second order or higher vanish in the limit $\Delta \to \infty$, since they contain bare propagators that vanish for $\Delta \to \infty$ (as argued in Sec. 3.1), the first-order contribution of $\Sigma^{R/A}$ (Hartree term) is finite at $\Delta_i = \infty$ even though it contains a bare propagator: As discussed at the end of Sec. 2.2.2, the Hartree term is given by an integral over $G^<$ (cf. Eq. (2.36)),[5] which gives a finite value $U\langle n_{\bar\sigma}\rangle$ that is independent of Δ and hence does not vanish in the limit $\Delta \to \infty$.

In equilibrium at half filling, we have $\langle n_{\bar\sigma}\rangle = 1/2$, such that the Hartree term is

$$(\Sigma_\sigma^{R/A})^{\Delta_i=\infty} = \Sigma_H = \frac{U}{2}\,. \tag{5.12}$$

In this case, we can avoid computing this term explicitly (e.g. when evaluating the SDE (3.5)) and instead simply add a constant value $U/2$ to the self-energy. Even further, at $B = 0$ and half filling, we have $\epsilon_\sigma = -U/2 = -\Sigma_H$. Therefore, we can absorb the Hartree term into the bare propagator by redefining $(G_0^R)^{-1} \mapsto (G_0^R)^{-1} - \Sigma_H$, which exactly compensates for ϵ_σ and thus simplifies Eq. (5.8) to

$$G_0^{R/A}(\nu) = \frac{1}{\nu \pm i\Delta}\,, \quad G_0^K(\nu) = -2iN_{\text{eff}}(\nu)\frac{\Delta}{\nu^2+\Delta^2}\,. \tag{5.13}$$

This is a valid choice since it only accounts for the constant Hartree shift of the single-particle levels, which has no effect on integrals over propagators that occur when computing diagrams.[6] On the other hand, within this form of G_0 its central peak is centered around $\nu = 0$ (cf. Fig. 6.2 below), which is beneficial for the numerical evaluation of integrals over G_0 (see the following Chapter 6). Therefore, we will use Eq. (5.13) when computing perturbation theory diagrams in Sec. 7.1 below.

Practically, in a numerical implementation we have to start the flow at a finite large value of Δ, such that Eq. (5.11) is not sufficient as initial condition. We usually choose $U = 1$ and $\Delta_i = 10.1$, such that $U/\Delta \ll 1$ is sufficiently small to be well in the weakly interacting regime. At this point, PT2 is already a good approximation and could serve as initial condition.

---

[5] In Eq. (2.36), $\Gamma_0 = \Gamma_0^{--|--} = U$, not $U/2$, since the Hartree term is evaluated in the contour basis (instead of the Keldysh basis where Γ_0 includes a prefactor 1/2, cf. Eq. (2.39)).

[6] Note that this is not necessarily the case for more complex models: If the bare propagator contains a momentum or lattice site dependence in the denominator, one cannot simply shift the frequency axis without qualitatively affecting the behavior of G_0.

However, in PT2 the vertex consists only of $\mathcal{K}_1$ diagrams (cf. Eq. (2.20)), while the $\mathcal{K}_{2^{(\prime)}}$ and $\mathcal{K}_3$ contributions are zero. This is obviously not an ideal starting point of the flow. Therefore, we initialize the flow by iterating the parquet equations with PT2 as input. At $U/\Delta \ll 1$, convergence is obtained very quickly after only ~ 5 iterations (also briefly discussed in Sec. 6.1 below).

Note that by keeping $U = 1$ fixed during the flow, in the numerics U is used as energy unit. This in particular implies that T_m/U is also fixed, i.e., T_m/Δ increases along the flow. If one would rather like to keep $T_m/\Delta =: \tilde{T}_m$ constant, one has $T_m = T_m(\Delta) = \tilde{T}_m \cdot \Delta$ along the flow, and thus

$$\Sigma^K_{\mathrm{res}}(\nu) = -2i \sum_m \Delta_m \tanh\left(\frac{\nu - \mu_m}{2\tilde{T}_m \Delta}\right) \tag{5.14}$$

inherits a complicated Δ dependence. This would lead to additional terms in S^K involving $\partial_\Delta \tanh((\nu - \mu_m)/2\tilde{T}_m\Delta)$, which is very sharply peaked and thus challenging for numerics, hence we will not exploit this route in the following. It might still be interesting to investigate it in the future, to be able to keep the temperature constant in units of the flow parameter Δ throughout the flow.

In the rest of this thesis, we will always assume $B = 0$ (i.e., SU(2) symmetry), half filling $\epsilon_\sigma = \epsilon = -U/2$ (i.e., particle-hole symmetry), and only a single reservoir in thermal equilibrium at temperature T. The extension to finite magnetic field, broken particle-hole symmetry and nonequilibrium is conceptually straightforward in the Keldysh formalism (preliminary nonequilibrium results have already been presented in [Agu20], Sec. 5.3), and all equations given up to this point are generic and do not require additional symmetries or equilibrium (except for explicit expressions for the SU(2)-symmetric case in Chapter 4, which are readily generalized to broken SU(2) symmetry, as also explained there). However, all these generalizations would involve further refinement of the numerics and are thus left for future work.

5.3 Physics of the SIAM

As already mentioned in the introduction, the SIAM is an old and well-studied model. Therefore, we neither aim to give a complete overview of the physical behavior it hosts and implications thereof, nor do we expect to add new fundamental insights in this regard. Instead, we only recapitulate briefly the most essential features, while the next chapters will focus on how well one can reproduce correlation functions of the SIAM on a quantitative level using Keldysh mfRG. A very good and comprehensive introduction to the physics of magnetic impurities in metals and the implications of the SIAM for this area was written by Hewson [Hew93].

The most striking feature of the SIAM is the emergence of the so-called Kondo scale. At half filling, the impurity level is singly occupied, with the impurity electron acting as a magnetic impurity immersed in the bath. At low energies (in an RG picture), charge fluctuations are suppressed and the interaction term effectively obtains the nature of an antiferromagnetic spin-spin interaction between the impurity spin and the total spin degree of freedom of the bath (as can be seen from a Schrieffer-Wolff transformation, projecting out charge fluctuations [SW66]). As a result, the impurity spin is screened by the bath, leading to the formation of a Kondo singlet between impurity and bath spin. This so-called Kondo effect happens at an energy scale that is exponentially small in the interaction, the Kondo temperature

$$T_K = \sqrt{\frac{U\Delta}{2}} \exp\left(\frac{\pi\Delta}{2U} - \frac{\pi U}{8\Delta}\right) \tag{5.15}$$

(see [FMW⁺18], Eq. (22), or (with a prefactor of 0.4107) [Hew93], Eq. (6.109) and the following text). The emergence of the Kondo scale can be nicely seen in the impurity spectral function

$$\begin{aligned}\mathcal{A}(\nu) &= -\frac{1}{\pi} \operatorname{Im} G^R(\nu) \\ &= \frac{1}{\pi\Delta} \frac{1 - \operatorname{Im}\Sigma^R(\nu)/\Delta}{\left(\nu - \epsilon - \operatorname{Re}\Sigma^R\right)^2/\Delta^2 + \left(1 - \operatorname{Im}\Sigma^R/\Delta\right)^2}\,,\end{aligned} \tag{5.16}$$

which characterizes the excitation spectrum of the impurity (cf. Fig. 5.2). In the noninteracting case ($\Sigma = 0$), the spectral function is simply given by a Lorentzian quasiparticle peak of width Δ at $\nu = \epsilon$ ($= 0$ at half filling), i.e., the bare energy level of the impurity broadened by the hybridization to the bath. At finite interaction U/Δ, new features arise: The so-called Hubbard bands at $\nu = \pm U/2$ originate from the single-particle excitations that now cost a finite interaction energy (also see Fig. 5.1), and the quasiparticle peak strongly narrows to a Kondo resonance of width T_K. Notably, the Kondo scale is an emergent scale, i.e., it cannot be explained from the bare parameters of the model (as opposed to the Hubbard bands, which simply reflect the single-particle levels).

In the Kondo regime, the Kondo temperature is exponentially suppressed with the interaction, $T_K \sim e^{-\pi U/8\Delta}$ for $U/\Delta \gg 1$ (Eq. (5.15)). Since at zero temperature T_K is related to the static spin susceptibility, $T_K = 1/(4\chi^R_{\text{sp}}(0))$ [FMW⁺18], we can also observe the Kondo regime by an exponential increase of $\chi^R_{\text{sp}}(0)$ with U/Δ for large interaction strength (cf. Fig. 5.3(a)). Quantitatively, Figs. 5.3(a) and (c) show that values $U/\Delta \gtrsim 5$ are required for exponential behavior to become visible. However, due to the exponentially small energy scale, the Kondo effect is a low-temperature effect: For $T \gtrsim T_K$, the Kondo resonance is strongly smeared out and even vanishes completely for $T \gg T_K$, as seen in Fig. 5.3(b). Likewise, an exponential increase of $\chi^R_{\text{sp}}(0)$ is only observable at sufficiently low temperature (Fig. 5.3(a)). For a fixed temperature T/U, the condition $T < T_K$ is only fulfilled up to a certain U/Δ (cf. Fig. 5.3(c)).

These observations pose significant challenges to our fRG approach: Truly large values of U/Δ are only accessible with a fully nonperturbative approach, but even a converged multiloop flow based on the parquet approximation (cf. Sec. 3.2.1) does introduce an error of 4^{th} order in the interaction. On the other hand, reaching low temperatures is also challenging for numerics, since the Keldysh propagator becomes increasingly sharp when lowering T (cf. Eq. (5.9c)). As further discussed in Sec. 6.4 below, even a temperature of $T/U = 0.01$ is currently challenging for our code (although this is not a fundamental problem and one can hope to improve on this in the future by means of numerical refinements). An observation of true Kondo behavior is therefore hard (if not impossible) to access within fRG.

The goal of the work presented here is different: We are aiming to evaluate the capabilities of Keldysh mfRG as a *quantitative* method in the regimes it can access, by comparing results to NRG, the gold standard for the SIAM in equilibrium. This is fundamental for establishing Keldysh mfRG as a valid method for applications beyond the reach of other methods.

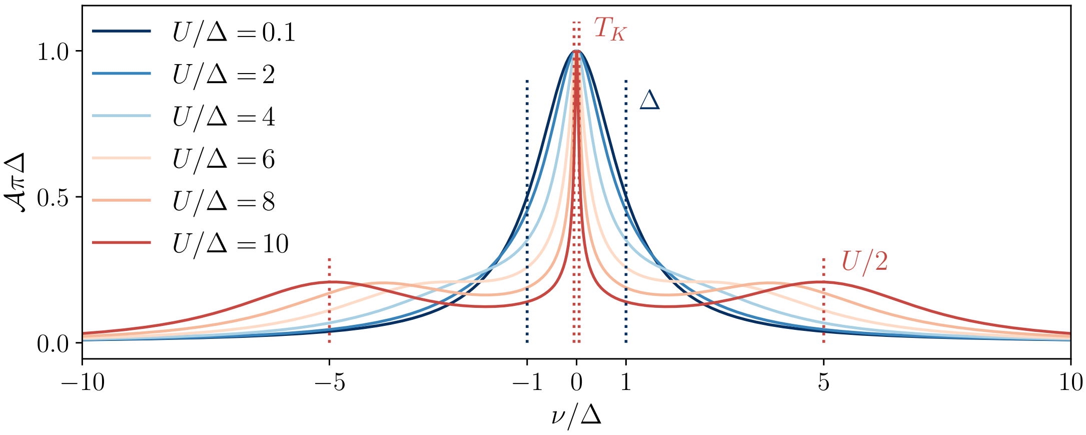

Figure 5.2 Spectral function of the SIAM for different interaction strengths U/Δ. Blue dotted lines indicate the scale of the hybridization $\pm\Delta$ which determines the width of the quasiparticle peak in the noninteracting case $U = 0$. Red dotted lines mark the scale of the Kondo temperature $\pm T_K$ and the position of the Hubbard bands $\pm U/2$ for $U/\Delta = 10$. Results are computed with NRG, using the routines of Seung-Sup Lee based on the `QSpace` tensor network library written by Andreas Weichselbaum [Wei12a, Wei12b, WvD07, LW16].

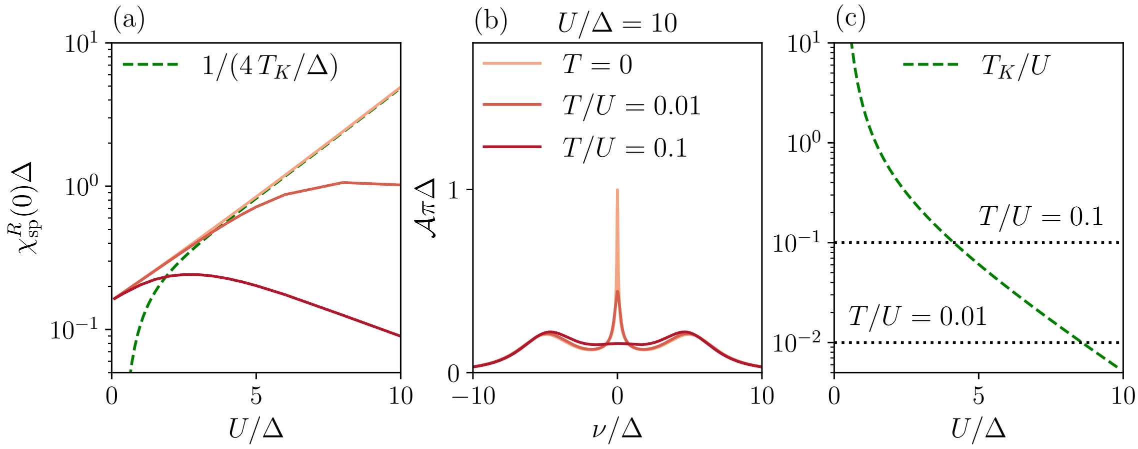

Figure 5.3 (a) Static spin susceptibility $\chi^R_{\mathrm{sp}}(0)$ as a function of U/Δ for different temperatures $T = 0$, $T/U = 0.01$, $T/U = 0.1$ (see legend of panel (b)). For $T = 0$, the inverse Kondo temperature (Eq. (5.15)) is directly related to $\chi^R_{\mathrm{sp}}(0)$; both increase exponentially for large U/Δ. (b) Spectral function for strong interaction $U/\Delta = 10$ and different temperatures $T = 0$, $T/U = 0.01$, $T/U = 0.1$. Increasing the temperature smears out the Kondo resonance; it completely vanishes at the highest temperature $T/U = 0.1$. (c) The Kondo temperature decreases exponentially as a function of U/Δ for sufficiently large U/Δ. Dashed lines indicate the temperatures $T/U = 0.01$ and $T/U = 0.1$ studied in the following chapters. $T < T_K$ is required in order to see Kondo physics, thus in the range of U/Δ where $T > T_K$, signatures of the Kondo effect are not accessible. Numerical results (χ_{sp} and $\mathcal{A}$) are computed with NRG, using the routines of Seung-Sup Lee based on the `QSpace` tensor network library written by Andreas Weichselbaum [Wei12a, Wei12b, WvD07, LW16].

6 Implementation details

In this chapter, we first list general ingredients of a numerical implementation of Keldysh mfRG (Sec. 6.1). Many details on our specific implementation are already introduced in [Agu20]. Here, we only give a short overview of the essential components of such a code. We then discuss two specific issues that arise in any real-frequency implementation, which require careful treatment: The sampling of frequency grid points (Sec. 6.2) and integration over frequencies (Sec. 6.3). These are only briefly mentioned in [Agu20] and have been further developed since then. In Section 6.4 we list all relevant parameters for fRG flows of which results are presented in Chapters 7–9, and we summarize in which regimes the code currently produces reliable results (and where it does not).

6.1 General structure

A very helpful guide for what is necessary to be able to perform mfRG calculations is given by the pseudocode in [KvD18b].

Objects, access, storage:

- The basic building blocks of the theory are the self-energy Σ and the vertex Γ, and the propagator G (or differentiated propagator S or $\partial_\Lambda G$) which connects them in bubbles and loops. Σ and Γ together form a state Ψ which will be computed along the fRG flow.

- It is useful to further decompose Γ according to the parametrization introduced in Chapter 4, since its individual constituents $\mathcal{K}_i^r$ enter the flow equations Eq. (4.27), (4.29), (4.31). For all these parts of the vertex, only a reduced number of Keldysh indices has to be stored, while their call operators need to know how to reconstruct “missing” components using symmetry transformations according to Table 4.2. A subtlety arises in the treatment of nonsymmetric vertices (cf. Sec. 4.3.2.3): A nonsymmetric vertex needs to be able to access its symmetry-related counterpart in order to be correctly reconstructed.

- Due to its simpler structure, the treatment of Σ is more straightforward, and the propagator G even only needs to have a reference to its self-energy to be generated via the Dyson equation $G = (G_0^{-1} - \Sigma)^{-1}$ (cf. Eq. (2.17)), since G_0 is known analytically (cf. Eq. (5.8) for the SIAM).

- The representation of the frequency dependence of Σ and Γ in numerics is nontrivial, since it requires us to represent functions of continuous variables via a finite number of data points. This is discussed in Sec. 6.2.

- For storing the results of Σ and Γ into a file, we use the data format `HDF5`, which is efficient for such hierarchical data structures.

Basic computations:

- From the basic building blocks, we want to compute diagrams, e.g. perturbation theory diagrams, the right-hand side of flow equations, the right-hand side of the parquet equations, etc. These involve bubbles for vertices and loops for self-energies.
- In bubbles and loops, we need to sum over internal Keldysh and spin indices (and potentially position indices) and integrate over frequencies (and potentially momenta), discussed in detail in Chapter 4.
- The Keldysh and spin sums only involve few summands and are thus straightforward to evaluate. Larger sums over spatial lattice site indices are ideally suited for vectorization [KMI⁺20, Rit21a], however, we will not elaborate on that, since the SIAM is zero-dimensional and has no such dependence.
- The frequency integration is the crucial part in the computation of bubbles and loops for us, since it is computationally expensive and difficult to do with high accuracy. We discuss this in detail in Sec. 6.3.

fRG flow:

- The computation of an fRG flow first requires a proper initial condition. Ideally, one would like to start the flow from the exact solution of some simple model, to which the model at hand can be smoothly connected via the flow parameter Λ (cf. Sec. 3.1). However, in practice one usually implements the regulator in a way that the exactly solvable model would be obtained at $\Lambda_i = \infty$, such that in numerics we have to start at some large but finite Λ_i, and one needs to find an approximate initial condition.

  If the regulator is chosen in a way that for large Λ_i the model is weakly interacting, a first attempt would be to use PT2 as initial condition. However, PT2 includes only diagrams contributing to $\mathcal{K}_1$ (cf. Eq. (2.20)), while $(\mathcal{K}_2)^{\Lambda=\Lambda_i} = (\mathcal{K}_3)^{\Lambda=\Lambda_i} = 0$ in PT2.

  An alternative starting point would be a converged solution of the parquet equations at Λ_i, obtained by iterating the SDE (3.5) and BSE (3.8) with e.g. PT2 as input until convergence. Since we expect a loop-converged mfRG flow to fulfill parquet self-consistency at all times during the flow (cf. Sec. 3.2.2), it is a reasonable choice to ensure it right from the start. Indeed, we have observed that for the SIAM a parquet-converged initial condition yields a more stable fRG flow (also mentioned in Chapter 5).[1]
- Eventually, for computing an fRG flow we need an ordinary differential equation (ODE) solver, which is again rather simple, since solving ODEs is a very well studied task. We use a 4th-order Runge-Kutta solver; higher accuracy could be achieved with an adaptive routine that automatically adjusts the step size. However, as discussed in Chapter 7, the ODE solver is currently only a minor error source.

Parallelization:

- For performance reasons, it is crucial to use parallelization. Fortunately, this is very straightforward in the context of fRG: Bubbles and loops need to be evaluated for each combination of external arguments independently. We use a hybrid `MPI`/`OpenMP` scheme to parallelize bubbles and loops over all external arguments.

In the following, we explain two crucial ingredients that have been improved upon compared to [Agu20] and are only briefly mentioned there: Storing the vertex on a nonlinear frequency grid, and frequency integration in bubbles and loops.

---

[1] Some inconsistencies attributed to a PT2 initialization are discussed in [Agu20], Sec. 5.2.4.

6.2 Frequency grid

Within the Keldysh formalism, the self-energy and the 4-point vertex are continuous functions of one or several frequency variables. However, in a numerical calculation, we need to represent them by a finite set of data points. To achieve this goal, we can think of two possible approaches:

(i) We can sample the functions on a discrete grid (and interpolate linearly between grid points), or

(ii) we can use a finite set of appropriate basis functions, and determine the expansion coefficients of self-energy and vertex in this basis numerically.[2]

Approach (ii) might potentially need less data points to properly resolve our functions of interest, compared to a naive discrete sampling, and could thus be computationally more efficient. However, this approach is also somewhat biased towards the set of basis functions: One simply cannot represent functions that are orthogonal to the chosen basis set. By contrast, in approach (i) the basis functions are effectively box functions of the size of the grid spacing, i.e., only features on a scale smaller than the grid spacing are ignored. Since self-energy and vertex are known at the beginning of the fRG flow, one can initially choose a grid that does resolve all essential features. Adaptively adjusting the grid during the flow allows to systematically control the error. For this reason, we use approach (i) here, leaving (ii) for future investigation.

Of course the discrete grid points in approach (i) do not necessarily have to be uniformly spaced over the sampled frequency range. Instead, one should place them on a nonlinear grid that resembles the behavior of the function to be represented, with a high density of grid points where the function has sharp features and changes strongly, and fewer points in slowly decaying tails. This reduces interpolation errors, since a linear interpolation scheme assumes the function to be piecewise linear between the grid points (cf. Fig. 6.2). Our choice of the frequency grid is specific for the SIAM, but the strategy of choosing it is quite generic. It is motivated by the following considerations:

- At the beginning of the flow, the physics is well captured by perturbation theory. We know the analytic form of the bare propagator, and we can expect the full propagator to behave very similarly as long as the interaction U/Δ is small. Self-energy and vertex inherit a similar behavior in perturbation theory.
- The propagator (and thus self-energy and vertex) have peak-like nontrivial structure around zero frequency for a system with particle-hole symmetry $\mu = 0$ (breaking particle-hole symmetry shifts the interesting features with the chemical potential $\mu \neq 0$). The nontrivial structure requires a dense grid in order to be properly resolved.
- The width of the central features is primarily determined by the hybridization Δ, which changes during the flow. We thus rescale the grid with Δ accordingly in order to guarantee that the interesting features are well resolved at all times during the flow.
- The Keldysh propagator (and equivalently the Keldysh self-energy and Keldysh-like components of the vertex) additionally have structure on a scale of the temperature $(\omega - \mu) \leq T$ (cf. Eq. (2.28)). For low temperatures $T \ll \Delta$, these features are thus much sharper than those induced by other physical scales.

---

[2] A similar scheme is applied routinely for parametrizing the fermionic part of the momentum-dependence of translationally invariant lattice models, using a so-called form-factor expansion [HS09, LdlPR^{+}17]. In that context, this approach is beneficial, since suitable basis functions follow quite naturally from the lattice symmetries.

- The propagator (and thus self-energy and vertex) have power-law tails (potentially with logarithmic corrections), which require less grid points. However, since functions are approximated by zero outside the frequency grid, a large frequency range is necessary in order to properly capture the slow power-law decay.

These physical requirements can be met by a grid with the following behavior:

- A quadratically increasing density of points around μ, with most points ω_j lying in a window of width $\alpha\Delta$ for some constant α (e.g. $\alpha \sim 10$), and $\min(\omega_j - \mu) < T$, and
- a power-law decaying density of points $\sim 1/\omega$ for large frequencies.

We implement the frequency grid $\{\omega_j\}$ by applying an explicit mapping function $f_\omega(\Omega)$ to an equidistant grid $\{\Omega_j\}$. This is beneficial for the following reason: If one integrates over some function F (self-energy or vertex), the adaptive integrator (see Sec. 6.3 below) needs to be able to evaluate the function at an arbitrary frequency ω, which requires to (linearly) interpolate between the stored discrete grid points $\omega_j < \omega < \omega_{j+1}$,

$$F(\omega) = \frac{\omega_{j+1} - \omega}{\omega_{j+1} - \omega_j}\, F(\omega_j) + \frac{\omega - \omega_j}{\omega_{j+1} - \omega_j}\, F(\omega_{j+1})\,. \tag{6.1}$$

This in turn requires to find the closest stored frequency points ω_j, ω_{j+1}. Having $\{\omega_j\}$ defined via an equidistant grid $\{\Omega_j\}$ allows to reduce this problem to finding the closest points $\Omega_j < \Omega < \Omega_{j+1}$, where $\Omega = f_\Omega(\omega)$, with the inverse mapping $f_\Omega = f_\omega^{-1}$. Finding the closest point on an equidistant grid is achieved by rounding a floating point number to an integer, which can be evaluated much faster than any search algorithm.

The requirements listed above are met using the mapping function (shown in Fig. 6.1)

$$f_\omega : (-1,1) \to \mathbb{R}\,, \quad f_\omega(\Omega) = \omega_s \operatorname{sgn}\Omega\, \frac{\Omega^2}{\sqrt{1-\Omega^2}}\,, \tag{6.2}$$

with the inverse function[3]

$$f_\Omega : \mathbb{R} \to (-1,1)\,, \quad f_\Omega(\omega) = \frac{\operatorname{sgn}\omega}{\omega_s}\sqrt{\frac{\sqrt{\omega^4 + 4\,\omega_s^2\,\omega^2} - \omega^2}{2}} = \frac{\omega}{\omega_s}\sqrt{\frac{\sqrt{1 + 4\left(\frac{\omega_s}{\omega}\right)^2} - 1}{2}}\,, \tag{6.3}$$

and $\omega_s = \alpha\Delta$, with some constant α that still needs to be determined. Here the quadratic scaling $f_\omega \sim \Omega^2$ around $\Omega = 0$ together with an appropriately chosen scale ω_s should ideally guarantee that the scale of the temperature is properly resolved, $\min(\omega_j - \mu) < T$.[4]

The procedure for obtaining the frequency grid $\{\omega_j\}$ can then be summarized in the following steps (cf. Fig. 6.1):

- Set the minimal and maximal values $\omega_{\min}$, $\omega_{\max}$ of the frequency grid $\{\omega_j\}$ at which the function to be resolved has well decayed to zero, such that all relevant features are captured within the interval $[\omega_{\min}, \omega_{\max}]$.

---

[3] The second expression on the right is simpler and thus slightly faster to evaluate numerically, but the $1/\omega$ appearing is a problem for $\omega = 0$. Therefore, we use the first expression, where ω only appears in the numerator.

[4] This is currently not fulfilled for the grids used for $\mathcal{K}_2$ and $\mathcal{K}_3$ at the beginning of the flow, due to the tradeoff between good resolution at small and at large frequencies with a finite number of grid points. This leads to an effective temperature scale $T_{\text{eff}} = \min(\omega_j - \mu) > T$ in $\mathcal{K}_2$ and $\mathcal{K}_3$. Resolving this issue would either require significantly more frequency grid points (resulting in much higher numerical costs) or a modification of the mapping function, potentially subdividing the full frequency range into intervals with different mapping functions.

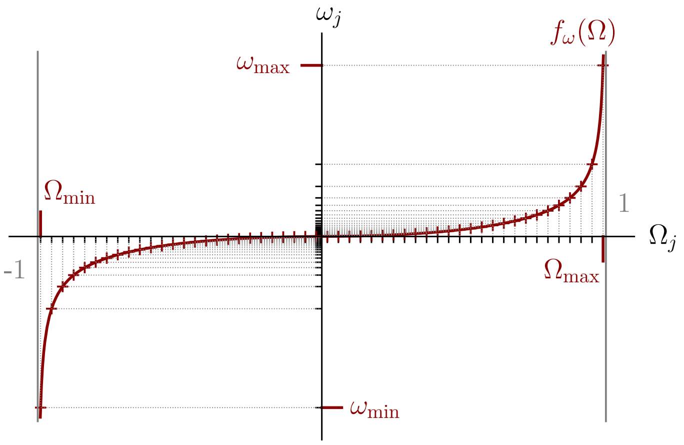

Figure 6.1 Non-linear frequency grid $\{\omega_j\}$ obtained via a transformation $f_\omega(\Omega)$ (Eq. (6.2)) from an auxiliary linear grid $\{\Omega_j\}$. The limits Ω_{min}, Ω_{max} of the latter are obtained from given values of ω_{min}, ω_{max} through the inverse transformation $f_\Omega(\omega)$ (Eq. (6.3)).

- Compute the corresponding minimal and maximal values of the auxiliary linear grid $\{\Omega_j\}$, $\Omega_{\text{min}} = f_\Omega(\omega_{\text{min}})$, $\Omega_{\text{max}} = f_\Omega(\omega_{\text{max}})$.
- The (physical) frequency grid points are given by $\omega_j = f_\omega(\Omega_j)$, with Ω_j sampled equidistantly from $[\Omega_{\text{min}}, \Omega_{\text{max}}]$ with a given number N_ω of grid points,

$$\Omega_j = \Omega_{\text{min}} + j\,\frac{\Omega_{\text{max}} - \Omega_{\text{min}}}{N_\omega - 1}\,, \qquad j = 0, \dots, N_\omega - 1\,. \tag{6.4}$$

Note that we use a number of different grids for all objects to be sampled, with a differing number of grid points N_ω and different parameters α, ω_{min}, ω_{max}: A grid for the self-energy, a grid for $\mathcal{K}_1^r$, an ω grid and a ν grid for $\mathcal{K}_2^r$, and an ω, ν, and ν' grid for $\mathcal{K}_3^r$. The grid parameters α, ω_{min}, ω_{max} are currently determined by hand in a somewhat heuristic way: We analyze the data produced by test runs, fix ω_{min}, ω_{max} such that the values $F(\omega_{\text{min}})$, $F(\omega_{\text{max}})$ of the function to be sampled are reasonably small,[5] and adjust α such that a reasonable frequency resolution is obtained. (Explicit values used for computing the results presented in Chapters 7–9 are given in Sec. 6.4 below.) A robust criterion for determining those parameters automatically throughout the flow is highly desirable and currently work in progress [Ge21].

6.3 Frequency integration

When computing diagrams, one needs to integrate over internal frequencies. For bubbles $B_r(\Gamma_L, \Gamma_R)$, these integrals read (cf. Eq. (4.9))

$$B_r(\omega_r, \nu_r, \nu'_r) = \frac{\alpha_r}{2\pi i} \int \mathrm{d}\nu''_r\, \Gamma_L(\omega_r, \nu_r, \nu''_r)\, \Pi_r(\omega_r, \nu''_r)\, \Gamma_R(\omega_r, \nu''_r, \nu'_r)\,, \tag{6.5}$$

---

[5] Note that for $\mathcal{K}_2$ and $\mathcal{K}_3$, the values have to be small along the boundaries of the combined 2d or 3d frequency grid, since frequency integrals are performed along various paths through frequency space, in particular when inserting $\mathcal{K}_2^r$ or $\mathcal{K}_3^r$ into a bubble in channel $r' \neq r$.

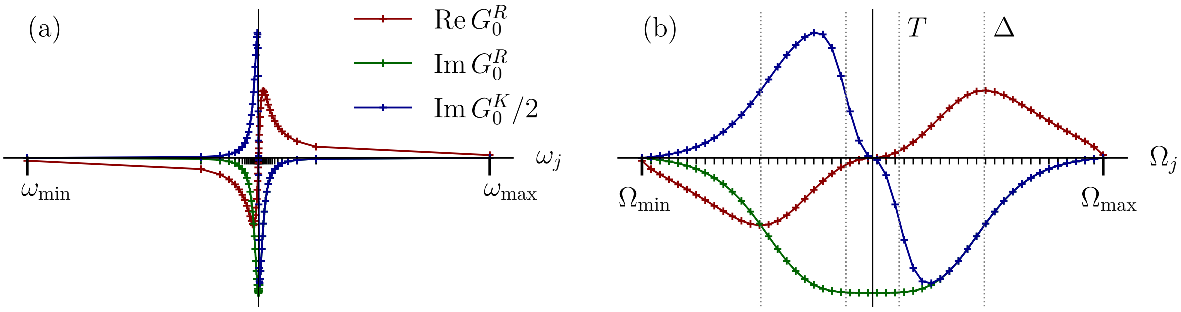

Figure 6.2 Illustration of the nonlinear frequency grid: Retarded and Keldysh component of the bare propagator G_0 (Eq. (5.13)), plotted over (a) the physical frequency grid $\{\omega_j\}$, and (b) the auxiliary grid $\{\Omega_j\}$. The transformation $f_\omega(\Omega)$ (Eq. (6.2)) is chosen in such a way that G_0 is smooth and has no sharp features on the auxiliary grid, such that on the physical grid the density of grid points is highest around the sharp features at $\omega = 0$. This minimizes interpolation errors: If the grid $\{\omega_j\}$ was chosen linearly with the same number of grid points, the resolution of the features at $\omega = 0$ would be much worse.

and for loops $L(\Gamma, G)$ (cf. Eq. (4.11))

$$L(\nu) = -\int \frac{\mathrm{d}\nu'}{2\pi i} \Gamma(\nu\nu'|\nu\nu')\, G(\nu')\,, \tag{6.6}$$

again ignoring the dependencies and sums over all other indices (spin, Keldysh index etc.).

Since vertex and self-energy (entering through the propagator) in the integrand are only known at discrete numerical frequency grid points (see previous section), we need to evaluate these integrals numerically as well. However, while nontrivial features only appear at small frequencies and decay in the limit $\nu_r'' \to \infty$, the integrals still have to be evaluated over the full real frequency axis. We simplify this problem using the following trick: We split up the integrals into three parts,

$$\int_{-\infty}^{\infty} \mathrm{d}\nu_r''(\dots) = \underbrace{\int_{-\infty}^{\nu_{\mathrm{min}}} \mathrm{d}\nu_r''(\dots)}_{\text{analytical treatment}} + \underbrace{\int_{\nu_{\mathrm{min}}}^{\nu_{\mathrm{max}}} \mathrm{d}\nu_r''(\dots)}_{\text{numerical evaluation}} + \underbrace{\int_{\nu_{\mathrm{max}}}^{\infty} \mathrm{d}\nu_r''(\dots)}_{\text{analytical treatment}}\,, \tag{6.7}$$

where we compute numerically only the (complicated) central part within a finite frequency window $[\nu_{\mathrm{min}}, \nu_{\mathrm{max}}]$, while the asymptotic tails can be evaluated analytically within some approximations, under the assumption that all nontrivial features have decayed to zero in those tails.

In the following two subsections we first describe the numerical integration procedure of the central subinterval and then derive analytical expressions for the values of the tail integrals.

6.3.1 Numerical integration

6.3.1.1 Adaptive integrator

Computing numerical integrals with high accuracy is a crucial ingredient for obtaining correct results of an fRG flow. At the same time, the integrator is also critical for the performance of the computation, since evaluating integrals constitutes the computationally most expensive part of the code. For these reasons, we use an adaptive integration routine which determines automatically where to evaluate the integrand within the integration domain: Regions with sharp features require many evaluation points in order to get a high accuracy, while in regions where the integrand is smooth fewer evaluations suffice, which increases the performance of the computation. We have observed that such an adaptive integrator is not only beneficial, but really indispensable for the problem at hand: Non-adaptive routines like a simple trapezoidal or Simpson rule on an equidistant grid have proven insufficient as they often led to systematically wrong results.

The general strategy of an adaptive integrator for computing some integral $\int_a^b F(x)\,\mathrm{d}x$ is as follows:

- Approximate the integral using some n-point integration rule $\int_a^b F(x)\,\mathrm{d}x \approx \sum_{j=1}^{n} F(x_j)\,w_j$, with nodes x_j and corresponding weights w_j.
- Use another higher-point integration rule and estimate the error by the difference of the results of the two rules.
- If the error is small enough (i.e., below some predefined accuracy), the integral is considered to be converged. Otherwise, the integration domain is subdivided, and the procedure is repeated for each subinterval until convergence.

The integrator we use is an adaptive 4-point Gauss-Lobatto routine with 7-point Kronrod extension and 13-point Kronrod extension as error estimate, which is due to a webnote of the numerical recipes book [PTVF07]. The benefit of Gauss-Lobatto rules (compared to e.g. the widely-used Gauss-Kronrod rules) is that the nodes x_j include the end points of the integration domain. This allows us to subdivide the domain at the nodes of the integration rule and thereby reuse points that have been computed previously, which is preferential in terms of performance. Similarly, the Kronrod extensions of a Gauss-Lobatto rule reuse all points from a corresponding lower-point rule and simply add additional points (similar for Gauss-Kronrod rules), which effectively allows to get two different rules from one set of evaluation points.

The nodes x_j of the 4-point Gauss-Lobatto rule with 7-point and 13-point Kronrod extension are distributed as follows:

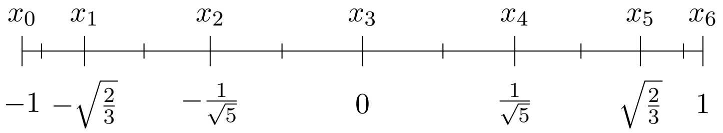

Here the lower row indicates the values of the nodes for integration boundaries $a = -1$, $b = 1$ (for other values of a, b, the values have to be rescaled correspondingly). The 4-point Gauss-Lobatto rule (GL4) and 4-point Gauss-Lobatto with 7-point Kronrod extension (GLK7) use the following points:

$$\mathrm{GL4}(x_0, x_6) = \sum_{j\in\{0,2,4,6\}} F(x_j)\,w_j\,, \quad \mathrm{GLK7}(x_0, x_6) = \sum_{j=0}^{6} F(x_j)\,w_j\,. \tag{6.8}$$

The smaller marks between the nodes $x_0, \ldots, x_6$ in the graphical representation above indicate the additional 6 points that are added in the 13-point Kronrod extension (GLK13), which are only known numerically (these and the weights w_j are found in [PTVF07]).

In summary, the recursive algorithm of the integrator can be depicted as follows:

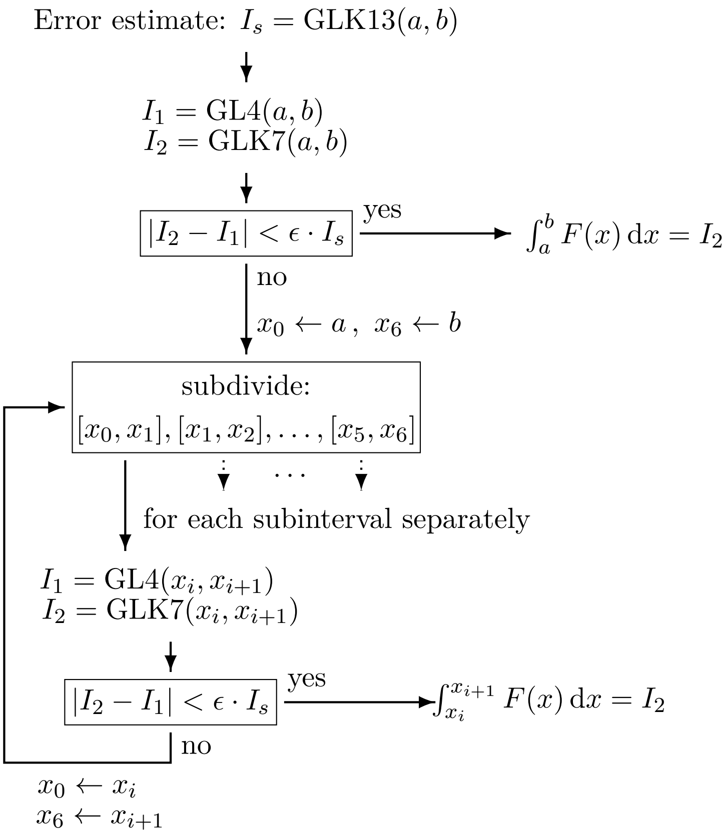
Error estimate: $I_s = \mathrm{GLK13}(a,b)$
$I_1 = \mathrm{GL4}(a,b)$
$I_2 = \mathrm{GLK7}(a,b)$
$|I_2 - I_1| < \epsilon \cdot I_s$
yes
$\int_a^b F(x)\,\mathrm{d}x = I_2$
no
$x_0 \leftarrow a\,,\ x_6 \leftarrow b$
subdivide:
$[x_0,x_1],[x_1,x_2],\dots,[x_5,x_6]$
for each subinterval separately
$I_1 = \mathrm{GL4}(x_i,x_{i+1})$
$I_2 = \mathrm{GLK7}(x_i,x_{i+1})$
$|I_2 - I_1| < \epsilon \cdot I_s$
yes
$\int_{x_i}^{x_{i+1}} F(x)\,\mathrm{d}x = I_2$
no
$x_0 \leftarrow x_i$
$x_6 \leftarrow x_{i+1}$

Note that the error estimate I_s is determined only once for the full integral and then reused for each subinterval, in order to avoid infinite recursions in subintervals. We set the relative accuracy to $\epsilon = 10^{-6}$, which gives converged results for all tested integrals.

6.3.1.2 Guiding the integrator

As argued before, the integrator should obtain results as accurate as possible with the smallest possible number of evaluations of the integrand. We can assist the integrator in this regard by using our knowledge of the problem to optimize the input, i.e., the integrand and the integration domain, in a way that simplifies the problem for the integrator.

First, we should try to keep the integrand as simple as possible. In the preceding chapters, we have always studied the dependence on different quantum numbers (frequency, Keldysh index, spin) independently, and dropped all other indices and sums for clarity of the notation. While this is justified conceptually, it is helpful to study the joint dependence on frequencies, Keldysh indices and spin in order to simplify expressions for numerics. Consider e.g. the frequency integration and the Keldysh sum of the bubbles (cf. Eqs. (4.9) and (4.41)),

$$B_r^{i_0}(\omega_r,\nu_r,\nu'_r) = \frac{\alpha_r}{2\pi i}\int \mathrm{d}\nu''_r \sum_{i_2\in\mathcal{I}_\Pi} \Gamma_L^{i_1^r(i_0,i_2)}(\omega_r,\nu_r,\nu''_r)\,\Pi_r^{i_2}(\omega_r,\nu''_r)\,\Gamma_R^{i_3^r(i_0,i_2)}(\omega_r,\nu''_r,\nu'_r) \quad (6.9\mathrm{a})$$

$$= \frac{\alpha_r}{2\pi i}\sum_{i_2\in\mathcal{I}_\Pi}\int \mathrm{d}\nu''_r\, \Gamma_L^{i_1^r(i_0,i_2)}(\omega_r,\nu_r,\nu''_r)\,\Pi_r^{i_2}(\omega_r,\nu''_r)\,\Gamma_R^{i_3^r(i_0,i_2)}(\omega_r,\nu''_r,\nu'_r)\,. \quad (6.9\mathrm{b})$$

Clearly, the two expressions in Eq. (6.9) are equivalent, since the integral over the internal frequency ν''_r and the sum over the internal Keldysh index i_2 can safely be exchanged.

However, in expression (6.9a), the integrand of the frequency integral involves a sum of 9 different contributions $i_2 \in \mathcal{I}_\Pi$. Each of these summands will have a different dependence on the integration variable ν_r'' with a different shape of nontrivial features, such that the sum can show a very complicated behavior as a function of ν_r'', making it hard for the integrator to reliably find and resolve all of its structure. On the contrary, in the second expression (6.9b) each summand is integrated separately, which considerably simplifies the task for the integrator and thus should be preferred. Indeed, we have observed that using Eq. (6.9a) can lead to systematic errors in the results (e.g. violation of particle-hole symmetry, violation of causality (cf. Sec. 7.2.1)), which are cured by applying Eq. (6.9b). The same reasoning holds for self-energy loops, even though the Keldysh sum in the loop only includes three terms (cf. Eq. (4.44)), and it also applies for internal spin sums in the t bubble and the loop (Eq. (4.35c) and Eq. (4.36)), which equivalently should be performed after the frequency integration. Note that computing several integrals instead of only one is *not* more expensive computationally, since both expressions (6.9a) and (6.9b) involve the same number of evaluations of Γ_L, Π, and Γ_R. In Eq. (6.9b), more integrals have to be computed compared to Eq. (6.9a), but the evaluation of each integrand is numerically cheaper. One might even expect a slight speedup using Eq. (6.9b), since for each summand the integrator only needs to perform many subdivisions in the frequency range where this summand has nontrivial features, and not around the features of all other summands.

Another knob to turn in order to assist the integrator is the extent of the integration domain. Since the integrator starts to evaluate the integrand at relatively few points within the integration domain, it is possible that sharp features lying between these nodes are missed altogether. In this case, the different integration rules could agree with high accuracy such that the integrator believes to be converged, while the result is actually wrong. One can enhance the robustness of the integrator by manually subdividing the integration domain at points where we expect nontrivial features to lie. Consider e.g. the bubble integrals Eq. (4.6): The propagators are centered around $\pm\frac{\omega_r}{2}$, thus the integrator will have sharp features at these points. If we subdivide the integration domain at $-\frac{\omega_r}{2} \pm \Delta$ and $\frac{\omega_r}{2} \pm \Delta$ (as also done in [TRK+20]), these features are centered in the intervals $[\pm\frac{\omega_r}{2} - \Delta, \pm\frac{\omega_r}{2} + \Delta]$ and will not be missed by the integrator. Similarly, the propagator in the loop integral Eq. (4.11) is centered around $\nu = 0$, therefore the loop integral should be subdivided at $\pm\Delta$.

Let us emphasize again that the issues discussed in this subsection are not of conceptual nature, but purely numerical problems. In principle, one should be able to circumvent them by arbitrarily increasing the robustness and accuracy of the integration routine. However, this comes at the price of increased numerical cost, since any adaptive integrator is by construction tailored to find a balance between robustness and speed. Using a nonadaptive routine, e.g. with a node distance corresponding to the smallest spacing of the grid on which the integrand is sampled, is not affordable in this context, since it would enormously increase the numerical costs.

6.3.2 Analytic integration of asymptotic tails

Now we derive expressions for the contributions of the asymptotic tails to the integrals according to Eq. (6.7), i.e.,

$$\int_{\text{tails}} \mathrm{d}\nu_r''(\dots) = \int_{-\infty}^{\nu_{\min}} \mathrm{d}\nu_r''(\dots) + \int_{\nu_{\max}}^{\infty} \mathrm{d}\nu_r''(\dots)\,. \tag{6.10}$$

6.3.2.1 Bubble integrals

In the bubbles, the expression to be computed is (cf. Eq. (4.9))

$$B_r^{\text{tails}}(\omega_r,\nu_r,\nu_r') = \frac{\alpha_r}{2\pi i}\int_{\text{tails}} \mathrm{d}\nu_r''\,\Gamma_L(\omega_r,\nu_r,\nu_r'')\,\Pi_r(\omega_r,\nu_r'')\,\Gamma_R(\omega_r,\nu_r'',\nu_r')\,. \tag{6.11}$$

We first make several approximations to simplify this expression, which allow us to compute it explicitly.

Vertices: The left and right vertex have decayed to constants in the tails,

$$\Gamma_L(\omega_r,\nu_r,\nu_r''<\nu_{\text{min}}) \approx \Gamma_L(\omega_r,\nu_r,-\infty) = \Gamma_L(\omega_r,\nu_r,+\infty) \approx \Gamma_L(\omega_r,\nu_r,\nu_r''>\nu_{\text{max}})\,, \tag{6.12a}$$
$$\Gamma_R(\omega_r,\nu_r''<\nu_{\text{min}},\nu_r') \approx \Gamma_R(\omega_r,-\infty,\nu_r') = \Gamma_R(\omega_r,+\infty,\nu_r') \approx \Gamma_R(\omega_r,\nu_r''>\nu_{\text{max}},\nu_r')\,. \tag{6.12b}$$

This can be understood from the asymptotic behavior of the different asymptotic classes. When computing a bubble in channel r, the vertex can be decomposed as

$$\Gamma = \Gamma_0 + \mathcal{K}_1^r + \mathcal{K}_2^r + \mathcal{K}_{2'}^r + \mathcal{K}_3^r + \gamma_{\bar{r}}\,. \tag{6.13}$$

For $|\nu_r''|$ large enough, in Γ_L (Γ_R), $\mathcal{K}_{2'}^r$ ($\mathcal{K}_2^r$) and $\mathcal{K}_3^r$ have decayed to zero (numerically, they are exactly zero, as soon as ν_r'' is outside the finite frequency box in which the vertices are stored). The same holds for $\gamma_{\bar{r}}$ according to Eq. (4.16). Γ_0, $\mathcal{K}_1^r$, and $\mathcal{K}_2^r$ ($\mathcal{K}_{2'}^r$) do not depend on ν_r''.

Thus, we obtain

$$B_r^{\text{tails}}(\omega_r,\nu_r,\nu_r') \approx \frac{\alpha_r}{2\pi i}\,\Gamma_L(\omega_r,\nu_r,\pm\infty)\underbrace{\left[\int_{\text{tails}} \mathrm{d}\nu_r''\,\Pi_r(\omega_r,\nu_r'')\right]}_{=:I_{B,r}^{\text{tails}}(\omega_r)}\Gamma_r(\omega_r,\pm\infty,\nu_r')\,. \tag{6.14}$$

Propagators:

- For small $|\omega_r|$, $|\nu_r''\pm\frac{\omega_r}{2}|$ is large in the tails (i.e., for large $|\nu_r''|$). We thus approximate
$$G^K(\nu_r''>\nu_{\text{max}}) \approx 0 \approx G^K(\nu_r''<\nu_{\text{min}})\,, \tag{6.15}$$
since $G^K(\nu_r'') \sim 1/(\nu_r''\pm\frac{\omega_r}{2})^2 \ll G^{R/A}(\nu_r'') \sim 1/(\nu_r''\pm\frac{\omega_r}{2})$ (cf. Eq. (5.9)). Likewise, we only compute the tail integrals for nondifferentiated bubbles and approximate
$$\dot{B}_r^{\text{tails}} \approx 0\,, \tag{6.16}$$
since the single-scale propagator $S(\nu_r'') \sim (G(\nu_r''))^2$ (cf. Eq. (5.10), and correspondingly $\partial_\Lambda G$) decays more quickly than G. Furthermore, we assume that the self-energy has decayed to its asymptotic (Hartree) value in the tails,
$$\Sigma^{R/A}(\nu_r''>\nu_{\text{max}}) \approx \Sigma_H \approx \Sigma^{R/A}(\nu_r''<\nu_{\text{min}}) \tag{6.17}$$
(with $\Sigma_H = U/2$ for half filling).
- For large $\omega_r \sim \nu_{\text{max}}$ ($\omega_r \sim \nu_{\text{min}}$), we have $|\nu_r''\pm\frac{\omega_r}{2}| \gtrsim \frac{\nu_{\text{max}}}{2}$ ($\lesssim \frac{\nu_{\text{min}}}{2}$) for $\nu_r''>\nu_{\text{max}}$ ($\nu_r''<\nu_{\text{min}}$). If ν_{max} and $|\nu_{\text{min}}|$ are chosen large enough, the arguments above should still hold.

Thus, in the Keldysh sum in B_r^{tails} (cf. Eq. (4.41)), we only compute four different terms for each channel r, namely Π_r^{RR}, Π_r^{RA}, Π_r^{AR}, Π_r^{AA}, i.e., those terms where both propagators are either G^R or G^A, and (cf. Eq. (5.9a))

$$G^{\eta}(\nu) = \frac{1}{\nu - \epsilon + \eta\, i\Delta - \Sigma^{\eta}(\nu)} \approx \frac{1}{\nu - \epsilon - \Sigma_H + \eta\, i\Delta} = \frac{1}{\nu - \epsilon' + \eta\, i\Delta}\,, \tag{6.18}$$

with $\eta = \pm$ for R/A, and $\epsilon' = \epsilon + \Sigma_H (= 0$ for half filling).

With this, we can compute the corresponding four integrals $(I_B^{\text{tails}})^{\eta_1\eta_2}$. The general structure of these integrals is (for simplicity using ν instead of ν_r'' as integration variable)

$$I_B^{\text{tails}} = \left(\int_{-\infty}^{\nu_{\text{min}}} + \int_{\nu_{\text{max}}}^{\infty} \right) \mathrm{d}\nu\, \frac{1}{\nu + \alpha}\, \frac{1}{\nu + \beta} =: I_B^{\text{tail},-} + I_B^{\text{tail},+}\,. \tag{6.19}$$

We use partial fraction decomposition,

$$\frac{1}{\nu + \alpha}\, \frac{1}{\nu + \beta} = \frac{1}{\beta - \alpha}\, \frac{1}{\nu + \alpha} + \frac{1}{\alpha - \beta}\, \frac{1}{\nu + \beta}\,, \tag{6.20}$$

to obtain

$$\begin{aligned} \int_{\nu_1}^{\nu_2} \mathrm{d}\nu \frac{1}{\nu + \alpha}\, \frac{1}{\nu + \beta} &= \frac{1}{\alpha - \beta} \Big[\ln(\nu_1 + \alpha) - \ln(\nu_2 + \alpha) - \ln(\nu_1 + \beta) + \ln(\nu_2 + \beta) \Big] \\ &= \frac{1}{\alpha - \beta} \left[\ln \frac{(\nu_1 + \alpha)(\nu_2 + \beta)}{(\nu_1 + \beta)(\nu_2 + \alpha)} + 2\pi i n \right]\,, \end{aligned} \tag{6.21}$$

where the branch $n \in \mathbb{N}$ of the complex logarithm still has to be determined. We thus obtain

$$I_B^{\text{tail},-} = \int_{-\infty}^{\nu_{\text{min}}} \mathrm{d}\nu \frac{1}{\nu + \alpha}\, \frac{1}{\nu + \beta} = \frac{1}{\alpha - \beta}\, \ln \frac{|\nu_{\text{min}}| - \beta}{|\nu_{\text{min}}| - \alpha}\,, \tag{6.22a}$$

$$I_B^{\text{tail},+} = \int_{\nu_{\text{max}}}^{\infty} \mathrm{d}\nu \frac{1}{\nu + \alpha}\, \frac{1}{\nu + \beta} = \frac{1}{\alpha - \beta}\, \ln \frac{\nu_{\text{max}} + \alpha}{\nu_{\text{max}} + \beta}\,, \tag{6.22b}$$

where the branch $n = 0$ follows from $\lim_{\nu_{\text{min}} \to -\infty} I_B^{\text{tail},-} \overset{!}{=} 0 \overset{!}{=} \lim_{\nu_{\text{max}} \to \infty} I_B^{\text{tail},+}$. In summary, we have

$$I_{B,r}^{\text{tails}} = \frac{1}{\alpha_r - \beta_r}\, \ln \frac{(\nu_{\text{max}} + \alpha_r)(|\nu_{\text{min}}| - \beta_r)}{(\nu_{\text{max}} + \beta_r)(|\nu_{\text{min}}| - \alpha_r)}\,. \tag{6.23}$$

The coefficients α_r, β_r differ between the channels a, t and p, and special care has to be taken for the case $\alpha_r = \beta_r$. For channels a and t, we have

$$\Pi_{a,t}^{\eta_1\eta_2} = G^{\eta_1}(\nu_{a,t}'' - \tfrac{\omega_{a,t}}{2})\, G^{\eta_2}(\nu_{a,t}'' + \tfrac{\omega_{a,t}}{2}) = \frac{1}{\nu_{a,t}'' \underbrace{- \tfrac{\omega_{a,t}}{2} - \epsilon' + \eta_1 i\Delta}_{\alpha_{a,t}}} \cdot \frac{1}{\nu_{a,t}'' \underbrace{+ \tfrac{\omega_{a,t}}{2} - \epsilon' + \eta_2 i\Delta}_{\beta_{a,t}}}\,, \tag{6.24}$$

and for channel p

$$\begin{aligned}\Pi_p^{\eta_1\eta_2} = G^{\eta_1}(\tfrac{\omega_p}{2}+\nu''_p)\,G^{\eta_2}(\tfrac{\omega_p}{2}-\nu''_p) &= \frac{1}{\nu''_p+\frac{\omega_p}{2}-\epsilon'+\eta_1 i\Delta}\cdot\frac{1}{-\nu''_p+\frac{\omega_p}{2}-\epsilon'+\eta_2 i\Delta} \\ &= -\frac{1}{\nu''_p\underbrace{+\frac{\omega_p}{2}-\epsilon'+\eta_1 i\Delta}_{\alpha_p}}\cdot\frac{1}{\nu''_p\underbrace{-\frac{\omega_p}{2}+\epsilon'-\eta_2 i\Delta}_{\beta_p}}\,, \end{aligned} \tag{6.25}$$

factoring out an overall minus sign to have the same structure as above. We obtain

$$\begin{aligned}&(I^{\text{tails}}_{B,\,a,t})^{\eta_1\eta_2}(\omega_{a,t}) \\ &\quad= \frac{1}{-\omega_{a,t}+(\eta_1-\eta_2)i\Delta}\ln\frac{(\nu_{\max}-\frac{\omega_{a,t}}{2}-\epsilon'+\eta_1 i\Delta)(|\nu_{\min}|-\frac{\omega_{a,t}}{2}+\epsilon'-\eta_2 i\Delta)}{(\nu_{\max}+\frac{\omega_{a,t}}{2}-\epsilon'+\eta_2 i\Delta)(|\nu_{\min}|+\frac{\omega_{a,t}}{2}+\epsilon'-\eta_1 i\Delta)}\,, \end{aligned} \tag{6.26a}$$

$$\begin{aligned}&(I^{\text{tails}}_{B,p})^{\eta_1\eta_2}(\omega_p) \\ &\quad= -\frac{1}{\omega_p-2\epsilon'+(\eta_1+\eta_2)i\Delta}\ln\frac{(\nu_{\max}+\frac{\omega_p}{2}-\epsilon'+\eta_1 i\Delta)(|\nu_{\min}|+\frac{\omega_p}{2}-\epsilon'+\eta_2 i\Delta)}{(\nu_{\max}-\frac{\omega_p}{2}+\epsilon'-\eta_2 i\Delta)(|\nu_{\min}|-\frac{\omega_p}{2}+\epsilon'-\eta_1 i\Delta)}\,. \end{aligned} \tag{6.26b}$$

We still need to consider the cases where the denominators vanish. This is the case for $\eta_1 = \eta_2$ and $\omega_{a,t} \to 0$ in the channels a and t, and for $\eta_1 = -\eta_2$ and $\omega_p \to 2\epsilon'$ in the p channel. Expanding the log in $\omega_{a,t}$, ω_p, we obtain at $\eta_1 = \eta_2$, $\eta_1 = -\eta_2$, respectively,

$$(I^{\text{tails}}_{B,\,a,t})^{\eta_1\eta_1}(\omega_{a,t}) \overset{\omega_{a,t}\to 0}{\longrightarrow} \frac{1}{\nu_{\max}-\epsilon'+\eta_1 i\Delta}+\frac{1}{|\nu_{\min}|+\epsilon'-\eta_1 i\Delta}\,, \tag{6.27a}$$

$$(I^{\text{tails}}_{B,p})^{\eta_1,-\eta_1}(\omega_p) \overset{\omega_p\to 2\epsilon'}{\longrightarrow} -\frac{1}{\nu_{\max}+\eta_1 i\Delta}-\frac{1}{|\nu_{\min}|-\eta_1 i\Delta}\,. \tag{6.27b}$$

6.3.2.2 Loop integrals

For the self-energy loop, we have to compute

$$\begin{aligned} L^{\text{tails}}(\nu) &= -\int\limits_{\text{tails}} \frac{\mathrm{d}\nu'}{2\pi i}\,\Gamma(\nu\nu'|\nu\nu')\,G(\nu') \\ &= -\int\limits_{\text{tails}} \frac{\mathrm{d}\nu'}{2\pi i}\Big\{\Gamma_0+\gamma_a\Big(\nu'{-}\nu,\tfrac{\nu+\nu'}{2},\tfrac{\nu+\nu'}{2}\Big)+\gamma_p\Big(\nu{+}\nu',\tfrac{\nu-\nu'}{2},\tfrac{\nu-\nu'}{2}\Big)+\gamma_t(0,\nu',\nu)\Big\}\,G(\nu')\,. \end{aligned} \tag{6.28}$$

First, we substitute $\nu_{\min} \mapsto \tilde{\nu}_{\min} = \nu_{\min} - |\nu|$, $\nu_{\max} \mapsto \tilde{\nu}_{\max} = \nu_{\max} + |\nu|$, such that

$$\int_{\text{tails}} \mathrm{d}\nu'_r(\dots) = \int_{-\infty}^{\tilde{\nu}_{\min}} \mathrm{d}\nu'_r(\dots) + \int_{\tilde{\nu}_{\max}}^{\infty} \mathrm{d}\nu'_r(\dots)\,, \tag{6.29}$$

while the integral over the interval $[\tilde{\nu}_{\min}, \tilde{\nu}_{\max}]$ is computed numerically. With this substitution, γ_a and γ_p (for which all three frequencies depend on ν') have decayed for $\nu' > \tilde{\nu}_{\max}$, $\nu' < \tilde{\nu}_{\min}$, as similarly argued for the bubble integrals. We remain with

$$\begin{aligned} L^{\text{tails}}(\nu) &\approx -\frac{1}{2\pi i}\left(\Gamma_0 + \gamma_t(0,\pm\infty,\nu)\right)\int_{\text{tails}} \mathrm{d}\nu'\, G(\nu') \\ &= -\frac{1}{2\pi i}\left(\Gamma_0 + \mathcal{K}_1^t(0) + \mathcal{K}_{2'}^t(0,\nu)\right)\underbrace{\int_{\text{tails}} \mathrm{d}\nu'\, G(\nu')}_{I_L^{\text{tails}}} \,. \end{aligned} \tag{6.30}$$

For the propagator, we can assume the same form as in Eq. (6.18). For the retarded and advanced propagator, we obtain

$$(I_L^{\text{tails}})^\eta = \ln\frac{|\tilde{\nu}_{\text{min}}| + \epsilon' - \eta\, i\Delta}{\tilde{\nu}_{\text{max}} - \epsilon' + \eta\, i\Delta}\,, \tag{6.31}$$

where the branch of the complex logarithm again has been determined by considering the limit $|\tilde{\nu}_{\text{min}}|, \tilde{\nu}_{\text{max}} \to \infty$. The Keldysh propagator could again be neglected, since it decays much faster than the retarded and advanced one. In equilibrium, we can however also compute it explicitly by making use of the FDT (Eq. (2.28)). For $\nu' \gg T, \mu$, we can approximate $\tanh((\nu'-\mu)/2T) \approx \operatorname{sgn}(\nu')$, from which we obtain

$$(I_L^{\text{tails}})^K \approx 2i\left(\arctan\left(\frac{\tilde{\nu}_{\text{max}} - \epsilon'}{\Delta}\right) - \arctan\left(\frac{|\tilde{\nu}_{\text{min}}| + \epsilon'}{\Delta}\right)\right)\,. \tag{6.32}$$

For particle-hole symmetry $\epsilon' = 0$ and a symmetric grid $|\tilde{\nu}_{\text{min}}| = \tilde{\nu}_{\text{max}}$, this contribution vanishes identically.

The tail contribution of the differentiated loop $\dot{L}^{\text{tails}}$ follows similarly, by replacing the regular propagator G with the single-scale propagator S in Eq. (6.30). Here we have (cf. Eq. (5.10a))[6]

$$S^\eta(\nu) = -\eta\, i\frac{1}{(\nu - \epsilon' + \eta\, i\Delta)^2} \tag{6.33}$$

for the retarded and advanced component, and the Keldysh component in equilibrium again follows from the FDT. The resulting integrals read

$$(\dot{I}_L^{\text{tails}})^\eta = -\eta\, i\left(\frac{1}{\tilde{\nu}_{\text{max}} - \epsilon' + \eta\, i\Delta} - \frac{1}{\tilde{\nu}_{\text{min}} - \epsilon' + \eta\, i\Delta}\right) \tag{6.34}$$

for the retarded and advanced component, and

$$(\dot{I}_L^{\text{tails}})^K = -2i\left(\frac{\tilde{\nu}_{\text{max}} - \epsilon'}{(\tilde{\nu}_{\text{max}} - \epsilon')^2 + \Delta^2} + \frac{\tilde{\nu}_{\text{min}} - \epsilon'}{(\tilde{\nu}_{\text{min}} - \epsilon')^2 + \Delta^2}\right) \tag{6.35}$$

for the Keldysh component, which again vanishes in the particle-hole-symmetric case with symmetric grid.

6.4 Numerical parameters and validity of the numerics

In the following Chapters 7 (Sections 7.2 and 7.3), 8 and 9, we present mfRG results for the SIAM with SU(2) and particle-hole symmetry in equilibrium at two different temperatures $T/U = 0.01$ and $T/U = 0.1$. In Chapter 7, we compare results for three different sets of numerical parameters (summarized in Table 6.1) which we call N_1, N_2, N_3: From N_1 to N_2, we increase the density of frequency grid points, and from N_2 to N_3, we increase the number of steps of the ODE solver (effectively decreasing the ODE step size, see details below). This allows us to evaluate the influence of these numerical parameters on the results by means of various checks analyzed in Sections 7.2 and 7.3. For results shown in Chapters 8 and 9, we use the highest-resolution data set N_3.

---

[6] Note that for the substitution $\Delta = (\Gamma + \Lambda)/2$ mentioned in Footnote 4 in Sec. 5.2, we again have to include a factor of 1/2, since $S^\Lambda = \frac{1}{2}S^\Delta$.

Table 6.1 Numerical parameters for three different runs N_1, N_2, N_3: Number of frequency grid points for Σ, $\mathcal{K}_1$, $\mathcal{K}_2$ (bosonic × fermionic) and $\mathcal{K}_3$ (bosonic × fermionic × fermionic), and number of steps of the (static) 4th-order Runge-Kutta ODE solver.

	N_Σ, $N_{\mathcal{K}_1}$	$N_{\mathcal{K}_2} = N_{\mathcal{K}_2,\omega} \times N_{\mathcal{K}_2,\nu}$	$N_{\mathcal{K}_3} = N_{\mathcal{K}_3,\omega} \times N_{\mathcal{K}_3,\nu} \times N_{\mathcal{K}_3,\nu'}$	N_{ODE}
N_1	201	51 × 51	21 × 21 × 21	65
N_2	501	101 × 101	41 × 41 × 41	65
N_3	501	101 × 101	41 × 41 × 41	115

For the frequency grids (cf. Sec. 6.2), we use the following parameters: $\omega_s = \alpha\Delta$, with

$$\alpha_\Sigma = 10\,, \tag{6.36a}$$
$$\alpha_{\mathcal{K}_1,\omega} = 5\,, \tag{6.36b}$$
$$\alpha_{\mathcal{K}_2,\omega} = 15\,, \quad \alpha_{\mathcal{K}_2,\nu} = 20\,, \tag{6.36c}$$
$$\alpha_{\mathcal{K}_3,\omega} = 10\,, \quad \alpha_{\mathcal{K}_3,\nu} = \alpha_{\mathcal{K}_3,\nu'} = 10\,, \tag{6.36d}$$

and $\omega_{\max} = -\omega_{\min} = 15 \cdot \omega_s$ for all grids. As mentioned in Sec. 6.2, these parameters have been set by hand through data analysis in a somewhat heuristic way; a more robust and automated scheme for determining the grid parameters should certainly be implemented in the future. For the ODE solver, we use predefined (nonadaptive) but decreasing step size along the flow, since we expect the physics to be increasingly complicated for decreasing Δ. We implement this by a substitution from a linear to a nonlinear grid: For given Δ_i, Δ_f, we define

$$\lambda_i = \frac{\sqrt{2}}{a}\sqrt{\sqrt{(\Delta_i - \Delta_f)^4 + a^2(\Delta_i - \Delta_f)^2} - (\Delta_i - \Delta_f)^2}\,, \quad \lambda_f = 0\,. \tag{6.37}$$

We then obtain Δ steps as[7]

$$\Delta_j = \Delta_f + \frac{a}{2}\frac{\lambda_j}{\sqrt{1-\lambda_j^2}}\,, \quad j = 0, \dots, N_{\text{ODE}} - 1\,, \quad \text{with} \tag{6.38a}$$
$$\lambda_j = \lambda_i + j\,\frac{\lambda_f - \lambda_i}{N_{\text{ODE}} - 1} \overset{\lambda_f = 0}{=} \lambda_i\,\frac{N_{\text{ODE}} - 1 - j}{N_{\text{ODE}} - 1}\,. \tag{6.38b}$$

Since Δ decreases during the flow, $\Delta_f < \Delta_i$, we have $\Delta_{j+1} < \Delta_j$ and $\lambda_{j+1} < \lambda_j$. For all results shown below we use $\Delta_i/U = 10.1$, $\Delta_f/U = 0.1$, $a = 5$, and the values of N_{ODE} shown in Table 6.1. Note that each step $\Delta_j \to \Delta_{j+1}$ is computed as a 4th-order Runge-Kutta step, i.e., it is subdivided into 4 equally-spaced substeps. As mentioned in Sec. 6.1 above, an algorithm that chooses the ODE step size adaptively would be preferential in the long term;

---

[7] For the substitution $\Delta = (\Gamma + \Lambda)/2$ of Footnote 4 in Sec. 5.2, we again have to slightly modify the definitions accordingly: With $\Delta_f = \Gamma/2$, we have $\Lambda_i = 2(\Delta_i - \Delta_f)$, $\Lambda_f = 0$, and $\Lambda_j = a\lambda_j/\sqrt{1-\lambda_j^2}$.

however, as seen from the tests in Sections 7.2 and 7.3 below, the ODE solver is currently only a subdominant source of numerical errors.

NRG benchmark results shown in Chapters 7 and 8 have been computed by Fabian Kugler using the routines of Seung-Sup Lee, based on the `QSpace` tensor network library written by Andreas Weichselbaum [Wei12a, Wei12b, WvD07, LW16].

Validity of the numerics: We study results for 1-loop, 2-loop, and 3-loop flows. For low temperature $T/U = 0.01$, the 3-loop flow currently breaks down around $U/\Delta \approx 4.5$, along with a violation of causality (see Sec. 7.2.1 below).[8] This problem does not occur at higher temperature $T/U = 0.1$, where we can reach much higher U/Δ without a breakdown of the flow or violation of causality. In general, lower temperatures are expected to be increasingly challenging for the numerics due to the sharper drop in the Keldysh propagator (cf. Eq. (2.28)). As of now, it is however not clear if the breakdown of the 3-loop flow is indeed caused by insufficient numerical accuracy or by a systematic bug in the code, since it is not ameliorated by improving the numerical parameters; identifying the reason is still ongoing work. The problem is however likely to be rooted in the center term $\dot{\gamma}_{r,C}^{(3)}$ of the 3-loop equation (3.10c), which is particularly demanding for numerics due to its double-bubble structure that involves the insertion of a temporarily stored nonsymmetric vertex (also see the discussion in Sec. 4.3.2.3).

As a consequence, we will not show data for loop orders higher than $\ell = 3$ in the following, and we will not include multiloop corrections to the self-energy flow ($\dot{\Sigma}_{\bar{t}}$, $\dot{\Sigma}_t$ in Eq. (3.12)), which start in loop order $\ell = 3$, since they involve an insertion of $\dot{\gamma}_{\bar{t},C}$. The 3-loop results at $T/U = 0.01$ can only be trusted for $U/\Delta \lesssim 3$, which is also confirmed by further tests in Sections 7.2 and 7.3 below. This value is no coincidence: As shown by Yosida and Yamada [YY70, Yam75a, YY75, Yam75b], the "small parameter" in the perturbation expansion of the SIAM is $U/\pi\Delta$. One should thus distinguish the regimes $U/\Delta < \pi$ and $U/\Delta > \pi$: In the former, $U/\pi\Delta$ is small and the perturbation series is expected to converge quickly. On the contrary, for $U/\Delta > \pi$ one starts to enter the strongly-correlated regime where pure perturbation theory will not be sufficient, but instead resummation schemes including infinitely many orders are indispensable.

We clearly see this transition in many of the results presented in the next chapters: While the flow fulfills all tests and perfectly reproduces NRG benchmark results for $U/\Delta \lesssim 3$, it seems to be considerably more challenging to correctly capture the physics evolving for larger U/Δ.

---

[8] Recall that T_K/U changes during the flow (cf. Sec. 5.3). At $U/\Delta \approx 4.5$, we have $T_K/U \approx 0.08$, i.e., $T < T_K$ is still fulfilled for $T/U = 0.01$ (but not for $T/U = 0.1$). In order to observe Kondo physics, it would however be necessary to reach even higher $U/\Delta \gtrsim 5$.

7 Perturbation theory and consistency checks

In this chapter, we present a series of tests and consistency checks to which we have subjected our code. We start with computing the simplest diagrams one can think of, namely those contributing to lowest-order perturbation theory. For the SIAM, there are exact perturbation theory results available to compare to. We then continue to evaluate various well-known relations, both generic and SIAM-specific ones, that have to be fulfilled for correlation functions computed from a full fRG flow. These tests have proven extremely useful for several reasons:

- Computing perturbation theory diagrams helped to develop an intuition for Keldysh diagrammatics, and in particular to guide our understanding of how to compute diagrams numerically. This in particular involved the optimization of the frequency grid and frequency integration, the results of which have been summarized in Chapter 6.
- A set of (ideally exact) benchmark results is indispensable for finding bugs and errors when implementing a numerical code. Accordingly, having all available benchmark tests pass gives strong confidence in the validity of the code.
- Having a set of reliable tests, in particular generic (model-independent) ones, is crucial when extending the code to more complex models, since they allow to potentially detect bugs or errors for each new set of functionality that is implemented.

While tests which have to be fulfilled exactly (i.e., up to numerical noise), such as symmetry relations, can detect bugs in the implementation when failing, other tests are only fulfilled up to a certain accuracy given by approximations in the numerics (e.g. by using a finite frequency grid and a finite integration accuracy), or approximations of the method (e.g. the PA (cf. Sec. 3.2.1)). These tests thus provide understanding of the validity of certain approximations and control over numerical accuracy. After presenting perturbation theory results in Section 7.1, which serve as a minimal consistency check, in Sections 7.2 and 7.3 we will systematically evaluate numerical errors, identify potential problems and point out possibilities how to improve on them. We will comment on systematic deviations from exact results due to intrinsic approximations of the method in Chapter 8.

7.1 4^{th}-order perturbation theory

7.1.1 Zero-temperature perturbation theory

The second-order perturbation theory contribution to the vertex can be computed analytically. In the Matsubara formalism, this has been done by Yosida and Yamada in 1970 already [YY70]. In the Keldysh formalism, we can do an analogous calculation in the limit $T \to 0$. At the particle-hole symmetric point, we have (cf. Eq. (5.13))

$$G_0^{R/A}(\nu) = \frac{1}{\nu \pm i\Delta}\,, \tag{7.1}$$

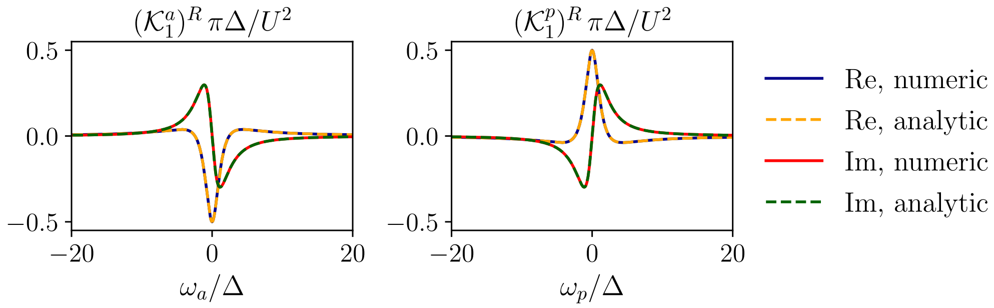

Figure 7.1 Real and imaginary part of the retarded component of $\mathcal{K}_1^a$ (left) and $\mathcal{K}_1^p$ (right) in second-order perturbation theory at $T = 0$ as a function of the bosonic transfer frequency, comparing numerical results computed at $U = 1$, $\Delta = 10$, to the exact analytical result.

and in the limit $T \to 0$, the FDT (2.28) simplifies to

$$G_0^K(\nu) \xrightarrow{T\to 0} \operatorname{sgn}(\nu)(G_0^R(\nu) - G_0^A(\nu))\,. \tag{7.2}$$

We can evaluate any of the retarded components in the a channel (cf. Eq. (4.59a)), e.g. $(\mathcal{K}_1^a)^R_{\uparrow\downarrow} = (\mathcal{K}_1^a)^{21|22}_{\uparrow\downarrow}$ $(= \mathcal{T}_3\bar{B}_1^a$ in Table 4.2):

$$(\mathcal{K}_1^a)^{R,\,\mathrm{PT2}}_{\uparrow\downarrow}(\omega_a) = (\mathcal{K}_1^a)^{21|22,\,\mathrm{PT2}}_{\uparrow\downarrow}(\omega_a) =$$

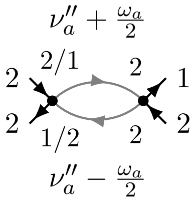
$\nu_a'' + \frac{\omega_a}{2}$
2/1
2
2
1
2
2
1/2
2
$\nu_a'' - \frac{\omega_a}{2}$

$$\begin{aligned}
&= \left(\frac{U}{2}\right)^2 \int \frac{\mathrm{d}\nu_a''}{2\pi i}\Big[G_0^A(\nu_a'' - \tfrac{\omega_a}{2})\,G_0^K(\nu_a'' + \tfrac{\omega_a}{2}) + G_0^K(\nu_a'' - \tfrac{\omega_a}{2})\,G_0^R(\nu_a'' + \tfrac{\omega_a}{2})\Big] \\
&= -U^2 \frac{1}{2\pi\Delta}\,\frac{1}{4 + (\frac{\omega_a}{\Delta})^2}\Big\{4\,\tfrac{\Delta}{\omega_a}\arctan\tfrac{\omega_a}{\Delta} - \ln\Big[1 + (\tfrac{\omega_a}{\Delta})^2\Big] \\
&\qquad\qquad + 2i\Big(\arctan\tfrac{\omega_a}{\Delta} + \tfrac{\Delta}{\omega_a}\ln\Big[1 + (\tfrac{\omega_a}{\Delta})^2\Big]\Big)\Big\}\,.
\end{aligned} \tag{7.3}$$

The evaluation of the integrals over two retarded and advanced propagators is analogous to those appearing in Sec. 6.3.2.1, and the arctan comes from the decomposition of the complex logarithm into real and imaginary parts. The contribution from the p channel follows analogously,

$$(\mathcal{K}_1^p)^{R,\,\mathrm{PT2}}_{\uparrow\downarrow}(\omega_p) = (\mathcal{K}_1^p)^{21|22,\,\mathrm{PT2}}_{\uparrow\downarrow}(\omega_p) =$$

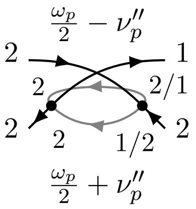
$\frac{\omega_p}{2} - \nu''_p$
2
1
2
2/1
2
2
2
1/2
$\frac{\omega_p}{2} + \nu''_p$

$$\begin{aligned}
&= \left(\frac{U}{2}\right)^2 \int \frac{\mathrm{d}\nu''_p}{2\pi i} \Big[G_0^K(\tfrac{\omega_p}{2} - \nu''_p)\, G_0^R(\tfrac{\omega_p}{2} + \nu''_p) + G_0^R(\tfrac{\omega_p}{2} - \nu''_p)\, G_0^K(\tfrac{\omega_p}{2} + \nu''_p)\Big] \\
&= U^2 \frac{1}{2\pi\Delta} \frac{1}{4 + (\frac{\omega_p}{\Delta})^2} \Big\{ 4\, \tfrac{\Delta}{\omega_p} \arctan \tfrac{\omega_p}{\Delta} - \ln \Big[1 + (\tfrac{\omega_p}{\Delta})^2\Big] \\
&\qquad + 2i \Big(\arctan \tfrac{\omega_p}{\Delta} + \tfrac{\Delta}{\omega_p} \ln \Big[1 + (\tfrac{\omega_p}{\Delta})^2\Big]\Big) \Big\}\,, \qquad (7.4)
\end{aligned}$$

which only differs by a minus sign from the result in the a channel. As shown in Fig. 7.1, these results are perfectly reproduced by our numerical code. Note that in the numerics we have also evaluated the diagrams at exactly $T = 0$ by replacing $N_{\mathrm{eff}}(\nu) = \tanh(\nu/2T) \to \mathrm{sgn}(\nu)$ in the bare Keldysh propagator (Eq. (5.13)). In perturbation theory, this is unproblematic, since only a single integral has to be evaluated with only bare vertices and propagators entering (unlike a full mfRG flow, where full objects are successively inserted into bubbles and loops, and we do observe problems related to the sharp drop of the Keldysh propagator at low T, see the previous discussion in Sections 5.3 and 6.4).

7.1.2 Zero-frequency perturbation theory

While analytical results can be derived for PT2 at $T = 0$, already at third order the log and arctan from the second-order expressions Eqs. (7.3) and (7.4) would make the integrand very complicated, and exact results have not been reported so far. However, one can obtain analytic expressions at higher orders if all external frequency arguments are set to zero. Hewson [Hew01] has computed $\Gamma_{\uparrow\downarrow}(0,0,0,0)$ up to 4th order in U in the Matsubara formalism, and of course this results translates automatically to the fully retarded components in Keldysh formalism (those components where only one Keldysh index is 1), since an analytic continuation is trivial at zero frequency. The fully advanced components (only one Keldysh index is 2) have the same value (since it is real) at the particle-hole symmetric point. Only a factor of $-1/2$ has to be added due to the structure of the bare Keldysh vertex (cf. Eqs. (2.15) and (2.39)). With this prefactor, Hewson's result (Eq. (57) of [Hew01]) reads

$$\Gamma_{\uparrow\downarrow}(0,0,0,0) = -\frac{U}{2} \left\{ 1 + \left(15 - \frac{3\pi^2}{2}\right) \left(\frac{U}{\pi\Delta}\right)^2 + \mathcal{O}\left(\left(\frac{U}{\pi\Delta}\right)^4\right) \right\} . \qquad (7.5)$$

In first order, there is only the bare vertex, and in second order, the two nonvanishing diagrams exactly cancel (cf. Eqs. (7.3), (7.4), or Fig. 7.1). In third order, one obtains a nontrivial finite result, namely, three diagrams with a value of $-\frac{U}{2}(U/\pi\Delta)^2$ and six diagrams with a value of $-\frac{U}{2}(2 - \pi^2/4)(U/\pi\Delta)^2$ [Hew01], which sum up to the contribution given in Eq. (7.5). At fourth order again all diagrams cancel, which is however far from trivial to see.

In the following, we show all diagrams contributing to $\Gamma_{\uparrow\downarrow}$ up to 4th order, and their corresponding numerical values of the fully retarded components at $T = 0$ and $\omega_r = \nu_r = \nu'_r = 0$ as a function of U/Δ. We show all pairs of diagrams that cancel each order, and all diagrams that contribute a finite value. For the sketches of diagrams, we use different colors to indicate the spin: Dark blue corresponds to spin ↑, light blue to spin ↓. The spin of green lines is summed over (separately for each green p bubble), with dark and light green lines having opposite spins. (Red lines in the $\mathcal{K}_1^t$ diagram in 2^{nd} order indicate that this diagram is zero regardless of the spin of these lines.) For clarity, we do not display prefactors in front of the diagrams: Every t bubble implies a minus sign, and all p bubbles have a prefactor of 1/2.

1^{st} and 2^{nd} order:

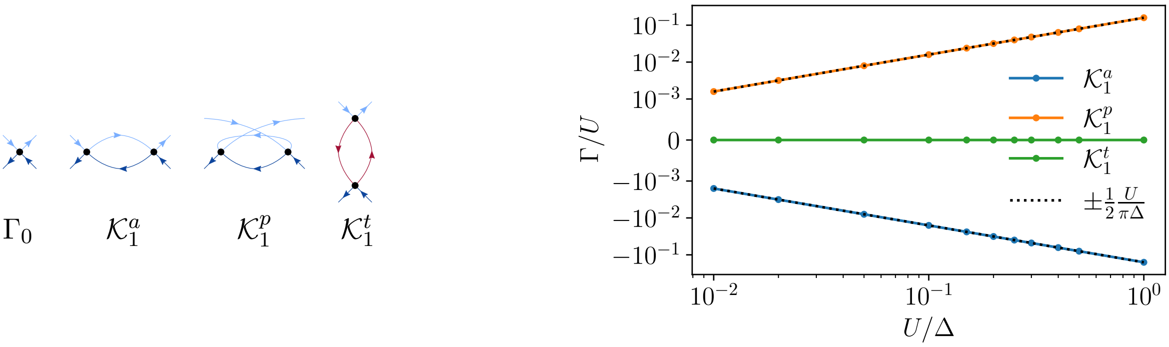

Figure 7.2 Vertex diagrams in 1^{st} (bare vertex Γ_0) and 2^{nd} order (only $\mathcal{K}_1$ diagrams). $\mathcal{K}_{1\uparrow\downarrow}^t$ is zero, since the red lines can neither have spin ↑ nor ↓. Diagrams in the a and p channel cancel. The analytical values can be read off from Eqs. (7.3) and (7.4).

3^{rd} order:

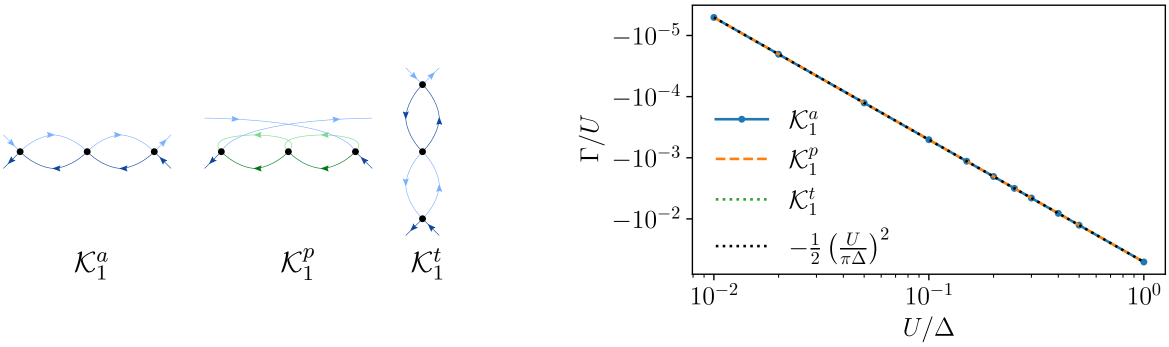

Figure 7.3 $\mathcal{K}_1$ diagrams in 3^{rd} order. All three diagrams give the same result [Hew01].

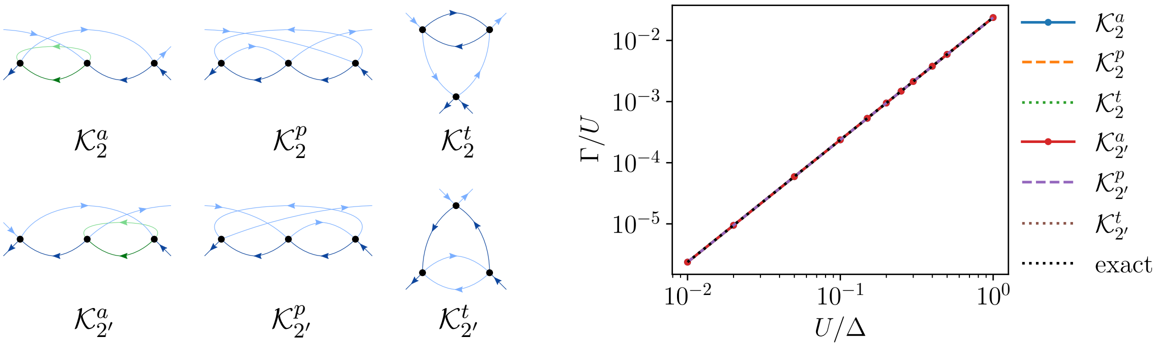

Figure 7.4 $\mathcal{K}_2$ (top row) and $\mathcal{K}_{2'}$ (bottom row) diagrams in 3^{rd} order. For diagrams not appearing here, the ↑↓ component is zero due to the spin structure (cf. $\mathcal{K}_1^t$ in 2^{nd} order). All diagrams give the same result, the exact analytical value is $\mathcal{K}_{2^{(\prime)}}^r = -\frac{1}{2}(2-\frac{\pi^2}{4})(\frac{U}{\pi\Delta})^2$ [Hew01].

4th order:

$\mathcal{K}_1$ diagrams:

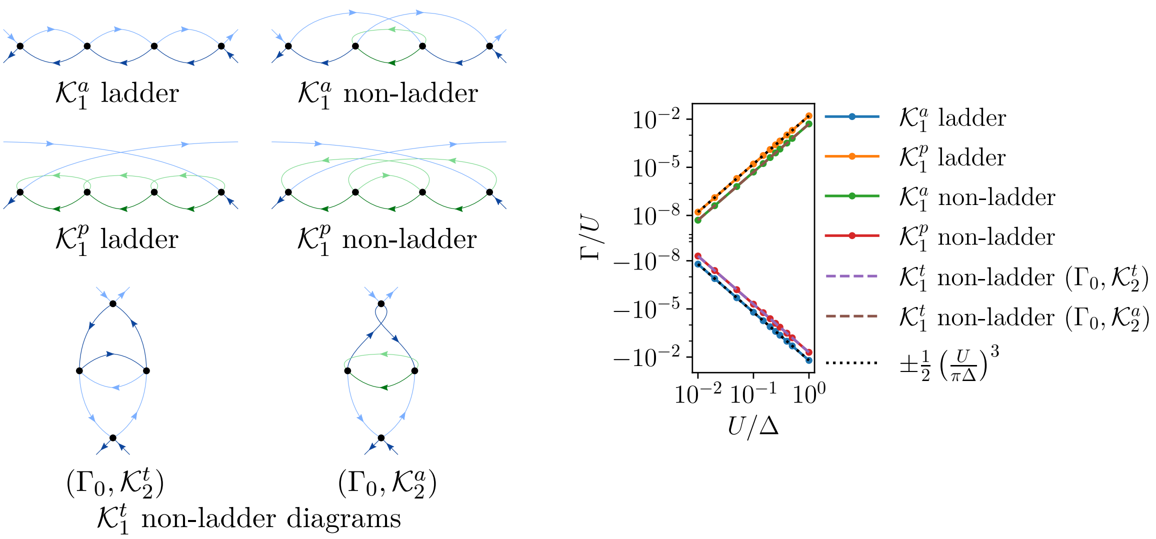
$\mathcal{K}_1^a$ ladder
$\mathcal{K}_1^a$ non-ladder
$\mathcal{K}_1^p$ ladder
$\mathcal{K}_1^p$ non-ladder
$(\Gamma_0, \mathcal{K}_2^t)$
$(\Gamma_0, \mathcal{K}_2^a)$
$\mathcal{K}_1^t$ non-ladder diagrams
10^{-2}
10^{-5}
10^{-8}
-10^{-8}
-10^{-5}
-10^{-2}
Γ/U
10^{-2} 10^{-1} 10^{0}
U/Δ
$\mathcal{K}_1^a$ ladder
$\mathcal{K}_1^p$ ladder
$\mathcal{K}_1^a$ non-ladder
$\mathcal{K}_1^p$ non-ladder
$\mathcal{K}_1^t$ non-ladder $(\Gamma_0, \mathcal{K}_2^t)$
$\mathcal{K}_1^t$ non-ladder $(\Gamma_0, \mathcal{K}_2^a)$
$\pm\frac{1}{2}\left(\frac{U}{\pi\Delta}\right)^3$

Figure 7.5 $\mathcal{K}_1$ diagrams in 4th order. In the a and p channel, diagrams can be divided into ladder and non-ladder-type diagrams. In the t channel, the ↑↓ component of the ladder diagram is zero. The ladder (non-ladder) diagrams in the a and p channel cancel. The non-ladder diagrams in the t channel cancel each other. The exact result for the ladder diagrams is known, since these diagrams factor into a product of three 2nd-order diagrams.

$\mathcal{K}_2$ diagrams:

$\mathcal{K}_{2'}$ diagrams follow by mirroring the $\mathcal{K}_2$ diagrams along the vertical (for a and p channels) or horizontal axis (for the t channel) and give the same values for $\omega_r = \nu_r = \nu'_r = 0$, they are thus not depicted explicitly in 4th order.

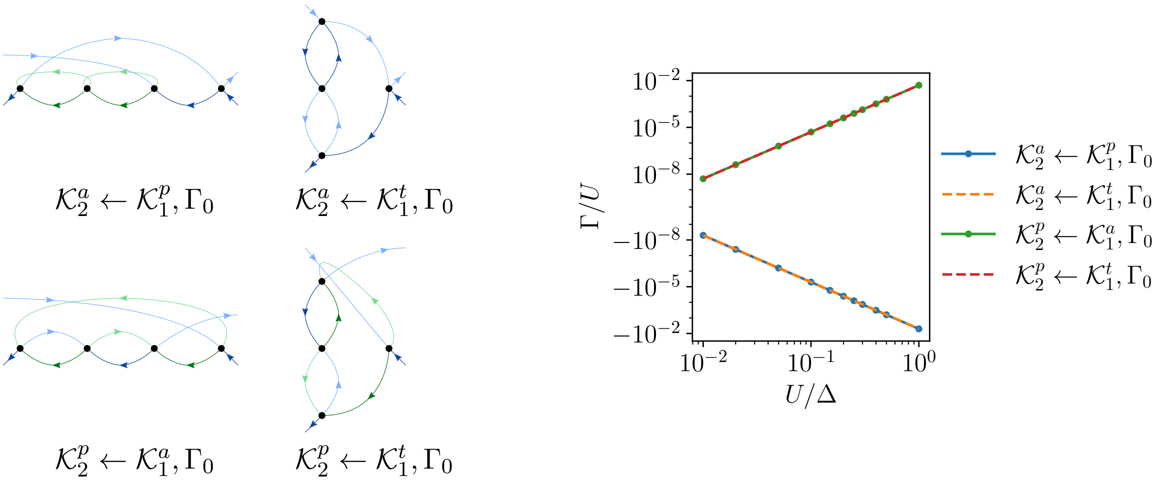
$\mathcal{K}_2^a \leftarrow \mathcal{K}_1^p, \Gamma_0$
$\mathcal{K}_2^a \leftarrow \mathcal{K}_1^t, \Gamma_0$
$\mathcal{K}_2^p \leftarrow \mathcal{K}_1^a, \Gamma_0$
$\mathcal{K}_2^p \leftarrow \mathcal{K}_1^t, \Gamma_0$
10^{-2}
10^{-5}
10^{-8}
-10^{-8}
-10^{-5}
-10^{-2}
Γ/U
10^{-2} 10^{-1} 10^{0}
U/Δ
$\mathcal{K}_2^a \leftarrow \mathcal{K}_1^p, \Gamma_0$
$\mathcal{K}_2^a \leftarrow \mathcal{K}_1^t, \Gamma_0$
$\mathcal{K}_2^p \leftarrow \mathcal{K}_1^a, \Gamma_0$
$\mathcal{K}_2^p \leftarrow \mathcal{K}_1^t, \Gamma_0$

Figure 7.6 $\mathcal{K}_2$ diagrams in 4th order obtained by inserting a 3rd-order $\mathcal{K}_1$ diagram. Diagrams in the a and p channel cancel (t diagrams are again zero due to the spin structure).

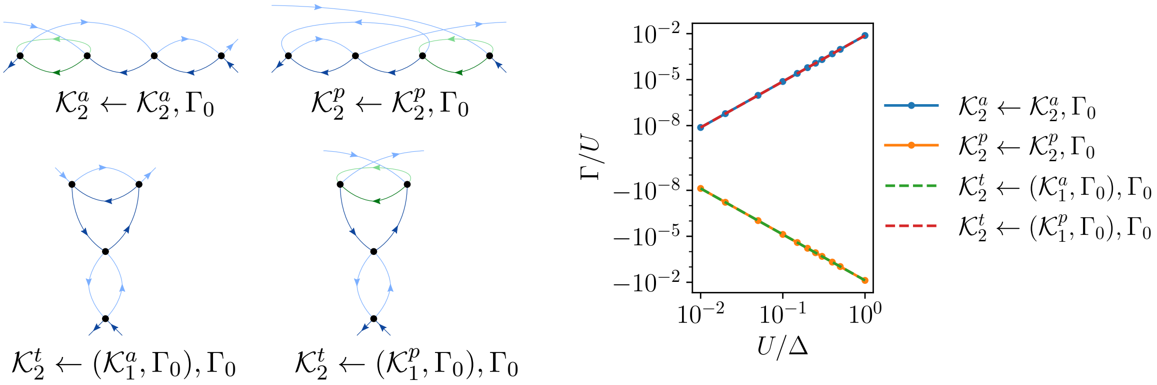
$\mathcal{K}_2^a \leftarrow \mathcal{K}_2^a, \Gamma_0$
$\mathcal{K}_2^p \leftarrow \mathcal{K}_2^p, \Gamma_0$
$\mathcal{K}_2^t \leftarrow (\mathcal{K}_1^a, \Gamma_0), \Gamma_0$
$\mathcal{K}_2^t \leftarrow (\mathcal{K}_1^p, \Gamma_0), \Gamma_0$
10^{-2}
10^{-5}
10^{-8}
-10^{-8}
-10^{-5}
-10^{-2}
Γ/U
10^{-2}
10^{-1}
10^{0}
U/Δ
$\mathcal{K}_2^a \leftarrow \mathcal{K}_2^a, \Gamma_0$
$\mathcal{K}_2^p \leftarrow \mathcal{K}_2^p, \Gamma_0$
$\mathcal{K}_2^t \leftarrow (\mathcal{K}_1^a, \Gamma_0), \Gamma_0$
$\mathcal{K}_2^t \leftarrow (\mathcal{K}_1^p, \Gamma_0), \Gamma_0$

Figure 7.7 $\mathcal{K}_2$ diagrams in 4th order obtained by inserting a 3rd-order $\mathcal{K}_2^r$ diagram in channel r. Diagrams in the a and p channel cancel, and the two t diagrams cancel separately.

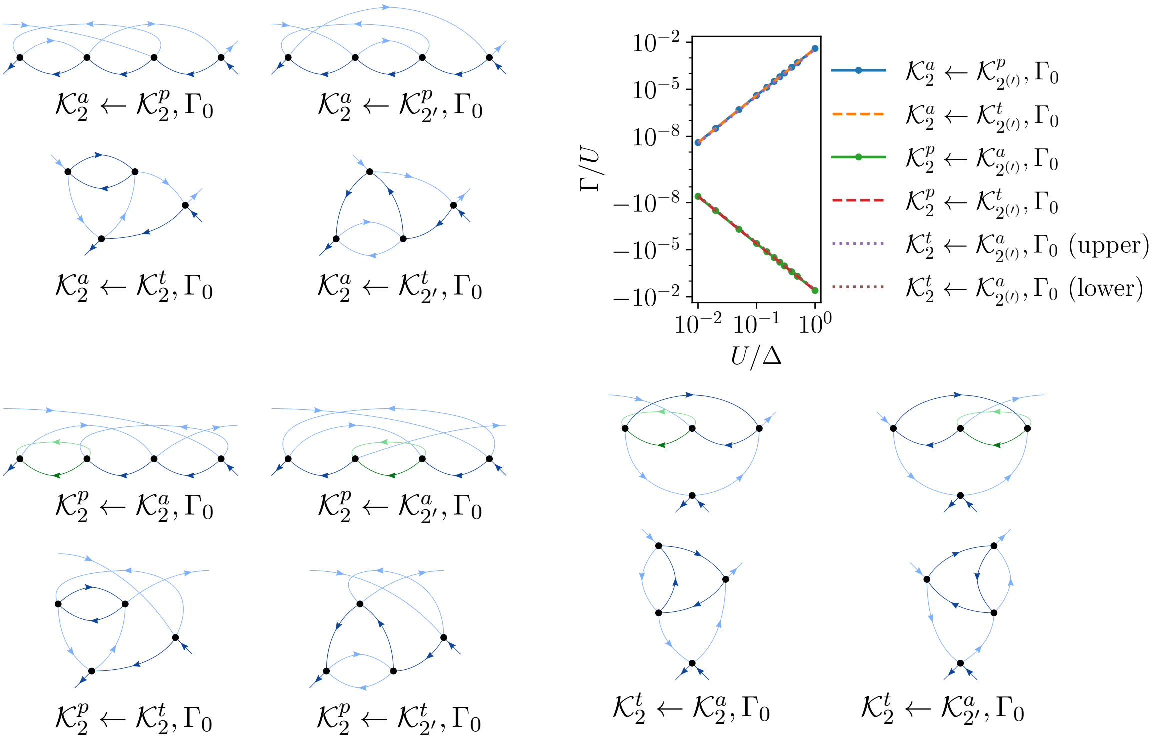
$\mathcal{K}_2^a \leftarrow \mathcal{K}_2^p, \Gamma_0$
$\mathcal{K}_2^a \leftarrow \mathcal{K}_{2'}^p, \Gamma_0$
$\mathcal{K}_2^a \leftarrow \mathcal{K}_2^t, \Gamma_0$
$\mathcal{K}_2^a \leftarrow \mathcal{K}_{2'}^t, \Gamma_0$
10^{-2}
10^{-5}
10^{-8}
-10^{-8}
-10^{-5}
-10^{-2}
Γ/U
10^{-2}
10^{-1}
10^{0}
U/Δ
$\mathcal{K}_2^a \leftarrow \mathcal{K}_{2^{(\prime)}}^p, \Gamma_0$
$\mathcal{K}_2^a \leftarrow \mathcal{K}_{2^{(\prime)}}^t, \Gamma_0$
$\mathcal{K}_2^p \leftarrow \mathcal{K}_{2^{(\prime)}}^a, \Gamma_0$
$\mathcal{K}_2^p \leftarrow \mathcal{K}_{2^{(\prime)}}^t, \Gamma_0$
$\mathcal{K}_2^t \leftarrow \mathcal{K}_{2^{(\prime)}}^a, \Gamma_0$ (upper)
$\mathcal{K}_2^t \leftarrow \mathcal{K}_{2^{(\prime)}}^a, \Gamma_0$ (lower)
$\mathcal{K}_2^p \leftarrow \mathcal{K}_2^a, \Gamma_0$
$\mathcal{K}_2^p \leftarrow \mathcal{K}_{2'}^a, \Gamma_0$
$\mathcal{K}_2^p \leftarrow \mathcal{K}_2^t, \Gamma_0$
$\mathcal{K}_2^p \leftarrow \mathcal{K}_{2'}^t, \Gamma_0$
$\mathcal{K}_2^t \leftarrow \mathcal{K}_2^a, \Gamma_0$
$\mathcal{K}_2^t \leftarrow \mathcal{K}_{2'}^a, \Gamma_0$

Figure 7.8 $\mathcal{K}_2$ diagrams in 4th order obtained by inserting a 3rd-order $\mathcal{K}_2^{r'}$ diagram in channel r, with $r' \neq r$. Diagrams in the a and p channel cancel. In the t channel, the upper two diagrams (containing $\mathcal{K}_1^p$ in 2nd order) and the lower two diagrams (containing $\mathcal{K}_1^t$ in 2nd order) cancel. (Inserting $\mathcal{K}_{2^{(\prime)}}^p$ in 3rd order in the t channel gives zero due to the spin structure.)

$\mathcal{K}_3$ diagrams:

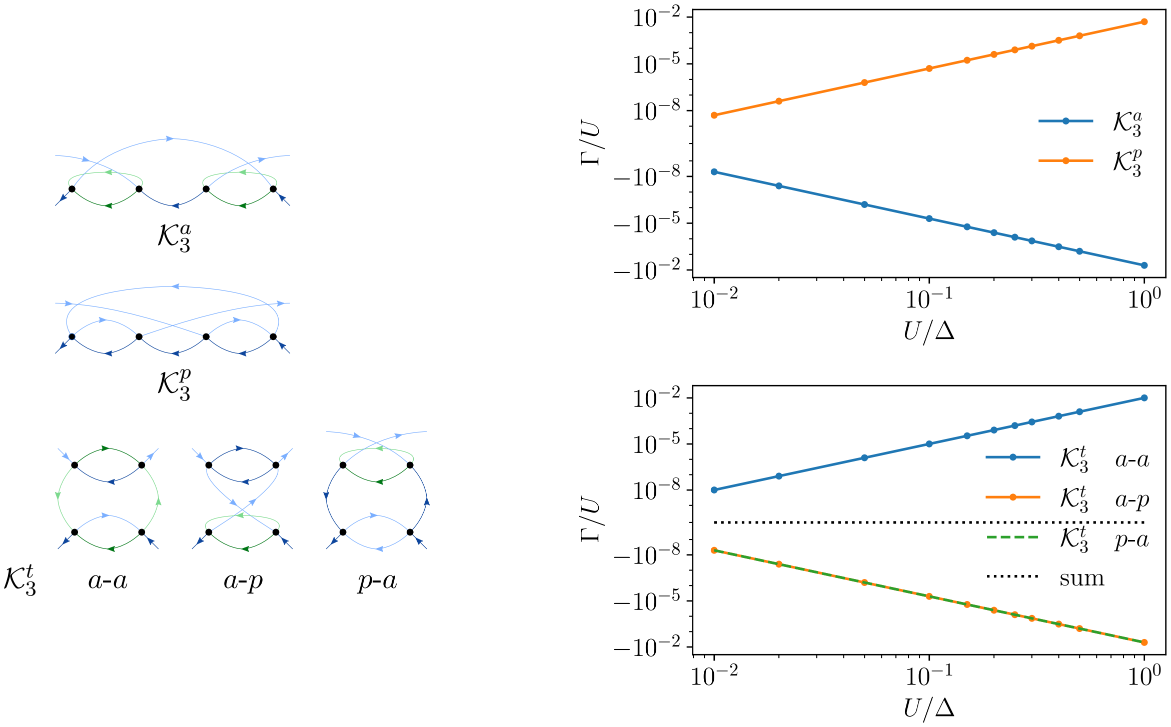

Figure 7.9 $\mathcal{K}_3$ diagrams in 4th order. In the t channel, one can insert $\mathcal{K}_1^a$ and $\mathcal{K}_1^p$ on both sides of the bubble. The p-p insertion is zero due to the spin structure. Diagrams in the a and p channel cancel, and the three t diagrams cancel separately. Notice that the a-a diagram in $\mathcal{K}_3^t$ does *not* come with a prefactor 1/2 despite having an internal spin sum, since it does not contain any p bubble. Therefore, it corresponds to two spin-resolved diagrams for the two possible spins of the green lines, in contrast to diagrams with a (green) p bubble, where the prefactor 1/2 effectively accounts for the spin sum.

7.2 Generic properties of correlation functions

7.2.1 Causality

By definition, the retarded propagator has to be causal (cf. Eq. (2.26)), $G^R(t<0) \overset{!}{=} 0$. In Fourier space, this property directly translates to $G^R(\nu)$ being analytic in the upper half of the complex frequency plane: Using the Fourier transform Eq. (2.27), we have

$$G^R(t<0) = \int \frac{\mathrm{d}\nu}{2\pi}\, e^{i\nu|t|}\, G^R(\nu) = \int \frac{\mathrm{d}\nu}{2\pi}\, e^{i\,\mathrm{Re}(\nu)|t|}\, e^{-\mathrm{Im}(\nu)|t|}\, G^R(\nu)\,. \tag{7.6}$$

The integral can be evaluated by closing the contour in the upper half of the complex plane $\mathrm{Im}(\nu) > 0$, and it gives zero if $G^R(\nu)$ has no poles in the upper half plane. Given the form (5.9a) of G^R, this leads to the requirement

$$\mathrm{Im}\,\Sigma^R(\nu) - \Delta \overset{!}{\leq} 0\,. \tag{7.7}$$

For a decoupled impurity (so-called Hubbard atom) with $\Delta = 0$, one obtains the stronger constraint

$$\mathrm{Im}\,\Sigma^R(\nu) \overset{!}{\leq} 0\,, \tag{7.8}$$

and in fact, one can impose this constraint generically, also for finite $\Delta > 0$, which is confirmed by NRG benchmark data. It is particularly important that the code always fulfills this constraint, since $\mathrm{Im}\,\Sigma^R - \Delta \approx 0$ would lead to a vanishing imaginary part in the denominator of G^R and thus to a true divergence of G^R, which is extremely difficult if not impossible to handle numerically. And indeed, at low temperature $T/U = 0.01$, starting in 3-loop, our implementation currently starts to violate the constraint (7.8) around $\nu \approx 0$ at intermediate U/Δ. This problem increases during the flow, and as $\mathrm{Im}\,\Sigma^R(0) - \Delta \approx 0$ around $U/\Delta \approx 4.5$, the flow breaks down, as mentioned above. At higher temperature $T/U = 0.1$, causality is fulfilled throughout the flow in all loop orders.

7.2.2 Kramers-Kronig relation

For any causal correlation function f (i.e., a function that is analytic in the upper half plane), the Kramers-Kronig relation connects the real and imaginary part,

$$\mathrm{Re}\, f(\omega) = \frac{1}{\pi}\,\mathcal{P}\!\int_{-\infty}^{\infty} \mathrm{d}\omega'\, \frac{\mathrm{Im}\, f(\omega')}{\omega' - \omega}\,, \tag{7.9}$$

where $\mathcal{P}$ denotes the Cauchy principal value. (This relation can also be inverted to obtain the imaginary from the real part.) Since the Kramers-Kronig relation is a very generic property of causal functions, it can serve as test how well analytic properties of correlation functions are captured within a numerical computation. In Fig. 7.10, we show 3-loop results for the retarded self-energy Σ^R and the retarded spin susceptibility χ^R_{sp} (related to the retarded component of $\mathcal{K}_1^a$, cf. Eq. (4.21)). For both functions, we compare the real part directly obtained from the fRG flow with the one obtained from the imaginary part via Eq. (7.9). We see that the Kramers-Kronig relation is almost perfectly fulfilled at weak coupling $U/\Delta = 1$, while small deviations appear at $U/\Delta = 3$, in particular for the self-energy. Note that besides having a finite resolution, the frequency grids are also bounded by their corresponding minimal/maximal frequencies ω_{min}, ω_{max}. Since the Kramers-Kronig relation involves an integral over the whole frequency axis, it is particularly sensitive to effects of such a finite

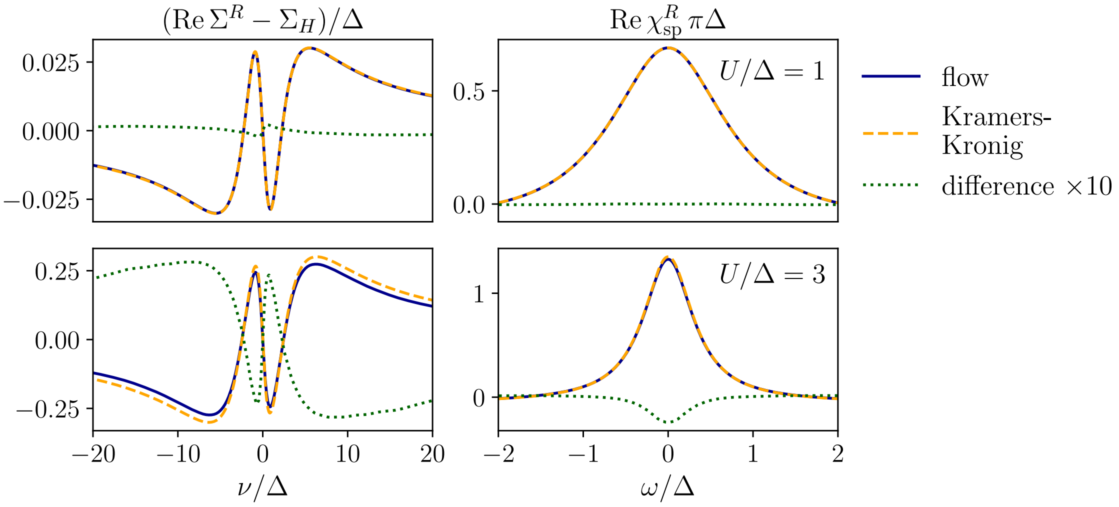

Figure 7.10 Real part of the retarded self-energy (left) and the retarded spin susceptibility (right) at $U/\Delta = 1$ (upper panels) and $U/\Delta = 3$ (lower panels), computed directly from an fRG flow and via the Kramers-Kronig relation from the imaginary part of the fRG result, and the difference of the two methods. Results are obtained from a 3-loop flow at $T/U = 0.01$, for the data set N_3 (cf. Table 6.1). While at weak coupling the agreement is almost perfect, at intermediate coupling the Kramers-Kronig relation is violated in particular in the tails of the self-energy.

frequency box, outside which the sampled functions Σ^R and χ^R_{sp} effectively drop to zero. Therefore, it is expected that increasing ω_{max} would improve these results (of course, however, at the price of increased numerical cost, if the density of grid points is kept unchanged).

To study the violation of Kramers-Kronig more systematically and evaluate how it is influenced by the numerical parameters, we define an integrated relative error as a measure for the deviation,

$$\frac{\int \mathrm{d}\nu \left| f^{\mathrm{flow}}(\nu) - f^{\mathrm{Kramers-Kronig}}(\nu) \right|}{\int \mathrm{d}\nu \left| f^{\mathrm{flow}}(\nu) \right|}, \tag{7.10}$$

for $f = \Sigma^R, \chi^R_{\mathrm{sp}}$. The result is shown in Fig. 7.11 for different loop orders and different numerical parameters (cf. Table 6.1). As expected, the error is enhanced continuously during the flow, since small deviations in the beginning are inserted again and again into the right-hand side of the flow equations. Increasing the number of frequency grid points ($N_1 \to N_2$) systematically improves the results for all loop orders. On the contrary, a smaller step size of the ODE solver ($N_2 \to N_3$) actually worsens the results. This might seem contradictive at first glance, since a smaller ODE step size should reduce the error induced by the ODE solver. A possible explanation might be that this ODE error is actually much smaller than other errors such as the interpolation error of the frequency grid. A nonnegligible error caused by inserting slightly incorrect results into the flow equation in each ODE step would then cause an error that increases with the number of steps and is not compensated by the reduced ODE error due to the smaller step size.

7.2.3 Fluctuation-dissipation theorems

Next, we test the fulfillment of FDTs for the self-energy and the spin susceptibility, which should hold generically in equilibrium. For the self-energy, at half filling ($\mu = 0$) according to

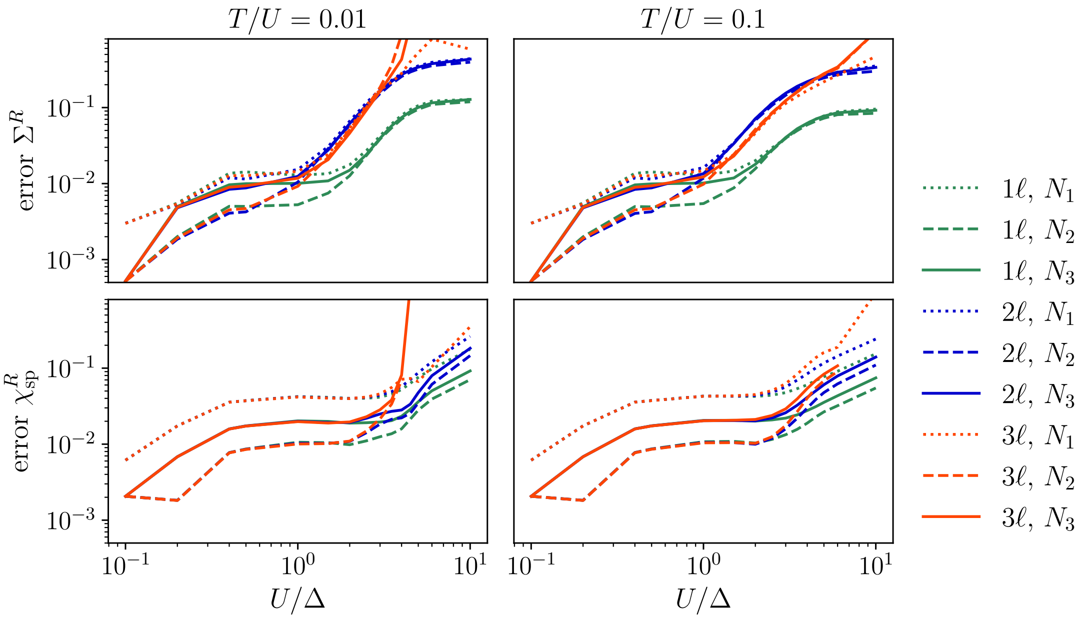

Figure 7.11 Integrated relative violation (Eq. (7.10)) of the Kramers-Kronig relation (Eq. (7.9)) for retarded self-energy (upper panels) and spin susceptibility (lower panels), as a function of U/Δ. Results are shown for $T/U = 0.01$ (left) and $T/U = 0.1$ (right), obtained from 1-, 2-, and 3-loop flows with different numerical parameters (cf. Table 6.1). The error continuously accumulates during the flow, but can be reduced by increasing the density of the frequency grid ($N_1 \to N_2$).

Eq. (2.32) we have

$$\operatorname{Re}\Sigma^K(\nu) = 0\,, \quad \operatorname{Im}\Sigma^K(\nu) = 2\tanh\left(\frac{\nu}{2T}\right)\operatorname{Im}\Sigma^R(\nu)\,. \tag{7.11}$$

Similarly, for χ_{sp} Eq. (4.62) translates to

$$\operatorname{Re}\chi^K_{\mathrm{sp}}(\omega) = 0\,, \quad \operatorname{Im}\chi^K_{\mathrm{sp}}(\omega) = 2\coth\left(\frac{\omega}{2T}\right)\operatorname{Im}\chi^R_{\mathrm{sp}}(\omega)\,. \tag{7.12}$$

The real parts of Σ^K and χ^K_r for all channels $r = a, p, t$ (and thus also for χ^K_{sp}) vanish up to numerical precision (error $< 10^{-15}$) in any loop order and for all choices of numerical parameters. For the imaginary parts, we compare the left and right-hand side of the FDTs in Fig. 7.12. Similar to the Kramers-Kronig relation, at weak coupling $U/\Delta = 1$ the agreement is almost perfect, while at intermediate $U/\Delta = 3$ small deviations start to evolve, in particular at small frequencies.

Again, we define an integrated relative error,

$$\frac{\int \mathrm{d}\nu \left|\operatorname{Im}\Sigma^K(\nu) - 2\tanh\left(\frac{\nu}{2T}\right)\operatorname{Im}\Sigma^R(\nu)\right|}{\int \mathrm{d}\nu \left|\operatorname{Im}\Sigma^K(\nu)\right|}\,, \quad \frac{\int \mathrm{d}\omega \left|\operatorname{Im}\chi^K_{\mathrm{sp}}(\omega) - 2\coth\left(\frac{\omega}{2T}\right)\operatorname{Im}\chi^R_{\mathrm{sp}}(\omega)\right|}{\int \mathrm{d}\omega \left|\operatorname{Im}\chi^K_{\mathrm{sp}}(\omega)\right|}\,, \tag{7.13}$$

to study the deviation more systematically, see Fig. 7.13. As for Kramers-Kronig, the results significantly improve by increasing the density of frequency grid points ($N_1 \to N_2$), while the error does not decrease by increasing the number of ODE steps ($N_2 \to N_3$). Remarkably,

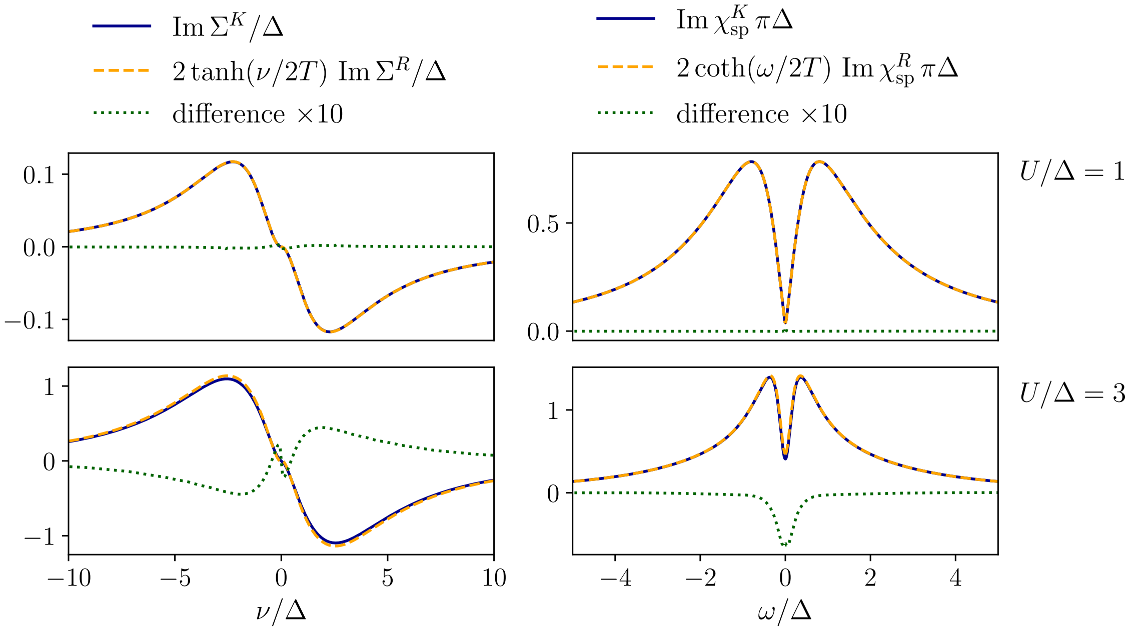

Figure 7.12 Left and right side of the FDT for self-energy (left, Eq. (7.11)) and spin susceptibility (right, Eq. (7.12)), and their difference, at $U/\Delta = 1$ (upper panels) and $U/\Delta = 3$ (lower panels). Results are obtained from a 3-loop flow at $T/U = 0.01$. While at weak coupling the agreement is almost perfect, at intermediate coupling the FDTs are slightly violated at small frequencies $\nu, \omega \lesssim \Delta$ both for Σ and χ_{sp}.

the error in the FDT for Σ first decreases along the flow before increasing again, which indicates that the initial condition of the frequency grid parameters is not optimally chosen. And indeed, further evaluation shows that at the beginning of the flow, the violation of the self-energy FDT is strongest for few points at high frequencies. These significantly influence the integrated error due to the high weight of the integration measure at very large frequencies, where frequency points are lying far apart. This points to an insufficient frequency resolution at high frequencies, which should thus be further optimized in the future, e.g. by increasing the numerical frequency window, or choosing a different decay of the grid mapping function at high frequencies (cf. Sec. 6.2). For the FDTs, another likely cause of error might be insufficient resolution on the scale $\omega \sim T$, since our choice of frequency grid (cf. Sec. 6.2) is a compromise between good resolution at small, intermediate and high frequencies, $T \ll \Delta \ll \omega_{\mathrm{max}}$, and cannot achieve perfect resolution at all scales. However, the fulfillment of the FDTs does not improve for higher temperature $T/U = 0.1$ compared to $T/U = 0.01$, which lets us conclude that finite resolution at small frequencies is only a subdominant error source.

7.3 Specific properties of the SIAM

We now turn toward properties of the SIAM spectral function (Eq. (5.16)). At zero frequency, with $\mathrm{Re}\,\Sigma^R(0) = 0$ (at half filling) we have

$$\mathcal{A}(0)\pi\Delta = \frac{1}{1 - \mathrm{Im}\,\Sigma^R(0)/\Delta}\,. \tag{7.14}$$

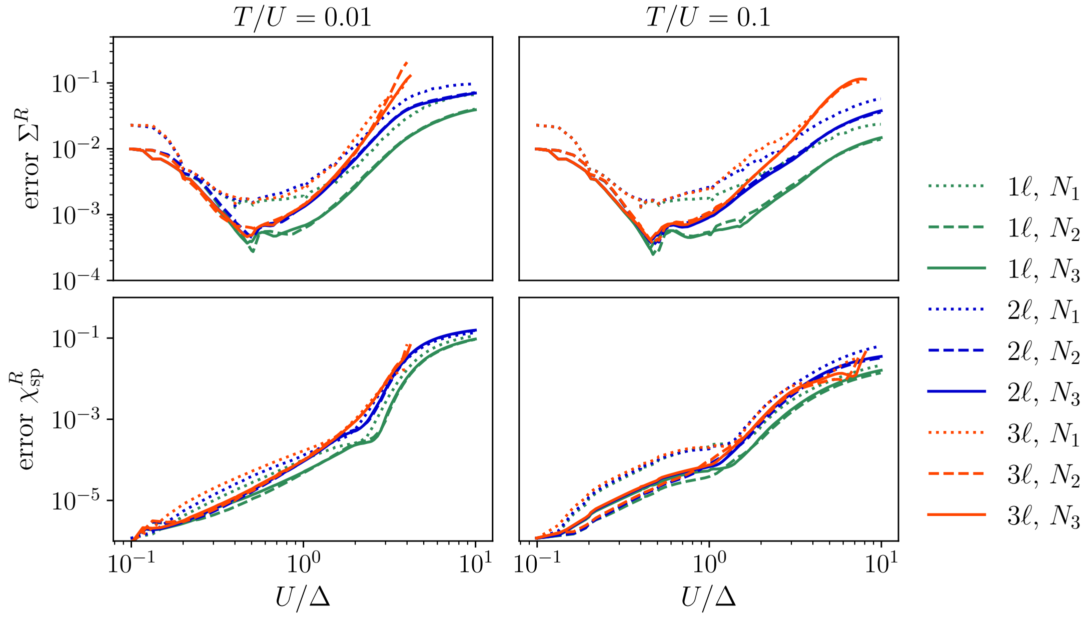

Figure 7.13 Integrated relative violation (Eq. (7.13)) of the equilibrium FDTs for retarded self-energy (Eq. (7.11), upper panels) and spin susceptibility (Eq. (7.12), lower panels), as a function of U/Δ. Results are shown for $T/U = 0.01$ (left) and $T/U = 0.1$ (right), obtained from 1-, 2-, and 3-loop flows with different numerical parameters (cf. Table 6.1). The error can again be suppressed by increasing the density of the frequency grid. A decrease of the self-energy error with increasing U/Δ points to a suboptimal choice of frequency grid parameters for the initial condition, which is partially compensated in the early iterations of the flow.

In PT2 (Eq. (3.14) of [Yam75a]),

$$\Sigma^R(\nu) = -\left(3 - \frac{\pi^2}{4}\right)\left(\frac{U}{\pi\Delta}\right)^2 \nu - i\,\frac{\Delta}{2}\left(\frac{U}{\pi\Delta}\right)^2 \left[\left(\frac{\nu}{\Delta}\right)^2 + \left(\frac{\pi T}{\Delta}\right)^2\right] + \mathcal{O}\left(\left(\frac{U}{\pi\Delta}\right)^4\right), \tag{7.15a}$$

$$\Rightarrow \Sigma^R(0) = -i\,\frac{\Delta}{2}\left(\frac{U}{\pi\Delta}\right)^2 \left(\frac{\pi T}{\Delta}\right)^2 + \mathcal{O}\left(\left(\frac{U}{\pi\Delta}\right)^4\right), \tag{7.15b}$$

which yields

$$\mathcal{A}(0)\pi\Delta = \frac{1}{1 + \frac{1}{2}\left(\frac{U}{\pi\Delta}\right)^2\left(\frac{\pi T}{\Delta}\right)^2} + \dots \tag{7.16}$$

At $T = 0$, the well-known Friedel sum rule follows,

$$\mathcal{A}(0)\pi\Delta \overset{!}{=} 1\,, \tag{7.17}$$

while $\mathcal{A}(0)\pi\Delta < 1$ at $T > 0$ (and $U > 0$). In Fig. 7.14, we show results for the spectral function at zero frequency, comparing to the PT2 result of Eq. (7.16) and also to NRG, which can be considered to be numerically exact even for large U/Δ. We see almost no difference between the data sets N_1, N_2, N_3, which proves convergence in the numerical parameters. Deviations from NRG are obviously due to the perturbative nature of the PA,

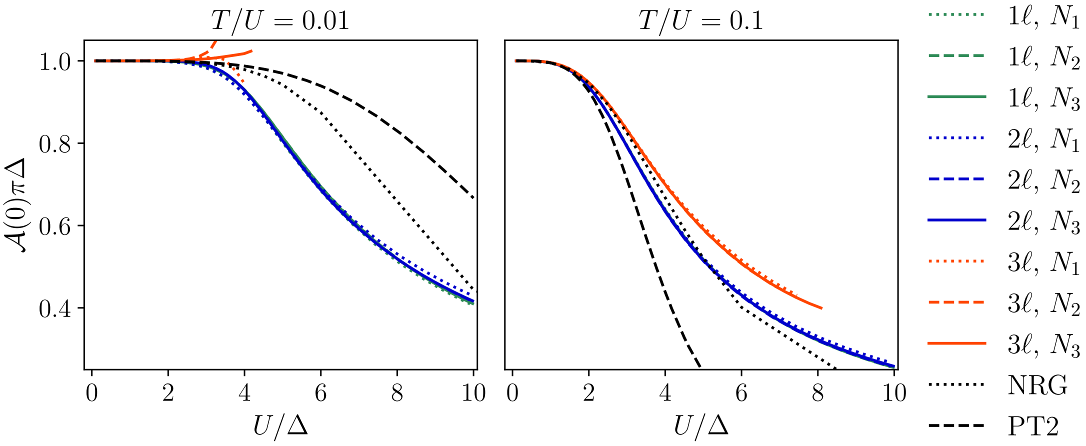

Figure 7.14 Spectral function at $\nu = 0$ (yielding the Friedel sum rule for $T = 0$ or $U = 0$) as a function of U/Δ. Results are shown for $T/U = 0.01$ (left) and $T/U = 0.1$ (right), obtained from 1-, 2-, and 3-loop flows with different numerical parameters (cf. Table 6.1). We compare the results to NRG and PT2 (Eq. (7.16)). The results seem to be fully converged in the numerical parameters, since all lines lie almost perfectly on top of each other. Note that 3-loop at $T/U = 0.01$ starts to produce unsensible results at $U/\Delta \sim 4$, shortly before the divergence of the flow.

but in particular for $T/U = 0.1$, even one-loop fRG is much closer to NRG than the PT2 result.

Next, we analyze the normalization of the spectral function. Since $\mathcal{A}$ is essentially a probability density,

$$\int_{-\infty}^{\infty} \mathrm{d}\nu \mathcal{A}(\nu) \overset{!}{=} 1 \tag{7.18}$$

has to be strictly fulfilled. Note that we can analytically integrate $\mathcal{A}$ outside the frequency range on which the self-energy is sampled (in a similar spirit as for bubble and loop integrals in Sec. 6.3.2), since for $\Sigma^R = \Sigma_H$ we simply have (cf. Eq. (5.16))

$$\mathcal{A}(\nu) = \frac{1}{\pi} \frac{\Delta}{\nu^2 + \Delta^2} . \tag{7.19}$$

We show the deviation from perfect normalization in Fig. 7.15. At small U/Δ, increasing the frequency resolution from N_1 to N_2 considerably reduces the error from the permille to the subpermille region. At $U/\Delta \gtrsim 3$, the error increases up to a few percent. This suggests that merely shrinking the frequency grid with Δ (cf. Sec. 6.2) is not sufficient from this point on, because most likely Σ^R has not sufficiently decayed to Σ_H at the boundaries of the frequency interval on which it is sampled (but is still approximated by zero outside this interval). As a result, spectral weight is missing in the tails of $\mathcal{A}$. It should be possible to reduce this issue by providing a more robust frequency grid, adjusting the grid boundaries with a strict criterion on how small $\Sigma^R - \Sigma_H$ has to be there. For the 3-loop flow at $T/U = 0.01$, the integral over the spectral function becomes significantly larger than 1, i.e., $\mathcal{A}$ has too much spectral weight. This can be directly attributed to the violation of causality (cf. Sec. 7.2.1), i.e., $\operatorname{Im} \Sigma^R > 0$, which obviously leads to unphysical results.

Let us now summarize the results of the tests presented in this chapter: In general, numerical errors are rather small, but they systematically increase during the flow due to the structure of the flow equations, which require iterative re-insertion of previous results when computing the next step in the flow. Therefore, care should be taken if one wants to reach

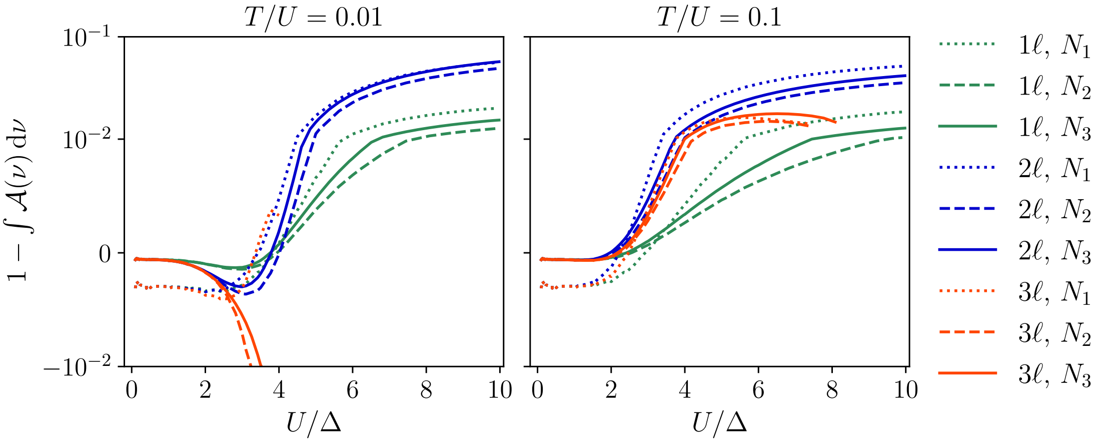

Figure 7.15 Error in the normalization of the spectral function as a function of U/Δ. Results are shown for $T/U = 0.01$ (left) and $T/U = 0.1$ (right), obtained from 1-, 2-, and 3-loop flows with different numerical parameters (cf. Table 6.1).

large values of U/Δ. Errors can typically be further reduced by increasing the density of frequency grid points, while the finite ODE step size seems to be a subdominant error source. Next steps should aim for a more flexible frequency grid, since we have seen indications that the boundaries of the frequency grid are not optimally chosen, in particular for large U/Δ, where a simple rescaling of the grid with Δ does not seem to fully capture the behavior of the sampled functions any more (as opposed to the regime of small U/Δ). This would come with a tradeoff between good resolution at small and at high frequencies, and between high resolution and numerical costs: To increase the grid boundaries ω_{min}, ω_{max}, one has to increase the number of frequency grid points or accept a lower density of grid points at small frequencies.

A different strategy for improving the high-frequency resolution would be to extrapolate self-energy and vertex functions outside the finite frequency grid on which they are sampled, according to some power law. In the Keldysh formalism, analytically finding the exact power-law decay is most likely difficult (if not impossible) due to the logarithmic corrections appearing (see the second-order expressions found in Sec. 7.1.1). However, one might determine the exponent and coefficients of an approximate power law by fitting the numerically sampled tails, thereby improving the high-frequency asymptotic behavior compared to simply cutting of the tails at ω_{min}, ω_{max}.

8 Dynamical and static properties

After having evaluated the validity of the numerics and discussed how to control errors caused by numerical approximations in the last chapter, we now present results for dynamical and static properties of the single-impurity Anderson model. As motivated in the introduction and also in Sec. 5.3, the main goal will be to answer the following question: How well can we reproduce known results quantitatively using Keldysh mfRG, and to which extent do the results improve by including the full vertex frequency dependence and multiloop terms? To this end, we compare our 1-loop, 2-loop, and 3-loop results to (numerically exact) NRG benchmark data, and we also compare to the approximation scheme used in all previous works on Keldysh fRG (e.g. [JMS07, Jak09, JPS10a, SBvD17, WvD19]), namely, a 1-loop flow (without Katanin substitution [Kat04]) with only $\mathcal{K}_1$ and only static self-energy feedback and static interchannel vertex feedback (abbreviated $\mathcal{K}_1$SF in the following).

In this simplified 1-loop scheme, the flow equations are Eq. (3.1a) and Eq. (3.1b) (with $\Gamma^{(6)} = 0$). The vertex only includes $\mathcal{K}_1$, $\Gamma \approx \Gamma_0 + \sum_r \mathcal{K}_1^r(\omega_r)$. The self-energy entering the flow equations via (full and single-scale) propagators is approximated by a static level shift $\Sigma^R \approx \operatorname{Re}\Sigma^R(\mu)$, $\Sigma^K \approx 0$. At half filling, this amounts to $\Sigma \approx \Sigma_H$, i.e., all propagators in the flow equations (3.1a) and (3.1b) are essentially bare ones, G_0 and $S_0 = \partial_\Delta G_0$ (in the sense of Eq. (5.13), with only a constant Hartree self-energy). Furthermore, vertices $\mathcal{K}_1^{r'}$ entering the flow equation for channel $r \neq r'$ are also approximated by a static constant, $\tilde{\mathcal{K}}_1^a = \mathcal{K}_1^a(\omega_a = 0)$, $\tilde{\mathcal{K}}_1^p = \mathcal{K}_1^p(\omega_p = 2\mu)$ $(= \mathcal{K}_1^p(\omega_p = 0)$ at half filling$)$, $\tilde{\mathcal{K}}_1^t = \mathcal{K}_1^t(\omega_t = 0)$. The vertex flow equations for $\mathcal{K}_1$SF read (summation over internal indices is understood)

$$\dot{\mathcal{K}}_1^r(\omega_r) = \left(\Gamma_0 + \mathcal{K}_1^r(\omega_r) + \sum_{r' \neq r} \tilde{\mathcal{K}}_1^{r'}\right) \left(\frac{\alpha_r}{2\pi i} \int \mathrm{d}\nu_r'' \, \dot{\Pi}_r(\omega_r, \nu_r'')\right) \left(\Gamma_0 + \mathcal{K}_1^r(\omega_r) + \sum_{r' \neq r} \tilde{\mathcal{K}}_1^{r'}\right) . \tag{8.1}$$

We organize this chapter as follows. We start by presenting results for dynamical correlation functions in Section 8.1, namely, the spectral function, the self-energy, and the spin susceptibility. In Section 8.2 we show various static properties and investigate the fulfillment of a one-particle Ward identity and the so-called Korringa-Shiba relation. In Section 8.3 we study the fulfillment of a sum rule that follows from Pauli's principle, and in Section 8.4 we evaluate a two-particle Ward identity related to particle number conservation. Sum rules and Ward identities provide important internal consistency checks for the method, since their fulfillment is often required for obtaining valid physical results. All results presented below are computed with the parameter set N_3 at two different temperatures $T/U = 0.01$ and $T/U = 0.1$ (cf. Table 6.1).[1] Note that since U/Δ increases during the flow, T/Δ does so as well for fixed T/U. This is important to keep in mind in particular for relations studied in the following which are only exactly fulfilled at $T = 0$. Keeping T/Δ constant during the

---

[1] At $T/U = 0.1$, the $\mathcal{K}_1$SF flow diverges at some $U/\Delta < 4$ (also see Fig. 8.5), while being stable at smaller $T/U = 0.01$. For this reason, we cannot show results for this scheme for $T/U = 0.1$ and $U/\Delta = 4$ in Figs. 8.1, 8.2, 8.3 and 8.8. The cause of this divergence is not clear, but a possible explanation is that even though including static interchannel feedback, a bare $\mathcal{K}_1$ flow is similar to resumming ladder diagrams, which are prone to divergences [KvD18b]. We will however not further study this issue, since the $\mathcal{K}_1$SF scheme is anyhow somewhat heuristic, and we can do better in a systematic way by including the full vertex frequency dependence.

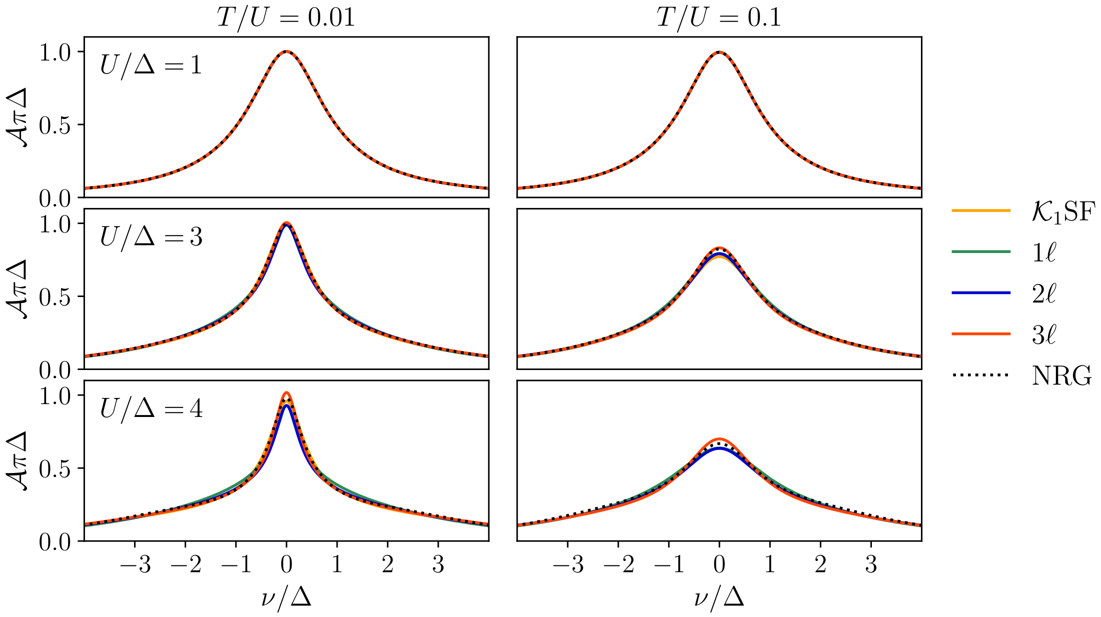

Figure 8.1 Spectral function for different interaction strengths $U/\Delta = 1$ (top row), $U/\Delta = 3$ (center row), $U/\Delta = 4$ (bottom row) and different temperatures $T/U = 0.01$ (left column) and $T/U = 0.1$ (right column), computed with a full 1-, 2-, and 3-loop flow, comparing to NRG and the $\mathcal{K}_1$SF approximation. All flows accurately reproduce NRG results.

flow would require modifications in the single-scale propagator (cf. end of Sec. 5.2) and has not been attempted here. For the values $U/\Delta = 1, 3, 4$ shown below, the Kondo temperature is $T_K/U \approx 2.3, 0.2, 0.1$.

8.1 Dynamical correlation functions

We begin by showing results for the spectral function (Eq. (5.16)) for different interaction strengths and different temperatures in Fig. 8.1. We see that all approximation schemes, $\mathcal{K}_1$SF and a full 1-, 2-, and 3-loop flow, almost perfectly reproduce the NRG benchmark data even for $U/\Delta = 4$. However, even though often studied, the spectral function is not an ideal quantity for benchmark purposes. The fact that the results of all flows agree almost perfectly, and differences are hardly visible, is actually no surprise, since at not too large U/Δ the dominant contribution to the spectral function is given by G_0, which is analytically known and therefore identical for all curves in Fig. 8.1, with only subleading corrections due to the self-energy. The only nontrivial information we can extract from Fig. 8.1 is that at $T/U = 0.1$ and $U/\Delta = 3$, the 3-loop flow is closest to the NRG result, while at $T/U = 0.01$ and $U/\Delta = 4$ we see first signatures of a value $\mathcal{A}(0)\pi\Delta > 1$ in 3-loop, which is related to the violation of the constraint (7.8) and thus a precursor of the breakdown of the flow.

In order to get a better impression how well spectral information is reproduced, in Fig. 8.2 we show the retarded self-energy, which encodes all nontrivial information (i.e., correlation effects) in the spectral function. Here, we see deviations from NRG much clearer (the difference to NRG is also explicitly shown in Fig. 8.2): At weak interaction $U/\Delta = 1$, again all flows produce consistent results, with only few percent deviation from NRG. At $T/U = 0.01$ and higher U/Δ, interestingly, NRG is best reproduced by the very simple $\mathcal{K}_1$SF approximation, while in particular 3-loop significantly deviates from NRG at $U/\Delta = 4$.

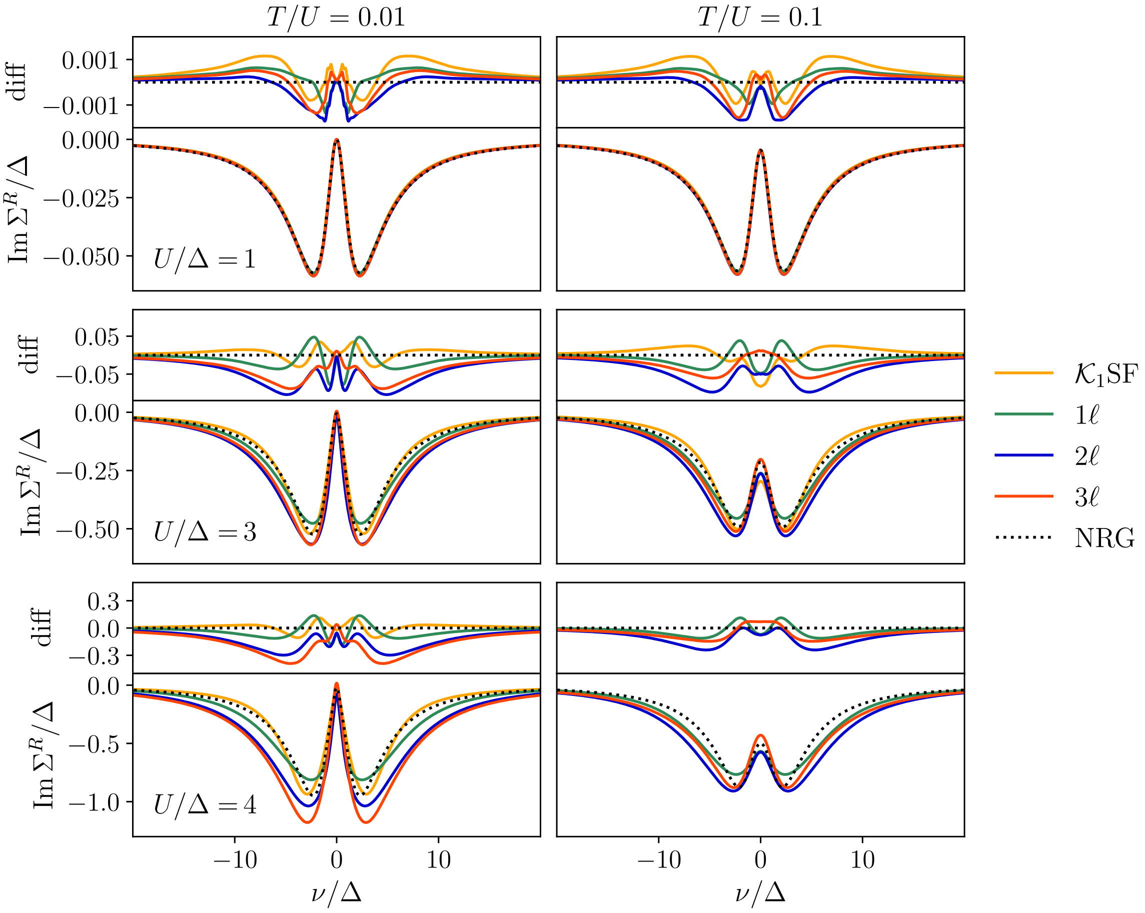

Figure 8.2 Imaginary part of the retarded self-energy for different interaction strengths $U/\Delta = 1$ (top row), $U/\Delta = 3$ (center row), $U/\Delta = 4$ (bottom row) and different temperatures $T/U = 0.01$ (left column) and $T/U = 0.1$ (right column), computed with a full 1-, 2-, and 3-loop flow, comparing to NRG and the $\mathcal{K}_1$SF approximation. For each value of U and T, “diff” is the difference between the fRG flows and NRG, $\mathrm{Im}\,(\Sigma^R_{\mathrm{fRG}} - \Sigma^R_{\mathrm{NRG}})/\Delta$. At lower temperature $T/U = 0.01$, $\mathcal{K}_1$SF best reproduces NRG results. At $T/U = 0.1$, the results show indications of an oscillatory behavior with increasing ℓ, expected to approach the PA for $\ell \to \infty$.

(This is however close to the breakdown of the 3-loop flow, as mentioned before.) At higher temperature $T/U = 0.1$, the 2-loop result lies constantly below the 1-loop result, and 3-loop above 2-loop. This indicates an oscillatory behavior with increasing loop order, which has been observed before [KvD18c, THK$^+$19]. For higher loop order, we expect convergence, while the converged result should reproduce the PA and will thus slightly deviate from NRG. This can also be seen in the difference of the sequence 1-loop, 2-loop, 3-loop to NRG: The converged result is expected to be close to the 3-loop result, which does deviate from NRG.

While the $\mathcal{K}_1$SF scheme is optimized for producing an accurate spectral function [Jak09] and does indeed perform better in this regard than a flow with the full vertex frequency dependence, it dramatically fails to correctly reproduce the spin susceptibility, see Fig. 8.3. Here the full flows agree well with NRG results, again showing an improvement of the results with increasing loop order, but $\mathcal{K}_1$SF differs by a factor of almost 1.5 even for small $U/\Delta = 1$. The comparison of Figs. 8.2 and 8.3 shows that $\mathcal{K}_1$SF is not a controlled approximation: Some quantities such as the self-energy are reproduced extremely well, while for others strong deviations occur.

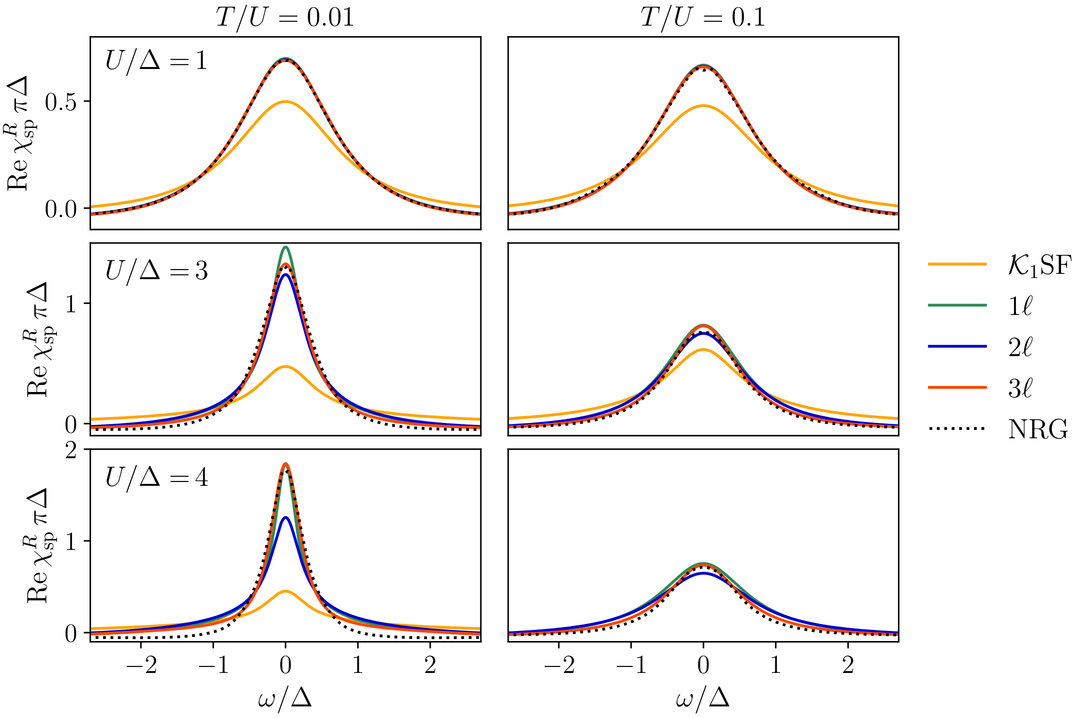

Figure 8.3 Real part of the retarded spin susceptibility for different interaction strengths $U/\Delta = 1$ (top row), $U/\Delta = 3$ (center row), $U/\Delta = 4$ (bottom row) and different temperatures $T/U = 0.01$ (left column) and $T/U = 0.1$ (right column), computed with a full 1-, 2-, and 3-loop flow, comparing to NRG and the $\mathcal{K}_1$SF approximation. Increasing the loop order improves results, while $\mathcal{K}_1$SF strongly deviates from NRG already for $U/\Delta = 1$.

The spin susceptibility can be directly accessed from $\mathcal{K}_1^a$ via Eq. (4.21). However, it can also be obtained from the formal definition of the susceptibilities in Eq. (4.17), by connecting two pairs of propagators on both sides of the full vertex (and adding a connected pair of propagators). In Fig. 8.4, we compare the former (“flowing”) and the latter (“post-processed”) way of computing χ_{sp}. Formally, Eq. (4.21) follows from Eq. (4.17) through the BSE, as argued in Sec. 4.1.3. An exact agreement of the flowing and post-processed susceptibility is thus only required for a loop-converged multiloop flow that by construction fulfills parquet self-consistency. For a truncated multiloop flow or the $\mathcal{K}_1$SF approximation, comparing the two ways of computing χ_{sp} gives a useful internal consistency check between the one- and two-particle level. We see in Fig. 8.4 that for $\mathcal{K}_1$SF already at $U/\Delta = 1$ strong deviations are visible, while even a one-loop flow with full vertex frequency dependence well fulfills this consistency also at higher $U/\Delta = 3$. Note that the post-processed susceptibility for $\mathcal{K}_1$SF is closer to the 3-loop result (and thus to NRG) than the flowing one, but still shows significant deviations in particular at higher $U/\Delta = 3$.

8.2 Static properties

We now turn toward static properties, in order to compare more systematically how the results evolve for different loop orders as a function of the interaction strength U/Δ. We first study the static spin susceptibility (i.e., the value of χ^R_{sp} of Fig. 8.3 at frequency $\omega = 0$) in the left column of Fig. 8.5, again at two different temperatures $T/U = 0.01$ and

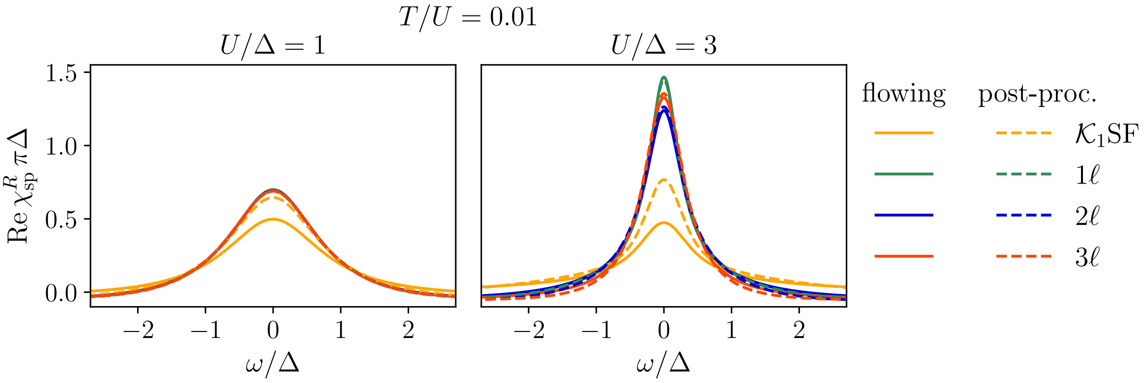

Figure 8.4 Real part of the retarded spin susceptibility for temperature $T/U = 0.01$ and different interaction strengths $U/\Delta = 1$ (left) and $U/\Delta = 3$ (right), computed in the $\mathcal{K}_1$SF approximation and with a full 1-, 2-, and 3-loop flow. "Flowing" results (solid lines) are directly obtained from $\mathcal{K}_1^a$ via Eq. (4.21), while "post-processed" results (dashed lines) are computed from the full vertex via Eq. (4.17). Both results are consistent for ℓ-loop flows with full vertex frequency dependence, while $\mathcal{K}_1$SF shows significant deviations.

$T/U = 0.1$. As discussed in Sec. 5.3, the static spin susceptibility is a good predictor for Kondo physics: The exponential suppression of the Kondo temperature with the interaction U is reflected in an exponential increase of $\chi^R_{\mathrm{sp}}(0)$ at large U/Δ. Unfortunately, as already anticipated in Sec. 5.3, none of the fRG flows does show this behavior in the large-U regime; instead, the susceptibility decreases after reaching a maximum at intermediate U. At the lower temperature $T/U = 0.01$, the 3-loop flow reproduces NRG remarkably well up to an interaction strength $U/\Delta \sim 4$. However, no reliable statements can be made beyond that point before curing the aforementioned numerical issues, leading to the breakdown of the flow. The $\mathcal{K}_1$SF approximation results in a qualitatively wrong behavior of χ^R_{sp} as a function of U/Δ, again indicating its failure to accurately capture vertex properties (as already seen in Fig. 8.3).

Next, we compute the quasiparticle weight

$$Z = \left(1 - \frac{\mathrm{d}\Sigma^R(\nu)}{\mathrm{d}\nu}\bigg|_{\nu=0}\right)^{-1}, \tag{8.2}$$

which is a measure for the strength of correlation effects: In order to describe the bare quasiparticle peak of the spectral function at $\nu = 0$, we can Taylor-expand the self-energy, $\Sigma^R(\nu) = \Sigma_H + \nu\,\partial_\nu \mathrm{Re}\,\Sigma^R|_{\nu=0} + \mathcal{O}(\nu^2) = \Sigma_H + \nu(1 - Z^{-1}) + \mathcal{O}(\nu^2)$ (since $\mathrm{Im}\,\Sigma^R$ is symmetric around $\nu = 0$, cf. Fig. 8.2, it does not contribute to the first-order term). Inserting the first-order approximation into the spectral function (Eq. (5.16)) yields the quasiparticle (qp) contribution

$$\mathcal{A}_{\mathrm{qp}}(\nu) = \frac{1}{\pi\Delta}\frac{1}{1 + Z^{-2}\left(\frac{\nu}{\Delta}\right)^2}, \tag{8.3}$$

with spectral weight

$$\int \mathrm{d}\nu \mathcal{A}_{\mathrm{qp}}(\nu) = Z\,. \tag{8.4}$$

In the noninteracting case, we have $Z = 1$, i.e., the spectral function is fully described by a bare quasiparticle peak, $\mathcal{A} = \mathcal{A}_{\mathrm{qp}}$. If $Z < 1$, correlation effects introduce new spectral features

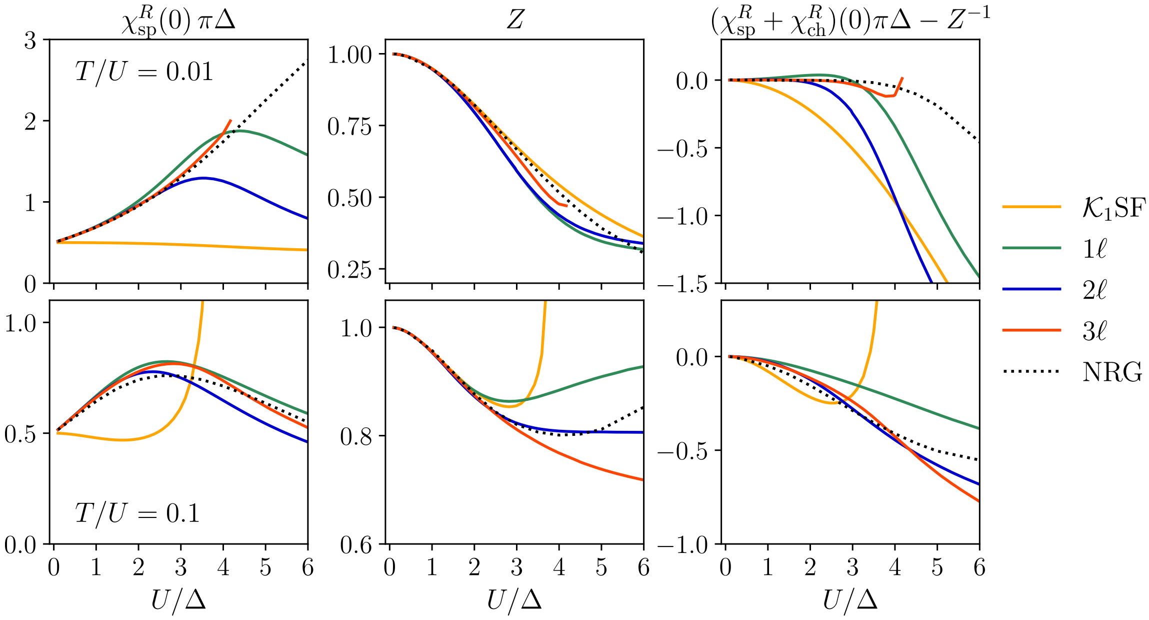

Figure 8.5 Static retarded spin susceptibility χ^R_{sp} (left column), quasiparticle weight Z (center column), and difference between left and right-hand side of the Ward identity (8.5) (right column), as functions of the interaction strength U/Δ. Results are shown at $T/U = 0.01$ (upper row) and $T/U = 0.1$ (lower row), computed with a full 1-, 2-, and 3-loop flow, comparing to NRG and the $\mathcal{K}_1$SF approximation.

(e.g. the exponentially narrow Kondo resonance with a very small quasiparticle weight), and for $Z = 0$ the quasiparticle peak would completely disappear, indicating a spectral gap related to Mott-insulating behavior e.g. in the Hubbard model.

The result for Z is plotted in the center column of Fig. 8.5. We see that in particular for low temperature $T/U = 0.01$, the quasiparticle weight strongly decreases for increasing interaction U. The NRG behavior is reproduced quite well by all loop orders and also by $\mathcal{K}_1$SF, the latter resulting from the good resolution of the self-energy within the $\mathcal{K}_1$SF approximation (cf. Fig. 8.2). At higher temperature $T/U = 0.1$, correlation effects seem to be smeared out by thermal fluctuations, and interestingly this seems to be more difficult to be captured in mfRG, since at large U/Δ loop convergence is by far not reached at $\ell = 3$. It might be interesting to see how higher loop orders and in particular multiloop corrections to the self-energy modify this behavior.

8.2.1 One-particle Ward identity

The sum of static spin and charge susceptibilities is related to the quasiparticle weight by means of a (one-particle) Ward identity (Eq. (4.12) of [Yam75a]),

$$(\chi^R_{\mathrm{sp}} + \chi^R_{\mathrm{ch}})(0)\,\pi\Delta = Z^{-1}\,. \tag{8.5}$$

This identity provides a useful internal consistency check for the method by enabling a connection between self-energy and vertex: Z is by definition (Eq. (8.2)) a property of the self-energy, while the susceptibilities are obtained from the $\mathcal{K}_1$ classes of the vertex (Eq. (4.21)). In the right column of Fig. 8.5, we show the difference between the left and right-hand side of Eq. (8.5). Note that the Ward identity is derived at $T = 0$ and does not

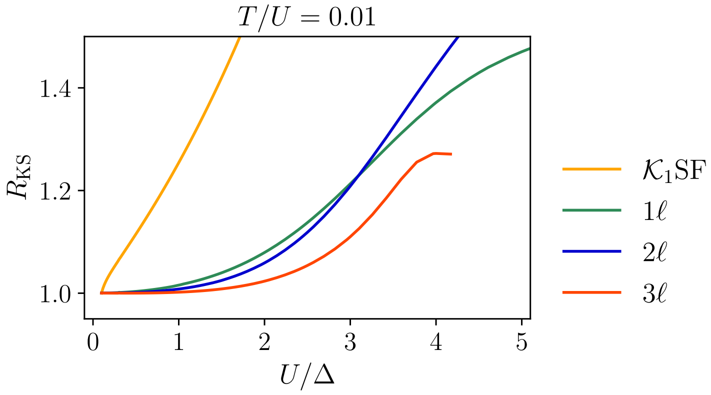

Figure 8.6 Korringa-Shiba ratio (8.7) at $T/U = 0.01$ as a function of the interaction strength U/Δ. Results are computed in the $\mathcal{K}_1$SF approximation and with a full 1-, 2-, and 3-loop flow. The Korringa-Shiba relation is better fulfilled for increasing loop order, while being strongly violated for $\mathcal{K}_1$SF already at small U/Δ.

necessarily need to be fulfilled at higher temperature; hence we again compare to the NRG result. At $T/U = 0.01$, 3-loop again gives the best agreement with NRG up to $U/\Delta \sim 4$, after which the corresponding flow becomes unstable. At higher temperature $T/U = 0.1$, loop-convergence again seems to be slower. Note that $\mathcal{K}_1$SF deviates quite strongly even at small U/Δ, which is expected since it well captures Σ and Z, but not χ.

8.2.2 Korringa-Shiba relation

Another connection between static properties of quite immediate physical interpretation is the so-called Korringa-Shiba relation [Shi75]

$$\lim_{\omega\to 0} \frac{\mathrm{Im}\,\chi^R_{\mathrm{sp}}(\omega)}{\omega} = 2\pi(\chi^R_{\mathrm{sp}}(0))^2 \,. \tag{8.6}$$

Since $\mathrm{Im}\,\chi^R_{\mathrm{sp}} \sim \omega$ for small ω, the left-hand side corresponds to the slope of $\mathrm{Im}\,\chi^R_{\mathrm{sp}}$ at $\omega = 0$, which can be interpreted as inverse spin relaxation time [Shi75], while the right-hand side is again the static spin susceptibility (squared). To check this relation, we define a Korringa-Shiba ratio

$$R_{\mathrm{KS}} = \frac{\lim_{\omega\to 0} \mathrm{Im}\,\chi^R_{\mathrm{sp}}(\omega)/\omega}{2\pi(\chi^R_{\mathrm{sp}}(0))^2} \overset{!}{=} 1\,, \tag{8.7}$$

shown in Fig. 8.6. The Korringa-Shiba relation is again derived at $T = 0$, thus we only show results for the smaller temperature $T/U = 0.01$. Obviously, R_{KS} deviates from 1 for large U/Δ, since T/Δ also increases during the flow. At small U/Δ, we see a significant improvement from 1-loop to 2-loop to 3-loop, while $\mathcal{K}_1$SF strongly violates the Korringa-Shiba relation.

After having confirmed consistency relations for static properties, in the next two sections 8.3 and 8.4 we evaluate two dynamical relations with important physical implications.

8.3 Sum rule for susceptibility

For the equal-spin particle-hole susceptibility $\chi_{\sigma\sigma} = (\chi_t)_{\sigma\sigma}$ (Eq. (4.18)), the following sum rule holds:

$$\int_{-\infty}^{\infty} \frac{d\omega}{2\pi i}\, \chi^K_{\sigma\sigma}(\omega) = \langle n_\sigma^2 \rangle - \langle n_\sigma \rangle^2 = \langle n_\sigma \rangle (1 - \langle n_\sigma \rangle) \overset{\text{half filling}}{=} \frac{1}{4}\,. \tag{8.8}$$

The second equality follows from the Pauli principle which requires that $n_\sigma^2 = n_\sigma$, since the eigenvalues of the particle number operator n_σ can either be 0 or 1. This sum rule is thus an excellent test how well a (numerical) method fulfills the Pauli principle. The first equality can be derived from the corresponding sum rule in the Matsubara formalism [VT97, CGKH$^+$21],

$$\frac{1}{\beta} \sum_n \chi_{\sigma\sigma}(i\omega_n) = \chi_{\sigma\sigma}(\tau = 0) = \langle n_\sigma^2 \rangle - \langle n_\sigma \rangle^2\,, \tag{8.9}$$

with the bosonic Matsubara frequencies $i\omega_n = 2\pi i n/\beta$, $n \in \mathbb{Z}$, with $\beta = 1/T$. Here the first equality is simply the definition of the Fourier transform of $\chi_{\sigma\sigma}(\tau = 0)$ on the Matsubara axis, and the second equality follows from the definition of χ (Eq. (4.18)), obtained from the 4-point correlation function (Eq. (2.18)) by connecting two pairs of legs and subtracting the disconnected part $\langle n_\sigma \rangle^2$. In order to analytically continue Eq. (8.9) to the real frequency axis to obtain Eq. (8.8), we can write the Matsubara sum of $\chi_{\sigma\sigma}(i\omega)$ over frequencies in the upper half plane as a contour integral of $\chi_{\sigma\sigma}(i\omega \to \omega + i0^+)$ along the real axis:

$$\begin{aligned}
\frac{1}{\beta} \sum_n \chi_{\sigma\sigma}(i\omega_n) &= \frac{1}{\beta} \sum_{n\neq 0} \chi_{\sigma\sigma}(i\omega_n) + \frac{1}{\beta}\, \chi_{\sigma\sigma}(i\omega_0) \\
&\overset{(1)}{=} \frac{2}{\beta} \sum_{n>0} \chi_{\sigma\sigma}(i\omega_n) + \frac{1}{\beta}\, \chi_{\sigma\sigma}(0) \\
&\overset{(2)}{=} \frac{1}{2\pi i} \int_{-\infty}^{\infty} d\omega \coth\left(\frac{\omega + i0^+}{2T}\right) \chi_{\sigma\sigma}(\omega + i0^+) + \frac{1}{\beta}\, \chi_{\sigma\sigma}(0) \\
&\overset{(3,4)}{=} \frac{1}{2\pi i} \left[\mathcal{P} \int_{-\infty}^{\infty} d\omega \coth\left(\frac{\omega}{2T}\right) 2\chi^R_{\sigma\sigma}(\omega) - i\pi\, \frac{2}{\beta}\, \chi_{\sigma\sigma}(0) \right] + \frac{1}{\beta}\, \chi_{\sigma\sigma}(0) \\
&= \frac{1}{2\pi i}\, \mathcal{P} \int_{-\infty}^{\infty} d\omega\, 2 \coth\left(\frac{\omega}{2T}\right) \left[\operatorname{Re} \chi^R_{\sigma\sigma}(\omega) + i \operatorname{Im} \chi^R_{\sigma\sigma}(\omega) \right] \\
&\overset{(5)}{=} \frac{1}{2\pi i} \int d\omega\, 2i \coth\left(\frac{\omega}{2T}\right) \operatorname{Im} \chi^R_{\sigma\sigma}(\omega) \overset{\text{Eq. (4.62)}}{=} \frac{1}{2\pi i} \int d\omega\, \chi^K_{\sigma\sigma}(\omega)\,.
\end{aligned} \tag{8.10}$$

Here we have used the following observations:

(1) $\chi_{\sigma\sigma}$ is symmetric, since in $\langle n_\sigma^2 \rangle$ the two operators n_σ can trivially be exchanged.

(2) $\coth\left(\frac{\omega}{2T}\right)$ has poles at the bosonic Matsubara frequencies $i\omega_n$, with corresponding residue $2/\beta$. We can thus use the residue theorem for the contour 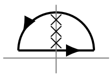 , with the radius of the semicircle going to infinity.

(3) $\coth\left(\frac{\omega}{2T}\right)$ has a simple pole at $\omega = 0$, thus

$$\coth\left(\frac{\omega + i0^+}{2T}\right) = \frac{1}{\omega + i0^+} \underbrace{\left[(\omega + i0^+) \coth\left(\frac{\omega + i0^+}{2T}\right) \right]}_{\text{regular}}\,. \tag{8.11}$$

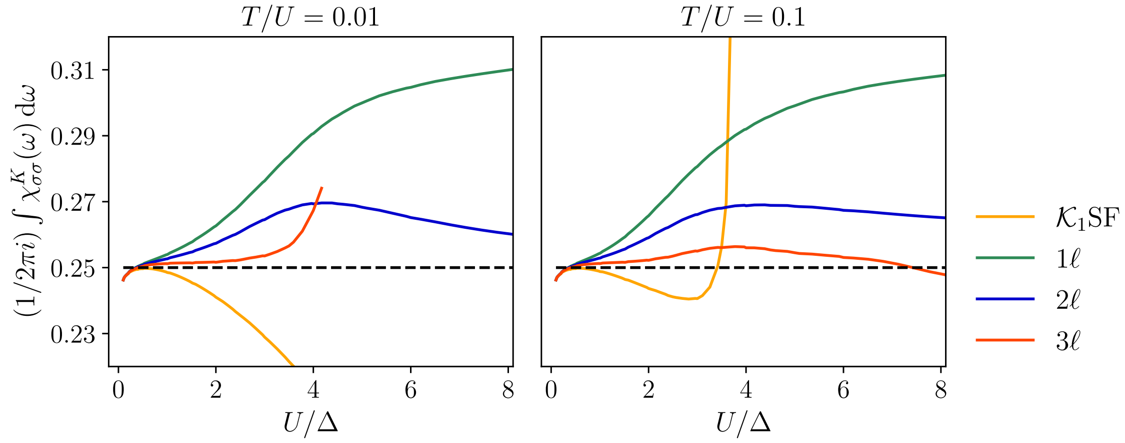

Figure 8.7 Testing the fulfillment of the sum rule (8.8) for the Keldysh component of the equal-spin particle hole susceptibility $\chi^K_{\sigma\sigma}$ as a function of the interaction strength U/Δ. Results are computed in the $\mathcal{K}_1$SF approximation and with a full 1-, 2-, and 3-loop flow. The black dashed line indicates the exact value of 1/4 that the integral over $\chi^K_{\sigma\sigma}$ should give. We see significant improvement with increasing loop order.

For integrating the pole we can use the Dirac identity $\frac{1}{\omega+i0^+} = \mathcal{P}\frac{1}{\omega} - i\pi\delta(\omega)$, with $\lim_{\omega\to 0}\omega\coth\left(\frac{\omega}{2T}\right) = 2T = \frac{2}{\beta}$.

(4) In the way we have defined the susceptibilities, namely, via two-particle correlation functions (Eq. (4.17)), they acquire a factor of 2 in the Keldysh rotation compared to the Matsubara susceptibilities. Therefore, when analytically continuing χ, one obtains $\chi_{\sigma\sigma}(i\omega \to \omega + i0^+) = 2\chi^R_{\sigma\sigma}(\omega)$.

(5) $\mathrm{Re}\,\chi^R_{\sigma\sigma}(\omega)$ is symmetric and coth antisymmetric, hence $\mathcal{P}\int \mathrm{d}\omega \coth\left(\frac{\omega}{2T}\right)\mathrm{Re}\,\chi^R_{\sigma\sigma}(\omega) = 0$.

The result of the left-hand side of Eq. (8.8) obtained from numerics is shown in Fig. 8.7, comparing to the value of 1/4 required by the Pauli principle. We see a strong improvement of the sum rule with increasing loop order up to the highest U/Δ reachable. While for $T/U = 0.01$ we of course have to restrict to $U/\Delta < 4$ for 3-loop, for higher temperature $T/U = 0.1$ we even obtain significant improvement up to interactions as high as $U/\Delta = 8$. This is a very important observation, since a violation of a concept as fundamental as the Pauli principle would considerably question the validity of results for physical observables.

8.4 Two-particle Ward identity

We conclude this chapter by presenting the results for a two-particle Ward identity that follows from particle number conservation (i.e., U(1) symmetry) (derived in [HBSvD17], Eqs. (C24), (C26)):

$$\tilde{\Phi}(\nu) = -2\,\mathrm{Im}\,\Sigma^R(\nu)\,, \tag{8.12}$$

with

$$\tilde{\Phi}(\nu) = \frac{\Delta}{i\pi}\int_{-\infty}^{\infty} \mathrm{d}\nu' G^A(\nu')G^R(\nu')\Big[\Gamma^{12|21}(\nu'\nu|\nu\nu') \\ - (1-2\,n_F(\nu'))\left(\Gamma^{12|22}(\nu'\nu|\nu\nu') - \Gamma^{22|21}(\nu'\nu|\nu\nu')\right)\Big]\,. \tag{8.13}$$

This Ward identity is particularly important for computing transport properties: It is a prerequisite for the derivation of a conductance formula in [HBSvD17], needed to compute the linear conductance from equilibrium calculations. In a recent study of quantum transport through a quantum point contact (simulated by a one-dimensional chain with a potential barrier) [WvD19], it was shown that this Ward identity is violated in the $\mathcal{K}_1$SF approximation, with direct implications on physical results. [WvD19] concludes that a more sophisticated methodology is indispensable for making reliable statements about physical properties.

In Fig. 8.8, we show both the left ($\tilde{\Phi}$, dotted lines) and right-hand side ($-2\,\mathrm{Im}\,\Sigma^R$, solid lines) of Eq. (8.12) as a function of ν/Δ, again for different U/Δ and different temperatures. We see that while $\mathcal{K}_1$SF significantly violates the Ward identity even at $U/\Delta = 1$, this violation is cured already on the one-loop level by including the full vertex frequency dependence. From the structure of Eq. (8.13) it is clear that a $\mathcal{K}_1$-based approximation cannot properly capture the behavior of $\tilde{\Phi}$: E.g. in the a channel only the static value $\mathcal{K}_1^a(\omega_a = 0)$ contributes to $\tilde{\Phi}$ (cf. Eq. (4.5)), while the integral over the frequency-dependent classes $\mathcal{K}_2^a$, $\mathcal{K}_{2'}^a$ and $\mathcal{K}_3^a$ is neglected. At $U/\Delta = 3$, the full 1-loop flow does slightly violate the Ward identity, but the deviation is much smaller than for $\mathcal{K}_1$SF, and it can be even further reduced by including 2- and 3-loop contributions. At $U/\Delta = 4$ we should again not fully trust 3-loop at $T/U = 0.01$, but at $T/U = 0.1$ the violation of the Ward identity is still significantly reduced by increasing the loop order.

We conclude that including the full vertex frequency dependence is indispensable for the fulfillment of Eq. (8.12), and a small violation at intermediate U/Δ can be further suppressed in multiloop fRG.

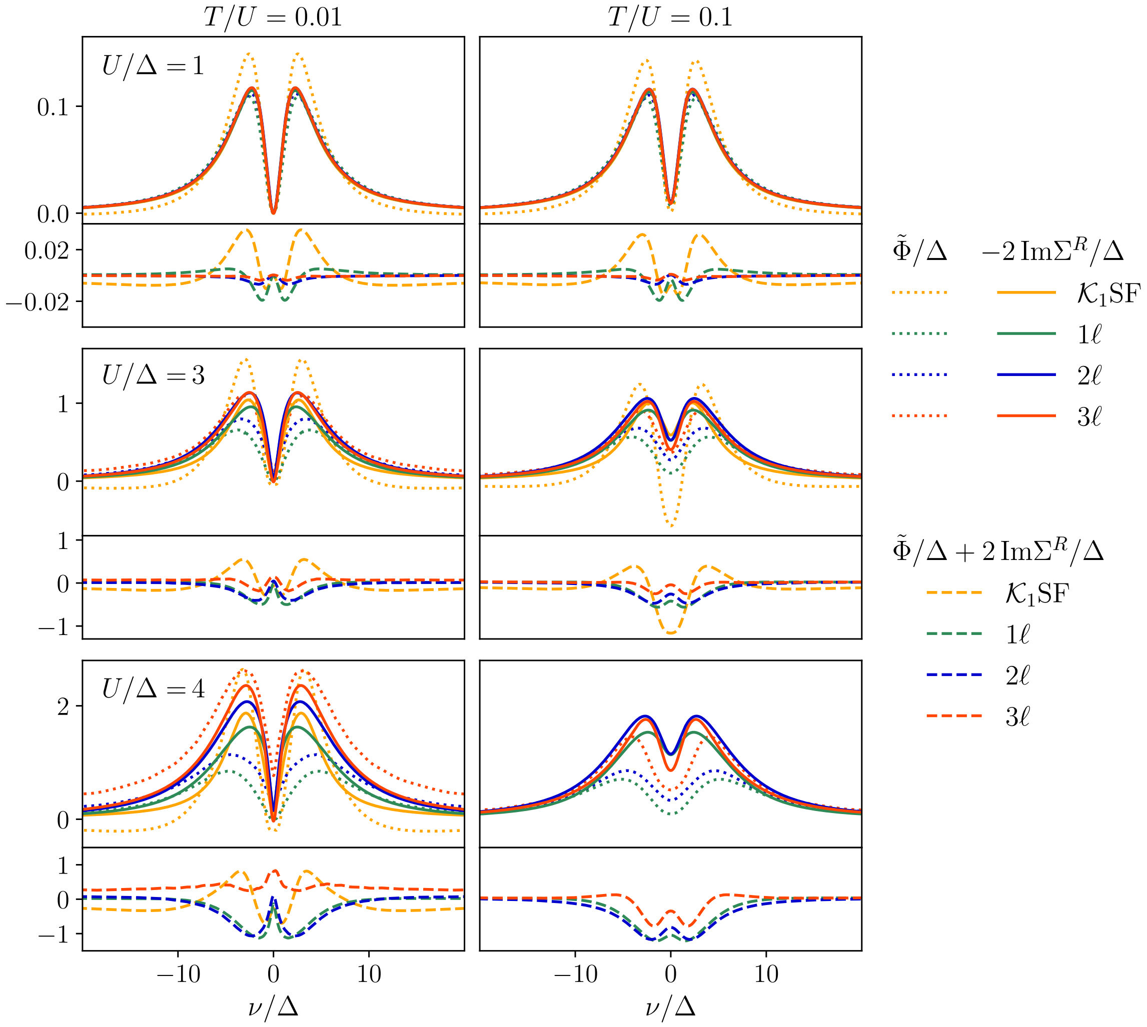

Figure 8.8 Left side (dotted) and right side (solid) of the Ward identity (8.12) and their difference (dashed) as a function of the fermionic frequency ν, for different interaction strengths $U/\Delta = 1$ (top row), $U/\Delta = 3$ (center row), $U/\Delta = 4$ (bottom row) and different temperatures $T/U = 0.01$ (left column) and $T/U = 0.1$ (right column), computed with a full 1-, 2-, and 3-loop flow, comparing to the $\mathcal{K}_1$SF approximation. Including the full vertex frequency dependence significantly improves the fulfillment of the Ward identity, and the deviation further decreases with increasing loop order ℓ.

9 Frequency-dependent two-particle vertex

In this chapter, we present results for the two-particle vertex of the SIAM. As discussed in Chapter 4, the full vertex is a huge object, which consists of two spin components (for SU(2) symmetry) and 15 nonzero Keldysh components, each depending on three real frequencies. In the following, we only show a small subset of the full data computed during the fRG flow. We restrict to the different-spin component $\Gamma_{\uparrow\downarrow}$ (if not indicated otherwise), to a selection of exemplary Keldysh components, and we plot the vertex in the two-dimensional frequency plane at $\omega_t = 0$ as a function of $(\nu, \nu') := (\nu_t, \nu'_t)$, i.e., the natural fermionic frequencies of the t channel. This frequency plane is interesting since it physically corresponds to the effective interaction of a hole and an electron with spins ↓ and ↑ and energies ν, ν' without energy transfer ($\omega_t = 0$) (cf. Eq. (4.5)):

$$\Gamma_{\uparrow\downarrow}(\nu,\nu') := \Gamma_{\uparrow\downarrow}(\omega_t = 0, \nu_t = \nu, \nu'_t = \nu') = \qquad . \tag{9.1}$$

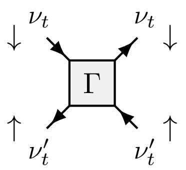

We show data of a 3-loop flow at temperature $T/U = 0.01$ for weak and intermediate bare interaction strength $U/\Delta = 0.5$ and $U/\Delta = 2.5$, which are both well in the regime where we can fully trust the current version of our numerics.

The results are shown in Fig. 9.1, decomposed into the asymptotic classes $\mathcal{K}_1$, $\mathcal{K}_2 + \mathcal{K}_{2'}$, $\mathcal{K}_3$, each summed over the three diagrammatic channels a, p, t. At weak interaction $U/\Delta = 0.5$, the vertex is dominated by the $\mathcal{K}_1$ contribution, which is predominantly determined by the two nonzero second-order perturbation diagrams (depicted on the left of Fig. 7.2). For comparison, the PT2 results are shown in the top row of Fig. 9.1. $\mathcal{K}_{2^{(\prime)}}$ and $\mathcal{K}_3$ are considerably smaller in magnitude. This changes at intermediate $U/\Delta = 2.5$: The maxima of $\mathcal{K}_1$ and $\mathcal{K}_{2^{(\prime)}}$ are of similar size, and $\mathcal{K}_3$ is only by a factor of ~ 2 smaller. Both $\mathcal{K}_{2^{(\prime)}}$ and $\mathcal{K}_3$ contain a lot of nontrivial structure that is absent at the $\mathcal{K}_1$ level. Even further, some Keldysh components of $\mathcal{K}_1$ (e.g. the $11|11$ component) are zero altogether due to the parity symmetries (cf. Eq. (4.48)), but nonzero at the $\mathcal{K}_2$ and $\mathcal{K}_3$ level. We have seen in Chapter 8 that neglecting this information within the $\mathcal{K}_1$SF approximation can lead to incorrect results for physical observables.

To analyze the structure of the vertex components in more detail and disentangle individual features, we further decompose $\mathcal{K}_i$ into the diagrammatic channels $r = a, p, t$ for $U/\Delta = 2.5$; results are shown in Fig. 9.2. In order to explain the features present in each channel, let us consider how the natural frequencies of the channels are reflected in the t parametrization depicted here, using Eq. (A.2). Firstly, all results are shown in the frequency plane $\omega_t = 0$, i.e., $\nu_a = \nu'_a$, $\nu_p = \nu'_p$. The diagonals in Fig. 9.2 are represented as follows:

$$\text{main diagonal:} \quad \nu_t = \nu'_t \quad \Rightarrow \quad \omega_a = 0\,, \quad \nu_a = \nu_t\,, \quad \omega_p = 2\nu_t\,, \quad \nu_p = 0\,, \tag{9.2a}$$

$$\text{antidiagonal:} \quad \nu_t = -\nu'_t \quad \Rightarrow \quad \omega_a = 2\nu_t\,, \quad \nu_a = 0\,, \quad \omega_p = 0\,, \quad \nu_p = -\nu_t\,. \tag{9.2b}$$

On the coordinate axes, we have

$$\nu_t = 0 \quad \Rightarrow \quad \omega_a = -\nu'_t\,,\ \nu_a = \nu'_t/2\,,\ \omega_p = \nu'_t\,,\ \nu_p = \nu'_t/2 \quad \Rightarrow \quad \nu_a = -\omega_a/2\,,\ \nu_p = \omega_p/2\,, \tag{9.3a}$$

$$\nu'_t = 0 \quad \Rightarrow \quad \omega_a = \nu_t\,,\quad \nu_a = \nu_t/2\,,\ \omega_p = \nu_t\,,\ \nu_p = -\nu_t/2 \quad \Rightarrow \quad \nu_a = \omega_a/2\,,\quad \nu_p = -\omega_p/2\,. \tag{9.3b}$$

With this, we can explain the individual features: The components of $\mathcal{K}_1^a$ are dominated by strong peaks along the main diagonal, i.e., by the static value at $\omega_a = 0$. Similarly, $\mathcal{K}_1^p$ shows peaks at the antidiagonal corresponding to $\omega_p = 0$. Of course $\mathcal{K}_1^t$ is constant in the $\omega_t = 0$ plane, since it does not depend on $\nu = \nu_t$ and $\nu' = \nu'_t$. Note that the peaks in $\mathcal{K}_1^a$ are much sharper and larger in value than those in $\mathcal{K}_1^p$ at $U/\Delta = 2.5$, which explains the asymmetry between the two diagonals at this interaction strength in Fig. 9.1. This is in contrast to the weakly interacting limit where the two PT2 diagrams in the a and p channel cancel exactly (cf. Sec. 7.1.1) and thus form a symmetric cross-like structure in the top row of Fig. 9.1. The peak heights of $\mathcal{K}_1^a$ are not only larger than those in the p channel, but also larger than the static values of $\mathcal{K}_1^t$. Since $(\mathcal{K}_1^a)_{\uparrow\downarrow} \sim \chi_{\mathrm{sp}}$ (Eq. (4.21)), large values of $\mathcal{K}_1^a$ physically correspond to strong spin fluctuations in the local moment regime of the SIAM.

The classes $\mathcal{K}_2^{a/p} + \mathcal{K}_{2'}^{a/p}$ similarly show strong features along $\omega_a = 0$, $\omega_p = 0$, respectively. Additionally, weaker features along the coordinate axes $\nu = 0$, $\nu' = 0$ are visible. In the parametrizations of the a and p channel, according to Eq. (9.3) these correspond to $\nu_{a/p} = \pm\omega_{a/p}/2$, i.e., they result from the frequency structures of the a and p bubble, respectively: As seen in Eq. (4.6), these frequency combinations correspond to the maxima of the propagators in the bubbles. In the t channel, the dominant features are lying along the coordinate axes, i.e., they correspond to the static values of $\mathcal{K}_2^t$ and $\mathcal{K}_{2'}^t$, respectively. Note that for the 12|12 component there is no peak at $\nu = 0$, since $(\mathcal{K}_2^t)_{\uparrow\downarrow}^{12|12} = 0$ (but $(\mathcal{K}_{2'}^t)_{\uparrow\downarrow}^{12|12} \neq 0$), see Table 4.2. (Im $(\mathcal{K}_2^t)_{\uparrow\downarrow}^{12|22}$ is nonzero but has a node at $\omega_t = 0$ and is thus not visible in Fig. 9.2.)

On the $\mathcal{K}_3$ level, the behavior is largely similar to that observed for $\mathcal{K}_2$. Here, we see slightly more pronounced features along the antidiagonal (main diagonal) in the a (p) channel, corresponding to $\nu_a = \nu'_a = 0$ ($\nu_p = \nu'_p = 0$).

Finally, we sum up all asymptotic classes and diagrammatic channels and show the full vertex Γ in the same frequency plane in Fig. 9.3. Due to very recent progress on NRG methodology [KLvD21, LKvD21], one can now also compute four-point functions directly from NRG (which used to be restricted to the one-particle level before). In Fig. 9.3, we compare our mfRG results to NRG data computed by Seung-Sup Lee. For illustration purposes, we restrict our attention to the (fully retarded) Keldysh component $\Gamma^{12|22}$. For weak interaction $U/\Delta = 0.5$, we obtain very good agreement between the two methods, and at intermediate interaction $U/\Delta = 2.5$, we still have good qualitative agreement, with all nontrivial features being equally captured by both methods. Note that while NRG is numerically exact on the one-particle level, on the two-particle level it still suffers from issues related to broadening of discrete spectral data [LKvD21]. This is very likely the reason for the small oscillations visible in the NRG data of $\Gamma_{\uparrow\downarrow}$ at $U/\Delta = 0.5$. Furthermore, due to the scheme within which the vertex is obtained from the four-point correlator $G^{(4)}$ in NRG, other Keldysh components are currently obtained with lower accuracy than the one shown in Fig. 9.3 [LKvD21]. In our Keldysh mfRG approach, we do not have this issue: Symmetries between the Keldysh components are built into the formalism (cf. Chapter 4), such that all Keldysh components are obtained with the same accuracy, always respecting the (enforced) crossing symmetries. The good quantitative agreement with NRG on the one-particle level (see Chapter 8), together with the excellent agreement between flowing and post-processed susceptibilities (cf. Fig. 8.4), reflecting consistency between the one- and two-particle level, gives good reason to believe that to date Keldysh mfRG provides the most accurate spectral data for four-point functions on the real-frequency axis at weak to intermediate interaction strength.

The good agreement between fRG and NRG is also very encouraging for a future implementation of Keldysh DMF^{2}RG (mentioned in the introduction): Within this framework, one would use mfRG in order to compute nonlocal extensions of DMFT by using a real-frequency DMFT vertex (computed with NRG as impurity solver) as initial condition for the mfRG flow. A good agreement at the fRG–NRG interface for the SIAM as a “benchmark model” gives confidence that this scheme will be realizable in the near future.

We now continue by presenting the results of the second project discussed in this thesis in Part II, before concluding the thesis in Chapter 11.

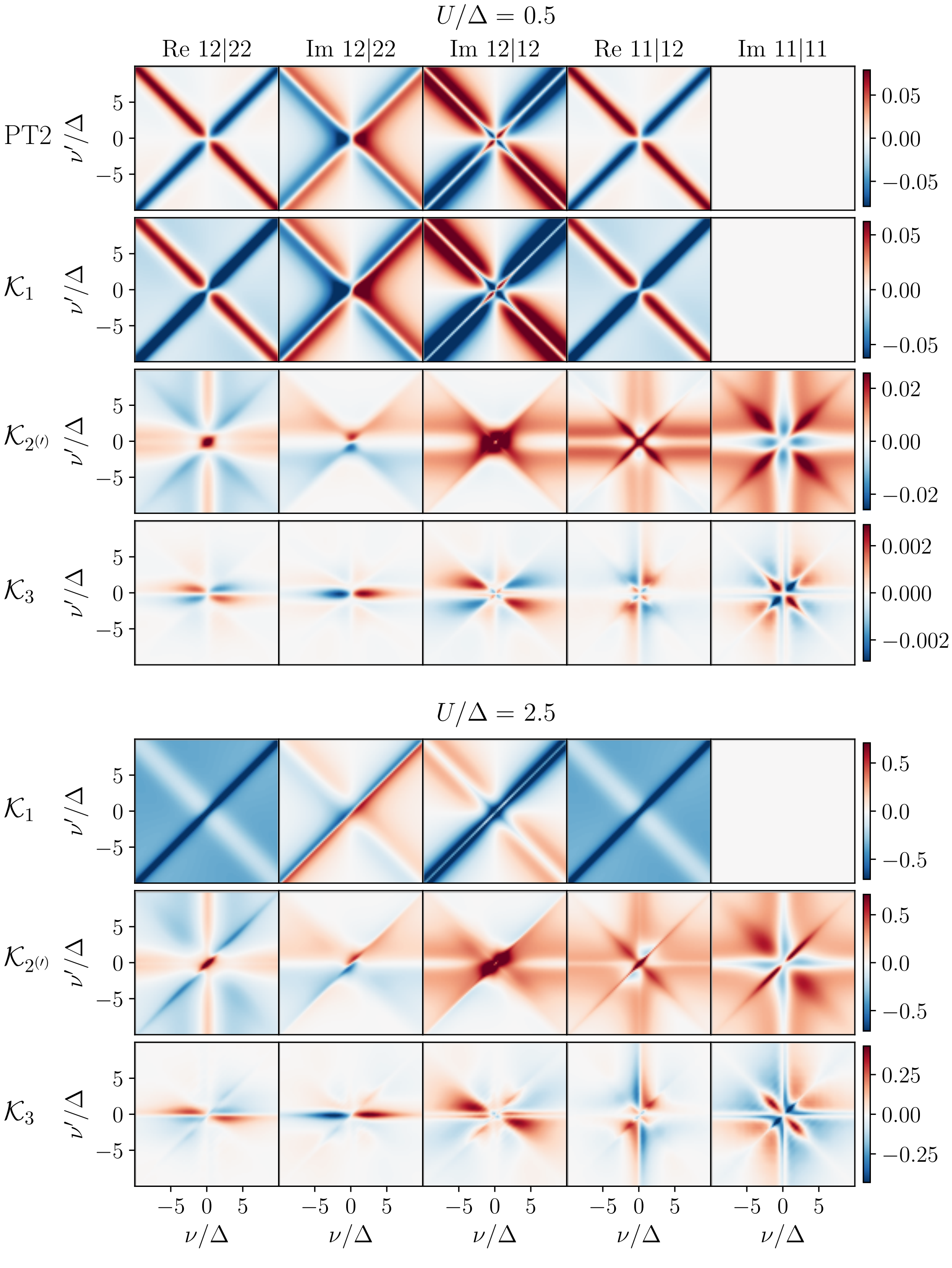

Figure 9.1 Real and imaginary parts of various Keldysh components of the equal-spin component of the asymptotic classes $\mathcal{K}_i/U = \sum_r \mathcal{K}_i^r/U$ at weak and intermediate interaction strength $U/\Delta = 0.5$ (top) and $U/\Delta = 2.5$ (bottom). Results are obtained from a 3-loop fRG flow. For $U/\Delta = 0.5$, we additionally compare to bare second-order perturbation theory (PT2, top row).

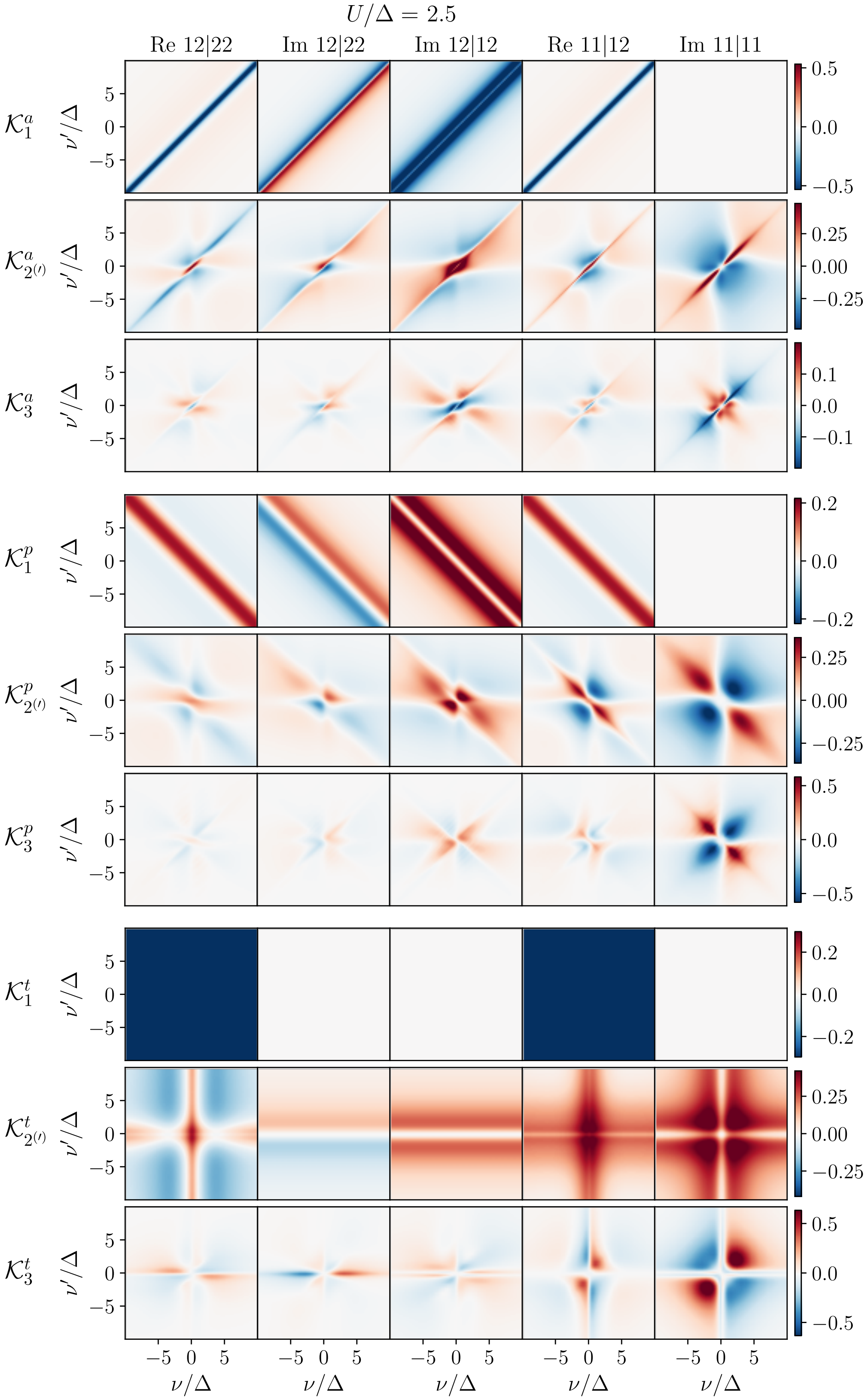

Figure 9.2 Same as Fig. 9.1 at $U/\Delta = 2.5$, divided into the diagrammatic channels a, p, t.

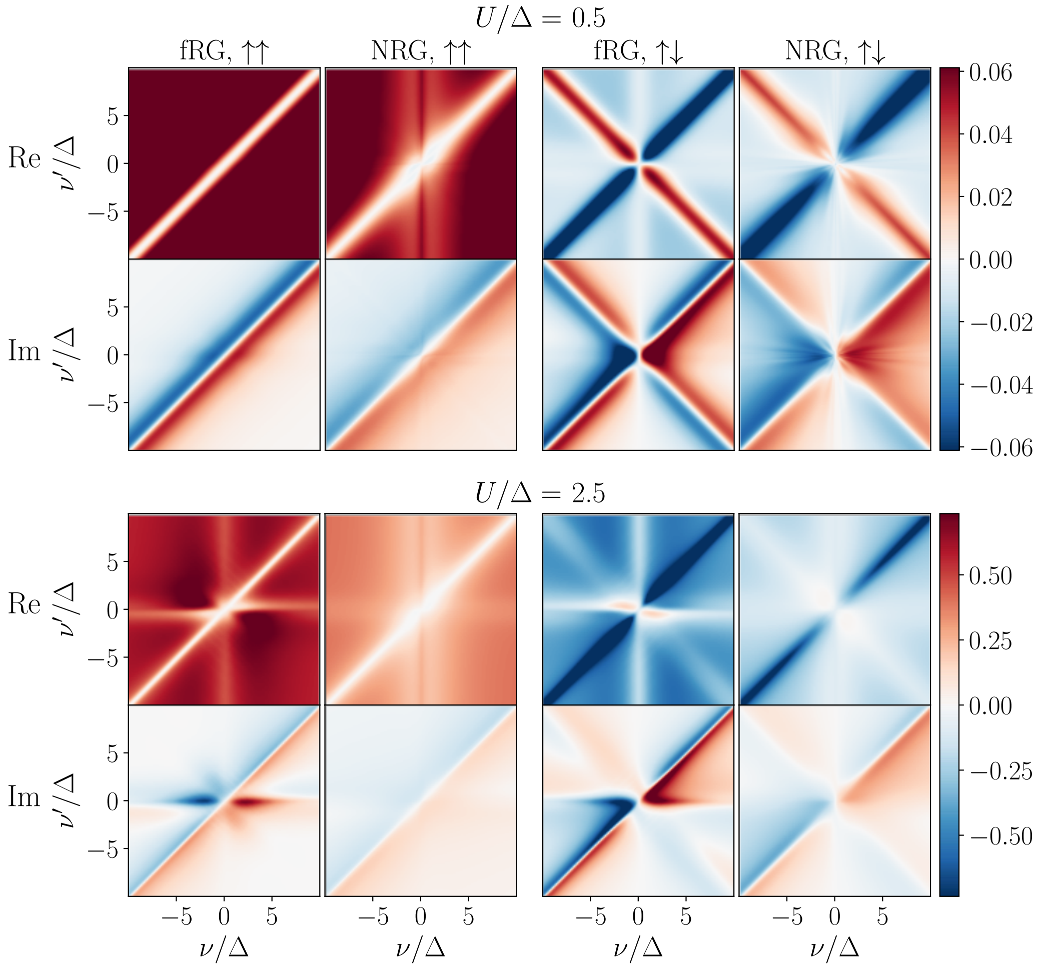

Figure 9.3 Fully retarded Keldysh component $(\Gamma^{12|22}(\nu,\nu') - \Gamma_0)/U$ of the full vertex (Eq. (9.1)). We show real and imaginary part of the equal-spin and different-spin components $\Gamma_{\uparrow\uparrow}$ (left) and $\Gamma_{\uparrow\downarrow}$ (right) at weak and intermediate interaction strength $U/\Delta = 0.5$ (top) and $U/\Delta = 2.5$ (bottom). We compare 3-loop fRG results to NRG results. The latter are computed by Seung-Sup Lee with the recent extension of NRG to four-point functions [KLvD21, LKvD21]. Both methods agree very well for $U/\Delta = 0.5$ and still show good qualitative agreement at $U/\Delta = 2.5$.

Part II

NRG+CFT analysis of a three-channel spin-orbital Kondo model

10 Non-Fermi-liquid behavior in a three-channel spin-orbital Kondo model

10.1 Overview

We now present the results of the project introduced in Sec. 1.1.2, aiming for a detailed understanding of non-Fermi-liquid behavior in Hund metals. In Publication P1 (reprinted on pages 114–137), we introduce the three-channel spin-orbital Kondo model that we will be using to describe the essential degrees of freedom relevant for Hund physics. We discuss its weak-coupling RG flow in order to get some intuition on the fixed points it hosts, and then study the strong-coupling RG flow using NRG. In two somewhat technical sections, we explain our generalization of the Affleck–Ludwig CFT approach from a spin impurity to one with a spin and orbital degree of freedom. With this methodology, we obtain analytical explanations for the finite-size spectrum of the model and the exponents of power-law behavior in the dynamical spin and orbital susceptibilities. In particular, we investigate the NFL fixed point obtained by screening of the orbital sector below the orbital Kondo scale T_{orb}, and also the transition towards the Fermi-liquid fixed point below T_{sp}, where both spin and orbital degrees of freedom are screened. The transition between NFL and FL turns out to be governed by the presence of the NFL fixed point, but constitutes a separate regime which we coin "spin-splitting" regime, characterized by an energy scale T_{ss} lying between T_{sp} and T_{orb}. Finally, we make a connection between the results for the Kondo-type model and the Anderson-type model it is derived from, the latter being the prototypical model for real Hund metals (as described in Sec. 1.1.2). We find that the spin-splitting regime, indirectly governed by the NFL fixed point, is the one that can also be observed in the corresponding Anderson model. The Supplemental Material (reprinted on pages 138–140) contains tables with technical details necessary for the CFT analysis.

In Publication P2 (reprinted on pages 142–149), we extend the analysis from the NFL fixed point to the full phase diagram of the model by independently varying its couplings. The NFL fixed point studied in detail in P1 corresponds to a single point (called NFL*) in this phase diagram. In addition, we find an FL, an SFL, and a different NFL phase. These phases and the power laws in the susceptibilities observed within them can again be explained by CFT arguments. We also find that the phases are connected by quantum phase transitions, showing characteristic power-law suppression of the corresponding coherence scales toward the phase boundaries. This provides an explanation for the strong suppression of the Fermi liquid scale in real Hund metals. The Supplemental Material (reprinted on pages 150–165) contains some more details on the phase transitions and the CFT analysis as well as results for further dynamical and static properties omitted in the main text. The numerical work for P2 has been carried out by Yilin Wang. The author of this thesis has contributed to the CFT analysis and the interpretation and discussion of the results, as well as to the writing of the manuscript.

Erratum: In Fig. 1(d) of publication P1 (p. page 117 below, p. 031052-4 of the original publication), fat, faint dashed lines showing the weak-coupling RG flow (and correctly described in the caption) were missing. We provide the corrected version in Fig. 10.1 below, along with its original caption. An erratum will be published soon also on the journal webpage.

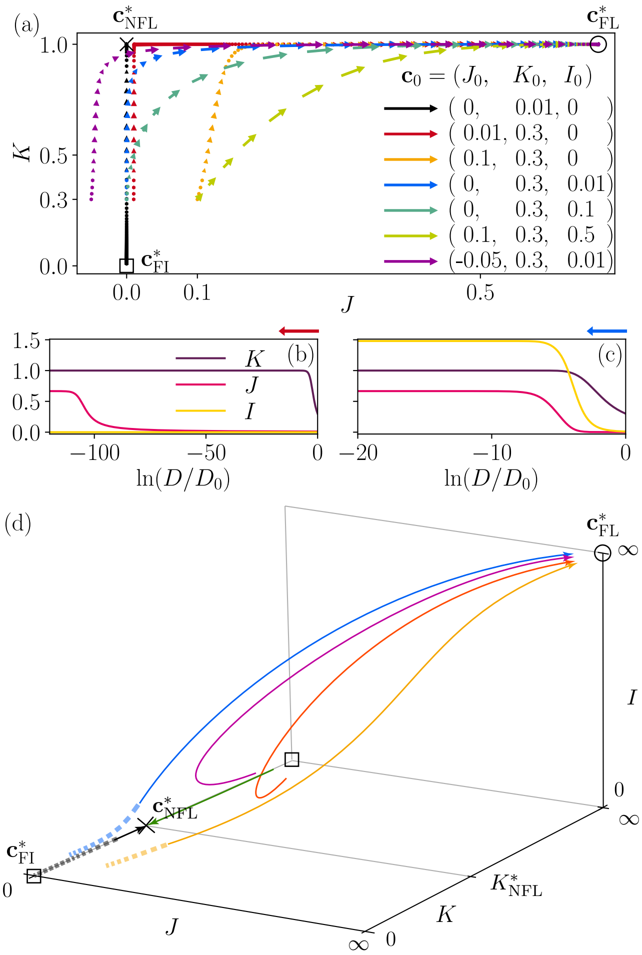

Figure 10.1 (a) RG flow of the coupling vector $\mathbf{c} = (J, K, I)$ (projected into the J-K plane), obtained by solving the weak-coupling RG equations (2) (Eqs. (8–10) of Ref. [9]) for various initial values, $\mathbf{c}_0 = (J_0, K_0, I_0)$. Arrows depict the gradient vector, $-[\mathrm{d}/(\mathrm{d}\ln D)](J, K)$ at equal steps of $\ln D$. (b),(c) Weak-coupling RG flow of $\mathbf{c}(D)$ for (b) $\mathbf{c}_0 = (0.01, 0.3, 0)$ [red arrows in (a)] and (c) $(0, 0.3, 0.01)$ [blue arrows in (a)]. (d) Qualitative depiction of the conjectured RG flow in the full J-K-I space, for all couplings non-negative. Fat, faint dashed lines show the solutions $\mathbf{c}(D)$ of the weak-coupling equations (2), initialized at $K_0 \ll K^*_{\mathrm{NFL}}$ with $(J_0, I_0) = (0, 0)$ (black), $(> 0, 0)$ (yellow) or $(0, > 0)$ (blue), and plotted only in the weak-coupling regime [beyond the latter, Eqs. (2) loose validity]. Solid lines, drawn by hand, qualitatively show the flow expected beyond the weak-coupling regime, including trajectories initialized at $K_0 \gg K^*_{\mathrm{NFL}}$, with $(J_0, I_0) = (0, 0)$ (green), $(> 0, 0)$ (orange) or $(0, > 0)$ (purple). The black squares, cross and circle depict fixed points.

Uncovering Non-Fermi-Liquid Behavior in Hund Metals: Conformal Field Theory Analysis of an $\mathrm{SU}(2) \times \mathrm{SU}(3)$ Spin-Orbital Kondo Model

by

E. Walter,[1] K. M. Stadler,[1] S.-S. B. Lee,[1] Y. Wang,[2] G. Kotliar,[2,3]
A. Weichselbaum,[2,1] and J. von Delft[1]

[1] Arnold Sommerfeld Center for Theoretical Physics, Center for NanoScience, and
Munich Center for Quantum Science and Technology,
Ludwig-Maximilians-Universität München, 80333 Munich, Germany

[2] Condensed Matter Physics and Materials Science Department,
Brookhaven National Laboratory, Upton, New York 11973, USA

[3] Department of Physics and Astronomy, Rutgers University,
Piscataway, New Jersey 08854, USA

reprinted on pages 114–137

with permission from
***Phys. Rev. X* 10, 031052 (2020)**,
DOI: 10.1103/PhysRevX.10.031052.

© 2020 American Physical Society

Supplemental Material reprinted on pages 138–140.

PHYSICAL REVIEW X **10,** 031052 (2020)

Uncovering Non-Fermi-Liquid Behavior in Hund Metals: Conformal Field Theory Analysis of an $\mathrm{SU}(2)\times\mathrm{SU}(3)$ Spin-Orbital Kondo Model

E. Walter,[1] K. M. Stadler,[1] S.-S. B. Lee,[1] Y. Wang,[2] G. Kotliar,[2,3] A. Weichselbaum,[2,1] and J. von Delft[1]
[1]*Arnold Sommerfeld Center for Theoretical Physics, Center for NanoScience,*
and Munich Center for Quantum Science and Technology,
Ludwig-Maximilians-Universität München, 80333 Munich, Germany
[2]*Condensed Matter Physics and Materials Science Department, Brookhaven National Laboratory,*
Upton, New York 11973, USA
[3]*Department of Physics and Astronomy, Rutgers University, Piscataway, New Jersey 08854, USA*

(Received 12 August 2019; revised 27 May 2020; accepted 7 July 2020; published 3 September 2020)

Hund metals have attracted attention in recent years due to their unconventional superconductivity, which supposedly originates from non-Fermi-liquid (NFL) properties of the normal state. When studying Hund metals using dynamical mean-field theory, one arrives at a self-consistent “Hund impurity problem” involving a multiorbital quantum impurity with nonzero Hund coupling interacting with a metallic bath. If its spin and orbital degrees of freedom are screened at different energy scales, $T_{\mathrm{sp}} < T_{\mathrm{orb}}$, the intermediate energy window is governed by a novel NFL fixed point, whose nature had not yet been clarified. We resolve this problem by providing an analytical solution of a paradigmatic example of a Hund impurity problem, involving two spin and three orbital degrees of freedom. To this end, we combine a state-of-the-art implementation of the numerical renormalization group, capable of exploiting non-Abelian symmetries, with a generalization of Affleck and Ludwig’s conformal field theory (CFT) approach for multichannel Kondo models. We characterize the NFL fixed point of Hund metals in detail for a Kondo model with an impurity forming an $\mathrm{SU}(2)\times\mathrm{SU}(3)$ spin-orbital multiplet, tuned such that the NFL energy window is very wide. The impurity’s spin and orbital susceptibilities then exhibit striking power-law behavior, which we explain using CFT arguments. We find excellent agreement between CFT predictions and numerical renormalization group results. Our main physical conclusion is that the regime of spin-orbital separation, where orbital degrees of freedom have been screened but spin degrees of freedom have not, features anomalously strong local spin fluctuations: the impurity susceptibility increases as $\chi^{\mathrm{imp}}_{\mathrm{sp}} \sim \omega^{-\gamma}$, with $\gamma > 1$.

DOI: 10.1103/PhysRevX.10.031052

Subject Areas: Condensed Matter Physics, Mesoscopics, Strongly Correlated Materials

I. INTRODUCTION

A. Motivation: Hund metals

Hund metals are multiorbital materials with broad bands which are correlated via the ferromagnetic Hund coupling J_H, rather than the Hubbard interaction U. The coupling J_H implements Hund’s rule, favoring electronic states with maximal spin, which causes Hund metals to be fundamentally different from Mott insulators. This is a new exciting area of condensed matter physics; for a recent review with numerous references, see Ref. [1]. Hund metals are a very diverse class of materials, including transition metal oxides with partially filled d shells, such as the iron-based pnictide and selenide superconductors, the ruthenates, and many others [1–13].

The iron-based superconductors, in particular, raised much interest in recent years because of the unconventional nature of their superconductivity. It has been argued that the Hund nature of their normal state is essential for the onset of superconductivity [14]. In particular, spin fluctuations with a power-law divergent susceptibility $\propto \omega^{-\gamma}$, with $\gamma > 1$, have been evoked in an explanation for the anomalously large ratio of $2\Delta_{\max}/T_c$ observed experimentally, where $\Delta_{\max}$ is the maximum superconducting gap and T_c the critical temperature [14]. The normal state of Hund metals is of great interest on its own, since it typically shows bad-metal behavior [6,15,16]. Motivated by these considerations, computational and experimental studies of Hund metals have begun to uncover their rich physics in recent years [4,5,8,11,12,17–21].

Published by the American Physical Society under the terms of the Creative Commons Attribution 4.0 International license. Further distribution of this work must maintain attribution to the author(s) and the published article’s title, journal citation, and DOI.

When studying Hund metals in the context of dynamical mean-field theory (DMFT), the problem of a crystal lattice with many strongly interacting lattice sites is mapped onto a "Hund impurity," coupled self-consistently to an effective noninteracting metallic bath. A Hund impurity has both spin *and* orbital degrees of freedom and a finite Hund coupling, favoring a large local spin.

A particularly fascinating consequence of the interplay between spin and orbital degrees of freedom is the phenomenon of spin-orbital separation (SOS): Kondo screening of Hund impurity models occurs in two stages, and the energy scales below which free spin and orbital degrees are screened differ, $T_{\mathrm{sp}} < T_{\mathrm{orb}}$ [8,9,22–24]. The low-energy regime below T_{sp} shows Fermi-liquid (FL) behavior. The intermediate SOS window $[T_{\mathrm{sp}}, T_{\mathrm{orb}}]$, by contrast, shows incoherent behavior, featuring almost fully screened orbital degrees of freedom coupled to almost free spin degrees of freedom. The incoherent regime has been conjectured to have non-Fermi-liquid (NFL) properties and argued to be relevant for the bad-metal behavior of Hund metals [8,25]. However, the nature of the putative underlying NFL state has not yet been clarified.

A major obstacle for analyzing the conjectured NFL regime of Hund metals has been a lack of detailed, analytical understanding of the basic properties of Hund impurity models, since theoretical work has overwhelmingly focused on Kondo models without orbital degrees of freedom. In this work, we overcome this obstacle in the context of an instructive case study of a specific Hund impurity model.

Before specifying the latter in detail, though, let us put our study into perspective by providing a brief historical overview of Hund impurity models.

B. Brief history of Hund impurity models

Hund impurity models are natural multiorbital generalizations of single-orbital magnetic impurity models such as the Kondo model used by Kondo in 1964 to explain the resistance minimum in magnetic alloys [26]. The search for a detailed understanding of the Kondo model beyond Kondo's perturbative calculation was a cornerstone toward the development of renormalization group techniques, starting with Anderson's poor man's scaling approach [27] and culminating in Wilson's numerical renormalization group (NRG) [28]. These methods confirmed that below a characteristic Kondo temperature the metallic bath screens the impurity spin, leading to the formation of a singlet state between impurity and conduction electrons.

Following these findings, naturally the question arises: What happens if the impurity has multiple orbitals? In particular, electrons on a multiorbital impurity experience not only a Coulomb interaction stabilizing a magnetic moment on the impurity, but also a Hund coupling, enforcing the effect of Hund's rule to maximize the total impurity spin. These two interactions lead to an intricate interplay, crucially depending on the number of electrons on the impurity. Indeed, it had been observed already in the 1960s that the Kondo scale for impurities in transition metal alloys with partially filled d shells decreases exponentially as the shell filling approaches $1/2$ [29,30], drawing attention to the question of understanding Kondo screening in the presence of multiple orbitals. Coqblin and Schrieffer [31] developed a generalization of the Kondo model for multiorbital impurities, yet only involving the spin degree of freedom. Okada and Yosida [32] included orbital degrees of freedom and in particular pointed out the importance of a finite Hund coupling, enforcing the effect of Hund's rule in such multiorbital systems. However, theoretical tools for analyzing a model with nonzero Hund coupling away from half filling were lacking at the time.

Later, Nozières and Blandin [33] studied a spin Kondo impurity immersed in a metallic bath with multiple orbital channels. A major conclusion of their work was that such models lead to overscreening of the impurity spin and NFL behavior, if the number of channels exceeds twice the impurity spin ($k > 2S$). This generated great theoretical interest in multichannel Kondo models, including exact Bethe solutions providing information on thermodynamical properties [34–39], and NRG studies [40,41]. Affleck and Ludwig (AL) [42–46] developed a powerful conformal field theory (CFT) approach for studying the strong-coupling fixed points of such multiband Kondo models, providing analytical results for finite-size spectra and the scaling behavior of correlation functions. However, their work was restricted to pure spin impurities without nontrivial orbital structure. Thus, their methods have not yet been applied to Hund impurity models, including orbital degrees of freedom and a finite Hund coupling.

In this work, we fill this long-standing void and provide a detailed and comprehensive analysis of a prototypical Hund impurity model (specified below). We achieve this by advancing and combining two powerful complementary techniques that both arose in the very context of Kondo physics: An *analytical* solution based on AL's celebrated CFT approach, generalized from a pure spin impurity to one with spin and orbital structure, and a quasiexact *numerical* solution using a state-of-the-art implementation of Wilson's NRG, allowing studies of multiorbital systems by fully exploiting Abelian and non-Abelian symmetries. This allows us to achieve a detailed understanding of the NFL behavior arising in this Hund impurity model.

C. Minimal models for Hund metals

We next describe the considerations motivating the specific choice of model studied below.

A minimal model for Hund metals has been proposed in Ref. [8]. It is a three-orbital Hubbard-Hund model, and it has been studied extensively in Refs. [2,6,9,11,22–24,47].

A treatment of this model by DMFT at $1/3$ filling yields a self-consistent Hund impurity model. More specifically, one obtains a self-consistent three-orbital Anderson-Hund (3oAH) model, in which bath and impurity both have spin *and* orbital degrees of freedom. The impurity hosts two electrons forming an antisymmetric orbital triplet and a symmetric spin triplet ($S = 1$), reflecting Hund's rule. At energies so low that charge fluctuations can be treated by a Schrieffer-Wolff transformation [9], the 3oAH model maps onto a three-channel spin-orbital Kondo (3soK) model whose impurity forms a (3×3)-dimensional $\mathrm{SU}(2) \times \mathrm{SU}(3)$ spin-orbital multiplet.

The 3oAH model exhibits SOS [8,9,22–24]. Within the SOS window $[T_{\mathrm{sp}}, T_{\mathrm{orb}}]$, the imaginary part of the spin susceptibility scales as $\chi_{\mathrm{sp}}^{\mathrm{imp}} \sim \omega^{-6/5}$ [22,47]. The fact that the exponent, $\gamma = 6/5$, is larger than 1 has been argued to lead to the anomalous superconducting state of the iron pnictide Hund metals, as mentioned above [14]. However, the origin of this power law has remained unclear. One impediment toward finding an explanation is the fact that for the 3oAH model the orbital and spin screening scales cannot be tuned independently. The SOS window turns out to be rather small, masking the NFL behavior expected to occur within it.

In this paper, we sidestep this limitation by instead studying the 3soK model and treating its exchange couplings as independent parameters, freed from the shackles of their 3oAH origin. We tune these such that the regime of SOS is very wide, with $T_{\mathrm{sp}} \ll T_{\mathrm{orb}}$. This enables us to characterize the NFL fixed point obtained for $T_{\mathrm{sp}} = 0$, which also governs the intermediate NFL window if $T_{\mathrm{sp}} \ll T_{\mathrm{orb}}$. We compute fixed-point spectra and the scaling behavior of dynamical spin and orbital susceptibilities using both NRG and CFT, with mutually consistent results. In particular, we find an analytical explanation for the peculiar power law $\chi_{\mathrm{sp}}^{\mathrm{imp}} \sim \omega^{-6/5}$: It turns out to be governed (albeit somewhat indirectly) by the NFL fixed point mentioned above. Finally, we demonstrate the relevance of these 3soK results for the low-energy behavior of the 3oAH model by employing a hybrid Anderson-Kondo model which smoothly interpolates between the physics of the 3soK and 3oAH models. This interpolation shows that our new results also shed light on previous DMFT results for a self-consistent 3oAH model [22,47].

Our CFT analysis builds on that devised by AL [42–46] for the k-channel Kondo model, describing k spinful channels exchange coupled to an impurity with spin S, but no orbital degrees of freedom. If $k > 2S$, the impurity spin is overscreened. AL described the corresponding NFL fixed point using a charge-spin-orbital $\mathrm{U}(1) \times \mathrm{SU}(2)_k \times \mathrm{SU(k)}_2$ Kac-Moody (KM) decomposition of the bath states, and fusing the spin degrees of freedom of impurity and bath using $\mathrm{SU}(2)_k$ fusion rules. Here we generalize this strategy to our situation, where the impurity has spin *and* orbital "isospin" degrees of freedom: the NFL fixed point at $T_{\mathrm{sp}} = 0$ can be understood by applying $\mathrm{SU}(3)_2$ fusion rules in the orbital sector, leading to orbital overscreening. If T_{sp} is nonzero (but $\ll T_{\mathrm{orb}}$), the overscreened orbital degrees of freedom couple weakly to the impurity spin, driving the system to a FL fixed point. There both spin and orbital degrees of freedom are fully screened, in a manner governed by $\mathrm{SU}(6)_1$ fusion rules.

The paper is structured as follows. Section II defines the 3soK model and discusses its weak-coupling renormalization group (RG) flow. Section III presents our NRG results. Section IV gives a synopsis of our CFT results, summarizing all essential insights and arguments, while Sec. V elaborates the corresponding CFT arguments in more detail. Section VI discusses a hybrid Anderson-Kondo model which interpolates between the 3soK model and the 3oAH model. Section VII summarizes our conclusions. The Appendix revisits a two-channel spin-orbital Kondo model studied by Ye in 1997 [48], pointing out the similarities and differences between his work and ours.

II. MODEL, PERTURBATIVE RG FLOW

We study the 3soK model proposed in Ref. [9]. $H_{\mathrm{bath}} = \sum_{pm\sigma} \varepsilon_p \psi^{\dagger}_{pm\sigma} \psi_{pm\sigma}$ describes a symmetric, flat-band bath, where $\psi^{\dagger}_{pm\sigma}$ creates an electron with momentum p and spin σ in orbital $m \in \{1, 2, 3\}$. The bath couples to the impurity spin $\mathbf{S}$ and orbital isospin $\mathbf{T}$ via

$$H_{\mathrm{int}} = J_0 \mathbf{S} \cdot \mathbf{J}_{\mathrm{sp}} + K_0 \mathbf{T} \cdot \mathbf{J}_{\mathrm{orb}} + I_0 \mathbf{S} \cdot \mathbf{J}_{\text{sp-orb}} \cdot \mathbf{T}. \quad (1)$$

Here $\mathbf{S}$ are SU(2) generators in the $S = 1$ representation, normalized as $\mathrm{Tr}(S^{\alpha} S^{\beta}) = \frac{1}{2} \delta^{\alpha\beta}$, and $\mathbf{T}$ are SU(3) generators in the representation with Young diagram $\ydiagram{1,1}$, and $\mathrm{Tr}(T^a T^b) = \frac{1}{2} \delta^{ab}$. $\mathbf{J}_{\mathrm{sp}}$, $\mathbf{J}_{\mathrm{orb}}$, and $\mathbf{J}_{\text{sp-orb}}$ are the bath spin, orbital, and spin-orbital densities at the impurity site, with $J^{\alpha}_{\mathrm{sp}} = \psi^{\dagger}_{m\sigma} \frac{1}{2} \sigma^{\alpha}_{\sigma\sigma'} \psi_{m\sigma'}$, $J^{a}_{\mathrm{orb}} = \psi^{\dagger}_{m\sigma} \frac{1}{2} \tau^{a}_{mm'} \psi_{m'\sigma}$, $J^{\alpha, a}_{\text{sp-orb}} = \psi^{\dagger}_{m\sigma} \frac{1}{2} \sigma^{\alpha}_{\sigma\sigma'} \frac{1}{2} \tau^{a}_{mm'} \psi_{m'\sigma'}$ (summation over repeated indices is implied), where fields are evaluated at the impurity site, $\psi^{\dagger}_{m\sigma}(r = 0)$, and σ^{α} $[\tau^{a}]$ are Pauli [Gell-Mann] matrices, with normalization $\mathrm{Tr}(\sigma^{\alpha} \sigma^{\beta}) = 2\delta^{\alpha\beta}$ $[\mathrm{Tr}(\tau^{a} \tau^{b}) = 2\delta^{ab}]$. We use Young diagrams as labels for irreducible representations (irreps) of the SU(3) group. An alternative notation, also frequently used, would be to label SU(3) irreps by their dimension: $\bullet = 1$, $\ydiagram{1} = 3$, $\ydiagram{1,1} = \bar{3}$, where $\bar{3}$ refers to the conjugate represenation of 3, $\ydiagram{2} = 6$, $\ydiagram{2,2} = \bar{6}$, $\ydiagram{2,1} = 8$, etc.

The Hamiltonian has $\mathrm{U}(1)_{\mathrm{ch}} \times \mathrm{SU}(2)_{\mathrm{sp}} \times \mathrm{SU}(3)_{\mathrm{orb}}$ symmetry. We label its symmetry multiplets by $Q = (q, S, \lambda)$, with q the *bath* particle number relative to half filling (the 3soK impurity has no charge dynamics; hence we may choose $q_{\mathrm{imp}} = 0$), S the total spin, and λ a Young diagram denoting an SU(3) representation. The values of the spin, orbital, and spin-orbital exchange couplings, J_0, K_0, I_0, can be derived from the 3oAH model by a Schrieffer-Wolff transformation [9]. When the 3oAH model is studied in the regime relevant for Hund metals, i.e., with a ferromagnetic on-site Hund coupling J_H favoring maximization of the local spin, and with a local filling n_d differing by $\simeq 1$ from half filling, the resulting 3soK exchange couplings J_0, K_0, I_0 are typically all positive, i.e., antiferromagnetic. [This can be inferred from Eqs. (4)–(7) of Ref. [9].] Furthermore, when the weak-coupling RG flow of the 3soK model is studied in the presence of finite $K_0 > 0$ and $I_0 > 0$, one finds that J_0 flows toward positive values regardless of whether its initial value is chosen positive or negative [the latter case is illustrated by the purple arrows in Fig. 1(a)]. Hence, we here focus on positive exchange couplings only. However, instead of using values obtained from a Schrieffer-Wolff transformation, here we take the liberty of choosing J_0, K_0, I_0 to be independent, tuning them such that $T_{\mathrm{sp}} \ll T_{\mathrm{orb}}$. This is in extension of the 3oAH model, in which T_{sp} is only at most about an order of magnitude smaller than T_{orb}.

Aron and Kotliar [9] have performed a perturbative analysis of the RG flow of the 3soK model. Their Eqs. (8)–(10) describe the flow of the coupling vector, $\mathbf{c}(D) = (J, K, I)$, upon reducing the half-bandwidth D starting from $\mathbf{c}_0 = (J_0, K_0, I_0)$ at D_0. For the 3soK model, these equations read

$$\begin{aligned}
\beta_J &= -\left(1 - \frac{3}{2}J\right)\left(J^2 + \frac{2}{9}I^2\right) + \cdots, \\
\beta_K &= -\frac{3}{2}(1 - K)\left(K^2 + \frac{1}{2}I^2\right) + \cdots, \\
\beta_I &= -\frac{3}{2}\left[\left(\frac{4}{3}J + 2K - J^2 - K^2\right)I - \frac{5}{18}I^2 - \frac{17}{36}I^3\right] + \cdots,
\end{aligned} \tag{2}$$

where $\beta_J = dJ/d\ln D$, etc., with energies in units of D_0. Figure 1 illustrates the resulting RG flow. There are several fixed points. The free-impurity fixed point, $\mathbf{c}^*_{\mathrm{FI}} = (0, 0, 0)$, is unstable: for any nonzero $\mathbf{c}_0$, one or more couplings flow toward strong coupling, and the D values where J or K become of order unity yield estimates of T_{sp} and T_{orb}, respectively. For $\mathbf{c}_0 = (0, K_0 \neq 0, 0)$ [black arrows in Fig. 1(a)], the system flows toward a NFL fixed point, $\mathbf{c}^*_{\mathrm{NFL}} = (0, 1, 0)$. This fixed point is unstable against nonzero J_0 or I_0. For $I_0 = 0$, the flow equations for J and K are decoupled, such that for a small but nonzero $J_0 \ll K_0$ (red arrows) the flow first closely approaches $\mathbf{c}^*_{\mathrm{NFL}}$, until J grows large, driving it toward a FL fixed point $\mathbf{c}^*_{\mathrm{FL}}$. Figure 1(b) shows that the NFL regime ($J \ll K$) governed by $\mathbf{c}^*_{\mathrm{NFL}}$ can be large. For $I_0 \neq 0$, the J and K flows are coupled, hence the growth of K triggers that of J, accelerating the flow toward $\mathbf{c}^*_{\mathrm{FL}}$. In this case, the NFL energy window is rather small [cf. Fig. 1(c)]. For example, for $\mathbf{c}_0 = (0.1, 0.3, 0.5)$ (light green arrows), typical for the values obtained through a Schrieffer-Wolff 3oAH to 3soK mapping, the RG flow does not approach $\mathbf{c}^*_{\mathrm{NFL}}$ very closely; thus fully developed NFL behavior is not observed.

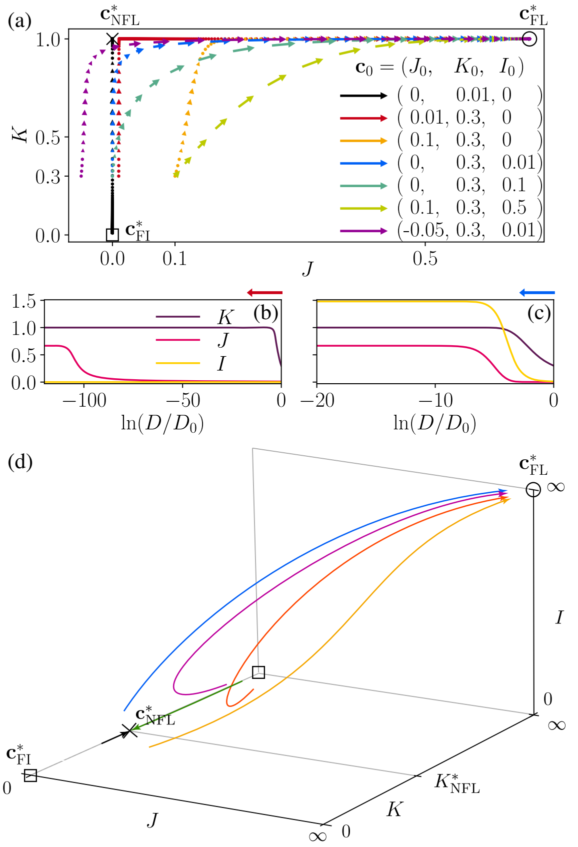

FIG. 1. (a) RG flow of the coupling vector $\mathbf{c} = (J, K, I)$ (projected into the J-K plane), obtained by solving the weak-coupling RG equations (2) [Eqs. (8)–(10) of Ref. [9]] for various initial values, $\mathbf{c}_0 = (J_0, K_0, I_0)$. Arrows depict the gradient vector $-[d/(d\ln D)](J, K)$ at equal steps of $\ln D$. (b),(c) Weak-coupling RG flow of $\mathbf{c}(D)$ for (b) $\mathbf{c}_0 = (0.01, 0.3, 0)$ [red arrows in (a)] and (c) (0,0.3,0.01) [blue arrows in (a)]. (d) Qualitative depiction of the conjectured RG flow in the full J-K-I space, for all couplings non-negative. Fat, faint dashed lines show the solutions $\mathbf{c}(D)$ of the weak-coupling equations (2), initialized at $K_0 \ll K^*_{\mathrm{NFL}}$ with $(J_0, I_0) = (0, 0)$ (black), $(> 0, 0)$ (yellow), or $(0, > 0)$ (blue), and plotted only in the weak-coupling regime [beyond the latter, Eqs. (2) lose validity]. Solid lines, drawn by hand, qualitatively show the flow expected beyond the weak-coupling regime, including trajectories initialized at $K_0 \gg K^*_{\mathrm{NFL}}$, with $(J_0, I_0) = (0, 0)$ (green), $(> 0, 0)$ (orange), or $(0, > 0)$ (purple). The black squares, cross, and circle depict fixed points.

Figure 1(d) offers a qualitative depiction of the conjectured RG flow in the full J-K-I space, for all couplings non-negative. Fat, faint dashed lines show the solutions $\mathbf{c}(D)$ of the weak-coupling Eqs. (2). However, these equations lose validity once the couplings are no longer small (and their above-mentioned predictions that $K^*_{\mathrm{NFL}} = K^*_{\mathrm{FL}} = 1$ should not be trusted). Solid lines, drawn by hand, qualitatively depict the flow expected beyond the weak-coupling regime, based on the following considerations.

First, for $K_0 > 0$ and $J_0 = I_0 = 0$, the NRG analysis of Sec. III suggests that the flow proceeds along a trajectory where I and J remain zero, reaching a NFL fixed point, $\mathbf{c}^*_{\rm NFL} = (0, K^*_{\rm NFL}, 0)$ at a finite value of $K^*_{\rm NFL}$. This fixed point is stable, approached by RG flow both from below and above. Correspondingly, the line $J_0 = I_0 = 0$ contains another fixed point at $K_0 = \infty$, which is unstable. To understand the latter point heuristically, consider taking K_0 very large. Then the system will attempt to screen its local orbital degree of freedom, with representation ⊟, into an orbital singlet. Doing so by binding just a bath single electron, spin up or down, would break spin symmetry. Hence, it must bind two bath electrons, spin up and down, yielding a local orbital degree of freedom yet again, with representation □. Thus, choosing K_0 very large is equivalent to initializing the model with local orbital representation □ and small initial coupling (presumably $\sim 1/K_0$). This would grow under the RG flow; hence $K_0 = \infty$ is an unstable fixed point, just as $K_0 = 0$. (This argumentation is entirely analogous to that familiar from the two-channel Kondo model [33]; for the present 3soK model, it is further elaborated in Ref. [49].)

For $K_0 > 0$ and J_0, I_0 both non-negative but not both zero, the NRG analysis of Sec. V E suggests that the flow always ends up at a unique FL fixed point $\mathbf{c}^*_{\rm FL}$. Hence $\mathbf{c}^*_{\rm NFL}$ is unstable against turning on J_0 or I_0. The fixed point $\mathbf{c}^*_{\rm FL}$ features a fully screened spin and orbital singlet ground state and an excitation spectrum with SU(6) symmetry. This implies that as the flow approaches $\mathbf{c}^*_{\rm FL}$, all three couplings J, K, and I tend to infinity, with relative values such that the fixed-point Hamiltonian has SU(6) symmetry, i.e., $3J = 2K = I$ [9].

III. NRG RESULTS

To study the RG flow in a quantitatively reliable manner, we solve the 3soK model using NRG [28,50,51], exploiting non-Abelian symmetries using QSpace [50]. The bath is discretized logarithmically and mapped to a semi-infinite "Wilson chain" with exponentially decaying hoppings, and the impurity coupled to site 0. The chain is diagonalized iteratively while discarding high-energy states, thereby zooming in on low-energy properties: the (finite-size) level spacing of a chain ending at site k is of order $\omega_k \propto \Lambda^{-k/2}$, where $\Lambda > 1$ is a discretization parameter. The RG flow can be visualized using NRG eigenlevel spectra, showing how the chain's lowest-lying eigenenergies $\mathcal{E}$ evolve when k is increased by plotting the dimensionless rescaled energies $E = (\mathcal{E} - \mathcal{E}_{\rm ref})/\omega_k$ versus ω_k for odd k. The E-level flow is stationary (ω_k independent) while ω_k traverses an energy regime governed by one of the system's fixed points, but changes during crossovers between fixed points.

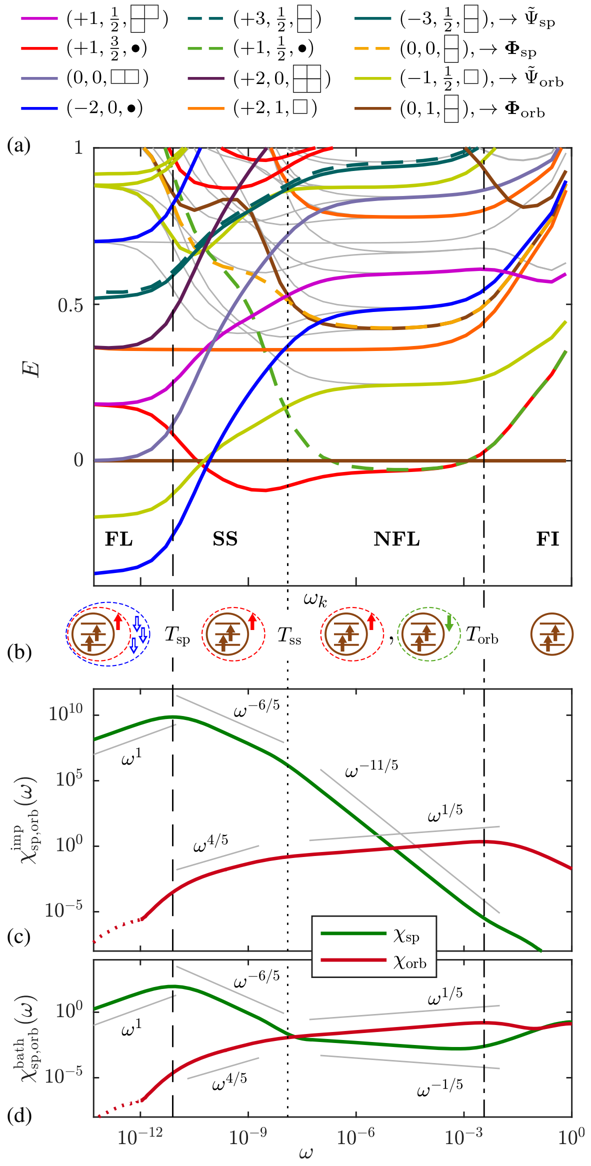

FIG. 2. NRG results for $\mathbf{c}_0 = (J_0, K_0, I_0) = (10^{-4}, 0.3, 0)$. (a) Finite-size eigenlevel spectrum computed by NRG, with $\mathcal{E}_{\rm ref} = \mathcal{E}(0, 1, ⊟)$ as reference energy. Quantum numbers $Q = (q, S, \lambda)$ are shown at the top, and → indicates boundary operators obtained via double fusion. (NRG parameters: $\Lambda = 2.5$; number of kept multiplets, $N_{\rm keep} = 3000$; half-bandwidth of the bath, $D = 1$.) (b) Illustrations of the ground states encountered during the flow. (c),(d) Imaginary part of the spin and orbital susceptibilities of (c) the impurity and (d) the bath site coupled to it (Wilson chain site $k = 0$). Gray lines show power laws predicted by CFT. Vertical lines show the crossover scales for orbital and spin screening, $T_{\rm orb}$ and $T_{\rm sp}$, marking the maxima of $\chi^{\rm imp}_{\rm orb}$ and $\chi^{\rm imp}_{\rm sp}$, and for spin splitting $T_{\rm ss}$, marking kinks in $\chi^{\rm imp,bath}_{\rm sp,orb}$.

To analyze the NFL regime in detail, we choose $I_0 = 0$ and $J_0 \ll K_0$, so that the SOS window becomes very large, with $T_{\mathrm{sp}} \lll T_{\mathrm{orb}}$. Figure 2(a) shows the NRG eigenlevel flow diagram for $\mathbf{c}_0 = (10^{-4}, 0.3, 0)$. We discern four distinct regimes, separated by three scales, T_{sp}, T_{ss}, T_{orb}.

- (i) The *free-impurity* (FI) regime, $\omega_k > T_{\mathrm{orb}}$, involves an unscreened impurity, with ground state multiplet $Q = (0, 1, \begin{smallmatrix}\square\\\square\end{smallmatrix})$ (flat brown line).
- (ii) In the NFL regime, $T_{\mathrm{ss}} < \omega_k < T_{\mathrm{orb}}$, two degenerate multiplets, $(1, \frac{1}{2}, \bullet)$ and $(1, \frac{3}{2}, \bullet)$ (dashed green and red lines) become the new ground state multiplets. Below the scale T_{orb}, the impurity orbital isopin is thus screened into an orbital singlet • by binding one bath electron, which couples to the impurity spin 1 to yield a total spin of $\frac{1}{2}$ or $\frac{3}{2}$.
- (iii) In the *spin-splitting* (SS) regime, $T_{\mathrm{sp}} < \omega_k < T_{\mathrm{ss}}$, the effects of nonzero J_0 become noticeable, splitting apart $(1, \frac{1}{2}, \bullet)$ and $(1, \frac{3}{2}, \bullet)$, the latter drifting down.
- (iv) In the FL regime, $\omega_k < T_{\mathrm{sp}}$, $(-2, 0, \bullet)$ becomes the new ground state multiplet. Below the scale T_{sp}, the spin $3/2$ is thus screened into a spin singlet by binding three bath holes, yielding a *fully* screened impurity. Note the equidistant level spacing, characteristic of a FL.

To further elucidate the consequences of orbital and spin screening, we computed the impurity's zero-temperature orbital and spin susceptibilities,

$$\chi^{\mathrm{imp}}_{\mathrm{orb}}(\omega) = -\frac{1}{8\pi}\sum_a \mathrm{Im}\langle T^a \| T^a\rangle_\omega, \tag{3a}$$

$$\chi^{\mathrm{imp}}_{\mathrm{sp}}(\omega) = -\frac{1}{3\pi}\sum_\alpha \mathrm{Im}\langle S^\alpha \| S^\alpha\rangle_\omega, \tag{3b}$$

where $\langle X \| X\rangle_\omega$ refers to the Fourier-transformed retarded correlation functions $-i\Theta(t)\langle[X(t), X(0)]\rangle$ with frequency ω, and analogous susceptibilities, $\chi^{\mathrm{bath}}_{\mathrm{orb}}$, $\chi^{\mathrm{bath}}_{\mathrm{sp}}$ (involving $\mathbf{J}_{\mathrm{orb}}$, $\mathbf{J}_{\mathrm{sp}}$) for the bath site coupled to it. To this end we used full-density-matrix (FDM) NRG [52] and adaptive broadening of the discrete NRG data [53].

Figures 2(c) and 2(d) show these susceptibilities on a log-log scale. $\chi^{\mathrm{imp}}_{\mathrm{orb}}$ and $\chi^{\mathrm{imp}}_{\mathrm{sp}}$ each exhibit a maximum, at two widely different scales, T_{orb} and T_{sp}, coinciding with the onset of the stationary NFL or FL regimes in Fig. 2(a), respectively. Moreover, the four susceptibilities $\chi^{\mathrm{imp,bath}}_{\mathrm{orb,sp}}$ all exhibit kinks at a coinciding energy scale T_{ss}, matching the onset of the SS regime in Fig. 2(a). If ω lies within one of the regimes NFL, SS, or FL, the susceptibilities all show behavior consistent with power laws (gray lines). These power laws can all be explained by CFT, as discussed in Sec. IV. Here we focus on their qualitative features, which by themselves give striking clues about the nature of orbital and spin screening.

In the NFL regime, where $\chi^{\mathrm{imp}}_{\mathrm{orb}}$ decreases with decreasing ω, it exhibits the *same* power law as $\chi^{\mathrm{bath}}_{\mathrm{orb}}$. In this sense, the impurity's orbital isospin has taken on the same character as that of the bath site it couples to, indicative of orbital screening—in the parlance of AL's CFT analysis, it has been "absorbed" by the bath. This power law $\omega^{1/5}$ is nontrivial, differing from the ω^1 expected for a fully screened local degree of freedom. This indicates that the local orbital degree of freedom, even while being screened, is still somehow affected by the spin sector. The converse is also true: the onset of orbital screening at T_{orb} is accompanied by a change in behavior for both spin susceptibilities, $\chi^{\mathrm{imp}}_{\mathrm{sp}}$ and $\chi^{\mathrm{bath}}_{\mathrm{sp}}$. Both increase with decreasing ω, with *different* powers, indicative of the absence of spin screening in the NFL regime. The exponent for the impurity spin susceptibility, $\chi^{\mathrm{imp}}_{\mathrm{sp}} \sim \omega^{-11/5}$, is remarkably large in magnitude. (For comparison, for the standard spin-1/2, single-channel Kondo model, $\chi^{\mathrm{imp}}_{\mathrm{sp}} \sim \omega^{-1}$ for $\omega \gtrsim T_{\mathrm{sp}}$.) The highly singular $\omega^{-11/5}$ behavior—our perhaps most unexpected result—indicates that the strength of spin fluctuations is strongly amplified by the onset of orbital screening. Our CFT analysis below will reveal the reason for this: orbital screening is accompanied by a renormalization of the local bath spin density at the impurity site.

Upon entering the SS regime, all susceptibility lines show a kink, i.e., change in power law, such that the impurity and bath exponents match not only in the orbital sector, $\chi^{\mathrm{imp}}_{\mathrm{orb}} \sim \chi^{\mathrm{bath}}_{\mathrm{orb}}$, but now also in the spin sector, $\chi^{\mathrm{imp}}_{\mathrm{sp}} \sim \chi^{\mathrm{bath}}_{\mathrm{sp}}$. The latter fact indicates clearly that bath and impurity spin degrees of freedom have begun to interact with each other. However, this is only a precursor to spin screening, since the spin susceptibilities still increase with decreasing ω, albeit with a smaller exponent, $\chi^{\mathrm{imp,bath}}_{\mathrm{sp}} \sim \omega^{-6/5}$, than in the NFL regime. However, since the exponent $\gamma = 6/5$ is larger than 1, spin fluctuations are anomalously large also in this regime. Importantly, this regime persists also for parameters corresponding to the more realistic 3oAH model. Indeed, previous DMFT studies for a self-consistent 3oAH model have yielded behavior for $\chi^{\mathrm{imp}}_{\mathrm{sp}}$ which in the SOS regime is consistent with an exponent of $\gamma = 6/5$, as further discussed in Secs. IV and VI. Moreover, as mentioned in the Introduction, anomalously large spin fluctuations are of direct relevance for the superconducting state of the iron pnictide Hund metals: in Ref. [14], strong spin fluctuations with $\gamma > 1$ were a key ingredient for a proposed explanation for the anomalously large ratio of $2\Delta_{\mathrm{max}}/T_c$ observed experimentally.

Full spin screening eventually sets in in the FL regime, where the spin susceptibilities $\chi^{\mathrm{imp,bath}}_{\mathrm{sp}}$ show the ω^1 behavior characteristic of a FL. We expect this behavior also for the orbital susceptibilities, but have not been able to observe it directly, since our results for $\chi^{\mathrm{imp,bath}}_{\mathrm{orb}}$ become numerically unstable when dropping below $\simeq 10^{-5}$ [as indicated by dotted lines in Figs. 2(c) and 2(d)].

In the following two sections we explain how the above NRG results can be understood using CFT arguments.

IV. CFT ANALYSIS: SYNOPSIS

This section presents a synopsis of our CFT analysis. It aims to be accessible also to readers without in-depth knowledge of AL's CFT work on Kondo models. We begin by summarizing AL's strategy for analyzing strong-coupling fixed points of quantum impurity models (Sec. IV A). We then apply it to the NFL fixed point (Sec. IV B) and the FL fixed point (Sec. IV C). A more elaborate discussion of CFT details follows in Sec. V.

A. General strategy

AL's strategy for determining spectra and correlation functions from CFT involves three key concepts:

(C1) *Independent excitations*.—The starting assumption is that the low-energy spectrum of a multiorbital Kondo Hamiltonian at a conformally invariant fixed point can be constructed from combinations of *independent* charge, spin, and orbital excitations. The excitation energies in each sector follow from the commutation relations of certain charge, spin, and orbital operators (these form a so-called Kac-Moody algebra); this is expressed in Eqs. (4) and (12).

(C2) *Gluing conditions and fusion rules*.—The spectrum of excitations in each sector (charge, spin, orbital) is the same at the free and strong-coupling fixed points. However, the way in which these three types of excitations should be combined to obtain valid many-body excitations, specified by so-called *gluing conditions*, differs for the free and strong-coupling fixed points. At the former, excitations are glued together in such a manner that a free-fermion spectrum is recovered. At the latter, the impurity has been absorbed by the bath, implying changes in the gluing conditions relative to those of the free fixed point. These changes are governed by so-called *fusion rules*, which specify how the impurity degrees of freedom should be "added" to those of the bath. This is conceptually similar to angular momentum addition, but with additional constraints to respect the Pauli principle.

(C3) *Scaling dimensions*.—Once the fusion rules and thus the spectrum of valid many-body excitations is known, the conformal scaling dimensions of operators living at the impurity site can be determined by using the same fusion rules once more ("double fusion"). Because of conformal invariance, the functional form of correlation functions is fully determined by the scaling dimensions of their operators.

In practice, analyzing a conformally invariant strong-coupling fixed point thus consists of three steps: (C1) determine the independent excitations, (C2) use "single fusion" to obtain the strong-coupling gluing conditions, and (C3) use "double fusion" to obtain the scaling dimensions of operators living at the impurity site. Even though AL's justification of this strategy involved sophisticated CFT arguments, its application to an actual model is rather straightforward, once one has determined the appropriate fusion rules. For the 3soK model, we present tables with the explicit fusion rules in the Supplemental Material (SM) [54], and Table II shows details on the fusion procedure. These tables are also meant to serve as a guide for future applications of AL's methodology.

B. NFL regime

In the following, we follow this strategy for the NFL fixed point of the 3soK model.

(C1) The 3soK model, being spherically symmetric around the origin, describes an effectively one-dimensional system. In the imaginary-time formalism, the field describing the conduction band, $\psi(\tau + ir)$, lives on the upper half of the complex plane, with time τ on the real and the distance r from the impurity on the imaginary axis. The impurity at $r = 0$ constitutes a "boundary" at the real axis. The fixed points of the model, assumed to be scale invariant, can thus be described using $(1+1)$-dimensional boundary CFT.

The bath of the 3soK model trivially has $\mathrm{U}(1) \times \mathrm{SU}(2) \times \mathrm{SU}(3)$ symmetry. Moreover, since we assumed a flat band, i.e., a linear dispersion, it also has conformal symmetry. The combination of both leads to the symmetry $\mathrm{U}(1) \times \mathrm{SU}(2)_3 \times \mathrm{SU}(3)_2$, where $\mathrm{SU}(2)_3$ and $\mathrm{SU}(3)_2$ refer to generalizations of the familiar SU(2) and SU(3) algebras, known as Kac-Moody algebras [44,57,58]. The subscript on $\mathrm{SU}(2)_3$ states that only those spin representations are allowed which can be constructed from electrons living on 3 orbitals. In particular, spins larger than $3/2$ do not occur in this algebra. The subscript on $\mathrm{SU}(3)_2$ indicates analogous restrictions for the allowed SU(3) representations. (The consequences of these restrictions are made explicit in Tables S3 and S2 of the SM [54].)

According to AL [42–46], the fixed points can be analyzed as follows. First, standard $\mathrm{U}(1) \times \mathrm{SU}(2)_3 \times \mathrm{SU}(3)_2$ non-Abelian bosonization is used to decompose the bath Hamiltonian into charge, spin, and orbital contributions,

$$H_{\mathrm{bath}} \sim \int dr \left[\frac{1}{12} J_{\mathrm{ch}}^2(r) + \frac{1}{5} \mathbf{J}_{\mathrm{sp}}^2(r) + \frac{1}{5} \mathbf{J}_{\mathrm{orb}}^2(r)\right], \quad (4)$$

with $J_{\mathrm{ch}}(r) = \psi^{\dagger}_{m\sigma}(r)\psi_{m\sigma}(r)$, etc. (We omitted overall prefactors; for a detailed discussion, see Refs. [44,57].) Since J_{ch}, $\mathbf{J}_{\mathrm{sp}}$, $\mathbf{J}_{\mathrm{orb}}$ are generators of the U(1), $\mathrm{SU}(2)_3$, $\mathrm{SU}(3)_2$ Kac-Moody algebras, respectively, the eigenstates of H_{bath} can be organized into multiplets forming irreps of the corresponding symmetry groups, labeled by quantum numbers $Q_{\mathrm{bath}} = (q, S, \lambda)$. If the bath is put in a box of

TABLE I. Left: Five low-lying free-fermion multiplets ($|\mathrm{FS}\rangle$ denotes the Fermi sea), with quantum numbers (q, S, λ), multiplet dimensions d, and energies $E(q, S, \lambda)$. Center: "Single fusion" with an impurity $Q_{\mathrm{imp}} = (0, 1, \begin{smallmatrix}\square\\\square\end{smallmatrix})$ leads to multiplets with quantum numbers (q, S', λ'), dimensions d', eigenenergies $E' = E(q, S, \lambda')$, and excitation energies $\delta E' = E' - E'_{\mathrm{min}}$. Right: "Double fusion," which fuses multiplets from the middle column with an impurity in the conjugate representation $\bar{Q}_{\mathrm{imp}} = (0, 1, \square)$ [cf. Sec. V B, details on (C3)], yields the multiplets (q, S'', λ''). These characterize the CFT boundary operators $\hat{O}$, with scaling dimensions $\Delta = E(q, S, \lambda'')$. $\mathbf{\Phi}_{\mathrm{orb}}$ and $\mathbf{\Phi}_{\mathrm{sp}}$ are the leading boundary operators in the orbital and spin sectors, respectively. In the spin-splitting regime, their roles are taken by $\tilde{\mathbf{\Psi}}_{\mathrm{orb}}$ and $\tilde{\mathbf{\Psi}}_{\mathrm{sp}}$, respectively. "Bare" free-fermion versions of these boundary operators, having the same quantum numbers, are listed on the very right. For clarity, not all possible multiplets arising from single and double fusion are shown. A more comprehensive list is given in Table II.

	Free fermions					Single fusion					Double fusion					
State	q	S	λ	d	E	q	S'	λ'	d'	$\delta E'$	q	S''	λ''	Δ	$\hat{O}$	$\hat{O}_{\mathrm{bare}}$
$\lvert\mathrm{FS}\rangle$	0	0	$\bullet$	1	0	0	1	$\begin{smallmatrix}\square\\\square\end{smallmatrix}$	9	$\frac{1}{30}$	0	0	$\begin{smallmatrix}\square\square\\\square\end{smallmatrix}$	$\frac{3}{5}$	$\mathbf{\Phi}_{\mathrm{orb}}$	$\mathbf{T}, \mathbf{J}_{\mathrm{orb}}$
$\psi^{\dagger}_{m\sigma}\lvert\mathrm{FS}\rangle$	1	$\frac{1}{2}$	$\square$	6	$\frac{1}{2}$	1	$\{\frac{1}{2}, \frac{3}{2}\}$	$\bullet$	6	0		$\cdots$				
$\psi_{m\sigma}\lvert\mathrm{FS}\rangle$	-1	$\frac{1}{2}$	$\begin{smallmatrix}\square\\\square\end{smallmatrix}$	6	$\frac{1}{2}$	-1	$\frac{1}{2}$	$\square$	6	$\frac{4}{15}$	-1	$\frac{1}{2}$	$\square\square$	$\frac{9}{10}$	$\tilde{\mathbf{\Psi}}_{\mathrm{orb}}$	$(\psi^{\dagger}_{l\sigma}\psi_{l\sigma} - \psi^{\dagger}_{m\sigma}\psi_{m\sigma})\psi_{n\sigma}$, $\psi^{\dagger}_{l\sigma}\psi_{m\sigma}\psi_{n\sigma}$, $l \neq m \neq n$
$\mathbf{J}_{\text{sp-orb}}\lvert\mathrm{FS}\rangle$	0	1	$\begin{smallmatrix}\square\square\\\square\end{smallmatrix}$	24	1	0	0	$\begin{smallmatrix}\square\\\square\end{smallmatrix}$	3	$\frac{13}{30}$	0	1	$\bullet$	$\frac{2}{5}$	$\mathbf{\Phi}_{\mathrm{sp}}$	$\mathbf{J}_{\mathrm{sp}}$
$\cdots$	-3	$\frac{1}{2}$	$\begin{smallmatrix}\square\square\\\square\end{smallmatrix}$	16	$\frac{3}{2}$	-3	$\frac{1}{2}$	$\begin{smallmatrix}\square\\\square\end{smallmatrix}$	6	$\frac{14}{15}$	-3	$\frac{1}{2}$	$\bullet$	$\frac{9}{10}$	$\tilde{\mathbf{\Psi}}_{\mathrm{sp}}$	$\psi_{1\sigma}\psi_{2\sigma}\psi_{3\bar{\sigma}}$

finite size, the corresponding free-fermion excitation eigenenergies $E(q, S, \lambda)$ are discrete and simple functions of the quantum numbers [see Eq. (12)].

(C2) Next, we include the interaction with the impurity in the orbital sector ($K_0 > 0$, $J_0 = I_0 = 0$) to describe the properties of the NFL fixed point $\mathbf{c}^{*}_{\mathrm{NFL}}$. The bosonized H_{bath} is quadratic in $\mathbf{J}_{\mathrm{orb}}$, whereas the coupling term $H_{\mathrm{int}} = K_0\mathbf{T} \cdot \mathbf{J}_{\mathrm{orb}}(r = 0)$ is linear. The latter can thus be absorbed into the former, in the spirit of "completing the square." AL conjectured that at the strong-coupling fixed point, this replacement takes the form

$$\mathbf{J}_{\mathrm{orb}}(r) \mapsto \mathcal{J}_{\mathrm{orb}}(r) = \mathbf{J}_{\mathrm{orb}}(r) + \delta(r)\mathbf{T}, \qquad (5)$$

with $\mathcal{J}_{\mathrm{orb}}$ satisfying the same Kac-Moody algebra as $\mathbf{J}_{\mathrm{orb}}$. At the strong-coupling fixed point, the Hamiltonian can thus be expressed as $H = H_{\mathrm{bath}}[\mathbf{J}_{\mathrm{orb}}] + H_{\mathrm{int}} = H_{\mathrm{bath}}[\mathcal{J}_{\mathrm{orb}}]$ (more details can be found in Sec. V B and Ref. [43]).

It follows immediately that at the fixed point, the spectrum of irreps of the full Hamiltonian can be obtained by combining the irreps of bath and impurity degrees of freedom, $Q_{\mathrm{bath}} \otimes Q_{\mathrm{imp}} = \sum_{\oplus} Q'$, and using "fusion rules" to deduce the resulting irreps Q'. This is conceptually similar to coupling two SU(2) spins, $\mathbf{S}'' = \mathbf{S} + \mathbf{S}'$, decomposing the direct product of their irreps as $S \otimes S' = \sum_{\oplus} S''$, and deducing that S'' ranges from $|S - S'|$ to $S + S'$. However, in the present context, specific assumptions must be made about which degrees of freedom are involved in the screening processes and which are not, and for those which are, Kac-Moody fusion rules have to be used when combining irreps. For the present situation, we have $Q_{\mathrm{bath}} = (q, S, \lambda)$ and $Q_{\mathrm{imp}} = (0, 1, \begin{smallmatrix}\square\\\square\end{smallmatrix})$, and place ourselves *at* the NFL fixed point, where bath and impurity couple only in the orbital sector.

To find the allowed irreps $Q' = (q', S', \lambda')$, we therefore posit the following fusion strategy (inspired by and generalizing that of AL [42–46]). In the charge sector, $q_{\mathrm{imp}} = 0$ trivially implies that $q' = q$. In the orbital sector, the impurity's orbital isospin is coupled to that of the bath [Eq. (1)] and absorbed by it according to Eq. (5); hence, $\lambda \otimes \lambda_{\mathrm{imp}} = \sum_{\oplus} \lambda'$ is governed by the fusion rules of the $\mathrm{SU}(3)_2$ Kac-Moody algebra. By contrast, in the spin sector the impurity spin is a spectator, decoupled from the bath (we are *at* $\mathbf{c}^{*}_{\mathrm{NFL}}$, where $J_0 = I_0 = 0$); hence, $S \otimes S_{\mathrm{imp}} = \sum_{\oplus} S'$ is governed by the fusion rules of the SU(2) Lie algebra [not the $\mathrm{SU}(2)_3$ Kac-Moody algebra]. The set of excitations (q, S', λ') so obtained have energies given by $E(q, S, \lambda')$, not $E(q, S', \lambda')$, since H_{int} only acts in the orbital sector. A more complete discussion of our "fusion hypothesis" is given in Sec. V B. The resulting spectrum reproduces the NRG spectrum in the NFL fixed point regime (see Table II).

Table I exemplifies a few many-body states obtained via this fusion scheme (AL called it single fusion, in distinction from a second fusion step, discussed below). In particular, the degenerate ground state multiplets of $\mathbf{c}^{*}_{\mathrm{NFL}}$, $(1, \frac{1}{2}, \bullet)$ and $(1, \frac{3}{2}, \bullet)$ [cf. Fig. 2(a)], arise via fusion of a one-particle bath excitation, $(+1, \frac{1}{2}, \square)$, with the impurity $(0, 1, \begin{smallmatrix}\square\\\square\end{smallmatrix})$, schematically depicted in Fig. 2(b).

(C3) Next, we want to compute the leading scaling behavior of spin and orbital correlation functions at the impurity site, i.e., on the boundary of the CFT. The absorption of the impurity into the bath (bulk) Hamiltonian translates, in CFT language, to a change in the boundary condition imposed on the theory at $r = 0$. As a result, a new set of "boundary operators," i.e., local operators living at the impurity site, appear in the theory.

These fully characterize the strong-coupling fixed point. Each boundary operator can be viewed as the renormalized version, resulting from the screening process, of some bare local operator having the same quantum numbers.

According to AL, the boundary operators can be obtained via a second fusion step (double fusion) (cf. Refs. [44–46] and Appendix C of Ref. [57]). Each multiplet (q, S'', λ'') resulting from double fusion is associated with a boundary operator $\hat{O}$ with the same quantum numbers, and a scaling dimension given by $\Delta = E(q, S, \lambda'')$ (cf. Table I). The realization that the scaling dimensions of boundary operators are related to finite-size excitation energies is due to Cardy [59]. Using a conformal mapping, he mapped the complex upper half-plane to a strip of infinite length and finite width, in such a way that the nontrivial boundary condition of the half-plane is mapped to both boundaries of the strip. He then showed that the boundary operators of the half-plane and their scaling dimensions can be associated with the finite-size spectrum of a Hamiltonian defined along the width of this strip. Since the strip has two nontrivial boundaries, one on each side, the finite-size spectrum can be found using a double-fusion procedure. The scaling dimensions of the boundary operators fully determine their time- or frequency-dependent correlators, $\langle \hat{O}(t)\hat{O}(0)\rangle \sim t^{-2\Delta}$ and $\langle \hat{O}||\hat{O}\rangle_\omega \simeq \omega^{2\Delta-1}$.

To explain the power laws found in the NFL regime of Figs. 2(c) and 2(d), and particularly the fact that there $\chi^{\mathrm{imp}}_{\mathrm{orb}}$ and $\chi^{\mathrm{bath}}_{\mathrm{orb}}$ exhibit the *same* power law, while $\chi^{\mathrm{imp}}_{\mathrm{sp}}$ and $\chi^{\mathrm{bath}}_{\mathrm{sp}}$ do not, we posit that the local operators in the orbital and spin exchange terms of Eq. (1) are renormalized to

$$\mathbf{J}_{\mathrm{orb}} \mapsto \mathbf{\Phi}_{\mathrm{orb}}, \quad \mathbf{T} \mapsto \mathbf{\Phi}_{\mathrm{orb}}, \quad \mathbf{J}_{\mathrm{sp}} \mapsto \mathbf{\Phi}_{\mathrm{sp}}, \quad \mathbf{S} \mapsto \mathbf{S}. \tag{6}$$

Here $\mathbf{\Phi}_{\mathrm{orb}}$ has quantum numbers $(0, 0, \ydiagram{2,1})$ (same as $\mathbf{T}$, $\mathbf{J}_{\mathrm{orb}}$) and dimension $\Delta_{\mathrm{orb}} = \frac{3}{5}$, while $\mathbf{\Phi}_{\mathrm{sp}}$ has quantum numbers $(0, 1, \bullet)$ (same as $\mathbf{S}$, $\mathbf{J}_{\mathrm{sp}}$) and $\Delta_{\mathrm{sp}} = \frac{2}{5}$ (cf. Table I). The local impurity and bath orbital susceptibilities thus both scale as

$$\chi^{\mathrm{imp,bath}}_{\mathrm{orb}} \sim \langle \mathbf{\Phi}_{\mathrm{orb}}||\mathbf{\Phi}_{\mathrm{orb}}\rangle_\omega \sim \omega^{2\Delta_{\mathrm{orb}}-1} = \omega^{1/5}, \tag{7}$$

and the bath spin susceptibility as

$$\chi^{\mathrm{bath}}_{\mathrm{sp}} \sim \langle \mathbf{\Phi}_{\mathrm{sp}}||\mathbf{\Phi}_{\mathrm{sp}}\rangle_\omega \sim \omega^{2\Delta_{\mathrm{sp}}-1} = \omega^{-1/5}. \tag{8}$$

By contrast, the impurity spin $\mathbf{S}$ is not renormalized, because *at* the fixed point $\mathbf{c}^*_{\mathrm{NFL}}$, where $J_0 = 0$, it is decoupled from the bath. Thus its scaling dimension is zero. The leading behavior of $\chi^{\mathrm{imp}}_{\mathrm{sp}}$ is obtained by now taking $J_0 \neq 0$ but very small ($\ll K_0$), and doing second-order perturbation theory in the renormalized spin exchange interaction. Thus, $\chi^{\mathrm{imp}}_{\mathrm{sp}}$ is proportional to the Fourier transform of $\langle \mathbf{S}(t)\mathbf{S}(0)(\int dt' J_0 \mathbf{S}\cdot\mathbf{\Phi}_{\mathrm{sp}})^2\rangle$, and power counting yields

$$\chi^{\mathrm{imp}}_{\mathrm{sp}} \sim \omega^{2\Delta_{\mathrm{sp}}-3} = \omega^{-11/5}. \tag{9}$$

The above predictions are all borne out in Figs. 2(c) and 2(d).

The remarkably large negative exponent, $-\frac{11}{5}$, for $\chi^{\mathrm{imp}}_{\mathrm{sp}}$ reflects the fact that the renormalized spin exchange interaction $J_0 \mathbf{S}\cdot\mathbf{\Phi}_{\mathrm{sp}}$, with scaling dimension $\frac{2}{5} < 1$, is a relevant perturbation. Its strength, though initially miniscule if $J_0 \ll 1$, grows under the RG flow, causing a crossover away from $\mathbf{c}^*_{\mathrm{NFL}}$ for $\omega \lesssim T_{\mathrm{ss}}$. This is reflected in the level crossings around T_{ss} in the NRG eigenlevel flow of Fig. 2. In particular, the double-fusion parent multiplets for $\mathbf{\Phi}_{\mathrm{orb}}$ and $\mathbf{\Phi}_{\mathrm{sp}}$, namely $(0, 1, \ydiagram{1,1})$ and $(0, 0, \ydiagram{1,1})$, undergo level crossings with the downward-moving multiplets $(-1, \frac{1}{2}, \square)$ and $(-3, \frac{1}{2}, \ydiagram{1,1})$, respectively. These in turn are double-fusion parent multiplets for the boundary operators $\tilde{\Psi}_{\mathrm{orb}}$ and $\tilde{\Psi}_{\mathrm{sp}}$, with scaling dimensions $\tilde{\Delta}_{\mathrm{orb}} = \tilde{\Delta}_{\mathrm{sp}} = \frac{9}{10}$ (Table I). To explain the SS regime of Figs. 2(c) and 2(d), and particularly that there the power laws for χ^{imp} and χ^{bath} match in both the orbital *and* spin sectors, we posit the RG replacements

$$\mathbf{J}_{\mathrm{orb}} \mapsto \tilde{\Psi}_{\mathrm{orb}}, \qquad \mathbf{T} \mapsto \tilde{\Psi}_{\mathrm{orb}},$$
$$\mathbf{J}_{\mathrm{sp}} \mapsto \mathbf{S} + \tilde{\Psi}_{\mathrm{sp}}, \qquad \mathbf{S} \mapsto \mathbf{S} + \tilde{\Psi}_{\mathrm{sp}}.$$

Here $\mathbf{S} + \tilde{\Psi}_{\mathrm{sp}}$ is symbolic notation for some linear admixture of both operators, induced by the action of the renormalized spin exchange interaction. We thus obtain

$$\chi^{\mathrm{imp,bath}}_{\mathrm{orb}} \sim \langle \tilde{\Psi}_{\mathrm{orb}}||\tilde{\Psi}_{\mathrm{orb}}\rangle_\omega \sim \omega^{2\tilde{\Delta}_{\mathrm{orb}}-1} = \omega^{4/5}, \tag{10}$$

and the leading contribution to $\chi^{\mathrm{imp}}_{\mathrm{sp}}$ and $\chi^{\mathrm{bath}}_{\mathrm{sp}}$, obtained by perturbing $\langle \mathbf{S}(t)\mathbf{S}(0)\rangle$ to second order in $\mathbf{S}\tilde{\Psi}_{\mathrm{sp}}$ [60], is

$$\chi^{\mathrm{imp,bath}}_{\mathrm{sp}} \sim \omega^{2\tilde{\Delta}_{\mathrm{sp}}-3} = \omega^{-6/5}. \tag{11}$$

This reproduces the power laws found in Figs. 2(c) and 2(d).

Remarkably, $\chi^{\mathrm{imp}}_{\mathrm{sp}} \sim \omega^{-6/5}$ behavior has also been found in studies of the self-consistent 3oAH model arising in our DMFT investigations of the three-orbital Hubbard-Hund model for Hund metals. For the 3oAH model the spin-orbital coupling I_0 in Eq. (1) is always nonzero, so that a fully fledged NFL does not emerge—instead, T_{orb} and T_{ss} effectively coincide (as further discussed in Sec. VI). However, the SS regime between T_{sp} and $T_{\mathrm{ss}} \simeq T_{\mathrm{orb}}$ can be quite wide, typically at least an order of magnitude. In Fig. 3(c) of Ref. [22], the behavior of $\chi^{\mathrm{imp}}_{\mathrm{sp}}$ in this regime (between the vertical solid and black lines there) is consistent with $\omega^{-6/5}$ behavior. Though this fact was not noted in Ref. [22], it was subsequently pointed out in Ref. [14] (see Fig. S1 of their Supplemental Material).

Behavior consistent with $\chi_{\mathrm{sp}}^{\mathrm{imp}} \sim \omega^{-6/5}$ can also be seen in Figs. 5.1(c) and 5.1(d) of Ref. [47], as discussed on p. 152 therein. The explanation for this behavior presented here, via a CFT analysis of the NFL and SS regimes, is one of the main results of this work, and the justification for the first part of the title of this paper.

C. Fermi-liquid regime

As mentioned above, the low-energy regime below T_{sp} is a FL. The fixed-point spectrum at $\mathbf{c}_{\mathrm{FL}}^{*}$ can be obtained by fusing a free-fermion spectrum with an impurity with $Q_{\mathrm{imp}} = (1, \frac{3}{2}, \bullet)$, representing the effective local degree of freedom obtained after completion of orbital screening (see Table III). Since the ground state describes a fully screened orbital and spin singlet, it actually is the singlet of a larger symmetry group, $\mathrm{U}(1) \times \mathrm{SU}(6)$. Indeed, the fixed-point spectrum at $\mathbf{c}_{\mathrm{FL}}^{*}$ matches that of the $\mathrm{U}(1) \times \mathrm{SU}(6)$ symmetric Kondo model. We demonstrate this, using both NRG and CFT with $\mathrm{SU}(6)_1$ fusion rules, in Sec. V E (see Table IV). The FL nature of the ground state is also borne out by the ω^1 scaling of $\chi_{\mathrm{sp}}^{\mathrm{imp,bath}}$ in the FL regime of Figs. 2(c) and 2(d).

V. CFT ANALYSIS: DETAILS

We now provide technical details for our CFT analysis of the NFL and FL fixed points of the three-orbital Kondo model discussed in Secs. III and IV. We closely follow the strategy devised by Affleck and Ludwig for their pioneering treatment of the strong-coupling fixed points of Kondo models [42–46] (for pedagogical reviews, see Refs. [58,61] and Appendixes A–D of Ref. [57]). In a series of works, they considered a variety of Kondo models of increasing complexity. These include the standard one-channel, SU(2) spin Kondo model with a spin exchange interaction between bath and impurity with $\mathrm{U}(1) \times \mathrm{SU}(2)_1$ symmetry; a spinful k-channel bath coupled to an SU(2) impurity $[\mathrm{U}(1) \times \mathrm{SU}(2)_k \times \mathrm{SU}(\mathrm{k})_2$ symmetry], and a $\mathrm{SU}(N)$ k-channel bath coupled to an $\mathrm{SU}(N)$ impurity $[\mathrm{U}(1) \times \mathrm{SU}(\mathrm{N})_k \times \mathrm{SU}(\mathrm{k})_N$ symmetry].

Our 3soK model features a spinful three-channel bath and an $\mathrm{SU}(2)_{\mathrm{sp}} \times \mathrm{SU}(3)_{\mathrm{orb}}$ impurity $[\mathrm{U}(1) \times \mathrm{SU}(2)_3 \times \mathrm{SU}(3)_2$ symmetry]. The impurity multiplet is a direct product of a spin triplet ($S = 1$) and an orbital triplet ($\lambda = \begin{smallmatrix}\square\\\square\end{smallmatrix}$). Its direct-product structure is more general than any of the cases considered by AL. [A two-channel version of our model, with $\mathrm{U}(1) \times \mathrm{SU}(2)_2 \times \mathrm{SU}(2)_2$ symmetry, has been studied by Ye [48], which we discuss in the Appendix.] However, at the NFL fixed point $\mathbf{c}_{\mathrm{NFL}}^{*}$ of our model, where $J_0 = I_0 = 0$, the impurity's SU(2) spin is a decoupled, threefold degenerate spectator degree of freedom. Hence AL's analysis [46] can be employed, with $N = 3$ and $k = 2$ channels, modulo some minor changes to account for the impurity spin.

By contrast, in the spin-splitting crossover regime the spin exchange interaction comes to life, so that the impurity's SU(2) spin degrees of freedom cease to be mere spectators. This regime thus lies outside the realm of cases studied by AL; in particular, it is not manifestly governed by the NFL fixed point $\mathbf{c}_{\mathrm{NFL}}^{*}$, or any other well-defined fixed point. Correspondingly, our discussion of this crossover regime in Sec. V C 2 is more speculative than that of the NFL regime, though our heuristic arguments are guided by and consistent with our NRG results.

Finally, for our model's FL fixed point $\mathbf{c}_{\mathrm{FL}}^{*}$, we are again in well-chartered territory: it can be understood by applying AL's strategy to an SU(6) one-channel bath coupled to an SU(6) impurity $[\mathrm{U}(1) \times \mathrm{SU}(6)_1$ symmetry].

Below we assume the reader to be familiar with AL's work and just focus on documenting the details of our analysis. Section V A describes how the free-fermion bath spectrum is decomposed into charge, spin, and orbital excitations using $\mathrm{U}(1) \times \mathrm{SU}(2)_3 \times \mathrm{SU}(3)_2$ non-Abelian bosonization. Section V B derives the finite-size spectrum and boundary operators of the NFL fixed point via single and double fusion, using the fusion rules of the $\mathrm{SU}(3)_2$ Kac-Moody algebra in the orbital sector and the SU(2) Lie algebra in the spin sector. Section V C describes the computation of the spin and orbital susceptibilities in the NFL and SS regimes, linking AL's strategy for computing such quantities to the compact scaling arguments used in Sec. IV. Section V D presents our results for the impurity spectral function in the NFL regime. Finally, Sec. V E, devoted to the FL regime, shows how its spectrum can be derived using either $\mathrm{SU}(2)_3$ fusion rules in the spin sector or $\mathrm{SU}(6)_1$ fusion rules in the flavor (combined spin + orbital) sector.

A. Non-Abelian $\mathbf{U(1)\times SU(2)_3\times SU(3)_2}$ bosonization

(C1) The first step of AL's CFT approach for multichannel Kondo models is to use non-Abelian bosonization to decompose the bath degrees of freedom into charge, spin, and orbital excitations in a manner respecting the symmetry of the impurity-bath exchange interactions. Our 3soK model features a spinful three-channel bath, with $H_{\mathrm{bath}} = \sum_{pm\sigma} \varepsilon_p \psi_{pm\sigma}^{\dagger} \psi_{pm\sigma}$. We assume a linear dispersion, $\varepsilon_p = \hbar v_F p$, with $\hbar v_F = 1$. Using non-Abelian bosonization with the $\mathrm{U}(1) \times \mathrm{SU}(2)_3 \times \mathrm{SU}(3)_2$ Kac-Moody current algebra, the spectrum of bath excitations can be expressed as (see Refs. [42,44] or Appendix A of Ref. [57])

$$E(q, S, \lambda) = \frac{1}{12} q^2 + \frac{1}{5} \kappa_2(S) + \frac{1}{5} \kappa_3(\lambda) + \ell, \tag{12a}$$

$$\kappa_2(S) = S(S+1), \tag{12b}$$

$$\kappa_3(\lambda) = \frac{1}{3} (\lambda_1^2 + \lambda_2^2 + \lambda_1 \lambda_2 + 3\lambda_1 + 3\lambda_2). \tag{12c}$$

Here $\kappa_2(S)$ and $\kappa_3(\lambda)$ are the eigenvalues of the quadratic Casimir operators of the SU(2) and SU(3) Lie algebras, respectively [62]. $q \in \mathbb{Z}$ is the U(1) charge quantum number, $S \in \frac{1}{2}\mathbb{Z}$ the SU(2) spin quantum number, and $\lambda = (\lambda_1, \lambda_2)$ the SU(3) orbital quantum number, denoting a Young diagram with λ_j j-row columns:

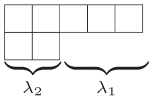

λ_1 = number of 1-row columns
λ_2 = number of 2-row columns

Finally, $\ell \in \mathbb{Z}$ counts higher-lying "descendent" excitations; for present purposes it suffices to set $\ell = 0$.

The free-fermion spectrum of H_{bath} is recovered from Eq. (12) by imposing free-fermion "gluing conditions," allowing only those combinations of quantum numbers (q, S, λ) for which $E(q, S, \lambda)$ is an integer multiple of 1/2. The resulting multiplets are listed in the left-hand column ("Free fermions") of Table II.

B. Non-Fermi-liquid fixed point

(C2) We now focus on the NFL fixed point of the 3soK model, at $\mathbf{c}^*_{\mathrm{NFL}}$, where $(J_0, K_0, I_0) = (0, 1, 0)$. According to AL's general strategy, the orbital isospin T can be then "absorbed" by the bath through the substitution

$$\mathbf{J}_{\mathrm{orb},n} \mapsto \mathcal{J}_{\mathrm{orb},n} = \mathbf{J}_{\mathrm{orb},n} + \mathbf{T}. \tag{13}$$

Here $\mathbf{J}_{\mathrm{orb},n}$ and $\mathcal{J}_{\mathrm{orb},n}$ are Fourier components (n being a Fourier index) of the bare and bulk orbital isospin currents, respectively, defined for a bath in a finite-sized box. (The local bath operator $\mathbf{J}_{\mathrm{orb}}$ is proportional to $\sum_{n\in\mathbb{Z}} \mathbf{J}_{\mathrm{orb},n}$.) The right-hand side of Eq. (13) is reminiscent of the addition of Lie algebra generators, $\mathbf{S}' = \mathbf{S} + \tilde{\mathbf{S}}$, when performing a direct product decomposition, $S \otimes \tilde{S} = \sum_{\oplus} S'$, of SU(2) multiplets. The terms added in Eq. (13), however, generate two *different* algebras: $\mathbf{J}_{\mathrm{orb},n}$ are generators of the $\mathrm{SU}(3)_2$ KM algebra, $\mathbf{T}$ of the SU(3) Lie algebra. AL proposed a remarkable fusion hypothesis for dealing with such situations (and confirmed its veracity by detailed comparisons to Bethe ansatz and NRG computations). For the present context their fusion hypothesis states: the eigenstates of the combined bath + impurity system can be obtained by combining (or "fusing") their orbital degrees of freedom, $\lambda \otimes \lambda_{\mathrm{imp}} = \sum_{\oplus} \lambda'$, using the fusion rules of the $\mathrm{SU}(3)_2$ KM algebra, as though the impurity's orbital multiplet were an $\mathrm{SU}(3)_2$, not SU(3), multiplet. The $\mathrm{SU}(3)_2$ fusion rules are depicted in Table S2 of the Supplemental Material [54].

Having discussed orbital fusion, we now turn to the spin sector—how should the impurity's spectator spin be dealt with? This question goes beyond the scope of AL's work, who did not consider impurities with spectator degrees of freedom. We have explored several spin fusion strategies and concluded that the following one yields spectra consistent with NRG: In parallel to orbital fusion, the bath and impurity spin degrees should be combined too, as

TABLE II. Fusion table for orbital screening at the NFL fixed point $\mathbf{c}^*_{\mathrm{NFL}}$ of the 3soK model. Left: The 14 lowest low-lying free-fermion multiplets (q, S, λ), with multiplet dimensions d and energies $E(q, S, \lambda)$, computed using Eqs. (12) and Table S1 of the SM [54]. Center: Single fusion with a $Q_{\mathrm{imp}} = (0, 1, \ydiagram{1,1})$ impurity, using SU(2) fusion rules in the spin sector and $\mathrm{SU}(3)_2$ fusion rules (listed in Table S2 of the SM [54]) in the orbital sector. This yields multiplets (q, S', λ'), with dimensions d', energies $E' = E(q, S, \lambda')$, and excitation energies $\delta E' = E' - E'_{\mathrm{min}}$. These are compared to the values, E_{NRG}, computed by NRG for $(J_0, K_0, I_0) = (0, 0.3, 0)$. The NRG energies have been shifted and rescaled such that the lowest energy is zero and the second-lowest values for E_{NRG} and $\delta E'$ match. The single-fusion and NRG spectra agree well (deviations ≲10%). Right: Double fusion, which fuses multiplets from the middle column with an impurity in the conjugate representation $\bar{Q}_{\mathrm{imp}} = (0, 1, \square)$, yields the quantum numbers (q, S'', λ''). These characterize the CFT boundary operators $\hat{O}$, with scaling dimensions $\Delta = E(q, S, \lambda'')$.

Free fermions					Single fusion, with $Q_{\mathrm{imp}} = (0, 1, \ydiagram{1,1})$						NRG	Double fusion, with $\bar{Q}_{\mathrm{imp}} = (0, 1, \square)$				
q	S	λ	d	E	q	S'	λ'	d'	E'	$\delta E'$	E_{NRG}	q	S''	λ''	Δ	$\hat{O}$
0	0	$\bullet$	1	0	0	1	$\ydiagram{1,1}$	9	$\frac{4}{15}$	$\frac{1}{30}$ (0.033)	0.033	0	0	$\bullet$	0	$\mathbb{1}$
														$\ydiagram{2,1}$	$\frac{3}{5}$	$\mathbf{\Phi}_{\mathrm{orb}}$
													1	$\bullet$	0	
														$\ydiagram{2,1}$	$\frac{3}{5}$	
													2	$\bullet$	0	
														$\ydiagram{2,1}$	$\frac{3}{5}$	

(Table continued)

TABLE II. *(Continued)*

Free fermions					Single fusion, with $Q_{\mathrm{imp}} = (0,1,\ydiagram{1,1})$						NRG	Double fusion, with $\bar{Q}_{\mathrm{imp}} = (0,1,\square)$				
q	S	λ	d	E	q	S'	λ'	d'	E'	$\delta E'$	E_{NRG}	q	S''	λ''	Δ	$\hat{O}$
$+1$	$\frac{1}{2}$	$\square$	6	$\frac{1}{2}$	$+1$	$\frac{1}{2}$	$\bullet$	2	$\frac{7}{30}$	0	0	$+1$	$\frac{1}{2}$	$\square$	$\frac{1}{2}$	
													$\frac{3}{2}$	$\square$	$\frac{1}{2}$	
							$\ydiagram{2,1}$	16	$\frac{5}{6}$	$\frac{3}{5}$ (0.6)	0.64	$+1$	$\frac{1}{2}$	$\square$	$\frac{1}{2}$	
														$\ydiagram{2,2}$	$\frac{9}{10}$	
													$\frac{3}{2}$	$\square$	$\frac{1}{2}$	
														$\ydiagram{2,2}$	$\frac{9}{10}$	
						$\frac{3}{2}$	$\bullet$	4	$\frac{7}{30}$	0	0	as above				
							$\ydiagram{2,1}$	32	$\frac{5}{6}$	$\frac{3}{5}$ (0.6)	0.64					
-1	$\frac{1}{2}$	$\ydiagram{1,1}$	6	$\frac{1}{2}$	-1	$\frac{1}{2}$	$\square$	6	$\frac{1}{2}$	$\frac{4}{15}$ (0.27)	0.28	-1	$\frac{1}{2}$	$\ydiagram{1,1}$	$\frac{1}{2}$	
														$\ydiagram{2}$	$\frac{9}{10}$	$\tilde{\Psi}_{\mathrm{orb}}$
													$\frac{3}{2}$	$\ydiagram{1,1}$	$\frac{1}{2}$	
														$\ydiagram{2}$	$\frac{9}{10}$	
							$\ydiagram{2,2}$	12	$\frac{9}{10}$	$\frac{2}{3}$ (0.67)	0.70	-1	$\frac{1}{2}$	$\ydiagram{1,1}$	$\frac{1}{2}$	
													$\frac{3}{2}$	$\ydiagram{1,1}$	$\frac{1}{2}$	
						$\frac{3}{2}$	$\square$	12	$\frac{1}{2}$	$\frac{4}{15}$ (0.27)	0.28	as above				
							$\ydiagram{2,2}$	24	$\frac{9}{10}$	$\frac{2}{3}$ (0.67)	0.70					
0	1	$\ydiagram{2,1}$	24	1	0	0	$\ydiagram{1,1}$	3	$\frac{2}{3}$	$\frac{13}{30}$ (0.43)	0.46	0	1	$\bullet$	$\frac{2}{5}$	$\mathbf{\Phi}_{\mathrm{sp}}$
														$\ydiagram{2,1}$	1	
							$\ydiagram{2}$	6	$\frac{16}{15}$	$\frac{5}{6}$ (0.83)	0.88	0	1	$\ydiagram{2,1}$	1	
						1	$\ydiagram{1,1}$	9	$\frac{2}{3}$	$\frac{13}{30}$ (0.43)	0.46	as above, with $S'' \in \{0,1,2\}$				
							$\ydiagram{2}$	18	$\frac{16}{15}$	$\frac{5}{6}$ (0.83)	0.88					
						2	$\ydiagram{1,1}$	15	$\frac{2}{3}$	$\frac{13}{30}$ (0.43)	0.46					
							$\ydiagram{2}$	30	$\frac{16}{15}$	$\frac{5}{6}$ (0.83)	0.88					
$+2$	0	$\ydiagram{2}$	6	1	$+2$	1	$\square$	9	$\frac{3}{5}$	$\frac{11}{30}$ (0.37)	0.39	$+2$	0	$\ydiagram{1,1}$	$\frac{3}{5}$	
														$\ydiagram{2}$	1	
													as above, with $S'' \in \{1,2\}$			
-2	0	$\ydiagram{2,2}$	6	1	-2	1	$\ydiagram{2,1}$	24	$\frac{14}{15}$	$\frac{7}{10}$ (0.7)	0.74	-2	0	$\square$	$\frac{3}{5}$	
														$\ydiagram{2,2}$	1	
													as above, with $S'' \in \{1,2\}$			
$+2$	1	$\ydiagram{1,1}$	9	1	$+2$	0	$\square$	3	1	$\frac{23}{30}$ (0.77)	0.82	$+2$	1	$\ydiagram{1,1}$	1	
														$\ydiagram{2}$	$\frac{7}{5}$	
							$\ydiagram{2,2}$	6	$\frac{7}{5}$	$\frac{7}{6}$ (1.17)	1.24	$+2$	1	$\ydiagram{1,1}$	1	
						1	$\square$	9	1	$\frac{23}{30}$ (0.77)	0.82	as above, with $S'' \in \{0,1,2\}$				
							$\ydiagram{2,2}$	18	$\frac{7}{5}$	$\frac{7}{6}$ (1.17)	1.24					
						2	$\square$	15	1	$\frac{23}{30}$ (0.77)	0.82					
							$\ydiagram{2,2}$	30	$\frac{7}{5}$	$\frac{7}{6}$ (1.17)	1.24					

(Table continued)

TABLE II. *(Continued)*

Free fermions					Single fusion, with $Q_{\mathrm{imp}} = (0,1,\ydiagram{1,1})$						NRG	Double fusion, with $\bar{Q}_{\mathrm{imp}} = (0,1,\ydiagram{1})$				
q	S	λ	d	E	q	S'	λ'	d'	E'	$\delta E'$	E_{NRG}	q	S''	λ''	Δ	$\hat{O}$
-2	1	$\ydiagram{1}$	9	1	-2	0	•	1	$\frac{11}{15}$	$\frac{1}{2}$ (0.5)	0.52	-2	1	$\ydiagram{1}$	1	
							$\ydiagram{2,1}$	8	$\frac{4}{3}$	$\frac{11}{10}$ (1.1)	1.16	-2	1	$\ydiagram{1}$ $\ydiagram{2,2}$	1 $\frac{7}{5}$	
						1	•	3	$\frac{11}{15}$	$\frac{1}{2}$ (0.5)	0.52	as above, with $S'' \in \{0,1,2\}$				
							$\ydiagram{2,1}$	24	$\frac{4}{3}$	$\frac{11}{10}$ (1.1)	1.16					
						2	•	5	$\frac{11}{15}$	$\frac{1}{2}$ (0.5)	0.52					
							$\ydiagram{2,1}$	40	$\frac{4}{3}$	$\frac{11}{10}$ (1.1)	1.16					
$+1$	$\frac{3}{2}$	$\ydiagram{2,2}$	24	$\frac{3}{2}$	$+1$	$\frac{1}{2}$	$\ydiagram{2,1}$	16	$\frac{43}{30}$	$\frac{6}{5}$ (1.2)	1.28	$+1$	$\frac{1}{2}$	$\ydiagram{1}$ $\ydiagram{2,2}$	$\frac{11}{10}$ $\frac{3}{2}$	
													$\frac{3}{2}$	$\ydiagram{1}$ $\ydiagram{2,2}$	$\frac{11}{10}$ $\frac{3}{2}$	
						$\frac{3}{2}$	$\ydiagram{2,1}$	32	$\frac{43}{30}$	$\frac{6}{5}$ (1.2)	1.28	as above				
						$\frac{5}{2}$	$\ydiagram{2,1}$	48	$\frac{43}{30}$	$\frac{6}{5}$ (1.2)	1.28					
-1	$\frac{3}{2}$	$\ydiagram{2}$	24	$\frac{3}{2}$	-1	$\frac{1}{2}$	$\ydiagram{1}$	6	$\frac{11}{10}$	$\frac{13}{15}$ (0.87)	0.92	-1	$\frac{1}{2}$	$\ydiagram{1,1}$ $\ydiagram{2}$	$\frac{11}{10}$ $\frac{3}{2}$	
													$\frac{3}{2}$	$\ydiagram{1,1}$ $\ydiagram{2}$	$\frac{11}{10}$ $\frac{3}{2}$	
						$\frac{3}{2}$	$\ydiagram{1}$	12	$\frac{11}{10}$	$\frac{13}{15}$ (0.87)	0.92	as above				
						$\frac{5}{2}$	$\ydiagram{1}$	18	$\frac{11}{10}$	$\frac{13}{15}$ (0.87)	0.92					
±3	$\frac{1}{2}$	$\ydiagram{2,1}$	16	$\frac{3}{2}$	±3	$\frac{1}{2}$	$\ydiagram{1,1}$	6	$\frac{7}{6}$	$\frac{14}{15}$ (0.93)	0.98	±3	$\frac{1}{2}$	• $\ydiagram{2,1}$	$\frac{9}{10}$ $\frac{3}{2}$	$\tilde{\Psi}_{\mathrm{sp}}$
													$\frac{3}{2}$	• $\ydiagram{2,1}$	$\frac{9}{10}$ $\frac{3}{2}$	
							$\ydiagram{2}$	12	$\frac{47}{30}$	$\frac{4}{3}$ (1.33)	1.41	±3	$\frac{1}{2}$	$\ydiagram{2,1}$	$\frac{3}{2}$	
													$\frac{3}{2}$	$\ydiagram{2,1}$	$\frac{3}{2}$	
						$\frac{3}{2}$	$\ydiagram{1,1}$	12	$\frac{7}{6}$	$\frac{14}{15}$ (0.93)	0.98	as above				
							$\ydiagram{2}$	24	$\frac{47}{30}$	$\frac{4}{3}$ (1.33)	1.41					
±3	$\frac{3}{2}$	•	4	$\frac{3}{2}$	±3	$\frac{1}{2}$	$\ydiagram{1,1}$	6	$\frac{53}{30}$	$\frac{23}{15}$ (1.53)	1.63	±3	$\frac{1}{2}$	• $\ydiagram{2,1}$	$\frac{3}{2}$ $\frac{21}{10}$	
													$\frac{3}{2}$	• $\ydiagram{2,1}$	$\frac{3}{2}$ $\frac{21}{10}$	
						$\frac{3}{2}$	$\ydiagram{1,1}$	12	$\frac{53}{30}$	$\frac{23}{15}$ (1.53)	1.63	as above				
						$\frac{5}{2}$	$\ydiagram{1,1}$	18	$\frac{53}{30}$	$\frac{23}{15}$ (1.53)	1.63					

$S \otimes S_{\mathrm{imp}} = \sum_{\oplus} S'$, but using the fusion rules of the SU(2) Lie algebra, not the $\mathrm{SU}(2)_3$ KM algebra. Heuristically, the difference—KM versus Lie—between the algebras governing orbital and spin fusion reflects the fact that the bath and impurity are *coupled* in the orbital sector, where the bath "absorbs" the impurity orbital isospin, but *decoupled* in the spin sector, where the impurity spin remains a spectator.

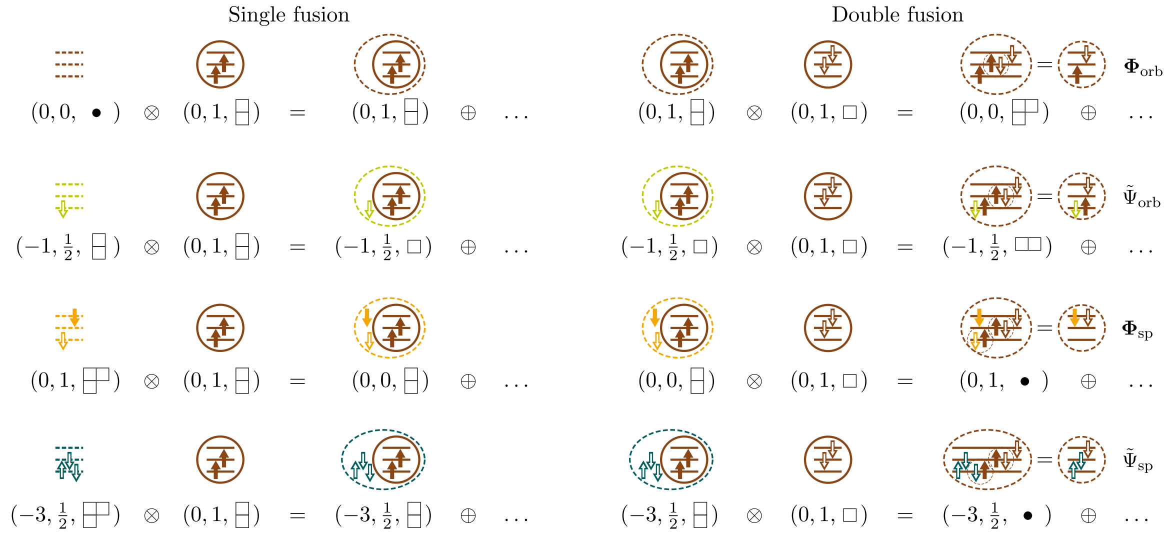

FIG. 3. Schematic depiction of single fusion (left) and double fusion (right), for the four multiplets giving rise to the boundary operators $\mathbf{\Phi}_{\rm orb}$, $\mathbf{\Phi}_{\rm sp}$, $\tilde\Psi_{\rm orb}$, $\tilde\Psi_{\rm sp}$ discussed in Sec. IV (corresponding to rows 1, 3, 4, 5 in Table I). Filled arrows represent electrons, empty arrows represent holes. An electron with spin ↑ and a hole with spin ⇓ (missing electron with spin ↑) can be combined to annihilate each other, as indicated by small dashed circles in the last column. Our illustrations depict the impurity using a fermionic representation, as would be appropriate for the 3oAH model, even though the 3soK impurity has no charge dynamics. In the "single fusion" column, excitations of the free bath are fused with the impurity, $Q_{\rm imp} = (0, 1, \begin{smallmatrix}\square\\\square\end{smallmatrix})$, to obtain the eigenmultiplets of the full system at the NFL fixed point. In the "double fusion" column (right), the single-fusion results are fused with the conjugate impurity representation, $\bar Q_{\rm imp} = (0, 1, \square)$. Each of the resulting multiplets is associated with a boundary operator having the same quantum numbers. Colors relate the multiplets obtained after single fusion to the corresponding lines in Fig. 2.

The fusion of bath and impurity degrees of freedom, called single fusion by AL, is illustrated schematically in the left-hand part of Fig. 3 for four selected multiplets. Table II gives a comprehensive list of low-lying multiplets obtained in this manner. On the left it enumerates the 14 lowest-lying multiplets, (q, S, λ), of the free bath, with dimensions d and energies $E(q, S, \lambda)$. Fusing these with a $Q_{\rm imp} = (0, 1, \begin{smallmatrix}\square\\\square\end{smallmatrix})$ impurity yields the multiplets (q, S', λ') listed in the center. Their energies are given by $E' = E(q, S, \lambda')$, not $E(q, S', \lambda')$, since at the NFL fixed point, where $J_0 = I_0 = 0$, the impurity spin is decoupled from the bath.

The single-fusion excitation energies, $\delta E' = E' - E'_{\rm min}$, relative to the lowest-lying multiplet ($E'_{\rm min} = 7/30$) are in good agreement (deviations $\lesssim 10\%$) with the values, $E_{\rm NRG}$, found by NRG (for $K_0 = 0.3$, $J_0 = I_0 = 0$) for multiplets with corresponding quantum numbers. The agreement improves upon decreasing the NRG discretization parameter Λ (here $\Lambda = 2.5$ was used). This remarkable agreement between CFT predictions and NRG confirms the applicability of the $\mathrm{SU}(2) \otimes \mathrm{SU}(3)_2$ fusion hypothesis proposed above.

(C3) As mentioned in Sec. IV, the fixed point $\mathbf{c}^*_{\rm NFL}$ is characterized by a set of local operators, called boundary operators by AL (since they live at the impurity site, i.e., at the boundary of the two-dimensional space-time on which the CFT is defined). These can be obtained by a second fusion step, called double fusion by AL: the multiplets (q, S', λ') obtained from single fusion are fused with the conjugate impurity representation, $\bar Q_{\rm imp} = (0, 1, \square)$, to obtain another set of multiplets, (q, S'', λ''), listed on the right-hand side of Fig. 3 and Table II. (The *conjugate* impurity representation has to be used for double fusion to ensure that the set of boundary operators contains the identity operator, $\bar\lambda \otimes \lambda = \mathbb{1}$.) Each such multiplet is associated with a boundary operator $\hat O$ with the same quantum numbers and scaling dimension, $\Delta = E'' = E(q, S, \lambda'')$. The operators called $\mathbf{\Phi}_{\rm orb}$ and $\mathbf{\Phi}_{\rm sp}$ are the leading boundary operators (with smallest scaling dimension) in the orbital and spin sectors, respectively. They determine the behavior of the orbital and spin susceptibilities in the NFL regime (see Sec. V C). In the spin-splitting regime, their role is taken by the operators $\tilde\Psi_{\rm orb}$ and $\tilde\Psi_{\rm sp}$, respectively, as discussed in Sec. IV.

C. Scaling behavior of the susceptibilities

In this section, we compute the leading frequency dependence of the dynamical spin and orbital susceptibilities. We begin with the NFL regime, where we directly follow the strategy used by AL in Sec. 3.3 of Ref. [44] and show how it reproduces the results presented in Sec. IV. Thereafter we discuss the SS regime, which has no analog in AL's work, using somewhat more heuristic arguments.

1. NFL regime

At the NFL fixed point, the impurity's orbital isospin $\mathbf{T}$ has been fully absorbed into the bath orbital current $\mathcal{J}_{\mathrm{orb}}$ [cf. Eq. (13)]. From this perspective, the impurity orbital susceptibility $\chi_{\mathrm{orb}}^{\mathrm{imp}}$ is governed by the leading local perturbation of the bulk orbital susceptibility, $\chi_{\mathrm{orb}}^{\mathrm{bulk}} \sim \langle \mathcal{J}_{\mathrm{orb}}^{\mathrm{bulk}} \| \mathcal{J}_{\mathrm{orb}}^{\mathrm{bulk}} \rangle_{\omega}$, where $\mathcal{J}_{\mathrm{orb}}^{\mathrm{bulk}}(t) = \int_{-\infty}^{\infty} \mathrm{d}x \mathcal{J}_{\mathrm{orb}}(t,x) \sim \mathcal{J}_{\mathrm{orb},n=0}$ is the bulk orbital current. The leading local perturbations are those combinations of boundary operators (found via double fusion; see Table II) having the smallest scaling dimensions and the same symmetry as the bare Hamiltonian [43–45].

In the orbital sector, the leading boundary operator is $\mathbf{\Phi}_{\mathrm{orb}}$, with quantum numbers $(0, 0, \yng(2,1))$ and scaling dimension $\Delta_{\mathrm{orb}} = \frac{3}{5}$ (cf. Tables I and II). The orbital current $\mathcal{J}_{\mathrm{orb}}$ has the same quantum numbers. Its first descendant $\mathcal{J}_{\mathrm{orb},-1}$ can be combined with $\mathbf{\Phi}_{\mathrm{orb}}$ to obtain an orbital SU(3) singlet boundary operator, $H'_{\mathrm{orb}} = \mathcal{J}_{\mathrm{orb},-1} \cdot \mathbf{\Phi}_{\mathrm{orb}}$, with scaling dimension $1 + \Delta_{\mathrm{orb}} = 1 + \frac{3}{5}$. This is the leading irrelevant (dimension > 1) boundary perturbation to the fixed-point Hamiltonian in the orbital sector. Its contribution to the impurity orbital susceptibility, $\chi_{\mathrm{orb}}^{\mathrm{imp}} \sim \chi_{\mathrm{orb}}^{\mathrm{bulk}}$, evaluated perturbatively to second order, is

$$\begin{aligned}\chi_{\mathrm{orb}}^{\mathrm{imp}}(\omega) \sim & \int_{-\infty}^{\infty} dt_1 \int_{-\infty}^{\infty} dt_2 \int_{-\infty}^{\infty} dt_3 e^{i\omega t_1} \\ & \times \langle \mathcal{J}_{\mathrm{orb}}^{\mathrm{bulk}}(t_1) \cdot \mathcal{J}_{\mathrm{orb}}^{\mathrm{bulk}}(0) H'_{\mathrm{orb}}(t_2) H'_{\mathrm{orb}}(t_3) \rangle \\ & \sim \omega^{2\Delta_{\mathrm{orb}}-1} = \omega^{1/5}. \end{aligned} \tag{14}$$

The last line follows by power counting ($\mathcal{J}_{\mathrm{orb}}^{\mathrm{bulk}}$ has dimension 0, each time integral dimension -1).

The local bath site coupled to the impurity will show the same behavior, $\chi_{\mathrm{orb}}^{\mathrm{bath}} \sim \omega^{1/5}$, since the orbital exchange interaction strongly couples its orbital isospin $\mathbf{J}_{\mathrm{orb}}$ to $\mathbf{T}$—indeed, $\mathcal{J}_{\mathrm{orb}}$ is constructed from a linear combination of both these operators [cf. Eq. (13)].

The above results can be obtained in a more direct way by positing that at the NFL fixed point, orbital screening causes both $\mathbf{T}$ and $\mathbf{J}_{\mathrm{orb}}$ to be renormalized into the same boundary operator $\mathbf{\Phi}_{\mathrm{orb}}$. We then obtain

$$\chi_{\mathrm{orb}}^{\mathrm{imp}}(\omega) \sim \chi_{\mathrm{orb}}^{\mathrm{bath}}(\omega) \sim \langle \mathbf{\Phi}_{\mathrm{orb}} \| \mathbf{\Phi}_{\mathrm{orb}} \rangle_{\omega} \sim \omega^{2\Delta_{\mathrm{orb}}-1}, \tag{15}$$

reproducing Eq. (14). This is the argument presented in Sec. IV.

We next turn to the spin sector. Exactly *at* the NFL fixed point, where $J_0 = I_0 = 0$, the impurity spin $\mathbf{S}$ is decoupled from the bath. *At* $\mathbf{c}_{\mathrm{NFL}}^{*}$ it hence has no dynamics, scaling dimension 0, and a trivial spin susceptibility, $\chi_{\mathrm{sp}}^{\mathrm{imp}}(\omega) \sim \delta(\omega)$. By contrast, $\chi_{\mathrm{sp}}^{\mathrm{bath}}$, the susceptibility of $\mathbf{J}_{\mathrm{sp}}$, the local bath spin coupled to the impurity, does show nontrivial dynamics at the fixed point. The reason is that some of the boundary operators induced by orbital screening actually live in the spin sector (a highly nontrivial consequence of non-Abelian bosonization and orbital fusion). The leading boundary operator in the spin sector is $\mathbf{\Phi}_{\mathrm{sp}}$, with quantum numbers $(0, 1, \bullet)$ and scaling dimension $\Delta_{\mathrm{sp}} = \frac{2}{5}$ (cf. Tables I and II). It can be combined with the first descendant of the (bare, unshifted) spin current to obtain a spin SU(2) singlet boundary operator, $H'_{\mathrm{sp}} = \mathbf{J}_{\mathrm{sp},-1} \cdot \mathbf{\Phi}_{\mathrm{sp}}$, with scaling dimension $1 + \Delta_{\mathrm{sp}} = 1 + \frac{2}{5}$. This is the leading irrelevant boundary perturbation to the fixed-point Hamiltonian in the spin sector. Its contribution to the local bath spin susceptibility, $\chi_{\mathrm{sp}}^{\mathrm{bath}} \sim \chi_{\mathrm{sp}}^{\mathrm{bulk}}$, evaluated to second order, is

$$\begin{aligned}\chi_{\mathrm{sp}}^{\mathrm{bath}}(\omega) \sim & \int_{-\infty}^{\infty} dt_1 \int_{-\infty}^{\infty} dt_2 \int_{-\infty}^{\infty} dt_3 e^{i\omega t_1} \\ & \times \langle \mathbf{J}_{\mathrm{sp}}^{\mathrm{bulk}}(t_1) \cdot \mathbf{J}_{\mathrm{sp}}^{\mathrm{bulk}}(0) H'_{\mathrm{sp}}(t_2) H'_{\mathrm{sp}}(t_3) \rangle \\ & \sim \omega^{2\Delta_{\mathrm{sp}}-1} = \omega^{-1/5}. \end{aligned} \tag{16}$$

This result, too, can be obtained more directly, by positing that $\mathbf{J}_{\mathrm{sp}}$ is renormalized to $\mathbf{\Phi}_{\mathrm{sp}}$, with

$$\chi_{\mathrm{sp}}^{\mathrm{bath}}(\omega) \sim \langle \mathbf{\Phi}_{\mathrm{sp}} \| \mathbf{\Phi}_{\mathrm{sp}} \rangle_{\omega} \sim \omega^{2\Delta_{\mathrm{sp}}-1}, \tag{17}$$

as argued in Sec. IV.

If the system is tuned very slightly away from the NFL fixed point, $J_0 \ll 1$, $I_0 = 0$, the impurity spin does acquire nontrivial dynamics, due to the action of the spin exchange interaction, $J_0 \mathbf{S} \cdot \mathbf{J}_{\mathrm{sp}}$. According to the above argument, orbital screening renormalizes it to $J_0 \mathbf{S} \cdot \mathbf{\Phi}_{\mathrm{sp}}$. Its second-order contribution to the impurity spin susceptibility is

$$\begin{aligned}\chi_{\mathrm{sp}}^{\mathrm{imp}}(\omega) \sim & \int_{-\infty}^{\infty} dt_1 \int_{-\infty}^{\infty} dt_2 \int_{-\infty}^{\infty} dt_3 e^{i\omega t_1} \\ & \times \langle \mathbf{S}(t_1) \cdot \mathbf{S}(0) (\mathbf{S} \cdot \mathbf{\Phi}_{\mathrm{sp}})(t_2) (\mathbf{S} \cdot \mathbf{\Phi}_{\mathrm{sp}})(t_3) \rangle \\ & \sim \omega^{2\Delta_{\mathrm{sp}}-3} = \omega^{-11/5}. \end{aligned} \tag{18}$$

The occurrence of such a large, negative exponent for the spin susceptibility is very unusual. It reflects the fact that near (but not at) the NFL fixed point the impurity spin is almost (but not fully) decoupled from the bath, and hence able to "sense" that orbital screening modifies the bath spin current in a nontrivial manner.

2. Spin-slitting regime

The renormalized exchange interaction $J_0 \mathbf{S} \cdot \mathbf{\Phi}_{\mathrm{sp}}$ is a relevant perturbation, with scaling dimension $\frac{2}{5} < 1$. It grows under the RG flow, eventually driving the system away from the NFL fixed point and into a crossover regime, $T_{\mathrm{sp}} < \omega < T_{\mathrm{ss}}$, called the spin-splitting regime in Sec. III. In the NRG flow diagram of Fig. 2(a), this regime is characterized by level crossings, extending over several

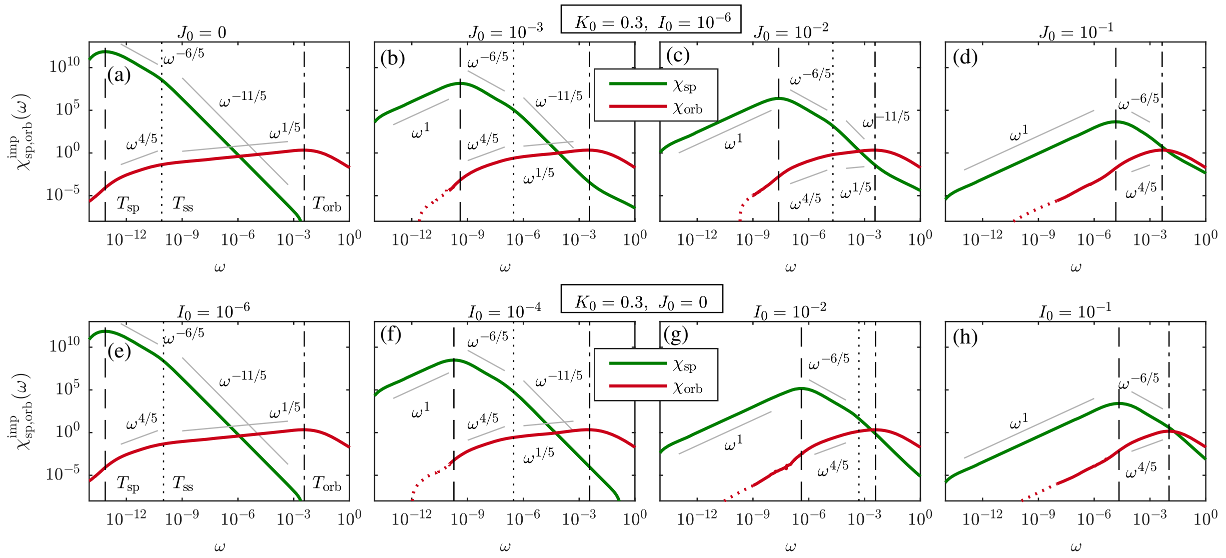

FIG. 4. Imaginary part of the zero-temperature impurity spin and orbital susceptibilities for the 3soK model. We keep $K_0 = 0.3$ fixed throughout, and (a)–(d) vary J_0 at fixed $I_0 = 10^{-6}$, or (e)–(h) vary I_0 at fixed $J_0 = 0$. (a)–(d) As J_0 is increased from 0 (left) to 10^{-1} (right), the width of the NFL regime $[T_{\rm ss}, T_{\rm orb}]$ shrinks, while that of the SS regime $[T_{\rm sp}, T_{\rm ss}]$ remains constant. (e)–(h) We find the same behavior when increasing I_0 with K_0 and J_0 kept fixed.

orders of magnitude in energy, rather than a stationary level structure. Hence the SS regime cannot be characterized by proximity to some well-defined fixed point. (A stationary level structure, characteristic of a FL fixed point, emerges only after another crossover, setting in at the scale $T_{\rm sp}$.) Nevertheless, Figs. 2(c) and 2(d) show that the local orbital and spin susceptibilities *do* exhibit well-defined power-law behavior in the SS regime:

$$\chi_{\rm orb}^{\rm imp,bath}(\omega) \sim \omega^{4/5}, \qquad \chi_{\rm sp}^{\rm imp,bath}(\omega) \sim \omega^{-6/5}. \tag{19}$$

We define the width of the SS regime as the energy range showing this behavior. It extends over about 3 orders of magnitude, independent of J_0 and I_0—increasing either of these couplings rigidly shifts the SS regime to larger energies without changing its width (see Fig. 4); i.e., the ratio $T_{\rm sp}/T_{\rm ss}$ is independent of these couplings.

The latter fact leads us to conjecture that the NFL fixed point does, after all, govern the SS regime too, though “from afar” rather than from up close. In technical terms, we conjecture that the leading behavior in the SS regime is governed by two different boundary operators, $\tilde{\mathbf{\Psi}}_{\rm orb}$ and $\tilde{\mathbf{\Psi}}_{\rm sp}$, with scaling dimensions $\tilde\Delta_{\rm orb} = \tilde\Delta_{\rm sp} = \frac{9}{10}$ (cf. Tables I and II) instead of the boundary operators $\mathbf{\Phi}_{\rm orb}$ and $\mathbf{\Phi}_{\rm sp}$ governing the NFL regime. This conjecture is encoded in the equation above Eq. (10). It states that $\mathbf{J}_{\rm orb}$ and $\mathbf{T}$ are both renormalized to $\tilde{\mathbf{\Psi}}_{\rm orb}$, causing $\chi_{\rm orb}^{\rm bath}$ and $\chi_{\rm orb}^{\rm imp}$ to scale with the same power,

$$\chi_{\rm orb}^{\rm bath,imp} \sim \langle \tilde{\mathbf{\Psi}}_{\rm orb} \| \tilde{\mathbf{\Psi}}_{\rm orb} \rangle_\omega \sim \omega^{2\tilde\Delta_{\rm orb}-1} = \omega^{4/5}, \tag{20}$$

and that $\mathbf{J}_{\rm sp}$ and $\mathbf{S}$ are both renormalized to $\mathbf{S} + \tilde{\mathbf{\Psi}}_{\rm sp}$, causing $\chi_{\rm sp}^{\rm bath}$ and $\chi_{\rm sp}^{\rm imp}$ to scale with the same power,

$$\chi_{\rm sp}^{\rm bath,imp} \sim \langle \tilde{\mathbf{\Psi}}_{\rm sp} \| \tilde{\mathbf{\Psi}}_{\rm sp} \rangle_\omega \sim \omega^{2\tilde\Delta_{\rm sp}-3} = \omega^{-6/5}. \tag{21}$$

The latter result is obtained in a manner analogous to Eq. (18), with $\mathbf{S} \cdot \mathbf{\Phi}$ replaced by $\mathbf{S}\tilde{\mathbf{\Psi}}_{\rm sp}$ [60].

D. Impurity spectral function

We next consider the leading frequency dependence of the impurity spectral function in the NFL regime. For a Kondo-type impurity, this function is given by $-(1/\pi){\rm Im}\mathcal{T}(\omega)$, where $\mathcal{T}(\omega) = \langle O_{m\sigma} \| O^\dagger_{m\sigma} \rangle_\omega$ is the impurity $\mathcal{T}$ matrix, with $O_{m\sigma} = [\psi_{m\sigma}, H_{\rm int}]$ [63].

As discussed in Sec. V C 1, the leading irrelevant boundary operators in the NFL regime are $H'_{\rm orb} = \mathcal{J}_{{\rm orb},-1} \cdot \mathbf{\Phi}_{\rm orb}$ and $H'_{\rm sp} = \mathbf{J}_{{\rm sp},-1} \cdot \mathbf{\Phi}_{\rm sp}$, with scaling dimensions $1 + \Delta_{\rm orb} = 1 + \frac{3}{5}$ and $1 + \Delta_{\rm sp} = 1 + \frac{2}{5}$, respectively. AL have shown that a boundary perturbation of this type, with dimension $1 + \Delta$, causes the $\mathcal{T}$ matrix to acquire a leading frequency dependence of ${\rm Im}\mathcal{T} \sim |\omega|^\Delta$ [45].

For $\omega > 0$, our NRG results are consistent with ${\rm Im}\mathcal{T} \sim \omega^{3/5}$ (cf. Fig. 5). This suggests that the prefactor of $H'_{\rm orb}$ is much larger than that of $H'_{\rm sp}$, presumably because the computation was done for $J_0 = I_0 = 0$. For $\omega < 0$, by contrast, our numerical results do not exhibit clear power-law

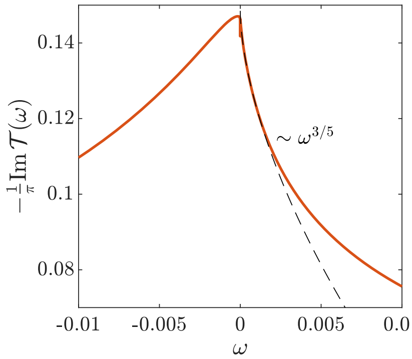

FIG. 5. Impurity spectral function, computed by FDM NRG [52], for $(J_0, K_0, I_0) = (0, 0.3, 0)$. For $\omega > 0$, the $\omega^{3/5}$ behavior is consistent with a boundary perturbation given by H'_{orb}. For $\omega < 0$, clear power law cannot be determined.

behavior for small $|\omega|$, implying that $\mathrm{Im}\mathcal{T}$ does not have particle-hole symmetry. This is not surprising: the 3soK model itself breaks particle-hole symmetry, since under a particle-hole transformation, the impurity's orbital multiplet $\begin{smallmatrix}\square\\\square\end{smallmatrix}$ is mapped to □. We suspect that the prefactor of the $|\omega|^{\Delta_{\mathrm{orb}}}$ contribution to $\mathrm{Im}\mathcal{T}$ vanishes for $\omega < 0$ for the impurity orbital representation $\begin{smallmatrix}\square\\\square\end{smallmatrix}$, such that only subleading boundary operators, with dimensions $\Delta \geq 9/10$ (cf. Table II), determine the small-ω scaling behavior. However, a detailed understanding of this matter is still lacking.

E. Fermi-liquid fixed point

In this section we show how the FL spectrum at the fixed point $\mathbf{c}^*_{\mathrm{FL}}$ can be derived analytically. This can be done in two complementary ways. The first uses $\mathrm{SU}(2)_3$ fusion in the spin sector, the second $\mathrm{SU}(6)_1$ fusion in the flavor (combined spin + orbital) sector.

1. Fermi-liquid spectrum via $\mathbf{SU(2)_3}$ *fusion*

It is natural to ask whether the FL spectrum at $\mathbf{c}^*_{\mathrm{FL}}$ can be derived from the NFL spectrum of $\mathbf{c}^*_{\mathrm{NFL}}$ via some type of fusion in the spin sector, reflecting spin screening induced by the spin exchange interaction. For example, we have tried the following simple strategy ("naive spin fusion"): when setting up the fusion table (Table II), the bath and impurity spin degrees of freedom are combined, $S \otimes S_{\mathrm{imp}} = \sum_{\oplus} S'$, using the fusion rules of the $\mathrm{SU}(2)_3$ KM algebra (Table S3 in the SM [54]) instead of the SU(2) Lie algebra, and the orbital degrees of freedom, $\lambda \otimes \lambda_{\mathrm{imp}} = \sum_{\oplus} \lambda'$, using $\mathrm{SU}(3)_2$ KM fusion rules (as before; see Table S2 in the SM [54]). Moreover, the energies of the resulting multiplets are computed as $E(q, S', \lambda')$, not $E(q, S, \lambda')$. However, this naive spin fusion strategy completely fails to reproduce the FL fixed point spectrum obtained by NRG, yielding completely different excitation energies and degeneracies.

We suspect that this failure is due to the fact that the RG flow does not directly pass from the NFL regime into the FL regime, but first traverses the intermediate SS regime.

TABLE III. Fusion table for spin screening at the FL fixed point $\mathbf{c}^*_{\mathrm{FL}}$ of the 3soK model. It has the same structure as Table II, but here single fusion of bath and impurity multiplets in the charge and spin sectors is performed using $\mathrm{U}(1) \times \mathrm{SU}(2)_3$ fusion rules (listed in Table S3 of the SM [54]). Moreover, we choose $Q_{\mathrm{imp}} = (1, \frac{3}{2}, \bullet)$ for the impurity, representing the effective local degree of freedom obtained after the completion of orbital screening. The resulting multiplets (q', S', λ) have eigenenergies $E' = E(q', S', \lambda)$ and excitation energies $\delta E' = E' - E'_{\mathrm{min}}$. The NRG energies, computed for $(J_0, K_0, I_0) = (10^{-4}, 0.3, 0)$, have been shifted and rescaled such that the lowest energy is zero and the second-lowest values for E_{NRG} and $\delta E'$ match. The single-fusion and NRG spectra agree very well (deviations $\lesssim$2%).

Free fermions					Single fusion, with $Q_{\mathrm{imp}} = (1, \frac{3}{2}, \bullet)$						NRG	Double fusion, with $\bar{Q}_{\mathrm{imp}} = (-1, \frac{3}{2}, \bullet)$			
q	S	λ	d	E	q'	S'	λ'	d	E'	$\delta E'$	E_{NRG}	q''	S''	λ''	Δ
0	0	•	1	0	+1	$\frac{3}{2}$	•	4	$\frac{5}{6}$	$\frac{1}{2}$	0.50	0	0	•	0
+1	$\frac{1}{2}$	□	6	$\frac{1}{2}$	+2	1	□	9	1	$\frac{2}{3}$	0.67	+1	$\frac{1}{2}$	□	$\frac{1}{2}$
−1	$\frac{1}{2}$	$\begin{smallmatrix}\square\\\square\end{smallmatrix}$	6	$\frac{1}{2}$	0	1	$\begin{smallmatrix}\square\\\square\end{smallmatrix}$	9	$\frac{2}{3}$	$\frac{1}{3}$	0.33	−1	$\frac{1}{2}$	$\begin{smallmatrix}\square\\\square\end{smallmatrix}$	$\frac{1}{2}$
0	1	$\begin{smallmatrix}\square&\square\\\square&\end{smallmatrix}$	24	1	+1	$\frac{1}{2}$	$\begin{smallmatrix}\square&\square\\\square&\end{smallmatrix}$	16	$\frac{5}{6}$	$\frac{1}{2}$	0.50	0	1	$\begin{smallmatrix}\square&\square\\\square&\end{smallmatrix}$	1
+2	0	□□	6	1	+3	$\frac{3}{2}$	□□	24	$\frac{13}{6}$	$\frac{11}{6}$	1.87	+2	0	□□	1
−2	0	$\begin{smallmatrix}\square&\square\\\square&\square\end{smallmatrix}$	6	1	−1	$\frac{3}{2}$	$\begin{smallmatrix}\square&\square\\\square&\square\end{smallmatrix}$	24	$\frac{3}{2}$	$\frac{7}{6}$	1.16	−2	0	$\begin{smallmatrix}\square&\square\\\square&\square\end{smallmatrix}$	1
+2	1	$\begin{smallmatrix}\square\\\square\end{smallmatrix}$	9	1	+3	$\frac{1}{2}$	$\begin{smallmatrix}\square\\\square\end{smallmatrix}$	6	$\frac{7}{6}$	$\frac{5}{6}$	0.84	+2	1	$\begin{smallmatrix}\square\\\square\end{smallmatrix}$	1
−2	1	□	9	1	−1	$\frac{1}{2}$	□	6	$\frac{1}{2}$	$\frac{1}{6}$	0.17	−2	1	□	1
+1	$\frac{3}{2}$	$\begin{smallmatrix}\square&\square\\\square&\square\end{smallmatrix}$	24	$\frac{3}{2}$	+2	0	$\begin{smallmatrix}\square&\square\\\square&\square\end{smallmatrix}$	6	1	$\frac{2}{3}$	0.68	+1	$\frac{3}{2}$	$\begin{smallmatrix}\square&\square\\\square&\square\end{smallmatrix}$	$\frac{3}{2}$
−1	$\frac{3}{2}$	□□	24	$\frac{3}{2}$	0	0	□□	6	$\frac{2}{3}$	$\frac{1}{3}$	0.34	−1	$\frac{3}{2}$	□□	$\frac{3}{2}$
±3	$\frac{1}{2}$	$\begin{smallmatrix}\square&\square\\\square&\end{smallmatrix}$	16	$\frac{3}{2}$	−2	1	$\begin{smallmatrix}\square&\square\\\square&\end{smallmatrix}$	24	$\frac{4}{3}$	1	0.99	−3	$\frac{1}{2}$	$\begin{smallmatrix}\square&\square\\\square&\end{smallmatrix}$	$\frac{3}{2}$
±3	$\frac{3}{2}$	•	4	$\frac{3}{2}$	−2	0	•	1	$\frac{1}{3}$	0	0.00	−3	$\frac{3}{2}$	•	$\frac{3}{2}$

In the latter, the degeneracy between the two degenerate ground state multiplets of the NFL regime, $(1, \frac{1}{2}, \bullet)$ and $(1, \frac{3}{2}, \bullet)$, is lifted, in a manner that seems to elude a simple description via a modified spin fusion rule.

Instead, the FL spectrum can be obtained via the following arguments. The ground state multiplet of the SS regime, $(1, \frac{3}{2}, \bullet)$, describes an effective local degree of freedom coupled to a bath in such a manner that one bath electron fully screens the impurity orbital isospin, while their spins add to a total spin of $\frac{1}{2} + 1 = \frac{3}{2}$ [see Fig. 2(b)]. Let us view this as an effective impurity with $Q_{\mathrm{imp}} = (1, \frac{3}{2}, \bullet)$. If we combine its charge and spin degrees of freedom with those of a *free* bath, using $q + q_{\mathrm{imp}} = q'$ and $S \oplus S_{\mathrm{imp}} = \sum_{\oplus} S'$, fused according to the $\mathrm{SU}(2)_3$ KM algebra, the resulting single-fusion spectrum fully reproduces the FL spectrum found by NRG, as shown in Table III.

2. *Fermi-liquid spectrum via* $\mathbf{SU(6)_1}$ *fusion*

The FL ground state of the 3soK model is a fully screened spin and orbital singlet. It is therefore natural to expect that the FL spectrum has a higher symmetry, namely that of the group $\mathrm{U}(1) \times \mathrm{SU}(6)$, which treats spin and orbital excitations on an equal footing.

This is indeed the case: we now show that the FL spectrum of the 3soK model discussed above matches that of an SU(6) Kondo model which does not distinguish between spin and orbital degrees of freedom. We consider a bath with six flavors of electrons, $H_{\mathrm{bath}} = \sum_p \sum_{\nu=1}^{6} \varepsilon_p \psi^{\dagger}_{p\nu} \psi_{p\nu}$ and an impurity-bath coupling of the form $J_U \mathbf{U} \cdot \mathbf{J}_{\mathrm{fl}}$. Here $\mathbf{J}_{\mathrm{fl}}$ is the flavor density at the impurity site, with $J^a_{\mathrm{fl}} = \psi^{\dagger}_{\nu} \frac{1}{2} \lambda^a_{\nu\nu'} \psi_{\nu'}$, where λ^a are SU(6) matrices in the fundamental representation, and $\mathbf{U}$ describes the impurity's SU(6) flavor isospin, chosen in the fully antisymmetric representation $\begin{smallmatrix}\square\\\square\end{smallmatrix}$. The latter has dimension 15, representing the $\binom{6}{2}$ ways of placing two identical particles into six available states.

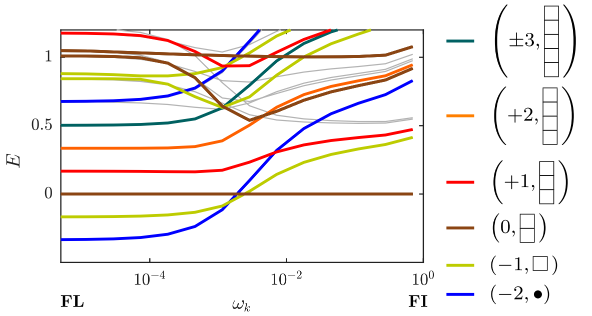

FIG. 6. NRG results for the SU(6) Kondo model with $J_U = 0.1$, shown using $\mathcal{E}_{\mathrm{ref}} = \mathcal{E}(0, \begin{smallmatrix}\square\\\square\end{smallmatrix})$ as reference energy. The computation was performed using QSpace [50] to exploit the model's full $\mathrm{U}(1) \times \mathrm{SU}(6)$ symmetry. (NRG parameters: $\Lambda = 2.5$, $N_{\mathrm{keep}} = 2000$, $D = 1$.)

Figure 6 shows the NRG finite-size eigenlevel flow for this model. It exhibits a single crossover from a free-impurity fixed point, with ground state multiplet $(q, \lambda) = (0, \begin{smallmatrix}\square\\\square\end{smallmatrix})$, to a FL fixed point, whose ground state multiplet $(-2, \bullet)$ involves complete screening of the impurity's flavor isospin degree of freedom.

This crossover can be described analytically by using non-Abelian bosonization followed by flavor fusion. We begin by using non-Abelian bosonization with the $\mathrm{U}(1) \times \mathrm{SU}(6)_1$ KM current algebra to express the bath excitation spectrum in the form

$$E(q, \lambda) = \frac{1}{12} q^2 + \frac{1}{7} \kappa_6(\lambda) + \ell, \tag{22a}$$

$$\begin{aligned} \kappa_6(\lambda) = {} & \frac{1}{12}(5\lambda_1^2 + 8\lambda_2^2 + 9\lambda_3^2 + 8\lambda_4^2 + 5\lambda_5^2) \\ & + \frac{1}{2}(5\lambda_1 + 8\lambda_2 + 9\lambda_3 + 8\lambda_4 + 5\lambda_5) \\ & + \frac{1}{6}(6\lambda_2\lambda_3 + 6\lambda_3\lambda_4 + 4\lambda_1\lambda_2 + 4\lambda_2\lambda_4 + 4\lambda_4\lambda_5 \\ & + 3\lambda_1\lambda_3 + 3\lambda_3\lambda_5 + 2\lambda_1\lambda_4 + 2\lambda_2\lambda_5 + \lambda_1\lambda_5), \end{aligned} \tag{22b}$$

with $\ell \in \mathbb{Z}$, where $\kappa_6(\lambda)$ is the quadratic Casimir for the representation $\lambda = (\lambda_1, \lambda_2, \lambda_3, \lambda_4, \lambda_5)$ of the SU(6) Lie algebra [62]. [The contributions from the two terms of Eq. (22a) are listed in Table S4 in the SM [54] for all q and λ values needed in Table IV.] The few lowest-lying (q, λ)

TABLE IV. Fusion table for flavor screening at the FL fixed point of the SU(6) Kondo model. The table has the same structure as the left and center parts of Table II, but here the free bath excitations are labeled (q, λ), their energies are computed using Eqs. (22) and Table S4 of the SM [54], and flavor fusion with $Q_{\mathrm{imp}} = (0, \begin{smallmatrix}\square\\\square\end{smallmatrix})$ is performed using $\mathrm{SU}(6)_1$ fusion rules (listed in Table S5 of the SM [54]). The resulting multiplets (q, λ') have eigenenergies $E' = E(q, \lambda')$, degeneracies d', and excitation energies $\delta E' = E' - E'_{\mathrm{min}}$. The FL spectrum, obtained by $\mathrm{U}(1) \times \mathrm{SU}(6)$ NRG calculations (Fig. 6) for $J_U = 0.1$, is shown on the right. It has been shifted and rescaled such that the lowest energy is zero and the second-lowest values for E_{NRG} and $\delta E'$ match. The single-fusion and NRG spectra agree very well (deviations $\lesssim 1\%$).

Free fermions				Single fusion, $Q_{\mathrm{imp}} = (0, \begin{smallmatrix}\square\\\square\end{smallmatrix})$					NRG
q	λ	d	E	q	λ'	d'	E'	$\delta E'$	E_{NRG}
0	$\bullet$	1	0	0	$\begin{smallmatrix}\square\\\square\end{smallmatrix}$	15	$\frac{2}{3}$	$\frac{1}{3}$	0.33
+1	$\square$	6	$\frac{1}{2}$	+1	$\begin{smallmatrix}\square\\\square\\\square\end{smallmatrix}$	20	$\frac{5}{6}$	$\frac{1}{2}$	0.50
−1	$\begin{smallmatrix}\square\\\square\\\square\\\square\\\square\end{smallmatrix}$	6	$\frac{1}{2}$	−1	$\square$	6	$\frac{1}{2}$	$\frac{1}{6}$	0.17
+2	$\begin{smallmatrix}\square\\\square\end{smallmatrix}$	15	1	+2	$\begin{smallmatrix}\square\\\square\\\square\\\square\end{smallmatrix}$	15	1	$\frac{2}{3}$	0.67
−2	$\begin{smallmatrix}\square\\\square\\\square\\\square\end{smallmatrix}$	15	1	−2	$\bullet$	1	$\frac{1}{3}$	0	0
±3	$\begin{smallmatrix}\square\\\square\\\square\end{smallmatrix}$	20	$\frac{3}{2}$	±3	$\begin{smallmatrix}\square\\\square\\\square\\\square\\\square\end{smallmatrix}$	6	$\frac{7}{6}$	$\frac{5}{6}$	0.84

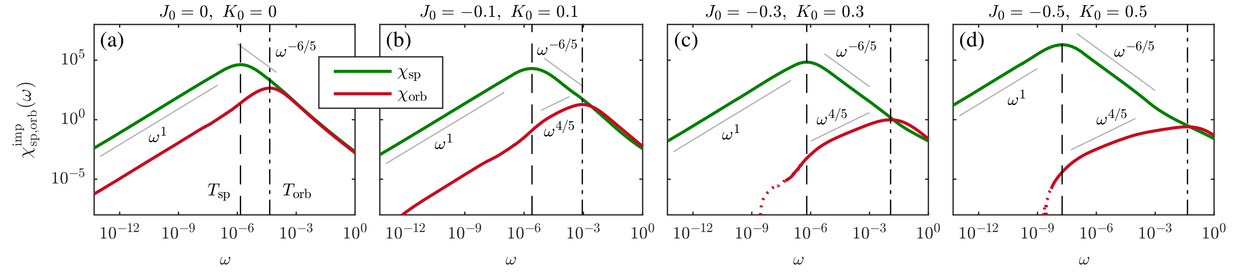

FIG. 7. Imaginary part of the impurity spin and orbital susceptibilities for the Anderson-Kondo model, with $U = 5$, $J_H = 1$, $\Gamma = 0.1$, $I_0 = 0$, and J_0, K_0 varying from (a) $J_0 = K_0 = 0$ (pure Anderson-Hund model) to (d) $-J_0 = K_0 = 0.5$. The energy scales for spin and orbital screening, T_{sp} and T_{orb}, are pushed apart with increasing $-J_0 = K_0$.

multiplets of the free bath, having $E(q,\lambda) \in \frac{1}{2}\mathbb{Z}$, are listed on the left-hand side of Table IV. The strong-coupling FL spectrum can be obtained by combining the bath and impurity flavor degrees of freedom, $\lambda \otimes \lambda_{\mathrm{imp}} = \sum_{\oplus} \lambda'$, using the fusion rules of the $\mathrm{SU}(6)_1$ KM algebra (see Table S5 in the SM [54]). The resulting multiplets (q, λ') are listed in the center of Table IV. Their eigenenergies fully match those from NRG.

VI. THREE-ORBITAL ANDERSON-KONDO MODEL

The 3soK model, which we study in detail above, is derived from the more realistic 3oAH model by a Schrieffer-Wolff transformation. In the following, we explore another route for smoothly connecting the physics of the two models, namely starting from the 3oAH model and then additionally turning on the spin and orbital exchange couplings of the 3soK model.

The Hamiltonian of the 3oAH model [22] has the following form: $H_{\mathrm{bath}} + H_{\mathrm{hyb}} + H_{\mathrm{3oAH}}$,

$$H_{\mathrm{3oAH}} = \frac{3}{4} J_H N_{\mathrm{imp}} + \frac{1}{2}\left(U - \frac{1}{2} J_H\right) N_{\mathrm{imp}}(N_{\mathrm{imp}} - 1) - J_H \mathbf{S}^2,$$
$$H_{\mathrm{hyb}} = \sum_{pm\sigma} V_p (f^\dagger_{m\sigma} \psi_{pm\sigma} + \mathrm{H.c.}),$$

with the impurity occupation $N_{\mathrm{imp}} = \sum_{m\sigma} f^\dagger_{m\sigma} f_{m\sigma}$, where $f^\dagger_{m\sigma}$ creates an impurity electron with spin σ in orbital m. A hybridization function, $\Gamma(\varepsilon) = \pi \sum_p |V_p|^2 \delta(\varepsilon - \varepsilon_p) \equiv \Gamma\Theta(D - |\varepsilon|)$, controls the hopping between the impurity and the bath. U is the local Coulomb interaction and J_H the Hund's coupling, favoring a large spin. To this Hamiltonian we add $J_0 \mathbf{S} \cdot \mathbf{J}_{\mathrm{sp}} + K_0 \mathbf{T} \cdot \mathbf{J}_{\mathrm{orb}}$, the Kondo-type spin and orbital exchange couplings between impurity and bath from Eq. (1), with $S^\alpha = f^\dagger_{m\sigma} \frac{1}{2} \sigma^\alpha_{\sigma\sigma'} f_{m\sigma'}$, $T^a = f^\dagger_{m\sigma} \frac{1}{2} \tau^a_{mm'} f_{m'\sigma}$. We treat J_0 and K_0 as free parameters and use them to "deform" the 3oAH model in a way that widens the SOS regime between T_{sp} and T_{orb}.

Figures 7(a)–7(d) show how the spin and orbital susceptibilities change upon increasing $|J_0|$ and $|K_0|$, with $J_0 < 0$ and $K_0 > 0$. A pure 3oAH model, with $(J_0, K_0) = (0, 0)$, clearly shows spin-orbital separation, but T_{sp} and T_{orb} differ by less than two decades [Fig. 7(a); see also Ref. [22]]. Though the SOS window is too small to reveal a true power law for $\chi^{\mathrm{imp}}_{\mathrm{sp}}$, the hints of $\omega^{-6/5}$ behavior are already discernable. Turning on the additional exchange coupling terms, with $J_0 < 0$ and $K_0 > 0$, causes T_{sp} to decrease and T_{orb} to increase, respectively, widening the SOS regime [Figs. 7(b)–7(d)]. For $(J_0, K_0) = (-0.5, 0.5)$ it spans more than 6 orders of magnitude, so that clear power laws, $\chi^{\mathrm{imp}}_{\mathrm{sp}} \sim \omega^{-6/5}$ and $\chi^{\mathrm{imp}}_{\mathrm{orb}} \sim \omega^{4/5}$, become accessible [Fig. 7(d)]. These power laws are consistent with our findings for the spin-splitting regime in Secs. III and V. This scenario is evidently smoothly connected to that of the pure 3soK model [Fig. 2(c)]. There the absence of charge fluctuations makes it possible to fully turn off the I_0 contribution implicitly present in the 3oAH model, thereby widening the SOS regime even further and allowing the true NFL regime to be analyzed in detail.

VII. CONCLUSION

While the main aim of this work was to understand NFL behavior in Hund metals, it has much wider implications, as already indicated in Sec. I. Let us assess these from several perspectives of increasing generality.

(i) We have used NRG and CFT to elucidate the NFL regime of a 3soK model, fine-tuned such that spin screening sets in at very much lower energies than orbital screening. We were able to analytically compute the scaling behavior of dynamical spin and orbital susceptibilities, finding $\chi^{\mathrm{imp}}_{\mathrm{orb}} \sim \omega^{1/5}$, $\chi^{\mathrm{imp}}_{\mathrm{sp}} \sim \omega^{-11/5}$ in the NFL regime and $\chi^{\mathrm{imp}}_{\mathrm{sp}} \sim \omega^{-6/5}$ in the spin-splitting regime. The main significance of these findings lies in the qualitative physical behavior which they imply. An orbital susceptibility decreasing with an exponent < 1, rather than the Fermi-liquid exponent 1, indicates that the orbital degrees of freedom, though screened, are still affected by the unscreened spin degrees of freedom. A spin susceptibility diverging as $\omega^{-\gamma}$, with $\gamma > 1$, indicates anomalously strong spin fluctuations. This seems to be a characteristic property of the incoherent regime of Hund metals. As pointed out in Sec. I, anomalously strong spin fluctuations have direct consequences for theories of the superconducting state of the iron pnictides [14].

(ii) We have uncovered the origin of hints of NFL behavior found previously for a 3oAH model and related models [1,3–5,8,22–24]. There the spin-orbital coupling I_0 is always nonzero, preventing RG trajectories from closely approaching the NFL fixed point. Nevertheless, even if they pass this fixed point "at a distance," it still leaves traces of NFL behavior for various observables, such as $\chi_{\mathrm{sp}}^{\mathrm{imp}} \sim \omega^{-6/5}$ behavior for the imaginary part of the impurity's dynamical spin susceptibility. We showed in Sec. VI how NFL behavior emerges if the 3oAH model is "deformed" by additionally turning on the spin and orbital exchange couplings of the 3soK model, thereby adiabatically connecting the SS regime of the 3soK model to the incoherent regime of the 3oAH model. Furthermore, it has been shown in Ref. [22] that DMFT self-consistency does not significantly influence the behavior of the susceptibilities in the 3oAH model. Thus our conclusions, in particular regarding the prevalence of strong spin fluctuations in the SOS regime, should also apply to DMFT calculations. Indeed, DMFT studies [22,47] of a self-consistent 3oAH model contain results for $\chi_{\mathrm{sp}}^{\mathrm{imp}}$ which, in the SOS window, are consistent with the $\omega^{-6/5}$ scaling found and explained here for the SS regime.

(iii) Taking a broader perspective, we have provided an analytic solution of a paradigmatic example of a "Hund impurity problem." We were able to address this fundamental type of problem by combining state-of-the-art multiorbital NRG with a suitable generalization of Affleck and Ludwig's CFT approach [42–46].

(iv) Regarding experimental relevance, Hund impurities are of central importance for understanding Hund metals, including almost all 4*d* and 5*d* materials, and even in the 5*f* actinides Hund's coupling is the main cause for electronic correlations. Our work illustrates paradigmatically why hints of NFL physics can generically be expected to arise in such systems. Moreover, *tunable* Hund impurities can be realized using magnetic molecules on substrates [64] or multilevel quantum dots, raising hopes of tuning Hund impurities in such a way that truly well-developed NFL behavior can be observed experimentally.

ACKNOWLEDGMENTS

We thank I. Affleck, A. Georges, M. Goldstein, O. Parcollet, E. Sela, and A. Tsvelik for helpful advice and, in particular, I. Brunner for technical advice regarding $\mathrm{SU}(3)_2$ fusion rules. E. W., K. M. S., and J. v. D. are supported by the Deutsche Forschungsgemeinschaft under Germany's Excellence Strategy—EXC-2111—390814868, and S.-S. B. L. by Grant No. LE3883/2-1. A. W. was supported by the U.S. Department of Energy, Office of Basic Energy Sciences, under Contract No. DE-SC0012704. G. K. was supported by the National Science Foundation Grant No. DMR-1733071. Y. W. was supported by the U.S. Department of Energy, Office of Science, Basic Energy Sciences as a part of the Computational Materials Science Program through the Center for Computational Design of Functional Strongly Correlated Materials and Theoretical Spectroscopy.

Note added.—Recently, a paper closely related to ours appeared [65], with similar goals, a complementary analysis (using NRG but not CFT), and conclusions consistent with ours.

APPENDIX: YE'S $\mathbf{SU(2)\times SU(2)}$ SPIN-ORBITAL KONDO MODEL

In this appendix, we revisit an $\mathrm{SU}(2)\times\mathrm{SU}(2)$ spin-orbital Kondo (2soK) model studied in a pioneering paper by Ye in 1997 [48]. It is a simpler cousin of our 3soK model, having a Hamiltonian of precisely the same form, with the following differences: the orbital channel index takes only two values, $m = 1, 2$; the local orbital current $\mathbf{J}_{\mathrm{orb}}$ is defined using Pauli (not Gell-Mann) matrices; and the impurity spin and orbital isospin operators, $\mathbf{S}$ and $\mathbf{T}$, are both SU(2) generators, in the representation $S = \lambda = \frac{1}{2}$.

In the context of the present study, Ye's paper is of interest because his Kondo impurity likewise features both spin and orbital degrees of freedom. From a conceptual perspective, his and our models differ only in the symmetry group, SU(2) versus SU(3) in the orbital sector, and the choice of impurity multiplet, $Q_{\mathrm{imp}} = (\frac{1}{2}, \frac{1}{2})$ versus $(1, \begin{smallmatrix}\square\\\square\end{smallmatrix})$. Moreover, he was able to obtain exact results for his model using Abelian bosonization. Below, we verify that when the NRG and CFT methodology used in the main text is applied to Ye's 2soK model, the results are consistent with his conclusions.

Before proceeding, however, let us also briefly address some differences between Ye's work and ours. Since he uses Abelian bosonization, his approach does not readily generalize to the $\mathrm{U}(1)\times\mathrm{SU}(2)\times\mathrm{SU}(3)$ impurity model considered here. Ye does mention very briefly that some of his results can also be obtained using non-Abelian bosonization, employing *simultaneous* fusion in the spin and orbital sectors. However, we show below that that fusion scheme is applicable only when particle-hole symmetry is present. This is the case for Ye's application, but not for our 3soK model. When particle-hole symmetry is absent, the fusion schemes needed for the spin and orbital are subtly different—indeed, clarifying these differences was the conceptually most challenging aspect of our work. Note that the particle-hole asymmetry of our 3soK model is not a

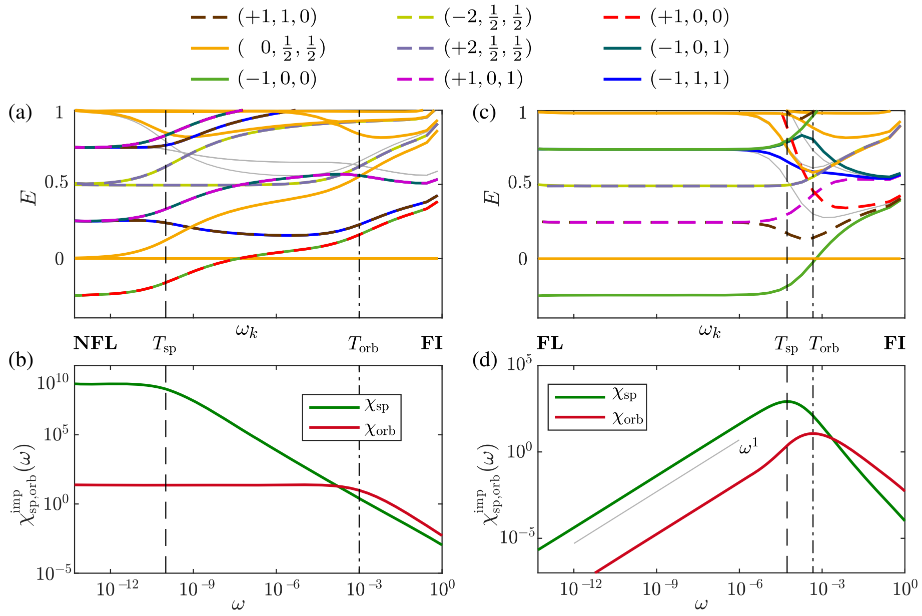

FIG. 8. NRG results for Ye's 2soK model, computed (a),(b) for $(J_0, K_0, I_0) = (0.1, 0.3, 0)$, respecting particle-hole symmetry, and (c), (d) for (0,0.3,0.05), breaking particle-hole symmetry. (a),(c) Eigenlevel flow diagrams, with quantum numbers (q, S, λ) shown at the top. The low-energy fixed points in (a) and (c) exhibit a NFL or FL spectrum, respectively, reproduced analytically in Table V or VI, respectively. (b),(d) Imaginary part of the impurity's spin and orbital susceptibilities. Vertical lines indicate the crossover scales for orbital screening T_{orb} (dash-dotted) and spin screening T_{sp} (dashed), marking when $\chi^{\mathrm{imp}}_{\mathrm{orb}}$ and $\chi^{\mathrm{imp}}_{\mathrm{sp}}$ (b) bend over to constant behavior or (d) reach their maxima, respectively. (NRG parameters: $\Lambda = 2.5$, $N_{\mathrm{keep}} = 2000$, $D = 1$.)

mere technical complication, but an essential ingredient of the physics of Hund metals, which typically feature fillings one particle away from half filling. Finally, note that Ye's model, involving an impurity with spin 1/2, is not relevant for Hund metals, where Hund's coupling favors local spins larger than 1/2.

1. $I_0 = 0$: NFL fixed point

For $I_0 = 0$, the 2soK model obeys particle-hole symmetry. Figure 8(a) shows the finite-size eigenlevel flow computed by NRG for $\mathbf{c}_0 = (J_0, K_0, I_0) = (0.1, 0.3, 0)$. The low-energy fixed-point spectrum features equidistant levels, but nevertheless has NFL properties, as predicted by Ye, in that it cannot be understood in terms of combinations of single-particle excitations. Remarkably, this fixed-point spectrum can be reproduced by CFT arguments. Using non-Abelian bosonization according to the $\mathrm{U}(1) \times \mathrm{SU}(2)_2 \times \mathrm{SU}(2)_2$ KM algebra, the spectrum of free bath excitations can be expressed as

$$E(q, S, \lambda) = \frac{1}{8} q^2 + \frac{1}{4} \kappa_2(S) + \frac{1}{4} \kappa_2(\lambda) + \ell, \tag{A1a}$$

$$\kappa_2(S) = S(S+1), \quad \kappa_2(\lambda) = \lambda(\lambda+1), \tag{A1b}$$

with $\ell \in \mathbb{Z}$, while $\kappa_2(S)$, $\kappa_2(\lambda)$ are the quadratic SU(2) Casimirs in the spin and orbital sectors, respectively. We now combine bath and impurity degrees of freedom using *simultaneous* fusion in the spin and orbital sectors, $S \otimes S_{\mathrm{imp}} = \sum_{\oplus} S'$ and $\lambda \otimes \lambda_{\mathrm{imp}} = \sum_{\oplus} \lambda'$, employing the fusion rules of the $\mathrm{SU}(2)_2 \times \mathrm{SU}(2)_2$ KM algebra (Table S7 in the SM [54]). This reproduces the NFL fixed-point spectrum found by NRG, as shown in Table V.

By contrast, we recall that for the 3soK model our attempts to use simultaneous spin and orbital fusion to obtain the FL ground state for $0 \neq J_0 \ll K_0$, $I_0 = 0$ were unsuccessful (cf. Sec. V E 1). Thus the 2soK and 3soK models provide an example and a counterexample for the success of simultaneous spin and orbital fusion, succeeding or failing for a NFL or FL fixed point spectrum, respectively.

We have also computed the imaginary parts of spin and orbital susceptibilities $\chi^{\mathrm{imp}}_{\mathrm{sp,orb}}(\omega)$. Figure 8(b) shows the results. Both functions approach constants in the zero-frequency limit, i.e., scale as ω^0. This can be understood in terms of the scaling dimensions of the leading boundary operators in the spin and orbital sectors, $\mathbf{\Phi}_{\mathrm{sp}}$ and $\mathbf{\Phi}_{\mathrm{orb}}$, which have dimensions $\Delta_{\mathrm{sp}} = \Delta_{\mathrm{orb}} = \frac{1}{2}$ (Table V). By the arguments of Sec. V C, we thus obtain

$$\chi^{\mathrm{imp}}_{\mathrm{sp,orb}} \sim \omega^{2\Delta_{\mathrm{sp,orb}}-1} \sim \omega^0,$$

as predicted by Ye. This resembles the behavior observed for the celebrated two-channel Kondo model, featuring a

TABLE V. Fusion table for the NFL fixed point of Ye's 2soK model. It is structured just as Table II for the 3soK model, but here the free bath excitations are computed using Eqs. (A2) and Table S6 of the SM [54], and single fusion of bath and impurity degrees of freedom is performed simultaneously in the spin and orbital sectors, using $\mathrm{SU}(2)_2 \times \mathrm{SU}(2)_2$ fusion rules (listed in Table S7 of the SM [54]). The resulting multiplets (q, S', λ') have energies $E' = E(q, S', \lambda')$ and excitation energies $\delta E' = E' - E'_{\mathrm{min}}$. The NRG energies, computed for $(J_0, K_0, I_0) = (0.1, 0.3, 0)$ [Fig. 8(a)], have been shifted and rescaled such that the lowest energy is zero and the second-lowest values for E_{NRG} and $\delta E'$ match. The single fusion and NRG spectra agree very well (deviations $\lesssim 1\%$).

Free fermions					Single fusion, with $Q_{\mathrm{imp}} = (0, \frac{1}{2}, \frac{1}{2})$						NRG	Double fusion, with $Q_{\mathrm{imp}} = (0, \frac{1}{2}, \frac{1}{2})$				
q	S	λ	d	E	q	S'	λ'	d'	E'	$\delta E'$	E_{NRG}	q	S''	λ''	Δ	$\hat{O}$
0	0	0	1	0	0	$\frac{1}{2}$	$\frac{1}{2}$	4	$\frac{3}{8}$	$\frac{1}{4}$	0.25	0	0	0	0	
														1	$\frac{1}{2}$	$\mathbf{\Phi}_{\mathrm{orb}}$
													1	0	$\frac{1}{2}$	$\mathbf{\Phi}_{\mathrm{sp}}$
														1	1	
±1	$\frac{1}{2}$	$\frac{1}{2}$	4	$\frac{1}{2}$	±1	0	0	1	$\frac{1}{8}$	0	0					
							1	3	$\frac{5}{8}$	$\frac{1}{2}$	0.5					
						1	0	3	$\frac{5}{8}$	$\frac{1}{2}$	0.5					
							1	9	$\frac{9}{8}$	1	0.99					
0	1	0	3	$\frac{1}{2}$	0	$\frac{1}{2}$	$\frac{1}{2}$	4	$\frac{3}{8}$	$\frac{1}{4}$	0.25					
0	0	1	3	$\frac{1}{2}$	0	$\frac{1}{2}$	$\frac{1}{2}$	4	$\frac{3}{8}$	$\frac{1}{4}$	0.25					
±2	0	0	1	$\frac{1}{2}$	±2	$\frac{1}{2}$	$\frac{1}{2}$	4	$\frac{7}{8}$	$\frac{3}{4}$	0.75					
±2	1	0	1	1	±2	$\frac{1}{2}$	$\frac{1}{2}$	4	$\frac{7}{8}$	$\frac{3}{4}$	0.75					
±2	0	1	1	1	±2	$\frac{1}{2}$	$\frac{1}{2}$	4	$\frac{7}{8}$	$\frac{3}{4}$	0.75					
±2	1	1	1	$\frac{3}{2}$	±2	$\frac{1}{2}$	$\frac{1}{2}$	4	$\frac{7}{8}$	$\frac{3}{4}$	0.75					

spin-1/2 impurity having no orbital isospin (obtained from Ye's model by using $\lambda = \bullet$ for the impurity orbital pseudospin, and setting $K_0 = I_0 = 0$).

2. $I_0 \neq 0$: FL fixed point

For $I_0 \neq 0$, particle-hole symmetry is broken. Figure 8(c) shows the eigenlevel flow computed by NRG for $\mathbf{c}_0 = (0, 0.3, 0.05)$. The low-energy fixed point is a FL, as predicted by Ye. Its spectrum shows the same equidistant set of energies as the NFL spectrum of $I_0 = 0$ [Fig. 8(a)], but the degeneracies are different. This fixed point *cannot* be understood by simultaneous fusion in the spin and orbital sector. However, it agrees with the FL spectrum of an SU(4) Kondo model with the higher symmetry $\mathrm{U}(1)_{\mathrm{ch}} \times \mathrm{SU}(4)_{\mathrm{fl}}$, defined in analogy to the SU(6) Kondo model from Sec. V E 2, with a flavor index $\nu = 1, \ldots, 4$ encoding both spin and orbital degrees of freedom. Using non-Abelian bosonization according to the $\mathrm{U}(1) \times \mathrm{SU}(4)_1$ KM algebra, the free bath spectrum can be expressed as

$$E(q, \lambda) = \frac{1}{8} q^2 + \frac{1}{5} \kappa_4(\lambda) + \ell, \tag{A2a}$$

$$\kappa_4(\lambda) = \frac{1}{8}(3\lambda_1^2 + 4\lambda_2^2 + 3\lambda_3^2 + 4\lambda_1\lambda_2 + 2\lambda_2\lambda_3 + 4\lambda_1\lambda_3 + 12\lambda_1 + 16\lambda_2 + 12\lambda_3), \tag{A2b}$$

with $\ell \in \mathbb{Z}$, where $\kappa_4(\lambda)$ is the quadratic Casimir for the $\lambda = (\lambda_1, \lambda_2, \lambda_3)$ representation of the SU(4) Lie algebra. [The contributions from the two terms of Eq. (A2) are listed in Table S8 of the Supplemental Material [54] for the lowest few q and λ values.] Combining the flavor degrees of freedom of bath and impurity, $\lambda \otimes \lambda_{\mathrm{imp}} = \sum_{\oplus} \lambda'$, using the

TABLE VI. Fusion table for the FL fixed point of the SU(4) Kondo model. It is structured just as Table IV for the SU(6) Kondo model, but here the free bath excitations are computed using Eqs. (A2) and Table S8 of the SM [54], and flavor fusion is performed using $\mathrm{SU}(4)_1$ fusion rules (Table S9 of the SM [54]). The NRG spectrum was computed for the 2soK model with $(J_0, K_0, I_0) = (0, 0.3, 0.05)$ [Fig. 8(c)]. The single-fusion and NRG spectra agree very well (deviations $\lesssim 1\%$).

Free fermions				Single fusion, $Q_{\mathrm{imp}} = (0, \square)$					NRG
q	λ	d	E	q	λ'	d'	E'	$\delta E'$	E_{NRG}
0	$\bullet$	1	0	0	$\square$	4	$\frac{3}{8}$	$\frac{1}{4}$	0.25
+1	$\square$	4	$\frac{1}{2}$	+1	$\begin{smallmatrix}\square\\\square\end{smallmatrix}$	6	$\frac{5}{8}$	$\frac{1}{2}$	0.50
−1	$\begin{smallmatrix}\square\\\square\\\square\end{smallmatrix}$	4	$\frac{1}{2}$	−1	$\bullet$	1	$\frac{1}{8}$	0	0
±2	$\begin{smallmatrix}\square\\\square\end{smallmatrix}$	6	1	±2	$\begin{smallmatrix}\square\\\square\\\square\end{smallmatrix}$	4	$\frac{7}{8}$	$\frac{3}{4}$	0.75
+3	$\begin{smallmatrix}\square\\\square\\\square\end{smallmatrix}$	4	$\frac{3}{2}$	+3	$\bullet$	1	$\frac{9}{8}$	1	1.00
−3	$\square$	4	$\frac{3}{2}$	−3	$\begin{smallmatrix}\square\\\square\end{smallmatrix}$	6	$\frac{13}{8}$	$\frac{3}{2}$	1.50

fusion rules of the $\mathrm{SU}(4)_1$ KM algebra, we recover the FL fixed point spectrum found by NRG. This is shown in Table VI. In the FL regime, the spin and orbital susceptibilities scale as $\chi^{\mathrm{imp}}_{\mathrm{sp,orb}} \sim \omega^1$ [Fig. 8(d)], as expected for a Fermi liquid and predicted by Ye.

[1] A. Georges, L. de' Medici, and J. Mravlje, *Strong Electronic Correlations from Hund's Coupling*, Annu. Rev. Condens. Matter Phys. **4**, 137 (2013).

[2] P. Werner, E. Gull, M. Troyer, and A. J. Millis, *Spin Freezing Transition and Non-Fermi-Liquid Self-Energy in a Three-Orbital Model*, Phys. Rev. Lett. **101**, 166405 (2008).

[3] K. Haule and G. Kotliar, *Coherence-Incoherence Crossover in the Normal State of Iron Oxypnictides and Importance of Hund's Rule Coupling*, New J. Phys. **11**, 025021 (2009).

[4] Z. P. Yin, K. Haule, and G. Kotliar, *Magnetism and Charge Dynamics in Iron Pnictides*, Nat. Phys. **7**, 294 (2011).

[5] Z. P. Yin, K. Haule, and G. Kotliar, *Kinetic Frustration and the Nature of the Magnetic and Paramagnetic States in Iron Pnictides and Iron Chalcogenides*, Nat. Mater. **10**, 932 (2011).

[6] L. de' Medici, J. Mravlje, and A. Georges, *Janus-Faced Influence of Hund's Rule Coupling in Strongly Correlated Materials*, Phys. Rev. Lett. **107**, 256401 (2011).

[7] J. Mravlje, M. Aichhorn, T. Miyake, K. Haule, G. Kotliar, and A. Georges, *Coherence-Incoherence Crossover and the Mass-Renormalization Puzzles in* $\mathrm{Sr_2RuO_4}$, Phys. Rev. Lett. **106**, 096401 (2011).

[8] Z. P. Yin, K. Haule, and G. Kotliar, *Fractional Power-Law Behavior and Its Origin in Iron-Chalcogenide and Ruthenate Superconductors: Insights from First-Principles Calculations*, Phys. Rev. B **86**, 195141 (2012).

[9] C. Aron and G. Kotliar, *Analytic Theory of Hund's Metals: A Renormalization Group Perspective*, Phys. Rev. B **91**, 041110(R) (2015).

[10] S. Hoshino and P. Werner, *Superconductivity from Emerging Magnetic Moments*, Phys. Rev. Lett. **115**, 247001 (2015).

[11] H. T. Dang, J. Mravlje, A. Georges, and A. J. Millis, *Electronic Correlations, Magnetism, and Hund's Rule Coupling in the Ruthenium Perovskites* $\mathrm{SrRuO_3}$ *and* $\mathrm{CaRuO_3}$, Phys. Rev. B **91**, 195149 (2015).

[12] J. Mravlje and A. Georges, *Thermopower and Entropy: Lessons from* $\mathrm{Sr_2RuO_4}$, Phys. Rev. Lett. **117**, 036401 (2016).

[13] M. Zingl, J. Mravlje, M. Aichhorn, O. Parcollet, and A. Georges, *Hall Coefficient Signals Orbital Differentiation in the Hund's Metal* $\mathrm{Sr_2RuO_4}$, npj Quantum Mater. **4**, 35 (2019).

[14] T.-H. Lee, A. Chubukov, H. Miao, and G. Kotliar, *Pairing Mechanism in Hund's Metal Superconductors and the Universality of the Superconducting Gap to Critical Temperature Ratio*, Phys. Rev. Lett. **121**, 187003 (2018).

[15] M. Yi, D. H. Lu, R. Yu, S. C. Riggs, J.-H. Chu, B. Lv, Z. K. Liu, M. Lu, Y.-T. Cui, M. Hashimoto, S.-K. Mo, Z. Hussain, C. W. Chu, I. R. Fisher, Q. Si, and Z.-X. Shen, *Observation of Temperature-Induced Crossover to an Orbital-Selective Mott Phase in* $A_x\mathrm{Fe}_{2-y}\mathrm{Se}_2$ *(*$A = \mathrm{K}$*, Rb) Superconductors*, Phys. Rev. Lett. **110**, 067003 (2013).

[16] F. Hardy, A. E. Böhmer, D. Aoki, P. Burger, T. Wolf, P. Schweiss, R. Heid, P. Adelmann, Y. X. Yao, G. Kotliar, J. Schmalian, and C. Meingast, *Evidence of Strong Correlations and Coherence-Incoherence Crossover in the Iron Pnictide Superconductor* $\mathrm{KFe_2As_2}$, Phys. Rev. Lett. **111**, 027002 (2013).

[17] A. Horvat, R. Žitko, and J. Mravlje, *Low-Energy Physics of Three-Orbital Impurity Model with Kanamori Interaction*, Phys. Rev. B **94**, 165140 (2016).

[18] A. Tamai, M. Zingl, E. Rozbicki, E. Cappelli, S. Riccò, A. de la Torre, S. M. Walker, F. Y. Bruno, P. D. C. King, W. Meevasana, M. Shi, M. Radović, N. C. Plumb, A. S. Gibbs, A. P. Mackenzie, C. Berthod, H. U. R. Strand, M. Kim, A. Georges, and F. Baumberger, *High-Resolution Photoemission on* $\mathrm{Sr_2RuO_4}$ *Reveals Correlation-Enhanced Effective Spin-Orbit Coupling and Dominantly Local Self-Energies*, Phys. Rev. X **9**, 021048 (2019).

[19] P. Werner and S. Hoshino, *Nickelate Superconductors—Multiorbital Nature and Spin Freezing*, Phys. Rev. B **101**, 041104(R) (2020).

[20] P. Coleman, Y. Komijani, and E. König, *The Triplet Resonating Valence Bond State and Superconductivity in Hund's Metals*, arXiv:1910.03168 [Phys. Rev. Lett. (to be published)].

[21] X. Chen, I. Krivenko, M. B. Stone, A. I. Kolesnikov, T. Wolf, D. Reznik, K. S. Bedell, F. Lechermann, and S. D. Wilson, *Unconventional Hund Metal in MnSi*, arXiv:1909.11195.

[22] K. M. Stadler, Z. P. Yin, J. von Delft, G. Kotliar, and A. Weichselbaum, *Dynamical Mean-Field Theory Plus Numerical Renormalization-Group Study of Spin-Orbital Separation in a Three-Band Hund Metal*, Phys. Rev. Lett. **115**, 136401 (2015).

[23] K. M. Stadler, G. Kotliar, A. Weichselbaum, and J. von Delft, *Hundness versus Mottness in a Three-Band Hubbard-Hund Model: On the Origin of Strong Correlations in Hund Metals*, Ann. Phys. (Amsterdam) **405**, 365 (2019).

[24] X. Deng, K. M. Stadler, K. Haule, A. Weichselbaum, J. von Delft, and G. Kotliar, *Signatures of Mottness and Hundness in Archetypal Correlated Metals*, Nat. Commun. **10**, 2721 (2019).

[25] S. Akhanjee and A. M. Tsvelik, *Analytically Tractable Model of Bad Metals*, Phys. Rev. B **87**, 195137 (2013).

[26] J. Kondo, *Resistance Minimum in Dilute Magnetic Alloys*, Prog. Theor. Phys. **32**, 37 (1964).

[27] P. W. Anderson, *A Poor Man's Derivation of Scaling Laws for the Kondo Problem*, J. Phys. C **3**, 2436 (1970).

[28] K. G. Wilson, *The Renormalization Group: Critical Phenomena and the Kondo Problem*, Rev. Mod. Phys. **47**, 773 (1975).

[29] J. R. Schrieffer, *The Kondo Effect—The Link between Magnetic and Nonmagnetic Impurities in Metals?*, J. Appl. Phys. **38**, 1143 (1967).

[30] M. D. Daybell and W. A. Steyert, *Localized Magnetic Impurity States in Metals: Some Experimental Relationships*, Rev. Mod. Phys. **40**, 380 (1968).

[31] B. Coqblin and J. R. Schrieffer, *Exchange Interaction in Alloys with Cerium Impurities*, Phys. Rev. **185**, 847 (1969).

[32] I. Okada and K. Yosida, *Singlet Ground State of the Localized d-Electrons Coupled with Conduction Electrons in Metals*, Prog. Theor. Phys. **49**, 1483 (1973).

[33] P. Nozières and A. Blandin, *Kondo Effect in Real Metals*, J. Phys. (Paris) **41**, 193 (1980).

[34] N. Andrei and C. Destri, *Solution of the Multichannel Kondo Problem*, Phys. Rev. Lett. **52**, 364 (1984).

[35] A. M. Tsvelik and P. B. Wiegmann, *Solution of the n-Channel Kondo Problem (Scaling and Integrability)*, Z. Phys. B **54**, 201 (1984).

[36] A. M. Tsvelik, *The Thermodynamics of Multichannel Kondo Problem*, J. Phys. C **18**, 159 (1985).

[37] A. M. Tsvelik and P. B. Wiegmann, *Exact Solution of the Multichannel Kondo Problem, Scaling, and Integrability*, J. Stat. Phys. **38**, 125 (1985).

[38] N. Andrei and A. Jerez, *Fermi- and Non-Fermi-Liquid Behavior in the Anisotropic Multichannel Kondo Model: Bethe Ansatz Solution*, Phys. Rev. Lett. **74**, 4507 (1995).

[39] A. Jerez, N. Andrei, and G. Zaránd, *Solution of the Multichannel Coqblin-Schrieffer Impurity Model and Application to Multilevel Systems*, Phys. Rev. B **58**, 3814 (1998).

[40] D. M. Cragg, P. Lloyd, and P. Nozieres, *On the Ground States of Some s-d Exchange Kondo Hamiltonians*, J. Phys. C **13**, 803 (1980).

[41] H. B. Pang and D. L. Cox, *Stability of the Fixed Point of the Two-Channel Kondo Hamiltonian*, Phys. Rev. B **44**, 9454 (1991).

[42] I. Affleck, *A Current Algebra Approach to the Kondo Effect*, Nucl. Phys. **B336**, 517 (1990).

[43] I. Affleck and A. W. W. Ludwig, *The Kondo Effect, Conformal Field Theory and Fusion Rules*, Nucl. Phys. **B352**, 849 (1991).

[44] I. Affleck and A. W. W Ludwig, *Critical Theory of Overscreened Kondo Fixed Points*, Nucl. Phys. **B360**, 641 (1991).

[45] I. Affleck and A. W. W. Ludwig, *Exact Conformal-Field-Theory Results on the Multichannel Kondo Effect: Single-Fermion Green's Function, Self-Energy, and Resistivity*, Phys. Rev. B **48**, 7297 (1993).

[46] A. W. W. Ludwig and I. Affleck, *Exact Conformal-Field-Theory Results on the Multi-Channel Kondo Effect: Asymptotic Three-Dimensional Space- and Time-Dependent Multi-Point and Many-Particle Green's Functions*, Nucl. Phys. **B428**, 545 (1994).

[47] K. M. Stadler, *A Model Study of Strong Correlations in Hund Metals. The Numerical Renormalization Group as Efficient Multi-Band Impurity Solver for Dynamical Mean-Field Theory*, Ph.D. thesis, Ludwig-Maximilians-Universität München, 2019.

[48] J. Ye, *Solution of the Two-Channel Spin-Flavor Kondo Model*, Phys. Rev. B **56**, R489 (1997).

[49] Y. Wang, E. Walter, S.-S. B. Lee, K. M. Stadler, J. von Delft, A. Weichselbaum, and G. Kotliar, *Global Phase Diagram of a Spin-Orbital Kondo Impurity Model and the Suppression of Fermi-Liquid Scale*, Phys. Rev. Lett. **124**, 136406 (2020).

[50] A. Weichselbaum, *Non-Abelian Symmetries in Tensor Networks: A Quantum Symmetry Space Approach*, Ann. Phys. (Amsterdam) **327**, 2972 (2012).

[51] A. Weichselbaum, *Tensor Networks and the Numerical Renormalization Group*, Phys. Rev. B **86**, 245124 (2012).

[52] A. Weichselbaum and J. von Delft, *Sum-Rule Conserving Spectral Functions from the Numerical Renormalization Group*, Phys. Rev. Lett. **99**, 076402 (2007).

[53] S.-S. B. Lee and A. Weichselbaum, *Adaptive Broadening to Improve Spectral Resolution in the Numerical Renormalization Group*, Phys. Rev. B **94**, 235127 (2016).

[54] See Supplemental Material at http://link.aps.org/supplemental/10.1103/PhysRevX.10.031052 for tables presenting detailed fusion rules and contributions to low-energy spectra, which includes Refs. [55,56].

[55] C. J. Cummins, *su(n) and sp(2n) WZW Fusion Rules*, J. Phys. A **24**, 391 (1991).

[56] P. Di Francesco, P. Mathieu, and D. Sénéchal, *Conformal Field Theory* (Springer, New York, 1997).

[57] J. von Delft, *2-Channel Kondo Scaling in Metal Nano-constrictions—A Conformal Field Theory Calculation of Scaling Function*, Ph.D. Thesis, Cornell University, 1995.

[58] A. W. W. Ludwig, *Field Theory Approach to Critical Quantum Impurity Problems and Applications to the Multichannel Kondo Effect*, Int. J. Mod. Phys. B **08**, 347 (1994).

[59] J. L. Cardy, *Conformal Invariance and Surface Critical Behavior*, Nucl. Phys. **B240**, 514 (1984).

[60] The quantum numbers of $\tilde{\Psi}_{\mathrm{orb}}$ differ from those of $\mathbf{\Phi}_{\mathrm{orb}}$ (and hence also of $\mathbf{T}$, $\mathbf{J}_{\mathrm{orb}}$), since the same is true for their parent states, reflecting the fact that the latter undergo a true level crossing. Ditto for $\tilde{\Psi}_{\mathrm{sp}}$ versus $\mathbf{\Phi}_{\mathrm{sp}}$ (and $\mathbf{S}$, $\mathbf{J}_{\mathrm{sp}}$). In contrast to $\mathbf{S} \cdot \mathbf{\Phi}_{\mathrm{sp}}$, it is hence not possible to couple $\mathbf{S}$ and $\tilde{\Psi}_{\mathrm{sp}}$ to a spin singlet, needed for computing $\chi_{\mathrm{sp}}^{\mathrm{imp,bath}}$. Instead, we speculate that the role of $(\int dt' S^a \Phi_{\mathrm{sp}}^a)^2$ could be taken, e.g., by $\int dt' S^a (\tilde{\Psi}_{\mathrm{sp}}^{\dagger})_{\sigma} \int dt'' S^a (\tilde{\Psi}_{\mathrm{sp}})_{\sigma}$.

[61] I. Affleck, *Conformal Field Theory Approach to the Kondo Effect*, Acta Phys. Polon. B **26**, 1869 (1995), https://www.actaphys.uj.edu.pl/R/26/12/1869/pdf.

[62] J. Fuchs and C. Schweigert, *Symmetries, Lie Algebras and Representations: A Graduate Course for Physicists* (Cambridge University Press, 1997), p. 335, Eq. (19.14).

[63] T. A. Costi, *Kondo Effect in a Magnetic Field and the Magnetoresistivity of Kondo Alloys*, Phys. Rev. Lett. **85**, 1504 (2000).

[64] A. A. Khajetoorians, M. Valentyuk, M. Steinbrecher, T. Schlenk, A. Shick, J. Kolorenc, A. I. Lichtenstein, T. O. Wehling, R. Wiesendanger, and J. Wiebe, *Tuning Emergent Magnetism in a Hund's Impurity*, Nat. Nanotechnol. **10**, 958 (2015).

[65] A. Horvat, R. Žitko, and J. Mravlje, *Non-Fermi-Liquid Fixed Point in Multi-Orbital Kondo Impurity Model Relevant for Hund's Metals*, arXiv:1907.07100.

Supplemental Material for "Uncovering Non-Fermi-Liquid Behavior in Hund Metals: Conformal Field Theory Analysis of an SU(2) × SU(3) Spin-Orbital Kondo Model"

E. Walter, K. M. Stadler, S.-S. B. Lee, Y. Wang, G. Kotliar, A. Weichselbaum, and J. von Delft

Citations and equation numbers refer to references and equations given in the main text.

Below we provide a number of tables needed for various non-Abelian bosonization and Kac-Moody fusion schemes used in the main text: $\mathrm{U}(1) \times \mathrm{SU}(2)_3 \times \mathrm{SU}(3)_2$, $\mathrm{U}(1) \times \mathrm{SU}(6)_1$, $\mathrm{U}(1) \times \mathrm{SU}(2)_2 \times \mathrm{SU}(2)_2$, and $\mathrm{U}(1) \times \mathrm{SU}(4)_1$.

The fusion rules for the $\mathrm{SU}(N)_k$ Kac-Moody (KM) algebra differ from those of the $\mathrm{SU}(N)$ Lie algebra in that some Young diagrams arising for the latter are forbidden for the former (such as Young diagrams with more than k columns, reflecting the fact that only two distinct spin species are available when constructing $\mathrm{SU}(N)_k$ representations). However, note that these fusion rules are in general more complicated than simply crossing out diagrams with more than k columns. For example, in Table S3 for $\mathrm{SU}(2)_3$, not all representations with $S'' \le 3/2$ are allowed. We constructed the KM fusion tables given below using a general recipe due to Cummins [55], explained in pedagogical detail in Sec. 16.2.4 of [56].

U(1)×SU(2)$_3$×SU(3)$_2$

Table S1. The few lowest values of the quantum numbers q, S and $\lambda = (\lambda_1, \lambda_2)$ labeling U(1) charge, $\mathrm{SU}(2)_3$ spin and $\mathrm{SU}(3)_2$ orbital multiplets, their contributions to the energies $E(q, S, \lambda)$ of Eq. (12a), and the dimensions d of the spin and orbital multiplets. $\kappa_2(S)$, $\kappa_3(\lambda)$ are given in Eqs. (12b), (12c).

q	0	±1	±2	±3	±4	±5
$\frac{1}{12}q^2$	0	$\frac{1}{12}$	$\frac{1}{3}$	$\frac{3}{4}$	$\frac{4}{3}$	$\frac{25}{12}$
S	0	$\frac{1}{2}$	1	$\frac{3}{2}$	2	$\frac{5}{2}$
$\frac{1}{5}\kappa_2(S)$	0	$\frac{3}{20}$	$\frac{2}{5}$	$\frac{3}{4}$	$\frac{6}{5}$	$\frac{7}{4}$
$d(S)$	1	2	3	4	5	6
(λ_1, λ_2)	(0,0)	(1,0)	(0,1)	(2,0)	(0,2)	(1,1)
λ	$\bullet$	$\ydiagram{1}$	$\ydiagram{1,1}$	$\ydiagram{2}$	$\ydiagram{2,2}$	$\ydiagram{2,1}$
$\frac{1}{5}\kappa_3(\lambda)$	0	$\frac{4}{15}$	$\frac{4}{15}$	$\frac{2}{3}$	$\frac{2}{3}$	$\frac{3}{5}$
$d(\lambda)$	1	3	3	6	6	8

Table S2. $\mathrm{SU}(3)_2$ fusion rules, listing various direct product decompositions of the form $\lambda \otimes \lambda' = \sum_\oplus \lambda''$. Crossed-out diagrams denote additional irreps occurring when considering direct product decompositions for SU(3) instead of $\mathrm{SU}(3)_2$.

$d(\lambda)$	$\kappa_3(\lambda)$	(λ_1, λ_2)	λ ╲ λ'	$\ydiagram{1}$	$\ydiagram{1,1}$
3	$\frac{4}{3}$	(1,0)	$\ydiagram{1}$	$\ydiagram{1,1} \oplus \ydiagram{2}$	$\bullet \oplus \ydiagram{2,1}$
3	$\frac{4}{3}$	(0,1)	$\ydiagram{1,1}$	$\bullet \oplus \ydiagram{2,1}$	$\ydiagram{1} \oplus \ydiagram{2,2}$
6	$\frac{10}{3}$	(2,0)	$\ydiagram{2}$	$\ydiagram{2,1} \oplus \cancel{\ydiagram{3}}$	$\ydiagram{1} \oplus \cancel{\ydiagram{3,1}}$
6	$\frac{10}{3}$	(0,2)	$\ydiagram{2,2}$	$\ydiagram{1,1} \oplus \cancel{\ydiagram{3,2}}$	$\ydiagram{2,1} \oplus \cancel{\ydiagram{3,3}}$
8	3	(1,1)	$\ydiagram{2,1}$	$\ydiagram{1} \oplus \ydiagram{2,2}$ $\oplus \cancel{\ydiagram{3,1}}$	$\ydiagram{1,1} \oplus \ydiagram{2}$ $\oplus \cancel{\ydiagram{3,2}}$

Table S3. $\mathrm{SU}(2)_3$ fusion rules, listing various direct product decompositions of the form $S \otimes S' = \sum_\oplus S''$. Crossed-out numbers denote additional irreps occurring when considering direct product decompositions for SU(2) instead of $\mathrm{SU}(2)_3$.

$d(S)$	$\kappa_2(S)$	S ╲ S'	$\frac{3}{2}$
1	0	0	$\frac{3}{2}$
2	$\frac{3}{4}$	$\frac{1}{2}$	$1 \oplus \cancel{2}$
3	2	1	$\frac{1}{2} \oplus \cancel{\frac{3}{2}} \oplus \cancel{\frac{5}{2}}$
4	$\frac{15}{4}$	$\frac{3}{2}$	$0 \oplus \cancel{1} \oplus \cancel{2} \oplus \cancel{3}$

U(1)×SU(6)$_1$

Table S4. The few lowest values of the quantum numbers q and $\lambda = (\lambda_1, \lambda_2, \lambda_3, \lambda_4, \lambda_5)$, labeling U(1) charge and SU(6)$_1$ flavor multiplets, their contributions to the eigenenergies $E(q, \lambda)$ of Eq. (22a), and the dimensions d of the flavor multiplets. Single-column Young diagrams with i boxes have $\lambda_j = \delta_{ij}$. $\kappa_6(\lambda)$ is given in Eq. (22b).

q	0	±1	±2	±3	±4	±5
$\frac{1}{12}q^2$	0	$\frac{1}{12}$	$\frac{1}{3}$	$\frac{3}{4}$	$\frac{4}{3}$	$\frac{25}{12}$
λ	•	□	$\begin{array}{\|c\|}\hline \\\hline \\\hline\end{array}$	$\begin{array}{\|c\|}\hline \\\hline \\\hline \\\hline\end{array}$	$\begin{array}{\|c\|}\hline \\\hline \\\hline \\\hline \\\hline\end{array}$	$\begin{array}{\|c\|}\hline \\\hline \\\hline \\\hline \\\hline \\\hline\end{array}$
$\frac{1}{7}\kappa_6(\lambda)$	0	$\frac{5}{12}$	$\frac{2}{3}$	$\frac{3}{4}$	$\frac{2}{3}$	$\frac{5}{12}$
$d(\lambda)$	1	6	15	20	15	6

Table S5. SU(6)$_1$ fusion rules, listing some direct product decompositions $\lambda \otimes \lambda' = \sum_{\oplus} \lambda''$, with $\lambda' = \begin{array}{|c|}\hline \\\hline \\\hline\end{array}$. Crossed-out diagrams denote additional irreps occurring when considering direct product decompositions for SU(6) instead of SU(6)$_1$.

$d(\lambda)$	$\kappa_6(\lambda)$	$(\lambda_1, \lambda_2, \lambda_3, \lambda_4, \lambda_5)$	λ' λ	$\begin{array}{\|c\|}\hline \\\hline \\\hline\end{array}$
1	0	(0,0,0,0,0)	•	$\begin{array}{\|c\|}\hline \\\hline \\\hline\end{array}$
6	$\frac{35}{12}$	(1,0,0,0,0)	□	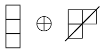
15	$\frac{14}{3}$	(0,1,0,0,0)	$\begin{array}{\|c\|}\hline \\\hline \\\hline\end{array}$	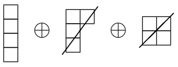
20	$\frac{21}{4}$	(0,0,1,0,0)	$\begin{array}{\|c\|}\hline \\\hline \\\hline \\\hline\end{array}$	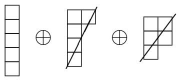
15	$\frac{14}{3}$	(0,0,0,1,0)	$\begin{array}{\|c\|}\hline \\\hline \\\hline \\\hline \\\hline\end{array}$	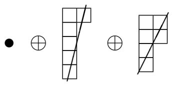
6	$\frac{35}{12}$	(0,0,0,0,1)	$\begin{array}{\|c\|}\hline \\\hline \\\hline \\\hline \\\hline \\\hline\end{array}$	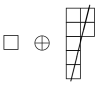

U(1)×SU(2)$_2$×SU(2)$_2$

Table S6. The few lowest values of the quantum numbers q, S and λ, labeling U(1) charge, SU(2)$_2$ spin and SU(2)$_2$ orbital multiplets, respectively, their contributions to the eigenenergies $E(q, S, \lambda)$ of Eq. (A1a), and the dimensions d of the spin and flavor multiplets. $\kappa_2(S)$ and $\kappa_2(\lambda)$ are given in Eq. (A1b).

q	0	±1	±2	±3
$\frac{1}{8}q^2$	0	$\frac{1}{8}$	$\frac{1}{2}$	$\frac{9}{8}$
S, λ	0	$\frac{1}{2}$	1	$\frac{3}{2}$
$\frac{1}{4}\kappa_2(S)$, $\frac{1}{4}\kappa_2(\lambda)$	0	$\frac{3}{16}$	$\frac{1}{2}$	$\frac{15}{16}$
$d(S)$, $d(\lambda)$	1	2	3	4

Table S7. SU(2)$_2$ fusion rules, listing various direct product decompositions of the form $S \otimes S' = \sum_{\oplus} S''$. Crossed-out numbers denote additional irreps occurring when considering direct product decompositions for SU(2) instead of SU(2)$_2$.

$d(S)$	$\kappa_2(S)$	S' S	$\frac{1}{2}$
1	0	0	$\frac{1}{2}$
2	$\frac{3}{4}$	$\frac{1}{2}$	$0 \oplus 1$
3	2	1	$\frac{1}{2} \oplus \cancel{\frac{3}{2}}$

$\mathbf{U(1)\times SU(4)_1}$

Table S8. The few lowest values of the quantum numbers q and $\lambda = (\lambda_1, \lambda_2, \lambda_3)$, labeling U(1) charge and $SU(4)_1$ flavor multiplets, their contributions to the eigenenergies $E(q, \lambda)$ of Eq. (A2a), and the dimensions d of the flavor multiplets. $\kappa_4(\lambda)$ is given in Eq. (A2b).

q	0	±1	±2	±3
$\frac{1}{8}q^2$	0	$\frac{1}{8}$	$\frac{1}{2}$	$\frac{9}{8}$
$(\lambda_1, \lambda_2, \lambda_3)$	(0,0,0)	(1,0,0)	(0,1,0)	(0,0,1)
λ	$\bullet$	$\square$	$\begin{array}{\|c\|}\hline \\ \hline \\ \hline\end{array}$	$\begin{array}{\|c\|}\hline \\ \hline \\ \hline \\ \hline\end{array}$
$\frac{1}{5}\kappa_4(\lambda)$	0	$\frac{3}{8}$	$\frac{1}{2}$	$\frac{3}{8}$
$d(\lambda)$	1	4	6	4

Table S9. $SU(4)_1$ fusion rules, listing some direct product decompositions $\lambda \otimes \lambda' = \sum_{\oplus} \lambda''$, with $\lambda' = \square$. Crossed-out diagrams denote additional irreps occurring when considering direct product decompositions for SU(4) instead of $SU(4)_1$.

$d(\lambda)$	$\kappa_4(\lambda)$	$(\lambda_1, \lambda_2, \lambda_3)$	$\lambda \backslash \lambda'$	$\square$
1	0	(0,0,0)	$\bullet$	$\square$
4	$\frac{15}{8}$	(1,0,0)	$\square$	$\begin{array}{\|c\|}\hline \\ \hline \\ \hline\end{array} \oplus \cancel{\begin{array}{\|c\|c\|}\hline & \\ \hline\end{array}}$
6	$\frac{5}{2}$	(0,1,0)	$\begin{array}{\|c\|}\hline \\ \hline \\ \hline\end{array}$	$\begin{array}{\|c\|}\hline \\ \hline \\ \hline \\ \hline\end{array} \oplus \cancel{\begin{array}{\|c\|c\|}\hline & \\ \hline & \\ \cline{1-1}\end{array}}$
4	$\frac{15}{8}$	(0,0,1)	$\begin{array}{\|c\|}\hline \\ \hline \\ \hline \\ \hline\end{array}$	$\bullet \oplus \cancel{\begin{array}{\|c\|c\|}\hline & \\ \hline & \\ \cline{1-1} & \\ \cline{1-1}\end{array}}$

Global Phase Diagram of a Spin-Orbital Kondo Impurity Model and the Suppression of Fermi-Liquid Scale

by

Y. Wang,[1] E. Walter,[2] S.-S. B. Lee,[2] K. M. Stadler,[2] J. von Delft,[2]
A. Weichselbaum,[1,2] and G. Kotliar,[1,3]
[1] Condensed Matter Physics and Materials Science Department,
Brookhaven National Laboratory, Upton, New York 11973, USA
[2] Arnold Sommerfeld Center for Theoretical Physics, Center for NanoScience, and
Munich Center for Quantum Science and Technology,
Ludwig-Maximilians-Universität München, 80333 München, Germany
[3] Department of Physics and Astronomy, Rutgers University,
Piscataway, New Jersey 08854, USA

reprinted on pages 142–149

with permission from
***Phys. Rev. Lett.* 124, 136406 (2020)**,
DOI: 10.1103/PhysRevLett.124.136406.
© 2020 American Physical Society

Supplemental Material reprinted on pages 150–165.

PHYSICAL REVIEW LETTERS **124,** 136406 (2020)

Global Phase Diagram of a Spin-Orbital Kondo Impurity Model and the Suppression of Fermi-Liquid Scale

Y. Wang,[1] E. Walter,[2] S.-S. B. Lee,[2] K. M. Stadler,[2] J. von Delft,[2] A. Weichselbaum,[1,2] and G. Kotliar[1,3]
[1]*Department of Condensed Matter Physics and Materials Science, Brookhaven National Laboratory, Upton, New York 11973, USA*
[2]*Arnold Sommerfeld Center for Theoretical Physics, Center for NanoScience, and Munich Center for Quantum Science and Technology, Ludwig-Maximilians-Universität München, 80333 Munich, Germany*
[3]*Department of Physics and Astronomy, Rutgers University, Piscataway, New Jersey 08856, USA*

(Received 4 November 2019; accepted 28 February 2020; published 3 April 2020)

Many correlated metallic materials are described by Landau Fermi-liquid theory at low energies, but for Hund metals the Fermi-liquid coherence scale T_{FL} is found to be surprisingly small. In this Letter, we study the simplest impurity model relevant for Hund metals, the three-channel spin-orbital Kondo model, using the numerical renormalization group (NRG) method and compute its global phase diagram. In this framework, T_{FL} becomes arbitrarily small close to two new quantum critical points that we identify by tuning the spin or spin-orbital Kondo couplings into the ferromagnetic regimes. We find quantum phase transitions to a singular Fermi-liquid or a novel non-Fermi-liquid phase. The new non-Fermi-liquid phase shows frustrated behavior involving alternating overscreenings in spin and orbital sectors, with universal power laws in the spin ($\omega^{-1/5}$), orbital ($\omega^{1/5}$) and spin-orbital (ω^{1}) dynamical susceptibilities. These power laws, and the NRG eigenlevel spectra, can be fully understood using conformal field theory arguments, which also clarify the nature of the non-Fermi-liquid phase.

DOI: 10.1103/PhysRevLett.124.136406

Introduction.—A very large number of correlated metallic materials are "bad metals," namely in a broad regimes of temperature T characterized by deviations from the Landau Fermi-liquid (FL) T^2 law [1] and their values of resistivity exceeding the Mott-Ioffe-Regel limit [2]. One class of bad metals are the Hund metals, i.e., 3d and 4d multiorbital systems where correlations derive from the Hund's coupling J_H [3–7]. They include ruthenates [8–13], iron pnictides and chalcogenides [14–20]. The Landau FL quasiparticles emerge only below a coherence scale T_{FL} which is much smaller than the natural energy scales of the problem, set by the electronic bandwidth. Why is T_{FL} so small in units of the bandwidth? This "naturalness problem" is a central problem of condensed matter physics which has attracted considerable attention in the community. Its solution should also provide a clue as to what reference system should be used to describe the anomalous behavior observed in a broad energy regime above T_{FL}, when no other instabilities such as magnetism or superconductivity intervene.

Two different directions have been followed to address this puzzle. The first invokes the proximity to quantum critical points (QCPs) [21–23], signaling the transition to an ordered phase, or to an unconventional one such as fractionalized Mott insulators [24,25]. An alternative starting point has been provided by the development of the combination of *ab initio* electronic structure and dynamical mean field theory (LDA + DMFT) [26–29]. Here, the excitations of a solid are understood in terms of atomic multiplets embedded in an effective medium, and the evolution of the electronic structure from atomic multiplet excitations into quasiparticles arises naturally as temperature is lowered. This approach has provided quantitative predictions in many materials of interest [3,19,28,30–36], where the *ab initio* LDA + DMFT calculations are in surprisingly good agreement with experiments. However, the solution of the LDA + DMFT equations is a complex problem, which generically yields a nonzero FL scale. Hence no connection with the ideas of QCPs was made. The question of how to reduce the FL scale to exactly zero and how to characterize the ensuing anomalous behavior above T_{FL} has remained open.

In this Letter, we provide an answer to this question by computing a global phase diagram of the simplest three-channel spin-orbital Kondo model which captures the essential physics of Hund metals, using the exact numerical renormalization group (NRG) method [37]. By tuning the spin or spin-orbital Kondo couplings into the ferromagnetic regimes, we push T_{FL} to be exactly zero and identify QCPs. We find quantum phase transitions to a singular-Fermi-liquid (SFL) phase and to a novel non-Fermi-liquid (NFL) phase showing frustrated behavior of alternating overscreenings in spin and orbital sectors, with universal power laws in dynamical susceptibilities. We use conformal field theory (CFT) arguments [38–43] to identify the nature of the NFL phase, analytically reproduce the NRG eigenlevel spectra and explain the power laws. Our global phase diagram provides a clear picture for understanding the

© 2020 American Physical Society

suppression of coherence in Hund metals in terms of proximity to QCPs.

Model and methods.—We study the three-channel spin-orbital Kondo (3soK) model derived from a realistic Anderson impurity model in [20,44] for the studies of Hund metals. $H_{\rm bath} = \sum_{pm\sigma} \varepsilon_p \psi^\dagger_{pm\sigma}\psi_{pm\sigma}$ describes a symmetric, flat-band bath with half-bandwidth $D = 1$, where $\psi^\dagger_{pm\sigma}$ creates an electron with momentum p and spin σ in orbital $m \in \{1,2,3\}$. The bath couples to the impurity spin $\mathbf{S}$ and orbital isospin $\mathbf{T}$ via

$$H_{\rm int} = J_0 \mathbf{S}\cdot\mathbf{J}_{\rm sp} + K_0 \mathbf{T}\cdot\mathbf{J}_{\rm orb} + I_0 \mathbf{S}\cdot\mathbf{J}_{\text{sp-orb}}\cdot\mathbf{T}. \quad (1)$$

Here $\mathbf{S}$ are SU(2) generators in the $S = 1$ representation, normalized as ${\rm Tr}(S^\alpha S^\beta) = \frac{1}{2}\delta_{\alpha\beta}$, and $\mathbf{T}$ are SU(3) generators in the $\bar{3}$, i.e., (01) representation [45] (orbital angular momentum takes $L = 1$ in this representation), and ${\rm Tr}(T^a T^b) = \frac{1}{2}\delta_{ab}$. $\mathbf{J}_{\rm sp}$, $\mathbf{J}_{\rm orb}$, and $\mathbf{J}_{\text{sp-orb}}$ are the bath spin, orbital and spin-orbital densities at the impurity site, with $J^\alpha_{\rm sp} = \psi^\dagger_{m\sigma}\frac{1}{2}\sigma^\alpha_{\sigma\sigma'}\psi_{m\sigma'}$, $J^a_{\rm orb} = \psi^\dagger_{m\sigma}\frac{1}{2}\tau^a_{mm'}\psi_{m'\sigma}$, $J^{\alpha,a}_{\text{sp-orb}} = \frac{1}{4}\psi^\dagger_{m\sigma}\sigma^\alpha_{\sigma\sigma'}\tau^a_{mm'}\psi_{m'\sigma'}$ (summation over repeated indices is implied) and normalized $\psi^\dagger_{m\sigma} = (1/\sqrt{N})\sum_p \psi^\dagger_{pm\sigma}$, and $\sigma^\alpha[\tau^a]$ are Pauli [Gell-Mann] matrices, with normalization ${\rm Tr}(\sigma^\alpha\sigma^\beta) = 2\delta_{\alpha\beta}$ $[{\rm Tr}(\tau^a\tau^b) = 2\delta_{ab}]$. J_0, K_0 and I_0 are bare spin, orbital and spin-orbital Kondo exchange couplings, and we treat them as independent parameters with positive and negative values describing antiferromagnetic (AFM) and ferromagnetic (FM) couplings, respectively. We take $K_0 = 0.3$ throughout.

We use the full-density-matrix NRG [46] method to solve this model, exploiting its full ${\rm U(1)_{ch}}\times{\rm SU(2)_{sp}}\times{\rm SU(3)_{orb}}$ symmetry using QSpace [45]. Symmetry labels $Q \equiv [q, S, (\lambda_1\lambda_2)]$ are used to label multiplets, where q is the bath particle number relative to half-filling of the bath (we choose $q_{\rm imp} = 0$ because the impurity site has no charge dynamics), S is the total spin, and $(\lambda_1\lambda_2)$ labels an SU(3) representation described by a Young diagram with $\lambda_1 + \lambda_2$ (λ_2) boxes in its first (second) row. The impurity multiplet has $Q_{\rm imp} = [0, 1, (01)]$. The bath is discretized logarithmically and mapped to a semi-infinite "Wilson chain" with exponentially decaying hoppings, and the impurity coupled to chain site $k = 0$. The chain is diagonalized iteratively while discarding high-energy states, thereby enlarging the low-energy properties: the finite-size level spacing of a chain ending at site $k \geq 0$ is of order $\omega_k \propto \Lambda^{-k/2}$. Here $\Lambda > 1$ is a discretization parameter, chosen to be 4 in this work. The RG flow can be visualized by combining the rescaled low-lying NRG eigenlevel spectra, $E = (\mathcal{E} - \mathcal{E}_{\rm ref})/\omega_k$ vs ω_k, with increasing even or odd k. The imaginary part of the impurity dynamical susceptibilities $\chi^{\rm imp}_{\rm sp}$, $\chi^{\rm imp}_{\rm orb}$ and $\chi^{\rm imp}_{\text{sp-orb}}$ were calculated at temperature $T = 10^{-16}$. Computational details are presented in the Supplemental Material [47].

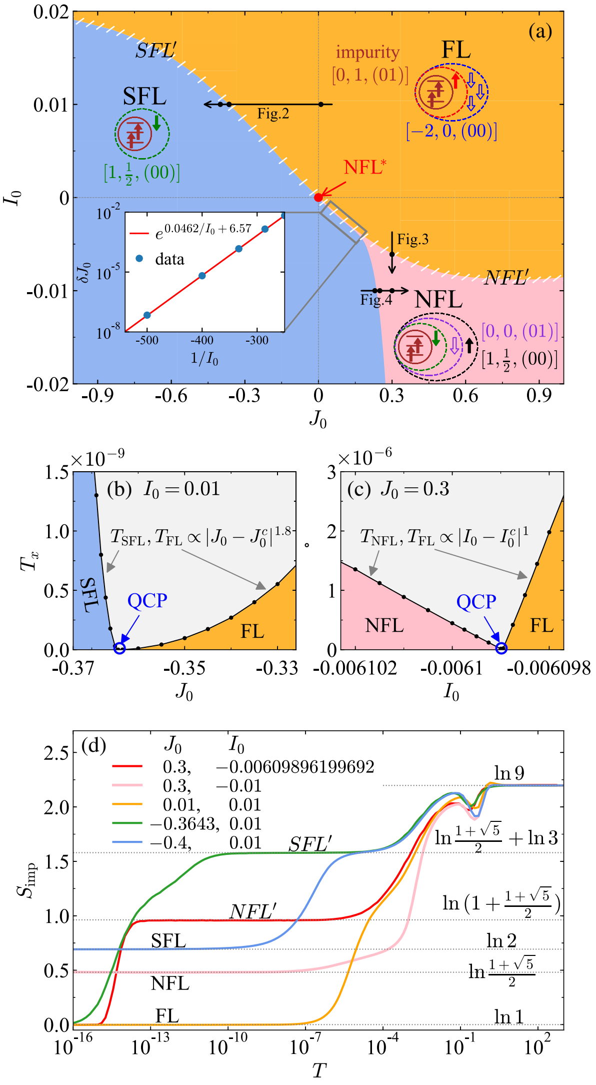

FIG. 1. (a) The calculated global phase diagram vs J_0 and I_0 at fixed $K_0 = 0.3$. Four low-energy fixed points are found: Fermi-liquid (FL, orange region); singular Fermi-liquid (SFL, blue region) with underscreened spin and fully screened orbital isospin; frustrated non-Fermi-liquid (NFL, pink region) with alternating spin and orbital overscreenings; and non-Fermi-liquid NFL* (red dot at $J_0 = 0$, $I_0 = 0$) with overscreened orbital isospin and degenerate impurity spin $\frac{1}{2}$, $\frac{3}{2}$. Cartoons depict the respective screening processes, where one dashed ellipse loosely represents an even number of Wilson shells. The indicated additional charge then is relative to half-filling, where filled (empty) arrows represent electrons (holes) with corresponding spin direction. The white-hatched region indicates the existence of an intermediate-energy crossover regime SFL' (NFL') enclosing the phase boundary between FL and SFL (NFL). The inset shows the "funnel width," δJ_0, of the NFL phase vs $1/I_0$ when $I_0 \to 0^-$. (b),(c) The onset energy scales T_x for ($x =$) FL, SFL and NFL vs (b) J_0 or (c) I_0, where quantum critical points are identified. (d) Impurity contribution to entropy $S_{\rm imp}$ as functions of temperature T.

Fixed points.—The calculated global phase diagram as a function of J_0 and I_0 is shown in Fig. 1(a). We first describe the low-energy fixed points found in the phase diagram. Throughout the entire regions where all three Kondo couplings are AFM, and for part of regions where J_0 or I_0 takes FM values (orange region), the system flows to a low-energy FL fixed point. This is seen in the NRG flow diagram and dynamical impurity susceptibilities χ^{imp} at $J_0 = I_0 = 0.01$ in Figs. 2(a) and 2(d). The ground state is a spin and orbital singlet, with impurity entropy $S_{\mathrm{imp}} = \ln 1$ [orange curve in Fig. 1(d)]. For small ω, all χ^{imp} follow a ω-linear behavior, characteristic of a FL.

When J_0 takes FM values and I_0 FM or small AFM values (blue region), the phase is governed by a low-energy SFL [48,58,59] fixed point where the spin is underscreened while the orbitals are fully screened. The transition from FL to SFL is analyzed in Fig. 2 for $I_0 = 0.01$. Figures 2(c) and 2(f), computed for $J_0 = -0.4$, show the NRG flow and χ^{imp} to the SFL fixed point. It has ground state $[+1, \frac{1}{2}, (00)]$ and S_{imp} approaches ln 2 at low energies [blue curve in Fig. 1(d)], signaling a residual spin of $\frac{1}{2}$. $\chi_{\mathrm{sp}}^{\mathrm{imp}}$ deviates slightly from a pure ω^{-1} power-law by a logarithmic correction at high energy and can be fitted by $\sim 1/[\omega \ln^2(\omega/T_{\mathrm{SFL}})]$ with T_{SFL} as an onset energy scale, consistent with the SFL results in [48]. $\chi_{\mathrm{orb}}^{\mathrm{imp}}$ shows ω-linear behavior at low energy, indicating fully screened orbital isospin. The coefficient of the impurity specific heat, $C_{\mathrm{imp}}(T)/T$ [47], shows divergent behavior [58], confirming the singular nature of this fixed point.

When I_0 takes strong FM and J_0 strong AFM couplings (pink region), we find a novel NFL fixed point, showing very interesting frustrated behavior of alternating overscreenings in spin and orbital sectors. Figure 3 analyzes the transition from FL to NFL at $J_0 = 0.3$. Figures 3(c), 3(f), 4(c), and 4(f) show the NRG flow and χ^{imp} towards the NFL fixed point. The two lowest multiplets with either orbital singlet, $[+1, \frac{1}{2}, (00)]$, or spin singlet, [0,0,(01)], are very close in energy. The dynamical susceptibilities follow perfect and universal power laws for the spin ($\omega^{-1/5}$), orbital ($\omega^{1/5}$) and spin-orbital (ω^{1}) operators. The impurity entropy S_{imp} evaluates to $\ln[(1+\sqrt{5})/2]$ [pink curve in Fig. 1(d)]. This value can be obtained from Eq. (6) in [49] for a general $\mathrm{SU}(N)_K$ Kondo model (K is the number of channels) with $N = 3$, $K = 2$, $Q = 2$ indicating $\mathrm{SU}(3)_2$ orbital overscreening, or with $N = 2$, $K = 3$, $Q = 1$ indicating $\mathrm{SU}(2)_3$ spin overscreening. Motivated by this, we follow the recently developed $\mathrm{SU}(2) \times \mathrm{SU}(3)$ CFT approach [43] to identify the nature of this fixed point. Its NRG eigenlevel spectra $Q' = [q', S', (\lambda_1'\lambda_2')]$ can be reproduced by applying either an $\mathrm{SU}(2)_3$ fusion procedure in the spin sector or an $\mathrm{SU}(3)_2$ fusion procedure in the orbital sector, i.e., fusing a spectrum of free fermions $Q = [q, S, (\lambda_1\lambda_2)]$, with an effective impurity multiplet labeling either $Q_{\mathrm{imp}}^{\mathrm{eff}} = [+1, \frac{1}{2}, (00)]$, or $Q_{\mathrm{imp}}^{\mathrm{eff}} = [0, 0, (01)]$. Double fusion of the spectrum Q' with the conjugate representation of the impurity multiplet, $\bar{Q}_{\mathrm{imp}}^{\mathrm{eff}} = [-1, \frac{1}{2}, (00)]$ or $\bar{Q}_{\mathrm{imp}}^{\mathrm{eff}} = [0, 0, (10)]$, yields the quantum numbers $Q'' = [q'', S'', (\lambda_1''\lambda_2'')]$ to characterize the CFT boundary operators, with scaling dimensions Δ, determining the behavior of dynamical susceptibilities.

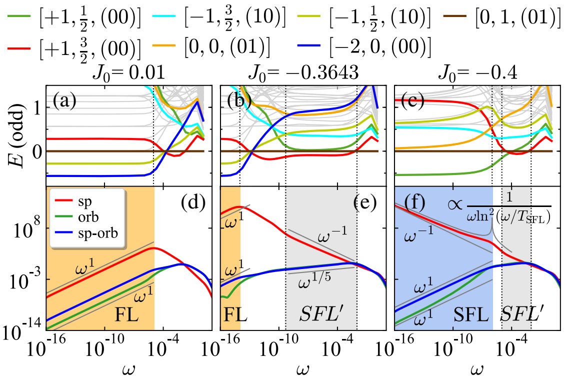

FIG. 2. The phase transition from FL to SFL at $I_0 = 0.01$. (a)–(c) NRG flow diagrams of a Wilson chain with odd length k, with the energy of the lowest [0,1,(01)] multiplet as the reference energy $\mathcal{E}_{\mathrm{ref}}$. The symmetry labels of selected multiplets are shown on top. (d)–(f) Impurity dynamical susceptibility $\chi^{\mathrm{imp}}(\omega)$.

Tables S1–S2 in the Supplemental Material [47] show the CFT results of the fixed point spectra and compare them with the NRG spectra at $J_0 = 0.3$, $I_0 = -0.01$. Both fusion procedures yield the same results, which reproduce the NRG spectra very well. The scaling dimension of the leading boundary operator in the spin, orbital and spin-orbital sectors are found to be $\Delta_{\mathrm{sp}} = \frac{2}{5}$, $\Delta_{\mathrm{orb}} = \frac{3}{5}$ and $\Delta_{\mathrm{sp\text{-}orb}} = 1$, respectively. They are also consistent with the CFT results in [49] for either a spin $\mathrm{SU}(2)_3$ Kondo model ($\Delta_{\mathrm{sp}} = 2/(2+3)$, $\Delta_{\mathrm{orb}} = 3/(2+3)$), or an orbital $\mathrm{SU}(3)_2$ Kondo model ($\Delta_{\mathrm{sp}} = 2/(3+2)$,

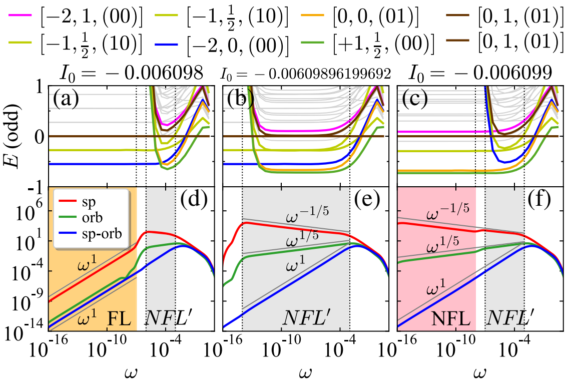

FIG. 3. Analogous to Fig. 2, but for the phase transition from FL to NFL at $J_0 = 0.3$.

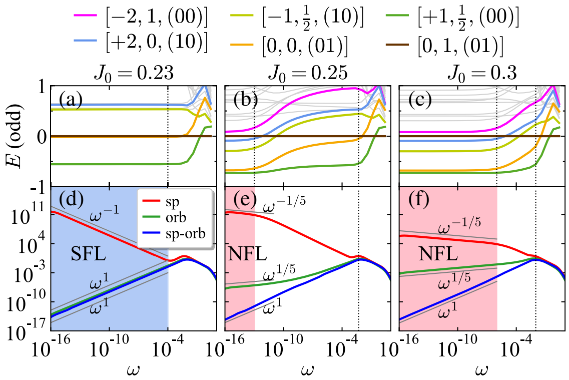

FIG. 4. Analogous to Fig. 2, but for the phase transition from SFL to NFL at $I_0 = -0.01$.

$\Delta_{\mathrm{orb}} = 3/(3+2)$). The power laws of dynamical susceptibilities can then be understood by the CFT procedure [43] $\chi_{\mathrm{sp}}^{\mathrm{imp}} \sim \omega^{2\Delta_{\mathrm{sp}}-1} = \omega^{-1/5}$, $\chi_{\mathrm{orb}}^{\mathrm{imp}} \sim \omega^{2\Delta_{\mathrm{orb}}-1} = \omega^{1/5}$ and $\chi_{\mathrm{sp\text{-}orb}}^{\mathrm{imp}} \sim \omega^{2\Delta_{\mathrm{sp\text{-}orb}}-1} = \omega^{1}$, respectively.

The impurity entropy and the CFT analysis both suggest that the spin $\mathrm{SU}(2)_3$ and orbital $\mathrm{SU}(3)_2$ Kondo models with overscreened fixed points are actually equivalent and complementary descriptions of this NFL fixed point. It indicates an alternating spin $\mathrm{SU}(2)_3$ and orbital $\mathrm{SU}(3)_2$ overscreening process by successively binding one electron or one hole, as illustrated by the cartoon picture at the bottom right of Fig. 1(a), similar in spirit to that of Nozières and Blandin [60]. To be specific, the strong AFM orbital coupling binds the bare impurity $Q_{\mathrm{imp}} = [0,1,(01)]$ and one bath electron $[+1,\frac{1}{2},(10)]$ into a fully screened orbital singlet with either spin $\frac{3}{2}$ or $\frac{1}{2}$: $[0,1,(01)] \otimes [+1,\frac{1}{2},(10)] \to [+1,\frac{3}{2},(00)] \oplus [+1,\frac{1}{2},(00)]$. In the FL phase, the spin $\frac{3}{2}$ multiplet has the lower energy; it can then bind three holes to form a fully screened spin and orbital singlet [43]: $[+1,\frac{3}{2},(00)] \otimes [-3,\frac{3}{2},(00)] \to [-2,0,(00)]$. By contrast, in the NFL regime, the spin $\frac{1}{2}$ multiplet has the lower energy since the spin-orbital coupling I_0 is strongly FM. Next, the AFM spin coupling attempts to screen the spin $\frac{1}{2}$ by coupling it to one hole, to yield a spin singlet,

$$\left[+1,\frac{1}{2},(00)\right] \otimes \left[-1,\frac{1}{2},(01)\right] \to [0,0,(01)], \tag{2a}$$

but the result is an overscreened orbital isospin. Screening the latter by binding an electron,

$$[0,0,(01)] \otimes \left[+1,\frac{1}{2},(10)\right] \to \left[+1,\frac{1}{2},(00)\right], \tag{2b}$$

leads back to an overscreened spin. Overall, this results in a neverending alternation of spin and orbital overscreening, favored by the fact that the multiplets [0,0,(01)] and $[+1,\frac{1}{2},(00)]$ are lowest in energy [see Figs. 3(c), 4(c)], with a very small energy difference.

The special point at $J_0 = I_0 = 0$ corresponds to an $\mathrm{SU}(3)_2$ NFL fixed point (NFL*) with overscreened orbitals and a degenerate impurity spin of $\frac{1}{2}, \frac{3}{2}$. The inset of Fig. 1(a) suggests that the region of NFL actually extends to this point. There we analyze the width of the NFL "funnel," defined by $\delta J_0 = J_0^{c1} - J_0^{c2}$, vs $1/I_0$, where J_0^{c1} (J_0^{c2}) is the phase boundary between FL (SFL) and NFL. It follows $\exp(0.0462/I_0 + 6.57)$, becoming zero only when $I_0 \to 0^-$.

Phase transitions.—T_{FL} on the FL side and T_{SFL} (T_{NFL}, the NFL scale) on the SFL (NFL) side go to zero as the phase boundary is approached. We find that T_{FL}, T_{SFL} and T_{NFL} follow power laws as functions of the control parameters J_0 and I_0, $|J_0 - J_0^c|^\alpha$ and $|I_0 - I_0^c|^\alpha$, to approach exactly zero at the critical values J_0^c and I_0^c, signaling the existence of QCPs [21,22]. The exponents found are $\alpha = 1.8$ in the FL-SFL transition, and $\alpha = 1$ for FL-NFL. We show $T_{\mathrm{FL/SFL}}$ as functions of J_0 at $I_0 = 0.01$ in Fig. 1(b), and $T_{\mathrm{FL/NFL}}$ as functions of I_0 at $J_0 = 0.3$ in Fig. 1(c). More data are shown in Fig. S5 [47].

When approaching the QCP in the FL-SFL transition as in Fig. 2 by decreasing J_0, the spin-orbital separation window [7,50] increases a lot, as seen in Figs. 2(b) and 2(e) for $J_0 = -0.3643$, and a wide crossover regime, *SFL′*, forms at intermediate energies. There the impurity entropy S_{imp} evaluates to $\ln[(1+\sqrt{5})/2] + \ln 3$ [green curve in Fig. 1(d)], corresponding to an orbital overscreened $\mathrm{SU}(3)_2$ fixed point, coupled to a fluctuating spin-1 moment. This is consistent with the recent findings in the region $I_0 = 0$ and $J_0 \to 0^+$ in [61]. $\chi_{\mathrm{orb}}^{\mathrm{imp}}$ follows a universal power-law of $\omega^{1/5}$, showing similarity with the NFL phase due to the same orbital $\mathrm{SU}(3)_2$ overscreening, while $\chi_{\mathrm{sp}}^{\mathrm{imp}}$ follows an approximate power law (with some non-power-law corrections, see the Supplemental Material [47]). Across the phase transition, the multiplet $[+1,\frac{1}{2},(00)]$ is pushed down to be the new ground state, while the original ground state $[-2,0,(00)]$ of the FL phase is pushed up to very high energy.

When approaching the QCP in the FL-NFL transition as illustrated in Fig. 3, the fine-tuning of I_0 generates a large crossover regime *NFL′* at intermediate energies [Figs. 3(b) and 3(e)], where the set of low-lying states is simply the union of those of the FL and NFL spectra (see Table S4 in the Supplemental Material [47]). *NFL′* thus represents a "level-crossing" scenario [47,51,52], involving two orthogonal low-energy subspaces whose levels cross when I_0 is tuned. When sufficiently close, both subspaces contribute to thermodynamic and dynamical properties. Here, the FL and NFL compete in the intermediate-energy regime, and I_0 determines either FL [Figs. 3(a) and 3(d)] or NFL [Figs. 3(c) and 3(f)] to be the low-energy fixed point.

The impurity entropy $S_{\mathrm{imp}}^{NFL'}$ evaluates to $\ln(e^{S_{\mathrm{imp}}^{\mathrm{FL}}} + e^{S_{\mathrm{imp}}^{\mathrm{NFL}}}) = \ln\{1 + [(1+\sqrt{5})/2]\}$ [red curve in Fig. 1(d)], not $\ln 1 + \ln[(1+\sqrt{5})/2]$, because the FL and NFL subspaces do not overlap. Hence the total effective impurity degrees of freedom are the *sum* of the contributions of those two sectors [47]. χ^{imp} of NFL' follow the same power laws as NFL because the NFL part dominates in this regime. For more details on NFL', see the Supplemental Material [47].

The transition from SFL to NFL shown in Fig. 4 confirms the picture of alternating overscreenings. Tuning J_0 to be more AFM, the state [0,0,(01)] is pushed down to be nearly degenerate with the ground state $[+1, \frac{1}{2}, (00)]$ [Fig. 4(b)], signaling the start of the alternating overscreening process. $\chi_{\mathrm{sp}}^{\mathrm{imp}}$ bends downward away from the ω^{-1} behavior towards an $\omega^{-1/5}$ dependence, while $\chi_{\mathrm{orb}}^{\mathrm{imp}}$ bends upward away from the ω-linear behavior towards an $\omega^{1/5}$ dependence. $\chi_{\text{sp-orb}}^{\mathrm{imp}}$ still follows ω^1.

Conclusion.—To summarize, we have presented a global phase diagram of the 3soK model. This allows us to follow the suppression of the coherence scale in Hund metals down to zero energy. The new NFL phase contains the essential ingredients needed to understand the actual incoherent behavior seen above T_{FL}. Recent advances in the physics of cold atoms might actually offer a concrete realization of the phase diagram of the model studied. Indeed it has been recently demonstrated that it is possible to simulate SU(N) impurity models with tunable exchange interactions reaching both FM and AFM regimes [62,63].

The iron pnictides display an intriguing QCP, as for example in $\mathrm{BaFe_2(As_{1-x}P_x)_2}$ [18,64–66], where a divergent electron mass and concomitant destruction of the FL state was observed. This QCP has motivated several theoretical studies [67–69]. Further progress from the perspective of this work would require the DMFT self-consistency condition and more realistic band structures. In the DMFT treatment of a lattice model, the SFL and the NFL phases are expected to turn into magnetically ordered states, but the impurity model studied here with its power-law singularities would describe the behavior above T_{FL}.

The approach presented here, which takes into account the Hund's coupling and the multiorbital nature, is in the same spirit as the ideas of local quantum criticality used to describe Kondo breakdown using impurity models [70], so it would then be also useful for unconventional quantum phase transitions observed in other heavy-fermion materials [71–74]. The global phase diagram of this 3soK model will also have potential impact on the studies of real multichannel spin and (or) orbital Kondo systems or quantum dots systems, for instance, generalize the studies in [75–79] to three-channel cases.

We thank H. Miao and R. Fernandes for helpful discussion. E. W., K. M. S., and J. vD. are supported by the Deutsche Forschungsgemeinschaft under Germany's Excellence Strategy–EXC-2111-390814868, and S.-S. B. L. by Grant No. LE3883/2-1. A. W. was supported by the U.S. Department of Energy, Office of Basic Energy Sciences, under Contract No. DE-SC0012704. Y. W. and G. K. were supported by the U.S. Department of Energy, Office of Science, Basic Energy Sciences as a part of the Computational Materials Science Program through the Center for Computational Design of Functional Strongly Correlated Materials and Theoretical Spectroscopy.

[1] L. D. Landau, E. M. Lifshitz, and L. P. Pitaevskij, in *Statistical Physics: Part 2: Theory of Condensed State*, Landau and Lifshitz Course of Theoretical Physics (Oxford, England, 1980).

[2] V. J. Emery and S. A. Kivelson, Superconductivity in Bad Metals, Phys. Rev. Lett. **74**, 3253 (1995).

[3] Z. P. Yin, K. Haule, and G. Kotliar, Kinetic frustration and the nature of the magnetic and paramagnetic states in iron pnictides and iron chalcogenides, Nat. Mater. **10**, 932 (2011).

[4] P. Werner, E. Gull, M. Troyer, and A. J. Millis, Spin Freezing Transition and Non-Fermi-Liquid Self-Energy in a Three-Orbital Model, Phys. Rev. Lett. **101**, 166405 (2008).

[5] L. Medici, J. Mravlje, and A. Georges, Janus-Faced Influence of Hund's Rule Coupling in Strongly Correlated Materials, Phys. Rev. Lett. **107**, 256401 (2011).

[6] A. Georges, L. Medici, and J. Mravlje, Strong correlations from Hund's coupling, Annu. Rev. Condens. Matter Phys. **4**, 137 (2013).

[7] K. M. Stadler, G. Kotliar, A. Weichselbaum, and J. von Delft, Hundness versus Mottness in a three-band Hubbard-Hund model: On the origin of strong correlations in Hund metals, Ann. Phys. (Amsterdam) **405**, 365 (2019).

[8] A. W. Tyler, A. P. Mackenzie, S. Nishizaki, and Y. Maeno, High-temperature resistivity of $\mathrm{Sr_2RuO_4}$: Bad metallic transport in a good metal, Phys. Rev. B **58**, R10107 (1998).

[9] A. P. Mackenzie, J. W. Reiner, A. W. Tyler, L. M. Galvin, S. R. Julian, M. R. Beasley, T. H. Geballe, and A. Kapitulnik, Observation of quantum oscillations in the electrical resistivity of $\mathrm{SrRuO_3}$, Phys. Rev. B **58**, R13318 (1998).

[10] M. Schneider, D. Geiger, S. Esser, U. S. Pracht, C. Stingl, Y. Tokiwa, V. Moshnyaga, I. Sheikin, J. Mravlje, M. Scheffler, and P. Gegenwart, Low-Energy Electronic Properties of Clean $\mathrm{CaRuO_3}$: Elusive Landau Quasiparticles, Phys. Rev. Lett. **112**, 206403 (2014).

[11] J. Mravlje, M. Aichhorn, T. Miyake, K. Haule, G. Kotliar, and A. Georges, Coherence-Incoherence Crossover and the Mass-Renormalization Puzzles in $\mathrm{Sr_2RuO_4}$, Phys. Rev. Lett. **106**, 096401 (2011).

[12] T. Kondo, M. Ochi, M. Nakayama, H. Taniguchi, S. Akebi, K. Kuroda, M. Arita, S. Sakai, H. Namatame, M. Taniguchi, Y. Maeno, R. Arita, and S. Shin, Orbital-Dependent Band Narrowing Revealed in an Extremely Correlated Hund's Metal Emerging on the Topmost Layer of $\mathrm{Sr_2RuO_4}$, Phys. Rev. Lett. **117**, 247001 (2016).

[13] X. Deng, K. Haule, and G. Kotliar, Transport Properties of Metallic Ruthenates: A DFT + DMFT Investigation, Phys. Rev. Lett. **116**, 256401 (2016).

[14] Y. Kamihara, T. Watanabe, M. Hirano, and H. Hosono, Iron-based layered superconductor La$[O_{1-x}F_x]$FeAs ($x = 0.05$–0.12) with $T_c = 26$ K, J. Am. Chem. Soc. **130**, 3296 (2008).

[15] G. R. Stewart, Superconductivity in iron compounds, Rev. Mod. Phys. **83**, 1589 (2011).

[16] F. Hardy, A. E. Böhmer, D. Aoki, P. Burger, T. Wolf, P. Schweiss, R. Heid, P. Adelmann, Y. X. Yao, G. Kotliar, J. Schmalian, and C. Meingast, Evidence of Strong Correlations and Coherence-Incoherence Crossover in the Iron Pnictide Superconductor KFe_2As_2, Phys. Rev. Lett. **111**, 027002 (2013).

[17] M. Yi, D. H. Lu, R. Yu, S. C. Riggs, J.-H. Chu, B. Lv, Z. K. Liu, M. Lu, Y.-T. Cui, M. Hashimoto, S.-K. Mo, Z. Hussain, C. W. Chu, I. R. Fisher, Q. Si, and Z.-X. Shen, Observation of Temperature-Induced Crossover to an Orbital-Selective Mott Phase in $A_xFe_{2-y}Se_2$ (A = K, Rb) Superconductors, Phys. Rev. Lett. **110**, 067003 (2013).

[18] P. Walmsley, C. Putzke, L. Malone, I. Guillamón, D. Vignolles, C. Proust, S. Badoux, A. I. Coldea, M. D. Watson, S. Kasahara, Y. Mizukami, T. Shibauchi, Y. Matsuda, and A. Carrington, Quasiparticle Mass Enhancement Close to the Quantum Critical Point in $BaFe_2(As_{1-x}P_x)_2$, Phys. Rev. Lett. **110**, 257002 (2013).

[19] K Haule and G Kotliar, Coherence-incoherence crossover in the normal state of iron oxypnictides and importance of Hund's rule coupling, New J. Phys. **11**, 025021 (2009).

[20] Z. P. Yin, K. Haule, and G. Kotliar, Fractional power-law behavior and its origin in iron-chalcogenide and ruthenate superconductors: Insights from first-principles calculations, Phys. Rev. B **86**, 195141 (2012).

[21] S. Sachdev, Quantum criticality: Competing ground states in low dimensions, Science **288**, 475 (2000).

[22] S. Sachdev, Quantum phase transitions, in *Handbook of Magnetism and Advanced Magnetic Materials* (Wiley-Interscience, , New Jersey, 2007).

[23] S. Sachdev, *Quantum Phase Transitions*, 2nd ed. (Cambridge University Press, Cambridge, England, 2011).

[24] S. Sachdev, Understanding correlated electron systems by a classification of mott insulators, Ann. Phys. (Amsterdam) **303**, 226 (2003).

[25] D.-H. Lee and J. M. Leinaas, Mott Insulators Without Symmetry Breaking, Phys. Rev. Lett. **92**, 096401 (2004).

[26] A. Georges, G. Kotliar, W. Krauth, and M. J. Rozenberg, Dynamical mean-field theory of strongly correlated fermion systems and the limit of infinite dimensions, Rev. Mod. Phys. **68**, 13 (1996).

[27] A. I. Lichtenstein, M. I. Katsnelson, and G. Kotliar, Finite-Temperature Magnetism of Transition Metals: An ab initio Dynamical Mean-Field Theory, Phys. Rev. Lett. **87**, 067205 (2001).

[28] M. Aichhorn, L. Pourovskii, V. Vildosola, M. Ferrero, O. Parcollet, T. Miyake, A. Georges, and S. Biermann, Dynamical mean-field theory within an augmented plane-wave framework: Assessing electronic correlations in the iron pnictide LaFeAsO, Phys. Rev. B **80**, 085101 (2009).

[29] K. Haule, C.-H. Yee, and K. Kim, Dynamical mean-field theory within the full-potential methods: Electronic structure of $CeIrIn_5$, $CeCoIn_5$, and $CeRhIn_5$, Phys. Rev. B **81**, 195107 (2010).

[30] G. Kotliar, S. Y. Savrasov, K. Haule, V. S. Oudovenko, O. Parcollet, and C. A. Marianetti, Electronic structure calculations with dynamical mean-field theory, Rev. Mod. Phys. **78**, 865 (2006).

[31] J. H. Shim, K. Haule, and G. Kotliar, Fluctuating valence in a correlated solid and the anomalous properties of δ-plutonium, Nature (London) **446**, 513 (2007).

[32] K. Haule, J. H. Shim, and G. Kotliar, Correlated Electronic Structure of $LaO_{1-x}F_xFeAs$, Phys. Rev. Lett. **100**, 226402 (2008).

[33] K. Haule and G. Kotliar, Arrested Kondo effect and hidden order in URu_2Si_2, Nat. Phys. **5**, 796 (2009).

[34] X. Deng, A. Sternbach, K. Haule, D. N. Basov, and G. Kotliar, Shining Light on Transition-Metal Oxides: Unveiling the Hidden Fermi Liquid, Phys. Rev. Lett. **113**, 246404 (2014).

[35] H. Shinaoka, S. Hoshino, M. Troyer, and P. Werner, Phase Diagram of Pyrochlore Iridates: All-In–All-Out Magnetic Ordering and Non-Fermi-Liquid Properties, Phys. Rev. Lett. **115**, 156401 (2015).

[36] M. Kim, J. Mravlje, M. Ferrero, O. Parcollet, and A. Georges, Spin-Orbit Coupling and Electronic Correlations in Sr_2RuO_4, Phys. Rev. Lett. **120**, 126401 (2018).

[37] R. Bulla, T. A. Costi, and T. Pruschke, Numerical renormalization group method for quantum impurity systems, Rev. Mod. Phys. **80**, 395 (2008).

[38] I. Affleck, A current algebra approach to the Kondo effect, Nucl. Phys. **B336**, 517 (1990).

[39] I. Affleck and A. W. W. Ludwig, The Kondo effect, conformal field theory and fusion rules, Nucl. Phys. **B352**, 849 (1991).

[40] I. Affleck and A. W. W. Ludwig, Critical theory of overscreened Kondo fixed points, Nucl. Phys. **B360**, 641 (1991).

[41] I. Affleck and A. W. W. Ludwig, Exact conformal-field-theory results on the multichannel Kondo effect: Single-fermion Green's function, self-energy, and resistivity, Phys. Rev. B **48**, 7297 (1993).

[42] A. W. W. Ludwig and I. Affleck, Exact conformal-field-theory results on the multi-channel Kondo effect: Asymptotic three-dimensional space- and time-dependent multi-point and many-particle Green's functions, Nucl. Phys. **B428**, 545 (1994).

[43] E. Walter, K. M. Stadler, S. S. B. Lee, Y. Wang, G. Kotliar, A. Weichselbaum, and J. von Delft, Uncovering non-fermi-liquid behavior in Hund metals: Conformal field theory analysis of a $SU(2) \times SU(3)$ spin-orbital Kondo model, arXiv:1908.04362.

[44] C. Aron and G. Kotliar, Analytic theory of Hund's metals: A renormalization group perspective, Phys. Rev. B **91**, 041110(R) (2015).

[45] A. Weichselbaum, Non-Abelian symmetries in tensor networks: A quantum symmetry space approach, Ann. Phys. (Amsterdam) **327**, 2972 (2012).

[46] A. Weichselbaum and J. von Delft, Sum-Rule Conserving Spectral Functions from the Numerical Renormalization Group, Phys. Rev. Lett. **99**, 076402 (2007).

[47] See the Supplemental Material at http://link.aps.org/supplemental/10.1103/PhysRevLett.124.136406 for computational details, more NRG flow diagrams and dynamical susceptibilities in Sec. S-I, more data of $T_{\rm FL}$, $T_{\rm SFL}$, and $T_{\rm NFL}$ as functions of J_0 and I_0 in Sec. S-II, CFT analysis in Sec. S-III, the detailed interpretation the "level-crossing" scenario and a proof of the impurity entropy $S_{\rm imp}$ of NFL' in Sec. S-IV, the impurity spectral functions $A_t(\omega)$ in Sec. S-V, the coefficients of specific heat $\gamma(T)$ in Sec. S-VI, the impurity static susceptibilities for SFL and NFL phases in Sec. S-VII, the energy difference of multiplets $[+1,\frac{1}{2},(00)]$ and $[+1,\frac{3}{2},(00)]$ along the phase boundary in Sec. S-VIII, the justification of the 3soK model in Sec. S-IX, the dependence on the discretization parameter Λ in Sec. S-X, and the irreducible representations of SU(3) in Sec. S-XI. The Supplemental Material includes Refs. [7,43,48–57].

[48] W. Koller, A. C. Hewson, and D. Meyer, Singular dynamics of underscreened magnetic impurity models, Phys. Rev. B **72**, 045117 (2005).

[49] O. Parcollet, A. Georges, G. Kotliar, and A. Sengupta, Overscreened multichannel SU(N) Kondo model: Large-N solution and conformal field theory, Phys. Rev. B **58**, 3794 (1998).

[50] K. M. Stadler, Z. P. Yin, J. von Delft, G. Kotliar, and A. Weichselbaum, Dynamical Mean-Field Theory Plus Numerical Renormalization-Group Study of Spin-Orbital Separation in a Three-Band Hund Metal, Phys. Rev. Lett. **115**, 136401 (2015).

[51] B. Sbierski, M. Hanl, A. Weichselbaum, H. E. Türeci, M. Goldstein, L. I. Glazman, J. von Delft, and A. İmamoğlu, Proposed Rabi-Kondo Correlated State in a Laser-Driven Semiconductor Quantum Dot, Phys. Rev. Lett. **111**, 157402 (2013).

[52] S.-S. B. Lee, J. von Delft, and M. Goldstein, Non-Fermi-liquid Kondo screening under Rabi driving, Phys. Rev. B **101**, 085110 (2020).

[53] T. A. Costi, Kondo Effect in a Magnetic Field and the Magnetoresistivity of Kondo Alloys, Phys. Rev. Lett. **85**, 1504 (2000).

[54] C. Hong, G. Yoo, J. Park, M.-K. Cho, Y. Chung, H.-S. Sim, D. Kim, H. Choi, V. Umansky, and D. Mahalu, Attractive coulomb interactions in a triple quantum dot, Phys. Rev. B **97**, 241115(R) (2018).

[55] A. Hamo, A. Benyamini, I. Shapir, I. Khivrich, J. Waissman, K. Kaasbjerg, Y. Oreg, F. von Oppen, and S. Ilani, Electron attraction mediated by coulomb repulsion, Nature (London) **535**, 395 (2016).

[56] G. Yoo, J. Park, S.-S. B. Lee, and H.-S. Sim, Anisotropic Charge Kondo Effect in a Triple Quantum Dot, Phys. Rev. Lett. **113**, 236601 (2014).

[57] A. Weichselbaum, S. Capponi, P. Lecheminant, A. M. Tsvelik, and A. M. Läuchli, Unified phase diagram of antiferromagnetic SU(N) spin ladders, Phys. Rev. B **98**, 085104 (2018).

[58] P. Coleman and C. Pépin, Singular fermi liquid behavior in the underscreened Kondo model, Phys. Rev. B **68**, 220405 (R) (2003).

[59] P. Mehta, N. Andrei, P. Coleman, L. Borda, and G. Zarand, Regular and singular fermi-liquid fixed points in quantum impurity models, Phys. Rev. B **72**, 014430 (2005).

[60] Ph. Nozires and A. Blandin, Kondo effect in real metals, J. Phys. France **41**, 193 (1980).

[61] A. Horvat, R. Zitko, and J. Mravlje, Non-fermi-liquid fixed point in multi-orbital Kondo impurity model relevant for Hund's metals, arXiv:1907.07100.

[62] F. Scazza, C. Hofrichter, M. Höfer, P. C. De Groot, I. Bloch, and S. Fölling, Observation of two-orbital spin-exchange interactions with ultracold SU(N)-symmetric fermions, Nat. Phys. **10**, 779 (2014).

[63] L. Riegger, N. D. Oppong, M. Höfer, D. R. Fernandes, I. Bloch, and S. Fölling, Localized Magnetic Moments with Tunable Spin Exchange in a Gas of Ultracold Fermions, Phys. Rev. Lett. **120**, 143601 (2018).

[64] S. Jiang, H. Xing, G. Xuan, C. Wang, Z. Ren, C. Feng, J. Dai, Z. Xu, and G. Cao, Superconductivity up to 30 k in the vicinity of the quantum critical point in $\mathrm{BaFe_2(As_{1-x}P_x)_2}$, J. Phys. Condens. Matter **21**, 382203 (2009).

[65] S. Kasahara, T. Shibauchi, K. Hashimoto, K. Ikada, S. Tonegawa, R. Okazaki, H. Shishido, H. Ikeda, H. Takeya, K. Hirata, T. Terashima, and Y. Matsuda, Evolution from non-Fermi- to Fermi-liquid transport via isovalent doping in $\mathrm{BaFe_2(As_{1-x}P_x)_2}$ superconductors, Phys. Rev. B **81**, 184519 (2010).

[66] E. Abrahams and Q. Si, Quantum criticality in the iron pnictides and chalcogenides, J. Phys. Condens. Matter **23**, 223201 (2011).

[67] R. M. Fernandes, S. Maiti, P. Wölfle, and A. V. Chubukov, How Many Quantum Phase Transitions Exist Inside the Superconducting Dome of the Iron Pnictides?, Phys. Rev. Lett. **111**, 057001 (2013).

[68] A. Levchenko, M. G. Vavilov, M. Khodas, and A. V. Chubukov, Enhancement of the London Penetration Depth in Pnictides at the Onset of Spin-Density-Wave Order Under Superconducting Dome, Phys. Rev. Lett. **110**, 177003 (2013).

[69] D. Chowdhury, B. Swingle, E. Berg, and S. Sachdev, Singularity of the London Penetration Depth at Quantum Critical Points in Superconductors, Phys. Rev. Lett. **111**, 157004 (2013).

[70] Q. Si, S. Rabello, K. Ingersent, and J. L. Smith, Locally critical quantum phase transitions in strongly correlated metals, Nature (London) **413**, 804 (2001).

[71] G. R. Stewart, Heavy-fermion systems, Rev. Mod. Phys. **56**, 755 (1984).

[72] H. Takagi, C. Urano, S. Kondo, M. Nohara, Y. Ueda, T. Shiraki, and T. Okubo, Transport properties of metallic $\mathrm{LiV_2O_4}$ single crystals–heavy mass Fermi liquid behavior, Mater. Sci. Eng. B **63**, 147 (1999).

[73] C. Urano, M. Nohara, S. Kondo, F. Sakai, H. Takagi, T. Shiraki, and T. Okubo, $\mathrm{LiV_2O_4}$ Spinel as a Heavy-Mass Fermi Liquid: Anomalous Transport and Role of Geometrical Frustration, Phys. Rev. Lett. **85**, 1052 (2000).

[74] P. Gegenwart, Q. Si, and F. Steglich, Quantum criticality in heavy-fermion metals, Nat. Phys. **4**, 186 (2008).

[75] P. Trocha, Orbital kondo effect in double quantum dots, Phys. Rev. B **82**, 125323 (2010).

[76] P. P. Baruselli, R. Requist, M. Fabrizio, and E. Tosatti, Ferromagnetic Kondo Effect in a Triple Quantum Dot System, Phys. Rev. Lett. **111**, 047201 (2013).

[77] L. Zhu, G. Woltersdorf, and J. Zhao, Observation of orbital two-channel Kondo effect in a ferromagnetic L10-MnGa film, Sci. Rep. **6**, 34549 (2016).

[78] L. Pan, Y. D. Wang, Z. H. Li, J. H. Wei, and Y. J. Yan, Kondo effect in double quantum dots with ferromagnetic RKKY interaction, J. Phys. Condens. Matter **29**, 025601 (2016).

[79] Z. Shi, E. M. Nica, and I. Affleck, Kondo effect due to a hydrogen impurity in graphene: A multichannel kondo problem with diverging hybridization, Phys. Rev. B **100**, 125158 (2019).

Supplemental Material for:
Global phase diagram of a spin-orbital Kondo impurity model and the suppression of Fermi-liquid scale

Y. Wang,[1] E. Walter,[2] S.-S. B. Lee,[2] K. M. Stadler,[2] J. von Delft,[2] A. Weichselbaum,[1, 2] and G. Kotliar[1, 3]

[1] *Department of Condensed Matter Physics and Materials Science, Brookhaven National Laboratory, Upton, New York 11973, USA*
[2] *Arnold Sommerfeld Center for Theoretical Physics, Center for NanoScience, and Munich Center for Quantum Science and Technology, Ludwig-Maximilians-Universität München, 80333 Munich, Germany*
[3] *Department of Physics and Astronomy, Rutgers University, Piscataway, New Jersey 08856, USA*

(Dated: March 18, 2020)

S-I. NRG FLOW DIAGRAMS AND DYNAMICAL SUSCEPTIBILITES

In Figs. S1-S3, we replot the NRG flow diagrams shown in the main text to add the flow diagrams of Wilson chains with even length k. Here we follow the standard convention that H_0, the Hamiltonian of the impurity together with the bath site at the location of the impurity, i.e., the bath site $k = 0$, is a Wilson chain of even length. We use $K_0 = 0.3$, $\Lambda = 4$ and half-bandwidth $D = 1$, throughout. In Fig. S1, we also add flow diagrams computed for $J_0 = -0.3643861$ and $J_0 = -0.3644$ to show more details of the phase transitions from FL to SFL. In Fig. S6, we compare the NRG flow diagrams of the NFL fixed point at $J_0 = 0.3, I_0 = -0.01$ with those at $J_0 = 0.6, I_0 = -0.13$. As we move from the former to the latter, i.e. deeper into the NFL regimes, the eigenvalues of the fixed point spectrum change; this is caused by particle-hole asymmetry and can be explained by the CFT analysis [see Table S3] in Sec. S-III.

The imaginary part of the dynamical susceptibilities of spin, orbital and spin-orbital operators at the impurity site or the zeroth bath site are defined as

$$\chi_{\text{sp}}^{\text{imp,bath}}(\omega) = -\frac{1}{3\pi}\text{Im}\sum_{\alpha}\langle S^{\alpha}||S^{\alpha}\rangle_{\omega}, \tag{S1a}$$

$$\chi_{\text{orb}}^{\text{imp,bath}}(\omega) = -\frac{1}{8\pi}\text{Im}\sum_{a}\langle T^{a}||T^{a}\rangle_{\omega}, \tag{S1b}$$

$$\chi_{\text{sp-orb}}^{\text{imp,bath}}(\omega) = -\frac{1}{24\pi}\text{Im}\sum_{\alpha,a}\langle S^{\alpha}T^{a}||S^{\alpha}T^{a}\rangle_{\omega}, \tag{S1c}$$

where, the operators S^{α} and T^{a} refer to either the impurity site (χ^{imp}) or the $k = 0$ bath site (χ^{bath}). The normalization averages over all correlators that are equivalent by the underlying symmetry.

In Fig. S4(a-e), we compare $\chi^{\text{imp}}(\omega)$ (solid lines) and $\chi^{\text{bath}}(\omega)$ (dashed lines). At the parameters we show, both follow the same behavior in the low-energy regimes of FL, SFL and NFL, and the intermediate-energy regimes *SFL′* and *NFL′*.

Figs. S4(f-j) reveal the power laws governing $\chi^{\text{imp}}(\omega)$ shown in the main text and in Figs. S1-S3, by showing the logarithmic derivative,

$$\alpha(\omega) = \frac{\text{d}(\log\chi^{\text{imp}}(\omega))}{\text{d}(\log\omega)}. \tag{S2}$$

If χ^{imp} follows a pure power law, ω^{α}, its logarithmic derivative gives the constant exponent, $\alpha(\omega) = \alpha$. For FL, $\chi^{\text{imp}}(\omega)$ is linear at small ω, $\alpha = 1$, for all the three susceptibilities [Fig. S4(f)], as expected for a FL. For *SFL′* [Fig. S4(g)], $\chi_{\text{orb}}^{\text{imp}}$ and $\chi_{\text{sp-orb}}^{\text{imp}}$ follow a well-defined power law with a constant value of $\alpha = 1/5$. By contrast, $\chi_{\text{sp}}^{\text{imp}}$ does not quite, since $\alpha(\omega)$ shows slight ω-dependence, indicating the presence of some non-power-law corrections. For SFL [Fig. S4(h)], $\alpha(\omega)$ for both spin and orbital first increases and then decreases, and finally approaches -1 and 1, respectively. This confirms the deviation from pure power-law behavior and the singular nature of this fixed point. However, $\chi_{\text{sp-orb}}^{\text{imp}}$ still follows a perfect power law. For *NFL′* [Figs. S4(i)] and NFL [Figs. S4(j)], χ^{imp} show well-defined power laws with $\alpha = -1/5$ for spin, $\alpha = 1/5$ for orbital and $\alpha = 1$ for spin-orbital, which are perfectly consistent with the CFT results presented in Sec. S-III.

S-II. DESTRUCTION OF FERMI-LIQUID SCALE

We define the orbital (spin) Kondo scale T_{orb} (T_{sp}) as the energy where $\chi_{\text{orb (sp)}}^{\text{imp}}$ is maximal. Fig. S5(a) shows T_{sp} (solid lines) and T_{orb} (dashed lines) as functions of $|J_0 - J_0^c|$ for two values of I_0, and Fig. S5(b) shows them as functions of $|I_0 - I_0^c|$ for two values of J_0, where J_0^c and I_0^c are the critical values at the phase transitions. T_{orb} remains large and almost constant throughout. By contrast, T_{sp} decreases in power-law fashion, $|J_0 - J_0^c|^{\alpha}$ and $|I_0 - I_0^c|^{\alpha}$, when approaching the phase boundary. Therefore, a spin-orbital separation (SOS) window [1, 2] forms near the phase boundary, where T_{sp} can be considered as the FL scale, $T_{\text{FL}} = T_{\text{sp}}$, of the problem. At the phase transitions, this FL scale vanishes, and a SFL or NFL scale arises. We define the energy scale characterizing the onset of SFL or NFL behavior [cf. Figs.1(b,c) in the main text], T_{SFL} or T_{NFL}, as the energy

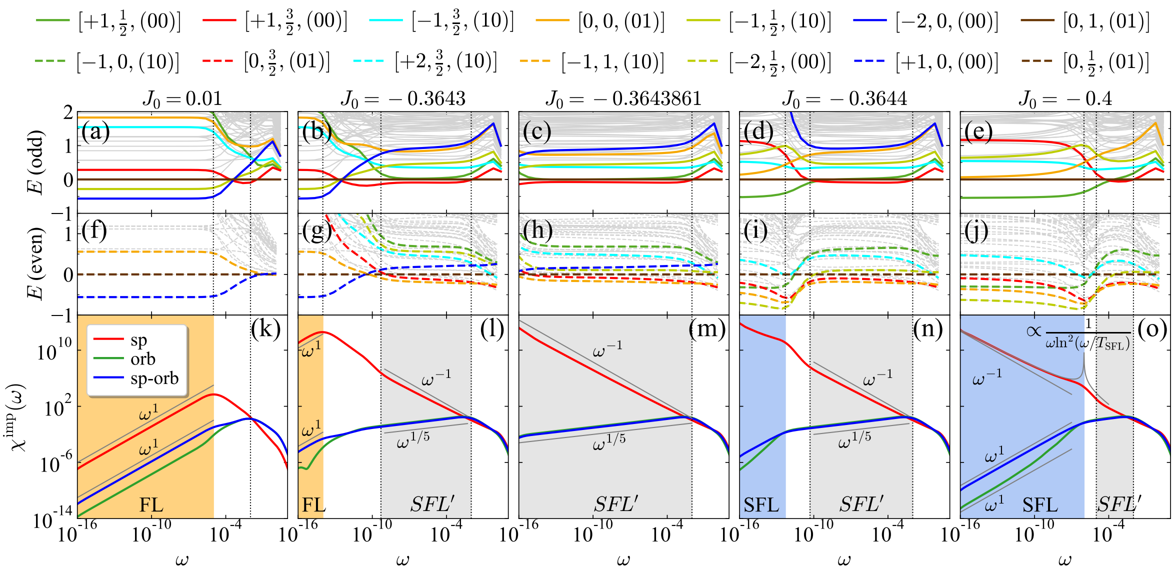

FIG. S1. The phase transition from FL to SFL, with $I_0 = 0.01$. (a-j) Lin-log plots of NRG flow diagrams of Wilson chain with (a-e) odd and (f-j) even length k as functions of the energy scale $\omega_k = \Lambda^{-k/2}$. The energy of multiplets $[0, 1, (01)]$ (brown solid) and $[0, \frac{1}{2}, (01)]$ (brown dashed) are chose as the reference energy $\mathcal{E}_{\mathrm{ref}}$ for odd and even lengths, respectively. The symmetry labels of selected multiplets are shown at the top. (k-o) Log-log plots of the impurity dynamical susceptibilities $\chi^{\mathrm{imp}}(\omega)$ for spin (red), orbital (green), and spin-orbital (blue) operators.

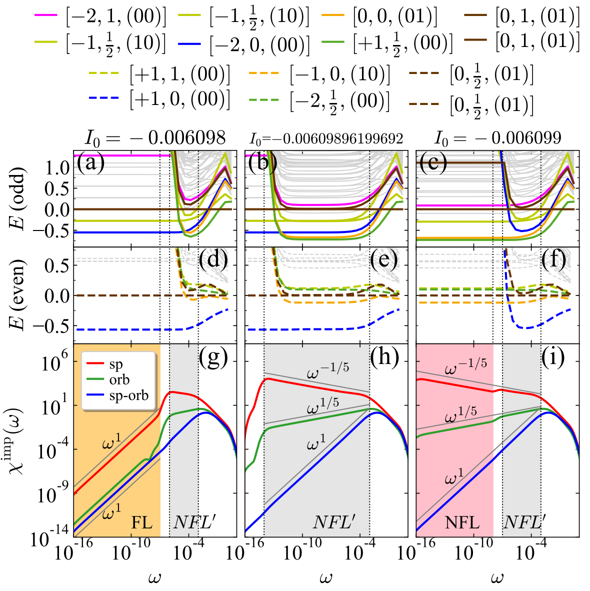

FIG. S2. Analogous to Fig. S1, but for the phase transition from FL to NFL, with $J_0 = 0.3$.

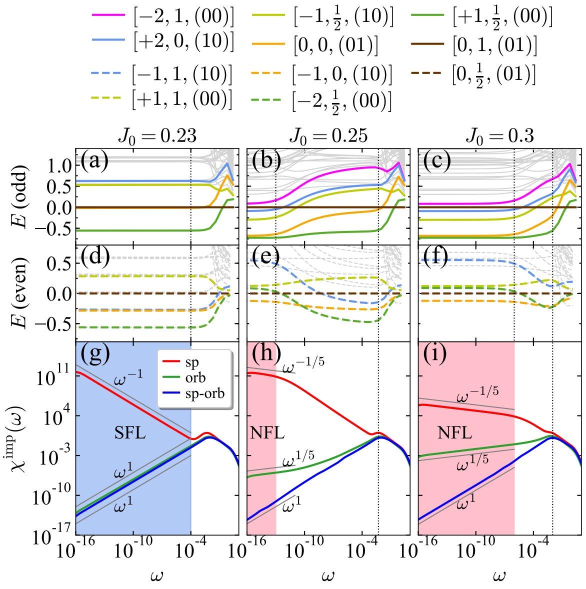

FIG. S3. Analogous to Fig. S1, but for the phase transition from SFL to NFL, with $I_0 = -0.01$.

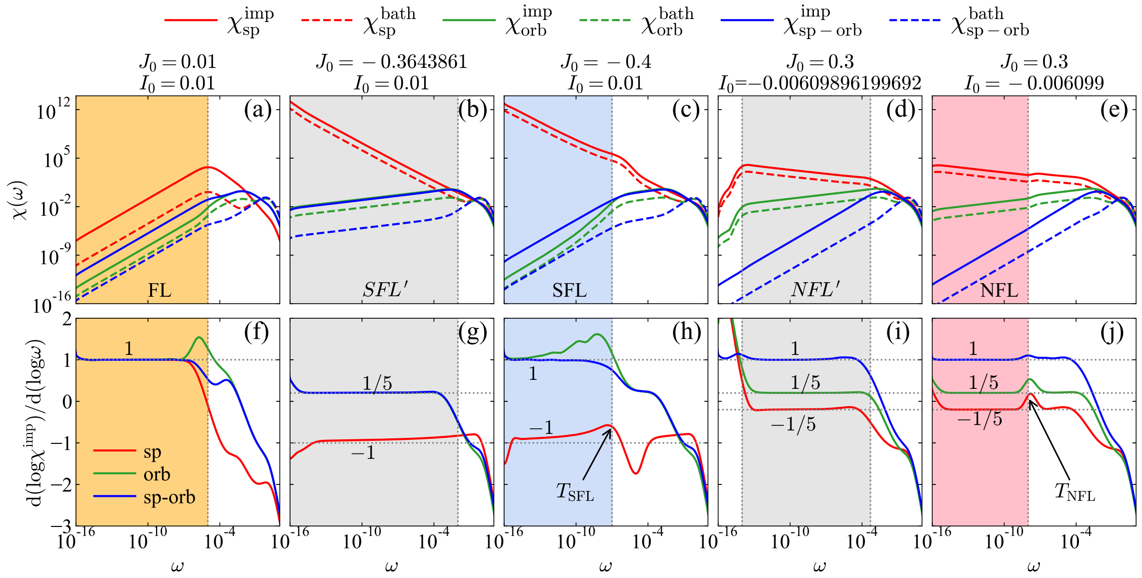

FIG. S4. (a-e) Log-log plots of dynamical susceptibilities at impurity site $\chi^{\rm imp}$ (solid) and the zeroth bath site $\chi^{\rm bath}$ (dashed). (f-j) Logarithmic derivative of the impurity dynamical susceptibilities, $\frac{d(\log\chi^{\rm imp})}{d(\log\omega)}$, plotted using the same logarithmic ω-axis as (a-e). The numbers displayed near the curves give the corresponding (asymptotic) power-law exponents.

where $d(\log\chi_{\rm sp}^{\rm imp}(\omega))/d(\log\omega)$ (Eq. S2) is maximal, as indicated by arrows in Figs. S4(h) and S4(j), respectively. Fig. S5(c) shows $T_{\rm SFL}$ and $T_{\rm NFL}$ as functions of $|J_0-J_0^c|$, and Fig. S5(d) shows them as functions of $|I_0-I_0^c|$. $T_{\rm SFL}$ or $T_{\rm NFL}$ follows the same power-law behavior as $T_{\rm FL}$ close to the phase boundary. The exponents found are α=1.8 in the FL-SFL transition, and α=1 for FL-NFL transition,

$$T_{\rm FL/SFL} \propto |J_0-J_0^c|^{1.8},\ |I_0-I_0^c|^{1.8}, \tag{S3a}$$

$$T_{\rm FL/NFL} \propto |J_0-J_0^c|^{1},\quad |I_0-I_0^c|^{1}. \tag{S3b}$$

S-III. CFT ANALYSIS

In this section, we follow the recently developed U(1)×SU(2)$_3$×SU(3)$_2$ conformal field theory (CFT) approach [3] to reproduce and understand the NRG finite-size spectra and the power laws of the dynamical susceptibilities for the NFL fixed point. We start with a brief summary of the main results of Walter *et al.* [3], and refer the reader to that paper and references therein for more details on the CFT approach. The energy of the lowest multiplet, $Q\equiv[q,S,(\lambda_1\lambda_2)]$, with charge q relative to half-filling, spin S, and SU(3) orbital label in Dynkin notation $(\lambda_1\lambda_2)\equiv(\lambda_1,\lambda_2)$, is given by

$$\begin{aligned} E(Q;\delta q) &= \tfrac{1}{12}(q+\delta q)^2 + \tfrac{1}{5}\kappa_2(S) + \tfrac{1}{5}\kappa_3(\lambda_1,\lambda_2), \\ \kappa_2(S) &= S(S+1), \\ \kappa_3(\lambda_1,\lambda_2) &= \tfrac{1}{3}(\lambda_1^2+\lambda_2^2+\lambda_1\lambda_2+3\lambda_1+3\lambda_2), \end{aligned} \tag{S4}$$

where κ_N represents the eigenvalues of the quadratic Casimir operator for SU(N). δq is a fitting parameter used to take into account particle-hole asymmetry effects, because the three-channel spin-orbital Kondo (3soK) model under consideration does not preserve particle-hole symmetry. Therefore δq depends on the choice of the Kondo couplings J_0, K_0 and I_0. Its specific value can be determined via fits to the NRG finite-size spectra. We simplify the formula by discarding the irrelevant constant term $\delta q^2/12$,

$$E(Q,\delta q) = \tfrac{1}{12}q^2 + \tfrac{\delta q}{6}q + \tfrac{1}{5}\kappa_2(S) + \tfrac{1}{5}\kappa_3(\lambda_1,\lambda_2). \tag{S5}$$

In the main text, the impurity entropy in the NFL regime was found to be, $S_{\rm imp} = \ln\frac{1+\sqrt{5}}{2}$, [see Fig. 1d]. This value can be obtained from either an SU(2)$_3$ Kondo model with overscreened spin, or an SU(3)$_2$ Kondo model with overscreened orbital. In the main text, we also observed that [see Figs. 3(c) and 4(c)] the two lowest NRG eigenstates, $[+1,\frac{1}{2},(00)]$ and $[0,0,(01)]$, are very close in energy, and argued that the NFL phase undergoes a never-ending alternation of spin and orbital overscreening process, converting $[+1,\frac{1}{2},(00)]$ to $[0,0,(01)]$ and back [cf. Eqs. (2a,b) in the main text]. We take this as a motivation to apply either an SU(2)$_3$ fusion procedure in the spin sector, or an SU(3)$_2$ fusion procedure in the orbital sector, i.e. fusing the spectrum of free fermions $Q\equiv[q,S,(\lambda_1\lambda_2)]$ with an effective impurity multiplet, $Q_{\rm imp}^{\rm eff}=[+1,\frac{1}{2},(00)]$ or $Q_{\rm imp}^{\rm eff}=[0,0,(01)]$, to get the spectra of the NFL fixed point $Q'\equiv[q',S',(\lambda_1'\lambda_2')]$. The energy of the free fermions and the NFL spectra

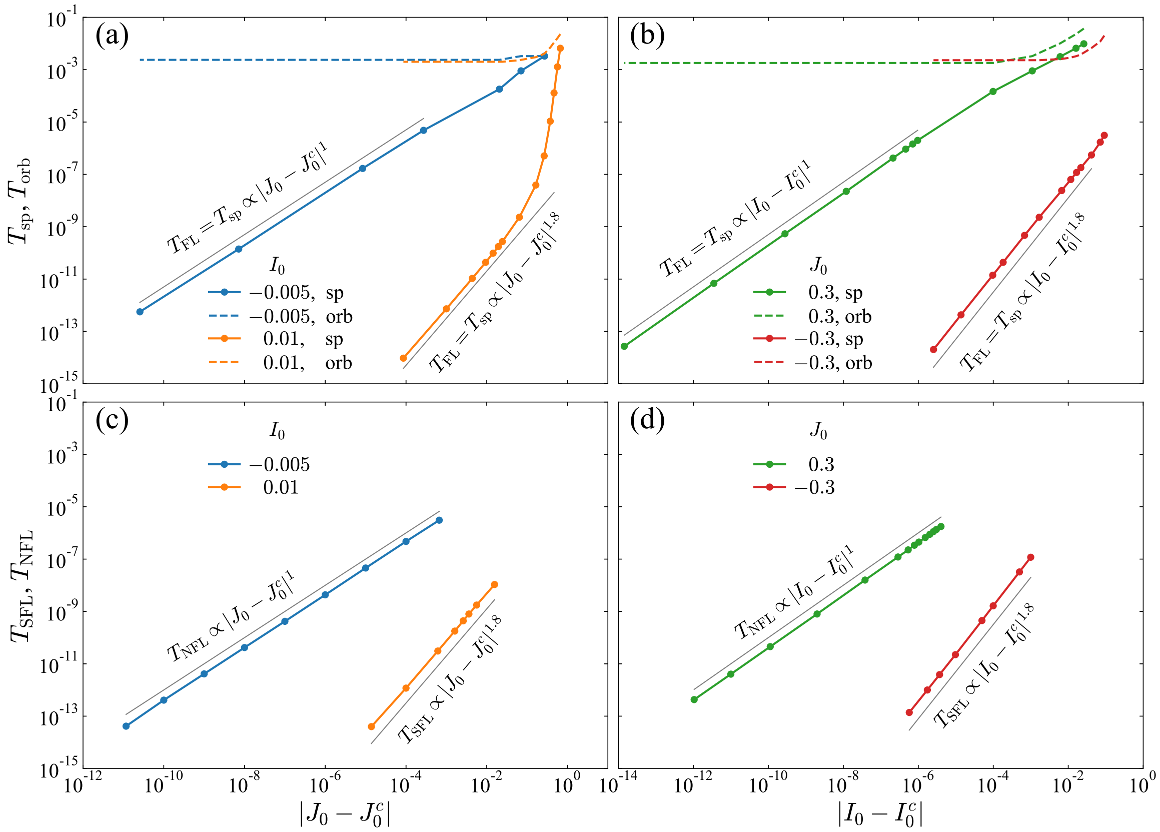

FIG. S5. Log-log plots of the spin and orbital Kondo scales, $T_{\rm sp}$ (solid lines) and $T_{\rm orb}$ (dashed lines), as functions of (a) $|J_0 - J_0^c|$ for two values of I_0, or (b) $|I_0 - I_0^c|$ for two values of J_0. Here, $T_{\rm sp}$ can be considered as the FL scale, $T_{\rm FL} = T_{\rm sp}$, of the problem. The corresponding SFL and NFL scales, $T_{\rm SFL}$ and $T_{\rm NFL}$, as functions of (c) $|J_0 - J_0^c|$, or (d) $|I_0 - I_0^c|$.

are given by $E(Q;0)$ and $E(Q';\delta q)$, respectively. Double fusion of the spectra Q' with the conjugate, i.e., dual representation of the effective impurity multiplet, $\bar{Q}^{\rm eff}_{\rm imp} = [-1, \frac{1}{2}, (00)]$ or $\bar{Q}^{\rm eff}_{\rm imp} = [0, 0, (10)]$, yields the quantum numbers $Q'' \equiv [q'', S'', (\lambda_1''\lambda_2'')]$, characterizing the CFT boundary operators with scaling dimensions given by $\Delta = E(Q'';\delta q)$.

Table S1 and Table S2 list the results of the two alternative fusion procedures with $Q^{\rm eff}_{\rm imp} = [+1, \frac{1}{2}, (00)]$ and $Q^{\rm eff}_{\rm imp} = [0, 0, (01)]$, respectively, and compare them with the energy $E_{\rm NRG}$, computed by NRG for odd-k Wilson chain at $J_0 = 0.3$ and $I_0 = -0.01$. Remarkably, the two fusion procedures yield the *same* fixed point spectrum, indicating that the SU(2)$_3$ and SU(3)$_2$ are actually equivalent and complementary descriptions of this NFL fixed point. Based on the CFT analysis, the energy difference of the mutiplets $[0, 0, (01)]$ and $[+1, \frac{1}{2}, (00)]$ is

$$E([0, 0, (01)]) - E([+1, \tfrac{1}{2}, (00)]) = \frac{1 - 5\delta q}{30}, \qquad \text{(S6)}$$

hence $[+1, \frac{1}{2}, (00)]$ is the ground state when $\delta q < 0.2$, otherwise, $[0, 0, (01)]$ is the ground state. Overall, we find for all of the explored region of the NFL phase that $|\delta q| \ll 1$. Hence the energies above are nearly degenerate. At $J_0 = 0.3$ and $I_0 = -0.01$, the NRG calculation shows that $[+1, \frac{1}{2}, (00)]$ is the ground multiplet and $[0, 0, (01)]$ the first excited one. In Tables S1-S2, $\delta E' = E' - E'([+1, \frac{1}{2}, (00)])$, is the excitation energy given by the CFT analysis. The NRG energies have been shifted and rescaled such that the ground state is zero and the values of $E_{\rm NRG}$ and $\delta E'$ match for the multiplet $[+1, \frac{1}{2}, (11)]$. Then δq is determined by matching $E_{\rm NRG}$ and $\delta E'$ for the multiplet $[0, 0, (01)]$, resulting in $\delta q \simeq 0.0433$. The remainder of the spectra $\delta E'$ and $E_{\rm NRG}$ show good agreement, with deviations smaller than 10%.

In Table S3, we perform the same fusion procedure as that in Table S2, but compared with the NRG results at $J_0 = 0.6$ and $I_0 = -0.13$, that is deep in the NFL phase diagram. The CFT can still perfectly reproduce the eigenlevel spectra in this region. It turns out that $\delta q \approx 0.2135$ is just above 0.2, such that the levels $[+1, \frac{1}{2}, (00)]$ and $[0, 0, (01)]$ have crossed, with the latter

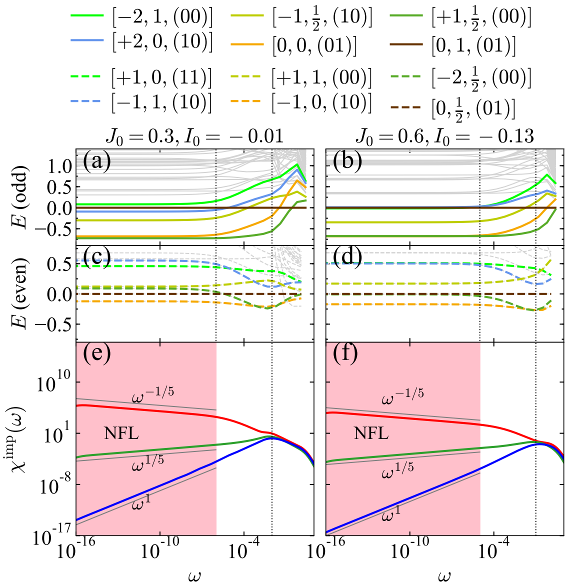

FIG. S6. (a-d) NRG flow diagrams and (e-f) impurity dynamical susceptibilities, comparing the cases (a,c,e) $J_0 = 0.3, I_0 = -0.01$ and (b,d,f) $J_0 = 0.6, I_0 = -0.13$. (a,b) odd-k and (c,d) even-k Wilson chains.

the new ground state. The remainder of the spectrum, which includes further level crossings, can also be perfectly reproduced by this value of δq. The CFT analysis explains the change of the NRG flow diagrams shown in Fig. S6.

With the double fusion procedure shown in Tables S1-S3, the scaling dimension of spin, orbital and spin-orbital operators are found to be $\Delta_{\text{sp}}{=}\frac{2}{5}$, $\Delta_{\text{orb}}{=}\frac{3}{5}$ and $\Delta_{\text{sp-orb}}{=}1$, respectively, as highlighted by color in Tables S1-S3. With this, the power laws of the dynamical susceptibilites are predicted by CFT as [3]

$$\chi^{\text{imp}}_{\text{sp}} \sim \omega^{2\Delta_{\text{sp}}-1} = \omega^{-1/5}, \tag{S7a}$$

$$\chi^{\text{imp}}_{\text{orb}} \sim \omega^{2\Delta_{\text{orb}}-1} = \omega^{1/5}, \tag{S7b}$$

$$\chi^{\text{imp}}_{\text{sp-orb}} \sim \omega^{2\Delta_{\text{sp-orb}}-1} = \omega^{1}. \tag{S7c}$$

in overall excellent agreement with the data in Figs. 3(f) and 4(f) in the main text, and Figs. S2(i), S3(i), S4(j), S6(e,f) in this Supplemental Material.

S-IV. INTERPRETATION OF *NFL′* REGIME

The *NFL′* regime appears as an intermediate fixed point in the NRG flow diagram [see Fig. 3(b) in the main text and Fig. S2(b,e) in this supplemental material], when the system is close to the phase boundary between the FL and NFL phases. The *NFL′* fixed-point spectrum is a "superposition" of the FL and NFL fixed-point spectra. To be more precise, the set of lowest-lying energy levels in the *NFL′* regime [Figs. S2(b,e)] is the union of the sets of the levels in the FL regime [Figs. S2(a,d)] and in the NFL regime [Figs. S2(c,f)] at iterations of the same parity (even or odd length). Table S4 shows this by listing the energy spectrum of *NFL′* for a Wilson chain with odd length at $J_0 = 0.3, I_0 = -0.00609896199692$ [Figs. S2(b)] and comparing it with the FL spectrum just before the phase transition at $I_0 = -0.006098$ [Figs. S2(a)] and the NFL spectrum just after the phase transition at $I_0 = -0.006099$ [Figs. S2(c)]. When the system is slightly away from the phase boundary, there is a reduction from *NFL′* to FL or NFL. During this 'crossover', a set of levels for either FL or NFL regime remains in the low-energy part of the NRG flow diagram, while the other set abruptly drifts towards higher energies due to the intrinsic exponential rescaling of NRG flow diagrams. Such an abrupt drift of a subset of levels is in stark contrast to the typically encountered smooth tangled fixed-point crossovers in impurity models.

The superposition nature of the *NFL′* fixed-point spectrum and the abrupt crossover indicate that the phase transition between the FL and NFL phase follows the "level-crossing" scenario. Within this scenario, the low-energy sector of the spectrum is the union of orthogonal subspaces. One subspace consists of the states $|E_i^{\text{FL}}\rangle$ at the FL fixed point, the other of the states $|E_i^{\text{NFL}}\rangle$ at the NFL fixed point, with their respective ground states at $i = 0$. At energy scales ω, T larger than the difference of the ground-state energies $|E_0^{\text{FL}} - E_0^{\text{NFL}}|$, both subspaces contribute to thermodynamic and dynamical properties, such as the impurity contribution to entropy S_{imp} and dynamical impurity susceptibility χ^{imp}. This corresponds to the *NFL′* regime appearing at earlier iterations in the NRG flow diagrams. As one proceeds with the NRG steps, the energy scale becomes smaller and eventually reaches $|E_0^{\text{FL}} - E_0^{\text{NFL}}|$. At this point, the higher lying fixed point starts to disappear from the low-energy physics, as clearly visible in the NRG flow diagram in Figs. S2(b,e). As an aside, we note that a similar level-crossing competition between two subspaces has been used to induce a two-stage Kondo effect in driven quantum dot systems [4, 5].

With $S_{\text{imp}} \equiv \ln g$, where $g^{\text{FL}}{=}1$ and $g^{\text{NFL}}{=}\frac{1}{2}(1+\sqrt{5})$, the level-crossing scenario leads to an additive behavior of g, i.e.,

$$S_{\text{imp}}^{\text{NFL}'} = \ln(g^{\text{FL}} + g^{\text{NFL}}) \ , \tag{S8}$$

which follows from elementary considerations based on the definition of the partition function. To derive this relation, we start from the partition function of the whole system (impurity plus bath). In the *NFL′* regime,

$$Z^{\text{NFL}'} = Z^{\text{FL}} + Z^{\text{NFL}}, \tag{S9}$$

with $Z^{\alpha} {\equiv} \sum_i \exp(-E_i^{\alpha}/T)$ at temperature T. This is the *sum* of partition functions for the NFL and FL regimes, since the FL and NFL subspaces are orthogonal to each other. Now the entropy is related to the partition function via the free energy $F = -T \ln Z$, having $S = -\frac{\partial}{\partial T} F$.

TABLE S1. Fusion table for the NFL fixed point. Left: The 12 lowest low-lying free fermion multiplets $Q = [q, S, (\lambda_1\lambda_2)]$ with degeneracy d and energies $E(Q; 0)$. Middle: "Single fusion" with an effective impurity multiplet $Q^{\mathrm{eff}}_{\mathrm{imp}} = [+1, \frac{1}{2}, (00)]$, using $\mathrm{SU}(2)_3$ fusion rules [3] in the spin sector. This yields multiplets $Q' = [q', S', (\lambda'_1\lambda'_2)]$ with degeneracy d' and energies $E' = E(Q'; \delta q)$. The excitation energies are $\delta E' = E' - E'_{\mathrm{min}}$, where $E'_{\mathrm{min}} = E'([+1, \frac{1}{2}, (00)]) = \frac{7+5\delta q}{30}$. These are compared to the values E_{NRG}, computed by NRG at $J_0 = 0.3, K_0 = 0.3, I_0 = -0.01$, where $[+1, \frac{1}{2}, (00)]$ is the ground state. The NRG energies have been shifted and rescaled such that the ground state is zero and the values of E_{NRG} and $\delta E'$ match for the multiplet $[+1, \frac{1}{2}, (11)]$. δq is then determined by matching E_{NRG} and $\delta E'$ for the multiplet $[0, 0, (01)]$, resulting in $\delta q = 0.0433$. Right: "Double fusion", which fuses multiplets from the middle column with an impurity in the conjugate representation $\bar{Q}^{\mathrm{eff}}_{\mathrm{imp}} = [-1, \frac{1}{2}, (00)]$, yields the quantum numbers $Q'' = [q'', S'', (\lambda''_1\lambda''_2)]$. These characterize the CFT boundary operators $\hat{O}$, with scaling dimensions $\Delta = E(Q''; \delta q)$.

free fermions					single fusion, with $Q^{\mathrm{eff}}_{\mathrm{imp}} = [+1, \frac{1}{2}, (00)]$						NRG	double fusion, with $\bar{Q}^{\mathrm{eff}}_{\mathrm{imp}} = [-1, \frac{1}{2}, (00)]$				
q	S	$(\lambda_1\lambda_2)$	d	E	q'	S'	$(\lambda'_1\lambda'_2)$	d'	E'	$\delta E'$	E_{NRG}	q''	S''	$(\lambda''_1\lambda''_2)$	Δ	$\hat{O}$
0	0	(00)	1	0	+1	$\frac{1}{2}$	(00)	2	$\frac{7+5\delta q}{30}$	0	0	0	0	(00)	0	$\mathbb{1}$
												0	1	(00)	$\frac{2}{5}$ $(= \Delta_{\mathrm{sp}})$	Φ_{sp}
+1	$\frac{1}{2}$	(10)	6	$\frac{1}{2}$	+2	0	(10)	3	$\frac{9+5\delta q}{15}$	$\frac{11+5\delta q}{30}$ (0.374)	0.369	+1	$\frac{1}{2}$	(10)	$\frac{3+\delta q}{6}$	
					+2	1	(10)	9	$\frac{3+\delta q}{3}$	$\frac{23+5\delta q}{30}$ (0.774)	0.809	+1	$\frac{1}{2}$	(10)	$\frac{3+\delta q}{6}$	
												+1	$\frac{3}{2}$	(10)	$\frac{33+5\delta q}{30}$	
−1	$\frac{1}{2}$	(01)	6	$\frac{1}{2}$	0	0	(01)	3	$\frac{4}{15}$	$\frac{1-5\delta q}{30}$ (0.026)	0.026	−1	$\frac{1}{2}$	(01)	$\frac{3-\delta q}{6}$	
					0	1	(01)	9	$\frac{2}{3}$	$\frac{13-5\delta q}{30}$ (0.426)	0.422	−1	$\frac{1}{2}$	(01)	$\frac{3-\delta q}{6}$	
												−1	$\frac{3}{2}$	(01)	$\frac{33-5\delta q}{30}$	
0	1	(11)	24	1	+1	$\frac{1}{2}$	(11)	16	$\frac{5+\delta q}{6}$	$\frac{3}{5}$ (0.600)	0.600	0	0	(11)	$\frac{3}{5}$ $(= \Delta_{\mathrm{orb}})$	Φ_{orb}
												0	1	(11)	1 $(= \Delta_{\text{sp-orb}})$	$\Phi_{\text{sp-orb}}$
					+1	$\frac{3}{2}$	(11)	32	$\frac{43+5\delta q}{30}$	$\frac{6}{5}$ (1.200)	1.223	0	1	(11)	1	
+2	0	(20)	6	1	+3	$\frac{1}{2}$	(20)	12	$\frac{47+15\delta q}{30}$	$\frac{4+\delta q}{3}$ (1.348)	1.432	+2	0	(20)	$\frac{3+\delta q}{3}$	
												+2	1	(20)	$\frac{21+5\delta q}{15}$	
−2	0	(02)	6	1	−1	$\frac{1}{2}$	(02)	12	$\frac{27-5\delta q}{30}$	$\frac{2-\delta q}{3}$ (0.652)	0.655	−2	0	(02)	$\frac{3-\delta q}{3}$	
												−2	1	(02)	$\frac{21-5\delta q}{15}$	
+2	1	(01)	9	1	+3	$\frac{1}{2}$	(01)	6	$\frac{7+3\delta q}{6}$	$\frac{14+5\delta q}{15}$ (0.948)	0.954	+2	0	(01)	$\frac{9+5\delta q}{15}$	
												+2	1	(01)	$\frac{3+\delta q}{3}$	
					+3	$\frac{3}{2}$	(01)	12	$\frac{53+15\delta q}{30}$	$\frac{23+5\delta q}{15}$ (1.548)	1.599	+2	1	(01)	$\frac{3+\delta q}{3}$	
−2	1	(10)	9	1	−1	$\frac{1}{2}$	(10)	6	$\frac{3-\delta q}{6}$	$\frac{4-5\delta q}{15}$ (0.252)	0.248	−2	0	(10)	$\frac{9-5\delta q}{15}$	
												−2	1	(10)	$\frac{3-\delta q}{3}$	
					−1	$\frac{3}{2}$	(10)	12	$\frac{33-5\delta q}{30}$	$\frac{13-5\delta q}{15}$ (0.852)	0.844	−2	1	(10)	$\frac{3-\delta q}{3}$	
+1	$\frac{3}{2}$	(02)	24	$\frac{3}{2}$	+2	1	(02)	18	$\frac{21+5\delta q}{15}$	$\frac{7+\delta q}{6}$ (1.174)	1.180	+1	$\frac{1}{2}$	(02)	$\frac{27+5\delta q}{30}$	
												+1	$\frac{3}{2}$	(02)	$\frac{9+\delta q}{6}$	
−1	$\frac{3}{2}$	(20)	24	$\frac{3}{2}$	0	1	(20)	18	$\frac{16}{15}$	$\frac{5-\delta q}{6}$ (0.826)	0.825	−1	$\frac{1}{2}$	(20)	$\frac{27-5\delta q}{30}$	
												−1	$\frac{3}{2}$	(20)	$\frac{9-\delta q}{6}$	
−3	$\frac{1}{2}$	(11)	16	$\frac{3}{2}$	−2	0	(11)	8	$\frac{14-5\delta q}{15}$	$\frac{7-5\delta q}{10}$ (0.678)	0.673	−3	$\frac{1}{2}$	(11)	$\frac{3-\delta q}{2}$	
					−2	1	(11)	24	$\frac{4-\delta q}{3}$	$\frac{11-5\delta q}{10}$ (1.078)	1.090	−3	$\frac{1}{2}$	(11)	$\frac{3-\delta q}{2}$	
												−3	$\frac{3}{2}$	(11)	$\frac{21-5\delta q}{10}$	
−3	$\frac{3}{2}$	(00)	4	$\frac{3}{2}$	−2	1	(00)	3	$\frac{11-5\delta q}{15}$	$\frac{1-\delta q}{2}$ (0.478)	0.470	−3	$\frac{1}{2}$	(00)	$\frac{9-5\delta q}{10}$	
												−3	$\frac{3}{2}$	(00)	$\frac{3-\delta q}{2}$	

TABLE S2. Fusion table for the NFL fixed point constructed in analogous to Table S1, but now using $\mathrm{SU}(3)_2$ fusion rules [3] in the orbital sector, with $Q^{\mathrm{eff}}_{\mathrm{imp}} = [0, 0, (01)]$ for single fusion and $\bar{Q}^{\mathrm{eff}}_{\mathrm{imp}} = [0, 0, (10)]$ for double fusion. The excitation energies are $\delta E' = E' - E'_{\mathrm{min}}$, where $E'_{\mathrm{min}} = E'([+1, \frac{1}{2}, (00)]) = \frac{7+5\delta q}{30}$. These are compared to the values E_{NRG}, computed by NRG at $J_0 = 0.3, K_0 = 0.3, I_0 = -0.01$, where $[+1, \frac{1}{2}, (00)]$ is the ground state (same as for Table S1). The values of E_{NRG} and $\delta E'$ match for the multiplet $[+1, \frac{1}{2}, (11)]$. δq is then determined by matching E_{NRG} and $\delta E'$ for the multiplet $[0, 0, (01)]$, resulting in $\delta q = 0.0433$.

free fermions					single fusion, with $Q^{\mathrm{eff}}_{\mathrm{imp}} = [0, 0, (01)]$						NRG	double fusion, with $\bar{Q}^{\mathrm{eff}}_{\mathrm{imp}} = [0, 0, (10)]$				
q	S	$(\lambda_1\lambda_2)$	d	E	q'	S'	$(\lambda'_1\lambda'_2)$	d'	E'	$\delta E'$	E_{NRG}	q''	S''	$(\lambda''_1\lambda''_2)$	Δ	$\hat{O}$
0	0	(00)	1	0	0	0	(01)	3	$\frac{4}{15}$	$\frac{1-5\delta q}{30}$ (0.026)	0.026	0	0	(00)	0	$\mathbb{1}$
												0	0	(11)	$\frac{3}{5}$ $(= \Delta_{\mathrm{orb}})$	Φ_{orb}
+1	$\frac{1}{2}$	(10)	6	$\frac{1}{2}$	+1	$\frac{1}{2}$	(00)	2	$\frac{7+5\delta q}{30}$	0	0	+1	$\frac{1}{2}$	(10)	$\frac{3+\delta q}{6}$	
					+1	$\frac{1}{2}$	(11)	16	$\frac{5+\delta q}{6}$	$\frac{3}{5}$ (0.600)	0.600	+1	$\frac{1}{2}$	(10)	$\frac{3+\delta q}{6}$	
												+1	$\frac{1}{2}$	(02)	$\frac{27+5\delta q}{30}$	
−1	$\frac{1}{2}$	(01)	6	$\frac{1}{2}$	−1	$\frac{1}{2}$	(10)	6	$\frac{3-\delta q}{6}$	$\frac{4-5\delta q}{15}$ (0.252)	0.248	−1	$\frac{1}{2}$	(01)	$\frac{3-\delta q}{6}$	
												−1	$\frac{1}{2}$	(20)	$\frac{27-5\delta q}{30}$	
					−1	$\frac{1}{2}$	(02)	12	$\frac{27-5\delta q}{30}$	$\frac{2-\delta q}{3}$ (0.652)	0.655	−1	$\frac{1}{2}$	(01)	$\frac{3-\delta q}{6}$	
0	1	(11)	24	1	0	1	(01)	9	$\frac{2}{3}$	$\frac{13-5\delta q}{30}$ (0.426)	0.422	0	1	(00)	$\frac{2}{5}$ $(= \Delta_{\mathrm{sp}})$	Φ_{sp}
												0	1	(11)	1 $(= \Delta_{\text{sp-orb}})$	$\Phi_{\text{sp-orb}}$
					0	1	(20)	18	$\frac{16}{15}$	$\frac{5-\delta q}{6}$ (0.826)	0.825	0	1	(11)	1	
+2	0	(20)	6	1	+2	0	(10)	3	$\frac{9+5\delta q}{15}$	$\frac{11+5\delta q}{30}$ (0.374)	0.369	+2	0	(01)	$\frac{9+5\delta q}{15}$	
												+2	0	(20)	$\frac{3+\delta q}{3}$	
−2	0	(02)	6	1	−2	0	(11)	8	$\frac{14-5\delta q}{15}$	$\frac{7-5\delta q}{10}$ (0.678)	0.673	−2	0	(10)	$\frac{9-5\delta q}{15}$	
												−2	0	(02)	$\frac{3-\delta q}{3}$	
+2	1	(01)	9	1	+2	1	(10)	9	$\frac{3+\delta q}{3}$	$\frac{23+5\delta q}{30}$ (0.774)	0.809	+2	1	(01)	$\frac{3+\delta q}{3}$	
												+2	1	(20)	$\frac{21+5\delta q}{15}$	
					+2	1	(02)	18	$\frac{21+5\delta q}{15}$	$\frac{7+\delta q}{6}$ (1.174)	1.180	+2	1	(01)	$\frac{3+\delta q}{3}$	
−2	1	(10)	9	1	−2	1	(00)	3	$\frac{11-5\delta q}{15}$	$\frac{1-\delta q}{2}$ (0.478)	0.470	−2	1	(10)	$\frac{3-\delta q}{3}$	
					−2	1	(11)	24	$\frac{4-\delta q}{3}$	$\frac{11-5\delta q}{10}$ (1.078)	1.090	−2	1	(10)	$\frac{3-\delta q}{3}$	
												−2	1	(02)	$\frac{21-5\delta q}{15}$	
+1	$\frac{3}{2}$	(02)	24	$\frac{3}{2}$	+1	$\frac{3}{2}$	(11)	32	$\frac{43+5\delta q}{30}$	$\frac{6}{5}$ (1.200)	1.223	+1	$\frac{3}{2}$	(10)	$\frac{33+5\delta q}{30}$	
												+1	$\frac{3}{2}$	(02)	$\frac{9+\delta q}{6}$	
−1	$\frac{3}{2}$	(20)	24	$\frac{3}{2}$	−1	$\frac{3}{2}$	(10)	12	$\frac{33-5\delta q}{30}$	$\frac{13-5\delta q}{15}$ (0.852)	0.844	−1	$\frac{3}{2}$	(01)	$\frac{33-5\delta q}{30}$	
												−1	$\frac{3}{2}$	(20)	$\frac{9-\delta q}{6}$	
±3	$\frac{1}{2}$	(11)	16	$\frac{3}{2}$	±3	$\frac{1}{2}$	(01)	6	$\frac{7\pm 3\delta q}{6}$	$\frac{14\pm 5\delta q}{15}$ (0.948/0.919)	0.954/0.894	±3	$\frac{1}{2}$	(00)	$\frac{9\pm 5\delta q}{10}$	
												±3	$\frac{1}{2}$	(11)	$\frac{3\pm\delta q}{2}$	
					±3	$\frac{1}{2}$	(20)	12	$\frac{47\pm 15\delta q}{30}$	$\frac{4\pm\delta q}{3}$ (1.348/1.319)	1.432/1.311	±3	$\frac{1}{2}$	(11)	$\frac{3\pm\delta q}{2}$	
±3	$\frac{3}{2}$	(00)	4	$\frac{3}{2}$	±3	$\frac{3}{2}$	(01)	12	$\frac{53\pm 15\delta q}{30}$	$\frac{23\pm 5\delta q}{15}$ (1.548/1.519)	1.599/1.579	±3	$\frac{3}{2}$	(00)	$\frac{3\pm\delta q}{2}$	
												±3	$\frac{3}{2}$	(11)	$\frac{21\pm 5\delta q}{10}$	

TABLE S3. Same fusion procedure as that in Table S2, but now compared to NRG data computed at $J_0 = 0.6, K_0 = 0.3, I_0 = -0.13$, where $[0, 0, (01)]$ becomes the ground state (in contrast to $[+1, \frac{1}{2}, (00)]$ used in Table S2). The excitation energies are defined as, $\delta E' = E' - E'_{\mathrm{min}}$, where $E'_{\mathrm{min}} = E'([0, 0, (01)]) = \frac{4}{15}$. The NRG energies have been shifted and rescaled such that the ground state is zero and the values of E_{NRG} and $\delta E'$ match for the multiplet $[0, 1, (01)]$. δq is then determined by matching E_{NRG} and $\delta E'$ for the multiplet $[+1, \frac{1}{2}, (00)]$, resulting in $\delta q = 0.2135$.

free fermions					single fusion, with $Q^{\mathrm{eff}}_{\mathrm{imp}} = [0, 0, (01)]$						NRG	double fusion, with $\bar{Q}^{\mathrm{eff}}_{\mathrm{imp}} = [0, 0, (10)]$				
q	S	$(\lambda_1\lambda_2)$	d	E	q'	S'	$(\lambda'_1\lambda'_2)$	d'	E'	$\delta E'$	E_{NRG}	q''	S''	$(\lambda''_1\lambda''_2)$	Δ	$\hat{O}$
0	0	(00)	1	0	0	0	(01)	3	$\frac{4}{15}$	0	0	0	0	(00)	0	$\mathbb{1}$
												0	0	(11)	$\frac{3}{5}$ $(= \Delta_{\mathrm{orb}})$	Φ_{orb}
+1	$\frac{1}{2}$	(10)	6	$\frac{1}{2}$	+1	$\frac{1}{2}$	(00)	2	$\frac{7+5\delta q}{30}$	$\frac{-1+5\delta q}{30}$ (0.002)	0.002	+1	$\frac{1}{2}$	(10)	$\frac{3+\delta q}{6}$	
					+1	$\frac{1}{2}$	(11)	16	$\frac{5+\delta q}{6}$	$\frac{17+5\delta q}{30}$ (0.602)	0.613	+1	$\frac{1}{2}$	(10)	$\frac{3+\delta q}{6}$	
												+1	$\frac{1}{2}$	(02)	$\frac{27+5\delta q}{30}$	
−1	$\frac{1}{2}$	(01)	6	$\frac{1}{2}$	−1	$\frac{1}{2}$	(10)	6	$\frac{3-\delta q}{6}$	$\frac{7-5\delta q}{30}$ (0.198)	0.196	−1	$\frac{1}{2}$	(01)	$\frac{3-\delta q}{6}$	
												−1	$\frac{1}{2}$	(20)	$\frac{27-5\delta q}{30}$	
					−1	$\frac{1}{2}$	(02)	12	$\frac{27-5\delta q}{30}$	$\frac{19-5\delta q}{30}$ (0.598)	0.605	−1	$\frac{1}{2}$	(01)	$\frac{3-\delta q}{6}$	
0	1	(11)	24	1	0	1	(01)	9	$\frac{2}{3}$	$\frac{2}{5}$ (0.400)	0.400	0	1	(00)	$\frac{2}{5}$ $(= \Delta_{\mathrm{sp}})$	Φ_{sp}
												0	1	(11)	1 $(= \Delta_{\mathrm{sp\text{-}orb}})$	$\Phi_{\mathrm{sp\text{-}orb}}$
					0	1	(20)	18	$\frac{16}{15}$	$\frac{4}{5}$ (0.800)	0.812	0	1	(11)	1	
+2	0	(20)	6	1	+2	0	(10)	3	$\frac{9+5\delta q}{15}$	$\frac{1+\delta q}{3}$ (0.405)	0.407	+2	0	(01)	$\frac{9+5\delta q}{15}$	
												+2	0	(20)	$\frac{3+\delta q}{3}$	
−2	0	(02)	6	1	−2	0	(11)	8	$\frac{14-5\delta q}{15}$	$\frac{2-\delta q}{3}$ (0.596)	0.595	−2	0	(10)	$\frac{9-5\delta q}{15}$	
												−2	0	(02)	$\frac{3-\delta q}{3}$	
+2	1	(01)	9	1	+2	1	(10)	9	$\frac{3+\delta q}{3}$	$\frac{11+5\delta q}{15}$ (0.805)	0.859	+2	1	(01)	$\frac{3+\delta q}{3}$	
												+2	1	(20)	$\frac{21+5\delta q}{15}$	
					+2	1	(02)	18	$\frac{21+5\delta q}{15}$	$\frac{17+5\delta q}{15}$ (1.205)	1.234	+2	1	(01)	$\frac{3+\delta q}{3}$	
−2	1	(10)	9	1	−2	1	(00)	3	$\frac{11-5\delta q}{15}$	$\frac{7-5\delta q}{15}$ (0.396)	0.391	−2	1	(10)	$\frac{3-\delta q}{3}$	
					−2	1	(11)	24	$\frac{4-\delta q}{3}$	$\frac{16-5\delta q}{15}$ (0.996)	1.015	−2	1	(10)	$\frac{3-\delta q}{3}$	
												−2	1	(02)	$\frac{21-5\delta q}{15}$	
+1	$\frac{3}{2}$	(02)	24	$\frac{3}{2}$	+1	$\frac{3}{2}$	(11)	32	$\frac{43+5\delta q}{30}$	$\frac{7+\delta q}{6}$ (1.202)	1.249	+1	$\frac{3}{2}$	(10)	$\frac{33+5\delta q}{30}$	
												+1	$\frac{3}{2}$	(02)	$\frac{9+\delta q}{6}$	
−1	$\frac{3}{2}$	(20)	24	$\frac{3}{2}$	−1	$\frac{3}{2}$	(10)	12	$\frac{33-5\delta q}{30}$	$\frac{5-\delta q}{6}$ (0.798)	0.799	−1	$\frac{3}{2}$	(01)	$\frac{33-5\delta q}{30}$	
												−1	$\frac{3}{2}$	(20)	$\frac{9-\delta q}{6}$	
±3	$\frac{1}{2}$	(11)	16	$\frac{3}{2}$	±3	$\frac{1}{2}$	(01)	6	$\frac{7\pm3\delta q}{6}$	$\frac{9\pm5\delta q}{10}$ (1.007/0.793)	1.033/0.791	±3	$\frac{1}{2}$	(00)	$\frac{9\pm5\delta q}{10}$	
												±3	$\frac{1}{2}$	(11)	$\frac{3\pm\delta q}{2}$	
					±3	$\frac{1}{2}$	(20)	12	$\frac{47\pm15\delta q}{30}$	$\frac{13\pm5\delta q}{10}$ (1.407/1.193)	1.527/1.209	±3	$\frac{1}{2}$	(11)	$\frac{3\pm\delta q}{2}$	
±3	$\frac{3}{2}$	(00)	4	$\frac{3}{2}$	±3	$\frac{3}{2}$	(01)	12	$\frac{53\pm15\delta q}{30}$	$\frac{3\pm\delta q}{2}$ (1.607/1.393)	1.695/1.474	±3	$\frac{3}{2}$	(00)	$\frac{3\pm\delta q}{2}$	
												±3	$\frac{3}{2}$	(11)	$\frac{21\pm5\delta q}{10}$	

TABLE S4. Demonstration that the NFL' fixed point spectrum is the union of the FL and NFL fixed point spectra near the phase transition. Second column: $E_{NFL'}$ of the intermediate-energy regime NFL' at $I_0 = -0.00609896199692$ [Fig. 3(b) and Fig. S2(b)]. Third column: the low-energy FL spectrum with ground state $[-2, 0, (00)]$ just before the phase transition at $I_0 = -0.006098$ [Fig. 3(a) and Fig. S2(a)]. Fourth column: the low-energy NFL spectrum with ground state $[+1, \frac{1}{2}, (00)]$ just after the phase transition at $I_0 = -0.006099$ [Fig. 3(c) and Fig. S2(c)]. All entries that relate or can be linked to FL are marked in red. The FL excitations can be obtained by adding electrons with energy $\epsilon_e = 0.275511$ or holes with energy $\epsilon_p = 1.553042$ on top of the ground state with energy E_g, as indicated in the column for E_{FL}.

Multiplets				$E_{NFL'}$	E_{FL}	E_{NFL}
q	S	$(\lambda_1\lambda_2)$	d	$@I_0 = -0.00609896199692$	$@I_0 = -0.006098$	$@I_0 = -0.006099$
$+1$	$\frac{1}{2}$	(00)	2	-0.717930		-0.729529 $(= E_g)$
0	0	(01)	3	-0.668562		-0.680530
-2	0	(00)	1	-0.550738	-0.551028 $(= E_g)$	
-1	$\frac{1}{2}$	(10)	6	-0.282883	-0.275517 $(\simeq E_g + \epsilon_e)$	
-1	$\frac{1}{2}$	(10)	6	-0.275324		-0.295054
$+2$	0	(10)	3	-0.0880684		-0.100011
0	1	(01)	9	0	0 $(\simeq E_g + 2\epsilon_e)$	
0	0	(20)	6	0.000037	0 $(\simeq E_g + 2\epsilon_e)$	
0	1	(01)	9	0.011703		0
-2	1	(00)	3	0.102149		0.089692
$+1$	$\frac{3}{2}$	(00)	4	0.275407	0.275518 $(\simeq E_g + 3\epsilon_e)$	
$+1$	$\frac{1}{2}$	(11)	16	0.275410	0.275518 $(\simeq E_g + 3\epsilon_e)$	
$+1$	$\frac{1}{2}$	(11)	16	0.313029		0.300831
-1	$\frac{1}{2}$	(02)	12	0.416507		0.404921
-2	0	(11)	8	0.451411		0.439442
$+2$	1	(10)	9	0.550783	0.551033 $(\simeq E_g + 4\epsilon_e)$	
$+2$	0	(02)	6	0.550791	0.551033 $(\simeq E_g + 4\epsilon_e)$	
$+2$	1	(10)	9	0.666084		0.654338
0	1	(20)	18	0.703088		0.690623
-1	$\frac{3}{2}$	(10)	12	0.741511		0.729522
$+3$	$\frac{1}{2}$	(01)	6	0.826154	0.826543 $(\simeq E_g + 5\epsilon_e)$	
-3	$\frac{1}{2}$	(01)	6	0.835829		0.823640
$+3$	$\frac{1}{2}$	(01)	6	0.911424		0.899222
-3	$\frac{1}{2}$	(01)	6	1.002497	1.002014 $(\simeq E_g + \epsilon_p)$	

The impurity contribution to the entropy is defined as the difference between the entropy of the whole system (impurity plus bath) and the entropy of the bath only,

$$\begin{aligned} S_{\rm imp} \equiv S_{\rm tot} - S_{\rm bath} &= \tfrac{\partial}{\partial T}\left[T\left(\ln Z_{\rm tot} - \ln Z_{\rm bath}\right)\right] \\ &= \ln\tfrac{Z_{\rm tot}}{Z_{\rm bath}} + \underbrace{\tfrac{1}{T}\left(U_{\rm tot} - U_{\rm bath}\right)}_{\simeq\ {\rm const}\ \cong\ \ln a} \qquad \text{(S10a)} \\ &\simeq \ln\left[\tfrac{a\, Z_{\rm tot}}{Z_{\rm bath}}\right]. \qquad \text{(S10b)} \end{aligned}$$

where $U{=}T^2\frac{\partial}{\partial T}\ln Z{\equiv}\langle E\rangle$ is the internal energy. The entropy is independent of the arbitrary choice of energy reference, as also apparent from the first line. Therefore both $Z_{\rm tot}$ and $Z_{\rm bath}$ can be computed relative to their respective ground state energies. Generally for gapless spectra then, the expectation values take $U_{\rm tot} \sim U_{\rm bath} \sim T$. Moreover, in the level-crossing scenario in the regime $|E_0^{\rm FL} - E_0^{\rm NFL}| \ll T$ (relative to the same energy reference), the two phases FL and NFL coexist, such that they also show similar energetics, i.e., $|U_{\rm FL} - U_{\rm NFL}| \ll T$. Therefore with $U_{\rm tot} = bU_{\rm FL} + (1-b)U_{\rm NFL} \simeq$ const for arbitrary $b \in [0,1]$, the last term in Eq. (S10a) resembles a constant, irrespective of having NFL', NFL, or FL. Eq. (S10b) implies that $g^x = e^{S^x_{\rm imp}} = a\frac{Z^x_{\rm tot}}{Z_{\rm bath}}$ for each of $x =$ FL, NFL and NFL'. Eq. (S8) for $S^{NFL'}_{\rm imp}$ then directly follows from Eq. (S9).

The level-crossing scenario also explains the same power laws of impurity susceptibilities $\chi^{\rm imp}$ in the NFL and NFL' regimes as well as the kinks of the susceptibilities at the crossover from the NFL' regime to the NFL regime [Fig. S2(i)]. In the NFL' regime, both FL and NFL subspaces contribute to the susceptibility independently,

$$\chi^{\rm imp} \simeq (\chi^{\rm FL} + \chi^{\rm NFL})/2. \qquad \text{(S11)}$$

For spin and orbital susceptibilities, the power exponents for $\chi^{\rm NFL}$ are smaller than 1, which is the power of $\chi^{\rm FL}$. Since the NFL' regime is already at low energies, the power law of $\chi^{\rm FL} + \chi^{\rm NFL}$ is dominated by that of $\chi^{\rm NFL}$ ($\omega^{-1/5}, \omega^{1/5} \gg \omega^1$ when $\omega < 1$). At the crossover from the NFL' regime to the NFL regime, the contribution of $\chi^{\rm FL}$ disappears, which results in the kinks.

S-V. IMPURITY SPECTRAL FUNCTIONS

The impurity spectral functions are calculated via the $\mathcal{T}$-matrix [6, 7], resulting in the local correlation function,

$$A_t(\omega) = -\tfrac{1}{\pi}\,{\rm Im}\Big(\pi^2\rho_0\langle O_{m\sigma}||O^\dagger_{m\sigma}\rangle_\omega\Big), \qquad \text{(S12)}$$

in the composite operator $O_{m\sigma} = [\psi_{m\sigma}, H_{\rm int}]$, where $\rho_0 = \frac{1}{2D}$ is the bare density of states with $D := 1$ the half-band width of the bath. The normalization ensures that $A_t \in [0,1]$ with $A_t = 1$ implying perfect transmission.

All of the spectral functions scale an asymmetric shape due to the absence of particle-hole symmetry. In the transition from FL to SFL [Fig. S7(a,b)], the spectral weight is close to the value 0.75 in the FL regime, while it decreases to about 0.4 in the crossover regime SFL' and further decreases to about 0.25 after entering the SFL regime. The spectral weight shows a jump from FL to NFL [Fig. S7(c,d)]. In the NFL regime, it is close to the value 0.4, which shows similarity with the crossover regime SFL'. The evolution of the spectral weight in the transition from SFL to NFL is smooth. In Figs. S7(e,f), we see the crossover of the spectral weight from 0.25 at high energy to 0.4 at low energy for $J_0 = 0.25$.

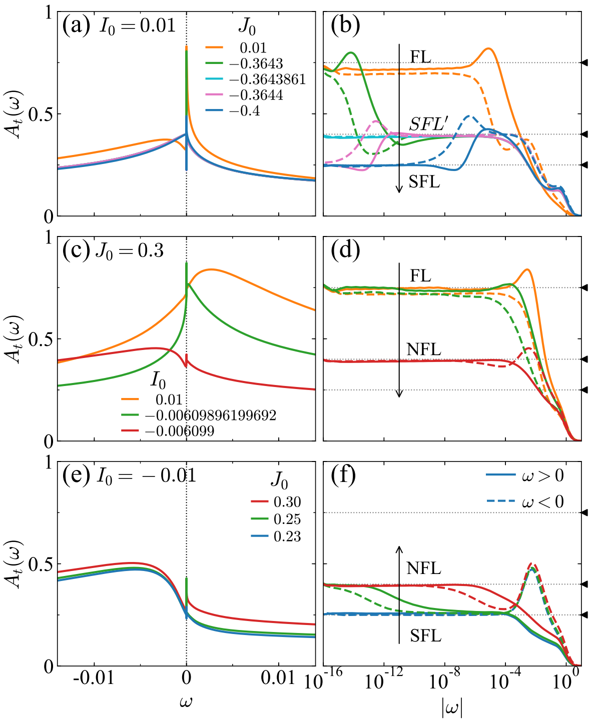

FIG. S7. Impurity spectral function $A_t(\omega)$. (a,b) transition from FL to SFL, (c,d) transition from FL to NFL, (e,f) transition from SFL to NFL. Lin-lin (Lin-log) plots in the left (right) column. In the right column, solid (dashed) lines are for $\omega > 0$ ($\omega < 0$). The grey dotted lines and the black arrows mark the spectral weight of 0.75, 0.4 and 0.25, respectively.

S-VI. THE COEFFICIENT OF IMPURITY SPECIFIC HEAT $\gamma = C_{\rm imp}/T$

Figs. S8(g-i) show the coefficient of the specific heat,

$$\gamma(T) = \frac{C_{\rm imp}(T)}{T} = \frac{\partial S_{\rm imp}(T)}{\partial T}, \qquad \text{(S13)}$$

as a function of temperature T for the FL, SFL and NFL fixed points. The corresponding impurity entropy $S_{\rm imp}$ [Figs. S8(d-f)] and the impurity dynamical susceptibilities of spin and orbital [Figs. S8(a-c)] are also plotted for comparison. $\gamma(T)$ takes a constant value for FL [Fig. S8(g)], as expected, while it follows an approximate power law behavior to diverge for SFL [Fig. S8(h)] and NFL [Fig. S8(i)]. For NFL, the power-law exponent is found to be $-1/5$, which can be obtained by the CFT argument for a SU(2)$_3$ Kondo model, $\gamma(T) \propto T^{\frac{2-3}{2+3}}$, see [8].

S-VII. THE IMPURITY STATIC SUSCEPTIBILITIES $\chi^{\text{static}}(T)$

Fig. S9 shows the impurity static susceptibilities $\chi^{\text{static}}_{\text{sp,orb}}(T)$ as functions of temperature T for SFL (a,c) and NFL (b,d) phases. For SFL, $\chi^{\text{static}}(T)$ follow $1/T$ behavior for spin [Fig. S9(a)] and constant for orbital [Fig. S9(c)] at low temperature, as expected for a decoupled impurity spin moment-$\frac{1}{2}$ and fully screened orbitals. For NFL, it follows $T^{-1/5}$ behavior for spin [Fig. S9(b)] at low temperature, which can be obtained by the CFT arguments for a SU(2)$_3$ Kondo model, $\chi^{\text{static}}_{\text{sp}} \propto T^{\frac{2-3}{2+3}}$, see [8]. While, for orbital, it follows $\frac{1}{\ln(T/T_0)} + C$ to approach a constant slowly at low temperature.

S-VIII. ENERGY DIFFERENCE OF MULTIPLETS $[+1, \frac{1}{2}, (00)]$ AND $[+1, \frac{3}{2}, (00)]$ ALONG THE PHASE BOUNDARY

Fig. S10 shows the energy difference δE between the multiplets $[+1, \frac{1}{2}, (00)]$ and $[+1, \frac{3}{2}, (00)]$ as a function of J_0 along the phase boundary between FL and SFL (NFL). I_0 is fine-tuned at fixed J_0 from the FL side, to induce a very large crossover regime of *SFL*$'$ or *NFL*$'$. The eigenlevel spectrum is taken at the odd Wilson site with the energy scale of $\omega_k = \Lambda^{-k/2} = 10^{-8}$ and then the desired energy difference δE is calculated. $[+1, \frac{3}{2}, (00)]$ has a lower energy when $J_0 < 0$, while $[+1, \frac{1}{2}, (00)]$ has a lower energy when $J_0 > 0$.

S-IX. JUSTIFICATION OF THE 3SOK MODEL

The 3soK model derives from a realistic three-orbitals Anderson impurity model H_{AIM} by the standard Schrieffer-Wolff transformation in the impurity subspace with total occupancy $N = 2$. The details are presented in the supplementary material in [9]. Here, we only give a brief summary of the results and justify the values of Kondo couplings used in this work. The three-orbitals Anderson impurity model H_{AIM} reads

$$\begin{aligned} H_{\text{AIM}} = H_{\text{imp}} + \sum_{p,m,\sigma} V_p \psi^\dagger_{pm\sigma} d_{m\sigma} + h.c. \\ + \sum_{p,m,\sigma} \epsilon_p \psi^\dagger_{pm\sigma} \psi_{pm\sigma}, \end{aligned} \tag{S14}$$

$$\begin{aligned} H_{\text{imp}} = \epsilon_d N + \frac{1}{2} U N(N-1) \\ + \frac{1}{2} J_H \sum_{mn,\sigma\sigma'} d^\dagger_{m\sigma} d^\dagger_{n\sigma'} d_{m\sigma'} d_{n\sigma}, \end{aligned} \tag{S15}$$

$$\begin{aligned} = \epsilon_d N + \frac{3}{4} J_H N + (U - \frac{J_H}{2}) \frac{N(N-1)}{2} \\ - J_H \boldsymbol{S}^2, \end{aligned} \tag{S16}$$

where, ϵ_d is the energy level of the impurity, U is Hubbard interaction and J_H is Hund's coupling, N is the total occupancy operator and $\boldsymbol{S}$ is total spin operator. After the Schrieffer-Wolff transformation, the 3soK model reads

$$H_{\text{3soK}} = H_{\text{int}} + H_{\text{bath}}, \tag{S17}$$

$$H_{\text{bath}} = \sum_{pm\sigma} \varepsilon_p \psi^\dagger_{pm\sigma} \psi_{pm\sigma}, \tag{S18}$$

$$H_{\text{int}} = J_0 \mathbf{S} \cdot \mathbf{J}_{\text{sp}} + K_0 \mathbf{T} \cdot \mathbf{J}_{\text{orb}} + I_0 \mathbf{S} \cdot \mathbf{J}_{\text{sp-orb}} \cdot \mathbf{T}, \tag{S19}$$

The bare Kondo couplings J_0, K_0 and I_0 are

$$J_0 = \frac{2}{3} \left[\frac{1}{\Delta E^-} - \frac{1}{3} \frac{1}{\Delta E^+} \right] V^2, \tag{S20}$$

$$K_0 = \left[\frac{1}{\Delta E^-} + \frac{4}{3} \frac{1}{\Delta E^+} \right] V^2, \tag{S21}$$

$$I_0 = 4 \left[\frac{1}{2} \frac{1}{\Delta E^-} + \frac{1}{3} \frac{1}{\Delta E^+} \right] V^2, \tag{S22}$$

with

$$V^2 = \sum_p V_p^2, \tag{S23}$$

$$\Delta E^+ = E^g_{N=3} - E^g_{N=2} = \epsilon_d + 2(U - J_H) > 0, \tag{S24}$$

$$\Delta E^- = E^g_{N=1} - E^g_{N=2} = -\epsilon_d - (U - J_H) > 0, \tag{S25}$$

where, E^g_N is the energy of the ground state in subspace with occupancy N, and ΔE^+ (ΔE^-) is the particle (hole) excitation energy, so $\epsilon_d = -(1+\alpha)(U - J_H)$ with $\alpha \in (0, 1)$.

Based on this Schrieffer-Wolff transformation, these three Kondo couplings are not independent. J_0 can be ferromagnetic when $\Delta E^- > 3\Delta E^+$, i.e. favors the virtual particle excitation processes, while K_0 and I_0 are always antiferromagnetic. However, it is worthwhile to treat them as independent parameters and study both the antiferromagnetic and ferromagnetic regimes to explore all the possible fixed points in the global phase diagram. Just as we show in this work, a SFL fixed point exists in the ferromagnetic regime of J_0 and a novel NFL fixed point exists in the ferromagnetic regime of I_0. Although this 3soK model derives from a realistic Anderson impurity model, it can also be viewed as a general multi-channel Kondo model with both spin and orbital degrees

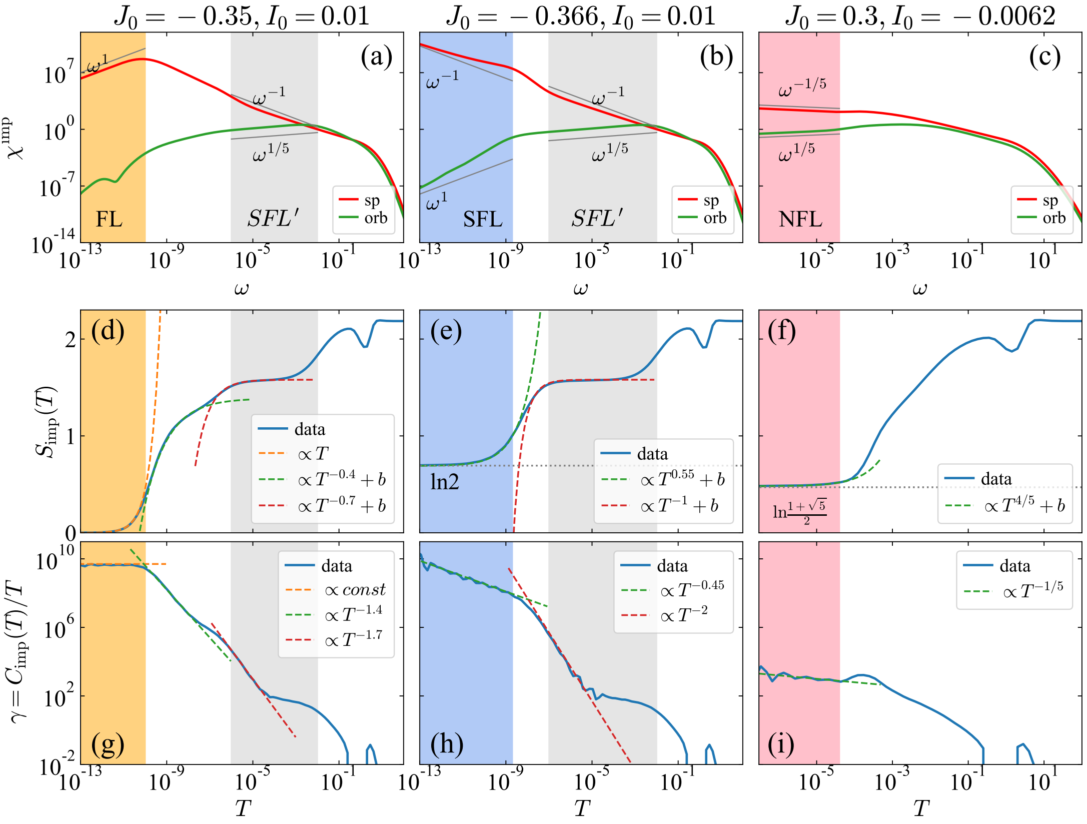

FIG. S8. (a-c) Log-log plots of the impurity dynamical susceptibilities of spin and orbital $\chi^{\rm imp}_{\rm sp,orb}(\omega)$ as a function of ω at temperature $T = 10^{-16}$. (d-f) Lin-log plots of the impurity contribution to the entropy $S_{\rm imp}$ as a function of T. (g-i) Log-log plots of the coefficient of the impurity contribution to the specific heat $\gamma(T) = C_{\rm imp}(T)/T$ as a function of T. The low-energy fixed points are FL (left), SFL (middle) and NFL (right).

of freedom. The ferromagnetic Kondo couplings may be realized in cold atoms systems [10, 11], as already mentioned in the main text. It may be also available in quantum dots in the near future based on the recent progress of experiments [12, 13], where they have realized negative Hubbard U. For triple dots having effectively negative U, it is possible to induce the strong anisotropy, including the sign flip of J_z [14]. This pursuit of negative U would finally reach to better controllability of the sign of Kondo couplings. The global phase diagram presented in this paper can serve as a guideline for further studies.

S-X. DEPENDENCE ON THE DISCRETIZATION PARAMETER Λ

To check the dependence on the NRG discretization parameter Λ, we calculate more results at $\Lambda = 3$ and $\Lambda = 5$. The results show that the overall phase diagram, including all the low-energy fixed points and intermediate-energy crossover regimes, doesn't change. Fig. S11 shows the NRG flow diagrams and the imaginary part of the impurity dynamical susceptibilities $\chi^{\rm imp}$ at $\Lambda = 3$. FL, SFL and NFL fixed points can be still obtained at $J_0 = 0.01, I_0 = 0.01$ [Figs. S11(a,d)], $J_0 = -0.4, I_0 = 0.01$ [Figs. S11(b,e)] and $J_0 = 0.3, I_0 = -0.01$ [Figs. S11(c,f)], respectively. Λ only shifts the phase boundary a little bit. For example, at $I_0 = 0.01$, the phase boundary from FL to SFL is about $J_0 = -0.36485$ at $\Lambda = 5$ and $J_0 = -0.3643861$ at $\Lambda = 4$, respectively. At $J_0 = 0.3$, the phase boundary from FL to NFL is about $I_0 = -0.006123125$ at $\Lambda = 5$ and $I_0 = -0.00609896$ at $\Lambda = 4$, respectively. As we have explained, the eigenstates and the power laws of those fixed points can be obtained by analytical CFT arguments, which are not related to the discretization; rather to the symmetries of the model, so the NRG results should be insensitive to the choice of Λ.

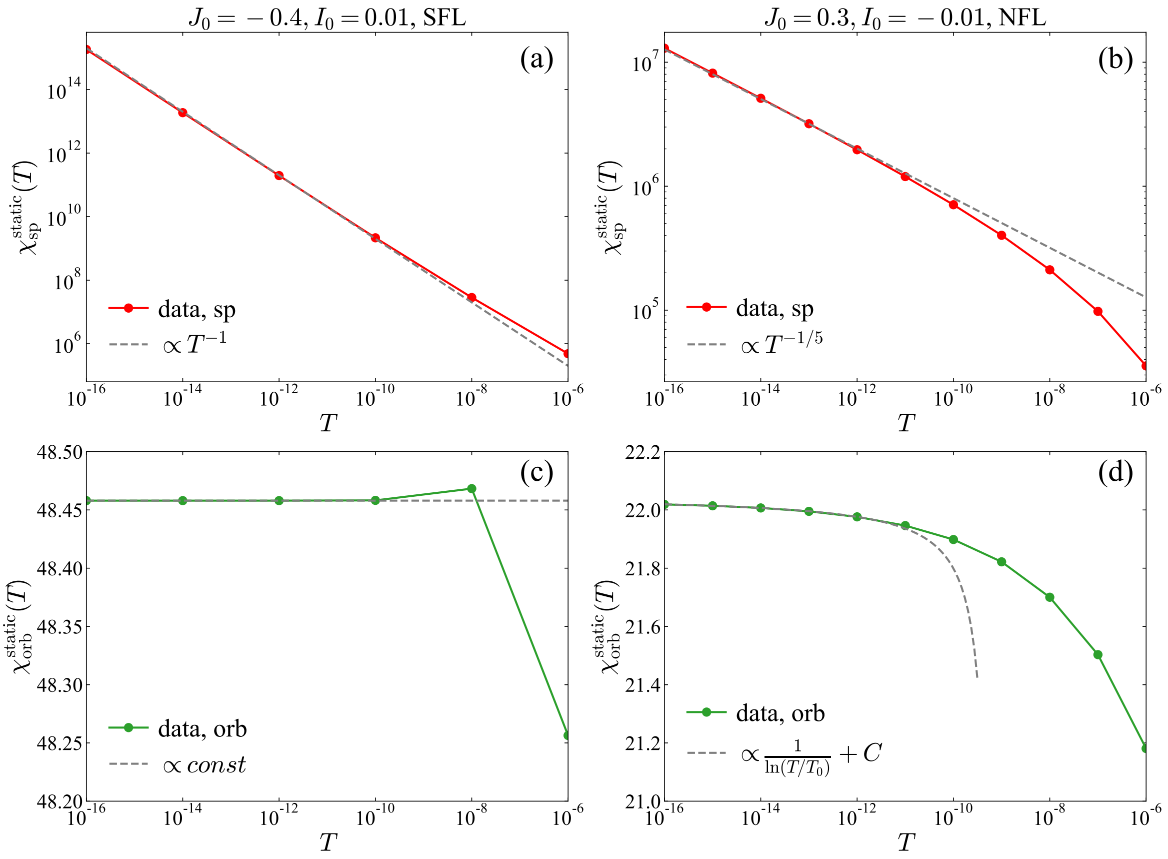

FIG. S9. (a-b) Log-log plots of the impurity static susceptibilities of spin $\chi_{\rm sp}^{\rm static}(T)$ as functions of temperature T. (c-d) Lin-log plots of the impurity static susceptibilities of orbital $\chi_{\rm orb}^{\rm static}(T)$ as functions of temperature T. (a,c) for SFL and (b,d) for NFL.

S-XI. IRREDUCIBLE REPRESENTATIONS OF SU(3)

We specify the irreducible representations (irreps) of SU(3) group using the Dynkin labels where we adopt the compact notation in [15, 16]. For SU(3), in particular, this implies that the label $(\lambda_1\lambda_2) \equiv (\lambda_1, \lambda_2)$ directly describes the Young tableau with two rows of $[\lambda_2 + \lambda_1, \lambda_2]$ number of boxes, respectively.

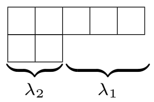

For a Young tableau, the vertical stacking of boxes means the anti-symmetric combination and the horizontal staking the symmetric combination. This way, $(10) \equiv \square \equiv \mathbf{3}$ is the defining irrep, with $(01) \equiv \ydiagram{1,1} \equiv \bar{\mathbf{3}}$ its dual; $(00) \equiv \bullet \equiv \mathbf{1}$ is the 1-dimensional scalar representation ('SU(3) singlet'); $(20) \equiv \ydiagram{2} \equiv \mathbf{6}$; $(02) \equiv \ydiagram{2,2} \equiv \bar{\mathbf{6}}$; $(11) \equiv \ydiagram{2,1} \equiv \mathbf{8}$, etc. Here the single bold number specifies the multiplet by its dimension. This convention, however, while frequently encountered, fails when multiple irreps have the same dimension beyond their dual [for example, (12) and (40) have the same dimension 15]. The adjoint or 'SU(3) spin operator' transforms in $(11) \equiv \ydiagram{2,1} \equiv \mathbf{8}$. The decompositions of the direct product of two irreps $(\lambda_1\lambda_2) \otimes (\lambda_1'\lambda_2') = \sum_\oplus (\lambda_1''\lambda_2'')$, are listed in Table S5.

Here, we take the local three-orbitals Hamiltonian for Hund's metal [1] with $\mathrm{U}(1)_{\rm ch} \times \mathrm{SU}(2)_{\rm sp} \times \mathrm{SU}(3)_{\rm orb}$ symmetry as an example to show the SU(3) representations, which are represented by the numbers in the parentheses in the second column of Fig. S12. The Hamiltonian reads,

$$H_{\rm loc} = \frac{3}{4} J_H N + (U - \frac{J_H}{2}) \frac{N(N-1)}{2} - J_H \boldsymbol{S}^2, \quad \text{(S26)}$$

where, U is the Hubbard interaction and J_H is the Hund's coupling, N is the total occupancy operator and $\boldsymbol{S}$ is the spin operator. The eigenlevels in each subspace with fixed total occupancy N are illustrated by the lines from bottom to top with the order of increasing energy. Their degeneracy are shown in the brackets on the left, and their symmetry labels are shown on the right.

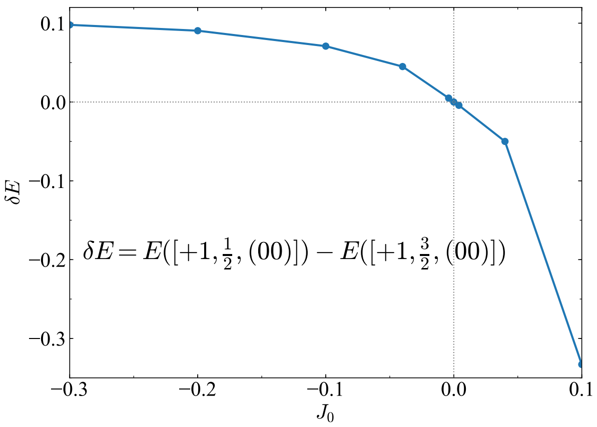

FIG. S10. Energy difference of multiplets $[+1,\frac{1}{2},(00)]$ and $[+1,\frac{3}{2},(00)]$ along the phase boundary.

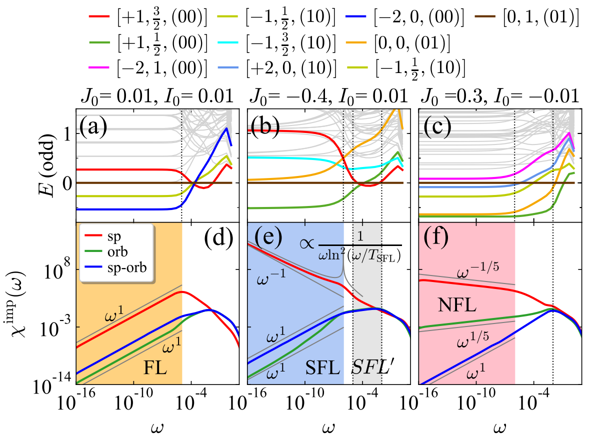

FIG. S11. (a)-(c) NRG flow diagrams and (d)-(f) imaginary part of the impurity dynamical susceptibilities calculated at the discretization parameter $\Lambda = 3$. (a,d) for FL phase, (b,e) for SFL phase and (c,f) for NFL phase.

TABLE S5. Decompositions of the direct product of two irreducible representations of SU(3): $(\lambda_1\lambda_2) \otimes (\lambda_1'\lambda_2') = \sum_\oplus (\lambda_1''\lambda_2'')$. The crossed-out terms do not appear in the SU(3)$_2$ fusion rules.

	(10)	(01)
(10)	(01) ⊕ (20)	(00) ⊕ (11)
(01)	(00) ⊕ (11)	(10) ⊕ (02)
(20)	(11) ⊕ $\cancel{(30)}$	(10) ⊕ $\cancel{(21)}$
(02)	(01) ⊕ $\cancel{(12)}$	(11) ⊕ $\cancel{(03)}$
(11)	(10) ⊕ (02) ⊕ $\cancel{(21)}$	(01) ⊕ (20) ⊕ $\cancel{(12)}$

To make the connection with the orbital angular momentum L, we add an extra term $-\frac{J_H}{4}\boldsymbol{L}^2$ to H_{loc} to break the orbital symmetry from SU(3) to SU(2), so we can see how the SU(3) representations are split into multiple SU(2) representations with integer orbital angular momentum. The results are shown in the third column of Fig. S12.

The ground multiplet with total occupancy $N = 2$ (red color in Fig. S12) is the impurity multiplet $[0, 1, (01)]$ we studied in this work, and the (01) representation of the SU(3)$_{\mathrm{orb}}$ group corresponds to the $L = 1$ representation of the SU(2)$_{\mathrm{orb}}$ group. Thus, the impurity multiplet takes orbital angular momentum $L = 1$ in the (01) representation. For this Hamiltonian, the reduction of the symmetry from SU(3)$_{\mathrm{orb}}$ to SU(2)$_{\mathrm{orb}}$ only affects the high energy multiplets. For example, the (20) representation is split into $L = 2$ and $L = 0$ representations, and the (11) representation is split into $L = 2$ and $L = 1$ representations.

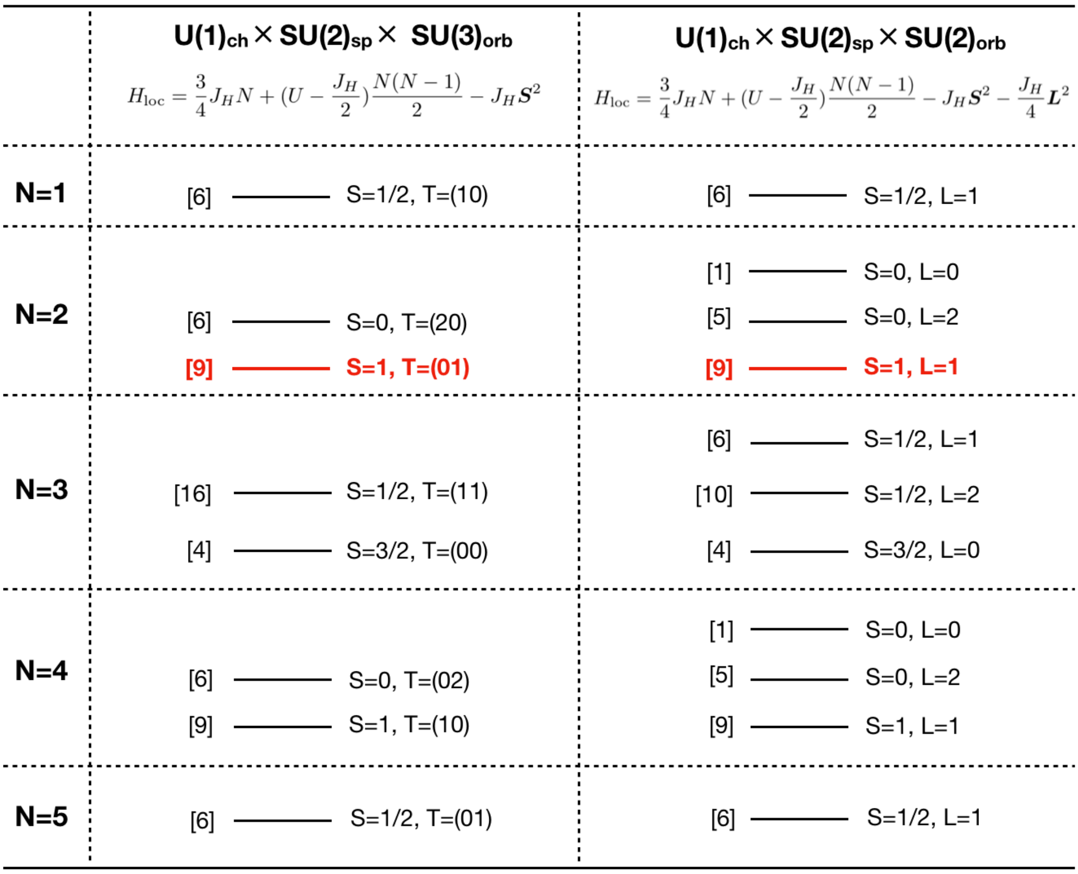
U(1)ch × SU(2)sp × SU(3)orb
$H_{\rm loc} = \frac{3}{4}J_H N + (U - \frac{J_H}{2})\frac{N(N-1)}{2} - J_H \boldsymbol{S}^2$
U(1)ch × SU(2)sp × SU(2)orb
$H_{\rm loc} = \frac{3}{4}J_H N + (U - \frac{J_H}{2})\frac{N(N-1)}{2} - J_H \boldsymbol{S}^2 - \frac{J_H}{4}\boldsymbol{L}^2$
N=1
[6] S=1/2, T=(10)
[6] S=1/2, L=1
N=2
[6] S=0, T=(20)
[9] S=1, T=(01)
[1] S=0, L=0
[5] S=0, L=2
[9] S=1, L=1
N=3
[16] S=1/2, T=(11)
[4] S=3/2, T=(00)
[6] S=1/2, L=1
[10] S=1/2, L=2
[4] S=3/2, L=0
N=4
[6] S=0, T=(02)
[9] S=1, T=(10)
[1] S=0, L=0
[5] S=0, L=2
[9] S=1, L=1
N=5
[6] S=1/2, T=(01)
[6] S=1/2, L=1

FIG. S12. Illustration of the multiplets of two different local Hamiltonians with three orbitals at large Hund's coupling J_H. One has SU(3) symmetry (second column) and another one has SU(2) symmetry (third column) in orbital sector. The numbers in the first column are the total occupancy numbers. The numbers in the brackets are the degeneracy of the multiplets. The numbers in the parentheses represent SU(3) representations. S and L represent spin and orbital angular momentum, respectively.

---

[1] K. M. Stadler, Z. P. Yin, J. von Delft, G. Kotliar, and A. Weichselbaum, "Dynamical mean-field theory plus numerical renormalization-group study of spin-orbital separation in a three-band Hund metal," Phys. Rev. Lett. **115**, 136401 (2015).

[2] K.M. Stadler, G. Kotliar, A. Weichselbaum, and J. von Delft, "Hundness versus Mottness in a three-band HubbardHund model: On the origin of strong correlations in Hund metals," Annals of Physics **405**, 365 – 409 (2019).

[3] E. Walter, K. M. Stadler, S. S. B. Lee, Y. Wang, G. Kotliar, A. Weichselbaum, and J. von Delft, "Uncovering non-fermi-liquid behavior in Hund metals: conformal field theory analysis of a SU(2) × SU(3) spin-orbital Kondo model," (2019), arXiv:1908.04362.

[4] B. Sbierski, M. Hanl, A. Weichselbaum, H. E. Türeci, M. Goldstein, L. I. Glazman, J. von Delft, and A. İmamoğlu, "Proposed Rabi-Kondo correlated state in a laser-driven semiconductor quantum dot," Phys. Rev. Lett. **111**, 157402 (2013).

[5] Seung-Sup B. Lee, Jan von Delft, and Moshe Goldstein, "Non-Fermi-liquid Kondo screening under Rabi driving," (2019), arXiv:1905.12617.

[6] T. A. Costi, "Kondo effect in a magnetic field and the magnetoresistivity of Kondo alloys," Phys. Rev. Lett. **85**, 1504–1507 (2000).

[7] Winfried Koller, Alex C. Hewson, and Dietrich Meyer, "Singular dynamics of underscreened magnetic impurity models," Phys. Rev. B **72**, 045117 (2005).

[8] Olivier Parcollet, Antoine Georges, Gabriel Kotliar, and Anirvan Sengupta, "Overscreened multichannel SU(N) Kondo model: Large-N solution and conformal field theory," Phys. Rev. B **58**, 3794–3813 (1998).

[9] Camille Aron and Gabriel Kotliar, "Analytic theory of Hund's metals: A renormalization group perspective," Phys. Rev. B **91**, 041110 (2015).

[10] F. Scazza, C. Hofrichter, M. Höfer, P. C. De Groot, I. Bloch, and S. Fölling, "Observation of two-orbital spin-exchange interactions with ultracold SU(N)-symmetric fermions," Nature Physics **10**, 779 EP – (2014), article.

[11] L. Riegger, N. Darkwah Oppong, M. Höfer, D. R. Fernandes, I. Bloch, and S. Fölling, "Localized magnetic moments with tunable spin exchange in a gas of ultracold fermions," Phys. Rev. Lett. **120**, 143601 (2018).

[12] Changki Hong, Gwangsu Yoo, Jinhong Park, Min-Kyun Cho, Yunchul Chung, H.-S. Sim, Dohun Kim, Hyungkook Choi, Vladimir Umansky, and Diana Mahalu, "Attractive coulomb interactions in a triple quantum dot," Phys. Rev. B **97**, 241115 (2018).

[13] A. Hamo, A. Benyamini, I. Shapir, I. Khivrich, J. Waissman, K. Kaasbjerg, Y. Oreg, F. von Oppen, and S. Ilani, "Electron attraction mediated by coulomb repulsion," Nature **535**, 395–400 (2016).

[14] Gwangsu Yoo, Jinhong Park, S.-S. B. Lee, and H.-S. Sim, "Anisotropic charge kondo effect in a triple quantum dot," Phys. Rev. Lett. **113**, 236601 (2014).

[15] Andreas Weichselbaum, "Non-abelian symmetries in tensor networks: A quantum symmetry space approach," Annals of Physics **327**, 2972 – 3047 (2012).

[16] A. Weichselbaum, S. Capponi, P. Lecheminant, A. M. Tsvelik, and A. M. Läuchli, "Unified phase diagram of antiferromagnetic su(n) spin ladders," Phys. Rev. B **98**, 085104 (2018).

11 Conclusion and outlook

Due to the decoupled nature of the two projects discussed in this thesis, we will divide the concluding remarks again into two parts.

Keldysh mfRG study of the single-impurity Anderson model: In Part I, we have introduced methodological advances in the parametrization of the Keldysh four-point vertex for fermionic theories with two-particle interactions, in particular exploiting both parity and crossing symmetries to reduce the number of independent Keldysh components of the vertex. We have also discussed how to construct bubbles and loops within this parametrization, which are necessary for computing the vertex in (m)fRG. Furthermore, we have presented details on our specific Keldysh mfRG implementation for the single-impurity Anderson model. We have thoroughly studied Keldysh perturbation theory for the SIAM and evaluated various properties of correlation functions obtained from a full mfRG flow, in order to gain understanding about sources of numerical errors. Finally, we have presented results for static and dynamical correlation functions on the one- and two-particle level, and investigated the fulfillment of sum rules and Ward identities.

We have seen that already on the one-loop level, including the full vertex frequency dependence tremendously improves results in various respects. The $\mathcal{K}_1$SF scheme used in all previous Keldysh fRG works, keeping only one frequency per diagrammatic channel, turns out not to be a well-controlled approximation: It provides good results for the self-energy and the spectral function, while stronger deviations occur for susceptibilities even in the weakly interacting regime. Instead, when including the full vertex frequency dependence, we can well reproduce benchmark results to high accuracy for all studied quantities and not too large interaction strength U/Δ.

We obtain further quantitative improvements by going from one-loop to multiloop fRG. In particular the Korringa-Shiba relation for the spin susceptibility, a sum rule following from the Pauli principle, and one- and two-particle Ward identities are systematically better fulfilled for increasing loop order. These relations provide important internal consistency checks which the validity of physical results strongly depends on. As a prime example, a violation of the two-particle Ward identity discussed in Sec. 8.4 is known to lead to inconsistent results for transport properties. Overall, our results show that Keldysh mfRG constitutes a *quantitative* method for computing real-frequency dynamical correlation functions within the regime of weak to intermediate interaction strength.

Up to now, we have only presented results up to loop order $\ell = 3$, without including self-energy multiloop corrections. This is due to the divergence of the 3-loop flow at low temperatures and large interaction strength, the origin of which has not yet been clarified. The immediate next steps therefore include further optimization of the numerics, in particular with a focus on the frequency grid on which self-energy and vertex are sampled. A flexibilization of the grid and potentially also higher-order interpolation schemes might be necessary (even though being numerically expensive) in order to get full control over numerical errors at low temperature and large interaction strength. Once this is achieved, full loop convergence should be easily reachable, which might further increase the interaction range where mfRG agrees with NRG benchmark results, before inevitable deviations due to the parquet approximation appear. The limitations of the PA could be overcome by means of DMF^{2}RG (see below).

As mentioned in Chapter 5, there are various possible generalizations of the model studied here, which can be straightforwardly implemented: One can break particle-hole symmetry by shifting the impurity levels through a gate voltage, or break SU(2) symmetry by splitting the spin components through a magnetic field, or one can add a second bath to the impurity and study nonequilibrium transport properties. The latter is beyond the reach of NRG, which is purely an equilibrium method. The conceptual prerequisites for these generalizations are all discussed in this thesis, but further refinements of the numerics might be necessary in order to control numerical errors arising from breaking those symmetries.

The (zero-dimensional) SIAM has primarily been studied for benchmark purposes, allowing to implement and systematically test our method against known results. However, we have designed our implementation in a modular way from the very beginning, aiming for future extensions to different models. Indeed, two different extensions are being implemented at the time of writing, which were already listed in the introduction (cf. Sec. 1.1.1): An extension for the Fermi-polaron problem, requiring a rotationally-invariant momentum dependence of the bath and the impurity, and an extension for the 2d Hubbard model, which requires a 2d lattice-momentum dependence. For both models, the dependence on frequencies, spin, and Keldysh indices can be treated in complete analogy to the parametrization introduced here, and can be captured within the current numerical implementation. Furthermore, we are aiming for a generalization from mfRG to DMF^{2}RG (discussed in Sec. 1.1.1), also in the context of the 2d Hubbard model: Here one starts an mfRG flow from a DMFT vertex, in order to incorporate nonlocal correlations beyond DMFT, or, from the fRG perspective, to elevate mfRG beyond the realm of the parquet approximation. In the Keldysh formalism, the DMFT vertex can be computed via NRG. The good agreement between mfRG and NRG for the SIAM on the two-particle level seen in Chapter 9 is a first important step on the route to this goal.

Non-Fermi-liquid behavior in a three-channel spin-orbital Kondo model: In Part II, we have reprinted published results on non-Fermi-liquid behavior in a three-channel spin-orbital Kondo model, which served as a minimal model for Hund metals. We have studied this model with a hybrid numerical and analytical approach, combining an accurate numerical description through NRG with analytical explanations obtained by a generalization of Affleck and Ludwig's CFT approach to fixed points of multichannel Kondo models. We have seen that in the parameter regime relevant for Hund metals, the two-stage screening process in the spin and orbital sector (coined spin-orbital separation) leads to four (not three) different regimes: At high energies, the impurity is only weakly coupled to the bath (free-impurity regime), while at low energies both spin and orbital degrees of freedom are screened, leading to a Fermi liquid. The intermediate SOS energy window of the three-channel spin-orbital Kondo model consists of two regimes: After orbital screening below T_{orb}, a non-Fermi-liquid fixed point is reached. A finite spin coupling drives the system away from this fixed point, leading to a crossover regime at the transition toward the Fermi liquid, which we call "spin-splitting" (SS) regime. For the NFL, SS, and FL regimes we were able to explain the fractional power laws in the dynamical spin and orbital susceptibilities through our CFT analysis. In particular, we can explain the superlinear divergence of the spin susceptibility in the NFL and SS regimes, which points to strong spin fluctuations that have been conjectured to be the origin of pairing in Hund metal superconductors. The orbital susceptibility is decreasing in these regimes due to the screening in the orbital sector. We have seen that surprisingly, the SS regime, even though not constituting a separate fixed point, also shows clear power-law behavior, which can be attributed to the presence of the NFL fixed point.

In the three-orbital Anderson-Hund model from which our Kondo-type model is derived (and which is believed to be relevant for actual Hund metals), the SOS window is much smaller. Here, the non-Fermi-liquid fixed point is not reached, but only passed at some distance. As a result, only the SS regime is visible in this model, while the NFL is masked by the onset of spin screening. Since the SS regime is however governed by the presence of the NFL fixed point, the power-law behavior observed there is an indication of non-Fermi-liquid physics.

In a second publication, we have extended the analysis of the three-channel spin-orbital Kondo model to its full phase diagram, which hosts various different phases that can all again be understood in terms of a CFT description. The Fermi-liquid phase, which is the ground state in the parameter regime relevant for Hund metals, is obtained after full spin and orbital screening. In a parameter regime dominated by a ferromagnetic spin-spin coupling, the ground state is a singular Fermi liquid, governed by screened orbital degrees of freedom and a residual fluctuating spin with a ferromagnetic coupling to the bath, which is marginal in the RG flow and thus approximately vanishes at low energies. Eventually, in a third region in the phase diagram (primarily determined by an antiferromagnetic spin-spin coupling and a ferromagnetic one in the combined spin-orbital sector) one obtains a quite exotic non-Fermi-liquid phase, featuring an alternating overscreening in the spin and orbital sector.

These different phases are connected by quantum phase transitions, showing characteristic power-law suppression of the coherence scales close to the phase boundaries. This observation has direct implications for the physics of Hund metals: The parameter regime relevant for Hund metals is in the Fermi-liquid phase, but close to its phase boundary. The presence of a quantum critical point at this phase boundary thus explains the unusually small Fermi-liquid coherence scale in Hund metals, which is accompanied by a rather large incoherent regime of non-Fermi-liquid nature at higher energies, studied in detail in the first publication.

Appendix A

Vertex frequency parametrizations

We reprint Eq. (4.5), defining the natural frequency parametrization in each channel:

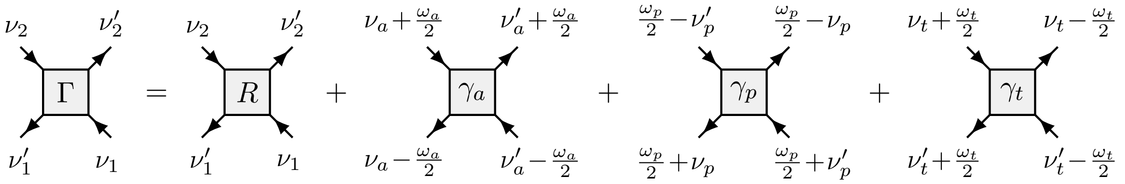
ν_2
ν_2'
Γ
ν_1'
ν_1
$=$
ν_2
ν_2'
R
ν_1'
ν_1
$+$
$\nu_a+\frac{\omega_a}{2}$
$\nu_a'+\frac{\omega_a}{2}$
γ_a
$\nu_a-\frac{\omega_a}{2}$
$\nu_a'-\frac{\omega_a}{2}$
$+$
$\frac{\omega_p}{2}-\nu_p'$
$\frac{\omega_p}{2}-\nu_p$
γ_p
$\frac{\omega_p}{2}+\nu_p$
$\frac{\omega_p}{2}+\nu_p'$
$+$
$\nu_t+\frac{\omega_t}{2}$
$\nu_t-\frac{\omega_t}{2}$
γ_t
$\nu_t'+\frac{\omega_t}{2}$
$\nu_t'-\frac{\omega_t}{2}$

(A.1)

All necessary transformations between those parametrizations can be read off (cf. [Agu20], Sec. 3.1):

$$
\begin{array}{lll}
\begin{array}{rcl}
\nu_1' &=& \nu_a-\frac{\omega_a}{2}\\
\nu_2' &=& \nu_a'+\frac{\omega_a}{2}\\
\nu_1 &=& \nu_a'-\frac{\omega_a}{2}\\
\nu_2 &=& \nu_a+\frac{\omega_a}{2}
\end{array}
& \Rightarrow &
\begin{array}{rclclcl}
\omega_a &=& \nu_2-\nu_1'=\nu_2'-\nu_1 &=& -\nu_p-\nu_p' &=& \nu_t-\nu_t'\\
\nu_a &=& \frac{\nu_1'+\nu_2}{2} &=& \frac{\omega_p+\nu_p-\nu_p'}{2} &=& \frac{\omega_t+\nu_t+\nu_t'}{2}\\
\nu_a' &=& \frac{\nu_2'+\nu_1}{2} &=& \frac{\omega_p-\nu_p+\nu_p'}{2} &=& \frac{-\omega_t+\nu_t+\nu_t'}{2}
\end{array}
\\[2ex]
\begin{array}{rcl}
\nu_1' &=& \frac{\omega_p}{2}+\nu_p\\
\nu_2' &=& \frac{\omega_p}{2}-\nu_p\\
\nu_1 &=& \frac{\omega_p}{2}+\nu_p'\\
\nu_2 &=& \frac{\omega_p}{2}-\nu_p'
\end{array}
& \Rightarrow &
\begin{array}{rclclcl}
\omega_p &=& \nu_1'+\nu_2'=\nu_1+\nu_2 &=& \nu_a+\nu_a' &=& \nu_t+\nu_t'\\
\nu_p &=& \frac{\nu_1'-\nu_2'}{2} &=& \frac{-\omega_a+\nu_a-\nu_a'}{2} &=& \frac{\omega_t-\nu_t+\nu_t'}{2}\\
\nu_p' &=& \frac{\nu_1-\nu_2}{2} &=& \frac{-\omega_a-\nu_a+\nu_a'}{2} &=& \frac{-\omega_t-\nu_t+\nu_t'}{2}
\end{array}
\\[2ex]
\begin{array}{rcl}
\nu_1' &=& \nu_t'+\frac{\omega_t}{2}\\
\nu_2' &=& \nu_t-\frac{\omega_t}{2}\\
\nu_1 &=& \nu_t'-\frac{\omega_t}{2}\\
\nu_2 &=& \nu_t+\frac{\omega_t}{2}
\end{array}
& \Rightarrow &
\begin{array}{rclclcl}
\omega_t &=& \nu_1'-\nu_1=\nu_2-\nu_2' &=& \nu_a-\nu_a' &=& \nu_p-\nu_p'\\
\nu_t &=& \frac{\nu_2'+\nu_2}{2} &=& \frac{\omega_a+\nu_a+\nu_a'}{2} &=& \frac{\omega_p-\nu_p-\nu_p'}{2}\\
\nu_t' &=& \frac{\nu_1'+\nu_1}{2} &=& \frac{-\omega_a+\nu_a+\nu_a'}{2} &=& \frac{\omega_p+\nu_p+\nu_p'}{2}
\end{array}
\end{array}
\tag{A.2}
$$

From these relations, the action of the symmetry transformations Eqs. (4.49) in the channel-dependent parametrizations can be readily derived:

$$
\begin{array}{llcccccc}
\mathcal{T}_1: & & & \nu_1 & \longleftrightarrow & \nu_2 & & \\
\\
 & \omega_a & = & \nu_2' - \nu_1 & \longleftrightarrow & \nu_2' - \nu_2 & = & -\omega_t \\
 & \nu_a & = & \frac{\nu_1'+\nu_2}{2} & \longleftrightarrow & \frac{\nu_1'+\nu_1}{2} & = & \nu_t' \\
 & \nu_a' & = & \frac{\nu_2'+\nu_1}{2} & \longleftrightarrow & \frac{\nu_2'+\nu_2}{2} & = & \nu_t \\
\\
 & \omega_p & = & \nu_1 + \nu_2 & \longleftrightarrow & \nu_2 + \nu_1 & = & \omega_p \\
 & \nu_p & = & \frac{\nu_1'-\nu_2'}{2} & \longleftrightarrow & \frac{\nu_1'-\nu_2'}{2} & = & \nu_p \\
 & \nu_p' & = & \frac{\nu_1-\nu_2}{2} & \longleftrightarrow & \frac{\nu_2-\nu_1}{2} & = & -\nu_p'
\end{array}
\tag{A.3a}
$$

$$
\begin{array}{llcccccc}
\mathcal{T}_2: & & & \nu_1' & \longleftrightarrow & \nu_2' & & \\
\\
 & \omega_a & = & \nu_2' - \nu_1 & \longleftrightarrow & \nu_1' - \nu_1 & = & \omega_t \\
 & \nu_a & = & \frac{\nu_1'+\nu_2}{2} & \longleftrightarrow & \frac{\nu_2'+\nu_2}{2} & = & \nu_t \\
 & \nu_a' & = & \frac{\nu_2'+\nu_1}{2} & \longleftrightarrow & \frac{\nu_1'+\nu_1}{2} & = & \nu_t' \\
\\
 & \omega_p & = & \nu_1 + \nu_2 & \longleftrightarrow & \nu_1 + \nu_2 & = & \omega_p \\
 & \nu_p & = & \frac{\nu_1'-\nu_2'}{2} & \longleftrightarrow & \frac{\nu_2'-\nu_1'}{2} & = & -\nu_p \\
 & \nu_p' & = & \frac{\nu_1-\nu_2}{2} & \longleftrightarrow & \frac{\nu_1-\nu_2}{2} & = & \nu_p'
\end{array}
\tag{A.3b}
$$

$$
\begin{array}{llcccccc}
\mathcal{T}_3: & & & \nu_1 & \longleftrightarrow & \nu_2 & & \\
 & & & \nu_1' & \longleftrightarrow & \nu_2' & & \\
\\
 & \omega_a & = & \nu_2' - \nu_1 & \longleftrightarrow & \nu_1' - \nu_2 & = & -\omega_a \\
 & \nu_a & = & \frac{\nu_1'+\nu_2}{2} & \longleftrightarrow & \frac{\nu_2'+\nu_1}{2} & = & \nu_a' \\
\\
 & \omega_p & = & \nu_1 + \nu_2 & \longleftrightarrow & \nu_2 + \nu_1 & = & \omega_p \\
 & \nu_p & = & \frac{\nu_1'-\nu_2'}{2} & \longleftrightarrow & \frac{\nu_2'-\nu_1'}{2} & = & -\nu_p \\
 & \nu_p' & = & \frac{\nu_1-\nu_2}{2} & \longleftrightarrow & \frac{\nu_2-\nu_1}{2} & = & -\nu_p' \\
\\
 & \omega_t & = & \nu_1' - \nu_1 & \longleftrightarrow & \nu_2' - \nu_2 & = & -\omega_t \\
 & \nu_t & = & \frac{\nu_2'+\nu_2}{2} & \longleftrightarrow & \frac{\nu_1'+\nu_1}{2} & = & \nu_t'
\end{array}
\tag{A.3c}
$$

$$\begin{array}{lccccccc}
\mathcal{T}_{\mathcal{C}}: & & & \nu_1' & \longleftrightarrow & \nu_1 & & \\
 & & & \nu_2' & \longleftrightarrow & \nu_2 & & \\
 & & & & & & & \\
 & \omega_a & = & \nu_2' - \nu_1 & \longleftrightarrow & \nu_2 - \nu_1' & = & \omega_a \\
 & \nu_a & = & \frac{\nu_1'+\nu_2}{2} & \longleftrightarrow & \frac{\nu_1+\nu_2'}{2} & = & \nu_a' \\
 & & & & & & & \\
 & \omega_p & = & \nu_1 + \nu_2 & \longleftrightarrow & \nu_1' + \nu_2' & = & \omega_p \\
 & \nu_p & = & \frac{\nu_1'-\nu_2'}{2} & \longleftrightarrow & \frac{\nu_1-\nu_2}{2} & = & \nu_p' \\
 & & & & & & & \\
 & \omega_t & = & \nu_1' - \nu_1 & \longleftrightarrow & \nu_1 - \nu_1' & = & -\omega_t \\
 & \nu_t & = & \frac{\nu_2'+\nu_2}{2} & \longleftrightarrow & \frac{\nu_2+\nu_2'}{2} & = & \nu_t \\
 & \nu_t' & = & \frac{\nu_1'+\nu_1}{2} & \longleftrightarrow & \frac{\nu_1+\nu_1'}{2} & = & \nu_t'
\end{array} \tag{A.3d}$$

These results are summarized in Table 4.1.

Appendix B

Multiloop flow equations in the single-boson exchange parametrization

Instead of the parquet channel decomposition Eq. (3.6),

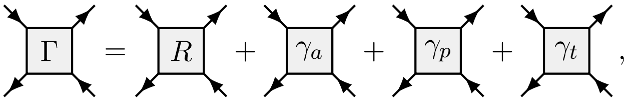

(B.1)

based on the two-particle reducibility of vertex diagrams, one can also decompose the vertex according to its reducibility w.r.t the bare interaction Γ_0, coined U reducibility. This results in the recently developed single-boson exchange (SBE) decomposition [KVC19, KV19], which allows for a physical interpretation of certain types of diagrams in terms of boson exchange processes. In studies of the two-dimensional Hubbard model, it has been shown that the SBE decomposition is a promising technique for computing the frequency and momentum dependences of the vertex [KLR20, KVC$^+$20, KKH21]. In a very recent one-loop fRG calculation of the vertex, it was found that some of its essential features are already captured by its U-reducible parts, which are much easier to compute numerically than the U-irreducible ones [BTH$^+$21]. SBE is particularly interesting in the context of DMF^{2}RG [TAB$^+$14, VTM19].

In the following, we first translate the SBE decomposition from the physical channels, in which it is formulated in the original papers, into the diagrammatic channels used throughout this thesis, and we relate its constituents to the asymptotic classes $\mathcal{K}_i^r$. We will see that the SBE and the conventional asymptotic decomposition Eq. (4.13) [WLT$^+$20] are in fact very closely related. We then derive multiloop flow equations in the SBE parametrization. A more comprehensive discussion of this analysis will be submitted for publication very soon [WGG$^+$21].

B.1 SBE decomposition in the diagrammatic channels

The SBE decomposition was originally defined in terms of the physical ch(arge), sp(in), and s(inglet pairing) channels [KVC19], which are superpositions of spin components of the diagrammatic channels a (=$\overline{\text{ph}}$ (particle-hole crossed)), p (=pp (particle-particle)), t (=ph (particle-hole)) [RVT12][1]:

$$\gamma^{\text{ch/sp}} = (\gamma_t)_{\uparrow\uparrow} \pm (\gamma_t)_{\uparrow\downarrow}\,, \tag{B.2a}$$

$$\gamma^{\text{s/t}} = (\gamma_p)_{\uparrow\downarrow} \mp (\gamma_p)_{\overline{\uparrow\downarrow}}\,. \tag{B.2b}$$

---

[1] The ch(arge) and sp(in) channels are called d(ensity) and m(agnetic) in [RVT12].

The t(riplet pairing) contribution in the particle-particle (p) channel does not show up in the SBE decomposition [KVC19]. On the level of the full vertex, we have [RVT12]

$$\Gamma^{\mathrm{ch/sp}} = \Gamma_{\uparrow\uparrow} \pm \Gamma_{\uparrow\downarrow} \tag{B.3}$$

(also see the discussion of susceptibilities in Sec. 4.1.2), where

$$\Gamma_{\uparrow\uparrow} = \Gamma_{\uparrow\downarrow} + \Gamma_{\overline{\uparrow\downarrow}} \tag{B.4}$$

for SU(2) symmetry (Eq. (4.34)), which we will assume throughout in the following.

The SBE decomposition of Γ in channel $\alpha = \mathrm{ch}, \mathrm{sp}$ is given by [KVC19][2]

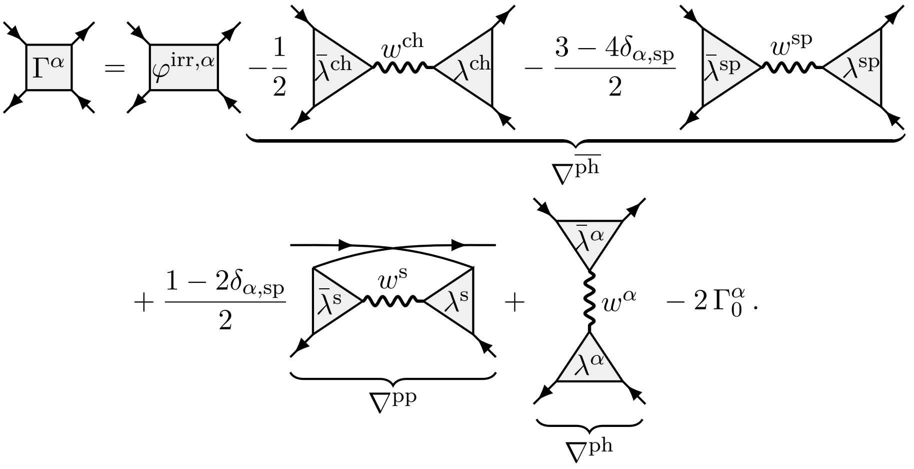
Γ^α
$=$
$\varphi^{\mathrm{irr},\alpha}$
$-\frac{1}{2}$
$\bar{\lambda}^{\mathrm{ch}}$
w^{ch}
λ^{ch}
$-\frac{3-4\delta_{\alpha,\mathrm{sp}}}{2}$
$\bar{\lambda}^{\mathrm{sp}}$
w^{sp}
λ^{sp}
$\nabla^{\overline{\mathrm{ph}}}$
$+\frac{1-2\delta_{\alpha,\mathrm{sp}}}{2}$
$\bar{\lambda}^{\mathrm{s}}$
w^{s}
λ^{s}
∇^{pp}
$+$
$\bar{\lambda}^\alpha$
w^α
λ^α
∇^{ph}
$-2\,\Gamma_0^\alpha\,.$

(B.5)

Here

$$w^\alpha(\omega_\alpha) = \Gamma_0^\alpha + \Gamma_0^\alpha\,\chi^\alpha(\omega_\alpha)\,\Gamma_0^\alpha \tag{B.6}$$

is called "screened interaction" in [KVC19], with

$$\Gamma_0^{\mathrm{ch/sp}} = (\Gamma_0)_{\uparrow\uparrow} \pm (\Gamma_0)_{\uparrow\downarrow} = \pm(\Gamma_0)_{\uparrow\downarrow}\,, \tag{B.7a}$$

$$\Gamma_0^{\mathrm{s}} = (\Gamma_0)_{\uparrow\downarrow} - (\Gamma_0)_{\overline{\uparrow\downarrow}} = 2(\Gamma_0)_{\uparrow\downarrow}\,, \tag{B.7b}$$

since $(\Gamma_0)_{\uparrow\uparrow} = 0$. $\bar{\lambda}^\alpha(\omega_\alpha, \nu_\alpha)$ and $\lambda^\alpha(\omega_\alpha, \nu'_\alpha)$ are three-point (fermion-boson) vertices obtained from the general three-point correlation functions by amputating the fermionic and bosonic legs. In [KVC19] it is also shown that for SU(2) and time-reversal symmetry one has $\bar{\lambda}^\alpha = \lambda^\alpha$. The diagrammatic contributions ∇^r contain those diagrams that are "U-reducible" in the corresponding channel r (U-r-reducible), i.e., diagrams that can be split into two parts w.r.t the channel r by removing a bare vertex Γ_0. All fully U-irreducible diagrams are contained in φ^{irr}. The term $-2\,\Gamma_0^\alpha$ is needed to avoid overcounting of the bare vertex, since ∇^r in each channel includes Γ_0: In lowest order, $\lambda^\alpha \approx \pm 1$ and $w^\alpha \approx \Gamma_0^\alpha$ [KVC19].

Now we express all constituents of the SBE decomposition in the diagrammatic channels a, p, t for the different-spin component $\Gamma_{\uparrow\downarrow}$, which is used throughout this thesis. This is convenient since the same-spin component can be obtained from the SU(2) relation (B.4), and thus only one component has to be computed explicitly. From Eq. (B.3) we obtain

---

[2] Note that in our convention of depicting diagrams, all diagrams are mirrored along the diagonal from the top left to bottom right (i.e., the bottom left and top right legs are exchanged) compared to the convention used in [KVC19]: The ph ($\overline{\mathrm{ph}}$) channel corresponds to the t (a) channel.

$\Gamma_{\uparrow\downarrow} = \frac{1}{2}(\Gamma^{\mathrm{ch}} - \Gamma^{\mathrm{sp}})$

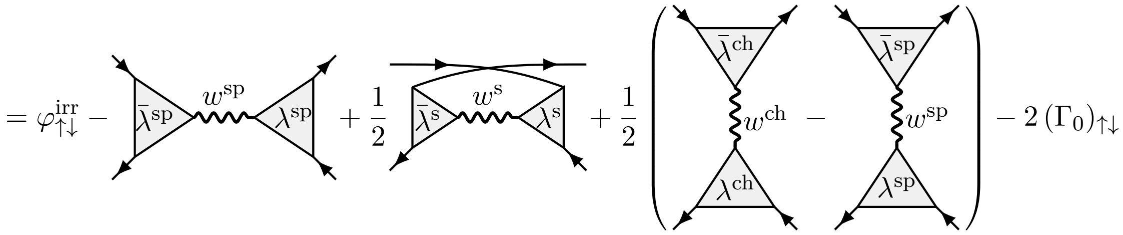
$= \varphi^{\mathrm{irr}}_{\uparrow\downarrow} -$
$\bar{\lambda}^{\mathrm{sp}}$
w^{sp}
λ^{sp}
$+ \frac{1}{2}$
$\bar{\lambda}^{\mathrm{s}}$
w^{s}
λ^{s}
$+ \frac{1}{2}$
$\bar{\lambda}^{\mathrm{ch}}$
w^{ch}
λ^{ch}
$-$
$\bar{\lambda}^{\mathrm{sp}}$
w^{sp}
λ^{sp}
$- 2\,(\Gamma_0)_{\uparrow\downarrow}$

(B.8)

with $\varphi^{\mathrm{irr}}_{\uparrow\downarrow} = \frac{1}{2}(\varphi^{\mathrm{irr,ch}} - \varphi^{\mathrm{irr,sp}})$. We can further decompose w^α and λ^α into different-spin and equal-spin components (see the definition of the particle-hole susceptibility in Eq. (4.18) and the definition of the three-point vertex e.g. in [vLKH$^+$18]),

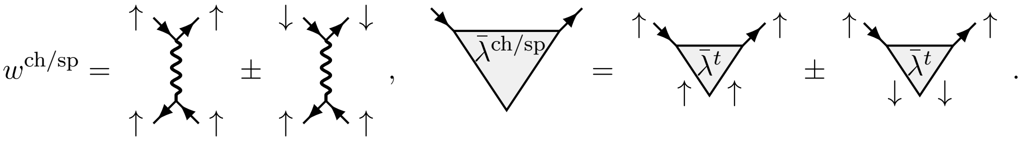
$w^{\mathrm{ch/sp}} =$
↑ ↑ ↑ ↑
$\pm$
↓ ↓ ↑ ↑
,
$\bar{\lambda}^{\mathrm{ch/sp}}$
$=$
↑ ↑ $\bar{\lambda}^{t}$ ↑ ↑
$\pm$
↑ ↑ $\bar{\lambda}^{t}$ ↓ ↓
.

(B.9)

Of course, due to SU(2) symmetry, all spins can be flipped, e.g.

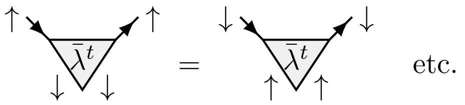
↑ ↑ $\bar{\lambda}^{t}$ ↓ ↓
$=$
↓ ↓ $\bar{\lambda}^{t}$ ↑ ↑
etc.

(B.10)

With this, we can decompose

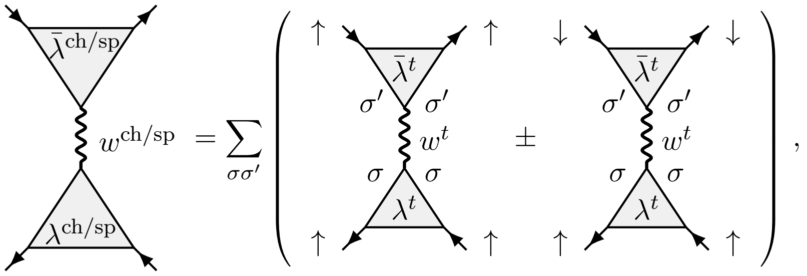
$\bar{\lambda}^{\mathrm{ch/sp}}$
$w^{\mathrm{ch/sp}}$
$\lambda^{\mathrm{ch/sp}}$
$= \sum_{\sigma\sigma'}$
↑ ↑ $\bar{\lambda}^{t}$ σ' σ' w^{t} σ σ λ^{t} ↑ ↑
$\pm$
↓ ↓ $\bar{\lambda}^{t}$ σ' σ' w^{t} σ σ λ^{t} ↑ ↑
,

(B.11)

and thus

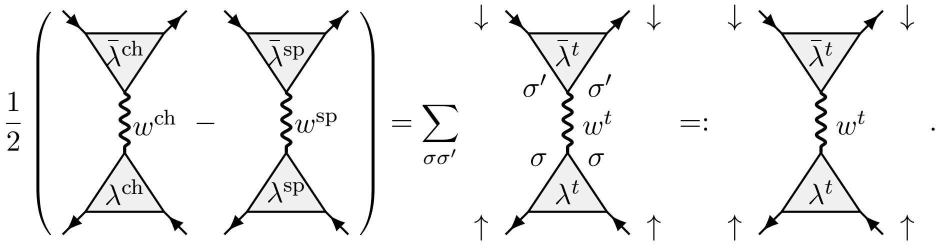
$\frac{1}{2}$
$\bar{\lambda}^{\mathrm{ch}}$
w^{ch}
λ^{ch}
$-$
$\bar{\lambda}^{\mathrm{sp}}$
w^{sp}
λ^{sp}
$= \sum_{\sigma\sigma'}$
↓ ↓ $\bar{\lambda}^{t}$ σ' σ' w^{t} σ σ λ^{t} ↑ ↑
$=:$
↓ ↓ $\bar{\lambda}^{t}$ w^{t} λ^{t} ↑ ↑
.

(B.12)

From crossing symmetry $\mathcal{S}_2$ (exchanging outgoing legs, cf. Eq. (2.41b)), we further have

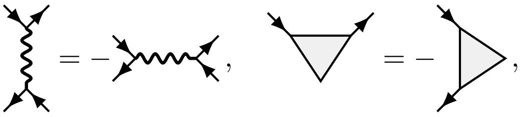

(B.13)

and thus

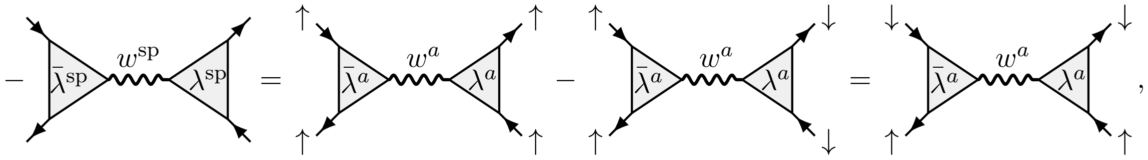
−
$\bar\lambda^{\mathrm{sp}}$
w^{sp}
λ^{sp}
=
$\bar\lambda^{a}$
w^{a}
λ^{a}
−
$\bar\lambda^{a}$
w^{a}
λ^{a}
=
$\bar\lambda^{a}$
w^{a}
λ^{a}
↑ ↑ ↑ ↑
↑ ↓ ↑ ↓
↓ ↓ ↑ ↑
,

(B.14)

where the last equality follows from SU(2) symmetry. Eventually, in the p channel we have with Eq. (B.2b)

$$w^{\mathrm{s}} = w^{p}_{\uparrow\downarrow} - w^{p}_{\overline{\uparrow\downarrow}} = 2\, w^{p}_{\uparrow\downarrow}\,, \tag{B.15}$$

where in the last equality $w^{p}_{\overline{\uparrow\downarrow}} = -w^{p}_{\uparrow\downarrow}$ directly follows from the crossing relation of the bare vertex Eq. (B.7b). Furthermore,

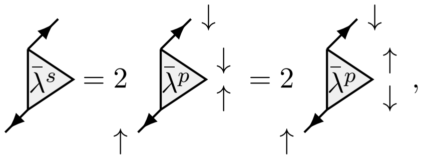
$\bar\lambda^{s}$
= 2
$\bar\lambda^{p}$
↓
↓
↑
↑
= 2
$\bar\lambda^{p}$
↓
↑
↓
↑
,

(B.16)

since the two legs on the right-hand side are both incoming and thus indistinguishable. Therefore, we have

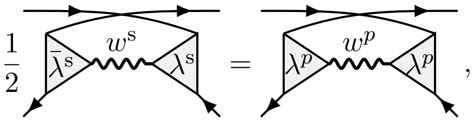
$\frac{1}{2}$
$\bar\lambda^{\mathrm{s}}$
w^{s}
λ^{s}
=
$\bar\lambda^{p}$
w^{p}
λ^{p}
,

(B.17)

with a factor of 4 included that accounts for the internal spin sum in the right diagram.

In summary, we obtain

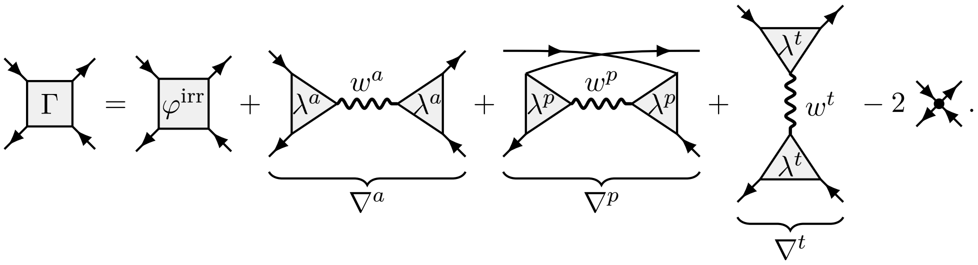
Γ
=
φ^{irr}
+
$\bar\lambda^{a}$
w^{a}
λ^{a}
+
$\bar\lambda^{p}$
w^{p}
λ^{p}
+
λ^{t}
w^{t}
$\bar\lambda^{t}$
− 2
.
∇^{a}
∇^{p}
∇^{t}

(B.18)

B.2 Relation between SBE and asymptotic decomposition

From Eq. (B.18), we can quite directly read off the relation between the SBE constituents w^r and λ^r and the asymptotic classes $\mathcal{K}_i^r$. A similar reasoning to the following considerations has been done in App. A of [BTH+21] within in the physical channel notation, and it transfers analogously to the diagrammatic channels.

With Eq. (B.6) and the definition of the susceptibilities in each channel in Sec. 4.1.2, $\Gamma_0^2\,\chi^r = \mathcal{K}_1^r$ (Eq. (4.19)), we see that

$$w^r(\omega_r) = \Gamma_0 + \mathcal{K}_1^r(\omega_r)\,. \tag{B.19}$$

Furthermore, as stated in Eq. (17) of [Kri19], one has

$$\lim_{\nu_r'\to\infty} \Gamma(\omega_r,\nu_r,\nu_r') = \bar{\lambda}^r(\omega_r,\nu_r)w^r(\omega_r) = \Gamma_0 + \mathcal{K}_1^r(\omega_r) + \mathcal{K}_2^r(\omega_r,\nu_r)\,, \tag{B.20a}$$

$$\lim_{\nu_r\to\infty} \Gamma(\omega_r,\nu_r,\nu_r') = w^r(\omega_r)\lambda^r(\omega_r,\nu_r') = \Gamma_0 + \mathcal{K}_1^r(\omega_r) + \mathcal{K}_{2'}^r(\omega_r,\nu_r')\,, \tag{B.20b}$$

where the last equality in each line stems from the definition of the asymptotic classes Eqs. (4.14), (4.15) in Sec. 4.1.2, and we have used that $\gamma_{r'\neq r}\to 0$ for $\nu_{r^{(\prime)}}\to\infty$ (Eq. (4.16)). With Eq. (B.19) we thus obtain

$$\bar{\lambda}^r(\omega_r,\nu_r) = 1 + \frac{\mathcal{K}_2^r(\omega_r,\nu_r)}{\Gamma_0 + \mathcal{K}_1^r(\omega_r)}\,, \qquad \lambda^r(\omega_r,\nu_r') = 1 + \frac{\mathcal{K}_{2'}^r(\omega_r,\nu_r')}{\Gamma_0 + \mathcal{K}_1^r(\omega_r)}\,. \tag{B.21}$$

The U-r-reducible part in each channel thus factorizes as

$$\begin{aligned}\nabla^r(\omega_r,\nu_r,\nu_r') &= \bar{\lambda}^r(\omega_r,\nu_r')\,w^r(\omega_r)\,\lambda^r(\omega_r,\nu_r')\\ &= \Gamma_0 + \mathcal{K}_1^r(\omega_r) + \mathcal{K}_2^r(\omega_r,\nu_r) + \mathcal{K}_{2'}^r(\omega_r,\nu_r') + \frac{\mathcal{K}_2^r(\omega_r,\nu_r)\,\mathcal{K}_{2'}^r(\omega_r,\nu_r')}{\Gamma_0 + \mathcal{K}_1^r(\omega_r)}\,.\end{aligned} \tag{B.22}$$

We see that ∇^r includes a part of $\mathcal{K}_3^r$ that can be fully expressed through functions that only depend on maximally two frequencies each. In the so-called SBE approximation $\varphi^{\mathrm{irr}}\approx 0$ [KVC19], which neglects all U-irreducible diagrams, one therefore includes some diagrams contributing to $\mathcal{K}_3$ (namely, the U-reducible ones), while the numerical complexity stays on the $\mathcal{K}_2$ level (only two-dimensional frequency dependencies have to be treated numerically). The validity and usefulness of this approximation is studied in [HLK21]. In the weak-coupling limit, the lowest-order $\mathcal{K}_3$ diagrams (4th order in the bare interaction) are already U-irreducible and thus not captured in the SBE approximation, which questions its validity in the perturbative regime. However, in the strong-coupling limit, [HLK21] provides quite convincing numerical proof of the usefulness of the SBE approximation, thus it might be interesting in the context of DMF^{2}RG. A similar conclusion can be drawn from the results of the first one-loop DMF^{2}RG study in the SBE decomposition [BTH$^+$21]. Furthermore, it seems that even if not neglected, φ^{irr} is usually more localized in frequency space than $\mathcal{K}_3$ and thus might be easier to treat numerically [BTH$^+$21].

B.3 Multiloop flow equations in the SBE decomposition

To derive multiloop flow equations for the SBE constituents, we first define

$$\Phi_r^{\mathrm{irr}} := \Gamma - \nabla^r \tag{B.23}$$

as the part of the full vertex that is U-r-irreducible, and

$$\varphi_r^{\mathrm{irr}} := \gamma_r - (\nabla^r - \Gamma_0)\,, \tag{B.24}$$

the U-r-irreducible part of the two-particle-reducible (Π-r-reducible) vertex. The latter definition is useful since φ_r^{irr} is contained in γ_r (nicely depicted as a Venn diagram in Fig. 6 of [KVC19]): ∇^r contains Γ_0, $\mathcal{K}_1^r$, $\mathcal{K}_2^r$, $\mathcal{K}_{2'}^r$ and those diagrams in $\mathcal{K}_3^r$ that are U-r-reducible, while φ_r^{irr} contains the part of $\mathcal{K}_3^r$ that is U-r-irreducible.

We now proceed analogously as in Section 4.1.4. We again only present the equations in the a channel explicitly; the contributions in the p and t channel follow by replacing a vertices and bubbles by p and t vertices and bubbles, respectively. First consider the one-loop flow equation (3.10a) for γ_a,

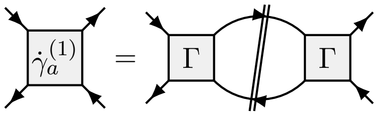
$\dot\gamma_a^{(1)}$
=
Γ
Γ
.

(B.25)

On the right-hand side, we insert the SBE decomposition w.r.t the a channel, $\Gamma = \nabla^a + \Phi_a^{\mathrm{irr}}$, to obtain

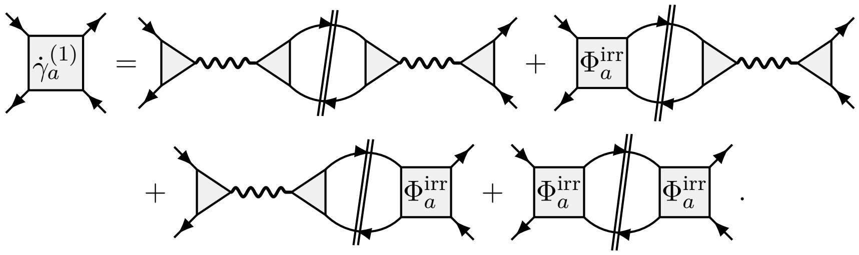
$\dot\gamma_a^{(1)}$
=
+
Φ_a^{irr}
+
Φ_a^{irr}
+
Φ_a^{irr}
Φ_a^{irr}
.

(B.26)

On the left-hand side of Eq. (B.25) we insert the decomposition $\gamma_a = \nabla^a - \Gamma_0 + \varphi_a^{\mathrm{irr}}$ (with $\dot\Gamma_0 = 0$),

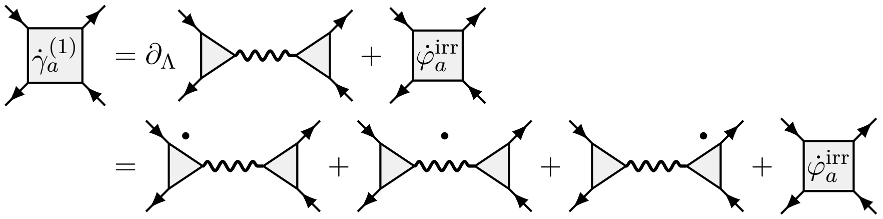
$\dot\gamma_a^{(1)}$
$= \partial_\Lambda$
+
$\dot\varphi_a^{\mathrm{irr}}$
=
+
+
+
$\dot\varphi_a^{\mathrm{irr}}$

(B.27)

By comparing the terms in Eqs. (B.26) and (B.27) in terms of their U-reducibility, we can readily deduce the one-loop contribution to the flow of the SBE constituents,

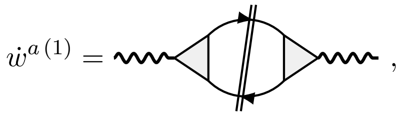

(B.28a)

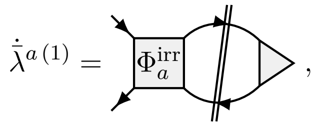
$\dot\lambda^{a\,(1)}$
=
Φ_a^{irr}
,

(B.28b)

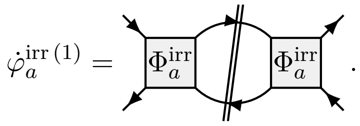
$\dot\varphi_a^{\mathrm{irr}\,(1)}$
=
Φ_a^{irr}
Φ_a^{irr}
.

(B.28c)

This agrees with the one-loop flow equations derived in [BTH+21]. The two-loop contribution (3.10a) follows in the same spirit. We obtain

$$\dot w^{a\,(2)} = 0\,, \tag{B.29a}$$

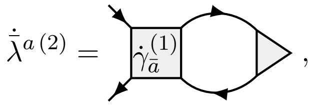
$\dot\lambda^{a\,(2)}$
=
$\dot\gamma_{\bar a}^{(1)}$
,

(B.29b)

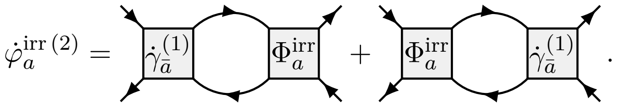
$\dot\varphi_a^{\mathrm{irr}\,(2)}$
=
$\dot\gamma_{\bar a}^{(1)}$
Φ_a^{irr}
+
Φ_a^{irr}
$\dot\gamma_{\bar a}^{(1)}$
.

(B.29c)

Here $\dot{\gamma}^{(1)}_{\bar{a}} = \dot{\gamma}^{(1)}_{p} + \dot{\gamma}^{(1)}_{t}$ can be constructed from $\dot{w}^{p,t\,(1)}$, $\dot{\lambda}^{p,t\,(1)}$ and $\dot{\varphi}^{\mathrm{irr}\,(1)}_{p,t}$ in analogy to Eq. (B.27) for $\dot{\gamma}^{(1)}_{a}$. Eventually, higher-loop contributions $\ell + 2 \geq 3$ read

$$\dot{w}^{a\,(\ell+2)} =$$

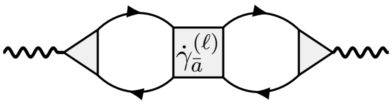
$\dot{\gamma}^{(\ell)}_{\bar{a}}$

, (B.30a)

$$\dot{\lambda}^{a\,(\ell+2)} =$$

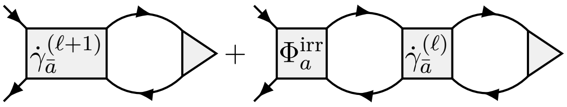
$\dot{\gamma}^{(\ell+1)}_{\bar{a}}$
+
Φ^{irr}_{a}
$\dot{\gamma}^{(\ell)}_{\bar{a}}$

, (B.30b)

$$\dot{\varphi}^{\mathrm{irr}\,(\ell+2)}_{a} =$$

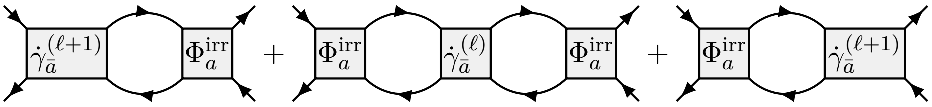
$\dot{\gamma}^{(\ell+1)}_{\bar{a}}$
Φ^{irr}_{a}
+
Φ^{irr}_{a}
$\dot{\gamma}^{(\ell)}_{\bar{a}}$
Φ^{irr}_{a}
+
Φ^{irr}_{a}
$\dot{\gamma}^{(\ell+1)}_{\bar{a}}$

. (B.30c)

List of Figures

5.1 (a) Sketch of the SIAM with two reservoirs, showing all relevant energy scales (for $B = 0$): Each reservoir $m = L, R$ is in thermal equilibrium at the temperature T_m and is filled up to its chemical potential μ_m. A difference in the chemical potentials leads to a voltage drop eV across the impurity. The single-particle energy levels ϵ and $\epsilon + U$ for the first and second electron on the impurity are broadened by the hybridization Δ (Eq. (5.5)) and can be shifted by the gate voltage eV_g. (b) For $V_g = 0$ and $\mu_L = -\mu_R$ (=0 in equilibrium), the impurity is singly occupied (i.e., half-filled), and fulfills particle-hole symmetry: Adding a second electron or removing the first electron from the impurity both costs an energy penalty $U/2$. 54

5.2 Spectral function of the SIAM for different interaction strengths U/Δ. Blue dotted lines indicate the scale of the hybridization $\pm\Delta$ which determines the width of the quasiparticle peak in the noninteracting case $U = 0$. Red dotted lines mark the scale of the Kondo temperature $\pm T_K$ and the position of the Hubbard bands $\pm U/2$ for $U/\Delta = 10$. Results are computed with NRG, using the routines of Seung-Sup Lee based on the `QSpace` tensor network library written by Andreas Weichselbaum [Wei12a, Wei12b, WvD07, LW16]. 59

5.3 (a) Static spin susceptibility $\chi^R_{\text{sp}}(0)$ as a function of U/Δ for different temperatures $T = 0$, $T/U = 0.01$, $T/U = 0.1$ (see legend of panel (b)). For $T = 0$, the inverse Kondo temperature (Eq. (5.15)) is directly related to $\chi^R_{\text{sp}}(0)$; both increase exponentially for large U/Δ. (b) Spectral function for strong interaction $U/\Delta = 10$ and different temperatures $T = 0$, $T/U = 0.01$, $T/U = 0.1$. Increasing the temperature smears out the Kondo resonance; it completely vanishes at the highest temperature $T/U = 0.1$. (c) The Kondo temperature decreases exponentially as a function of U/Δ for sufficiently large U/Δ. Dashed lines indicate the temperatures $T/U = 0.01$ and $T/U = 0.1$ studied in the following chapters. $T < T_K$ is required in order to see Kondo physics, thus in the range of U/Δ where $T > T_K$, signatures of the Kondo effect are not accessible. Numerical results (χ_{sp} and $\mathcal{A}$) are computed with NRG, using the routines of Seung-Sup Lee based on the `QSpace` tensor network library written by Andreas Weichselbaum [Wei12a, Wei12b, WvD07, LW16]. . 59

6.1 Non-linear frequency grid $\{\omega_j\}$ obtained via a transformation $f_\omega(\Omega)$ (Eq. (6.2)) from an auxiliary linear grid $\{\Omega_j\}$. The limits Ω_{min}, Ω_{max} of the latter are obtained from given values of ω_{min}, ω_{max} through the inverse transformation $f_\Omega(\omega)$ (Eq. (6.3)). 65

6.2 Illustration of the nonlinear frequency grid: Retarded and Keldysh component of the bare propagator G_0 (Eq. (5.13)), plotted over (a) the physical frequency grid $\{\omega_j\}$, and (b) the auxiliary grid $\{\Omega_j\}$. The transformation $f_\omega(\Omega)$ (Eq. (6.2)) is chosen in such a way that G_0 is smooth and has no sharp features on the auxiliary grid, such that on the physical grid the density of grid points is highest around the sharp features at $\omega = 0$. This minimizes interpolation errors: If the grid $\{\omega_j\}$ was chosen linearly with the same number of grid points, the resolution of the features at $\omega = 0$ would be much worse. . . 66

7.1 Real and imaginary part of the retarded component of $\mathcal{K}_1^a$ (left) and $\mathcal{K}_1^p$ (right) in second-order perturbation theory at $T = 0$ as a function of the bosonic transfer frequency, comparing numerical results computed at $U = 1$, $\Delta = 10$, to the exact analytical result. 78

7.2 Vertex diagrams in 1st (bare vertex Γ_0) and 2nd order (only $\mathcal{K}_1$ diagrams). $\mathcal{K}_{1\uparrow\downarrow}^t$ is zero, since the red lines can neither have spin ↑ nor ↓. Diagrams in the a and p channel cancel. The analytical values can be read off from Eqs. (7.3) and (7.4). 80

7.3 $\mathcal{K}_1$ diagrams in 3rd order. All three diagrams give the same result [Hew01]. . 80

7.4 $\mathcal{K}_2$ (top row) and $\mathcal{K}_{2'}$ (bottom row) diagrams in 3rd order. For diagrams not appearing here, the ↑↓ component is zero due to the spin structure (cf. $\mathcal{K}_1^t$ in 2nd order). All diagrams give the same result, the exact analytical value is $\mathcal{K}_{2^{(\prime)}}^r = -\frac{1}{2}(2-\frac{\pi^2}{4})(\frac{U}{\pi\Delta})^2$ [Hew01]. 80

7.5 $\mathcal{K}_1$ diagrams in 4th order. In the a and p channel, diagrams can be divided into ladder and non-ladder-type diagrams. In the t channel, the ↑↓ component of the ladder diagram is zero. The ladder (non-ladder) diagrams in the a and p channel cancel. The non-ladder diagrams in the t channel cancel each other. The exact result for the ladder diagrams is known, since these diagrams factor into a product of three 2nd-order diagrams. 81

7.6 $\mathcal{K}_2$ diagrams in 4th order obtained by inserting a 3rd-order $\mathcal{K}_1$ diagram. Diagrams in the a and p channel cancel (t diagrams are again zero due to the spin structure). 81

7.7 $\mathcal{K}_2$ diagrams in 4th order obtained by inserting a 3rd-order $\mathcal{K}_2^r$ diagram in channel r. Diagrams in the a and p channel cancel, and the two t diagrams cancel separately. 82

7.8 $\mathcal{K}_2$ diagrams in 4th order obtained by inserting a 3rd-order $\mathcal{K}_2^{r'}$ diagram in channel r, with $r' \neq r$. Diagrams in the a and p channel cancel. In the t channel, the upper two diagrams (containing $\mathcal{K}_1^p$ in 2nd order) and the lower two diagrams (containing $\mathcal{K}_1^t$ in 2nd order) cancel. (Inserting $\mathcal{K}_{2^{(\prime)}}^p$ in 3rd order in the t channel gives zero due to the spin structure.) 82

7.9 $\mathcal{K}_3$ diagrams in 4th order. In the t channel, one can insert $\mathcal{K}_1^a$ and $\mathcal{K}_1^p$ on both sides of the bubble. The p-p insertion is zero due to the spin structure. Diagrams in the a and p channel cancel, and the three t diagrams cancel separately. Notice that the a-a diagram in $\mathcal{K}_3^t$ does *not* come with a prefactor 1/2 despite having an internal spin sum, since it does not contain any p bubble. Therefore, it corresponds to two spin-resolved diagrams for the two possible spins of the green lines, in contrast to diagrams with a (green) p bubble, where the prefactor 1/2 effectively accounts for the spin sum. 83

7.10 Real part of the retarded self-energy (left) and the retarded spin susceptibility (right) at $U/\Delta = 1$ (upper panels) and $U/\Delta = 3$ (lower panels), computed directly from an fRG flow and via the Kramers-Kronig relation from the imaginary part of the fRG result, and the difference of the two methods. Results are obtained from a 3-loop flow at $T/U = 0.01$, for the data set N_3 (cf. Table 6.1). While at weak coupling the agreement is almost perfect, at intermediate coupling the Kramers-Kronig relation is violated in particular in the tails of the self-energy. 85

7.11 Integrated relative violation (Eq. (7.10)) of the Kramers-Kronig relation (Eq. (7.9)) for retarded self-energy (upper panels) and spin susceptibility (lower panels), as a function of U/Δ. Results are shown for $T/U = 0.01$ (left) and $T/U = 0.1$ (right), obtained from 1-, 2-, and 3-loop flows with different numerical parameters (cf. Table 6.1). The error continuously accumulates during the flow, but can be reduced by increasing the density of the frequency grid ($N_1 \to N_2$). 86

7.12 Left and right side of the FDT for self-energy (left, Eq. (7.11)) and spin susceptibility (right, Eq. (7.12)), and their difference, at $U/\Delta = 1$ (upper panels) and $U/\Delta = 3$ (lower panels). Results are obtained from a 3-loop flow at $T/U = 0.01$. While at weak coupling the agreement is almost perfect, at intermediate coupling the FDTs are slightly violated at small frequencies $\nu, \omega \lesssim \Delta$ both for Σ and χ_{sp}. 87

7.13 Integrated relative violation (Eq. (7.13)) of the equilibrium FDTs for retarded self-energy (Eq. (7.11), upper panels) and spin susceptibility (Eq. (7.12), lower panels), as a function of U/Δ. Results are shown for $T/U = 0.01$ (left) and $T/U = 0.1$ (right), obtained from 1-, 2-, and 3-loop flows with different numerical parameters (cf. Table 6.1). The error can again be suppressed by increasing the density of the frequency grid. A decrease of the self-energy error with increasing U/Δ points to a suboptimal choice of frequency grid parameters for the initial condition, which is partially compensated in the early iterations of the flow. 88

7.14 Spectral function at $\nu = 0$ (yielding the Friedel sum rule for $T = 0$ or $U = 0$) as a function of U/Δ. Results are shown for $T/U = 0.01$ (left) and $T/U = 0.1$ (right), obtained from 1-, 2-, and 3-loop flows with different numerical parameters (cf. Table 6.1). We compare the results to NRG and PT2 (Eq. (7.16)). The results seem to be fully converged in the numerical parameters, since all lines lie almost perfectly on top of each other. Note that 3-loop at $T/U = 0.01$ starts to produce unsensible results at $U/\Delta \sim 4$, shortly before the divergence of the flow. 89

7.15 Error in the normalization of the spectral function as a function of U/Δ. Results are shown for $T/U = 0.01$ (left) and $T/U = 0.1$ (right), obtained from 1-, 2-, and 3-loop flows with different numerical parameters (cf. Table 6.1). . 90

8.1 Spectral function for different interaction strengths $U/\Delta = 1$ (top row), $U/\Delta = 3$ (center row), $U/\Delta = 4$ (bottom row) and different temperatures $T/U = 0.01$ (left column) and $T/U = 0.1$ (right column), computed with a full 1-, 2-, and 3-loop flow, comparing to NRG and the $\mathcal{K}_1$SF approximation. All flows accurately reproduce NRG results. 92

8.2 Imaginary part of the retarded self-energy for different interaction strengths $U/\Delta = 1$ (top row), $U/\Delta = 3$ (center row), $U/\Delta = 4$ (bottom row) and different temperatures $T/U = 0.01$ (left column) and $T/U = 0.1$ (right column), computed with a full 1-, 2-, and 3-loop flow, comparing to NRG and the $\mathcal{K}_1$SF approximation. For each value of U and T, "diff" is the difference between the fRG flows and NRG, $\mathrm{Im}\,(\Sigma^R_{\mathrm{fRG}} - \Sigma^R_{\mathrm{NRG}})/\Delta$. At lower temperature $T/U = 0.01$, $\mathcal{K}_1$SF best reproduces NRG results. At $T/U = 0.1$, the results show indications of an oscillatory behavior with increasing ℓ, expected to approach the PA for $\ell \to \infty$. 93
8.3 Real part of the retarded spin susceptibility for different interaction strengths $U/\Delta = 1$ (top row), $U/\Delta = 3$ (center row), $U/\Delta = 4$ (bottom row) and different temperatures $T/U = 0.01$ (left column) and $T/U = 0.1$ (right column), computed with a full 1-, 2-, and 3-loop flow, comparing to NRG and the $\mathcal{K}_1$SF approximation. Increasing the loop order improves results, while $\mathcal{K}_1$SF strongly deviates from NRG already for $U/\Delta = 1$. 94
8.4 Real part of the retarded spin susceptibility for temperature $T/U = 0.01$ and different interaction strengths $U/\Delta = 1$ (left) and $U/\Delta = 3$ (right), computed in the $\mathcal{K}_1$SF approximation and with a full 1-, 2-, and 3-loop flow. "Flowing" results (solid lines) are directly obtained from $\mathcal{K}_1^a$ via Eq. (4.21), while "post-processed" results (dashed lines) are computed from the full vertex via Eq. (4.17). Both results are consistent for ℓ-loop flows with full vertex frequency dependence, while $\mathcal{K}_1$SF shows significant deviations. 95
8.5 Static retarded spin susceptibility χ^R_{sp} (left column), quasiparticle weight Z (center column), and difference between left and right-hand side of the Ward identity (8.5) (right column), as functions of the interaction strength U/Δ. Results are shown at $T/U = 0.01$ (upper row) and $T/U = 0.1$ (lower row), computed with a full 1-, 2-, and 3-loop flow, comparing to NRG and the $\mathcal{K}_1$SF approximation. 96
8.6 Korringa-Shiba ratio (8.7) at $T/U = 0.01$ as a function of the interaction strength U/Δ. Results are computed in the $\mathcal{K}_1$SF approximation and with a full 1-, 2-, and 3-loop flow. The Korringa-Shiba relation is better fulfilled for increasing loop order, while being strongly violated for $\mathcal{K}_1$SF already at small U/Δ. 97
8.7 Testing the fulfillment of the sum rule (8.8) for the Keldysh component of the equal-spin particle hole susceptibility $\chi^K_{\sigma\sigma}$ as a function of the interaction strength U/Δ. Results are computed in the $\mathcal{K}_1$SF approximation and with a full 1-, 2-, and 3-loop flow. The black dashed line indicates the exact value of 1/4 that the integral over $\chi^K_{\sigma\sigma}$ should give. We see significant improvement with increasing loop order. 99
8.8 Left side (dotted) and right side (solid) of the Ward identity (8.12) and their difference (dashed) as a function of the fermionic frequency ν, for different interaction strengths $U/\Delta = 1$ (top row), $U/\Delta = 3$ (center row), $U/\Delta = 4$ (bottom row) and different temperatures $T/U = 0.01$ (left column) and $T/U = 0.1$ (right column), computed with a full 1-, 2-, and 3-loop flow, comparing to the $\mathcal{K}_1$SF approximation. Including the full vertex frequency dependence significantly improves the fulfillment of the Ward identity, and the deviation further decreases with increasing loop order ℓ. 101

9.1 Real and imaginary parts of various Keldysh components of the equal-spin component of the asymptotic classes $\mathcal{K}_i/U = \sum_r \mathcal{K}_i^r/U$ at weak and intermediate interaction strength $U/\Delta = 0.5$ (top) and $U/\Delta = 2.5$ (bottom). Results are obtained from a 3-loop fRG flow. For $U/\Delta = 0.5$, we additionally compare to bare second-order perturbation theory (PT2, top row). 106

9.2 Same as Fig. 9.1 at $U/\Delta = 2.5$, divided into the diagrammatic channels a, p, t. 107

9.3 Fully retarded Keldysh component $(\Gamma^{12|22}(\nu,\nu') - \Gamma_0)/U$ of the full vertex (Eq. (9.1)). We show real and imaginary part of the equal-spin and different-spin components $\Gamma_{\uparrow\uparrow}$ (left) and $\Gamma_{\uparrow\downarrow}$ (right) at weak and intermediate interaction strength $U/\Delta = 0.5$ (top) and $U/\Delta = 2.5$ (bottom). We compare 3-loop fRG results to NRG results. The latter are computed by Seung-Sup Lee with the recent extension of NRG to four-point functions [KLvD21, LKvD21]. Both methods agree very well for $U/\Delta = 0.5$ and still show good qualitative agreement at $U/\Delta = 2.5$. 108

10.1 (a) RG flow of the coupling vector $\mathbf{c} = (J, K, I)$ (projected into the J-K plane), obtained by solving the weak-coupling RG equations (2) (Eqs. (8–10) of Ref. [9]) for various initial values, $\mathbf{c}_0 = (J_0, K_0, I_0)$. Arrows depict the gradient vector, $-[\mathrm{d}/(\mathrm{d}\ln D)](J, K)$ at equal steps of $\ln D$. (b),(c) Weak-coupling RG flow of $\mathbf{c}(D)$ for (b) $\mathbf{c}_0 = (0.01, 0.3, 0)$ [red arrows in (a)] and (c) $(0, 0.3, 0.01)$ [blue arrows in (a)]. (d) Qualitative depiction of the conjectured RG flow in the full J-K-I space, for all couplings non-negative. Fat, faint dashed lines show the solutions $\mathbf{c}(D)$ of the weak-coupling equations (2), initialized at $K_0 \ll K^*_{\mathrm{NFL}}$ with $(J_0, I_0) = (0, 0)$ (black), $(>0, 0)$ (yellow) or $(0, >0)$ (blue), and plotted only in the weak-coupling regime [beyond the latter, Eqs. (2) loose validity]. Solid lines, drawn by hand, qualitatively show the flow expected beyond the weak-coupling regime, including trajectories initialized at $K_0 \gg K^*_{\mathrm{NFL}}$, with $(J_0, I_0) = (0, 0)$ (green), $(> 0, 0)$ (orange) or $(0, > 0)$ (purple). The black squares, cross and circle depict fixed points. 112

Bibliography

[Aff90] Ian Affleck, *A current algebra approach to the Kondo effect*, Nucl. Phys. B **336** (1990), 517 – 532. See pages: 2 and 5

[Agu20] Santiago Aguirre Lamus, *Multiloop functional renormalization group in the Keldysh formalism — a study of the single-impurity Anderson model*, Master's thesis, Ludwig-Maximilians-Universität München, 2020. See pages: 28, 29, 40, 41, 42, 43, 47, 55, 57, 61, 62, and 171

[AK15] Camille Aron and Gabriel Kotliar, *Analytic theory of Hund's metals: A renormalization group perspective*, Phys. Rev. B **91** (2015), 041110. See page: 5

[AL91a] Ian Affleck and Andreas W. W. Ludwig, *Critical theory of overscreened Kondo fixed points*, Nucl. Phys. B **360** (1991), 641–696. See pages: 2 and 5

[AL91b] Ian Affleck and Andreas W. W. Ludwig, *The Kondo effect, conformal field theory and fusion rules*, Nucl. Phys. B **352** (1991), 849–862. See pages: 2 and 5

[AL93] Ian Affleck and Andreas W. W. Ludwig, *Exact conformal-field-theory results on the multichannel Kondo effect: Single-fermion Green's function, self-energy, and resistivity*, Phys. Rev. B **48** (1993), 7297–7321. See pages: 2 and 5

[And61] P. W. Anderson, *Localized Magnetic States in Metals*, Phys. Rev. **124** (1961), 41–53. See pages: 3 and 53

[And72] P. W. Anderson, *More Is Different*, Science **177** (1972), 393–396. See page: 1

[AT13] S. Akhanjee and A. M. Tsvelik, *Analytically tractable model of bad metals*, Phys. Rev. B **87** (2013), 195137. See page: 5

[BCP08] Ralf Bulla, Theo A. Costi, and Thomas Pruschke, *Numerical renormalization group method for quantum impurity systems*, Rev. Mod. Phys. **80** (2008), 395–450. See pages: 2 and 5

[BHP98] R. Bulla, A. C. Hewson, and Th. Pruschke, *Numerical renormalization group calculations for the self-energy of the impurity Anderson model*, J. Phys.: Condens. Matter **10** (1998), 8365–8380. See page: 3

[BHS$^+$13] Florian Bauer, Jan Heyder, Enrico Schubert, David Borowsky, Daniela Taubert, Benedikt Bruognolo, Dieter Schuh, Werner Wegscheider, Jan von Delft, and Stefan Ludwig, *Microscopic origin of the '0.7-anomaly' in quantum point contacts*, Nature **501** (2013), 73–78. See page: 3

[Bic04] N. E. Bickers, *Self-consistent many-body theory for condensed matter systems*, in: Sénéchal D., Tremblay A.-M., Bourbonnais C. (eds), Theoretical Methods for Strongly Correlated Electrons, CRM Series in Mathematical Physics, Springer, New York, 2004. See page: 23

[BPH97] R. Bulla, Th. Pruschke, and A. C. Hewson, *Anderson impurity in pseudo-gap Fermi systems*, J. Phys.: Condens. Matter **9** (1997), 10463–10474. See page: 3

[BTH$^+$21] Pietro M. Bonetti, Alessandro Toschi, Cornelia Hille, Sabine Andergassen, and Demetrio Vilardi, *Single boson exchange representation of the functional renormalization group for strongly interacting many-electron systems*, arXiv:2105.11749 [cond-mat.str-el] (2021). See pages: 32, 175, 178, 179, and 180

[CGKH$^+$21] Patrick Chalupa-Gantner, Fabian B. Kugler, Cornelia Hille, Jan von Delft, Sabine Andergassen, and Alessandro Toschi, *Fulfillment of sum rules and Ward identities in the multiloop functional renormalization group solution of the Anderson impurity model*, arXiv:2110.07455 [cond-mat.str-el] (2021). See pages: 3 and 98

[CGS$^+$18] P. Chalupa, P. Gunacker, T. Schäfer, K. Held, and A. Toschi, *Divergences of the irreducible vertex functions in correlated metallic systems: Insights from the Anderson impurity model*, Phys. Rev. B **97** (2018), 245136. See page: 26

[Dag94] Elbio Dagotto, *Correlated electrons in high-temperature superconductors*, Rev. Mod. Phys. **66** (1994), 763–840. See pages: 3 and 4

[dMMG11] Luca de' Medici, Jernej Mravlje, and Antoine Georges, *Janus-Faced Influence of Hund's Rule Coupling in Strongly Correlated Materials*, Phys. Rev. Lett. **107** (2011), 256401. See page: 4

[DSH$^+$19] Xiaoyu Deng, Katharina M. Stadler, Kristjan Haule, Andreas Weichselbaum, Jan von Delft, and Gabriel Kotliar, *Signatures of Mottness and Hundness in archetypal correlated metals*, Nat. Commun. **10** (2019), 2721. See pages: 4 and 5

[FMW$^+$18] Michele Filippone, Cătălin Paşcu Moca, Andreas Weichselbaum, Jan von Delft, and Christophe Mora, *At which magnetic field, exactly, does the Kondo resonance begin to split? A Fermi liquid description of the low-energy properties of the Anderson model*, Phys. Rev. B **98** (2018), 075404. See page: 58

[GdMM13] Antoine Georges, Luca de' Medici, and Jernej Mravlje, *Strong Correlations from Hund's Coupling*, Annu. Rev. Condens. Matter Phys. **4** (2013), 137–178. See pages: 4 and 5

[Ge20] Anxiang Ge, *Analytic continuation of correlators from the Matsubara to the Keldysh formalism*, Master's thesis, Ludwig-Maximilians-Universität München, 2020. See page: 18

[Ge21] Anxiang Ge, private communication, 2021. See pages: 49, 51, and 65

[GGGK$^+$98] D. Goldhaber-Gordon, J. Göres, M. A. Kastner, Hadas Shtrikman, D. Mahalu, and U. Meirav, *From the Kondo Regime to the Mixed-Valence Regime in a Single-Electron Transistor*, Phys. Rev. Lett. **81** (1998), 5225–5228. See page: 3

[GGSM$^+$98] D. Goldhaber-Gordon, Hadas Shtrikman, D. Mahalu, David Abusch-Magder, U. Meirav, and M. A. Kastner, *Kondo effect in a single-electron transistor*, Nature **391** (1998), 156–159. See page: 3

[Gie21] Marcel Gievers, private communication, 2021. See page: 4

[GJSS91] J. E. Gubernatis, Mark Jarrell, R. N. Silver, and D. S. Sivia, *Quantum Monte Carlo simulations and maximum entropy: Dynamics from imaginary-time data*, Phys. Rev. B **44** (1991), 6011–6029. See pages: 1 and 10

[GKKR96] Antoine Georges, Gabriel Kotliar, Werner Krauth, and Marcelo J. Rozenberg, *Dynamical mean-field theory of strongly correlated fermion systems and the limit of infinite dimensions*, Rev. Mod. Phys. **68** (1996), 13–125. See pages: 1, 3, and 4

[GML$^+$11] Emanuel Gull, Andrew J. Millis, Alexander I. Lichtenstein, Alexey N. Rubtsov, Matthias Troyer, and Philipp Werner, *Continuous-time Monte Carlo methods for quantum impurity models*, Rev. Mod. Phys. **83** (2011), 349–404. See page: 1

[GPM07] R. Gezzi, Th. Pruschke, and V. Meden, *Functional renormalization group for nonequilibrium quantum many-body problems*, Phys. Rev. B **75** (2007), 045324. See page: 3

[GRS$^+$17] O. Gunnarsson, G. Rohringer, T. Schäfer, G. Sangiovanni, and A. Toschi, *Breakdown of Traditional Many-Body Theories for Correlated Electrons*, Phys. Rev. Lett. **119** (2017), 056402. See page: 26

[Hal21] Johannes Halbinger, private communication, 2021. See pages: 28 and 37

[HBA$^+$13] F. Hardy, A. E. Böhmer, D. Aoki, P. Burger, T. Wolf, P. Schweiss, R. Heid, P. Adelmann, Y. X. Yao, G. Kotliar, J. Schmalian, and C. Meingast, *Evidence of Strong Correlations and Coherence-Incoherence Crossover in the Iron Pnictide Superconductor KFe_2As_2*, Phys. Rev. Lett. **111** (2013), 027002. See page: 4

[HBSvD17] Jan Heyder, Florian Bauer, Dennis Schimmel, and Jan von Delft, *Derivation of Oguri's linear conductance formula for interacting fermions within the Keldysh formalism*, Phys. Rev. B **96** (2017), 125141. See pages: 11, 14, 99, and 100

[Hew93] A. C. Hewson, *The Kondo Problem to Heavy Fermions*, Cambridge University Press, 1993. See pages: 3, 57, and 58

[Hew01] A. C. Hewson, *Renormalized perturbation calculations for the single-impurity Anderson model*, J. Phys.: Condens. Matter **13** (2001), 10011–10029. See pages: 79, 80, and 184

[HLK21] Viktor Harkov, Alexander I. Lichtenstein, and Friedrich Krien, *Parametrizations of local vertex corrections from weak to strong coupling: Importance of the Hedin three-leg vertex*, Phys. Rev. B **104** (2021), 125141. See page: 179

[HMPS04] R. Hedden, V. Meden, Th. Pruschke, and K. Schönhammer, *A functional renormalization group approach to zero-dimensional interacting systems*, J. Phys.: Condens. Matter **16** (2004), 5279–5296. See page: 3

[HS09] C. Husemann and M. Salmhofer, *Efficient parametrization of the vertex function, Ω scheme, and the t, t' Hubbard model at van Hove filling*, Phys. Rev. B **79** (2009), 195125. See pages: 24 and 63

[Hub63] J. Hubbard, *Electron correlations in narrow energy bands*, Proc. R. Soc. Lond. A **276** (1963), 238–257. See page: 4

[Jak09] Severin G. Jakobs, *Functional renormalization group studies of quantum transport through mesoscopic systems*, Ph.D. thesis, RWTH Aachen, 2009. See pages: 9, 11, 12, 14, 15, 17, 18, 21, 24, 53, 54, 55, 56, 91, and 93

[JMS07] Severin G. Jakobs, Volker Meden, and Herbert Schoeller, *Nonequilibrium Functional Renormalization Group for Interacting Quantum Systems*, Phys. Rev. Lett. **99** (2007), 150603. See pages: 2, 32, and 91

[JPS10a] Severin G. Jakobs, Mikhail Pletyukhov, and Herbert Schoeller, *Nonequilibrium functional renormalization group with frequency-dependent vertex function: A study of the single-impurity Anderson model*, Phys. Rev. B **81** (2010), 195109. See pages: 2, 3, 32, 55, and 91

[JPS10b] Severin G. Jakobs, Mikhail Pletyukhov, and Herbert Schoeller, *Properties of multi-particle Green's and vertex functions within Keldysh formalism*, J. Phys. A: Math. Theor. **43** (2010), 103001. See pages: 17 and 18

[Kam11] Alex Kamenev, *Field Theory of Non-Equilibrium Systems*, Cambridge University Press, 2011. See pages: 9, 11, 14, and 15

[Kat04] A. A. Katanin, *Fulfillment of Ward identities in the functional renormalization group approach*, Phys. Rev. B **70** (2004), 115109. See pages: 26 and 91

[KB62] Leo P. Kadanoff and Gordon A. Baym, *Quantum statistical mechanics*, Benjamin, New York, 1962. See page: 9

[KBS10] Peter Kopietz, Lorenz Bartosch, and Florian Schütz, *Introduction to the Functional Renormalization Group*, Springer Berlin Heidelberg, 2010. See pages: 1, 2, and 21

[Kel64] Leonid V. Keldysh, *Diagram technique for nonequilibrium processes*, Zh. Eksp. Teor. Fiz. **47** (1964), 1515–1527, [Sov. Phys. JETP **20** (1965), 1018]. See page: 9

[KHP$^+$08] C. Karrasch, R. Hedden, R. Peters, Th. Pruschke, K. Schönhammer, and V. Meden, *A finite-frequency functional renormalization group approach to the single impurity Anderson model*, J. Phys.: Condens. Matter **20** (2008), 345205. See page: 3

[KKH21] Friedrich Krien, Anna Kauch, and Karsten Held, *Tiling with triangles: parquet and GWγ methods unified*, Phys. Rev. Research **3** (2021), 013149. See page: 175

[Klö19] Christian Klöckner, *Functional renormalization group approach to correlated quantum systems far from equilibrium*, Ph.D. thesis, Freie Universität Berlin, 2019. See pages: 9 and 17

[KLR20] Friedrich Krien, Alexander I. Lichtenstein, and Georg Rohringer, *Fluctuation diagnostic of the nodal/antinodal dichotomy in the Hubbard model at weak coupling: A parquet dual fermion approach*, Phys. Rev. B **102** (2020), 235133. See page: 175

[KLvD21] Fabian B. Kugler, Seung-Sup B. Lee, and Jan von Delft, *Multipoint Correlation Functions: Spectral Representation and Numerical Evaluation*, Phys. Rev. X **11** (2021), 041006. See pages: 4, 104, 108, and 187

[KMI$^+$20] Dominik Kiese, Tobias Müller, Yasir Iqbal, Ronny Thomale, and Simon Trebst, *Multiloop functional renormalization group approach to quantum spin systems*, arXiv:2011.01269 [cond-mat.str-el] (2020). See page: 62

[KmWW80a] H. R. Krishna-murthy, J. W. Wilkins, and K. G. Wilson, *Renormalization-group approach to the Anderson model of dilute magnetic alloys. I. Static properties for the symmetric case*, Phys. Rev. B **21** (1980), 1003–1043. See page: 3

[KmWW80b] H. R. Krishna-murthy, J. W. Wilkins, and K. G. Wilson, *Renormalization-group approach to the Anderson model of dilute magnetic alloys. II. Static properties for the asymmetric case*, Phys. Rev. B **21** (1980), 1044–1083. See page: 3

[Kon64] J. Kondo, *Resistance Minimum in Dilute Magnetic Alloys*, Prog. Theor. Phys. **32** (1964), 37–49. See page: 1

[Kri19] Friedrich Krien, *Efficient evaluation of the polarization function in dynamical mean-field theory*, Phys. Rev. B **99** (2019), 235106. See page: 179

[Kub57] Ryogo Kubo, *Statistical-Mechanical Theory of Irreversible Processes. I. General Theory and Simple Applications to Magnetic and Conduction Problems*, J. Phys. Soc. Jpn. **12** (1957), 570–586. See page: 18

[Kub66] Ryogo Kubo, *The fluctuation-dissipation theorem*, Rep. Prog. Phys. **29** (1966), 255–284. See page: 18

[Kug18] Fabian B. Kugler, *Counting Feynman diagrams via many-body relations*, Phys. Rev. E **98** (2018), 023303. See page: 11

[Kug19] Fabian B. Kugler, *Renormalization group approaches to strongly correlated electron systems*, Ph.D. thesis, Ludwig-Maximilians-Universität München, 2019. See pages: 2, 21, 23, 25, and 28

[KV19] Friedrich Krien and Angelo Valli, *Parquetlike equations for the Hedin three-leg vertex*, Phys. Rev. B **100** (2019), 245147. See pages: 37 and 175

[KVC19] Friedrich Krien, Angelo Valli, and Massimo Capone, *Single-boson exchange decomposition of the vertex function*, Phys. Rev. B **100** (2019), 155149. See pages: 6, 37, 175, 176, and 179

[KVC$^+$20] Friedrich Krien, Angelo Valli, Patrick Chalupa, Massimo Capone, Alexander I. Lichtenstein, and Alessandro Toschi, *Boson-exchange parquet solver for dual fermions*, Phys. Rev. B **102** (2020), 195131. See page: 175

[KvD18a] Fabian B. Kugler and Jan von Delft, *Derivation of exact flow equations from the self-consistent parquet relations*, New J. Phys. **20** (2018), 123029. See pages: 2, 21, 23, 25, and 26

[KvD18b] Fabian B. Kugler and Jan von Delft, *Multiloop functional renormalization group for general models*, Phys. Rev. B **97** (2018), 035162. See pages: 2, 21, 23, 25, 61, and 91

[KvD18c] Fabian B. Kugler and Jan von Delft, *Multiloop Functional Renormalization Group That Sums Up All Parquet Diagrams*, Phys. Rev. Lett. **120** (2018), 057403. See pages: 2, 21, 23, 26, and 93

[KWHH08] Yoichi Kamihara, Takumi Watanabe, Masahiro Hirano, and Hideo Hosono, *Iron-Based Layered Superconductor La[$O_{1-x}F_x$]FeAs (x = 0.05-0.12) with T_c = 26 K*, J. Am. Chem. Soc. **130** (2008), 3296–3297. See page: 4

[LA94] Andreas W. W. Ludwig and Ian Affleck, *Exact conformal-field-theory results on the multi-channel Kondo effect: Asymptotic three-dimensional space- and time-dependent multi-point and many-particle Green's functions*, Nucl. Phys. B **428** (1994), 545–611. See pages: 2 and 5

[LCMK18] Tsung-Han Lee, Andrey Chubukov, Hu Miao, and Gabriel Kotliar, *Pairing Mechanism in Hund's Metal Superconductors and the Universality of the Superconducting Gap to Critical Temperature Ratio*, Phys. Rev. Lett. **121** (2018), 187003. See page: 4

[LdlPR$^+$17] J. Lichtenstein, D. Sánchez de la Peña, D. Rohe, E. Di Napoli, C. Honerkamp, and S.A. Maier, *High-performance functional Renormalization Group calculations for interacting fermions*, Comput. Phys. Commun. **213** (2017), 100–110. See page: 63

[LKvD21] Seung-Sup B. Lee, Fabian B. Kugler, and Jan von Delft, *Computing Local Multipoint Correlators Using the Numerical Renormalization Group*, Phys. Rev. X **11** (2021), 041007. See pages: 4, 104, 108, and 187

[LW16] Seung-Sup B. Lee and Andreas Weichselbaum, *Adaptive broadening to improve spectral resolution in the numerical renormalization group*, Phys. Rev. B **94** (2016), 235127. See pages: 59, 75, and 183

[MAM$^+$11] Jernej Mravlje, Markus Aichhorn, Takashi Miyake, Kristjan Haule, Gabriel Kotliar, and Antoine Georges, *Coherence-Incoherence Crossover and the Mass-Renormalization Puzzles in* Sr_2RuO_4, Phys. Rev. Lett. **106** (2011), 096401. See page: 4

[MS59] Paul C. Martin and Julian Schwinger, *Theory of Many-Particle Systems. I*, Phys. Rev. **115** (1959), 1342–1373. See page: 18

[MSH$^+$12] Walter Metzner, Manfred Salmhofer, Carsten Honerkamp, Volker Meden, and Kurt Schönhammer, *Functional renormalization group approach to correlated fermion systems*, Rev. Mod. Phys. **84** (2012), 299–352. See pages: 1, 2, and 21

[MV89] Walter Metzner and Dieter Vollhardt, *Correlated Lattice Fermions in $d = \infty$ Dimensions*, Phys. Rev. Lett. **62** (1989), 324–327. See pages: 1, 3, and 4

[NO88] John W. Negele and Henri Orland, *Quantum Many-Particle Systems*, Addison-Wesley Pub. Co., 1988. See pages: 11, 12, and 13

[PTVF07] William H. Press, Saul A. Teukolsky, William T. Vetterling, and Brian P. Flannery, *Numerical Recipes - The Art of Scientific Computing (3rd Edition)*, Cambridge University Press, 2007, Webnote 4 (Adapt). See page: 67

[Reu11] Johannes Reuther, *Frustrated quantum Heisenberg antiferromagnets: Functional renormalization-group approach in auxiliary-fermion representation*, Ph.D. thesis, Karlsruher Institut für Technologie, 2011. See page: 24

[RHT+18] G. Rohringer, H. Hafermann, A. Toschi, A. A. Katanin, A. E. Antipov, M. I. Katsnelson, A. I. Lichtenstein, A. N. Rubtsov, and K. Held, *Diagrammatic routes to nonlocal correlations beyond dynamical mean field theory*, Rev. Mod. Phys. **90** (2018), 025003. See pages: 1 and 3

[Rit21a] Marc K. Ritter, private communication, 2021. See page: 62

[Rit21b] Nepomuk Ritz, private communication, 2021. See page: 4

[RMJ16] J. F. Rentrop, V. Meden, and S. G. Jakobs, *Renormalization group flow of the Luttinger-Ward functional: Conserving approximations and application to the Anderson impurity model*, Phys. Rev. B **93** (2016), 195160. See page: 3

[Roh13] Georg Rohringer, *New routes towards a theoretical treatment of nonlocal electronic correlations*, Ph.D. thesis, TU Wien, 2013. See pages: 24, 33, and 38

[RVT12] G. Rohringer, A. Valli, and A. Toschi, *Local electronic correlation at the two-particle level*, Phys. Rev. B **86** (2012), 125114. See pages: 24, 28, 33, 175, and 176

[SBvD17] Dennis H. Schimmel, Benedikt Bruognolo, and Jan von Delft, *Spin Fluctuations in the 0.7 Anomaly in Quantum Point Contacts*, Phys. Rev. Lett. **119** (2017), 196401. See pages: 2, 3, 32, and 91

[Sch61] Julian Schwinger, *Brownian Motion of a Quantum Oscillator*, J. Math. Phys. **2** (1961), 407–432. See page: 9

[Sch17] Dennis H. Schimmel, *Transport through inhomogeneous interacting low-dimensional systems*, Ph.D. thesis, Ludwig-Maximilians-Universität München, 2017. See pages: 9, 11, 14, 21, and 24

[SCW+16] T. Schäfer, S. Ciuchi, M. Wallerberger, P. Thunström, O. Gunnarsson, G. Sangiovanni, G. Rohringer, and A. Toschi, *Nonperturbative landscape of the Mott-Hubbard transition: Multiple divergence lines around the critical endpoint*, Phys. Rev. B **94** (2016), 235108. See page: 26

[SEPD12] Richard Schmidt, Tilman Enss, Ville Pietilä, and Eugene Demler, *Fermi polarons in two dimensions*, Phys. Rev. A **85** (2012), 021602. See page: 4

[Shi75] H. Shiba, *The Korringa Relation for the Impurity Nuclear Spin-Lattice Relaxation in Dilute Kondo Alloys*, Prog. Theor. Phys. **54** (1975), 967–981. See page: 97

[SKWvD19] K. M. Stadler, G. Kotliar, A. Weichselbaum, and J. von Delft, *Hundness versus Mottness in a three-band Hubbard–Hund model: On the origin of strong correlations in Hund metals*, Ann. Phys. **405** (2019), 365–409. See pages: 4 and 5

[SRG+13] T. Schäfer, G. Rohringer, O. Gunnarsson, S. Ciuchi, G. Sangiovanni, and A. Toschi, *Divergent Precursors of the Mott-Hubbard Transition at the Two-Particle Level*, Phys. Rev. Lett. **110** (2013), 246405. See page: 26

[SS86] H.-B. Schüttler and D. J. Scalapino, *Monte Carlo studies of the dynamical response of quantum many-body systems*, Phys. Rev. B **34** (1986), 4744–4756. See pages: 1 and 10

[Ste11] G. R. Stewart, *Superconductivity in iron compounds*, Rev. Mod. Phys. **83** (2011), 1589–1652. See page: 4

[SW66] J. R. Schrieffer and P. A. Wolff, *Relation between the Anderson and Kondo Hamiltonians*, Phys. Rev. **149** (1966), 491–492. See pages: 3, 5, and 57

[SYvD$^+$15] K. M. Stadler, Z. P. Yin, J. von Delft, G. Kotliar, and A. Weichselbaum, *Dynamical Mean-Field Theory Plus Numerical Renormalization-Group Study of Spin-Orbital Separation in a Three-Band Hund Metal*, Phys. Rev. Lett. **115** (2015), 136401. See page: 5

[TAB$^+$14] C. Taranto, S. Andergassen, J. Bauer, K. Held, A. Katanin, W. Metzner, G. Rohringer, and A. Toschi, *From Infinite to Two Dimensions through the Functional Renormalization Group*, Phys. Rev. Lett. **112** (2014), 196402. See pages: 4, 26, 28, 37, and 175

[TGCR18] P. Thunström, O. Gunnarsson, Sergio Ciuchi, and G. Rohringer, *Analytical investigation of singularities in two-particle irreducible vertex functions of the Hubbard atom*, Phys. Rev. B **98** (2018), 235107. See page: 26

[THK$^+$19] Agnese Tagliavini, Cornelia Hille, Fabian B. Kugler, Sabine Andergassen, Alessandro Toschi, and Carsten Honerkamp, *Multiloop functional renormalization group for the two-dimensional Hubbard model: Loop convergence of the response functions*, SciPost Phys. **6** (2019), 9. See pages: 2, 26, and 93

[TRK$^+$20] Julian Thoenniss, Marc K. Ritter, Fabian B. Kugler, Jan von Delft, and Matthias Punk, *Multiloop pseudofermion functional renormalization for quantum spin systems: Application to the spin-1/2 kagome Heisenberg model*, arXiv:2011.01268 [cond-mat.str-el] (2020). See page: 69

[TW83] A. M. Tsvelick and P. B. Wiegmann, *Exact results in the theory of magnetic alloys*, Adv. Phys. **32** (1983), 453–713. See page: 3

[TZR$^+$19] A. Tamai, M. Zingl, E. Rozbicki, E. Cappelli, S. Riccò, A. de la Torre, S. McKeown Walker, F. Y. Bruno, P. D. C. King, W. Meevasana, M. Shi, M. Radović, N. C. Plumb, A. S. Gibbs, A. P. Mackenzie, C. Berthod, H. U. R. Strand, M. Kim, A. Georges, and F. Baumberger, *High-Resolution Photoemission on Sr_2RuO_4 Reveals Correlation-Enhanced Effective Spin-Orbit Coupling and Dominantly Local Self-Energies*, Phys. Rev. X **9** (2019), 021048. See page: 4

[vLKH$^+$18] Erik G. C. P. van Loon, Friedrich Krien, Hartmut Hafermann, Alexander I. Lichtenstein, and Mikhail I. Katsnelson, *Fermion-boson vertex within dynamical mean-field theory*, Phys. Rev. B **98** (2018), 205148. See page: 177

[VT97] Y. M. Vilk and A.-M. S. Tremblay, *Non-Perturbative Many-Body Approach to the Hubbard Model and Single-Particle Pseudogap*, J. Phys. I **7** (1997), 1309–1368. See pages: 33 and 98

[VTM19] Demetrio Vilardi, Ciro Taranto, and Walter Metzner, *Antiferromagnetic and d-wave pairing correlations in the strongly interacting two-dimensional Hubbard model from the functional renormalization group*, Phys. Rev. B **99** (2019), 104501. See pages: 4, 26, 28, 37, and 175

[Wei12a] Andreas Weichselbaum, *Non-abelian symmetries in tensor networks: A quantum symmetry space approach*, Ann. Phys. **327** (2012), 2972–3047. See pages: 5, 59, 75, and 183

[Wei12b] Andreas Weichselbaum, *Tensor networks and the numerical renormalization group*, Phys. Rev. B **86** (2012), 245124. See pages: 5, 59, 75, and 183

[Wei20] Lukas Weidinger, *Finite-ranged interactions and multiband effects in quantum point contacts – A functional renormalization group study*, Ph.D. thesis, Ludwig-Maximilians-Universität München, 2020. See page: 17

[Wet93] Christof Wetterich, *Exact evolution equation for the effective potential*, Phys. Lett. B **301** (1993), 90–94. See pages: 21 and 22

[WGG$^+$21] Elias Walter, Marcel Gievers, Anxiang Ge, Fabian Kugler, and Jan von Delft, *Multiloop flow equations for single-boson exchange fRG*, (in preparation), 2021. See page: 175

[WGTM08] Philipp Werner, Emanuel Gull, Matthias Troyer, and Andrew J. Millis, *Spin Freezing Transition and Non-Fermi-Liquid Self-Energy in a Three-Orbital Model*, Phys. Rev. Lett. **101** (2008), 166405. See page: 4

[WH02] Enke Wang and Ulrich Heinz, *Generalized fluctuation-dissipation theorem for nonlinear response functions*, Phys. Rev. D **66** (2002), 025008. See pages: 18, 19, 50, and 51

[WH20] Philipp Werner and Shintaro Hoshino, *Nickelate superconductors: Multiorbital nature and spin freezing*, Phys. Rev. B **101** (2020), 041104. See page: 4

[Wic50] G. C. Wick, *The Evaluation of the Collision Matrix*, Phys. Rev. **80** (1950), 268–272. See page: 12

[Wil75] Kenneth G. Wilson, *The renormalization group: Critical phenomena and the Kondo problem*, Rev. Mod. Phys. **47** (1975), 773–840. See pages: 2 and 5

[WLT$^+$20] Nils Wentzell, Gang Li, Agnese Tagliavini, Ciro Taranto, Georg Rohringer, Karsten Held, Alessandro Toschi, and Sabine Andergassen, *High-frequency asymptotics of the vertex function: Diagrammatic parametrization and algorithmic implementation*, Phys. Rev. B **102** (2020), 085106. See pages: 28, 31, and 175

[WSSvD18] Lukas Weidinger, Christian Schmauder, Dennis H. Schimmel, and Jan von Delft, *Functional renormalization group treatment of the 0.7 analog in quantum point contacts*, Phys. Rev. B **98** (2018), 115112. See page: 3

[WvD07] Andreas Weichselbaum and Jan von Delft, *Sum-Rule Conserving Spectral Functions from the Numerical Renormalization Group*, Phys. Rev. Lett. **99** (2007), 076402. See pages: 59, 75, and 183

[WvD19] Lukas Weidinger and Jan von Delft, *Keldysh Functional Renormalization Group Treatment of Finite-Ranged Interactions in Quantum Point Contacts*, arXiv:1912.02700 [cond-mat.str-el] (2019). See pages: 2, 3, 32, 91, and 100

[Yam75a] K. Yamada, *Perturbation Expansion for the Anderson Hamiltonian. II*, Prog. Theor. Phys. **53** (1975), 970–986. See pages: 3, 75, 88, and 96

[Yam75b] K. Yamada, *Perturbation Expansion for the Anderson Hamiltonian. IV*, Prog. Theor. Phys. **54** (1975), 316–324. See pages: 3 and 75

[YHK11a] Z. P. Yin, K. Haule, and G. Kotliar, *Kinetic frustration and the nature of the magnetic and paramagnetic states in iron pnictides and iron chalcogenides*, Nat. Mater. **10** (2011), 932–935. See page: 4

[YHK11b] Z. P. Yin, K. Haule, and G. Kotliar, *Magnetism and charge dynamics in iron pnictides*, Nat. Phys. **7** (2011), 294–297. See page: 4

[YHK12] Z. P. Yin, K. Haule, and G. Kotliar, *Fractional power-law behavior and its origin in iron-chalcogenide and ruthenate superconductors: Insights from first-principles calculations*, Phys. Rev. B **86** (2012), 195141. See pages: 4 and 5

[YLY$^+$13] M. Yi, D. H. Lu, R. Yu, S. C. Riggs, J.-H. Chu, B. Lv, Z. K. Liu, M. Lu, Y.-T. Cui, M. Hashimoto, S.-K. Mo, Z. Hussain, C. W. Chu, I. R. Fisher, Q. Si, and Z.-X. Shen, *Observation of Temperature-Induced Crossover to an Orbital-Selective Mott Phase in $A_xFe_{2-y}Se_2$ (A=K, Rb) Superconductors*, Phys. Rev. Lett. **110** (2013), 067003. See page: 4

[YY70] Kei Yosida and Kosaku Yamada, *Perturbation Expansion for the Anderson Hamiltonian*, Prog. Theor. Phys. **46** (1970), 244–255. See pages: 3, 75, and 77

[YY75] K. Yosida and K. Yamada, *Perturbation Expansion for the Anderson Hamiltonian. III*, Prog. Theor. Phys. **53** (1975), 1286–1301. See pages: 3 and 75

[ZH83] V. Zlatić and B. Horvatić, *Series expansion for the symmetric Anderson Hamiltonian*, Phys. Rev. B **28** (1983), 6904–6906. See page: 3

[ZR88] F. C. Zhang and T. M. Rice, *Effective Hamiltonian for the superconducting Cu oxides*, Phys. Rev. B **37** (1988), 3759–3761. See pages: 3 and 4